



K S Krishna Swamy

PHYSICS OF COMETS

Third Edition

PHYSICS OF COMETS

Third Edition

WORLD SCIENTIFIC SERIES IN ASTRONOMY AND ASTROPHYSICS

Editor: Jayant V. Narlikar

Inter-University Centre for Astronomy and Astrophysics, Pune, India

Published:

- Volume 1: Lectures on Cosmology and Action at a Distance Electrodynamics
F. Hoyle and J. V. Narlikar
- Volume 2: Physics of Comets (2nd Ed.)
K. S. Krishna Swamy
- Volume 3: Catastrophes and Comets*
V. Clube and B. Napier
- Volume 4: From Black Clouds to Black Holes (2nd Ed.)
J. V. Narlikar
- Volume 5: Solar and Interplanetary Disturbances
S. K. Alurkar
- Volume 6: Fundamentals of Solar Astronomy
A. Bhatnagar and W. Livingston
- Volume 7: Dust in the Universe: Similarities and Differences
K. S. Krishna Swamy
- Volume 8: An Invitation to Astrophysics
T. Padmanabhan
- Volume 9: Stardust from Meteorites: An Introduction to Presolar Grains
M. Lugardo
- Volume 10: Rotation and Accretion Powered Pulsars
P. Ghosh
- Volume 11: Find a Hotter Place!: A History of Nuclear Astrophysics
L. M. Celnikier
- Volume 12: Physics of Comets (3rd Edition)
K. S. Krishna Swamy

*Publication cancelled.

World Scientific Series in Astronomy and Astrophysics – Vol. 12



PHYSICS OF COMETS

Third Edition

K S Krishna Swamy

retired from the Tata Institute of Fundamental Research, Mumbai, India



World Scientific

NEW JERSEY • LONDON • SINGAPORE • BEIJING • SHANGHAI • HONG KONG • TAIPEI • CHENNAI

Published by

World Scientific Publishing Co. Pte. Ltd.

5 Toh Tuck Link, Singapore 596224

USA office: 27 Warren Street, Suite 401-402, Hackensack, NJ 07601

UK office: 57 Shelton Street, Covent Garden, London WC2H 9HE

British Library Cataloguing-in-Publication Data

A catalogue record for this book is available from the British Library.

PHYSICS OF COMETS (3rd Edition)

World Scientific Series in Astronomy and Astrophysics — Vol. 12

Copyright © 2010 by World Scientific Publishing Co. Pte. Ltd.

All rights reserved. This book, or parts thereof, may not be reproduced in any form or by any means, electronic or mechanical, including photocopying, recording or any information storage and retrieval system now known or to be invented, without written permission from the Publisher.

For photocopying of material in this volume, please pay a copying fee through the Copyright Clearance Center, Inc., 222 Rosewood Drive, Danvers, MA 01923, USA. In this case permission to photocopy is not required from the publisher.

ISBN-13 978-981-4291-11-8

ISBN-10 981-4291-11-0

Printed in Singapore.

Foreword

Only in recent years has the true nature of comets become evident. With this knowledge has come the realization that comets are almost certainly debris left over from the building of the outermost planets. This material must be typical of the gas and dust in the interstellar cloud from which the Sun and planetary system evolved. Thus, comets appear to offer us an opportunity to study primitive matter involved in the origin of the solar system, material that has been stored in deep freeze for 4.6×10^9 years. At the same time, the comets provide a link with interstellar solids, of which they are probably largely composed. The physical and chemical study of comets has now replaced classical celestial mechanics as the major focus of observational and theoretical research. Familiar areas of astronomical spectroscopy are approached from a somewhat unusual point of view in cometary studies, while comets provide an entirely new laboratory for an increased understanding of magneto-hydrodynamics. On the other extreme, the physics of amorphous ices and other solids can be applied to probe the internal structure, origin and activity of the comet nuclei. In summation, the study of comets has now become a manifold discipline with fascinating potential, particularly as the space age provides new observational input over the entire electromagnetic spectrum, coupled with the expectation of direct *in situ* studies and even the eventual return of samples from cometary nuclei. The marked progress in this direction is represented by the new results described in this book's revised (second) edition. The several missions to Halley's comet have filled in many lacunae of comet knowledge.

Fred L. Whipple

This page intentionally left blank

Preface

We are in an exciting era of cometary science. This has come about due to space mission to comets, launch of several satellites and ground based studies. The first major space adventure was in 1986 when six spacecraft passed through Comet Halley as close as 500 km from the nucleus. More recently, the far more adventures venture of the Deep Impact Mission to Comet Tempel 1 and Stardust Mission to Comet Wild 2 made it possible for the first time to look at the material in the deeper layers of the cometary nuclei and to study in the laboratory the collected cometary dust. All these studies have given rise to exciting and unexpected results which have raised some fundamental issues about comets and in turn on the solar system itself. For example, the detection of X-rays from comets was a real challenge in its understanding. The observed diversity in chemical composition among comets has direct bearing on the formation conditions in the solar nebula. The mineralogy of dust in IDPs, comets, meteorites, asteroids and circumstellar shell of stars are quite similar showing generic relationship between them.

In view of these exciting developments it is an appropriate time to revise and update the second edition of the book “Physics of Comets” published in 1997. Therefore extensive revision has been carried out in most of the chapters. Emphasis has been to include all the new results with the hope that the flavour of excitement may be conveyed to the reader. The general arrangement, purpose and level of the updated and revised edition of the book remains the same as that of second edition.

I am especially grateful to my colleagues, H.M. Antia who helped me in various ways and especially in the preparation of figures and S. Ramadurai for a thorough reading of the manuscript. I would also like to express my gratitude to my family and parents for their support and encouragement.

I would like to thank all the publishers and authors who have given permission for the reproduction of figures and tables. The help of Mr. Vivek Vengurlekar in the preparation of the manuscript is highly appreciated. My interaction with several astronomers have been very helpful and especially, the cometary experts like, M.F.A'Hearn, P.D. Feldman, W.F. Huebner, M.J. Mumma, C.R.O'Dell and J. Watanabe.

K S Krishna Swamy

204, Sigma Tower
Plot 32, Gorai Road
Borivali West
Mumbai 400 091, India

Contents

Foreword	v
Preface	vii
1. General Introduction	1
1.1. Historical Perspective	1
1.2. Discovery	4
1.3. Appearance	5
1.4. Statistics	6
1.5. Importance	9
1.6. Brightness	10
1.7. Main Characteristics	13
1.8. Spacecraft Encounters with Comets	19
1.9. An Overall View	23
Problems	30
References	30
2. Dynamics	33
2.1. Orbital Elements	33
2.2. Orbit in Space	35
2.2.1. Relevant equations	35
2.2.2. Orbital elements from position and velocity . .	40
2.2.3. Orbital elements from observations	41
Problems	45
References	46

3. Physical Aspects	47
3.1. Black Body Radiation	47
3.2. Perfect Gas Law	49
3.3. Dissociative Equilibrium	49
3.4. Doppler Shift	50
3.5. Spectroscopy	51
3.5.1. Atomic spectroscopy	51
3.5.2. Molecular spectroscopy	54
3.5.3. Chemical subgroups	57
3.6. Isotopic Effect	58
3.7. Franck-Condon Factors	59
3.8. Intensity of Emitted Lines	61
3.9. Boltzmann Distribution	64
3.10. Λ -Doubling	64
3.11. Photochemistry of Water	65
3.12. Silicate	67
3.13. Annealing	68
3.14. Carbon	69
3.15. Solar Radiation	70
3.16. Solar Wind	72
Problems	73
References	74
4. Spectra	75
4.1. Main Characteristics	76
4.2. Forbidden Transitions	90
4.3. Line-to-Continuum Ratio	92
Problems	93
References	93
5. Spectra of Coma	95
5.1. Fluorescence Process	95
5.1.1. Rotational structure	98
5.1.2. Vibrational structure	101
5.1.3. Comparison with observations	102
5.1.4. Case of C ₂ molecule	108
5.1.5. Prompt emission lines of OH	114
5.1.6. Molecules other than diatomic	118

5.1.7.	OH radio lines	118
5.1.8.	Oxygen lines	121
5.1.9.	Forbidden transitions	121
5.1.10.	Molecular band polarization	123
5.2.	Excitation Temperature	125
5.2.1.	Rotational temperature	125
5.2.2.	Vibrational temperature	128
5.3.	Abundances of Heavy Elements	128
5.4.	Isotopic Abundances	130
5.5.	Summary	137
Problems		137
References		138
6.	Gas Production Rates in Coma	141
6.1.	Theoretical Models	142
6.1.1.	From the total luminosity	142
6.1.2.	From surface brightness distribution	144
6.1.3.	From number densities	149
6.1.4.	Semi-empirical photometric theory	151
6.2.	Results	152
6.2.1.	OH and H	152
6.2.2.	H ₂ O, H ₂	158
6.2.3.	CN, C ₂ , C ₃ , NH	162
6.2.4.	CH, NH ₂	166
6.2.5.	CO, CO ₂	167
6.2.6.	CS, S ₂	169
6.2.7.	Ions	169
6.2.8.	Complex molecules	171
6.2.9.	O, C, N, S	176
6.3.	Analysis of Hydrogen Observations	183
6.3.1.	Analysis of Lyman α measurements	183
6.3.2.	Analysis of H α observations	189
6.4.	Related Studies	191
6.4.1.	Gas-phase chemistry in the coma	191
6.4.2.	In situ mass spectrometer for ions	194
6.4.3.	Temperature and velocity of the coma gas . .	196
6.5.	Parent Molecules	202
6.6.	Chemical Diversity	206
6.7.	Summary	207

Problems	207
References	208
7. Dust Tails	213
7.1. Dynamics	213
7.2. Anti-tail	220
7.3. Dust Trails	222
7.4. Sodium Gas Tails	222
7.5. Dust features	223
Problems	225
References	226
8. Light Scattering Theory	227
8.1. Mie Scattering Theory	228
8.1.1. Efficiency factors	228
8.1.2. Albedo	230
8.1.3. Scattered intensity	231
8.1.4. Polarization	232
8.2. Approximate Expressions	233
8.3. Computation of Cross Sections	233
8.4. Results	234
8.5. Particles of Other Types	238
8.6. Optical Constants	243
Problems	246
References	247
9. The Nature of Dust Particles	249
9.1. Visible Continuum	249
9.1.1. Albedo	255
9.1.2. Phase function	256
9.1.3. Dust production rate from continuum	257
9.1.4. Dust production from $A(\theta)f\rho$	259
9.2. Polarization	261
9.2.1. Linear polarization	261
9.2.2. Circular polarization	266
9.3. Grain Sizes	268
9.4. Infrared Measurements	269
9.4.1. Dust production from infrared observations . .	272

9.4.2.	Anti-tail	276
9.5.	Spectral Feature	278
9.5.1.	Silicate signature	279
9.5.2.	Mineralogy of dust particles	281
9.5.3.	The C-H stretch feature	288
9.5.4.	Ice signature	289
9.6.	Properties Derived from Direct Measurements	290
9.7.	Radiation Pressure Effects	294
9.8.	Summary	296
Problems		298
References		299
10.	Ion Tails	303
10.1.	Evidence for the Solar Wind	303
10.2.	Dynamical Aberration	304
10.3.	Theoretical Considerations	308
10.3.1.	Comparison with observations	314
10.4.	Instabilities and Waves	318
10.5.	Acceleration of Cometary Ions	321
10.6.	Large Scale Structures	323
10.6.1.	Tail rays or streamers	324
10.6.2.	Knots or condensations	325
10.6.3.	Oscillatory structure	325
10.6.4.	“Swan-like” feature	326
10.6.5.	Bend in the tail	326
10.6.6.	Disconnection events	328
10.7.	X-rays	330
10.8.	Summary	335
Problems		335
References		336
11.	Nucleus	339
11.1.	Morphology	339
11.2.	Theory of Vapourization	340
11.3.	Outbursts	348
11.4.	Albedo and Radius	350
11.5.	Mass, Density and Surface Gravity	353
11.6.	Rotation	355

11.7.	Nucleus Composition	359
11.8.	Mass Loss	360
11.9.	Structure	361
11.10.	Non-gravitational Forces	365
11.11.	Ortho to Para Ratio of Molecules	370
11.12.	Binary Systems	375
11.13.	Summary	376
	Problems	377
	References	377
12.	Origin	381
12.1.	Evidence for the Oort Cloud	381
12.2.	Evolution and Properties of Oort Cloud	384
12.2.1.	Short period comets	389
12.3.	Origin of the Oort Cloud	391
12.4.	Taxonomy	396
12.5.	Summary	398
	Problems	398
	References	399
13.	Relation to Other Solar System Studies	401
13.1.	Asteroids	401
13.2.	Meteorites	406
13.3.	Meteor Streams	411
13.4.	Particles Collected at High Altitudes	416
13.5.	Primordial Material	419
13.6.	Chemical Evolution	420
13.7.	Terrestrial Water	423
13.8.	Impact of Outside Bodies	424
13.9.	Overview	426
	Problems	431
	References	432
14.	Problems and Prospects	435
14.1.	Epilogue	435
14.2.	Future studies	437
	Index	441

CHAPTER 1

General Introduction

1.1. Historical Perspective

Among the various objects of the solar system, comets have attracted and fascinated the common man to a large extent for the last two thousand years or so. This information comes from the ancient records of paintings or drawings of comets on caves, clothes, etc. as well as from the observations of early writers. It was not until the sixteenth century that comets were demonstrated to be celestial objects. This came from the work of Tycho Brahe who observed the bright comet of 1577 AD with accurate instruments and from various locations in Europe. This really revolutionized the ideas about comets and from then on, observers took a serious view of comets and started making position measurements.

The complete credit for the discovery that comets are part of the solar system goes to Edmond Halley. Halley, using Newtonian mechanics, showed that the comets which had appeared in 1531, 1607 and 1682 are the one and the same with a period of about $75\frac{1}{2}$ years. He also noticed that the time interval between the successive perihelion passages was not the same. He concluded rightly that this could be due to the perturbation of the cometary orbit produced by the planets Jupiter and Saturn. Following these successes, he predicted that the same comet would return in 1758. As predicted, the comet did appear in 1758, though Halley, dead by then, was not there to witness the glorious triumph of his prediction. This comet is therefore named after him. In recent years this comet has been traced backwards through many centuries by several investigators through orbit calculations. Through this work, it has been possible to identify every appearance of the comet as shown by ancient records until about 240 BC. So far, it seems to have made about twenty-eight appearances.

Since early times, the appearance of a comet has been associated with disasters, calamities, tragedies and so on. One beneficial result of such wrong notions and ideas is that the appearances of most comets are recorded. These observations have proved very valuable to modern astronomers. Although there were many bright comets which have been recorded since early times, somehow the Comet Halley seems to have attracted much more attention than the others. The comet which has been depicted in the Bayeux tapestry is the Comet Halley which appeared in 1066 AD (Fig. 1.1). The comet in the tapestry can be seen to hover above

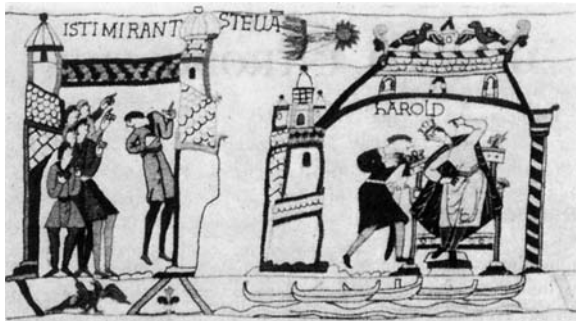


Fig. 1.1 A portion of the Bayeux tapestry showing the 1066 apparition of Comet Halley. The tapestry depicts the people pointing at the comet with fear for its effect on King Harold of England (Report of the Science Working Group. The International Halley, Watch, NASA, July 1980).

the English King Harold who is being told of the bad omen. Such types of association of Comet Halley with the occurrence of bad things on Earth have also been made for many other apparitions. The last apparition of Comet Halley in 1910 drew wide publicity (Fig. 1.2). It was very bright and enormous in extent. Actually the Earth passed through the tenuous gas of this comet's tail.

There was also the fear that a comet might collide with the Earth and bring disastrous consequences. There are several indirect observational evidences, such as the presence of Cretaceous-Tertiary boundary, Tunguska event and so on, which show that such events must have happened on the Earth in the past. The collision of Comet Shoemaker-Levy 9 with Jupiter during July 1994 has given supporting evidence, although the probability of such an event happening on the Earth is very small. With the passage of time some of the fears have been erased from the people's minds. Today the appearance of a bright comet in the sky like that of the Comet Ikeya-Seki of

BARNARD PICTURES OF HALLEY'S COMET

Taken at Yerkes Observatory
May 4, They Tally with Observa-
tion from Times Tower May 5.

VIEWED BY MISS PROCTOR

Negatives Show the Tail Extending
20 Degrees, Equivalent to 24,000,000
Miles in Length.

IN COMET'S TAIL ON WEDNESDAY

**European and American Astronomers
Agree the Earth Will Not Suffer in
the Passage.**

TELL THE TIMES ABOUT IT

**And of Proposed Observations—
Yerkes Observatory to Use Bal-
loons if the Weather's Cloudy.**

TAIL 46,000,000 MILES LONG?

Scarfed in a Filmy Bit of It, We'll
Whirl On In Our Dance Through
Space, Unharmed, and, Most
of Us, Unheeding.

SIX HOURS TO-NIGHT IN THE COMET'S TAIL

Few New Yorkers Likely to
Know It by Ocular Demostra-
tion, for It May Be Cloudy.

OUR MILLION-MILE JOURNEY

Takes Us Through 48 Trillion Cubic
Miles of the Tail, Weighing All Told
Half an Ounce!

BALLOON TRIP TO VIEW COMET.

Aeronaut Harmon Invites College
Deans to Join Him in Ascension.

MAY SEE COMET TO-DAY.

Harvard Observers Think It May Be
Visible in Afternoon.

MAY BE METEORIC SHOWERS.

Prof. Hall Doubts This, Though, but
There's No Danger, Anyway.

YERKES OBSERVATORY READY.

Experts and a Battery of Cameras and
Telescopes Already Prepared.

CHICAGO IS TERRIFIED.

Women Are Shutting Up Doors and
Windows to Keep Out Cyanogen.

Fig. 1.2 Some of the newspaper headlines which appeared in The New York Times during Comet Halley's appearance in 1910 (Report of the Science Working Group, *loc. cit.*).

1965, Comet West in 1975, Comet Hale-Bopp in 1995 or the Comet Hyakutake in 1996 is welcomed both by the scientists and the public at large. Scientists look forward to observing and studying these objects and understanding their nature. The public look forward to viewing a spectacular and colourful event in the sky.

During early times, comets were studied more from the point of their dynamics. This was made possible through the efforts of many pioneers in celestial mechanics. These extensive dynamical studies of various comets have shown, for the first time, the existence of some important physical effects like the presence of non-gravitational forces in comets. With the passage of time, cometary research has evolved from the study of dynamics

to the study of these objects *per se*. Specifically, in the last three or four decades, emphasis has been laid more in understanding the origin, physics and chemistry of these objects. The presence of complex organic molecules including molecules of biological interest in comets, which may have some relation to the existence of life on Earth, has interested biologists too, in the study of comets.

1.2. Discovery

Many comets are discovered by amateur astronomers who just scan the sky with a low-power telescope. They are called ‘comet seekers’. The comets are usually named after their discoverers. If two or even more observers find the same comet nearly simultaneously, all the names are attached to that comet. For example, the Comet Ikeya-Seki (1965 VIII) which was visible to the naked eye in 1965, was discovered by two Japanese amateurs, Ikeya and Seki. However, not all comets are found by amateurs. Many are being discovered nowadays by astronomers in their photographic plates taken from some other scientific study. A typical example of this class is Comet Kohoutek (1973 XII) discovered in 1973. Comets discovered by them are fainter as the professional astronomers have better instruments. Several comets have also been discovered through satellites, such as Solar Heliospheric Observatory (SOHO). In addition to the names of the discoverers, comets are also assigned temporary designations, indicating the year of their discovery followed by a small letter denoting the order of their discovery in that year. For example, the first two comets found in the year say 1968, are designated as 1968a and 1968b respectively. Later on when the orbits of all the comets discovered in that particular year are well determined, permanent designations are given. This consists of the year in which the comet passed nearest to the Sun i.e., perihelion, followed by a Roman numeral which indicates the order of perihelion passage during that year. Hence, the comets mentioned above will be given the permanent designations 1968I and 1968II and so on. If the comet is periodic, one also attaches P to the name of the comet. Thus the periodic Comet Encke is written as P/Encke.

However, in this system of naming of comets, there is the difficulty sometimes in deciding whether a particular object is a comet or a minor planet. e.g. 2060 Chiron, 1990 UL3=1990P=1990XVI. In addition, confusion can creep in when the better orbit of the comet becomes available

which could change the prediction of the order of perihelian passage by even a year. In view of this, a change in the cometary designation is being followed effective January 1, 1995. In the new system a year is divided into fortnights assigning successively the Roman alphabet A to Z (leaving out the letters I and Z). The designation of the comets consists of year followed by the alphabet representing the fortnight of observation and the order in which it was discovered. As for example, the third comet reported as discovered during the second half of February 1995 would be designated as 1995D3. If there is an indication of the nature of the object it could be expressed by preceding the designation with C/(for comet), P/(as now, for periodic comet), etc. Routine recoveries of periodic comets will not in future receive additional designations. The new scheme also proposes to retain the tradition of naming comets after their discoverers such as C/1996 B2(Hyakutake).

1.3. Appearance

Comets spend almost all their time at great distances from the Sun. The cometary activity starts showing up only when it approaches the Sun. At far-off distances from the Sun, it appears as a faint fuzzy patch of light. The fuzzy patch of light is a cloud of gas and dust called *coma*. The coma grows in size and brightens as it nears the Sun. In addition to the brightening of the coma, the *tail* starts developing and reaches its maximum extent at about the closest approach to the Sun. After its perihelion passage, the reverse process takes place in the sense that the comet starts fading away as it recedes from the Sun. These effects can be seen clearly in the time sequence photographs of Comet Halley, as shown in Fig. 1.3. Cometary activity is therefore transient in nature. These observations clearly show that the material composed of gas and dust must have come from a central compact solid source called the *nucleus* of comet. The diameter of the nucleus is extremely small and is estimated to be about 1 to 10 km. This size is so small that it appears as a point source and cannot be resolved even with the largest telescope. On the other hand, the diameter of the coma is much larger and lies in the range of about 10^4 to 10^5 km. The nucleus and the coma forms the *head* of a comet. The most characteristic feature of a comet is the tail which may extend up to about 10^7 to 10^8 km.

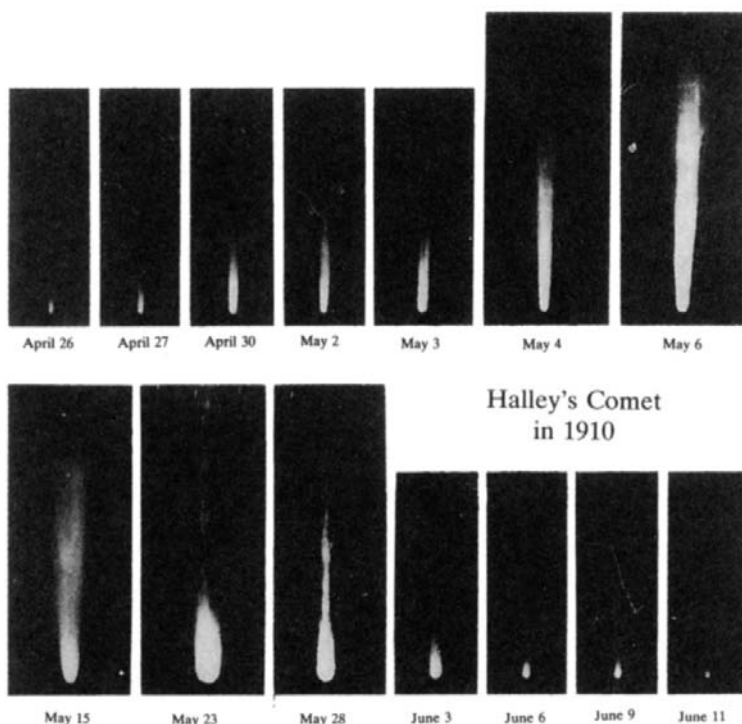


Fig. 1.3 Shows the time sequence photographs of Comet Halley in 1910 which brings out the transient nature of comets (Report of the Science Working Group, *loc. cit.*).

1.4. Statistics

The rate of discovery of comets has increased steadily since the beginning of the century. In recent times more and more fainter comets are also being discovered due to vast improvement in the observational techniques and also due to several systematic search programmes. On an average, around 25 to 30 comets are seen every year. Of these, the newly discovered comets are around 12 to 15 per year and the recoverable ones are around 13 to 15 per year. Comets are classified based on their orbital periods. The general convention which has been followed is that *short-period* comets are those which have periods (P) less than 200 years. Those which have periods greater than 200 years are called *long-period* comets. The short period comets are further subdivided into two classes. Comets with periods < 20 years are called Jupiter-family comets (JFCs) and cluster around Jupiter

(semi major axis ≤ 7.4 AU). Those comets whose periods is in the range $20 < P < 200$ years are called Halley- type comets (HTCs) with Comet Halley as prototype. The semi major axis lies in the range of around 7.4 to 34.2 AU. Halley - type comets may be considered as short-period extension of long-period comets. Among the newly discovered comets, about 8–10 are long period comets and 5 are short period ones. Most of these comets are generally faint. The bright comets and, in particular, the sun-grazing comets occur occasionally. Comets have been seen as close as 0.01 AU from the Earth. Comets have also been classified as ‘old’ and ‘new’ based purely on their orbital characteristics. Comets which have made several perihelion passages around the Sun are generally termed ‘old’ and those which are entering for the first time are called ‘new’. If the direction of motion of the comet is the same as that of the Earth’s motion, in its orbit, it is said to have a *direct* orbit. If they are in opposite directions, the comet is said to have a *retrograde* orbit.

More than 1000 Comets are known. The ratio of long-period to short-period comets is $\approx 5 : 1$. For Jupiter-family comets, the peak in the orbital period occurs around 7 to 8 years. The median orbital period of Halley-type comets is around 70.5 years. But in short-period comets, the period of a few years has also been seen as in the case of Comet Encke which has a period of 3.3 years. Among the long period comets, most of them seem to have parabolic and osculating elliptical orbits. It is of interest to know how far the comets reach away from the Sun in their orbit, which is called the *aphelion* distance. Figure 1.4 shows a histogram of the number of comets versus aphelion distance. A peak in the distribution occurs around 5 AU, which corresponds roughly to the distance of Jupiter which are the Jupiter-family comets. The general pattern of the histogram remain roughly the same with the addition of more comets. On the other hand, the long-period comets seem to peak around 4×10^4 AU (Fig. 12.1). Those with $a < 10^4$ AU are often called ‘returning’ comets and those with $a > 10^4$ AU are called dynamically ‘new’ comets. It is also found that for most of the comets the closest approach to the Sun, called the *perihelion* distance, is around 0.6 to 1.5 AU. The distribution of inclination to the ecliptic plane of short and long period comets are striking. The short period comets have inclinations < 20 to 30° and the median inclination is around 11° . The median inclination for Halley-type comets is around 64° . However, for long-period comets, the inclinations are randomly distributed. They also approach the Sun more or less isotropically. The short-period comets generally have direct orbits while long-period comets have both direct and retrograde orbits.

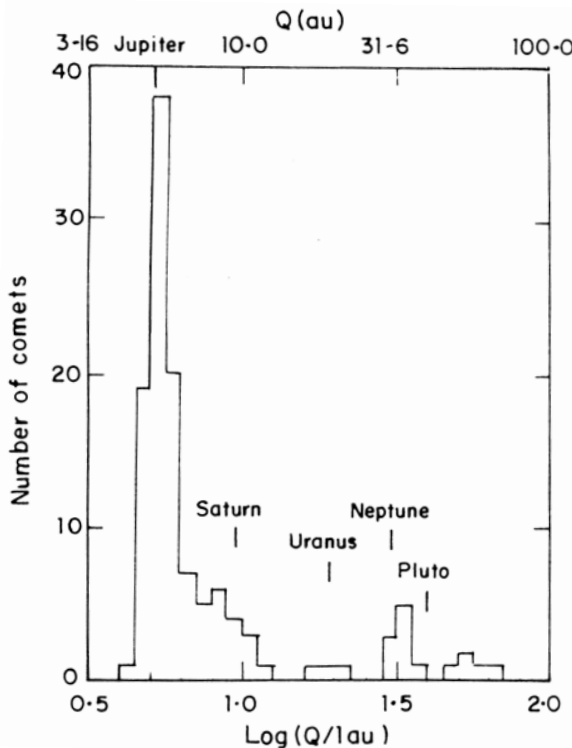


Fig. 1.4 Shows the distribution of the number of comets as a function of the aphelion distance for short period comets. The peak around Jupiter's distance can clearly be seen. Smaller peaks at the distances of other planets also appear to be present (Bailey, M.E., Clube, S.V.M. and Napier, W.M. 1990. *The Origin of Comets*, Pergamon Press).

There is a group of sun-grazing comets called Kreutz family of comets. Several hundred such comets have been discovered by satellites such as SOHO. This is because these comets are hardly visible from the earth due to their intrinsic faintness and also because of their peculiar orbit characteristics. They all appear to have the same orbital elements. The orbit of these comets indicate an aphelion distance of around 120–200 AU from the sun. This corresponds to a time period of revolution of around 500–1000 years. Their inclination peak is around 145° . This indicates that these sun-grazing comets are likely to have resulted from the break up of a very big comet into large number of parts, sometime in the past. These sun-grazing comets disappear during their approach to the sun. An example of such a comet is shown in Fig. 1.10.

Age of a comet is generally measured by the reciprocal of the semi major axis i.e. a^{-1} (AU $^{-1}$). New comets coming from the Oort cloud for the first time have $a > 10^4$ AU or $(1/a) < 100 \times 10^{-6}$ AU $^{-1}$. With successive passges the orbit shrinks gradually primarily due to planetary perturbations and hence the value of $(1/a)$ becomes larger and larger. Consequently, the increasing value of $(1/a)$ corresponds to increasing time with respect to the first approach to the solar system. In other words, $(1/a)$ gives a measure of the comet's age.

1.5. Importance

The study of comets is important from several points of view. Cometary activity arises basically from the solar heating of the nucleus, releasing the gas and dust, which finally are lost into the solar system. The time which the comet spends near the Sun is a very small fraction of its total period. So only a thin layer of the material of the nucleus is ablated at every perihelion passage and nothing much would have happened in the inner regions of the nucleus of a comet. The inner core of the comet may thus represent the composition of the original material at the time of its formation. Therefore it is hoped that a systematic study of the material of the nucleus of comets can give information with regard to the nature of the material present at the early phase of the solar nebula, 4 to 5 billion years ago, even before the formation of the Earth and the solar system. The isotopic anomalies seen in the cometary dust particles indicate the presence of presolar grains. i.e. they refer to grains produced in the circumstellar shell of stars. This indicate the presence of interstellar grains in comets. The highly complex molecules and organic compounds seen in comets can finally find their way on to the Earth. These might have played a key role in the complex scenario of chemical evolution finally leading to life on the Earth. The tail pointing away from the Sun arise primarily due to the interaction of the dust and gas of the cometary material with the solar radiation and solar wind. Therefore the study of cometary tails may throw light on the physical conditions of the interplanetary medium as well as of the solar wind and the solar activity. It is also of great interest from the point of view of Plasma Physics for the study of interactions, generation of instabilities and waves and so on, many of which cannot be produced under the laboratory conditions. In fact, the existence of the solar wind, i.e. the flow of high velocity charged particles from the Sun, was predicted by Biermann in the 1950s from the

study of the ion tails of comets. After a large number of revolutions around the Sun, the cometary activity may die out completely leading finally to a residual solid nucleus, which possibly may lead to an asteroid. Comets are also believed to be the sources of meteors and interplanetary dust. It is generally believed that the origin of comets is intimately related to the origin of the solar system, a problem of great current interest. Therefore, the study of comets can provide clues which may help in understanding the origin and evolution of the solar system. There is also generic relationship between comets with the interplanetary dust particles, meteorites, asteroids and interstellar matter. In addition to these possible interrelationships, the comets themselves are interesting objects to study, as their nature and origin are still not well understood.

1.6. Brightness

One of the uncertain facts about a comet is its brightness. The comet shines mostly due to the reflected sunlight at far-off distances from the Sun. The brightness depends upon three factors: (i) the distance r from the Sun to the comet; (ii) the nature of the comet and (iii) the distance Δ from the comet to the earth. The brightness depends upon the nature of the comet as it is the one which is producing the observed radiation.

The expected brightness of a comet I , can be written as

$$I = \frac{I_o}{r^2 \Delta^2} \phi(\alpha) \quad (1.1)$$

where $\phi(\alpha)$ is the appropriate phase function which is not important for the total brightness, I_o is the constant of proportionality, usually taken to be the brightness of the comet at $r = \Delta = 1$ AU. It has been found that the brightness of comets rarely follow a simple relation of the above type. Figure 1.5 shows results for a few comets. Mostly the power of r is greater than 2. One usually writes a modified form of Eq. (1.1) as

$$I = \frac{I_o}{r^n \Delta^2}. \quad (1.2)$$

The above equation can be written in terms of magnitudes as

$$m = m_0 + 5 \log \Delta + 2.5n \log r \quad (1.3)$$

where m refers to the total apparent magnitude and m_0 the absolute magnitude formally corresponding to $r = \Delta = 1$ AU. The study of a large number of comets has given a pretty good idea as to the variation of brightness with

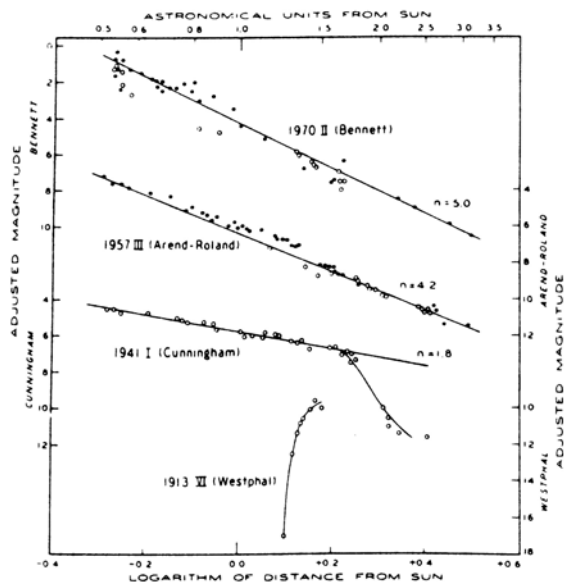


Fig. 1.5 The magnitude of the comet reduced to a standard distance of 1 AU from the Earth is plotted as a function of \log of the solar distance in AU. Circles and dots refer to observations made before and after perihelion respectively (Jacchia, L.G. 1974. *Sky and Telescope* **47**, 216; courtesy of *Sky and Telescope*).

Table 1.1 Parameters for brightness.

Comet	m_o	n
Arend-Rigaux	10.9	4
Tuttle	7.97	6
Kobayashi-Berger-Milon	7.34	3.8
West	5.94	2.4
Machholz	6.5	4
Meier	9.3	4
Klemola	9.7	4

Meisel, D.D. and Morris, C.S. 1982, In *Comets*, ed Wilkening, Univ. Arizona Press, Tucson

heliocentric distance r as well as the mean value of n . The value of m_o and n for some comets are given in Table 1.1.

Quite often it is found that it is not possible to find a single value of

n covering the whole range of the Sun-comet distance. In addition, the variation of the observed brightness, before and after perihelion passage, seems to require different values of n . Because n varies from comet to comet, a mean value for n has been derived, with the proper weightage given to the observations. The results of such a study based on carefully analyzed photometric data for more than 100 comets grouped into four classes are shown in Table 1.2. The range of parameters of the classes selected are,

- I (new) $1/a \times 10^6 \leq 50(\text{AU})^{-1}$; $(P) > 2.8 \times 10^6 \text{yr}$
- II $5 \times 10^{-5} < 1/a < 0.00215(\text{AU})^{-1}$; $10^4 < P < 2.8 \times 10^6 \text{yr}$
- III $0.00215 < 1/a < 0.01(\text{AU})^{-1}$; $10^3 < P < 10^4 \text{yr}$
- IV $0.01 < 1/a < 0.117(\text{AU})^{-1}$; $25 < P < 10^3 \text{yr}$

Table 1.2 Values of $\langle n \rangle$, $\langle q \rangle$ and $\sigma(n)$ for various comets.

Orbit Class	I	II	III	IV
Maximum period (yr)	∞	2.8×10^6	104	103
Minimum period (yr)	2.8×10^6	104	103	25
Pre-Perihelion Dominated				
Number of Comets	10	5	5	6
$\langle q \rangle (\text{AU})$	0.43	0.90	1.17	0.71
$\langle n \rangle$	2.45	3.11	3.32	3.83
$\sigma(n)$	± 0.35	± 0.71	± 0.52	± 0.49
Post-Perihelion Dominated				
Number of Comets	15	16	9	17
$\langle q \rangle (\text{AU})$	1.20	1.54	0.88	0.80
$\langle n \rangle$	3.16	3.87	4.48	4.94
$\sigma(n)$	± 0.26	± 0.58	± 0.53	± 0.79

(Whipple, F.L. 1991, In *Comets in the Post-Halley Era*, Eds. R.L. Newburn, Jr. et al., Kluwer Academic Publishers, p. 1259).

where P is the period. Table 1.2 give weighted mean perihelion distance $\langle q \rangle$, the weighted mean $\langle n \rangle$ and $\sigma(n)$ the mean error of $\langle n \rangle$. The mean value of n shows a variation with the comet class and with the age of the comet (i.e. inversely with the period). This is indicated for both pre-and post - q data. The post - q observations give a considerably larger value of $\langle n \rangle$ than the pre - q observations. In general, the large value of n required for comets arises due to the fact that the brightness is the sum total of the reflection component and the emission of gases from the coma. For the case of pure

reflection the value of n is 2. Therefore the expected brightness of a comet is a complicated function of the physical condition of the coma. However, in the absence of any knowledge or data on the comet, one can get an idea of the average behaviour of its brightness from Eq. (1.3) with a suitable value of n .

As remarked earlier the larger value of n arises due to the contribution of the emission component into the total light that is observed. The amount of emission depends upon the total number of the molecules present in the coma. In principle, it is possible to predict the brightness of a comet by relating it to the evaporation of the gases from the nucleus. This is a difficult practical problem. However, the problem is simplified if the comet has already been observed once before, for which the visual light curve is usually available. For such cases, one can use a simplified approach for predicting the expected brightness for its next apparition. In the visual spectral region, the emission is mainly due to the C_2 molecule. Therefore, to a first approximation one can assume the visible light is mainly due to the fluorescence process of the C_2 molecule, which depends upon the production rate of the C_2 molecule. This could in turn be related to the total hydrogen production rate which is very well studied in various comets. From such a procedure and using the observed light curve, it is possible to evaluate the unknown constants occurring in the photometric equation. Knowing the photometric equation, the calculation of the expected brightness of a comet as a function of r and Δ is quite simple. (Sec. 6.1.4).

There is still a simpler way than the above method. Since in Eq. (1.3) the value of n is uncertain, it can be written in a simplified form as

$$m = 5 \log \Delta + m(r) \quad (1.4)$$

where

$$m(r) = m_0 + 2.5n \log r.$$

From the observed light curve, the value of $m(r)$ can be calculated from Eq. (1.4) as a function of the time from the perihelion passage ($\equiv r$). Figure 1.6 shows the results of such calculations for Comet Crommelin (1984 IV) based on the last four apparitions. Based on Eq. (1.4) and the curve of Fig. 1.6, the expected brightness can be predicted.

1.7. Main Characteristics

Some of the main observed features in comets are the following:

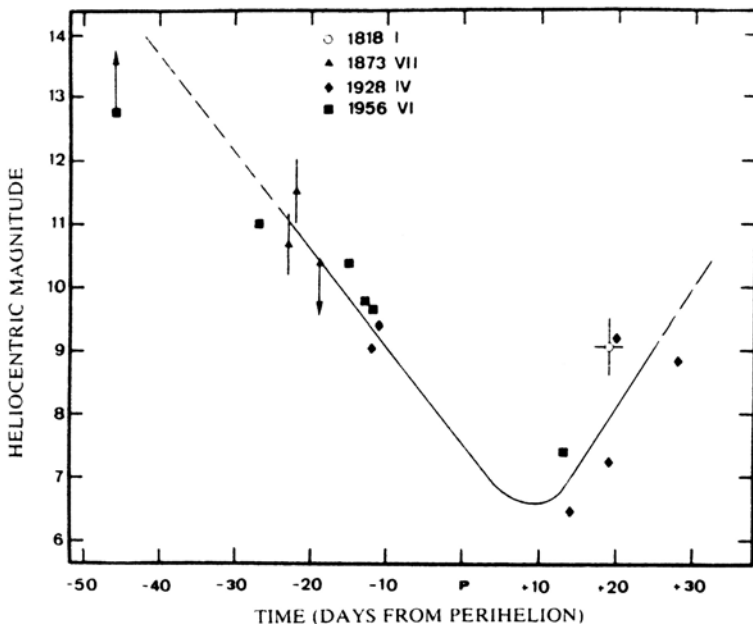


Fig. 1.6 A plot of the heliocentric magnitude of the Comet Crommelin as a function of time (equivalent to perihelion distance) from perihelion for four different appearances (Festou, M. 1983. *International Halley Watch News Letter No. 3*, p. 4).

Most of the comets seem to deviate from their predicted orbits. They are known to arrive into the solar vicinity earlier or later than the predictions based on Newtonian gravitation. The classic example for which the data exist for the last two centuries is Comet Encke, which has a period of 3.3 years. It arrives earlier every time by about $2\frac{1}{2}$ hours. The splitting of the nuclei of comets into two or more fragments has been seen in many comets. The best example is Comet West (1975VI) in which the nuclei split up into four components in a time span of a few days. This can be seen from Fig. 1.7. There appears to be some correlation between the time of fragmentation and the increase in brightness of the comet. This might mean that a spurt of cometary activity leads to fragmentation. For sun-grazing or planet grazing comets the splitting might also take place because of the tidal forces. The classic example is the nucleus of Comet Shoemaker-Levy 9 (D/1993 F2) which is believed to have fragmented into several pieces primarily due to the tidal forces exerted by Jupiter during its closest approach in July 1992. The spectacular feature of such an event

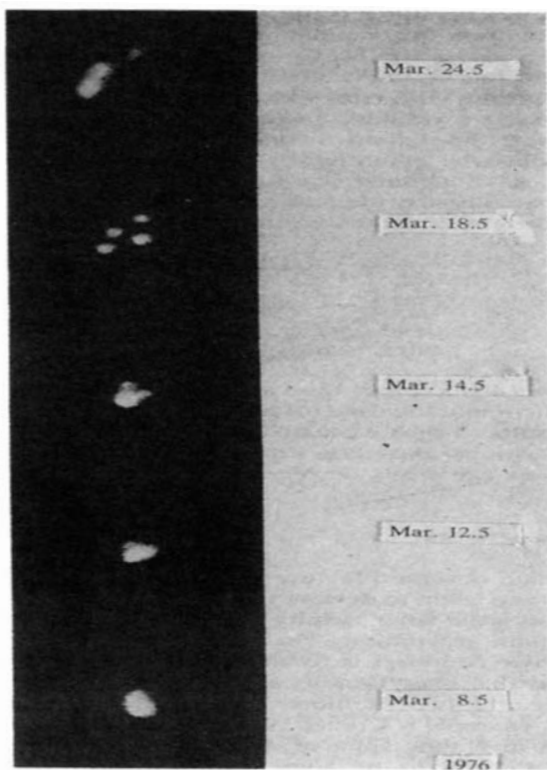


Fig. 1.7 Photograph shows the splitting of the nucleus of the Comet West 1975 VI into four parts in a time period of 10 days. The separation of the various components with time can easily be seen (Whipple, F.L. 1978. In *Cosmic Dust*, ed. J.A.M. McDonnell, New York: John Wiley and Sons, p. 1).

is that as many as 21 nuclei all in a line, were discovered in mid July 1993. (Fig. 1.8). The subsequent orbit of these fragments and their collision with Jupiter in July 1994 is schematically shown in Fig. 1.9.

Comets which come very close to the Sun can be completely destroyed. An example of this type is shown in Fig. 1.10 which was discovered accidentally in the satellite observation and shows the time sequence photograph of a comet. After its closest approach to the Sun, the comet was not visible at all, most probably due to complete evaporation or falling into Sun.

Many comets show a sudden increase in brightness of one to two magnitudes in a short time scale usually called *outbursts* or *flares*. These outbursts are not periodic in character. An outburst may mean a sudden release of

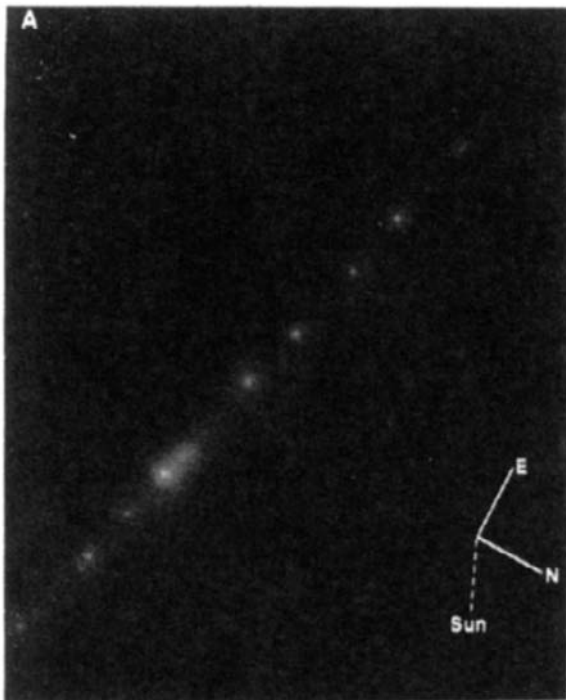


Fig. 1.8 Image of Shoemaker-Levy 9 taken with the Hubble space Telescope on July 1, 1993. The comet's heliocentric distance was 5.46 AU and the geocentric distance was 5.4 AU. The various fragments of the comet can clearly be seen. (Courtesy of H.A. Weaver and collaborators).

material from the nucleus. A classic example in which the flares have been seen very frequently is Comet Schwassmann-Wachmann 1. Figure 1.11 shows one such event for this comet. This comet has a period of 16.5 years and has been seen to brighten as much as 8 magnitudes. The flaring activity appears to be a general property of comets and is not associated with any particular type of comet. A strong outburst was seen in Comet Halley even at a heliocentric distance of around 14 AU.

In many comets successive halos coming out of the coma have also been seen. Comet Donati (1858VI) is an example of this class where the successive halos can distinctly be seen (Fig. 1.12). In many comets a broad fan-shaped coma coming out of the central condensation has also been seen.

The satellite observations in the Lyman α line of hydrogen at 1216 Å led to the discovery of the enormous extent of the hydrogen envelope (\sim

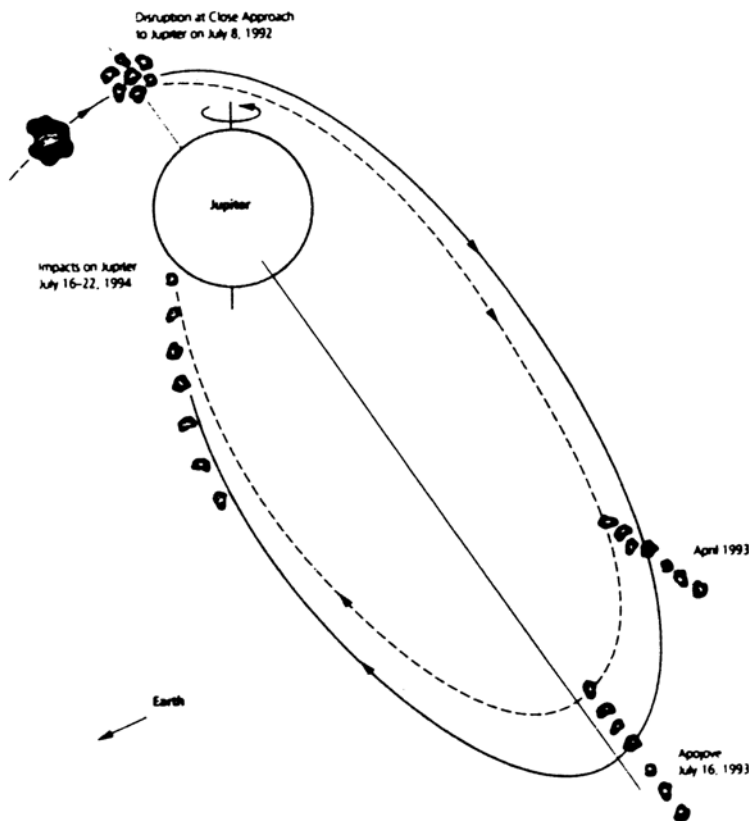


Fig. 1.9 The orbit of the Comet Shoemaker-Levy 9 around Jupiter is shown schematically. The comet which appears to have come close to Jupiter around July 8, 1992 was disintegrated due to Jupiter's tidal force. This comet discovered in March 25, 1993 had as much as 21 components. These components penetrated Jupiter's atmosphere during July 16 to 22, 1994 (Courtesy of Sekanina, Z., Chodas, P.W. and Yeomans, D.K.).

10^7 km) around the visible coma of about 10^4 to 10^5 km. The size of the hydrogen halo was found to be larger than the size of the Sun at the same distance. This can clearly be seen in the observations of Comet Kohoutek which is shown in Fig. 1.13.

The most characteristic feature of a comet is, of course, the presence of two tails. One is the *dust tail* which is curved, also called *Type II tail*. The other is the *plasma tail* which is straight, also called *Type I tail* or *ion*

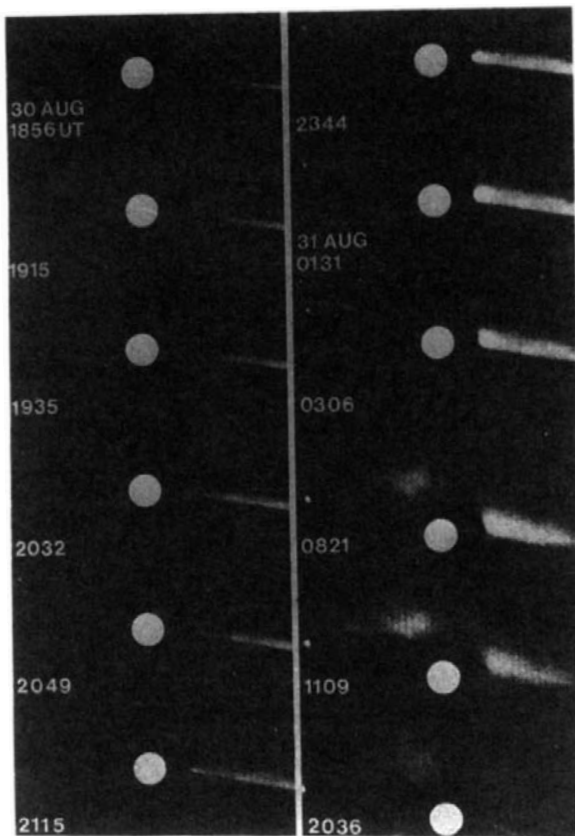


Fig. 1.10 Time sequence photographs taken between August 30, 18^h 56^m to August 31, 20^h 36^m by Solwind satellite show the disappearance of the comet. The comet enters from the right. The photographs are taken by Howard, R.A., Koomen, M.J. and Michels D.I. official US Navy photograph. (Courtesy of Howard, R.A. and collaborators).

tail. Figure 1.14 shows these two well-developed tails for the Comet Mrkos (1957V). Both the tails point to the direction away from the Sun. The nature of these two tails can be seen clearly in the colour photographs in which the dust tail appears yellowish and the plasma tail bluish in colour. Quite often a third short tail has also been seen in the direction towards the Sun. This is called the *anti-tail* of the comet. Figure 1.15 shows an example of this class for Comet Arend-Roland (1957 III).

The dust tail is generally very smooth and structureless. But this is not so in the case of the plasma tail. Large scale structures of various kinds

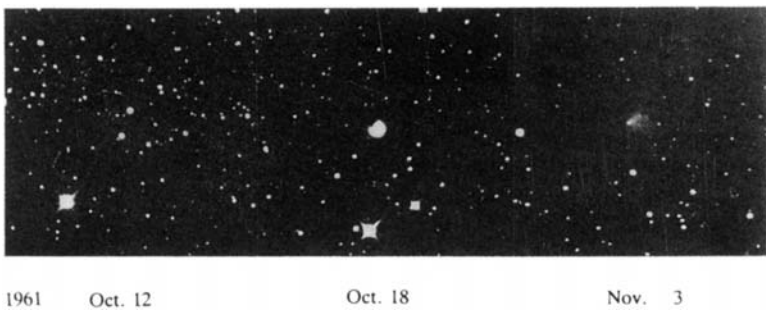


Fig. 1.11 An outburst seen in Comet Schwassmann-Wachmann 1. The position of the comet on October 12, is shown by lines in the margin. The comet is very bright on October 18, but has become faint by November 3 (Roemer, E. 1966. In *Nature and Origin of Comets*. Memoirs of the Society Royale de Sciences of Liege **12**, 15; Courtesy of E. Roemer, official US Navy photographs).

have been seen in the plasma tail of comets. As the name indicates, this tail is composed mainly of ions. Therefore many of the features seen in the laboratory plasma arising out of various physical processes as well as others, which cannot be seen in the laboratory plasma, have also been seen in the plasma tail of comets. For example features like oscillations, kinks, helices, knots, filaments, rays etc., have been seen in many comets. These indicate clearly the presence of complex interactions of the magnetic field with the tail plasma. Some typical large scale observed features in comets are shown in Figs. 1.16 to 1.18.

1.8. Spacecraft Encounters with Comets

The general nature of comets has been revealed mainly through indirect means from the studies of ground based observations, rockets, aeroplanes and satellites. However space mission to comets will provide an opportunity to make *in situ* measurements of a comet. Since this is almost like direct access, it will provide more detailed information about the nucleus. With this in view several space missions to comets have been undertaken. They are given in Table 1.3. The main objective of space missions are, to image the nucleus for its morphology; to determine the composition of gas and dust; and to understand the interaction of the solar wind with the cometary ionosphere.

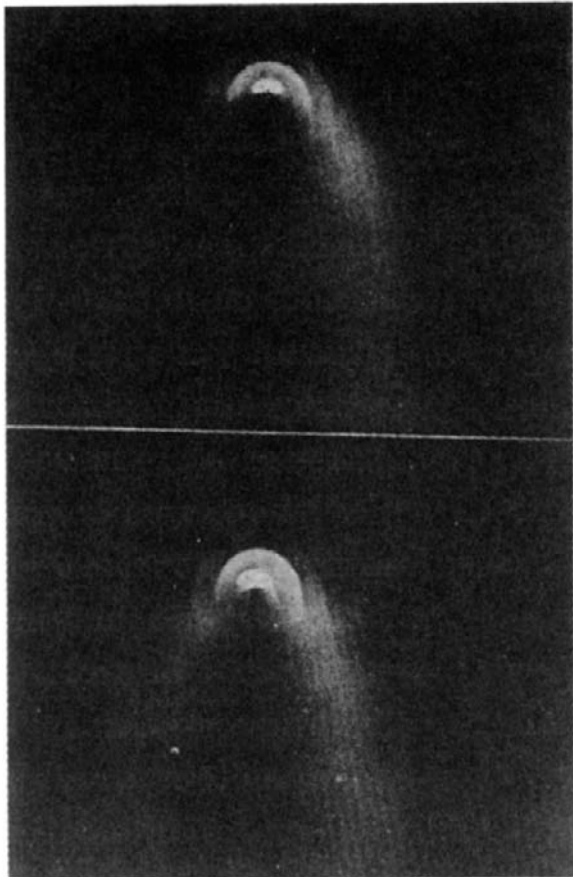


Fig. 1.12 Successive halos around Comet Donati (1858 VI) as observed visually by Bond on October 1858 (Whipple, F.L. 1981. In *Comets and Origin of Life*, ed. C. Ponnampерuma, Dordrecht: D. Reidel Publishing Company, p. 1).

Comet Halley was the first comet to be studied in great detail from several spacecrafts in 1986. Even prior to Comet Halley observations, *in situ* measurements of particles, fields and waves were carried out by the ICE satellite (International Cometary Explorer). It passed through the plasma tail of Comet Giacobini-Zinner on September 11, 1985.

During March 1986, around the time of the closest approach of Comet Halley to the Sun, six spacecrafts from various space agencies made detailed and extensive *in situ* measurements of various kinds in the coma of Comet Halley (Fig. 1.19). All the encounters took place on the Sunward side of

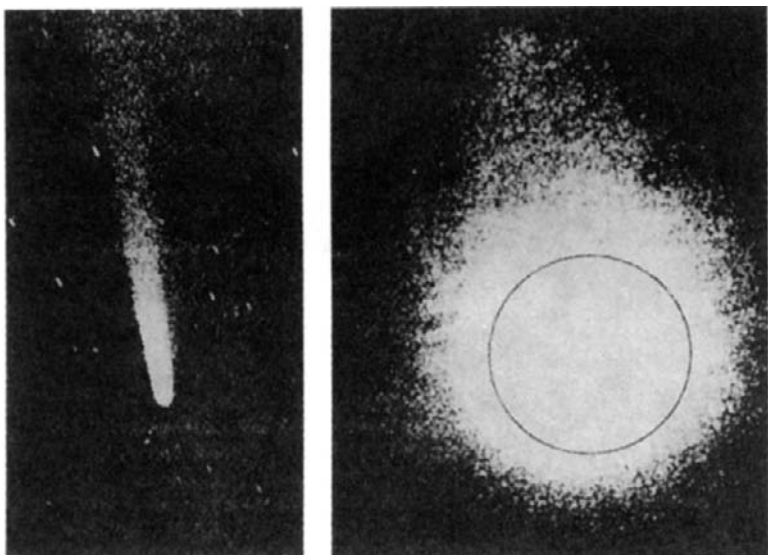


Fig. 1.13 Comet Kohoutek (1973 XII) as seen in visible (left) and in ultraviolet region taken in Lyman α line (right). Circle represents the apparent size of the Sun at the same distance. The vast extent of the hydrogen halo can clearly be seen. (Whipple, F.L. 1981, *loc. cit.*).

the comet. The closest approach to the nucleus was made by the European Space Agency's (ESA) Spacecraft Giotto, which passed at a distance of approximately 500 km from the nucleus. The Russian spacecrafts Vega 1 and 2 passed at distances of around 8000 km from the nucleus. The distances of the closest approach of the Japanese spacecrafts Suisei and Sakigake were around 1.5×10^5 km and 7.0×10^6 km respectively. The ICE spacecraft also passed through at a distance of around 0.2 AU upstream of Comet Halley later in March 1986. Another space encounter with a comet took place on July 10, 1992 when the Giotto Spacecraft, which was successfully redirected in July 1990, passed through the Comet P/Grigg-Skjellerup nucleus within 100 to 200 km.

The Comet Halley, with a period of about 76 yrs, moves in a retrograde motion with respect to the planets. Due to the retrograde motion of Comet Halley with respect to the Earth and the Spacecrafts, the relative encounter velocity was very high, ~ 68 km/sec. Since the gas and dust velocities in the coma are ~ 1 km/sec, the Giotto Spacecraft essentially saw the static situation while it passed through the coma as particles hit the spacecraft from the forward direction. The scientific payload on the spacecrafts, which



Fig. 1.14 Photograph of Comet Mrkos (1957V) taken on 27 August 1957 which shows the characteristic feature of the two tails, ion tail (straight) and the dust tail (curved). (Arpigny, C. 1977, *Proceedings of the Robert A. Welch Foundation Conferences on Chemical Research XXI*, Cosmochemistry, Houston).

passed through Comet Halley, had experiments for the study of flux and composition of neutrals, ions, electrons and dust, magnetic field and waves, imaging the nucleus, infrared spectra and ultraviolet images among others.

The space missions, Deep Space 1, Stardust and Deep Impact also made *in situ* measurements of various kinds in the Comets 19P/Borrelly, 81P/Wild 2 and 9P/Tempel 1 respectively. The cometary material from Comet Wild 2 was successfully brought back to the earth by Stardust mission. This is the first time, laboratory studies are being carried out on the real cometary dust particles.

The Deep Impact mission released a projectile which impacted on the surface of the nucleus of Comet Tempel 1 resulting in a crater on the nucleus. As a result, the vapourized ejecta from the deeper layers came out. This material was subjected to a thorough investigation, in addition to studying the crater itself. This gave an opportunity for the first time to study the material in the deeper layers of the nucleus of a comet. All these missions have met with tremendous success. They provide new insights into the nature of nucleus, coma, dust and the tails. These observations were supplemented by extensive observations of various kinds carried out with worldwide ground based telescopes, satellites, rockets and Kuiper Airborne



Fig. 1.15 Photograph of Comet Arend-Roland (1957III) which shows the anti-tail (sharp ray towards the left). Taken on 24 April 1957 (Whipple, F.L. 1981, *loc. cit.*).

Observatory, with sophisticated instrumentation by professionals and amateur astronomers to obtain as much coverage as possible, over the orbit of the comets. This co-ordinated effort of an unprecedented nature have not only confirmed our knowledge about comets, theories and hypothesis that existed before these measurements were made, but have also provided new and unexpected insight into the cometary phenomena.

1.9. An Overall View

The various aspects of cometary phenomena has come from studies carried out over the entire range of the electromagnetic spectrum from X-rays to radio region, from *in situ* measurement of comets and from laboratory studies of cometary dust particles brought back to earth. All these studies had a tremendous impact on Cometary Science.

The three major parts of a comet are the nucleus, the coma and the



Fig. 1.16 Comet Kohoutek showing the helical structure. Photograph was taken on 13 January 1974. The oscillations in the tail at far off distances from the head can clearly be seen. (Brandt, J.C. and Chapman, R.C. 1981. *Introduction to Comets*, Cambridge: Cambridge University Press, illustrations credited to Joint Observatory for Cometary Research (JOCR), NASA).

tail (Fig. 1.20). Most of the information about these three components has come basically from the study of spectra. Almost all the observed activities seen in a comet should be related directly or indirectly to the nucleus of a comet. A reasonable working model for the nucleus which is the *icy-conglomerate model* was first proposed by Whipple in the 1950's. In this model the nucleus was believed to be a discrete rotating body consisting of frozen water, complex molecules formed out of abundant elements H, C, N and O, and dust. All the subsequent observations of comets for the last four decades had supported this model by indirect means, basically through the observation of the dissociated products of H₂O (i.e. OH, H and O) and H₂O⁺. The first actual detection of H₂O in a comet came from the observation of Comet Halley in 1986, when well resolved rotational lines of the 2.7 μm band of H₂O were detected with observations carried out with the Kuiper Airborne Observatory. The nucleus contains around 80% of H₂O-ice and the rest is made up of other constituents. The single body nature of the nucleus, in contrast to that of 'loosely bound system',



Fig. 1.17 Photograph showing a big knot in the tail of Comet Kohoutek. This is generally called as ‘Swan-like’ feature. The photograph was taken on 11 January 1974 (Brandt, J.C. and Chapman, R.C. 1981, *loc. cit.* JOCR photograph).

Table 1.3 Spacecrafts to Comets.

Comet	Spacecraft	Launch date	Date of closest approach	Distance of closest approach (Km)	Period of Comet (yr)	Remarks
Halley	6 spacecrafts		March 1986	<i>Giotto</i> ~500	76	Out of 6 spacecrafts, <i>Giotto</i> mission was the closest
Borrelly	Deep Space 1	Oct.25, 1998	Sept.22, 2001	~2171	6.9	Extended mission to comet after asteroid flyby
Wild 2	Stardust	Feb.7, 1999	Jan.2, 2004	100-150	6.4	Returned to Earth on Jan.15, 2006 with cometary dust
Tempel 1	Deep Impact	Jan.12, 2005	July 4, 2005	~500	5.5	10^4 tons of material was excavated from the nucleus

was confirmed by the photographs taken of the nucleus of Comet Halley by Giotto Spacecraft when it was at a distance of 500 km from the nucleus, supporting the general concept of the Whipple model. The nucleus was observed to be irregular in shape and there were only a few active areas on its surface. The rotation of the nucleus of Comet Halley was also confirmed. All these results have been confirmed with further observations carried out with Deep Space 1 on Comet Borrelly; Stardust on Comet Wild 2; and Deep Impact on Comet Tempel 1. The shapes and sizes of the cometary



Fig. 1.18 Photograph of Comet Halley showing well developed streamers. Taken on 8 May 1910. (Report of the Science Working Group, *loc.cit.*).

nuclei have been determined from the images taken at different angles.

When the comet is far off from the Sun, the continuum spectrum seen is simply that of the reflected sunlight by the nucleus. As it approaches the Sun, the gas, mostly made up of complex molecules and the dust are released from the nucleus, due to solar heating. This then expands outwards into the vacuum at about 0.5 km/sec giving rise to the observed coma. The dimension of the visible coma is around 10^4 to 10^5 km, while the ultraviolet coma extends up to about 10^6 to 10^7 km. As the gas expands, it is subjected to various physical processes like dissociation, ionization, gas-phase

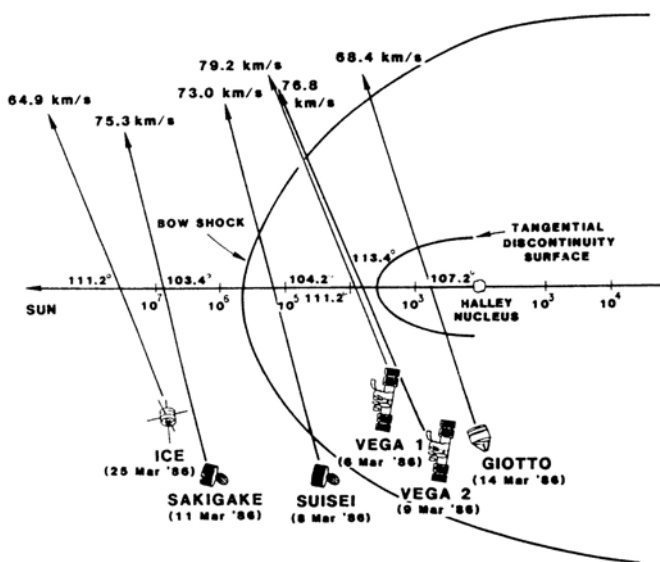


Fig. 1.19 The geometry of the six spacecraft flybys to Comet Halley. The distances are marked in logarithmic scale and the Sun is to the left of the Comet. The flyby dates for each mission are given at the bottom, flyby phase angle in the centre and flyby speeds at the top (Mendis, D.A. 1988. *Ann. Rev. Astron. Astrophys.* **26**, 11).

reactions, etc. Therefore, the gaseous material in the coma is modified to a large extent. The complex molecules released by the nucleus, generally known as *parent molecules*, ultimately give rise to simple molecules and radicals like CN, C₂, OH, CH, NH₂, etc., which are seen in the comet's emission spectra. The emission lines of various elements like Na, Si, Ca, Cr, etc., show up in sun-grazing comets. Through the study of the radio region, large number of molecules possibly the parent molecules of some of the observed species, have been identified.

The dust coming out of the nucleus is dragged outwards by the gas accompanying it. These dust particles are subjected to the radiation pressure of the Sun which pushes them in the direction away from the Sun. Since the dust particles lag behind as they stream away from the sun, they take a curved path. This gives rise to the observed curved nature of the dust tail. The tail that is usually seen in the sky is the dust tail, which is made visible through the scattering of the solar radiation by the dust particles in the tail. The tail extends up to about 10^7 km or so.

The understanding of the nature and composition of the dust parti-

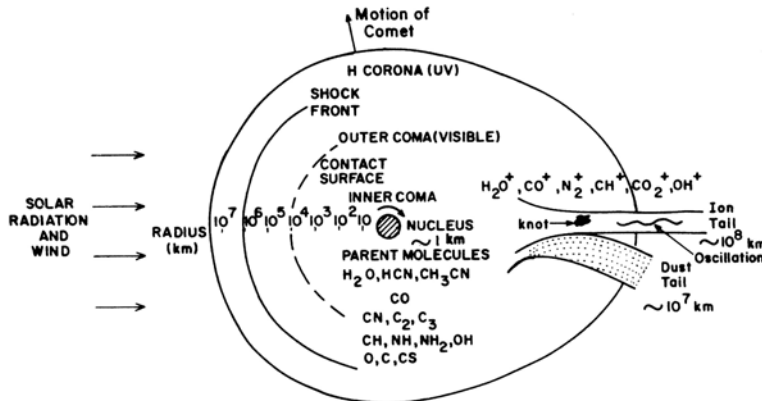


Fig. 1.20 Descriptive sketch of a comet.

cles came mostly from the interpretation of continuum, polarization and infrared radiation from comets. That the grain material could be some form of silicate, was inferred from the detection of broad emission features occurring around 10 and $20 \mu\text{m}$ in comets, which are characteristic features of all silicate materials. The silicate material could be of the olivine type which can be further inferred from the detection of a feature at $11.3 \mu\text{m}$ in the high resolution spectral observations of Comet Halley. There is another component of the grains in comets came from the discovery of CHON particles from the *in situ* measurements of Comet Halley. As the name indicates, these particles are mostly made up of H, C, N and O. This was also supported from the ground-based observations of Comet Halley and other comets by the detection of a broad emission feature around $3.4 \mu\text{m}$ attributed to C-H stretching bond of hydrocarbons. Therefore these studies indicated two major components for the grains in comets, namely silicate and some form of carbon.

More recent studies of Comets Tempel 1 and Wild 2 has shown the highly complex mineralogy of the cometary dust particles. They have shown the presence of silicates of various types, carbonates, water-ice, amorphous carbon, sulphides among others. The organics present in the dust particles are also highly complex. The surprising result was the observation of wide variation in the chemical composition among comets. The dust particles also contain material of low and high temperature condensates indicating that there must have been large scale mixing of material in the solar nebula. The presence of large numbers of small-sized grains, $\lesssim 0.1 \mu\text{m}$, which cannot

be detected through observations made in the visible region, was found to exist in comets in abundance. The grains in the coma can also act as a source of observed molecules which comprise the gas.

The solar radiation also breaks up the original molecules released by the nucleus and ionizes them. The ionized gas in the coma is swept outwards by a stream of charged particles present in the solar wind. These two are coupled through the interplanetary magnetic field. This gives rise to the plasma tail in the antisolar direction and extends up to about 10^7 to 10^8 km. Therefore, the structure and the dynamics of plasma tail are basically due to the interaction of the cometary plasma with the solar wind. The theoretical modelling of the interaction between the solar wind plasma and the cometary ions had predicted the existence of several gross features like bow shock, ionopause etc., which were confirmed based on the *in situ* measurements carried out on Comets Halley, Giacobini-Zinner, Borrelly, Tempel 1 and Wild 2 by the spacecrafts. Therefore the multi-layered structure and variations seen in comets arise due to complex interactions taking place in the plasma between electrons, heavy cometary ions, cometary protons and solar wind protons as they are being thermalised at different positions in the coma. The spectrum of the plasma tail shows mainly emissions from ions like H_2O^+ , CO^+ , CO_2^+ , N_2^+ , etc; of these the emission due to CO^+ is the dominant one. Since this emission spectrum lies in the blue spectral region, the ion tail appears blue in colour photographs.

The comets are believed to be members of the solar system inferred from the observed orbital characteristics of comets. The study based on the isotopic ratio of $^{12}\text{C}/^{13}\text{C}$ in many comets gives a value ~ 90 which is the same as the solar system value. Several other isotopic ratios seen in Comet Halley are also consistent with the solar system values. These results seem to suggest that the cometary material and the solar system material are similar in nature. With regard to the origin of comets, the widely accepted hypothesis is that of Oort. He pointed out that there appears to be a cometary reservoir whose aphelia is about 50,000 AU or more from the Sun. This is usually called the *Oort cloud*. It is estimated that there may be around 10^{12} comets in the Oort cloud. Many of the comets leaving this cloud are finally brought into the solar system due to stellar perturbations. This accounts for the steady influx of comets into the solar system. However, the long period comets coming from the Oort cloud faces serious problems in explaining the number and inclination of the observed short period comets. This has led to the hypothesis that the short period comets come from another population of comets from a region

beyond the orbit of Neptune, between 30 and 50 AU. This region is generally called the *Kuiper belt*. The origin of comets therefore is related to the origin of the Oort cloud and the Kuiper belt. Several hypotheses have been put forward to explain the origin of these clouds.

In the succeeding chapters, we would like to elaborate on some of these aspects. Before going into the actual subject matter, we would like to give a brief account of the physical background required for the interpretation of various observed phenomena.

Problems

1. What is the basis of the assumption that a comet possesses a nucleus at its centre? Since it is hard to see the nucleus of a comet directly, what is the best way to locate it?
2. Suppose a Comet A has $n = 3$ [Eq. (1.2)] in its 50th orbit around the Sun while Comet B has $n = 6$ in its first orbit around the Sun. Does one expect the same brightness variation of Comets A and B in their next orbits? Give reasons. Explain why the two values of n could be vastly different.
3. Is it possible for the comets to be in orbit around the Sun, but not seen from the Earth?
4. Discuss with examples that impact of comets on solar system objects is a natural phenomena.
5. Discuss the consequences of a comet hitting the Earth.
6. Compare the energy released by a 1 km size comet moving at 60 km/sec and suddenly coming to a stop with that of two 3500 lb cars colliding head-on at 50 km/hr.

References

Some of the references pertaining to cometary studies are the following:

1. Bailey, M.E., Clube, S.V.M. and Napier, W.M. 1990. *The origin of comets*. Pergamon Press, Oxford.
2. Brandt, J.C. and Chapman, R.D. 2004. *Introduction to comets*. 2nd Edition, Cambridge University Press, Cambridge.
3. Festou, M.C., Keller, H.U. and Weaver, H.A. (eds), 2005. *Comets II*, Univ. Arizona Press, Tucson.

4. Grewing, M., Praderie, F. and Reinhard, R. (eds). 1987. *Exploration of Halleys Comet*. Springer-Verlag, Berlin. (*Astron. Astrophys.*, **187**, 1-936, 1987).
 5. Huebner, W.F. (ed.) 1990. *Physics and Chemistry of Comets*. Springer-Verlag, Berlin.
 6. Lazzaro, D., Mello, S.F. and Fernandez, J.A. (eds.) 2006. *Asteroids, Comets and Meteors*, Cambridge University Press, Cambridge.
 7. Nature. 1986. *Encounters with Halley*, **321**, 259.
 8. Newburn, Jr., R.L., Neugebauer, M. and Rahe, J. (eds.). 1991. *Comets in the Post-Halley Era*. Vols. 1 and 2. Kluwer Publishers, Dordrecht.
 9. Wickramasinghe, N.C. 2009. *Astrobiology, Comets and the Origin of Life*, World Scientific Publishing Co., Singapore.
 10. Wilkening. L.(ed.). 1982. *Comets*, Univ. Arizona Press, Tucson.
- Deep Impact: The important and first of its kind results based on Deep Impact studies of Comet Tempel 1 are presented in the following publications:
11. Deep Impact 2005. *Science* (Special Issue), **310**, 257-283.
 12. A'Hearn, M.F. and Combi, M.R. (Eds). 2007. *Deep Impact Mission to Comet 9P/Tempel 1, Icarus* (Special Issue), **187**, 1-356 (Part I); **190**, 283-459 (Part II).
- Stardust: The important and first of its kind results based on *in situ* measurements and laboratory studies of collected dust particles from Comet Wild 2 from Stardust mission are presented in the following publications:
13. Stardust 2004. *Science* (Special Issue), **304**, 1762-1780.
 14. Stardust 2006. *Science* (Special Issue), **314**, 1707-1739.

This page intentionally left blank

CHAPTER 2

Dynamics

2.1. Orbital Elements

The objects in space are generally specified with respect to the ecliptic or to the equatorial system of coordinates. In the former the Earth's orbit around the Sun, i.e., the *ecliptic plane* is the reference frame, while in the latter it is the plane of the Earth's equator. The position of an object is specified by the *longitude* and the *latitude* in the ecliptic system and by the right ascension (α) and the declination (δ) in the equatorial system. The right ascension is measured from the vernal equinox, which is the point where the ecliptic plane cuts the Earth's equator. The declination is the angular distance from the north to the south of the celestial equator. The two systems can be transformed from one to the other through trigonometric relations.

The orbit of a body around the Sun is generally a conic section. In general, the conics are the *ellipse*, *parabola* and *hyperbola*. The *major axis* refers to the maximum diameter of the ellipse and it determines the size of the ellipse (Fig. 2.1). The *eccentricity* e of the ellipse is defined as the ratio of the distance between the center and a focus to the length of the semi major axis. An ellipse is completely defined by the eccentricity and the major axis. The value of e varies between 0 and 1. A *circle* is a special case of the ellipse when the eccentricity is zero. The parabola has an eccentricity equal to unity while a hyperbola has an eccentricity greater than one. In an elliptical orbit the closest and the farthest distance of the object from the Sun which is stationed at one of the foci is known as the *perihelion* and *aphelion* distances respectively.

The position of a comet in the sky is generally referred to the ecliptic system of coordinates. To define completely an orbit in space, six quantities

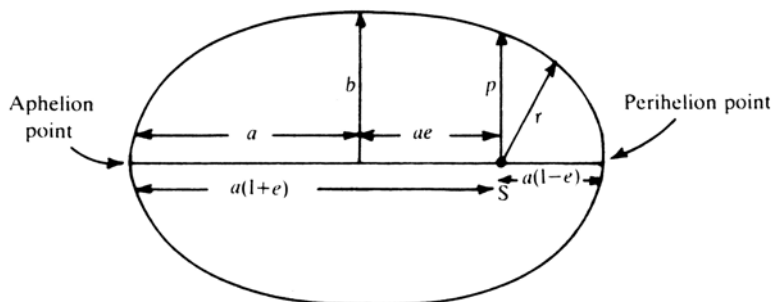


Fig. 2.1 Various parameters defined for an elliptical orbit. S denotes the position of the Sun occupying one of the foci.

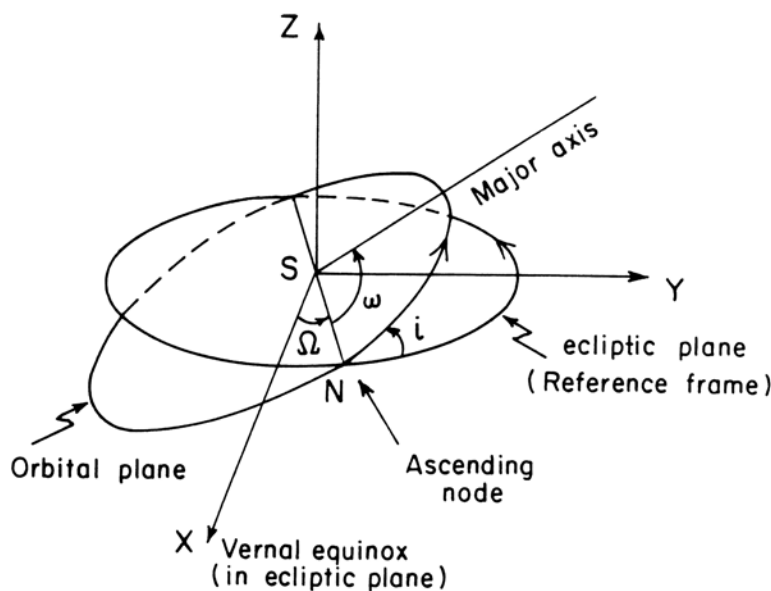


Fig. 2.2 The orbital elements required for specifying an orbit.

usually termed as *elements* of the orbit are to be specified (Fig. 2.2). They are the following:

a = length of the semi major axis;

e = eccentricity;

i = angle between the orbital plane and the plane of the ecliptic;

Ω = longitude of the ascending node. This is the angle from the vernal

equinox along the ecliptic plane to the point of intersection of orbital plane with the ecliptic plane;

ω = argument of the perihelion, which is the angle measured from the ascending node to the perihelion point.

The first two parameters specify the size and the shape of the orbit in its orbital plane, while the other three define the orientation of the orbit with respect to the ecliptic plane.

The sixth element is the *time parameter* which defines the position of the body in its orbit at that time. This is taken to be T , the time of perihelion passage. This gives a reference time to fix the body at other times in its orbit.

Therefore, the quantities, a, e, T and the angle i, ω, Ω define completely the position of the body and its orbit at any given time. For a parabolic orbit, the semi major axis which is infinite is replaced by the perihelion distance q , which defines the size of the parabola.

2.2. Orbit in Space

2.2.1. Relevant equations

The orbit of a comet is a conic section about the Sun and it can be defined under the Newtonian Gravitation.

The equation of motion of a comet of mass m around the Sun can be represented as

$$\left(\frac{d^2 \mathbf{r}}{dt^2} \right) = - \left(\frac{G(M_{\odot} + m)}{r^3} \right) \mathbf{r} \equiv \frac{\mu \mathbf{r}}{r^3} \quad (2.1)$$

where M_{\odot} is the mass of the Sun and G is the gravitational constant. Since $m \lesssim M_{\odot}$, $\mu = GM_{\odot}$ and \mathbf{r} is the position vector of the comet relative to the Sun, the use of plane polar coordinates r and θ in the orbital plane of motion allows one to separate the Eq. (2.1) into r and θ components, giving, for the r component

$$\ddot{r} - r\dot{\theta}^2 = -\frac{\mu}{r^2} \quad (2.2)$$

and for the θ component

$$r\ddot{\theta} + 2\dot{r}\dot{\theta} = 0 \quad (2.3)$$

Equation (2.3) can be written as

$$\frac{1}{r} \frac{d}{dt}(r^2\dot{\theta}) = 0. \quad (2.4)$$

The integration of the above equation gives the specific (means per unit mass) angular momentum integral

$$r^2\dot{\theta} = \text{constant} = h. \quad (2.5)$$

Specific energy integral is given by

$$E' = \frac{1}{2}(r^2 + r^2\dot{\theta}^2) - \frac{\mu}{r}. \quad (2.5a)$$

From the above system of equations, one can derive the polar equation for the conic section for an angle θ as

$$r = \frac{p}{1 + e \cos(\theta - \omega)} \quad (2.6)$$

where ω is constant, $p = h^2/\mu$ is the semi latus rectum and $e = \sqrt{1 + \frac{2E'h^2}{\mu^2}}$ is the eccentricity of the orbit and therefore the length of the semi major axis $a = -\frac{\mu}{2E'}$. ω is actually the angle that the major axis makes with the axis $\theta = 0$. At the perihelion point $\theta = \omega = 0$ and therefore the perihelion distance is given by $h^2/\mu(1 + e)$. The perihelion distance is also equal to $a(1 - e)$. Hence

$$h^2 = \mu a(1 - e^2). \quad (2.6a)$$

Equation (2.6) can be expressed as

$$r = \frac{a(1 - e^2)}{1 + e \cos(\theta - \omega)} = \frac{a(1 - e^2)}{1 + e \cos f} \quad (2.7)$$

where a is the semimajor axis and the angle f is known as the *true anomaly* (Fig. 2.3).

The other quantity of interest is the velocity of the object in its orbit. From Eqs. (2.1) and (2.4), the expression for the orbital speed of the particle can be obtained and it is given by

$$v^2 = \mu \left[\frac{2}{r} - \frac{1}{a} \right]. \quad (2.8)$$

The quantity $1/a$ is *+ve*, zero or *-ve* depending on whether the orbit is an ellipse, a parabola or a hyperbola. The velocity at the perihelion point for an ellipse is given by

$$v_p^2 = \frac{\mu}{a} \left(\frac{1 + e}{1 - e} \right); \quad (2.9)$$

similarly at the aphelion point, the expression for the velocity is given by

$$v_a^2 = \frac{\mu}{a} \left(\frac{1 - e}{1 + e} \right). \quad (2.10)$$

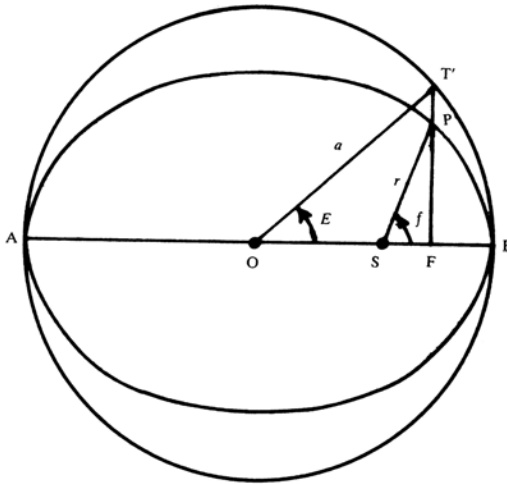


Fig. 2.3 Definition of eccentric anomaly E . f represents the true anomaly.

From Eq. (2.7) it is clear that the value of $\frac{1}{r}$ monotonically decreases from perihelion to aphelion, Eq. (2.8) would then suggest that the velocity of the object is maximum at perihelion and minimum at aphelion and varies along its orbit in between these, two limits.

Another quantity of interest is the heliocentric radial velocity of the object. For elliptical orbits, it can be shown from Eq. (2.7) by taking its time derivative that

$$\dot{r} = \mp \mu^{1/2} \left[\frac{a^2 e^2 - (a - r)^2}{ar^2} \right]^{1/2}. \quad (2.11)$$

The minus and positive signs refer to preperihelion and postperihelion radial velocities.

The *mean angular motion* n of the body in its orbit with the period P is by definition

$$n = \frac{2\pi}{P}. \quad (2.12)$$

Since Eq. (2.5) suggest that $h = r^2\dot{\theta} = \text{constant}$ and $\frac{1}{2}r^2\dot{\theta}$ is the areal velocity, the orbital period

$$\begin{aligned} P &= \frac{\text{Area of the ellipse}}{\text{areal velocity}} \\ &= \frac{2\pi a^2 \sqrt{1 - e^2}}{h} \end{aligned} \quad (2.12a)$$

$$P = 2\pi \sqrt{\frac{a^3}{\mu}}. \quad (2.13)$$

Hence

$$n = \mu^{1/2} a^{-3/2}. \quad (2.14)$$

If T represents the time of perihelion passage, the angle swept by the radius vector in a time interval $(t - T)$ is called the *mean anomaly* M and is defined as

$$M = n(t - T). \quad (2.15)$$

If a circle is drawn with OB as radius, then the line FP referring to the ellipse when extended perpendicular to the major axis cuts the circle at T' (Fig. 2.3). The angle $T'OB$ is called by definition *eccentric anomaly*, generally denoted as E . Since $PF/T'F = \sqrt{1 - e^2}$ for any point P on the orbit, it can be shown that

$$SF = x = a \cos E - ae$$

$$PF = y = a\sqrt{1 - e^2} \sin E$$

Therefore

$$r = \sqrt{x^2 + y^2} = a(1 - e \cos E) \quad (2.16)$$

. Further

$$\cos f = 1 - 2 \sin^2 \frac{f}{2} \quad (2.16a)$$

or

$$2r \sin^2 \frac{f}{2} = r(1 - \cos f) \quad (2.16b)$$

However

$$\cos f = \frac{SF}{r} = \frac{a \cos E - ae}{a(1 - e \cos E)} \quad (2.16c)$$

and

$$\sin f = \frac{PF}{r} = \frac{a(1 - e^2)^{1/2} \sin E}{a(1 - e \cos E)} \quad (2.16d)$$

Therefore the Eq. (2.16b) can be written as

$$2r \sin^2 f / 2 = a(1 + e)(1 - \cos E) \quad (2.16e)$$

similarly

$$2r \cos^2 f/2 = a(1 - e)(1 + \cos E)$$

Therefore

$$\tan f/2 = \left(\frac{1+e}{1-e} \right)^{1/2} \tan \frac{E}{2} \quad (2.17)$$

This is the relation which connects the eccentric anomaly E with the true anomaly f .

There is also a relation connecting the mean anomaly M and the eccentric anomaly E . This is generally referred to as *Kepler's* equation which is derived as follows:

The quantity $(t-T)/P$ represents the fractional area of the ellipse swept by SP with respect to the point B, where P is the orbital period. This is also equal to $n(t-T)/2\pi$. From the law of areas and the properties of the auxiliary circle, it follows that

$$\frac{n(t-T)}{2\pi} = \frac{M}{2\pi} = \frac{\text{area } BSP}{\text{area of ellipse}} = \frac{\text{area } BST'}{\text{area of circle}}$$

But $\text{Area } BST' = \text{area of circular sector BOT}' - \text{area SOT}'$

$$= \frac{a^2 E}{2} - \frac{a}{2} ae \sin E$$

Therefore

$$\frac{M}{2\pi} = \frac{a^2}{2} \frac{(E - e \sin E)}{\pi a^2}$$

or

$$E - e \sin E = M \quad (2.18)$$

which is the Kepler's equation.

The above relation can also be written as

$$E - e \sin E = n(t - T). \quad (2.19)$$

The corresponding relations for the parabolic case are

$$r = \frac{2q}{1 + \cos f} \quad (2.20)$$

$$v^2 = \frac{2\mu}{r} \quad (2.21)$$

$$\left(\frac{\mu}{2q^3} \right)^{1/2} (t - T) = \tan \frac{f}{2} + \frac{1}{3} \tan^3 \frac{f}{2} \quad (2.22)$$

where $q = a(1 - e)$, and for the hyperbolic case,

$$r = \frac{a(e^2 - 1)}{1 + e \cos f} \quad (2.23)$$

$$r = a(e \cosh F - 1) \quad (2.24)$$

$$\tanh \frac{F}{2} = \left(\frac{e-1}{e+1} \right)^{1/2} \tan \frac{f}{2} \quad (2.25)$$

$$v^2 = \mu \left(\frac{2}{r} + \frac{1}{a} \right) \quad (2.26)$$

$$e \sinh F - F = M = \left(\frac{\mu}{a^3} \right)^{1/2} (t - T). \quad (2.27)$$

2.2.2. Orbital elements from position and velocity

The position and the velocity of an object along its orbit can be obtained from the solution of the above equations. The reverse problem which is often of interest in cometary studies is to determine the elements of the orbit from a given set of position, velocity and time.

Let the position of the body in the heliocentric coordinate system at a time t be (x, y, z) and the velocity components $(\dot{x}, \dot{y}, \dot{z})$. Then

$$r^2 = x^2 + y^2 + z^2 \quad (2.28)$$

and

$$v^2 = \dot{x}^2 + \dot{y}^2 + \dot{z}^2. \quad (2.29)$$

Since r and v are known, the semimajor axis can be calculated from Eq. (2.8).

The areal constant h may be regarded as the vector product of \mathbf{r} and the orbital velocity \mathbf{v} of the comet relative to the Sun. If the components of \mathbf{h} along x, y and z directions are represented as h_x, h_y and h_z then,

$$\begin{aligned} h_x &= y\dot{z} - z\dot{y} \\ h_y &= z\dot{x} - x\dot{z} \\ h_z &= x\dot{y} - y\dot{x} \end{aligned} \quad (2.30)$$

and

$$h^2 = h_x^2 + h_y^2 + h_z^2 = \mu p.$$

Therefore the value of p the length of the semilatus rectum can be calculated. From a knowledge of p and a, e can be obtained from the relation

$$p = a(1 - e^2). \quad (2.31)$$

The projection of \mathbf{h} onto the three planes yz , zx and xy gives the following expressions

$$\begin{aligned} h \sin i \sin \Omega &= \pm h_x \\ h \sin i \cos \Omega &= \mp h_y \\ h \cos i &= h_z. \end{aligned} \quad (2.32)$$

Hence, the above equations give i and Ω . The upper sign and lower sign refer to the cases when i is less than or greater than 90° .

The value of $(\omega + f)$ can be derived from the following relations which relate the position of the point (x, y, z) in terms of the angles of the orbit.

$$\sin(\omega + f) = \frac{z}{r} \operatorname{cosec} i \quad (2.33)$$

and

$$\cos(\omega + f) = \frac{1}{r}(x \cos \Omega + y \sin \Omega).$$

The value of f can be obtained from the relation

$$r = \frac{(h^2/\mu)}{1 + e \cos f}. \quad (2.34)$$

Hence ω can be determined. The only other quantity remaining to be determined is the time of the perihelion passage T , which depends upon the conic section. For an elliptical orbit the eccentric anomaly E can be obtained from the Eqs. (2.16) or (2.17). knowing E, e, n and f , the value of T can be calculated from the Eq. (2.19).

Therefore all the elements a, e, i, ω, Ω and T can be determined. The procedure for the other two types of orbits are also similar. For parabolic and hyperbolic orbits, the Eqs. (2.22) and (2.27) may be used to evaluate T .

2.2.3. Orbital elements from observations

Since in general six elements are required to specify completely the orbit in space, it follows that six independent quantities must be obtained by the observations. A single observation gives only two quantities say, in terms of the angular coordinates α and δ of the body. Therefore in all, three different sets of observations are required to define its orbit.

Let the heliocentric equatorial rectangular coordinates of the comet and the Earth at any given time be denoted by (x, y, z) and (X, Y, Z) respectively with respect to the plane of the celestial equator. Let their heliocentric distances be r and R which are given by

$$r^2 = x^2 + y^2 + z^2$$

and

$$R^2 = X^2 + Y^2 + Z^2. \quad (2.35)$$

Then neglecting comet's mass,

$$\ddot{x} = -\frac{GMx}{r^3} \quad (2.36)$$

and for the Earth

$$\ddot{X} = -\frac{G(M + m_e)X}{R^3} \quad (2.37)$$

where M and m_e are the mass of the Sun and the Earth respectively.

Let the geocentric direction cosines of the comet be l, m and n and its geocentric distance be ρ . Then

$$x = X + l\rho$$

$$y = Y + m\rho$$

and

$$z = Z + n\rho. \quad (2.38)$$

The direction cosines l, m and n are given in terms of the observed position of the comet, right ascension α and declination δ , as

$$l = \cos \alpha \cos \delta$$

$$m = \cos \delta \sin \alpha$$

and

$$n = \sin \delta. \quad (2.39)$$

Equations (2.36), (2.37) and (2.38) give

$$\ddot{\rho}l + 2\dot{\rho}l + \rho\ddot{l} = -GM\frac{(X + l\rho)}{r^3} + G(M + m_e)\frac{X}{R^3} \quad (2.40)$$

or

$$\left(\ddot{\rho} + \frac{GM\rho}{r^3} \right) l + 2\dot{\rho}l + \rho\ddot{l} = -GX \left(\frac{M}{r^3} - \frac{M + m_e}{R^3} \right). \quad (2.41)$$

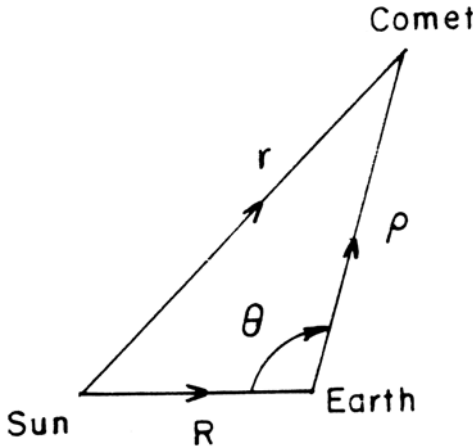


Fig. 2.4 Shows the geometry of the triangle with distances marked.

There will be two other equations in Y and Z . These equations may be solved to give $(\ddot{\rho} + (GM\rho/r^3))$, $2\dot{\rho}$ and ρ . Except for r , all other quantities are known or can be derived from the observed quantities; r can also be expressed in terms of ρ . From the triangle whose sides are R, r and ρ (Fig. 2.4) the following relation may be obtained:

$$r^2 = R^2 + \rho^2 - 2\rho R \cos \theta \quad (2.42)$$

where θ is the angle between R and ρ . The projection of R in the direction of ρ gives

$$R \cos \theta = -(lX + mY + nZ). \quad (2.43)$$

Therefore

$$r^2 = R^2 + \rho^2 + a_1 \rho \quad (2.44)$$

where

$$a_1 = 2(lX + mY + nZ).$$

Equations (2.41) and (2.44) can be solved for r and ρ . Knowing the values of r and ρ , the comet's heliocentric coordinates (x, y, z) and the velocity components $(\dot{x}, \dot{y}, \dot{z})$ can then be obtained from the relations

$$\begin{aligned} x &= X + l\rho \\ \dot{x} &= \dot{X} + l\dot{\rho} + l\rho \end{aligned} \quad (2.45)$$

and with similar equations for y, \dot{y}, z and \dot{z} . Knowing the position and velocity of the comet, the orbital elements and hence the orbit can be

determined from the method already discussed. The method outlined above is generally referred to as *Laplace's method*.

The actual computation involves a knowledge of the value l, m, n, X, Y, Z and their derivatives. The values of X, Y, Z are given in the Ephemeris. From this data the values of the first derivative can be found out. The calculation of geocentric direction cosines, their first and second derivatives can be deduced from three observations of the comet which are not too far off from each other. Let the dates of observation be t_1, t_2 and t_3 . The right ascension and declination for these three times are known. Here we will just show an approximate method of getting the first and second derivatives. In actual practice one can use various refined methods.

The average value of the first derivative of l for the time between t_1 and t_2 is given by

$$\dot{l}_{12} = \frac{l_2 - l_1}{t_2 - t_1}. \quad (2.46)$$

Similarly

$$\dot{l}_{23} = \frac{l_3 - l_2}{t_3 - t_2}. \quad (2.47)$$

If the time interval $(t_2 - t_1) \approx (t_3 - t_2)$, then the value of \ddot{l} at time t_2 is approximately equal to

$$\ddot{l}_2 = \frac{1}{2} [\dot{l}_{12} + \dot{l}_{23}]. \quad (2.48)$$

Similarly

$$\ddot{l}_2 = \frac{\dot{l}_{23} - \dot{l}_{12}}{\frac{1}{2}(t_3 - t_1)}. \quad (2.49)$$

Similar relations for the first and second derivatives and m and n can be obtained.

The elements obtained from three sets of observations define the initial orbit of the comet. For getting a better orbit it is necessary to have many more observations. The initial orbit can be improved further as more and more observations become available. In fact equations can be set up for the difference between the predicted and the observed positions. These can then be solved to get the corrections for the preliminary orbit elements. This procedure will eventually lead to a more accurate orbit. Such an orbit is called a 'definitive orbit'. The orbit calculated based on the six elements gives the position of the comet in space. In order to find the position of the comet in the plane of the sky, it is necessary to know the position of earth

in space. The geometrical position of the earth can be obtained from the ‘ephemeris’ which is used to find the position of the comet in the plane of the sky.

In the discussion so far, it is assumed that the comet is only under the influence of the Sun’s gravitational field. But in actual practice the orbit gets perturbed due to the planets as comets enter the solar system. The dominant effect arises mainly from the planets Jupiter and Saturn because of their large masses. When the comet is far off, the perturbation produced due to stars, has also to be considered. The calculations which include many of these perturbations have been carried out numerically. Through these efforts the dynamical evolution of comets has been studied.

Problems

1. The components of velocity of a body are $(0, 1, 3)$ corresponding to the position $(4, 2, 1)$. Calculate a and e . What is the nature of the orbit? Assume for simplicity $\mu = 1$.
2. The ecliptic heliocentric coordinates of position and velocity of a comet are $(4, 2, 3)$ and $(2, 2, 1)$ respectively on March 16, 1959. Find the elements of the orbit of the comet. Here again assume $\mu = 1$.
3. The time period of the Earth around the Sun is 1 year and its orbital velocity is 30 km/sec. Compute the distance from the Earth to the Sun.
4. Calculate the lifetime of comets which have aphelion distances of 5 AU and 5×10^4 AU, are almost in parabolic orbits and can survive 1000 perihelion passages.
5. The comet moving in an elliptical orbit has an eccentricity of 0.985. Compare its velocity at perihelion and aphelion.
6. Show that in elliptic motion about a focus under attraction μ/r^2 , the radial velocity is given by the equation

$$r^2 \dot{r}^2 = \frac{\mu}{a} \{a(1 + e) - r\} \{r - a(1 - e)\}$$

7. Calculate roughly the distance from the Sun beyond which Comet Halley spends about half of its total time period of 76 yrs.
8. Estimate the average values of r , dr/dt , dv/dt and the kinetic energy in an elliptical orbit taking time as an independent variable.
9. A satellite is orbiting in a circle at an altitude of 600 km. Knowing the radius and surface gravity of the Earth, calculate its orbital velocity

and period of revolution. If it is brought to an altitude of 400 km, what is the time period?

References

The solutions of the equations of Sec. 2.2.3 are specially discussed in:

1. Moulton, F.R. 1970. *An Introduction to Celestial Mechanics*, New York: Dover Publications Inc.
2. Roy. A.E. 1965. *The Foundations of Astrodynamics*, New York: The Macmillan Company.
3. Danby, J.M.A. 1988. *Foundations of Celestial Mechanics*, Richmond: Willmann-Bell, Inc.
- Orbit calculation with personal computer
4. Boulet, D.L. 1991. *Methods of Orbit determination with Micro Computer*: Richmond: Willmann-Bell, Inc.

CHAPTER 3

Physical Aspects

The gaseous material of a comet is immersed in the radiation field of the Sun. The study of the interaction between the two requires knowledge of some of the basic laws of radiation as well as of the spectroscopy of atoms and molecules. Here we will briefly review some of the relations which are used in subsequent chapters for interpreting the cometary observations.

3.1. Black Body Radiation

The energy radiated at different wavelengths by a black body (which absorbs all of the incident radiation) at temperature T is given by Planck's law

$$B_\lambda d\lambda = \frac{2hc^2}{\lambda^5} \frac{1}{e^{hc/\lambda kT} - 1} d\lambda \quad (3.1)$$

where h , k and c denote the Planck constant, Boltzmann constant and the velocity of light respectively. Figure 3.1 shows a plot of the Eq. (3.1) for several temperatures which shows clearly the shift of the maximum of the curve to shorter wavelengths with an increase in temperature. The wavelength corresponding to the peak of the curve λ_{\max} can be represented by the equation

$$\lambda_{\max} T = 0.2897 \quad (3.2)$$

known as Wien's displacement law. Figure 3.1 also shows that the total amount of the radiation emitted shifts gradually from the ultraviolet to the visible and to the infrared spectral regions as the temperature goes from a higher value to a lower value.

If the photon energy $h\nu$ is very much less than the thermal energy i.e. $h\nu \ll kT$, the Planck's formula simplifies to

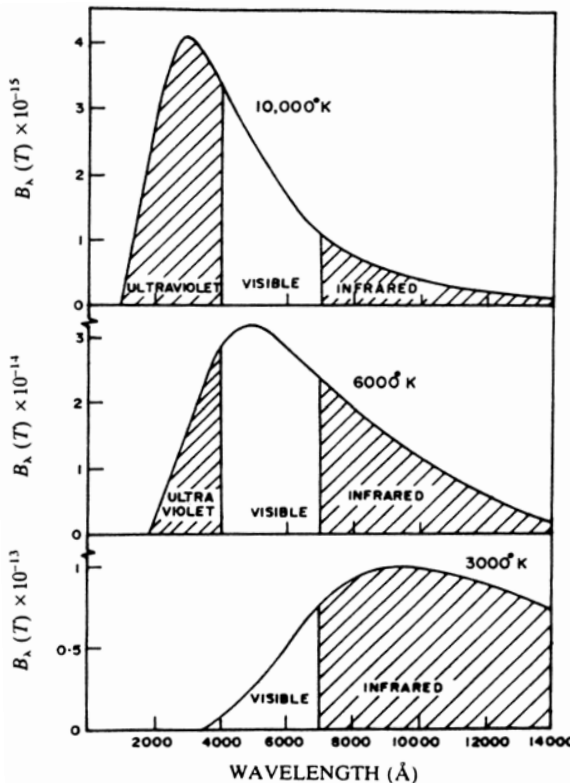


Fig. 3.1 The Planck function for various temperatures. The regions of ultraviolet, visible and infrared are clearly marked.

$$B_\nu(T) = \frac{2\nu^2 k T}{c^2} \quad (3.2a)$$

This is the well known *Rayleigh - Jeans law* which is valid for long wavelength region, such as radio wavelength region. This is extensively used in the study molecules in the radio region.

The energy density u_ν of the radiation field is related to B_ν through the relation

$$u_\nu = \frac{4\pi}{c} B_\nu(T) \quad (3.3)$$

The total energy density is given by

$$u = \int u_\nu dv = aT^4 \quad (3.4)$$

where a is the radiation constant. The relation (3.4) known as the *Stephan-Boltmann law*, shows that the energy density of the black body radiation depends upon the fourth power of temperature.

3.2. Perfect Gas Law

The particles of gas in a container which are constantly in motion collide with each other as well as with the walls of the container, giving rise to a resultant force and hence the pressure. The pressure is a function of the density of the gas and the temperature. For a perfect gas, in which the interatomic or intermolecular forces can be ignored, there is a simple mathematical relation between the pressure, density and temperature of the gas, called the *equation of state*. The equation of state for a perfect gas is given by

$$p = nkT \quad (3.5)$$

where p , n and T represent the pressure, density and temperature, respectively.

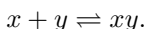
For a gas containing a number of non-interacting species of various types each exerting its own pressure, the total gas pressure is just the sum of the various components, i.e.

$$p = \sum p_i = \sum n_i kT. \quad (3.6)$$

3.3. Dissociative Equilibrium

If the gaseous medium is at a low temperature, the atoms can combine together to form molecules. These molecules in turn may dissociate giving back the atoms. Finally an equilibrium situation will be reached when the direct and the reverse processes balance each other. For such an equilibrium situation, it is possible to calculate the number of molecules formed out of the individual atoms for a given temperature.

Consider two atoms x and y combining together to form the diatomic molecule xy , i.e.



For the equilibrium situation one has the relation

$$\frac{p(x)p(y)}{p(xy)} = K(xy) \quad (3.7)$$

where $p(x)$, $p(y)$ and $p(xy)$ are partial pressures of x , y and xy respectively. $K(xy)$ is called the *equilibrium constant* or the *dissociation constant* of the reaction. The equilibrium constant depends upon the temperature and on various parameters of the molecule. An expression for the equilibrium constant can be obtained in an explicit form as

$$\begin{aligned} \log_{10}K_{xy}(T) &= \log_{10}\frac{p_x p_y}{p_{xy}} = -\frac{5040.4D}{T} + \frac{5}{2}\log_{10}T \\ &\quad + \frac{3}{2}\log_{10}M + \log_{10}\frac{Q_x Q_y}{Q_{xy}} + 4.41405. \end{aligned} \quad (3.8)$$

Here M is the reduced mass of the molecule equal to $(m_{xy}/(m_x+m_y))$ where m_x , m_y and m_{xy} are the masses of x , y and xy respectively. The Q 's are the *partition functions* and D is the energy required to dissociate the molecule called the *dissociation energy*. For many molecules of astrophysical interest the equilibrium constant can be calculated from Eq. (3.8) as all the relevant spectroscopic parameters are known. Since the equilibrium constant is a function of the temperature, one usually fits the calculated data with a polynomial expression of a suitable form.

3.4. Doppler Shift

The frequency of the emitted radiation depends upon the relative velocity of the source and the observer. The effect is produced only by the component of velocity in the direction towards or away from the observer called the *radial velocity*. The shift of the lines produced as a result of the above motion is termed as *Doppler shift* or *Doppler effect*. The expected shift for a source moving with the velocity v is given by

$$\frac{\Delta\lambda}{\lambda_o} = \frac{(\lambda - \lambda_o)}{\lambda_o} = \frac{v}{c} \quad (3.9)$$

where λ and λ_o are the observed and the laboratory wavelength respectively. The relative velocity of the source is denoted as positive if it is moving away from the observer and negative if it is moving towards the observer. In the

former case, the shift is towards longer wavelengths while in the latter case it is towards shorter wavelengths. From the measurement of the shift of the lines using Eq. (3.9), it is possible to determine the velocity of the source. Doppler shift has been used extensively in astronomy to derive the relative velocities of the various astronomical objects.

3.5. Spectroscopy

3.5.1. Atomic spectroscopy

Bohr's formalism of the absorption and emission processes in atoms is that the lines arise out of transitions between well-defined electron energy levels having definite quantum number. The wavelength of the emitted radiation arising out of the two energy levels E_1 and E_2 ($E_2 > E_1$) is represented by

$$\lambda = \frac{hc}{E_2 - E_1} \quad (3.10)$$

When the transition takes place from a lower level to a higher level, the energy is lost from the incident radiation and it gives rise to an *absorption* line. If the reverse process takes place it releases the energy and is known as the *emission* line.

The energy level diagram for the hydrogen atom, which has a single orbital electron around a proton, is shown in Fig. 3.2. The energy levels are defined by the principle quantum number n which can take values $n = 1, 2, \dots, \infty$. The *Lyman* series arises out of the transition from $n = 2, 3, \dots$ to $n = 1$. The Lyman α line corresponding to transition $n = 2$ to $n = 1$ has a wavelength of 1216 Å and is in the ultraviolet region. This line is very strong in comets. Most of the lines of the *Balmer* series lie in the visible spectral region. Similarly there are *Paschen*, *Brackett* and other series, whose lines lie mostly in the infrared region.

As n increases, the energy levels come closer and closer together and finally they coalesce. The transitions arising out of these highest levels give rise to a continuum. The excitation potential of a line is the energy required to excite the line. The excitation potential for the Lyman α line is 10.15 eV. The *ionisation potential* is the energy required to remove the electron *completely* from the atom. For the hydrogen atom this energy is 13.54 eV. For atoms with more electrons, the spectra becomes complicated.

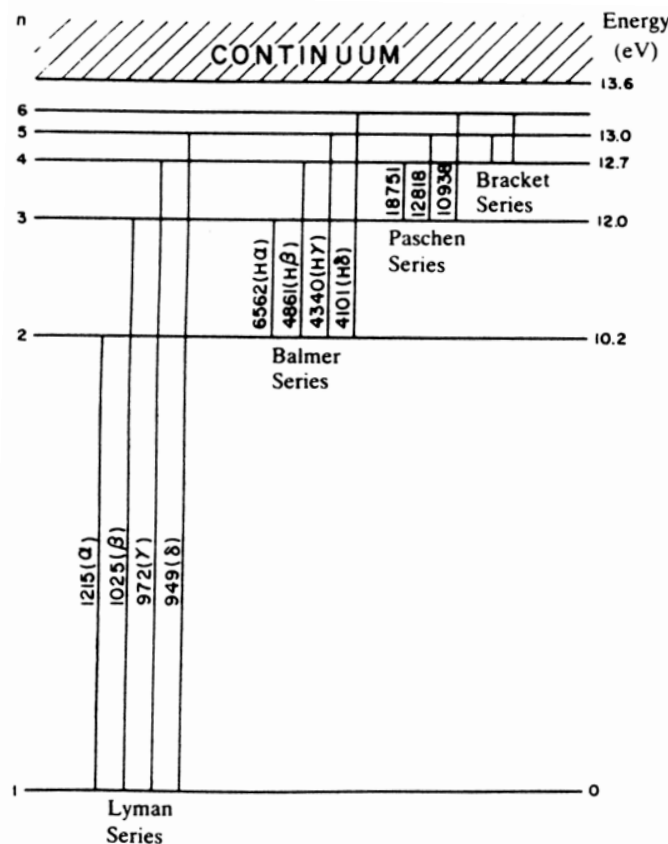


Fig. 3.2 Energy level diagram of the hydrogen atom showing various transitions.

However, the basic model on which they can be explained remains the same except that one has to consider various types of transitions.

Since the electrons in an atom have orbital and spin angular momenta around the nucleus, they are therefore characterised by three quantum numbers, n, l and j . They denote *total* quantum number, the *orbital angular momentum* quantum number and the *total angular momentum* quantum number. The quantum number j for the case of l and s coupling is given by

$$j = l + s$$

where s is the *spin* quantum number representing the spin of the electron and can take the values $+\frac{1}{2}$ and $-\frac{1}{2}$. For many electron systems, the vector sum of the above quantities has to be taken and is represented by the capital letters L , S and J . Therefore

$$L = \sum l_i, \quad S = \sum s_i, \quad \text{and} \quad J = L + S.$$

The J levels are in general degenerate with $(2J + 1)$ levels. They split up into $(2J + 1)$ levels in the presence of an external magnetic field. L can take values 0, 1, 2 up to $(n - 1)$ and they are represented as S, P, D, F,... terms. The value with $S = 0, \frac{1}{2}, 1, \dots$ denotes the *multiplicity* of the levels and refers to lines as *singlets*, *doublets*, *triplets*, etc. The level is generally written as

$$n^{(2S+1)} L_J$$

where n is the total quantum number, $(2S + 1)$ gives the multiplicity, J the total angular momentum and L is the term symbol.

In general, the transitions between various levels have to satisfy certain *selection* rules. For electric dipole transitions the selection rules are the following:

$$\begin{aligned}\Delta J &= 0, \pm 1 \quad \text{with} \quad J = 0 \not\rightarrow J = 0 \\ \Delta L &= 0, \pm 1 \\ \Delta S &= 0.\end{aligned}$$

In situations where dipole transitions are forbidden it is possible to observe magnetic or quadrupole transitions. These are called *forbidden* lines. The transition probabilities of these lines are much smaller than those of allowed transitions. Many of the forbidden lines have been observed in various astrophysical situations because of low density present in them. Collisions are infrequent in such an environment and hence forbidden lines can be seen. Many of these lines cannot usually be observed under normal laboratory conditions. The forbidden lines are generally denoted with a square bracket. For example the forbidden line $\lambda = 6300 \text{ \AA}$ of oxygen arising out of 1D level is denoted as $O[{}^1D]$. If the atom is neutral, it is designated by putting I in front of the chemical symbol, like OI, NI, ... The symbols II, III,... represent atoms in singly ionized, doubly ionized states like NII, NIII,...

3.5.2. Molecular spectroscopy

Many of the diatomic and complex molecules are abundant in objects like the Sun, the cool stars and comets. If the two atoms in the diatomic molecule are of the same type, it is called a *homonuclear* molecule. Examples of this type are H₂, N₂, O₂ etc. If the two atoms are of different types, like CN, CH, OH, etc., it is called a *heteronuclear* molecule. The spectrum of even the simplest diatomic molecule shows complicated behaviour comprising different bands and each band itself is made up of many lines. This is due to the fact that the two atoms in the molecule can vibrate individually along the common axis as well as rotate along the axis perpendicular to the common axis. The total energy of the molecule is the sum total of the kinetic and potential energies of the electrons and the nuclei. This is generally represented in terms of the potential energy curves which give the variation of the potential energy as a function of the internuclear separation. The energy required to separate a stable molecule into its components is called the *dissociation energy* of the molecule. The various vibrational energies of the molecule are denoted by the *vibrational* quantum number v and can take values 0, 1, 2,... Each vibrational level is further split up into various rotational levels denoted by the rotational quantum number J . Therefore each electronic state has many vibrational levels, each of which in turn has several rotational levels as shown schematically in Fig. 3.3. A transition can take place between vibrational and rotational levels of the two electronic states. The total energy E, of the molecule can be represented as a sum of the electronic (E_{e1}), vibrational (E_{vib}) and rotational (E_{rot}) energies, namely

$$E_{\text{total}} = E_{e1} + E_{\text{vib}} + E_{\text{rot}}. \quad (3.11)$$

In terms of actual energies

$$E_{e1} > E_{\text{vib}} > E_{\text{rot}}.$$

The electronic transitions give lines which fall in the visible and UV regions while those of rotational transitions lie in the infrared and far-infrared regions. The vibrational energy of the molecule can be represented as

$$\begin{aligned} G(v)hc \equiv E_{\text{vib}} &= hcw_e \left(v + \frac{1}{2} \right) - hcw_e x_e \left(v + \frac{1}{2} \right)^2 \\ &\quad + hcw_e y_e \left(v + \frac{1}{2} \right)^3 + \dots \end{aligned} \quad (3.12)$$

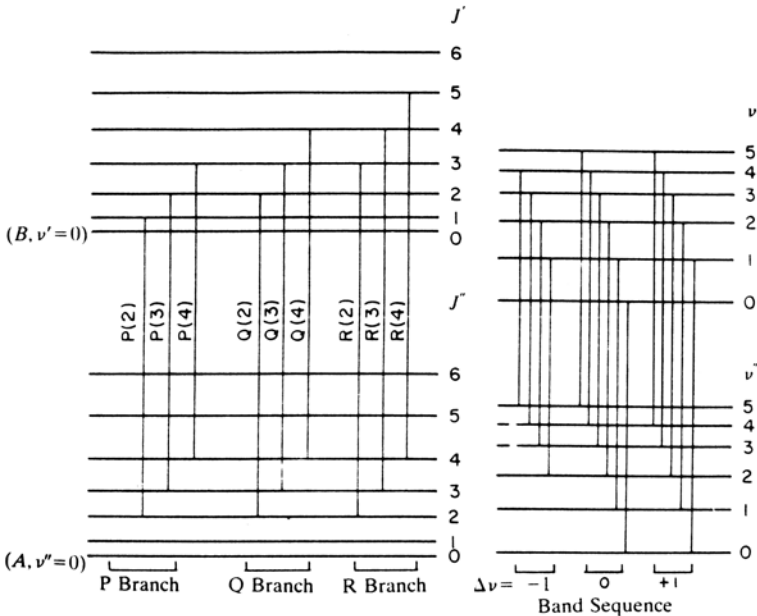


Fig. 3.3 Schematic representation of the vibrational and rotational levels of two electronic states A and B of a molecule. The left one shows the transitions involving P, Q and R branches. The right one shows the transitions which define the band sequence (see text).

where w_e , w_{ex_e} and w_{ey_e} are the spectroscopic constants of the molecule.

The expression for the rotational energy is of the form

$$F(J)hc = E_{\text{rot}} = \frac{\hbar^2}{8\pi^2 I} J(J+1) = hcBJ(J+1) \quad (3.13)$$

where $B = [h/(8\pi^2 cI)]$, J is the rotational quantum number and it can take values, $0, 1, 2, \dots$ I is the moment of inertia of the molecule. B is known as the *rotational constant* of the molecule. All the quantum numbers of the lower electronic level (T'') are denoted as double prime (''), like v'' and J'' , while that of the upper level (T') as prime ('') like v' and J' . Therefore, the wave number (cm^{-1}) of the transition between the two electronic states is given by

$$\begin{aligned} \nu = \frac{1}{hc} & \{ [E_{\text{el}}(T') - E_{\text{el}}(T'')] + [E_{\text{vib}}(v') - E_{\text{vib}}(v'')] \\ & + [E_{\text{rot}}(J') - E_{\text{rot}}(J'')] \}. \end{aligned} \quad (3.14)$$

The classification of the electronic states of a molecule is based on a scheme similar to that employed for atoms. L , i.e., $(L_1 + L_2)$ and S , i.e., $(S_1 + S_2)$ are the total angular momenta of the two atoms in the molecule. The projections along the axis of the molecule are denoted as Λ and Σ . Λ can take values $0, 1, 2, \dots, L$. The designations used for these states are

$$\begin{array}{llllll} \text{for } \Lambda = & 0 & 1 & 2 & 3 & \dots \\ & \Sigma & \Pi & \Delta & \Phi & \dots & (\text{for molecules}) \\ \text{similar to } & S & P & D & F & \dots & \text{in the atomic case.} \end{array}$$

The total angular momentum Ω is given by

$$\Omega = \Lambda + \Sigma$$

which is similar to the case of quantum number J in the atomic case. The selection rules for the electronic transitions are

$$\begin{aligned} \Delta\Lambda &= 0, \pm 1 \\ \Delta\Sigma &= 0 \end{aligned}$$

and

$$\Delta\Omega = 0, \pm 1.$$

The transition between any two electronic states, is determined by the vibration-rotation structure of the two states involved. There are no rigorous selection rules for the vibrational quantum number and so the transition can take place between any two vibrational levels of the two electronic states. A pure vibrational transition between the two electronic states, called a *band* is denoted as (v', v'') , i.e., the quantum number of the upper level is written first. Thus for example $(2, 0)$ means a transition from the upper vibrational level $v' = 2$ to the lower vibrational level $v'' = 0$. Pure vibrational transitions in a given electronic state are allowed for heteronuclear molecules but not for homonuclear molecules like C_2 , N_2 , etc.

Each of the vibrational bands is further split up into a large number of rotational lines. The selection rule for the rotational quantum number J is given by $\Delta J = J' - J'' = 0, \pm 1$. However, if $\Lambda = 0$, only $\Delta J = \pm 1$ is allowed. Therefore, the rotational transitions give rise to three series of lines called P, Q and R branches corresponding to $\Delta J = -1, 0, +1$ (Fig. 3.3).

The rotational lines of a given vibrational band cannot in general be resolved in low resolution spectra and therefore it results in a blended feature. It can be resolved with a higher spectral resolution. For some molecules the bands arising for the same change in the vibrational quantum number in going from the upper to the lower electronic state have wavelengths very close to each other. Therefore these bands cannot be resolved and give rise to blended features known as *band-sequences* (Fig. 3.3). For example, $\Delta v = 0$ of the Swan band sequence for the C_2 molecule occurs around $\lambda = 5165 \text{ \AA}$ (Fig. 4.1). To separate the bands from the band-sequences, it is necessary to go in for even higher resolutions. To resolve rotational structure, still higher resolutions are required (Fig. 5.17).

As in the atomic case, the molecular term can be written as

$$Z^{(2S+1)}\Lambda_{\Omega}$$

where Z represents the designation of the electronic state, $(2S + 1)$ the multiplicity where S is the electron spin, Ω the total angular momentum and Λ is the kind of term like Σ, Π , etc. As a typical case, the designation of some of the band systems are given below for illustrative purposes.

$(B^2\Sigma - X^2\Sigma)$ of the CN system and $(A^2\Pi - X^2\Sigma)$ of the CO^+ system and so on.

3.5.3. Chemical subgroups

Certain chemical subgroups of atoms in a complex molecule, such as $-CH_2-$ (methylene), $-CH_3$ (methyl) etc. vibrate at characteristic stretching and bending frequencies for that group. This gives rise to absorption or emission lines at or near the same frequency regardless of the structure of the rest of the molecule. Therefore infrared spectra can be used as a diagnostic of the chemical subgroup present in the material. The chemistry dominated by the cosmically abundant H, C, N and O atoms and the diagnostic bands fall almost exclusively in the near and mid-infrared region between 2.5 and 25 μm . The various spectral signatures in the mid-infrared region arising out of subgroups composed of H, C, N and O is shown in Fig. 3.4. Figure 3.4 show that hydrocarbons have characteristic frequency in the 3–3.4 μm and 5–8 μm regions depending on the exact chemical composition and configuration of the larger molecules containing the spectrally active groups. Therefore, infrared spectra is used extensively to classify species and subgroup by chemical type, like aliphatic vs aromatic hydrocarbons etc. As for example, the 3.4 μm emission feature seen

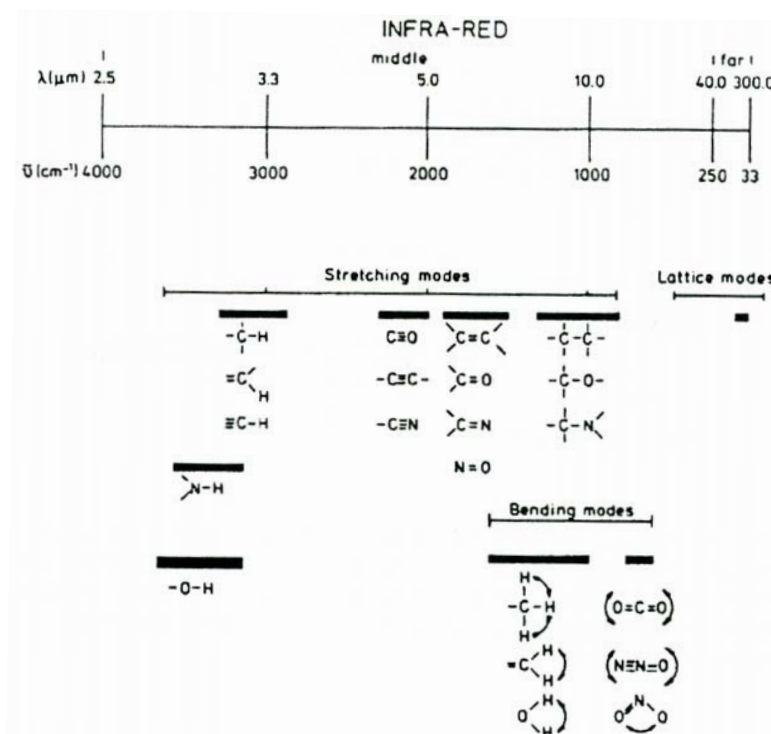


Fig. 3.4 The vibrational frequency ranges of various molecular groups (Allamandola, L.J. 1984. In *Galactic and Extragalactic Infrared Spectroscopy*, Eds. M.F. Kessler and J.P. Phillips, D. Reidel Publishing Company, p. 5: with kind permission of Springer Science and Business Media).

from astronomical sources is generally attributed to C-H stretching modes of $-\text{CH}_2-$ and $-\text{CH}_3$ groups in aliphatic hydrocarbons. This feature will be seen in all biological molecules.

3.6. Isotopic Effect

The diatomic molecules which have the same atomic number but have slightly different masses can give rise to a separation of the lines. This is known as *isotopic shift*. The difference in the emitted frequencies between the two isotopic molecules arises through the difference in the reduced masses of the two molecules. The spectroscopic constants of the isotopic molecules (i) and the ordinary molecule are related by the following rela-

tions.

$$w_e(i) = \rho w_e$$

$$w_e x_e(i) = \rho^2 w_e x_e$$

and

$$w_e y_e(i) = \rho^3 w_e y_e \quad (3.15)$$

where

$$\rho = \left[\frac{\mu}{\mu(i)} \right]^{\frac{1}{2}}$$

Here μ denotes the reduced mass of the molecule. The amount of the shift depends upon the ratio of the masses and on the value of the vibrational quantum number v . In the case when only the first term in the energy term included, the isotopic shift is given by

$$\Delta\nu_{\text{shift}} = (1 - \rho) \left[\left(v' + \frac{1}{2} \right) \omega'_e - \left(v'' + \frac{1}{2} \right) \omega''_e \right] \quad (3.16)$$

Therefore, the isotopic shift is a function of the value of $(1 - \rho)$. The larger the deviation from unity, the greater will be the shift of the lines. The sign of $(1 - \rho)$ indicates the type of shift expected. The negative sign implies a shift towards shorter wavelengths. For example, the $(1,0)$ band of the blue degraded Swan $\Delta v = +1$ sequence occurs around 4737 Å while that of ^{12}C ^{13}C occurs around 4745 Å.

The isotopic mass difference also has an effect on the rotational constant B which in turn changes the rotational levels as

$$F^i(J) = \rho^2 B J(J+1). \quad (3.17)$$

Therefore, the isotopic effect could also be seen in the rotational spectra of the molecules.

3.7. Franck-Condon Factors

The electronic transitions in a molecule give rise to several types of intensity patterns depending on the type of the molecule. For example, for some molecules $(0, 0)$ transitions is the strongest, while for others the strongest line may be for a different value (v', v'') . The observed variations in the intensity distributions can be understood in terms of the *Franck-Condon principle*. The basic idea is the following. The electron jump takes place

from one electronic state to another preferentially at the turning points of any vibrational level. This is due to the fact that the time of passage between these two turning points is much shorter than the time spent at the turning points. Therefore, the relative position and velocity after the transition is the same as before the transition. Hence, if a transition takes place from a given value of v' of the upper state, the quantum number of the jumped lower state depends on the location and shape of the two potential curves. Figure 3.5 shows the expected results for two cases. In one case

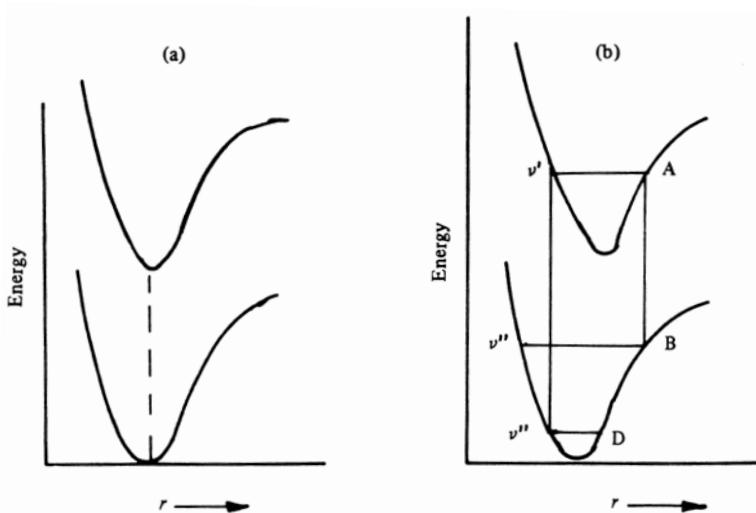


Fig. 3.5 Understanding of the expected intensity distribution in emission according to the Franck-Condon principle (see text). The minimum of the curve corresponds to the equilibrium position.

the minimum of the potential curves is nearly one above the other, while in the second case, one is shifted for higher values of r . Based on the Franck-Condon principle the $(0, 0)$ transition should be the strongest for case 1. For case 2, the strongest lines will be arising from the higher values of v' . For emission lines, there will be two values of v'' , corresponding to points B and D in Fig. 3.5 for which the intensity will be maximum. The locus of the strongest bands is a parabola called the *Condon parabola*. The Condon parabola can be calculated theoretically provided the potential curves are known. The Franck-Condon factors give a measure of the relative band intensities for an electronic transition.

3.8. Intensity of Emitted Lines

The intensity of a spectral line in emission, defined in ergs/sec, is given by

$$I_{21} = N_2 A_{21} h \nu_{21}. \quad (3.18)$$

Here N_2 is the number of the species in state 2 and ν_{21} is the frequency of the emitted radiation from state 2 to state 1. A_{21} is the *Einstein coefficient* which gives the probability for a spontaneous transition from state 2 to state 1, even without any external influence. The Einstein coefficient may be expressed in terms of a parameter called the *strength* S_{21} of a line as

$$g_2 A_{21} = \frac{64\pi^4 \nu_{21}^3}{3hc^3} S_{21} \quad (3.19)$$

where g_2 is the *statistical weight* or the *degeneracy* of the upper level. Other quantities have their usual meanings. The mean life of state 2 is

$$\tau_2 = \frac{1}{A_{21}}. \quad (3.20)$$

It is instructive to see the order of value of τ for various types of transitions. For electronic transitions $\tau \sim 10^{-8}$ sec ($A = 10^8$ sec $^{-1}$). For vibrational transitions $\tau \sim 10^{-3}$ sec ($A = 10^3$ sec $^{-1}$) and for rotational transitions $\tau \sim 1$ sec ($A = 1$ sec $^{-1}$). The Einstein values B_{12} and B_{21} represent the probability for the absorption and induced emission processes and is given by

$$g_2 B_{21} = g_1 B_{12} = \frac{8\pi^3}{3h^2} S_{21}. \quad (3.21)$$

The *total line strength* S_{21} of the molecular line is the product of electronic, vibrational and rotational components. Therefore

$$S_{21} = S_{e1} S_{vib} S_{rot}. \quad (3.22)$$

In general the probability of a transition between two states of eigenfunctions ψ' and ψ'' is given by the equation

$$R = \int \psi' \mu \psi'' dr \quad (3.23)$$

where μ is the dipole moment. R^2 is proportional to the transition probability. Usually S_{el} and S_{vib} are combined together as

$$(S_{e1} S_{vib}) \equiv S_{e1}^{\text{vib}} = \left| \int \psi_{v'} R_e \psi_{v''} dr \right|^2 \quad (3.24)$$

Here R_e is called the *electronic transition moment*. $\psi_{v'}$ and $\psi_{v''}$ are the eigenfunctions for the vibrational states v' and v'' . R_e itself is defined by the expression

$$R_e = \int \psi'_e \mu_e \psi''_e d\tau_e \quad (3.25)$$

where ψ_e 's are the electronic wavefunctions and μ_e refers to the electric dipole moment for the electrons. In general the electron wavefunction ψ_e also depends to some extent on the internuclear distance r . Hence R_e should also depend on r . However, since the variation of R_e with r is slow, this variation is often neglected and R_e is replaced by an average value of R_e . Therefore Eq. (3.24) becomes

$$S_{el}^{\text{vib}} = R_e^2(r_{v'v''}) \left| \int \psi_{v'} \psi_{v''} dr \right|^2 \quad (3.26)$$

where $r_{v'v''}$ is called the *r-centroid* and it is a characteristic internuclear separation which can be associated with a given band (v', v'') and is given by

$$r_{v'v''} = \frac{\int \psi_{v'} r \psi_{v''} dr}{\int \psi_{v'} \psi_{v''} dr}. \quad (3.27)$$

The integral over the products of the vibrational wavefunctions of the two states of Eq. (3.26) is known as the *overlap integral* and is generally called the *Franck-Condon factors* of the (v', v'') band. Therefore, Eq. (3.26) can be written as

$$S_{el}^{\text{vib}} = R_e^2(r_{v'v''}) q_{v'v''} \quad (3.28)$$

where

$$q_{v'v''} = \left| \int \psi_{v'} \psi_{v''} dr \right|^2.$$

Hence Eq. (3.22) becomes

$$S_{21} = R_e^2(r_{v'v''}) q_{v'v''} S_{\text{rot}}. \quad (3.29)$$

Hence the electronic transition moment R_e^2 refers to *r-centroid* $r_{v'v''}$ and S_{rot} is usually known as *Höln-London factors*. Equation (3.29) shows that the total strength of a molecular line is essentially given by the product of the three-strength factors, namely the electronic transition, Franck-Condon factors and the Höln-London factors.

The values of the electronic transition moment for any band basically has to come from the laboratory measurements of the intensity of the lines, as theoretical calculations are very difficult. Enormous amount of work has

been carried out in various laboratories over the world to extract this basic data from the line intensity measurements of various bands. But the data is still very meagre. So for most of the cases, one ends up using either the mean value or an approximate value for the electronic transition moment.

The Franck-Condon factors can be calculated from a knowledge of the wavefunction of the vibrational levels, which comes out of the solution of the Schrödinger equation. For this, the potential function $U(r)$ has to be expressed in a convenient and mathematical form. There are various representations of the potential curve. The well-known function is that of Morse and is generally called *Morse function*. This has been extensively used in the literature as it is quite simple and convenient. However it does not represent the potential curves for all the cases exactly. So other expressions for the potential have been suggested. The one that is commonly used in recent years is known as the *RKR potential* referring to the authors Rydberg, Klein and Rees, who proposed it. In this method, the potential curve is constructed point by point from the laboratory measured values of the vibrational and rotational levels. The potential curves obtained in this way are much superior in many cases compared to Morse potential representation. The advantage of this method is the fact that it uses experimentally determined values of the quantities. However, the disadvantage is that the experimental values are often not of good quality and, in addition, this method is quite cumbersome. Many people have written computer programs to evaluate $q_{v'v''}$ and r -centroids for given values of input parameters. For many molecules of astrophysical interest, the values of $q_{v'v''}$ have been published in the literature.

On the other hand, the rotational strength factors have to be calculated from the theory. They depend upon the structure of the molecule, type of coupling, type of transition involved, etc. Until recently there existed a lot of confusion in the definition and normalization of Hönl-London factors. This has been clarified by several workers. The expression for the Hönl-London factors has been evaluated for various cases of interest and is available in the literature. Computer programs have also been written to compute these factors.

It is also possible to get an estimate of the Einstein A value or the oscillator strength f , directly from the laboratory measurements of the intensity of lines. Various techniques and methods have been employed to measure these quantities. The measurements are however hard to make and so there are not many measurements available at the present time. Even if they are available, the values by different methods or by different observers

often disagree. Therefore, one has to make use of laboratory measured values along with the calculated quantities in any particular situation.

3.9. Boltzmann Distribution

The calculation of the intensities of lines involves a knowledge of the relative population of atoms or molecules in different excited states. In a thermal equilibrium in which every process is balanced by its inverse, the population distribution among various levels is described according to *Boltzmann formula*. The population distribution between two discrete states 1 and 2 with an energy separation $\epsilon_{12} = E_2 - E_1$ is given by the expression

$$\frac{n_2}{n_1} = \frac{g_2}{g_1} e^{-\epsilon_{12}/kT} \quad (3.30)$$

where g_1 and g_2 are the *statistical weights* of the two levels and for an atom it is equal to

$$g(J) = 2J + 1$$

where J is the total angular momentum quantum number. The expression can be used to calculate the population distribution in different levels for a given temperature. Conversely, with a knowledge of the population in two or more levels, the excitation temperature can be determined.

3.10. Λ -Doubling

The assumption that the interaction between the angular momentum due to rotation of the molecule as a whole and the electron orbital angular momentum can be neglected is valid only for the case of $\Lambda = 0$. This corresponds to the case of Σ states. However, for the electronic states Π, Δ, \dots , for which $\Lambda \neq 0$, this interaction splits the rotational energy levels. This is called *Λ -doubling*. The splitting of the levels is generally very small and is of the order of 1cm^{-1} or less. Therefore the transitions between these levels will give rise to lines which lie in the radio frequency region. For transitions of the type (${}^1\Sigma - {}^1\Sigma$) there is no Λ -doubling. But for others like (${}^2\Sigma - {}^2\Pi$), the effect of Λ -doubling can be seen. Λ -doubling is the characteristic feature of molecules like OH, CH, etc., which have large rotational constants. The OH radical has been studied more extensively than any other radical. The energy level diagram of the hydroxyl radical,

with only a few vibrational levels is shown in Fig. 3.6. The strong (0,0) band

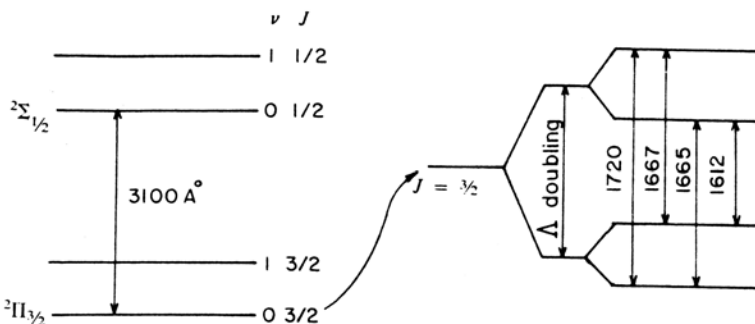


Fig. 3.6 Energy level diagram of the OH molecule and the associated Λ -doubling.

which is generally seen in emission in comets arises from the transitions as shown in Fig. 3.6. The lowest rotational level, corresponding to $v'' = 0$ and $J'' = 3/2$ is further expanded in Fig. 3.6 to show the Λ -splitting. The two Λ -doubling states are further split by the hyperfine interaction with the hydrogen nucleus. Therefore in all there are a total of four lines (Table 3.1). All these lines have been seen from many astronomical sources.

Table 3.1 Radio lines of the OH molecule.

Frequency (MHz)	Relative Intensities of lines	Transition probability (sec^{-1})
1612.23	1	4.50 (-12)
1665.40	5	2.47 (-11)
1667.36	9	2.66 (-11)
1720.53	1	3.24 (-12)

3.11. Photochemistry of Water

Extensive studies pertaining to photochemistry of water has been carried out through laboratory and theoretical studies. All these studies have shown that there are a large number of channels through which water can go through depending upon the impinging energy of the photon. The resulting fragments can further divide in several ways. All these possible

pathways are given in Table 3.2.

Table 3.2 Water photodissociation products.

Reaction		Threshold wavelength (\AA)
(a)	$\text{H}_2\text{O} + h\nu \rightarrow \text{OH} + \text{H}$	2424.6
	$\rightarrow \text{OH}(\text{A}^2\Sigma^+) + \text{H}$	1357.1
	$\rightarrow \text{H}_2 + \text{O}({}^1\text{D})$	1770
	$\rightarrow \text{H}_2 + \text{O}({}^1\text{S})$	1450
	$\rightarrow \text{H} + \text{H} + \text{O}({}^3\text{P})$	1304
	$\rightarrow \text{H}_2\text{O}^+ + e^-$	984
	$\rightarrow \text{H} + \text{OH}^+ + e^-$	684.4
	$\rightarrow \text{H}_2 + \text{O}^+ + e^-$	664.4
	$\rightarrow \text{OH} + \text{H}^+ + e^-$	662.3
(b)	$\text{OH} + h\nu \rightarrow \text{O} + \text{H}$	2823.0
	$\rightarrow \text{OH}^+ + e^-$	928
	$\text{H}_2 + h\nu \rightarrow \text{H} + \text{H}$	844.79
	$\rightarrow \text{H}_2^+ + e^-$	803.67
	$\rightarrow \text{H} + \text{H}^+ + e^-$	685.8
	$\text{O} + h\nu \rightarrow \text{O}^+ + e^-$	910.44
	$\text{H} + h\nu \rightarrow \text{H}^+ + e^-$	911.75

(a) Main pathways. (b) Fragment pathways. Adapted from Feldman, P.D., Cochran, A.L. and Combi, M.R. 2005, In *Comets II*, Eds. M.C. Festou, H.U. Keller and H.A. Weaver, Univ. Arizona Press, Tucson, p. 425.

In the first reaction the product $\text{OH}(\text{A}^2\Sigma^+)$ is produced in the highly excited state which decays giving rise to “*prompt*” emission lines. In the third reaction, the product is in the metastable levels $\text{O}({}^1\text{D})$ and $\text{O}({}^1\text{S})$ which give rise to forbidden lines.

These results are of direct relevance to comets as water is the dominant molecular specie in the coma of comets at heliocentric distances of around 1AU. In fact most of the products as mentioned in Table 3.2 have been observed in comets through spectroscopic means.

Among all the photo-dissociation fragments of H_2O , the velocity distribution of H in the reaction producing the products of H and OH is completely dominated by non-thermal component. This arises due to the fact that there is excess energy available over and above the energy required to overcome the chemical bond energy. This excess energy is imparted to the H atoms which result in the velocity of $\sim 17.8 \text{ km/sec}$. OH radical has

an excess velocity ~ 1.05 km/sec.

3.12. Silicate

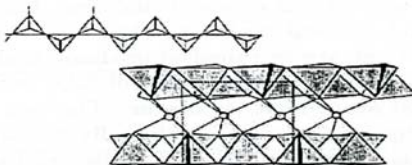
There are various types of silicates. They differ in their chemical composition and mineral structure. The basic building block of silicate material is SiO_4 . They are tetrahedral in shape. In the tetrahedron, the four oxygen atoms of SiO_4 are located one at each corner, while Si atom is at its centre. The two main forms of silicate material of interest are Olivine and Pyroxene (Fig. 3.7). Olivines can be considered as solid solutions of

Silicate structure

Pyroxenes: $\text{MgFeSi}_2\text{O}_6$ or
 $\text{Mg}_{2-x}\text{Fe}_{1-x}\text{SiO}_3$

Solid solution series of $\text{MgSiO}_3/\text{FeSiO}_3$: $\xrightarrow{\text{MgSiO}_3}$ Enstatite 0-5 Ma% FeO Bronzite 5-15 Ma% FeO Hypersthene >15 Ma% FeO $\xrightarrow{\text{FeSiO}_3}$ Ferrosilite <10 Ma% MgO

Chain silicates: $[\text{SiO}_3]^{2-}_{\infty}$



Olivines: $\text{Mg}_{2x}\text{Fe}_{2-2x}\text{SiO}_4$

Solid solution series of $\text{Mg}_2\text{SiO}_4/\text{Fe}_2\text{SiO}_4$: $\xrightarrow{\text{Mg}_2\text{SiO}_4}$ Forsterite <10 Ma% FeO Olivine 10-30 Ma% FeO Hortolomite $\xrightarrow{\text{Fe}_2\text{SiO}_4}$ Fayalite <10 Ma% MgO

Neso silicates: $[\text{SiO}_4]^{4-}$

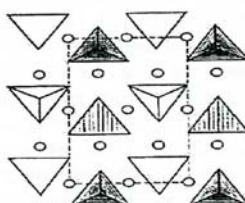


Fig. 3.7 Different forms of Olivines and Pyroxenes and their structure (Henning, Th. 1999, In *Asymptotic Giant Branch Stars*, Eds. T. Le Bertre, A. Lebre and C. Waelkens, IAU Symposium 191, ASP Conference Publications, p. 221:By the kind permission of the Astronomical Society of the Pacific Conference Series).

Mg_2SiO_4 and Fe_2SiO_4 , while Pyroxenes of MgSiO_3 and FeSiO_3 . They can be represented by a general formula as $\text{Mg}_{2x}\text{Fe}_{2-2x}\text{SiO}_4$ for olivine and $\text{Mg}_x\text{Fe}_{1-x}\text{SiO}_3$ for pyroxenes. The value of x can take values between 1 and 0. The end members of olivine class are Forsterite ($x = 1$, Mg_2SiO_4) and Fayalite ($x = 0$, Fe_2SiO_4). The corresponding ones for pyroxene are Enstatite ($x = 1$, MgSiO_3) and Ferrosilite ($x = 0$, FeSiO_3). Pyroxene has chain-like structure while olivine has island-like structure. In the case of amorphous silicate, long range order is absent due to blending of structures and only short-range order exists. The two crystalline silicates exhibit both short-range and long-range order. The degree of long-range order (amorphous to crystalline) has a considerable effect on the spectroscopic properties of the material. For example, amorphous silicate exhibit broad smooth spectral features, while crystalline silicates show sharp and distinct features. Amorphous and crystalline silicates are present in cometary dust.

3.13. Annealing

Amorphous silicate is the most common form present in astronomical objects. In fact the dominant component of silicate in the interstellar medium is amorphous silicate. Since crystalline silicate is present in comets, it is important to understand how amorphous silicate can be transformed to crystalline silicate.

The transformation of amorphous to crystalline state is possible by the process of annealing in which the ordered arrangement of silicate tetrahedra is brought about by atomic diffusion. In this process, thermal diffusion brings about rearrangement of the structural units (tetrahedra) which results in long-range order. Diffusion in solids is a result of activation of lattice defects. Therefore the poorly ordered state of the amorphous material slowly drifts towards more energetically favourable positions leading to macro-crystalline structure.

Several experiments have been carried out to see the actual change over from the amorphous state to crystalline state. Magnesium silicate which showed a broad feature at $9.3 \mu\text{m}$ to start with showed two features at 9.8 and $11.0 \mu\text{m}$ after annealing at 1027 K . These features and the spectral feature at $20 \mu\text{m}$ showed the formation of olivine. The change over from amorphous to crystalline can take anywhere between a few hours to a day or so. In the change over process the band length or angle within the SiO_4 tetrahedron is not altered but simply leads to ordered arrangement of the

SiO_4 units. As an example the annealing of $\text{CaMgSi}_2\text{O}_6$ smoke is shown in Fig. 3.8.

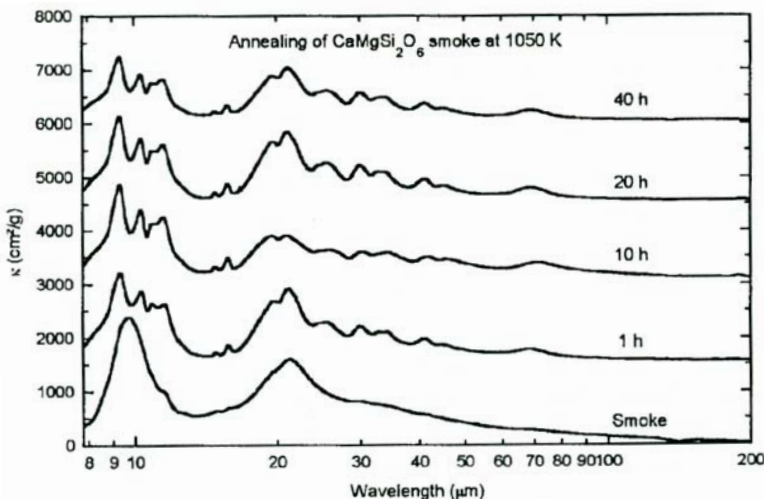


Fig. 3.8 Annealing of $\text{CaMgSi}_2\text{O}_6$ smoke at 1050K and for times from 1 to 40 hours. The development of structures in the curve can clearly be seen. The curves for 1 to 40 hours are shifted vertically for clarity (Colangeli, L., Henning, Th., Brucato, J.R. *et al.* 2003. *Astron. Astrophys. Rev.*, **11**, 97).

3.14. Carbon

Carbon can exist both in crystalline and amorphous form. Some of the forms of carbon are graphite, diamond and amorphous carbon. Amorphous carbon does not exhibit a long-range order in their arrangement. There are several classes of materials of this category which depend mostly on their appearance, for example, glassy carbon or soot. Aliphatic molecules have open structures, while aromatic molecules have ring structures, like benzene, C_6H_6 . Benzene is the building block for a wide range of hydrocarbon molecules. Molecules with several aromatic rings are called Polycyclic Aromatic Hydrocarbons (PAHs). PAHs are the most thermodynamically stable hydrocarbon compounds that exist in the gaseous form. PAHs can exist in neutral and ionized states. The size of PAHs could be around 25 to 100 carbon atoms. Therefore wide variety of PAHs can exist under astrophysical conditions including comets. PAHs possess rich spectra with specific

spectral signature, a high photo-stability and also contain abundant carbon. The mid infrared region (2 to 25 μm) is where the fundamental vibrational modes of PAHs and their overtones are active. The C - H out-of-plane bending feature occurs at around 11 μm , C-C stretching around 6 μm and C-H in-plane bending around 8.7 μm . A series of emission lines at 3.3, 6.2, 7.7, 8.6 and 11.3 μm seen in astronomical objects is generally attributed to PAHs. However no specific molecule has been identified.

3.15. Solar Radiation

The subject of the study of the total amount of energy as well as the spectral distribution in the solar spectrum is an old one. It is of great interest in various fields. It has therefore been studied extensively in the entire range of the electromagnetic spectrum. The detailed and extensive measurements are carried out in the case of the Sun because of its proximity, it being a typical main sequence star and also because of its effects on the Earth's environment. It also turns out that most of the phenomena that one observes from a comet is associated directly or indirectly with the radiation field of the Sun.

The surface temperature of the Sun is about 6000°K. According to Planck's distribution law [Eq. (3.1)] most of the energy is concentrated in the visible region of the spectrum. Therefore the amount of energy measured from the Earth corrected for the atmospheric transmission gives a good estimate of the total energy of radiation. Of course, one should try to allow for the UV and IR radiation which is cut off by the Earth's atmosphere. The intensity of the solar radiation as seen from the Earth's atmosphere at the Earth's mean distance from the Sun is called the *solar constant*. To get the solar constant value, extensive ground based measurements have been carried out. The average value for the solar constant is found to be $\sim 1.95 \text{ cal/cm}^2/\text{min}$.

The spectral energy distribution in the visible region is quite smooth and can be represented well by a black body of temperature 6000°K. Superposed on it are the absorption lines of the gases of the solar atmosphere. For measuring the solar emission in the UV region, it is necessary to go above the Earth's atmosphere. Such observations have been carried out using rockets and satellites. The solar flux decreases very rapidly to shorter wavelength. As one goes towards the UV spectral region, the number of emission lines arising out of different ionization levels of the various ele-

ments increases. In fact below around 1500 Å, the major portion of the energy is in emission lines rather than in the continuum (Fig. 3.9). As one

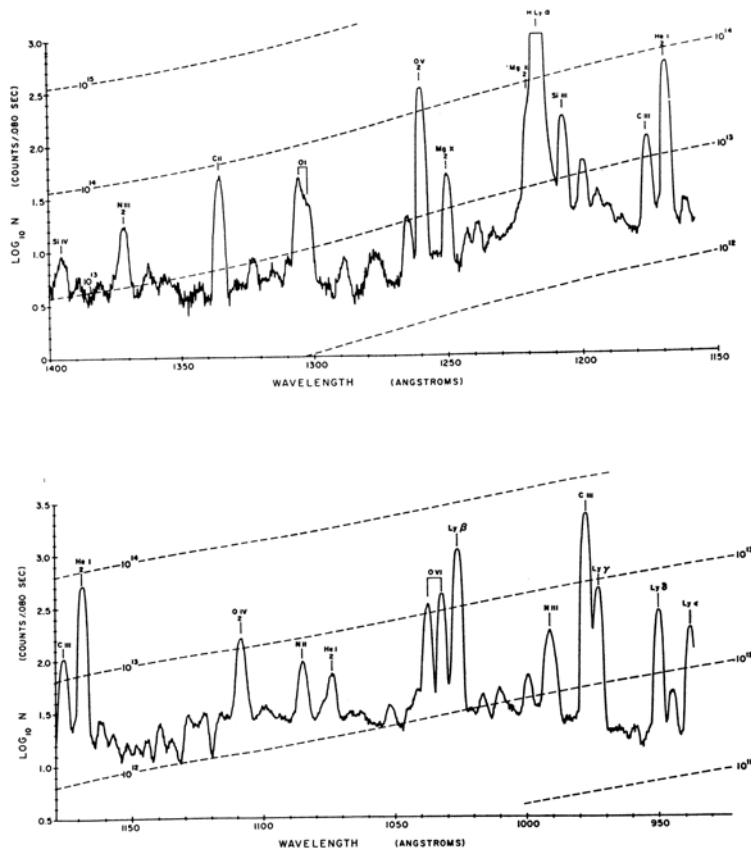


Fig. 3.9 A representative spectral distribution of the quiet Sun between 1150 to 1400 Å (Dupree, A.K. and Reeves, E.M. 1971. *Ap. J.* **165**, 599).

goes towards shorter and shorter wavelength, one is essentially seeing the higher and higher temperature regions, namely the chromosphere and the corona of the Sun, from where the emission lines arise. Therefore the shape of the continuum radiation in the UV and far UV regions depend to certain extent on the resolution of the instrument. The higher the resolution of the instrument the more the number of weak lines can be resolved. The intense lines in the UV region are the Lyman α and Lyman β occurring at 1215.7 Å and 1025.7 Å, respectively. They have fluxes of about 3×10^{11} and

2×10^9 photons/cm²/sec at the top of the atmosphere as compared to the continuum level in the same region of about 10^8 photons/cm²/sec. Lyman α and Lyman β emission lines are quite important as they can dissociate, ionize or excite the species. There could be some uncertainty in the data in the UV region. In addition, the emission could vary with the solar conditions as for example, whether the Sun is quiet or flares are present and so on. The solar UV flux also varies considerably with 27 day solar rotation period. It also varies with 11 year solar activity cycle which can cause the solar flux to vary by a factor of 2 to 4 at wavelength shorter of 1000 Å.

It will become clear later on that the emission and absorption lines, strong as well as weak present in the solar spectrum, as well as their variations play a crucial role in the formation of spectral line in a cometary atmosphere.

3.16. Solar Wind

The solar plasma from the corona that flows out continuously into the interplanetary medium is called the *solar wind*. The possible existence of such plasma flows came from the pioneering investigations of Biermann based on the study of plasma tail of comets. The theoretical work of Parker in the 1950's based on the hydrodynamic expansion of the solar corona predicted the expected nature of the solar wind. The theory also showed that the magnetic field originating in the photosphere and dragged into the interplanetary medium takes the form of an Archimedean spiral structure. The observations carried out with satellites later on confirmed Parker's theory of the solar wind. The actual interplanetary magnetic field measurements have established the Archimedean spiral structure for the magnetic field. The mean values obtained from observations for some of the physical parameters of interest for the solar wind near the Earth are the following: number density of electrons or protons, $N_e \sim N_p \approx 5/\text{cm}^3$; velocity $\approx 450 \text{ km/sec}$; electron temperature $\sim 1.5 \times 10^5 \text{ }^\circ\text{K}$; magnetic field $\approx 2.5\gamma$ where $\gamma = 10^{-5}$ gauss. However, it is well known that the Sun is not quiet all the time and lot of activities of violent nature do take place on the surface of the Sun, like flares, bursts, etc. These have a great effect on many of the geomagnetic activities. In fact there is an almost one-to-one relation between the disturbance occurring on the Sun and the effect observed on the terrestrial atmosphere. The existence of such a correlation has been known since early times. These effects arise basically due to the fact that a

disturbance on the surface of the Sun releases suddenly a large amount of plasma which is coupled through interplanetary magnetic field. Therefore, the average physical properties of the solar wind change with the solar conditions. During disturbed periods the solar wind velocity and the density at 1 AU could vary by a factor of two or so. The magnitude as well as the direction of the magnetic field also change. The extensive measurements made with satellites have given an enormous amount of information with regard to the variation of physical quantities with heliocentric distance for quiet as well as for disturbed solar conditions. These measurements have also shown the presence of magnetic sector boundaries in the magnetic field which have opposite polarity. These regions are separated by null surfaces where the magnetic field is zero. Since the plasma tail of a comet and the solar wind are coupled to each other through interplanetary magnetic fields (Chap. 10), the interpretation of the observed cometary features requires a knowledge of the exact conditions of the solar wind at the time of observation.

Problems

1. Derive Eq. (3.1) in frequency units.
2. Calculate the wavelength of vibrational bands of the Swan system ($d^3\Pi - a^3\Pi$) for the C_2 molecule and ($B - X$) transitions of the H_2 molecule for $v''=0,1,2$ and $v'=0,1$. This will help in understanding the meaning of band sequence. What instrumental resolution is required to resolve vibrational and rotational structure of the Swan bands.
3. Derive the expression for the isotopic shift for the vibrational and rotational transitions including second order terms.
4. Calculate the isotopic shift between $^{12}C^{12}C$ and $^{12}C^{13}C$ for the (1,0) band of the Swan system.
5. Calculate the frequency and wavelength of the line arising out of the transition between $n = 109$ to 108 in hydrogen and carbon atoms. Discuss its significance.
6. Is there a Doppler effect when the observer or the source moves at right angles to the line joining them? How can the Doppler effect be determined when the motion has a component at right angles to the line?
7. Make an estimate of the temperature of the Sun from the fact that it can be seen.

8. Explain why the spectrum of the Sun at wavelengths less than 1500 Å consists entirely of emission lines.
9. What evidence do we have, direct and indirect, of the existence and properties of solar wind?
10. What is the probable mechanism responsible for the generation of the solar wind?
11. Sun's radiation striking the Earth has an intensity of 1400 watts/meter². Assuming the Earth is a flat disk at right angles to the Sun's rays and that the incident energy is completely absorbed, calculate the radiation force acting on the earth. Compare it with the force due to the Sun's gravitational attraction.
12. Calculate the Einstein A-value for the rotational transitions 2 to 1 in the ground electronic state and compare it with the value for the electronic transitions between A and X levels for the CO molecule.

References

1. Herzberg, G. 1950. *Molecular Spectra and Molecular Structure 1. Spectra of Diatomic Molecules*, New York: Van Nostrand Reinhold Company.

CHAPTER 4

Spectra

The main goals of the study of spectra are to identify the species responsible for the observed lines and to obtain information about their abundances and the physical conditions present in the source. It is no exaggeration to say that our present understanding about various aspects of cometary phenomena has come directly or indirectly from the study of their spectra.

The first photographic observations in the visible region was carried out in 1864. This was gradually superceded by photoelectric detectors of various kinds followed by charged coupled devices (CCDs). Therefore it is possible to make high spectral resolution observations with the existing large size optical telescopes.

The observations in the UV spectral region below 3000 Å was carried out first with rockets and then by Orbiting Astronomical observatory (OAO-2) in 1970. This was followed by the launching of International Ultraviolet Explorer (IUE) in 1978, Hubble Space Telescope (HST) in 1990 and Far Ultraviolet Spectroscopic Explorer (FUSE) in 1999. These satellites made it possible to explore the spectral region from around 3000 Å down to about 900 Å. The observations carried out with Röntgen Satellite (ROSAT), Extreme Ultraviolet Explorer (EUVE) and Chandra X-ray observatory have extended the wavelength limit to X-ray region of around 1 Å.

In the near infrared region, observations have been carried out with balloons and with the Keck telescope, Infrared Telescope Facility (IRTF), Subaru telescope etc. at Mauna Kea in Hawai with sensitive detectors. Kuiper Airborne observatory (KAO) was very helpful in making observations in the infrared. Infrared Space Observatory (ISO) made it possible to study far-infrared spectral region with high resolving power. This has been followed by Spitzer Space Observatory (SSO) which has opened up

new avenue for making infrared observations.

The availability of large size radio telescopes has made it possible to study molecules in the millimetre and radio wavelength regions.

4.1. Main Characteristics

The identification of the spectra of comets is one of the active areas of study. This is due to the combination of many factors such as better instruments, availability of space vehicles, computation techniques, etc. The identification of the lines in the spectra of a comet is quite a complex and difficult task. The usual procedure is to look for the coincidences between the laboratory wavelength of lines and the observed wavelenghts in the spectra of a comet which have been corrected for the velocity effect (Chap. 3). With this method many of the well-known atoms and molecules which are seen in other astronomical objects have been identified in the spectra of comets. With better resolution as well as going into new spectral regions, many more new species have been identified.

The extensive spectral observations carried out on Comet Halley which have been compiled in the Atlas of Cometary Spectra, show the vast extent of the lines which could not be identified. There are also large number of unidentified lines in the high dispersion ($\lambda/\Delta\lambda = 60,000$) visible spectrum of Comet 122P/de Vico. Therefore much work remains to be done in the area of identification of lines. It is appropriate at this point to mention the fact that the problem of identification of lines is intimately connected with the availability of spectroscopic data pertaining to various atoms and molecules. In addition, the astrophysical environment is vastly different from those of laboratory conditions. Therefore many of the lines that may be present in the astronomical spectra cannot be produced under laboratory conditions. Hence laboratory data is not available for each and every transition for all the atoms and molecules. Therefore, there could always be lines in the astronomical spectra which cannot be identified. It is interesting to note that several transitions were observed first in the cometary spectra before being studied in the laboratory. The well-known case is the bands of the ion CO^+ , generally called the Comet-Tail System. Other examples are the bands of C_3 and H_2O^+ .

The observations carried out in the visual spectral region of around 3000 to 8000 Å have been the main source of information for the study of spectra of cometary atmosphere for the last several decades. These

studies had limitations due to photographic techniques and also most of the spectroscopic observations could be made only on bright comets at small heliocentric distances. Early observations were also limited to spectra taken at low spectral resolution. In recent years many of these limitations have been overcome. Based on the spectra in the visual region, it is possible to arrive at some general pattern regarding the main characteristic features of the spectra of comets.

At large heliocentric distances, the comet appears as a point source. This is due to the reflection of the solar radiation by the nucleus. For heliocentric distances, $r \gtrsim 3$ AU, the spectrum is mainly the continuum radiation arising mostly due to the scattered solar radiation by the dust particles present in the cometary atmosphere. The emission lines of the various molecules appear roughly in a sequence as the comet approaches the Sun. The molecular bands first to appear are those of CN at $r \sim 3$ AU followed by the emission from C₃ and NH₂($r \sim 2$ AU). Thereafter at $r \sim 1.5$ AU the emission from C₂ (Swan bands), CH, OH and NH appear in the spectrum. They are often strong enough to reveal their structure. At $r < 1.5$ AU emission from CO⁺, OH⁺, N₂⁺ and CH⁺ appear. Emission from Na appear around 0.8 AU. The relative intensity of emission bands and continuum varies from comet to comet. In sun-grazing comets, say for $r \sim 0.1$ AU, numerous metallic emission lines crowd the spectrum.

The spectrum of a plasma tail shows mostly the presence of ionized species and generally at $r < 2$ AU. The notable exceptions include the Comet Humason (1962 VIII) where CO⁺ was seen even at $r > 6$ AU. Among the observed ions in the plasma tail of a comet, the emission from CO⁺ dominate.

As a typical case, Fig. 4.1 shows the spectra of Comet Encke in the visual region taken at a resolution (full width at half maximum intensity) of $\Delta\lambda = 7$ Å. The Swan band sequences corresponding to $\Delta v = -1, 0$ and +1 of the C₂ molecule (d³II - a³ II), whose wavelengths lie around 5635, 5165 and 4737 Å respectively, are the strongest in the spectra. The vibrational structure could be resolved with better resolution spectra. The resolution of the rotational structure requires still higher resolution. In fact it has been possible to resolve completely the rotational structure.

The spectra of Comet Halley taken at a spectral resolution of 0.07 Å beautifully shows the rotational structure of the (0, 0) Swan band of the C₂ molecule(Fig. 5.17). The spectra taken in recent times by instruments with very high resolving power, $\lambda/\Delta\lambda \approx 60,000$, shows in great detail, the rotational structure of individual bands. Since the Swan bands of the C₂

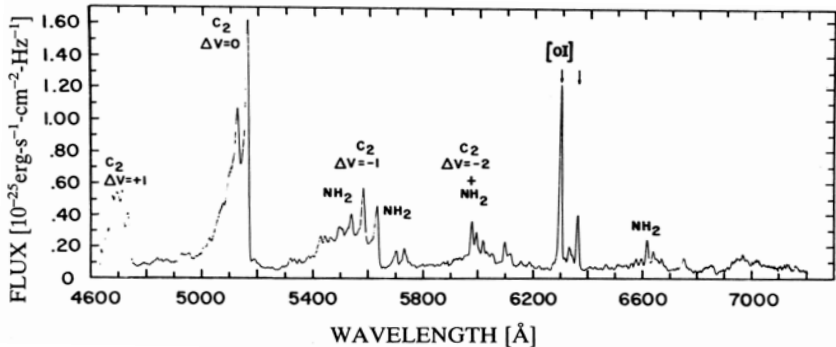


Fig. 4.1 Typical scanner spectrum of Comet Encke using the 3-m Lick Observatory Telescope in the visual region. *Courtesy of Spinrad.*

molecule dominate the spectrum in the visual region, to a first approximation, it also determines the ‘visual diameter’ of the head of the comet. It may also be noted that the wavelength of $\Delta v = +1$ band sequence of the isotopic molecule $^{12}\text{C}^{13}\text{C}$ (4745 \AA), is shifted by about 7 \AA with respect to that of $^{12}\text{C}^{12}\text{C}$ (4737 \AA) and it has been seen in the spectra of many comets. Unfortunately this isotopic feature is blended strongly with the emission from the NH_2 molecule ($(\tilde{A}_2\text{A}_1 - \tilde{X}_2\text{B}_1)$ system). Other bands of NH_2 can also be seen. Several other isotopic lines have been seen.

The emission due to C_3 molecule has a broad feature extending roughly from 3950 to 4140 \AA , with a strong peak around 4050 \AA . The identification of C_3 feature in comets was difficult as the laboratory analysis was not available. Laboratory studies have confirmed the observed lines as due to C_3 molecule and it has a complex spectra. Until its identification, this broad feature was simply known as ‘ 4050 \AA ’ Group. Various transitions of the CN molecule, both the red ($\lambda \sim 7800 \text{ \AA} - 1 \mu\text{m}$) and the violet ($\lambda \sim 3600 - 4200 \text{ \AA}$) systems corresponding to transitions ($A^2\Pi - X^2\Sigma^+$) and ($B^2\Sigma^+ - X^2\Sigma^+$) have been identified. The violet system of CN is one of the prominent feature in the spectra of comets. The rotational structure of $\text{CN}(0, 0)$ band is well-resolved (Fig. 5.1). High spectral resolution observations of the violet system of CN molecule resolve completely the isotopic feature which has been used to derive $^{12}\text{C}/^{13}\text{C}$ ratio. For CH molecule, both the systems ($A^2\Delta - X^2\Pi$) and ($B^2\Sigma - X^2\Pi$) have been seen. The wavelength of $(0, 0)$ band of $(A - X)$ is at 4314 \AA and that of $(B - X)$ is at 3886 \AA . The $(A - X)$ band is weaker than the $(B - X)$ band. The $(0, 0)$ band of $(A - X)$ transitions has been observed at high resolution.

The lines of (0, 0) band of the NH molecule arising out of ($A^3\Pi_i - X^3\Sigma$) transitions lie in the region of 3345 and 3375 Å. The (0, 0) and (1, 1) bands corresponding to ($A^2\Sigma^+ - X^2\Pi$) of OH at 3090 Å and 3140 Å, which is close to the atmospheric cut-off were detected from ground-based observations. The rotational structure was partially resolved. Numerous lines belonging to ($A^3\Pi - X^3\Sigma$) system of OH⁺ ($\lambda \sim 3500$ Å) have been identified. The lines of H₂O⁺ ($\lambda \sim 5500 - 7500$ Å) were identified for the first time in Comet Kohoutek. The bands of ($A^2\Pi - X^2\Sigma$) of CO⁺ around $\lambda \sim (3400 - 6300$ Å) has been seen. The lines of CH⁺ seen in a cometary spectra is the (0, 0) band at 4230 Å belonging to ($A^1\Pi - X^1\Sigma$) transitions. The ($B^2\Sigma_u^+ - X^1\Sigma_g^+$) (0, 0) band of N₂⁺ at 3914 Å has been seen (See Sec. 6.2.7).

The lines arising out of metals, K, Ca, Fe, V, Cr, Mn, Ni and Cu have been seen in the sun-grazing Comet Ikeya–Seki. The sodium D lines at 5890 and 5896 Å also show up for $r \lesssim 1.4$ AU.

The very first lines emitted by OH following the dissociation of H₂O called ‘Prompt emission’ lines have been seen in UV (~ 3100 Å) (Sec. 5.1.5) and infrared ($\sim 3 \mu\text{m}$) regions (see Sec. 6.2.2.)

The use of rockets and satellites has made it possible to extend the observations into the ultraviolet region. This is the region of the spectrum say from 1000 to 4000 Å where the abundant atomic and molecular species have their resonance transitions. In fact the spectra of comets taken in the ultraviolet region has clearly demonstrated the richness of molecular emissions in this spectral region. Comet West in 1976 provided a good opportunity to secure high quality spectra in the UV region as the comet was quite bright. For illustration, the rocket spectra of this comet covering the wavelength region from 1600 to 4000 Å is shown in Fig. 4.2. Many molecules like CS, CN⁺ and others were identified for the first time based on the spectra of Fig. 4.2 and others. The wavelength of the (0, 0) band of CS arising out of the electronic transition ($A^1\Pi - X^1\Sigma^+$) is at 2576 Å. The wavelength of the (0, 0) band of CN⁺ arising out of ($^1\Sigma - ^1\Sigma$) transition is at 3185 Å. The (0, 0) transition, ($A - X$) of OH at 3090 Å which was weak when observed from the ground is found to be very strong when observed outside the Earth’s atmosphere. The rotational structure of OH bands has also been resolved completely.

The strong emission ($A^1\Pi - X^1\Sigma^+$) bands of CO commonly referred to as the Fourth Positive system occurring around 1500 Å region were also identified for the first time in Comet West. Figure 4.3 shows the spectrum covering this spectral range. The Cameron band system near 2050 Å arising out of dipole forbidden triplet and singlet electronic states ($a^3\Pi - X^1\Sigma^+$) of

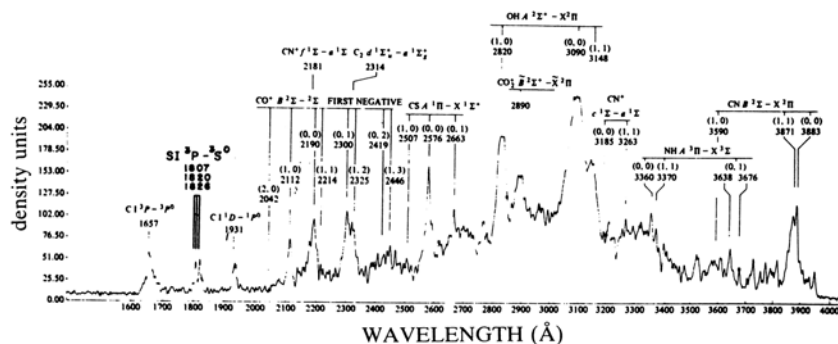


Fig. 4.2 Rocket spectrum of Comet West in the 1600 to 4000 Å spectral region. The richness of molecular emissions can be seen. *Courtesy of Andy Smith.*

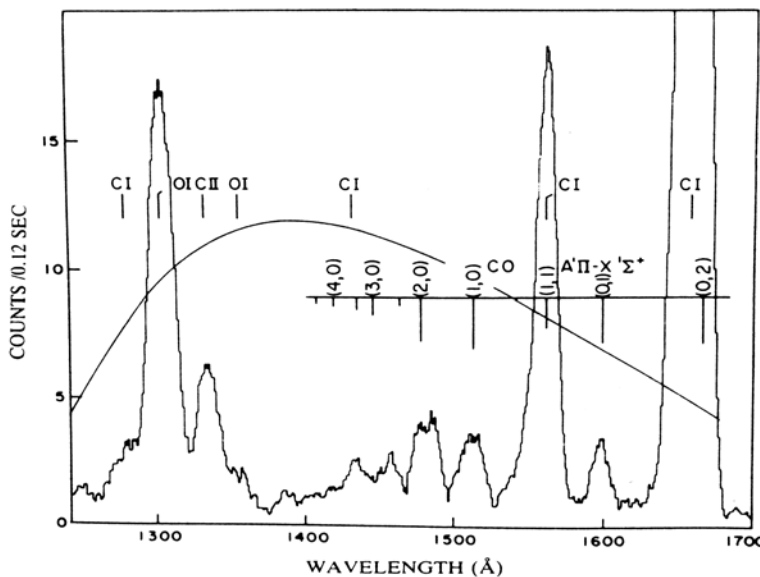


Fig. 4.3 Low resolution spectrum of Comet West taken from an Aerobee rocket in the wavelength region 1300 to 1700 Å which shows bands of CO molecule (Feldman, P.D. and Brune, W.H. 1976, *Ap. J.*, **209**, L45).

CO was observed with HST for the first time in 1991 in Comet Hartley 2 (1991 XV). After its detection, it was also shown to be present in the earlier data acquired with IUE in several others comets. Several other bands of CO belonging to Hopfield–Birge system ($B^1\Sigma^+ - X^1\Sigma^+$), ($C^1\Sigma^+ - X^1\Sigma^+$)

and ($E^1\Pi - X^1\Sigma^+$), have been seen in the spectral region 1075 and 1155 Å obtained with FUSE (See Fig. 4.6). The presence of CO_2^+ ion in comets came from the detection of the bands of ($\tilde{A}^2\Pi - \tilde{X}^2\Pi$) system in the region 3300–3900 Å. The ($\tilde{B}^2\Sigma - \tilde{X}^2\Pi$) double band system whose wavelength occurs around 2890 Å has also been identified. In the region of 2000 to 2600 Å the First Negative bands ($B^2\Sigma^+ - X^2\Sigma^+$) of CO^+ are generally very strong. The Mulliken System of the C_2 molecule corresponding to $\Delta v = 0$ has a wavelength around 2300 Å. This feature is present in Fig. 4.2. The relevant spectra of Comet Bradfield is shown in Fig. 4.4. Several strong

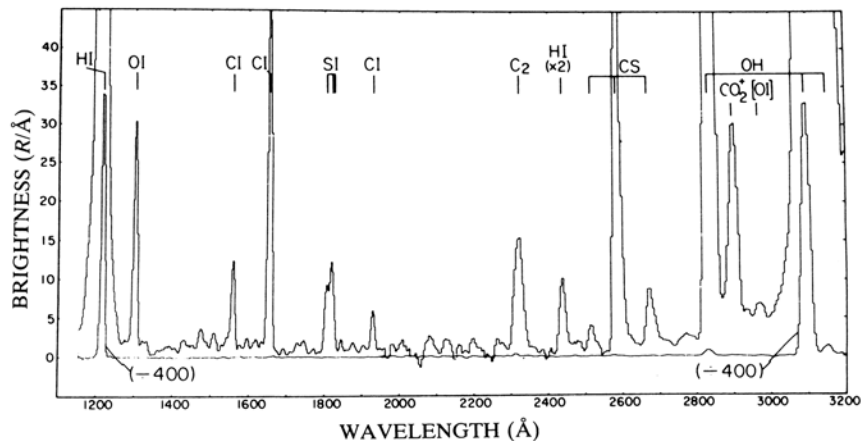


Fig. 4.4 The ultraviolet spectrum of Comet Bradfield 1979 X obtained from the International Ultraviolet Explorer (Weaver, H.A., Feldman, P.D., Festou, M.C. and A'Hearn, M. F. 1981. *Ap. J.*, **251**, 809).

emission bands of ($B^3\Sigma_u - X^3\Sigma_g$) of the S_2 molecule have been identified in the wavelength region of 2800–3100 Å based on the beautiful spectra of the Comet IRAS–Araki–Alcock (1983VII) as shown in Fig. 4.5. The P_1 lines of H_2 Lyman system ($B^1\Sigma^+ - X^1\Sigma_g^+$) were detected for the first time in Comet C/2001A2 (LINEAR) with FUSE as shown in Fig. 4.6.

The earlier reported detection of lines of N_2^+ in the low resolution spectra of comets are not seen in the high spectral resolution observations of some recent comets (See Sec. 6.2.7).

The dissociation of the molecular species should finally lead to their constituent atoms such as H, O, C, N and S. These lines lie in the UV region. Shortward of 1800 Å, the spectrum is dominated by multiplets of CI at 1561 Å, 1657 Å, OI at 1304 Å and CII at 1335 Å. Many weak CI

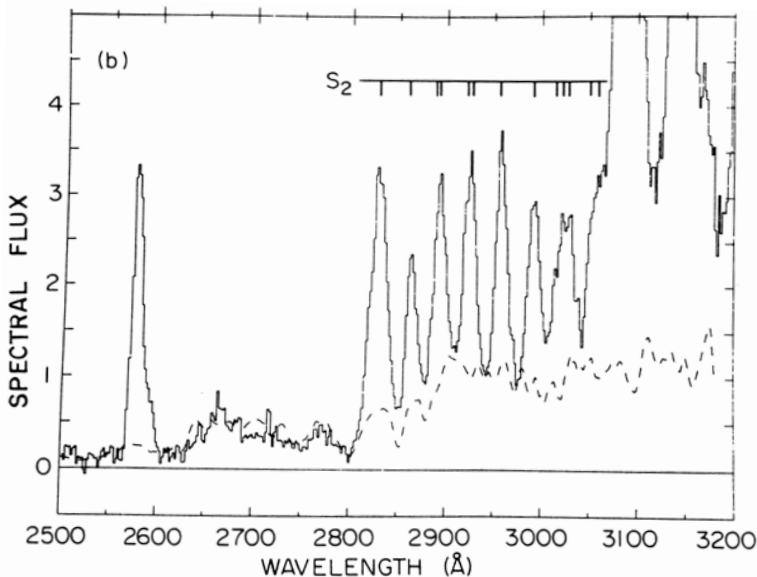


Fig. 4.5 The spectrum of Comet IRAS–Araki–Alcock in the wavelength region 2500 to 3200 Å obtained with the International Ultraviolet Explorer Spacecraft. The image No. LWR 15908 was taken on May 11, 1983 with the nucleus centred, when the comet was 0.032 AU from the Earth. The new features corresponding to (B–X) system of S₂ are identified (A'Hearn, M.F., Feldman, P.D. and Schleicher, D.G. 1983, *Ap. J.*, **274**, L99).

features are also present. The lines of SI multiplet at 1807, 1820 and 1826 Å were detected for the first time in Comet West. (Figs. 4.2 and 4.4). Two other multiplets of S are sometimes seen at 1429 and 1479 Å.

Some of the molecules detected through their spectral characteristics are given in Table 4.1.

The observations made with the orbiting astronomical observatory (OAO–2) satellite in 1970 on Comet Kohoutek and on other comets in the light of the hydrogen Lyman α line at 1216 Å led to the discovery of a hydrogen halo around the visible coma (Fig. 1.13). This important observation also led to the realization that the mass loss rates from comets are much higher than previous estimates which were based on observations in the visual spectral region.

The first X-ray detection from a comet was from Comet Hyakutake in 1996 (Fig. 10.15). The X-ray spectra obtained on Comet LINEAR from Chandra X-ray observatory in the energy range 0.2 to 0.8 KeV showed that

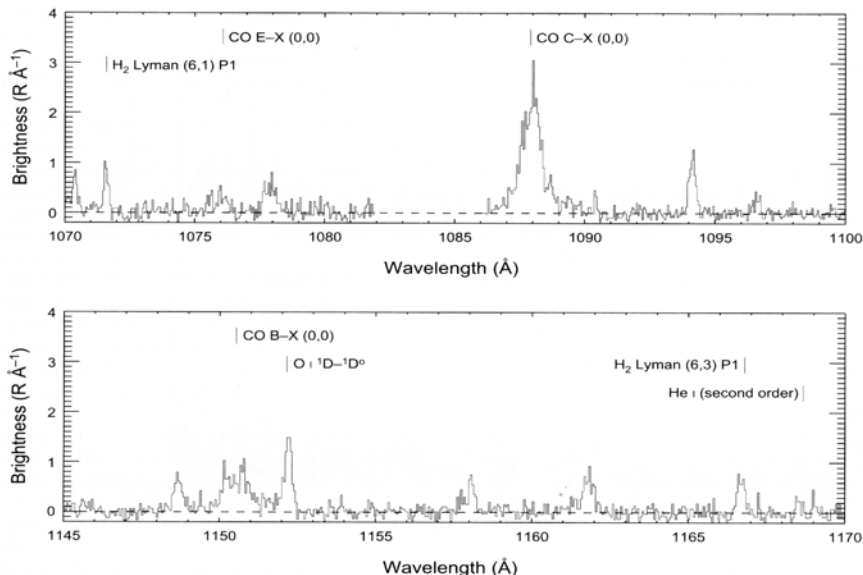


Fig. 4.6 The lines of H_2 seen in the FUSE spectrum of Comet C/2001 A2 (LINEAR) on July 12, 2001. (Feldman, P.D., Weaver, H.A. and Burgh, E.B. 2002. *AP.J.*, **576**, L91, Reproduced by Permission of the AAS).

the spectra was dominated by the emission arising out of highly charged ions of C, N and O (Sec. 10.7).

The extension of observations into the infrared region is important as this spectral region is characterized by vibration–rotation transitions of many molecules. Some of the bands of the CN red system ($A^2\Pi - X^2\Sigma$) occurring around $\lambda \sim 8000 \text{ \AA}$ were first seen in the Comet Mrkos (1957 V) based on photographic spectra. This has later been observed from many comets. Several other bands of CN can also be seen. Many weak features of NH_2 and the Phillips bands of C_2 are present. High resolution spectra has resolved the rotational structure.

At wavelengths larger than $1 \mu\text{m}$, lines of several molecules have been detected. In particular the first and direct detection of H_2O in Comet Halley came from the high resolution observation of ν_3 vibrational band at $2.7 \mu\text{m}$ with the Kuiper Airborne Observatory (Fig. 4.7). In the spectral region around $2.9 \mu\text{m}$ multiple nonresonant fluorescent lines of H_2O called *hot bands* have been seen.

Table 4.1 Some of the observed spectroscopic features of molecules.

Molecule	Transition	Wavelength (Å) (0,0) band
OH	A $^2\Sigma^+ - X ^2\Pi_i$	3085
CN	B $^2\Sigma^+ - X ^2\Sigma^+$	3883
	A $^2\Pi - X ^2\Sigma^+$	7873 ^a
C ₂	d $^3\Pi_g - a ^3\Pi_u$	5165
	A $^1\Pi_u - X ^1\Sigma_g^+$	7715 ^b
	D $^1\Sigma_u^+ - X ^1\Sigma_g^+$	2313
C ₃	A $^1\Pi_u - X ^1\Sigma_g^+$	3950-4140*
CH	A $^2\Delta - X ^2\Pi$	4314
	B $^2\Sigma - X ^2\Pi$	3886
CS	A $^1\Pi - X ^1\Sigma^+$	2576
CO	A $^1\Pi_u - X ^1\Sigma^+$	1300-1800*
	a $^3\Pi_g - X ^1\Sigma^+$	1900-2200*
	B $^1\Sigma^+ - X ^1\Sigma^+$	1150.5
	C $^1\Sigma^+ - X ^1\Sigma^+$	1087.9
	E $^1\Pi - X ^1\Sigma^+$	1076.1
NH	A $^3\Pi_i - X ^3\Sigma^-$	3360
NH ₂	A ² A ₁ - X ² B ₁	4500-7350*
H ₂	B $^1\Sigma^1 - X ^1\Sigma_g^+$	1071.6, 1166.8 ^c
S ₂	B $^3\Sigma_u - X ^3\Sigma_g$	2800-3050*
CH ⁺	A $^1\Pi - X ^1\Sigma^+$	4230
OH ⁺	A $^3\Pi - X ^3\Sigma^-$	3565
CO ⁺	A $^2\Pi - X ^2\Sigma^+$	4273 ^a
	B $^2\Sigma^+ - X ^2\Sigma^+$	2190
N ₂ ⁺	B $^2\Sigma^+ - X ^2\Sigma^+$	3914
H ₂ O ⁺	A ² A ₁ - X ² B ₁	4270-7540*
CO ₂ ⁺	A $^2\Pi_u - X ^2\Pi_g$	2800-5000*
	B $^2\Sigma_u - X ^2\Pi_g$	2890

*Range of wavelength.

a. (2,0), b. (3,0), c. (6,1) and (6,3)

Feldman, P.D. *et al.* 2002, *Ap. J.*, **576**, L91.

Weaver, H. 1998, Comets, In The Scientific Impact of the Goddard High Resolution spectrophotograph, eds. J.C. Brandt *et al.* ASP Conf. series No. 143, p. 213.

Feldman *et al.* 2005, In *Comets*, eds. M.C. Festou, H.U.Keller and H.A. Weaver, Univ. Arizona Press, Tucson, p. 425.

In the 3 μm region strong emissions from hydrocarbons are present. This is shown in Fig. 4.8 where the emissions from CH₄ (Methane), C₂H₂ (Acetylene) and C₂H₆ (Ethane) can clearly be seen. A broad emission feature around 3.4 μm observed from ground and *in situ* measurements

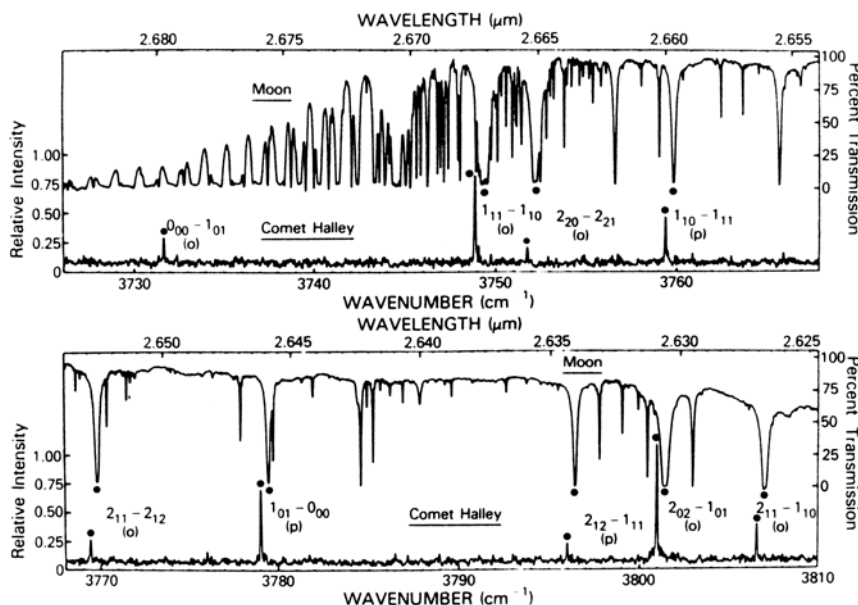


Fig. 4.7 High resolution infrared spectroscopic observations of the ν_3 band ($2.7 \mu\text{m}$) of H_2O in Comet Halley taken from NASA's Kuiper Airborne Observatory on December 24, 1985. The lines originating from Ortho (O) and Para (P) H_2O are resolved completely. The spectra of the Moon is also shown for comparison (Mumma, M.J., Weaver, H.A., Larson, H.P., Davis, D.S. and Williams, M. 1986. *Science* **232**, 1523).

of Comet Halley and subsequently in other comets, is attributed to C–H stretch vibrations of organics (Fig. 4.9). Most of the observed features are attributed to methanol (CH_3OH).

Since the molecule CO_2 has no allowed radio transitions, it does not fluoresce in the UV or optical regions. It can only be observed in the infrared region. Although ν_3 band of CO_2 at $4.25 \mu\text{m}$ is very strong, but cannot be observed from the ground because of strong absorption from terrestrial CO_2 . It has been detected by Vega spacecraft in Comet Halley and later on in other comets with ISO. The infrared lines of CO at $4.7 \mu\text{m}$ arising out of V(1, 0) IR band was clearly detected in Comet Hyakutake (C/1996 B2).

Polycyclic Aromatic Hydrocarbon molecules (PAHs) are commonly seen from interstellar medium near 3.28 , 7.6 and $11.9 \mu\text{m}$. Some of these features have been seen in Comet 9P/Tempel 1 from the observations carried out with Spitzer Space Observatory (Sec. 9.5.2).

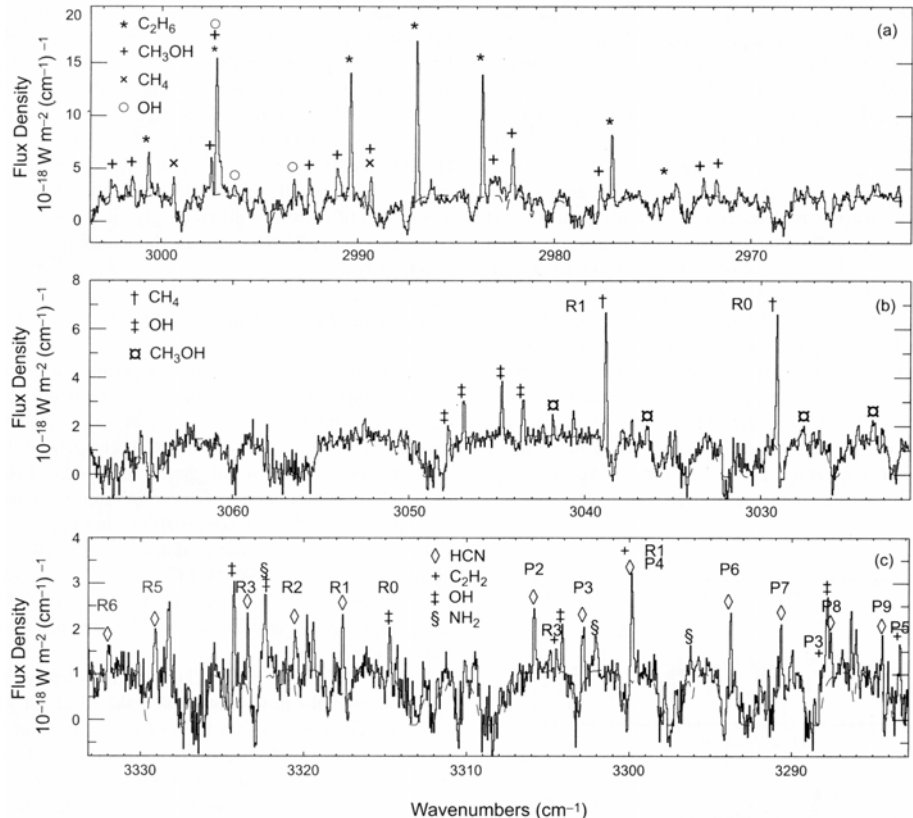


Fig. 4.8 High dispersion spectra in the $3 \mu\text{m}$ region of Comet C/1999 H1 (Lee) which shows the lines of various hydrocarbons. The spectra was obtained on August 21, 1999. (Adapted from Mumma, M.J. *et al.* 2001. *Ap. J.*, **546**, 1183, Reproduced by permission of the AAS).

The infrared observations in the region 1 to $30 \mu\text{m}$ of many comets have shown the presence of two strong broad emission features around $10 \mu\text{m}$ and $20 \mu\text{m}$. These features are generally attributed to silicate materials (Sec. 9.5).

Most of the polyatomic and complex molecules have rotational transitions whose wavelengths lie in the millimetre and centimetre region, i.e. radio frequency regions. Studies based on interstellar matter showed that interstellar clouds are dominated by molecules of simple, complex as well as of biological importance. It was immediately felt that many of these molecules may also be present in the cometary material. If found, it will

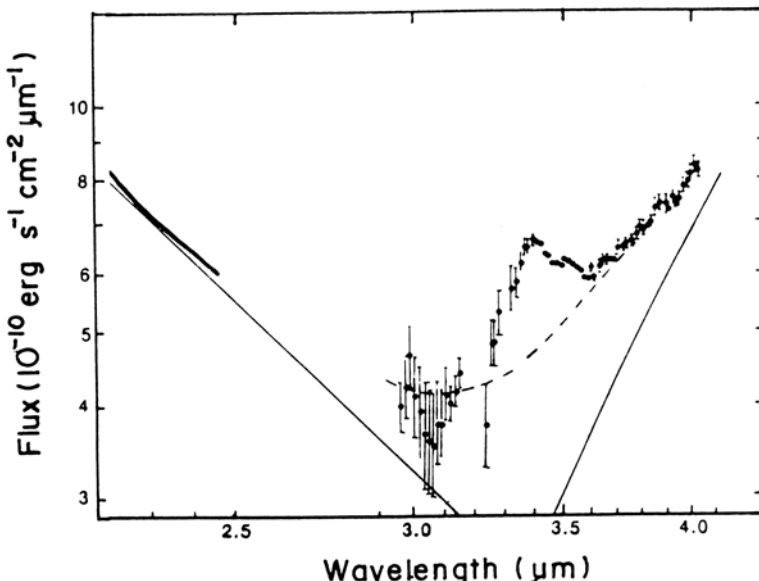


Fig. 4.9 The infrared spectrum of Comet Halley taken on March 31, 1986 ($r = 1.17$ AU) shows the presence of a broad emission feature around $3.4 \mu\text{m}$. The dashed line refers to the continuum for a black body of 350 K and the scattered sunlight (Wickramasinghe, D.T. and Allen, D.A. 1986. *Nature* **323**, 44).

have a great implication with regard to the origin of comets. They could also possibly be the parent molecules (Chap. 6) of cometary radicals. Therefore searches for many of these molecules have been carried out on many comets in the frequency range 80 – 460 GHz from ground based radio telescopes. Large number of molecules have been identified. A typical observed spectra from Comet Hale–Bopp (C/1995O1) is shown in Fig. 4.10 which exhibit lines of CH_3OH , SO and HC_3N .

Glycine ($\text{NH}_2\text{CH}_2\text{COOH}$), an amino acid has been detected for the first time in the dust particles of Comet Wild 2.

With regard to the spectra of diatomic molecules, the Λ –doubling of OH around 18 cm was first detected in Comet Kohoutek in 1974. Since then these lines have been monitored regularly in almost all the comets.

The possible presence of noble gases (He, Ne, Ar, Kr and Xe) whose lines lie in the far UV spectral region ($\lambda \lesssim 1200\text{ \AA}$) has been looked for, but not detected. The detection of noble gases which are highly volatile and chemically inactive should provide clues with regard to the thermal history of the nucleus of a comet.

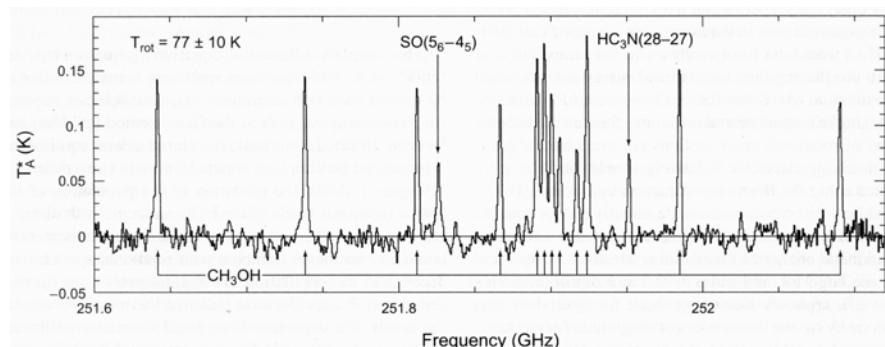


Fig. 4.10 Radio spectrum of Comet Hale-Bopp Showing the lines of molecules CH_3OH (twelve $J_3 - J_2$ A lines), SO (5_6-4_5 line) and HC_3N ($J(28-27)$ line) (Lis, D.C. *et al.* 1999. *Earth, Moon and Planets*, **78**, 13).

The studies carried out on several comets has shown the presence of various kinds of molecules of varying complexity (~ 50), but smaller than those detected from the interstellar medium (~ 150). Many of these molecules are likely to be parent molecules sublimated from the cometary ices. Many of the molecules present in the interstellar medium but not seen from comets does not mean that they are not present in comets. This could be due to the fact that the detection of a line depend upon various factors, such as column density of the specie, timing of the observation, possible destruction etc.

There are large number of unidentified features that are present in the spectra of comets in the UV, visible and radio regions. Many of these unidentified features could be due to some already known species (atoms, radicals, ions, simple molecules, complex molecules). Therefore the identification of these features require further laboratory studies as well as theoretical investigations.

The detection of continuum emission at 3.71 cm from Comet Kohoutek in 1974 has not been detected in other comets even with more sensitive instruments. However continuum at millimetre wavelengths have been detected from Comets Halley, Hyakutake and Hale–Bopp.

The *in situ* mass spectrometer studies of Comet Halley has given lot of new information about the species present in the coma. They have given rise to the identification of a large number of new species, which is difficult to detect through traditional spectroscopic means.

A compilation of some of the observed atomic and molecular species

in comets is given in Table 4.2. It should, however, be pointed out that the cometary coma must contain many more molecules than observed so far. The following interesting points may be noted regarding species of Table 4.2.

Table 4.2 Some of the observed species in comets.

Neutrals :	H, C, O, S, Na, K, Ca, V, Cr, Mn, Fe, Co, Ni, Cu C ₂ , CH, CN, CO, CS, OH, NH, S ₂ , SO, H ₂ C ₃ , NH ₂ , H ₂ O, HCN, H ₂ S, CO ₂ , HNC, OCS, SO ₂ , CS ₂ H ₂ CO, NH ₃ , HNCO, H ₂ CS, CH ₄ , C ₂ H ₂ , C ₂ H ₆ HCOOH, HC ₃ N, CH ₃ CN, CH ₃ OH, CH ₃ CHO, NH ₂ CHO, HCOOCH ₃ , HOCH ₂ CH ₂ OH, NH ₂ CH ₂ COOH
Ions:	C ⁺ , CO ⁺ , CH ⁺ , CN ⁺ , H ₂ O ⁺ , HCO ⁺ , H ₃ O ⁺ , CO ₂ ⁺
Dust:	Silicate CHON

1. H₂ has been detected.
2. PAHs have been detected.
3. The very first emission lines emitted by OH after the dissociation of H₂O called Prompt Emission lines have been seen.
4. The molecules detected are composed of the most abundant elements in the universe, namely H,C, O and N.
5. Most of the elements detected comes from sun-grazing comets, presumably arising from the vapourization of refractory grains.
6. Most of the species detected are organic, indicating the importance of carbon, similar to the case of interstellar molecules.
7. Highly Complex organic molecules belonging to homologous series, Alkanes, Alcohols, Aldehydes, Carboxylic acids and Cyanopolyyynes have been detected.
8. NH, NH₂ and NH₃ have all been seen.
9. Hydrocarbon such as CH₄, C₂H₂ and C₂H₆ are present.
10. One important element missing from the list is nitrogen. This is due to the fact that the resonance transition of nitrogen, which is at 1200 Å,

is very close to the strong hydrogen Lyman α line. Hence, it is very hard to detect this line. But nitrogen can be inferred from the strong CN emission lines.

11. N₂ has not been detected.
12. Most of the observed species are radicals or ions which are physically stable, but chemically highly reactive. This means that they cannot exist as such in the nucleus. So the general belief is that these radicals are the by-products of the break-up of some complex molecules. This has led to what is generally termed as ‘parent–daughter’ hypothesis for the observed species. Several possible parent molecules have been detected.
13. The predominance of radicals implies low densities in the coma which in turn means that the collisions may not be very important. However, very close to the nucleus they have to be considered.
14. Most of the products of water photodissociation have been observed.
15. There is a wide variation in the chemical composition of comets.
16. Ethylene glycol (HOCH₂CH₂OH) is the most abundant organic molecule inspite of its complexity.
17. Detection of amino acid Glycine (NH₂CH₂COOH) in cometary dust indicate that building blocks of life are prevalent in space.
18. Grains mostly made up of C,H,N and O called ‘CHON’ particles are present in comets. These grains contain highly complex molecules.
19. The observed anomalous isotopic ratio of elements indicate the presence of presolar grains.
20. Silicate dust mineralogy is highly complex.
21. Dust contain both high and low temperature condensates indicating that large scale mixing of material must have taken place in the solar nebula.

4.2. Forbidden Transitions

So far we have been discussing the spectra arising out of the allowed dipole transitions which have a mean lifetime of $\sim 10^{-8}$ sec.

Many forbidden lines arising out of several atoms have been seen from various types of astronomical objects, including comets. The mean lifetime for magnetic dipole and electric quadrupole transitions are $\sim 10^{-3}$ and 1 sec respectively.

The well-known auroral red lines of 6300.23 Å and 6363.87 Å, the green

line of 5577.35 Å of neutral oxygen atom have been seen in many comets. The red lines originate from the ^1D upper level while the green lines arise from the ^1S level as can be seen from the energy level diagram of neutral oxygen atom (Fig. 4.11). In the beginning there was some confusion as to

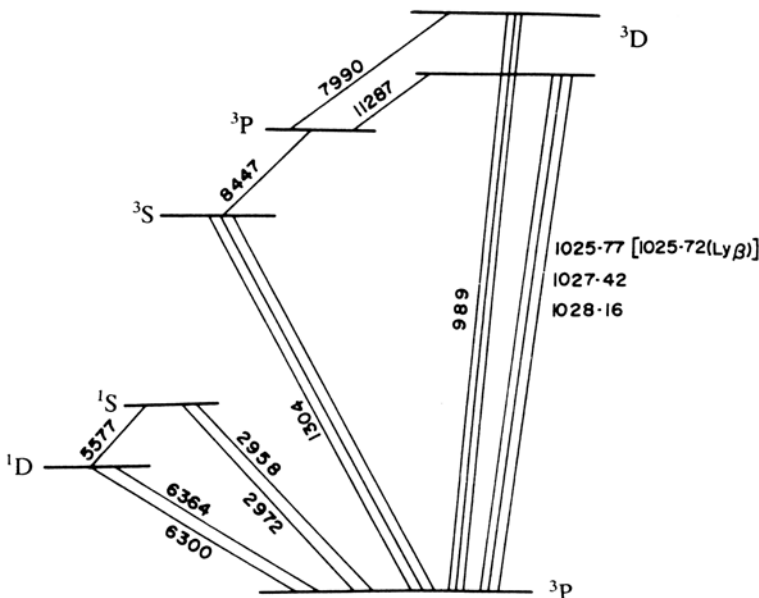


Fig. 4.11 Energy level diagram of oxygen atom showing various transitions.

whether these lines were due to the Earth's atmosphere or were intrinsic to the comet. This was finally resolved based on high dispersion spectra. The red lines observed in the spectra of a comet should be Doppler shifted in a manner similar to other cometary molecular emissions, if they are intrinsic to the comet, while that of atmospheric origin should not be shifted. Based on such arguments it was conclusively shown that [OI] lines are of cometary origin. In fact the observations carried out with Fabry–Perot instrument can separate the lines arising out of the earth's atmosphere and from the comet quite well. The life time of the ^1D state is about 130 sec and that of ^1S is less than 1 sec. The red doubled at 6300.34 and 6363.77 Å ($^1\text{D} - ^3\text{P}$) and the green line at 5577.34 Å ($^1\text{S} - ^1\text{D}$) arise out of 'prompt' emission, as the photodissociation of H₂O lead directly oxygen atoms in ^1D and ^1S states (Sec. 3.11). Oxygen atoms that are excited to the ^1S state decays to

3P state only 5% of the time and rest 95% to 1D state. The line 2972 Å has also been detected. The intensity of the red doublet is quite strong as can be seen from Fig. 4.1. The green line is weak compared to the red line. The green line is also blended with the cometary C₂ Swan band. Even so, the green line has been detected. Since red doublet lines are strong in comets, they have been observed regularly and studied extensively in comets.

As in the case of oxygen, the forbidden lines of carbon arising out of $^1D - ^3P$ transition at 9823 and 9849 Å has also been seen. The presence of carbon atoms in the 1D state (lifetime of 4000 sec) comes from the observation of the resonance scattered $^1P - ^1D$ transitions at 1931 Å.

4.3. Line-to-Continuum Ratio

Based on the spectra in the visual spectral region, one can classify the observed spectra of comets into two categories: (1) strong continuum and (2) strong molecular line emissions. Although at present a large number of observations exist on comets taken since early times they are however not homogeneous. This is due to the fact that the spectra have been taken with different instruments as well as at different heliocentric distances. Also all the available spectra are not of a very good quality. This is particularly so for earlier spectral observations. Therefore, it is hard to make any real meaningful ratio of continuum to line emission in comets. Nonetheless several attempts have been made to use the available observations in order to see any trend in the line to continuum ratios. One such study was based on a homogeneous set of observations of about 85 comets. A statistical study of these comets showed a wide variation in the line to continuum ratios among these comets (Sec. 9.1.4).

It may be noted that the spectra of comets is entering a new era due to the availability of sensitive instruments and detectors which can provide high spatial, spectral and temporal observations. It is also possible to get 2-dimensional images. In addition, the Earth's atmosphere is no more a hindrance for making observations in various spectral regions due to the use of rockets and satellites.

As can be seen from the general discussion of cometary spectra presented so far, comets are very rich in emissions arising out of various kinds of molecules. The next logical step is to extract the physical conditions of the gaseous material present in the coma from a study of these lines, which will be discussed in the following chapter.

Problems

1. Describe the spectra of a Comet at far of distance from the Sun and very close to the Sun. Why is there a difference?
2. Cometary spectra show only the emission lines. Explain.
3. Suppose one were to observe an absorption line in the spectra and the optical depth required is 0.1. Calculate the column density of sodium atoms for the D1 line.
4. What are the various criteria that may be used for a firm identification of an unknown line in a cometary spectrum.
5. What is meant by forbidden line? Describe the conditions under which forbidden lines occur. Mention some specific examples and discuss what we can learn from them.

References

A good account of the spectra of comets can be found in the following:

1. Arpigny, C. 1965. *Ann. Rev. Astr. Ap.* **3**, 351.
 2. Swings, P. and Haser. L., 1956. *Atlas of Representative Cometary Spectra* Liege: The Institute of Astrophysique.
 3. Arpigny, C., Rahe. J., Donn. B., Dossin, B. and Wyckoff, S. 1997. *Atlas of Cometary Spectra*, Kluwer, Dordrecht, Netherlands.
 4. Cochran, A.L. and Cochran, W.D. 2002. *Icarus*, **157**, 297.
- A discussion of the observations in the Ultraviolet (5), Visible (5,6), Infrared (7,8) and Radio (8,9) region can be found in
5. Feldman, P.D., Cochran, A. and Combi, M.R., 2005. In *Comets II*, eds, M.C. Festou, H.U. Keller and H.A. Weaver, University of Arizona Press, Tucson, p.425.
 6. A'Hearn, M.F. 1982. In *Comets*, ed. L.L. Wilkening, Univ. Arizona Press, Tucson p. 433.
 7. Hanner, M.S. and Tokunaga, A.T. 1991. In *Comets in the Post Halley Era*. eds. R.C. Newburn, M. Neugebauer and J. Rahe. Kluwer Academic Publishers p. 93.
 8. Bockelee-Morvan, D., Crovisier, D., Mumma, M.J., and Weaver, H.A. 2005. In *Comets II*, eds, M.C. Festou, H.U. Keller and H.A. Weaver, Univ. Arizona Press, Tucson, P.391.
 9. Crovisier, J. and Schloerb, F.P. 1991. In *Comets in the Post Halley Era*. eds. R.C. Newburn, M. Neugebauer and J. Rahe. Kluwer Aca-

demic Publishers, p. 149.

The first observational results for Comet Kohoutek using Fabry–Perot instrument is given in

10. Huppler, D., Reynolds, R.J., Roesler, F.L., Scherb, F. and Tranger, J. 1975. *Ap.J.*, **202**, 276.

The detection of amino acid Glycine is reported in the following paper

11. Elsila, J.E., Glavin, D.P. and Dworkin, J.P. 2009. *Meteorites and Planetary Science*, **44**, 1323.

The reference for the study of gas to dust ratio is the following

12. A'Hearn, M.F. *et al.* 1995. *Icarus*, **118**, 223.

CHAPTER 5

Spectra of Coma

In the last chapter, we discussed the general characteristics of the spectra of comets. As was pointed out, the analysis of these spectral lines can give information about the temperature, pressure and the physical processes responsible for producing the lines, in addition to the abundances of the species. Here we would like to discuss in some detail a few of these aspects, with special reference to the cometary spectra.

5.1. Fluorescence Process

In order to analyse cometary spectra it is necessary to know the mechanism responsible for the excitation of cometary emissions. The absorption of solar radiation in their resonance transitions which then trickle down to give the radiation is called the *resonance* fluorescence process. Whether the mechanism of excitation is due to the collision process with atoms, molecules or ions, or due to the resonance fluorescence process is governed by the relative time scales for the two processes. The collision time scale is given by

$$\tau_{\text{coll}} \approx \frac{1}{n\sigma v} \quad (5.1)$$

where n , σ and v denote the number density, the collision crosssection and the velocity of the species respectively. Using for the collision cross-section with neutral atoms or ions, a typical value $\sigma \sim 10^{-16} - 10^{-17} \text{ cm}^2$ and $v \approx 1 \text{ km/sec}$, $n \approx 10^5/\text{cm}^3$, the characteristic collision time scale turns out to be

$$\tau_{\text{coll}} \approx 10^7 \text{ sec.} \quad (5.2)$$

This time scale is much larger than the typical time scale for absorption of solar radiation in the visible region of say C₂ and CN at a distance of 1 AU,

which is about 10 to 100 sec. Therefore for typical cometary conditions the absorption of solar radiation is the main excitation process. Another observation which also supports the above conclusion is that the line emissions seen in a cometary spectra arise mostly from the ground electronic state of the molecule and this involves a lot of energy. It can therefore be brought about only by the absorption of the solar radiation. However, the striking success for the process came from the work of Swings. He noticed that the relative intensity of rotational lines of the CN (0, 0) band seemed to have peculiar minimum and maximum intensities at certain locations. The pattern also changed with the Sun-Comet distance, as can be seen from Fig. 5.1, which shows a marked difference between the two spectra taken about 10 days apart. Comparing the position of the observed lines with the solar spectrum, it was found that the position of minimum intensity corresponded to the regions of less flux in the solar radiation field as compared to that of maximum intensity positions. This in turn was related to the presence or absence of absorption lines called *Fraunhofer lines*. In other words, there existed a definite correlation between the absorbed solar radiation by the molecule and the corresponding emission intensity. Since the comet has a variable velocity around its orbit, the frequency of the radiation that the molecule in the comet absorbs depends upon this velocity due to the Doppler shift effect. Therefore the observed intensity pattern should change depending upon whether the Fraunhofer lines come in the way of absorption or not. These are also consistent with the observed intensity patterns. This effect is generally called the ‘Swings effect’.

Let us further examine the validity of the resonance fluorescence excitation process from a detailed analysis of the rotational and vibrational spectra of molecules. The calculation of intensities of lines or a synthetic spectrum requires the knowledge of the population distribution in different energy levels of the molecule. This is a complicated problem as it is necessary to simultaneously consider the different electronic, vibrational and rotational levels of the molecule in the level population calculation. The nature of the energy levels depends upon the type and structure of the molecule. Just as an example to show the complexity of the energy level diagram of the molecules, Fig. 5.2 shows the various energy levels and the transitions that have to be considered for the OH molecule. Therefore it is rather difficult to give a general set of equations for the calculation of the population distribution of molecules. Instead, one has to consider each molecule on a more or less individual basis depending on its energy level structure. However, there are some simple diatomic molecules for which the

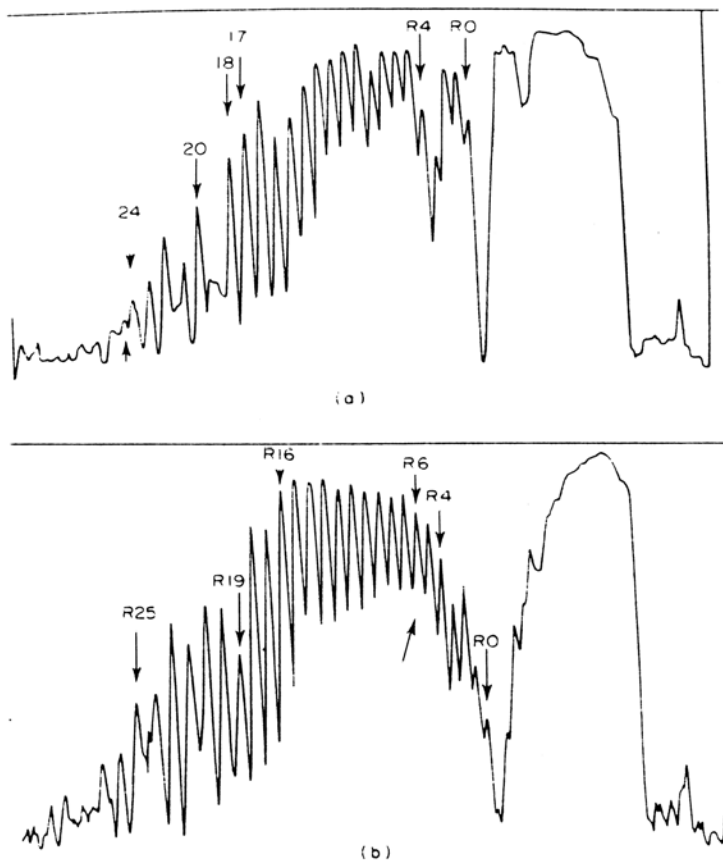


Fig. 5.1 The microdensitometer tracings in the spectral region of CN violet band of Comet Ikeya 1963 1.(a) and (b) refer to the spectra taken on the 3rd and 13th of March 1963 respectively. The variations in the band structure between the two spectra can be seen. (Taken from Whipple, F.L. 1978. In *Cosmic Dust*. ed. J.A.M. McDonnell, New York; John Wiley and Sons. p. 1).

energy levels are such that it is a good approximation to consider vibrational and rotational transitions separately. Therefore it is appropriate to outline the method for the cases of vibrational and rotational levels treated separately. The formalism can easily be adapted to take into account the complexities of the molecule of interest. Earlier studies indicated that the C₂ molecule appears to deviate from the general behaviour of all other molecules. Therefore, the case of C₂ molecule will be considered separately.

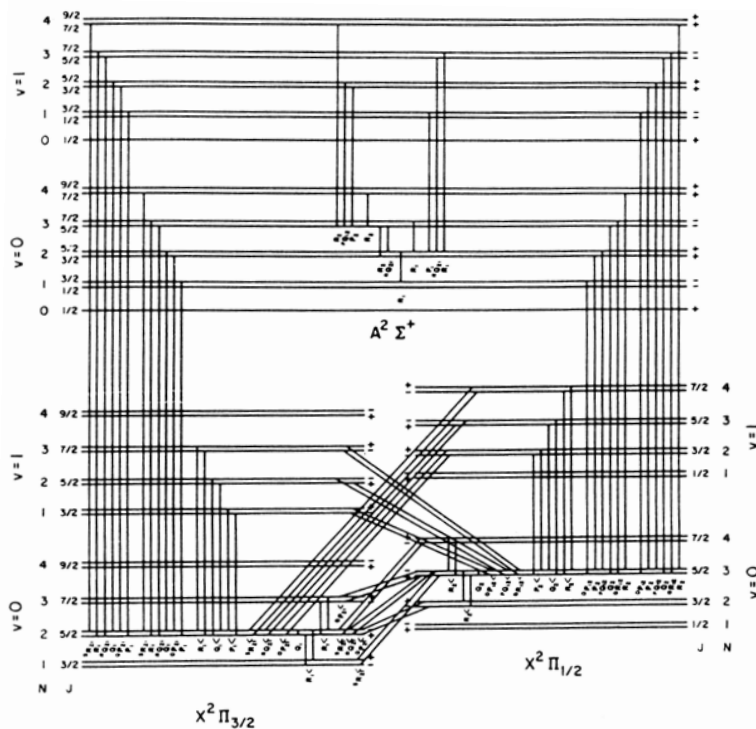


Fig. 5.2 The energy level diagram of OH molecule showing electronic, vibrational and rotational structure and the various transitions between them (Schleicher, D.G. and A'Hearn, M.F., 1988. *Ap.J.* **331**, 1058).

5.1.1. Rotational structure

Consider the case of rotational structure for a given vibrational band of a diatomic molecule. The intensity of a line depends, among other things, on the fraction of the species in different rotational levels. The Boltzmann's law for the distribution of population in different rotational levels for an assumed temperature is not a good approximation due to the fact that the presence of Fraunhofer lines in the solar spectrum tends to make the population distribution in various rotational levels irregular. In addition, the collisions which tend to produce the Boltzmann distribution, are rather infrequent due to low densities present in a cometary atmosphere. Therefore, it becomes necessary to determine the resulting population distribution from the solution of the statistical equilibrium equations which take into account the absorption and the emission processes. For the pure radiative

case, the number of molecules in an upper rotational state N_j is determined by the balance between the number of molecules entering and leaving this particular state. This can be written as

$$\frac{dN_j}{dt} = \sum_{P,Q,R} N_i B_{ij} \rho_{ij} - N_j \sum_{P,Q,R} A_{ji} \quad (5.3)$$

where N_i is the number of molecules in the lower rotational state i , such that $i < j$. The summation is over P, Q and R branches. The A 's and B 's are the Einstein coefficients and ρ is the radiation density corresponding to the wavelength of the transition. ρ has to be corrected for the radial velocity (Chap. 3) of the comet through the relation

$$\lambda_{\text{exc}} = \lambda_{\text{lab}} \left(1 - \frac{v}{c} \right) \quad (5.4)$$

where v is the radial velocity of the comet with respect to the Sun which can be calculated as the orbit is known.

The detailed energy distribution of the solar radiation field with the Fraunhofer lines present has also to be used in the calculation of ρ . This requires a very high dispersion scan of the solar spectrum in the region of interest. Sometimes for simplicity and to a first approximation, 'blocking coefficients' (γ_λ) are used, which give a measure of the degree of absorption in a given range of wavelengths. Therefore multiplying the mean radiation field with the blocking coefficients, takes into account the effect of Fraunhofer lines in an approximate manner. However, the detailed energy distribution should be used as far as possible.

Since the physical conditions do not change drastically within the time of observation, one can use $(dN_j/dt) = 0$ which implies a steady state condition. Therefore, Eq. (5.3) reduces to

$$\sum_{P,Q,R} N_i B_{ij} \rho_{ij} = N_j \sum_{P,Q,R} A_{ji}. \quad (5.5)$$

A similar expression can be written for the transitions in the lower rotational state as

$$\sum_{P,Q,R} N_j A_{ji} + N_{i+1} A_{i+1}^{\text{rot}} = N_i \left[\sum_{P,Q,R} B_{ij} \rho_{ij} + A_i^{\text{rot}} \right] \quad (5.5a)$$

where A^{rot} represents the transition rate for pure rotational transitions in the lower electronic state, which should be included for a heteronuclear molecule. The total number of equations involved depends upon the number of rotational levels in the upper and lower states. A simultaneous solution of

these equations with the added condition that the sum total of populations in all the levels is equal to unity, i.e.

$$\sum_{t=1}^{i+j} N_t = 1 \quad (5.6)$$

gives the relative populations in various rotational levels. For illustrative purposes, Fig. 5.3 shows the relative populations of the rotational levels of $(0, 0)$ band of $B^2\Sigma^+ - X^2\Sigma^+$ transition of the CN molecule for various heliocentric distances. It shows clearly that with decrease in distance lot more rotational levels are populated.

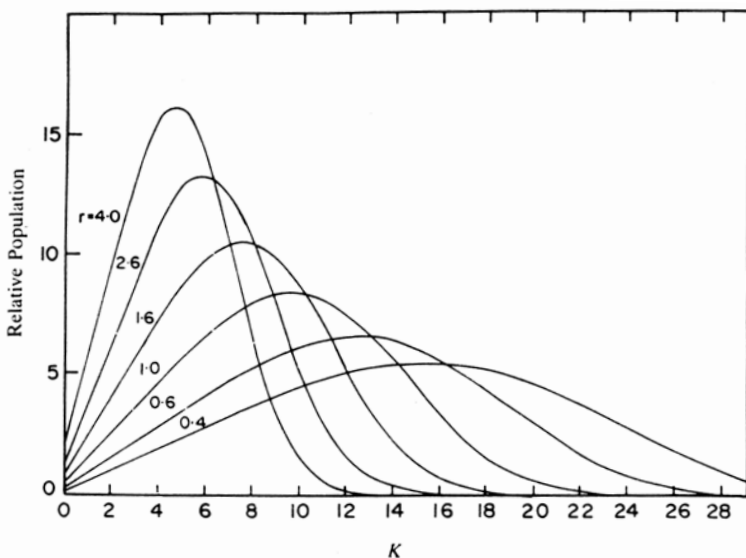


Fig. 5.3 The figure gives the relative population distribution of rotational levels for the ground state of CN in comets for different heliocentric distances. (Arpigny, C. 1964. *Ann. d'Ap.* **27**, 393).

In general the excitation by solar radiation of pure rotational levels is negligible due to weakness of solar flux at the wavelength of rotational transitions. However at large heliocentric distances the rotational excitation from the 2.7 K cosmic background radiation may become important and has to be considered in the fluorescence calculations.

5.1.2. Vibrational structure

Let us now consider the vibrational bands of diatomic molecules. The relative populations in different vibrational levels have to be obtained from the solution of the statistical equilibrium equations written for each vibrational level. Since many electronic transitions can arise from the same ground state, it is necessary to take into account all these electronic transitions in addition to the vibrational transitions. The statistical equilibrium of any vibrational level is determined as before, by a balance between the transitions into and out of that particular level. The equations for the lower and upper electronic states i and j respectively for a homonuclear molecule can be written as follows. For the vibrational levels of the lower electronic state

$$N_i \sum_{k=m}^p B_{ik} \rho_{ik} = \sum_{k=m}^p N_k (B_{ki} \rho_{ki} + A_{ki}), \quad i = 1, 2, \dots, (m-1) \quad (5.7)$$

and for the vibrational levels of the upper electronic state

$$N_j \sum_{l=1}^{m-1} (B_{jl} \rho_{jl} + A_{jl}) = \sum_{l=1}^{m-1} N_l B_{lj} \rho_{lj}, \quad j = m, p. \quad (5.8)$$

Here N is the fraction of molecules in different vibrational levels, such that $\sum_{t=1}^p N_t = 1$. The A 's and B 's are the Einstein coefficients, ρ is the energy density of the solar radiation.

For heteronuclear molecules, the vibrational transitions within the ground electronic state of the molecule are permitted. This term has to be included in the above equations. For upper electronic states, these transitions are not important as the probability for electronic transitions is much greater than that of vibrational transitions. The Einstein A value for the vibrational transitions $v \rightarrow v'$ is given by the expression

$$A_{vv'}^{\text{vib}} = \frac{64\pi^4 \nu^3}{3hc^3} |R_{vv'}|^2. \quad (5.9)$$

Here $|R_{vv'}|^2$ represent the vibrational matrix elements. These could be calculated from quantum mechanics provided the variation of the dipole moment function is known. However for most of the molecules the variation of the dipole moment function is not known. For such cases, one can approximate $|R_{vv'}|^2$ as

$$|R_{vv'}|^2 = \mu_1^2 |R'_{vv'}|^2 \quad (5.10)$$

where μ_1 is the coefficient of the linear term in the dipole moment expansion and

$$R'_{v+p,v} = \left[\frac{r_e^2 B}{\omega_e} x_e^{p-1} \frac{(v+p)!}{p^2 v!} \right]^{1/2} \quad (5.11)$$

where $p = v' - v$ and the other parameters are the usual spectroscopic constants of the molecule. This expression is a good approximation if $(v + v')x_e \lesssim 1$. This condition is generally satisfied for most of the molecules of astrophysical interest.

5.1.3. Comparison with observations

The intensities or the synthetic profile of the bands can easily be calculated from the knowledge of the population distribution in different rotational or vibrational levels. The calculated profiles can then be convolved with the Gaussian profile of instrumental resolution corresponding to the observations. The results of such calculations for the rotational profile of the (0, 0) band of $B^2\Sigma^+ - X^2\Sigma^+$ transition of the CN molecule for various cases is compared with the observed profile for Comet Mrkos in Fig. 5.4. They clearly indicate that the observed profile agrees well with the expected profile when the effects of Fraunhofer lines are taken into account.

A more detailed and sophisticated synthetic spectrum of the same band has been calculated. The calculated profile agrees very well with the observed profile of several comets (Fig. 5.5). Such comparisons for the (0, 0) band or bands arising from $A^1\Pi - X^1\Sigma^+$ transitions for several other molecules such as CO, CS and OH have also been carried out for various comets. They also show good agreement.

In a similar way, the expected intensities of various vibrational bands of the molecules CO, CO^+ , CS, CN, CN^+ etc. can be calculated based on the resonance fluorescence process. As a typical case, Table 5.1 shows a comparison of the expected and the observed intensities of lines for the molecules CO^+ and CS. The results for several other molecules also show a similar agreement.

It is interesting to note that the total excitation rate to $A^1\Pi$ state of CO by the absorption of solar radiation in the 1500 Å region leading to resonance fluorescence in the $CO(A-X)$ system is around 1 to $2 \times 10^{-6}s^{-1}$ at 1 AU. This is much smaller than the excitation rate by solar radiation

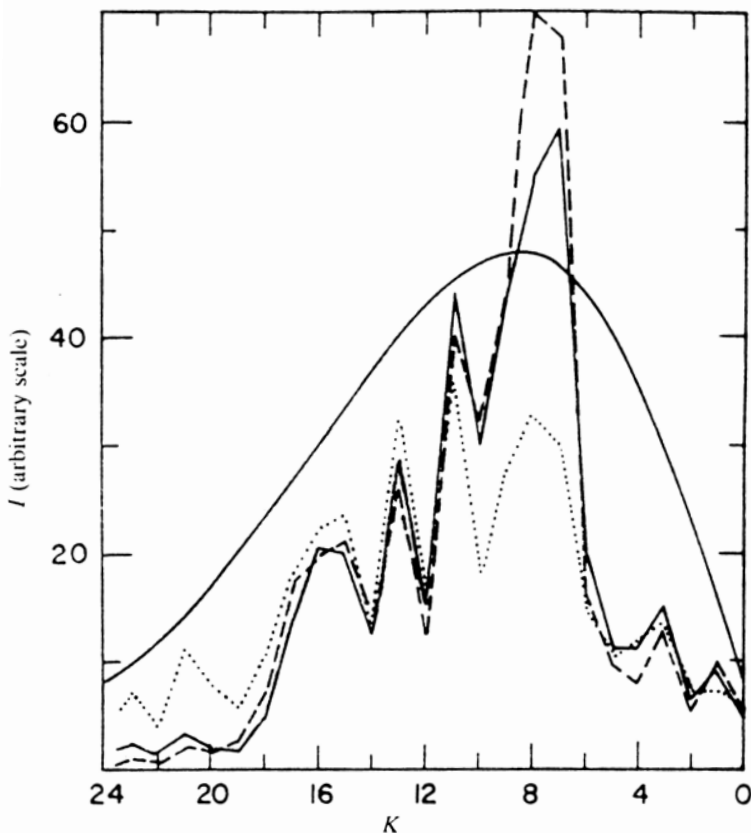


Fig. 5.4 Comparison of the expected and the observed (solid curve) intensity distribution in the R-branch of the violet (0, 0) band of CN system for Comet Mrkos. The continuous curve refers to results based on Boltzmann distribution for 500°K. The dotted and dashed curves refer to results based on statistical equilibrium calculations without and with Fraunhofer lines taken into account, (Arpigny, C 1964, *loc. cit.*).

of the CO v(1, 0) band at $4.7 \mu\text{m}$, which is around $2.6 \times 10^{-4} \text{s}^{-1}$ at 1 AU. This indicates that the populations of the ground state rotational levels are controlled mainly by vibrational excitation with solar radiation. The extension of cometary spectra into the ultraviolet region has made it possible to look for some of the transitions which lie in the ultraviolet region. In some cases there could be some disagreement between the calculated and the observed intensities. This could arise due to the fact that there may be disagreement in the observations and also there could be uncertainties in

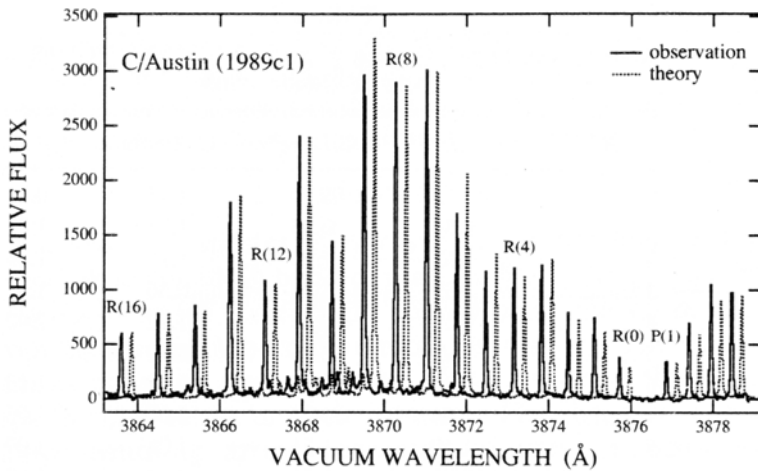


Fig. 5.5 Comparison of the observed R-branch lines of (0,0) band of ($B^2\Sigma^+ - X^2\Sigma^+$) system of CN from Comet Austin with the calculated spectrum based on resonance fluorescence process. The calculated spectrum is shifted by 0.25 Å for easier comparison (Wyckoff *et al.* 2000. *Ap.J.*, **535**, 991).

Table 5.1 (A-X) Bands of CO^+ and CS.

Band (CO^+)	Computed*	Observed ^a	Band (CS)	Computed ⁺	Observed
(0,0)	0.11	0.12	(0,0)	1.0	1.0 ^b 1.0 ^c
(1,0)	0.63	0.60	(1,0)	0.03	0.05
(2,0)	1.00	1.00	(0,1)	0.13	0.12 0.11
(3,0)	1.20	1.16	(1,1)	0.07	0.08
(4,0)	0.67	0.64	(0,2)	0.01	0.01
(5,0)	0.28	0.40	(1,2)	0.03	0.012

a. Comet Humason (1961e) (Arpigny, C. 1964. *Ann.d'Ap.* **27**, 406)

b. Comet West (Smith, A.M., Stecher, T.P. and Casswell, L. 1980. *Ap. J.* **242**, 402)

c. Comet Bradfield (Feldman, P.D. *et al.* 1980, *Nature* **286**, 132)

*(Krishna Swamy, K.S. 1979, *Ap. J.* **227**, 1082; Magnani, L. and A'Hearn, M.F. 1986, *Ap. J.* **302**, 477).

+(Krishna Swamy, K.S. 1981. *Astr. Ap.* **97**, 110; Sanzovo, G.C., Singh, P.D. and Huebner, W.F. 1993. *AJ*. **106**, 1237).

the oscillator strengths, variation of electronic transition moment with the r-centroid and other parameter which enter into the model calculation.

For those molecules for which the oscillator strengths are not available, it may be possible to reverse the problem and get an estimate for the oscillator strength of the transitions from a comparison of the expected

and the observed intensities of lines.

From the discussion so far, it is clear that the resonance fluorescence process is very successful in explaining the observed band spectra of various molecules in comets. So far, only the effect of the radial component of the velocity of the comet in its orbit leading to Doppler shift of lines has been considered. This is the well known Swings-effect. In addition, it is necessary to consider the velocity of the gas in the coma. As the gas comes out of the nucleus, it expands outwards in all directions. Therefore, the resultant Doppler shift of the solar radiation depends upon these two components. The resultant velocity will be different at different locations in the comet and hence the relative intensities of the same feature should vary with position in the coma. Such an effect was first noticed by Greenstein in the Comet Mrkos. This is generally called Greenstein effect. This can be seen clearly from Fig. 5.6 where the relative intensities of CN(0, 0) lines at three different locations in the Comet Seki are shown. To take care of the effect of internal motions in the solution of statistical equilibrium equations, it is necessary to know the distribution of velocities of the species as a function of the distance from the nucleus. This has to be derived on the basis of a simple physical model. One such model could be that the gaseous material is flowing out of the nucleus with a uniform velocity. The model could be made more complicated by including the resistance force due to the solar wind and so on. In addition to the orderly motion discussed so far, there may also be motions present purely of random character. It is even harder to consider this type of velocity in the model calculation. Therefore the subject of the various kinds of gaseous motions in comets is quite complicated and it is hard to disentangle one from the other. In principle, if one has a very high dispersion spectrum, it is possible to construct a detailed model including the effect of all the velocities, which can reproduce the observations well.

There are also other complications that have to be taken into account. In the above treatment it is assumed that the coma is optically thin. For reasonable value for the absorption cross section, $\sigma \approx 10^{-17} - 10^{-18} \text{ cm}^2$ for molecules, the optical depth effect ($\tau = N\sigma \gtrsim 1$) has to be considered for the molecules with a large column density N , which imply large production rates of the molecules. Since for most of the cometary species the optical depth $\tau \lesssim 1$, the optically thin assumption is a very good approximation for most of the lines. But for some resonance lines such as Lyman α line of hydrogen at 1216 Å and the rotational lines of the H₂O molecule, the optical depth could be significant and therefore could affect the molecular excitation through radiative trapping. Another complication arises for

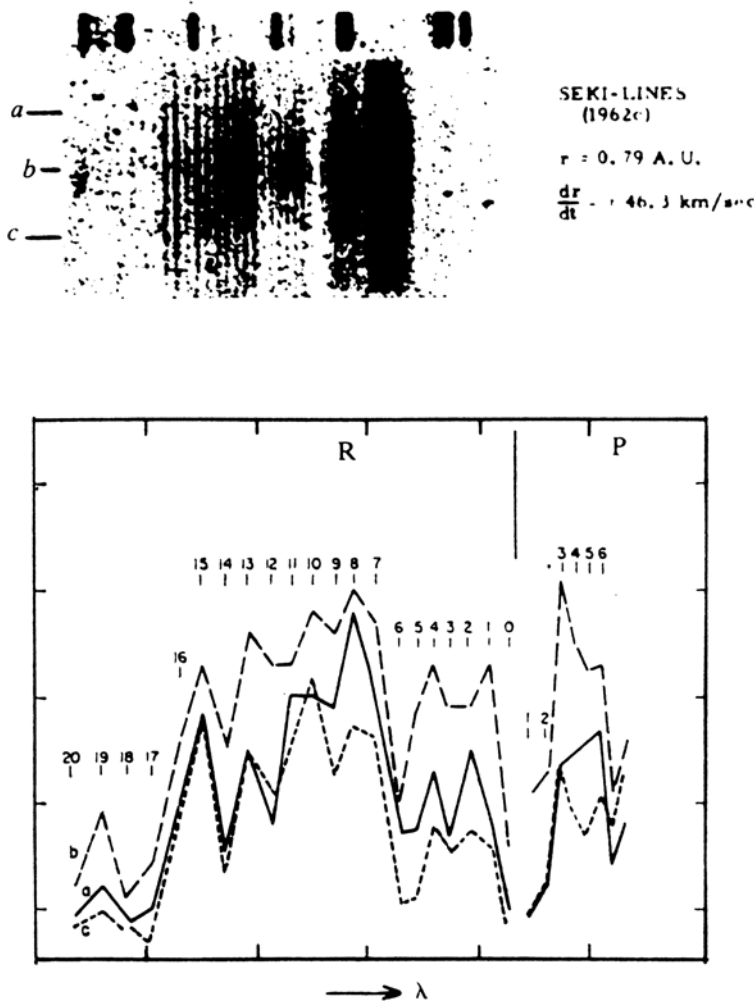


Fig. 5.6 Top section shows the rotational lines of (0,0) band of the violet CN system in Comet Seki-Lines. The lower portion represents the tracings of the spectra in the regions a, b and c. (Arpigny, C. 1965. *Mem. Acad. Roy. Belg. Cl 8°*, Vol. 35, No. 5).

molecules with short lifetimes. It is possible that such molecules may decay even before the fluorescence equilibrium is reached, which require several cycles of excitation and de-excitation. These have to be treated based on time dependent calculations.

In addition to the radiative process collisional excitation and de-

excitation could also be important. Since the density to a first approximation varies with distance from the nucleus as r^{-2} , the collisions can be an important excitation process close to the nucleus, \sim a few thousand kilometers for molecules with production rates $\sim 10^{29}/\text{sec}$. In the inner coma, the molecules will be more in thermodynamic equilibrium rather than fluorescence equilibirum. As one moves outwards there will be a region where both thermodynamic and fluorescence equilibria will be operating. Finally at large distances, fluorescence equilibrium takes over. Since the observed intensities or profile of emission lines are an average over the line of sight in the coma, it is necessary to integrate over the whole volume, including both collision and radiative processes. For collision effects, one generally considers the collision of the molecule with H₂O as it is the most abundant molecule in the coma. However, other species might have to be considered if they turn out to be important. For example, the production rate of CO is much larger than that of H₂O in comets at large heliocentric distances and therefore collisional excitation is due to that of CO.

The collision de-excitation rate is given by

$$C_{\text{coll}} = n_{\text{H}_2\text{O}} \sigma_{\text{coll}} \bar{v} \quad (5.12)$$

where σ_{coll} is the collision cross section for rotational transitions of the molecules produced by collisions with H₂O, $n_{\text{H}_2\text{O}}$ is the number density of H₂O molecules and \bar{v} is the mean relative velocity between H₂O and the molecule and is given by

$$\bar{v} = \frac{8kT}{\pi} \left[\frac{1}{m_{\text{H}_2\text{O}}} + \frac{1}{m_{\text{mol}}} \right]. \quad (5.13)$$

Here T is the temperature of the gas, $m_{\text{H}_2\text{O}}$ and m_{mol} are the masses of the two molecules. The excitation cross sections can be obtained from the de-excitation crosssections from the detailed balance condition

$$\sigma(l \rightarrow u) = \sigma(u \rightarrow l) \frac{g_u}{g_l} \exp \left[-\frac{E_u - E_l}{kT_{\text{kin}}} \right] \quad (5.14)$$

where u and l refer to upper and lower levels and T_{kin} the temperature that characterises the colliding particles.

The modelling of the collision process in the coma is rather uncertain due to uncertainties in the collision cross sections between the molecular species and the H₂O molecule and the temperature of the coma gas. However the best available data is generally made use of in such calculations. The variation of the H₂O density with distance from the nucleus is also required and is generally calculated based on Haser's model (Sec. 6.1.2).

The time evolution of the profiles, until it attains the equilibrium state, can be investigated based on the time dependent population distribution. As an example, the results for the case of A-X(0, 0) band of CS is shown in Fig. 5.7 for different initial population distributions. Such calculations are important when comparing with observations made closer to the nucleus.

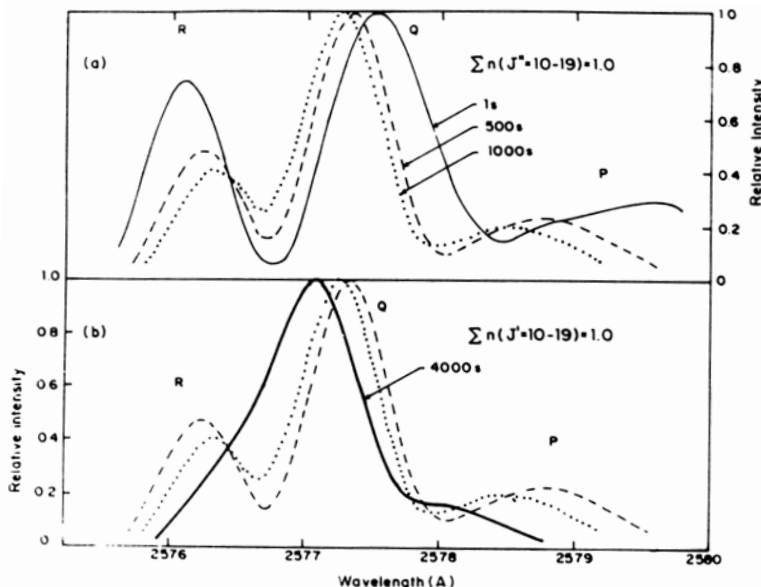


Fig. 5.7 Time evolution of the synthetic profile of P, Q and R branches of the (0, 0) band of CS molecule for the case when the initial population ($t = 0$) is distributed over the rotational levels in the lower level $J'' = 10$ to 19 (a) or upper levels $J' = 10$ to 19 (b) at 4000 km from the nucleus. The time for each curve is marked. The curves are for a spectral resolution of 0.8 Å corresponding to Halley's data ($r=1.1$ au, $Q(H_2O)=3.0 \times 10^{29} s^{-1}$, $T = 300$ K; Krishna Swamy, K.S. and Tarafdar, S.P. 1993. *Astr. Ap.* **271**, 326).

5.1.4. Case of C_2 molecule

One exception to the general behaviour of the resonance fluorescence excitation process appeared to be the case of the C_2 molecule. This was noticed as early as 1953 and showed that the calculated relative band strengths did not agree with the observed relative strengths. There was a discrepancy of nearly a factor of two between the expected and the observed intensities. Early investigators had expressed this discrepancy in terms of the

vibrational temperature of the C_2 molecule. Therefore it is also called ‘the problem of low vibrational temperature of C_2 ’. The observed difference was also found to be dependent upon the heliocentric distance of the comet.

The excitation mechanism which populates the upper energy states also determine the vibrational level population in the lowest electronic state. The initial population distribution produced at the time of formation of the molecule is masked by the excitation and decays, finally leading to the equilibrium population distribution. The resulting population distribution in the bottom triplet state should therefore be close to the Boltzmann distribution corresponding to the colour temperature of the Sun in the Swan band region. However the observed distribution gives a lower value ~ 3500 K. This discrepancy was rather disturbing in view of the fact that the C_2 Swan bands are the strongest in the visual region of a cometary spectrum and this had questioned the basic fluorescence excitation mechanism itself. The problem of low vibrational temperature of C_2 has finally been resolved based on a new physical effect which seems to operate very effectively in the case of the C_2 molecule as can be understood from the energy level diagram of the C_2 molecule shown in Fig. 5.8. The Swan bands which are strong in the cometary spectra arise from the triplet state, which lies about 714 cm^{-1} higher than the ground singlet state. This had given rise to another interesting problem which also eluded a reasonable explanation. i.e. why is it that Swan bands are strong in a cometary spectrum even though they do not arise from the ground state of the molecule, contrary to the normal situation. It was therefore not clear whether this reflected the preferential formation of the triplet state at the time of formation of the C_2 molecule or the fact that only the weak lines of the singlet series are expected in the spectra. In Fig. 5.8 the vibrational levels of the electronic states $a^3\Pi_u$ and $b^3\Sigma_g^-$ of the triplet states are also shown. It shows that the vibrational levels of the ground triplet electronic state, for $v'' > 4$, lies at a higher energy level compared to those of the $b^3\Sigma_g^-$ state. Therefore the transitions from higher vibrational levels of the $a^3\Pi_u$ electronic state can decay to lower lying vibrational levels through the vibrational levels of the $b^3\Sigma_g^-$ electronic state. The result of such transitions is to depopulate the higher vibrational levels of the $a^3\Pi_u$ state giving rise to more concentration in the lower vibrational levels which implies a non-Boltzmann type of population distribution (Fig. 5.9). This effect is in a sense equivalent in principle to vibrational transitions in the ground state of the molecule. Therefore even though C_2 is a homonuclear molecule wherein transitions between the lowest lying vibrational levels are forbidden, there is a physical mechanism by

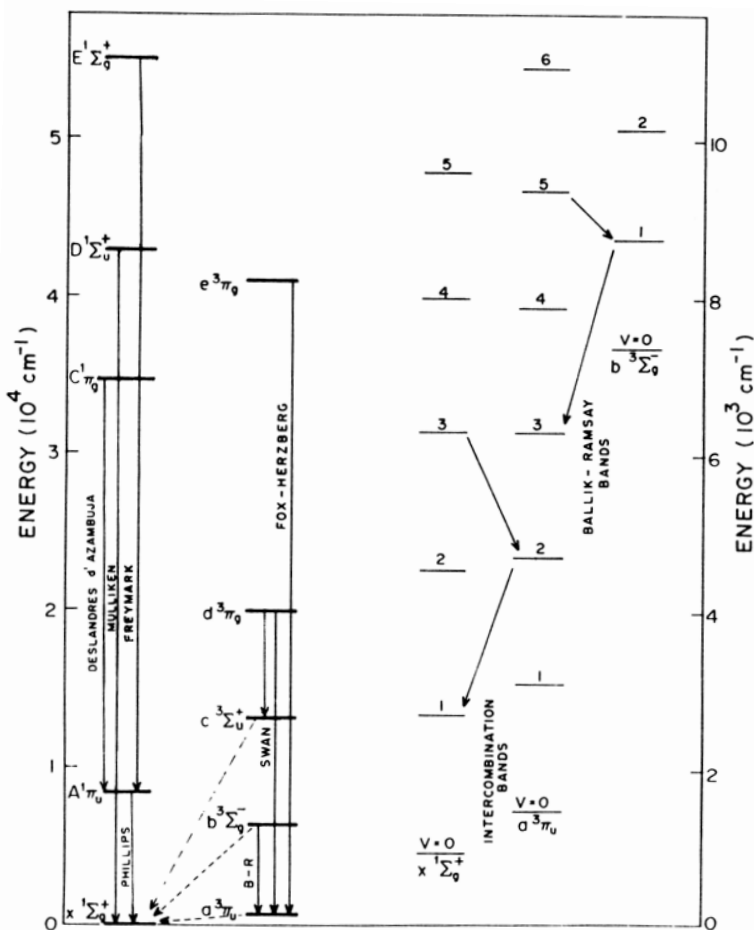


Fig. 5.8 Energy level diagram for the C_2 molecule. The electronic structure is shown on the left-hand side. The singlet electronic state is the ground state of the molecule. Various transitions are shown. B-R indicates the Ballik-Ramsay bands. The vibrational levels of three lowest electronic states are shown on the right-hand side.

which the population from higher levels cascade radiatively to lower vibrational levels in the ground electronic state of the molecule. This increases the concentration in the lower levels thereby simulating a lower excitation temperature. Since the rate of spontaneous downward transitions would be fixed, this process would become relatively more important in the lower radiation field at greater heliocentric distances, so that the vibrational tem-

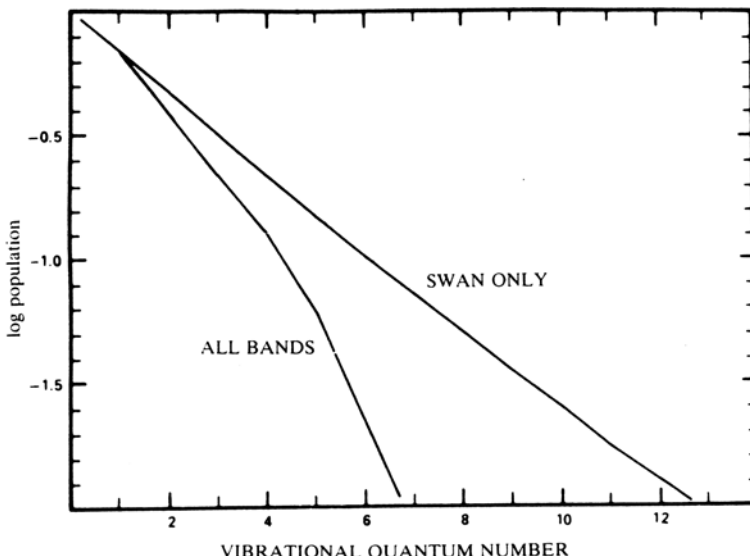


Fig. 5.9 The expected vibrational population distribution in the $a^3\Pi_u$ state is shown for the cases when Fox-Herzberg, Ballik-Ramsay and Swan bands (referred as All bands) or only Swan bands are included in the calculations. (Krishna Swamy, K.S. and O'Dell, C.R. 1977. *Ap. J.*, **216**, 158). The deviation occurs due to new depopulation mechanism discussed in the text.

perature would be expected to drop with increasing heliocentric distance.

In order to calculate the expected intensities of Swan and Phillips systems, the modelling of the C_2 molecule has to be carried out taking into account simultaneously both the singlet and triplet states. The model developed includes a total of ten electronic states with several vibrational levels in each of the electronic state. The forbidden singlet-triplet ground state transitions is the link between the singlet and triplet states for which the electronic transition moment is taken as a variable parameter.

The solution of the statistical equilibrium equations of such a system gives the population distribution in various levels. The resulting population distribution in the ground state as shown in Fig. 5.9 clearly shows the importance of the depopulation mechanism discussed earlier.

The expected band sequence flux ratios can be calculated from a knowledge of the steady state relative populations in different vibrational levels. The total energy emitted in a band sequence for a given value of

$\Delta v = (v' - v'')$ can be written as

$$F(\Delta v) \approx \sum_{V''} n_{V''} \sum_{\Delta v} B_{V''} v' \rho_{V''v'} P_{v'v''} n_{v'',v''}. \quad (5.15)$$

Here $n_{V''}$ is the level population and $P_{v'v''}$ is the probability that when an absorption takes place from the state v'' to v' state, it will come back to state v'' . The above expression can be written as

$$F(\Delta v) \approx \sum_{V''} n_{V''} PR(V'', \Delta v) \quad (5.16)$$

where $PR(V'', \Delta v)$ denotes the production rate. The production rates can be calculated from a knowledge of the molecular parameters and are given in Table 5.2.

Table 5.2 Production rates for Swan band sequences.

v''	$\frac{PR(v'', \Delta v)}{PR(v''=0, \Delta v=0)}$		
	$\Delta v = -1$	$\Delta v = 0$	$\Delta v = +1$
0	0.2745	1.000	0.0813
1	0.3167	0.6333	0.3484
2	0.3255	0.4153	0.5335
3	0.3109	0.2450	0.6509
4	0.2813	0.1351	0.7168
5	0.2438	0.0700	0.7449
6	0.2030	0.0368	0.7454
7	0.1643	0.0249	0.7328
8	0.1299	0.0265	0.7182
9	0.1004	0.0371	0.7108
10	0.0747	0.0523	0.7151
11	0.0531	0.0669	0.7180
12	0.0383	0.0673	0.6402
13	0.0277	0.0564	0.0517

This table shows that for the band sequence $\Delta v = 0$ the contribution comes mostly from the lowest states, while for $\Delta v = +1$, higher states also contribute appreciably. Figure 5.10 shows a comparison of the expected $\Delta v = +1$ Swan band sequence flux ratios for several values of the electronic transition moment, $|Re|^2$ for the ground state singlet-triplet transitions, with observations of Comet Halley. The expected variation from the model for transition moment $\sim 2.5 \times 10^{-6}$ gives a good fit to the observed variation. The calculated intensities can also explain the observed

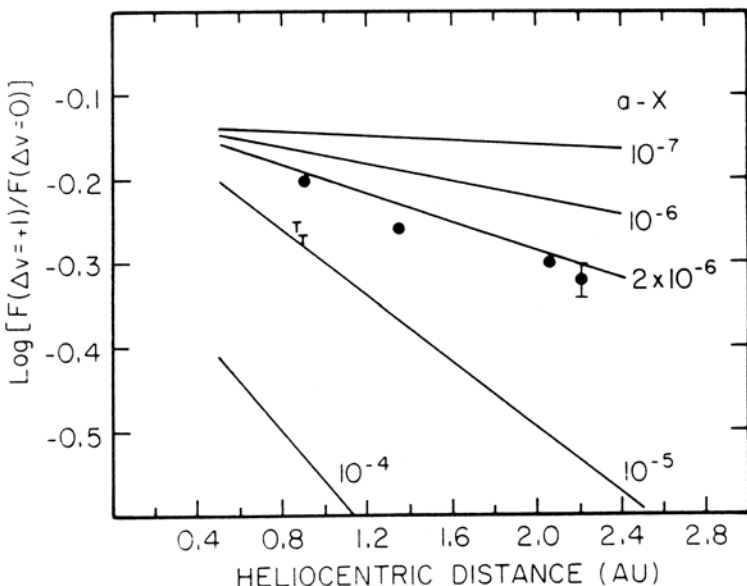


Fig. 5.10 A comparison of the expected and the observed Swan band flux ratios plotted as a function of the heliocentric distance. The continuous lines are the model based dependence shown for several values of transition moment for the lowest singlet triplet transitions. The filled circles show the observed dependence for Comet Halley (O'Dell, C.R., Robinson, R.R., Krishna Swamy, K.S. McCarthy, P.J. and Spinrad, H. 1988. *Ap. J.* **334**, 476).

flux ratios for the Mulliken system of the C_2 molecule. The results of these calculations also explain the observed result that the intensities of the Swan bands are stronger compared to those of the Phillips bands. These investigations also show that the forbidden singlet-triplet transitions are quite important. The wavelength of these transitions lies in the infrared spectral region.

The molecule CO has a structure very similar to that of the C_2 molecule containing both singlet and triplet electronic states. The singlet electronic state is the ground state of the molecule. However, the strong bands of CO seen in a cometary spectra arise out of singlet states ($A^1\Pi - X^1\Sigma^+$) in contrast to the case of the C_2 molecule which arise from the triplet states ($d^3\Pi_g - a^3\Pi_u$). It is therefore of interest to know the physical reason for the inversion in intensities of the singlet and triplet series for the case of the C_2 molecule. This arises basically due to the difference in the energy level structures of the two molecules as can be seen below.

Consider the simple case of two levels with population n_1 and n_2 corresponding to the lowest singlet and triplet states of the molecule with energy separation ΔE . The resulting population in the upper and lower levels, n_2 and n_1 depend essentially on the rate of the absorption and emission processes and this can be written as

$$\frac{n_2}{n_1} \propto \left(\frac{B\rho}{A} \right). \quad (5.17)$$

Here A and B are the Einstein coefficients and ρ is the energy density of the solar radiation. The ratio of the change in population for two values of ΔE is given by

$$\left[\frac{\text{Triplet}}{\text{Singlet}} \right]_{\Delta E_1} / \left[\frac{\text{Triplet}}{\text{Singlet}} \right]_{\Delta E_2} = \left(\frac{\lambda_1}{\lambda_2} \right)^5 \frac{F_{\odot}(\lambda_1)}{F_{\odot}(\lambda_2)}. \quad (5.18)$$

Here $F_{\odot}(\lambda)$ represents the solar flux. The above equation shows a strong dependence on the wavelength. Therefore the relative intensities of singlet-singlet to triplet-triplet transitions of a molecule depend strongly on the energy separation between the lowest singlet and triplet states which are the 714cm^{-1} for C_2 and 49000 cm^{-1} for CO .

Let us now consider the rotational structure of C_2 molecule. The Swan bands of the C_2 system arise out of $3\pi_0$, $3\pi_1$ and $3\pi_2$ states. The relative population in different rotational levels of each of these substates for a given vibrational transition can be obtained from the solution of statistical equilibrium equations of lower and upper states. For vibrational population distribution, the values based on statistical equilibrium equations can be used. The synthetic profile resulting out of the superposition of many lines arising out of the various bands and corrected for the instrumental effect is compared with the observed profile in Fig. 5.11.

5.1.5. *Prompt emission lines of OH*

Laboratory studies have demonstrated that the photodissociation of water creates a fraction of OH in the highly excited rotational levels (upto $J' \approx 22$ of $v' = 0$ and upto $J' \approx 17$ of $v' = 1$) of the electronic state $\text{A}^2\Sigma^+$ (see also Sec. 6.2.2). Since the lifetime of OH formed in the electronic state $\text{A}^2\Sigma^+$ is much shorter than the collision time, the OH formed in the electronic state $\text{A}^2\Sigma^+$ quickly trickles down to ground electronic state $\text{X}^2\Pi$ by spontaneous emission giving rise to emission lines in the UV region, ($\text{A}-\text{X}$) bands. This type of transition lines are called *prompt emission* lines as the dissociation fragment emit promptly after its production. The wavelength

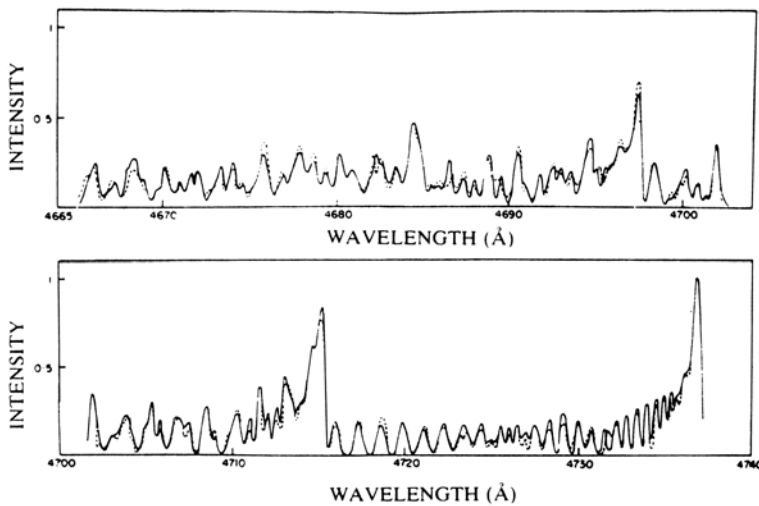


Fig. 5.11 Comparison of the calculated (continuous) and observed (dashed) spectra of $\Delta v = +1$ sequence of the C₂ Swan system for Comet West. (Observations are from Lambert, D.L. and Danks, A.C. 1983. *Ap. J.* **268** 428; spectral resolution (FWHM)=0.3 Å).

of these emission lines comprising P – and Q doublets of the (0, 0) band lie in the wavelength region of 3100 to 3250 Å. The prompt emission lines of OH are much weaker than the solar resonance fluorescence lines of OH arising from the ground electronic state X²Π.

These studies are of direct relevance to comets as the photodissociation of H₂O by solar Lyman α photons in the coma should lead to OH in highly excited rotational states of A²Σ⁺ giving rise to prompt emission lines of (A–X) transitions in the UV region. For detecting these lines in a comet, observations have to be carried out very close to the nucleus where OH molecules will still be in the excited electronic state A²Σ⁺ produced after the photodissociation of H₂O.

Comet Hyakutake gave the first opportunity to look for these lines, as the comet came close to the earth, $\Delta=0.11$ AU, that made it possible to make spectral observations very close to the nucleus. The observations were carried out with Kitt Peak 4 m Mayall Telescope on 26 March 1996 when the comet was at $r = 1.02$ AU. All the expected lines (as per Laboratory studies) of P - and Q lines of OH upto rotational quantum number 22 of the (0, 0) band are detected for the first time in the spectra covering the wavelength region from 3100 to 3250 Å. This is shown in Figs. 5.12 and 5.13. The intensities of the lines decrease downwards from the rotational quantum

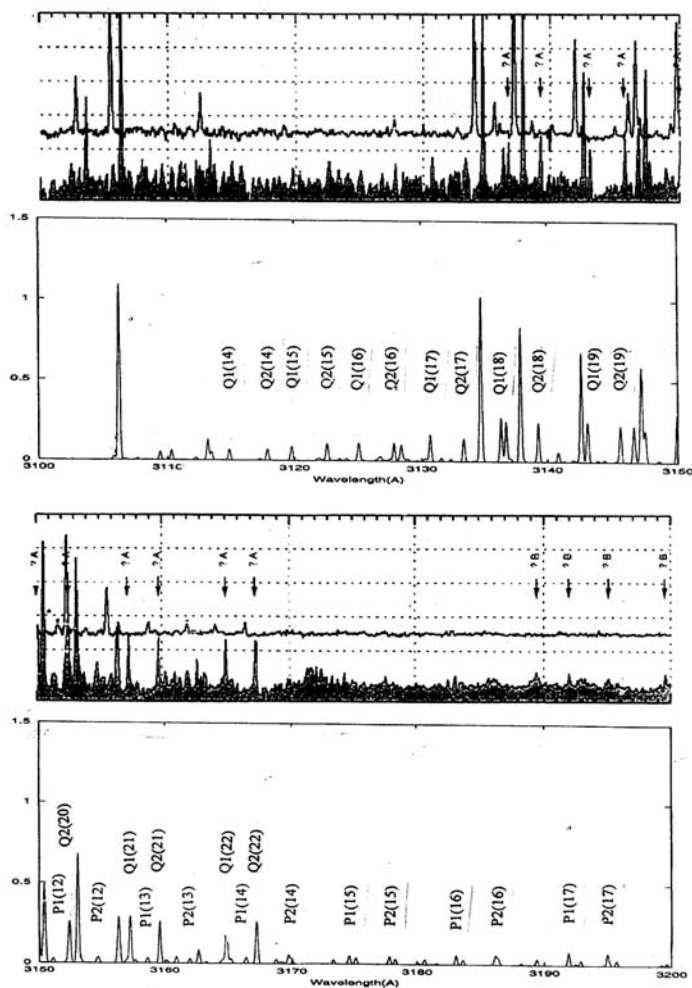


Fig. 5.12 The Prompt Emission lines of P and Q doublet of OH arising from the highly excited rotational levels of $A^2\Sigma$ state ($(A - X)$ transition) was observed for the first time in Comet Hyakutake on 26 March 1996 ($r = 1.02$ AU and $\Delta = 0.11$ AU) in the wavelength region 3100 to 3250 Å. The above figures cover the wavelength region from 3100 to 3200 Å. Many of the lines marked as A and B in the spectra are the prompt emission lines of OH. These are compared with the computed spectra (lower panels) which is summed over resonance fluorescence and prompt emission lines. (Meier, R. et al. 1998. *Icarus*, **136**, 268; A'Hearn, M.F., Krishna Swamy, K.S. and Wellnitz, D.D. 2007. *Bull. Am. Astro. Soc.*, **39**, 507).

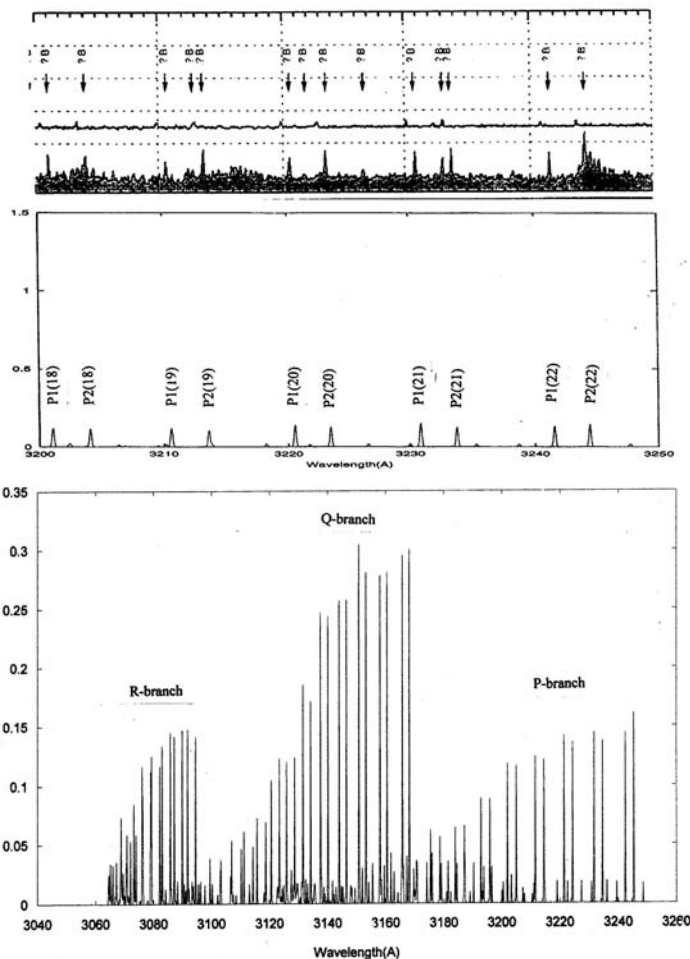


Fig. 5.13 The Prompt Emission lines of P and Q doublet of OH arising from the highly excited rotational levels of $A^2\Sigma$ state ((A - X) transition) was observed for the first time in Comet Hyakutake on 26 March 1996 ($r = 1.02$ AU and $\Delta = 0.11$ AU) in the wavelength region 3100 to 3250 Å. The above figures cover the wavelength region from 3200 to 3250 Å. Many of the lines marked B in the spectra are the prompt emission lines of OH. These are compared with the computed spectra (lower panels) which is summed over resonance fluorescence and prompt emission lines. The expected intensities of P, Q and R lines are also shown. (Meier, R. et al. 1998, *Icarus*, **136**, 268; A'Hearn, M.F., Krishna Swamy, K.S. and Wellnitz, D.D. 2007, *Bull. Am. Astro. Soc.*, **39**, 507).

number 22 in conformity with laboratory studies. The observed spectra is compared with the computed spectra which is summed over resonance fluorescence and prompt emission lines. The two are in good agreement. The weak features present alongwith P- and Q branches of (0, 0) band are due to prompt emission lines arising out of (1, 1) transitions. The strong features present in the calculated spectra are due to resonance fluorescence process. The expected intensity distribution of all the P,Q and R branch prompt emission lines are also shown in Fig. 5.13.

The importance of the detection of prompt emission lines of OH is that it can help in a better understanding of the cometary coma very close to the nucleus. In addition it can also help in the understanding of the photodissociation of H₂O process.

5.1.6. *Molecules other than diatomic*

The analysis of polyatomic molecules is more complicated than that of diatomic molecules. Therefore, their studies are limited in extent. The work done on molecules like H₂O, NH₂, CO₂⁺, NH₃, etc., indicate that the resonance fluorescence process is the major excitation mechanism for these molecules as well.

5.1.7. *OH radio lines*

The hydroxyl radical gives rise to lines in the radio region due to Λ -splitting of the levels (Table 3.1). The line at 1667 MHz which occurs at a wavelength of 18 cm was first detected in Comet Kohoutek in 1974. The most studied lines in comets are the 1665 and 1667 MHz lines. The intensity of the lines are found to be variable. Curiously, one finds that these lines have been seen in the emission as well as in the absorption which depend on the heliocentric distance of the comet. These observations can be explained by the fluorescence excitation process. Since the transitions between the Λ -doublet levels are highly forbidden, in the absence of any other excitation mechanism, the levels should be populated according to their statistical weights at the coma temperature. The deviation from this equilibrium value is generally referred to as inversion or anti-inversion. The cosmic microwave background radiation of 2.7 K and the galactic sources can induce transitions. The line may be seen in absorption if the population is anti-inverted or in emission if the population is inverted due to stimulated emission. The Λ -doublet levels are actually populated through the process

of UV solar absorption lines from the ground state $^2\Pi_{3/2}$ ($v'' = 0, J = 3/2$) to the state $^2\Sigma^+$, $v = 0$ and $v = 1$ levels and then cascade back to the ground level. Since the UV absorption lines or the UV fluorescence efficiencies depend upon the comet heliocentric velocity (Swings effect, Fig. 5.14), the resulting relative population distributions in the four levels also depends critically on the heliocentric velocity of the comet and hence on the heliocentric distance. This can result in the lines of OH to be produced

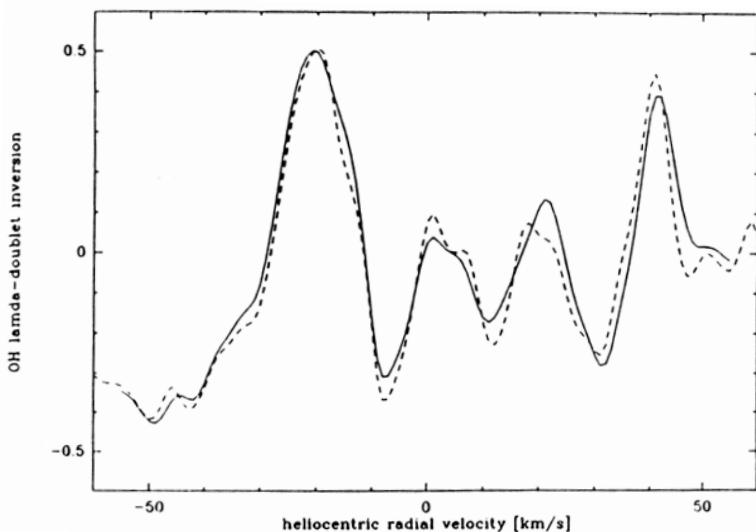


Fig. 5.14 The g-factor or the Fluorescence efficiency factor for the (0,0) band of OH is shown as a function of the heliocentric radial velocity. The variation in the value can clearly be seen arising due to Swings effect (Schleicher, D.G. and A'Hearn, M.F., 1988. *Ap.J.* **331**, 1058).

either in absorption or in emission. Such an effect can clearly be seen from the observation of Comet Kohoutek which is shown in Fig. 5.15. The upper section of the curve shows the observed peak antenna temperature of 1667 MHz line as a function of time. The lower section shows the expected inversion based on the ultraviolet pumping model and is given by $[(n_u - n_l)/(n_u + n_l)]$. Here n_u and n_l represent the projected densities of the upper and lower levels of the Λ -doublet. There is a one-to-one relation between the two curves. This mechanism has been verified for a large number of radial velocities as well as observations based on several comets. This explanation is generally accepted and is used in interpreting the 18 cm

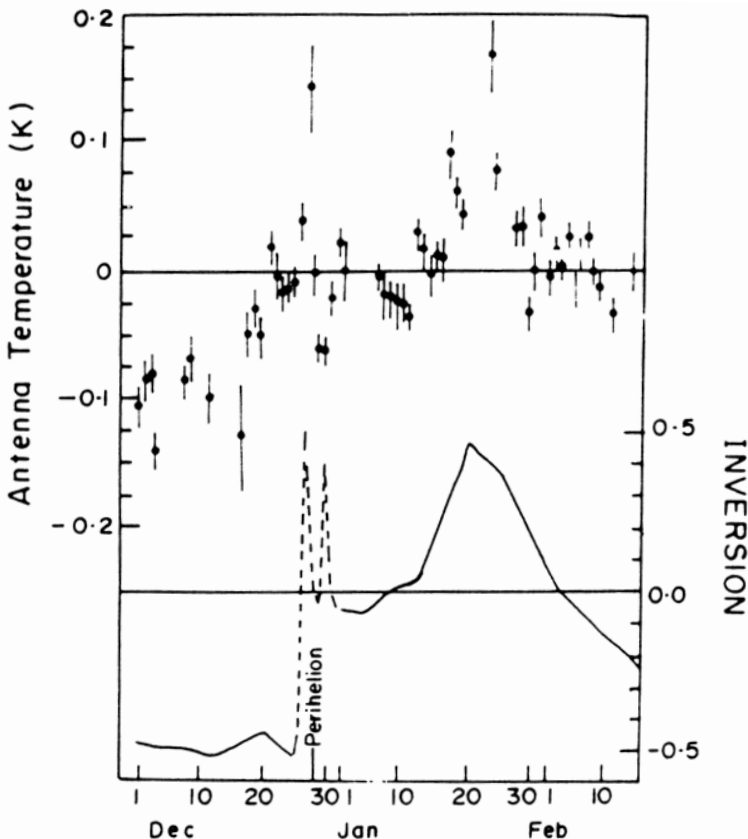


Fig. 5.15 The radio OH data for Comet Kohoutek. The top portion denotes the observed peak antenna temperature of the 1667 MHz line as a function of time. The lower portion denotes population inversion predicted by the ultraviolet pumping model as a function of time (Adapted from Biraud, F. Bourgois, G., Crovisier, J. Fillip, R., Gerard, E. and Kazes, I, 1974. *Astr. Ap.* **34**, 163).

observations. Therefore, the ultraviolet pumping of the OH radio lines is the dominant excitation mechanism. However, the collisions can also be quite effective as the Λ -doublet transitions are forbidden and the radiation field is weak. It is found that collisions with ions and electrons can be more important than even neutrals. This could have a severe effect in influencing the inversion in the inner coma of comets with high production rates. This is recognized as an important process in the calculation of radio emission from comets.

5.1.8. Oxygen lines

Allowed transitions. The triplet lines of oxygen at $\lambda=1304\text{ \AA}$ (1302.17 \AA) are very strong in the UV region of the cometary spectra (Fig. 4.4). Of particular interest are the Comets Kohoutek and West in which these lines have been seen and these comets had heliocentric velocities in the range of about 44 to 55 km/sec. To see whether the excitation process of these lines is through resonance fluorescence process, a high dispersion spectrum of the solar line at 1302.2 \AA is shown in Fig. 5.16. The line width of $\pm 40\text{ km/sec}$ corresponds to a Doppler shift of about $\pm 0.17\text{ \AA}$. For $\dot{r} > 40\text{ km/sec}$, the cometary absorption wavelength will be completely shifted from the solar line. Therefore, for comets with heliocentric velocity $\dot{r} \lesssim 30\text{ km/sec}$, the emission is produced by the resonance scattering of the solar lines. For higher velocities, either the line should be very weak which is not the case or there should be some other excitation mechanism. From the energy level diagram of the oxygen atom (Fig. 4.11) it can be seen that the line 1025.77 \AA is very close to the solar Lyman β line of hydrogen of 1025.72 \AA . Therefore excitation is produced mainly through chance coincidence with solar HI Lyman β and hence absorption takes place. It then goes through cascading process through intermediate levels leading finally to the emission line at 1304 \AA . This mechanism is well known in planetary nebulae as *Bowen mechanism*. The intensity of OI 1304 \AA multiplet produced by resonance scattering of the solar lines is much stronger than those produced by the Lyman β fluorescence. Therefore the intensity of the emission line 1304 \AA depends critically on the radial velocity (Swings effect), the width of the solar emission line and the width of cometary absorption line.

5.1.9. Forbidden transitions

The identification of the red oxygen doublet lines at 6300 and 6364 \AA in comets immediately raises the question of the excitation mechanism of these lines as they are electric dipole forbidden transitions. First of all, it is interesting to investigate whether the fluorescence process can or cannot explain these lines. The direct method to test this hypothesis is to compare the fluorescence efficiency rate for the red oxygen lines with those of ultraviolet resonance lines which is given in Table 5.3.

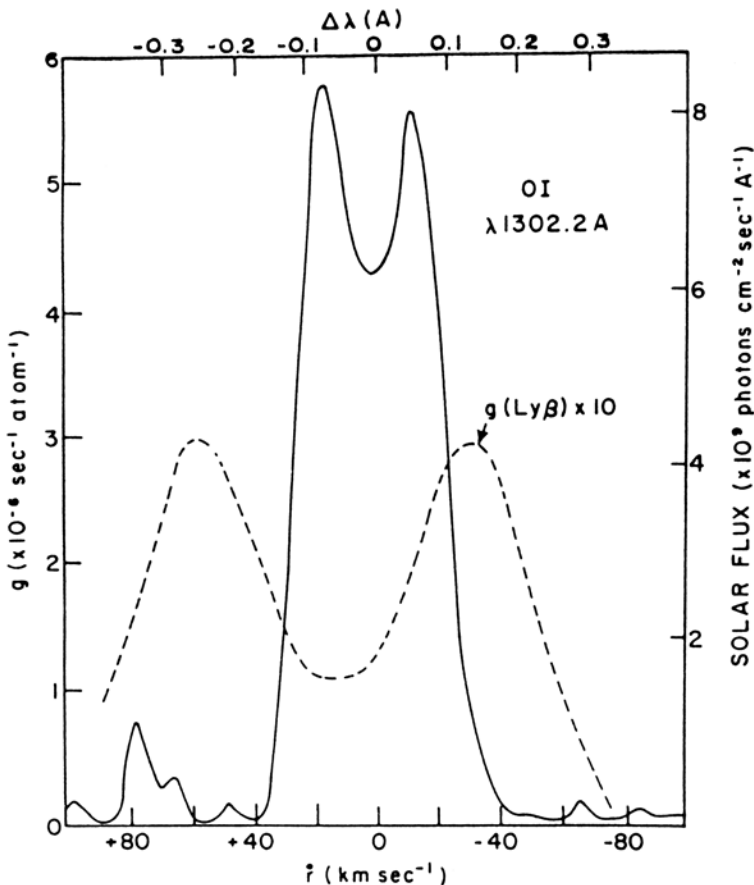


Fig. 5.16 High resolution profile 1302.2 Å line of OI in the Sun (Solid curve). The dashed curve represents the g-factor for fluorescence excited by solar Ly β as a function of heliocentric velocity (Feldman, P.D., Opel, C.B., Meier, R.R. and Nicolas, K.R. 1976. *The Study of Comets*, eds. B. Donn et al. NASA SP-393, Washington, D.C. p. 773).

The values show that the excitation to 1S_0 level (2972 Å) is negligible (Fig. 4.11). Also the expected intensities of the line 6300 Å can be calculated based on the observed intensities of the 1304 line and the g-factors of Table 5.3. The expected intensities of red lines are very much smaller than those of the observed values. Therefore, the resonance fluorescence process cannot be responsible for the excitation of forbidden oxygen lines. The collisional excitation is also inadequate for explaining the observed emission.

Table 5.3 Fluorescence efficiency factors at 1 AU for oxygen.

Line(Å)	g-factor*
	(photons/sec/atom)
989	1.6 (-8)
1027	0.4 to 1.5 (-6)
1304	0.6 to 1.5 (-5) ^a 1.1 to 3.9 (-7) ^b
2972	3.1 (-15)
5577	6.21(-14)
6300	4.2 (-10)
6364	1.3 (-10)

* See Chap. 6.

Number in the bracket refers to power of 10 (a) for solar absorption; (b) Lyman β induced fluorescence; (Festou, M.C. and Feldman, P.D. 1981, *Astr. Ap.* **103**, 154).

Therefore it is generally assumed that the photo dissociation of some molecules leave oxygen atoms in the excited ^1D state which then decay to 3P ground state giving rise to 6300 Å emission. ^1D state can be generated from the photodissociation of molecules H_2O , OH, CO_2 and CO (Sec. 6.2.9). However, the contributions from the photodissociation reactions of CO_2 and CO are much smaller than that of H_2O .

5.1.10. Molecular band polarization

The resonance fluorescence excitation process which is responsible for the observed emission lines in comets leads to two other important effects. The first being that even though the incident radiation is a natural one, the fluorescence lines should be linearly polarized. Secondly the total intensity of emission is not isotropic but depends upon the phase angle.

The linear polarization of emission bands in comets was first observed in Comet Cunningham 1941 I from the study of C_2 and CN bands. This was followed by observations of other comets. The polarization of C_2 (5140), C_3 (4060), CN (3871) and OH (3090) bands have been measured in Comets Halley and Hartley - Good 1985 XVII. The polarization of the bands of CO^+ (4260) and H_2O^+ (7000) has also been measured in Comet Halley.

The measured linear polarization in percentage for Comet Halley at a phase angle $\sim 50^\circ$ is around 3.9, 4.0, 3.8 and 1.8 for the molecules CN, C₂, C₃ and OH respectively.

There exists several studies pertaining to the polarization of fluorescence lines, both from experimental and theoretical points of view. The theoretical studies are based on the application of the principle of Zeeman splitting in a magnetic field. Therefore, the important parameter in determining the polarization in a molecular band $u \rightarrow l$ (u is the upper level and l is the lower level) is the Larmor frequency ν_L of the molecule. In the case of a strong magnetic field, $2\pi\nu_L > A_{u \rightarrow l}$ where $A_{u \rightarrow l}$ is the Einstein coefficient for the transition, the molecule will precess strongly in the upper state before de-excitation takes place and therefore it essentially loses memory of its unidirectional excitation process. The resultant effect being that the fluorescence emission line will be isotropic and unpolarized. For the other case of a weak magnetic field, $2\pi\nu_L < g_{l \rightarrow u}$, where $g_{l \rightarrow u}$ is the excitation rate of the band, the fluorescence cycle will lead to alignment of the molecule with respect to the direction of the excitation field. The typical values for a cometary molecular band is, $A_{u \rightarrow l} \sim 10^6/\text{sec}$ and $g_{l \rightarrow u} \sim 10^3$ to $10^{-1}/\text{sec}$. The general value of the magnetic field as measured by space-crafts in Comet Halley is of the order of a few 10 nT. This corresponds to $\nu_L \sim 10^2/\text{sec}$. These values show that

$$g_{l \rightarrow u} < 2\pi\nu_L < A_{u \rightarrow l}.$$

The resultant effect being that the molecules will precess in the lower state between the fluorescence cycles, but not in the upper state. This therefore preserves the polarization for the case of anisotropic excitation.

The excitation by unidirectional natural radiation leading to linear polarization of an emission line has maximum polarization for a phase angle of 90° (i.e. observed perpendicular to the exciting radiation). The expected variation of polarization with phase angle θ is given by the expression

$$P(\theta) = \frac{P_{\max} \sin^2 \theta}{1 + P_{\max} \cos^2 \theta} \quad (5.19)$$

and the total intensity should vary as

$$I_{\text{total}} = \frac{P_{\max} \cos^2 \theta + 1}{\frac{1}{3} P_{\max} + 1}. \quad (5.20)$$

Here P_{\max} represents the maximum polarization corresponding to $\theta = 90^\circ$. The value of P_{\max} depends upon different rotational quantum number J for

the P, Q and R branches of the band. Theoretical calculations are available for some of the transitions at the present time.

The value of P_{\max} for various molecular bands can be determined from the observed polarization and phase angle corresponding to the time of observation. The derived value of P_{\max} from observations for the C_2 and CN molecules is in agreement with the expected theoretical value of P_{\max} of 7.7%. The observed polarization variation also established the validity of the theoretical dependence given by Eq. (5.19). The P_{\max} values derived from observations for the C_3 molecule $\sim 6\%$ which is similar to that of C_2 and CN , but smaller than the expected value of 19%. During the 2003 apparition of Comet 2P/Encke the observed polarization of C_2 and CN were in good agreement with the theoretical calculations. However for C_3 the observed polarization was close to the value of CN and C_2 ($\sim 7\%$) except on one day when the observed polarization was 16.4% which is close to the expected value of 19%. The derived P_{\max} value for H_2O^+ and CO^+ is quite high $\sim 20\%$.

5.2. Excitation Temperature

The population distribution under thermal equilibrium is given by the Boltzmann law. Even though it does not represent a real situation, it can be used to a first approximation for estimating the excitation temperature. This excitation temperature is found to be not much different from the temperature obtained based on a detailed analysis of the level population in many cases.

5.2.1. Rotational temperature

The temperature determined from the application of the Boltzmann law to rotational lines is generally called the *rotational temperature*. For rotational levels, the exponential factor $e^{-E/kT}$ is given by $e^{-BJ(J+1)hc/kT}$ where B is the rotational constant of the molecule (Chap. 3). In addition, for each level there are $(2J + 1)$ states. The number of molecules in any rotational level J in terms of the total number N can be expressed as

$$N_J = \frac{N}{Q_{\text{rot}}} (2J + 1) e^{-BJ(J+1)hc/kT}. \quad (5.21)$$

Here Q_{rot} is the rotational partition function and is given by

$$Q_{\text{rot}} = \sum (2J + 1) e^{-BJ(J+1)hc/kT}. \quad (5.22)$$

The rotational population N_J , goes through a maximum and then decreases with an increase in J . For a given temperature, the maximum value of J for which the population is maximum can be evaluated from the above equation and is given by

$$J_{\max} = \sqrt{\frac{kT}{2Bhc}} - \frac{1}{2}. \quad (5.23)$$

The intensity of a rotational line in the emission can be written as (Chap. 3)

$$I_{\text{em}} = C\nu^4 S_J e^{-BJ(J+1)hc/kT}. \quad (5.24)$$

Here C is a constant and S_J is the Höln-London factor. T is the rotational temperature. A plot of $\log (I_{\text{em}}/S_J)$ as a function of $J(J + 1)$ results in a straight line. From the slope of the line the rotational temperature can be evaluated.

The above method has been applied to the case of cometary spectra to obtain the rotational temperature of various molecules. One can get a better estimate of the rotational temperature if the rotational levels are populated to high quantum numbers. In addition one requires the spectra of high dispersion for the lines to be resolved. Studies have been carried out for molecules like CH, CN, OH, C₂, etc. Except for the C₂ molecule, the rotational temperatures for all other molecules have values in the range of about 200 to 400°K. The rotational temperature for the C₂ molecule based on the profile analysis of well-resolved lines of Swan bands gives the temperature values in the range of about 3000 to 4000°K (Fig. 5.11). The vast difference in the rotational temperature between the C₂ and other molecules arises due to the fact that for heteronuclear molecules like CH, CN, etc., the transitions in the ground state of the molecule are possible; these radiate away the energy. This makes the temperature low. But for the homonuclear molecule C₂, such types of transitions are forbidden and hence give higher temperatures.

The (0, 0) band spectra of Swan system for Comet Halley taken at a high resolution of 0.06–0.08 Å (FWHM) resolved all the rotational lines of the R branch. The observed intensities of these rotational lines indicated the existence of two vastly different well defined Boltzmann temperature population distributions corresponding to those of lower and higher rotational levels. In particular, the low rotational levels with $J' \lesssim 15$ gave a rotational temperature, $T_{\text{rot}} \sim 600 -- 700$ K, while the higher levels gave a rotational temperature, $T_{\text{rot}} \sim 3200$ K. The synthetic spectra based on

time-dependent rotational population distribution with resonance fluorescence excitation process show that a reasonably good fit over the whole wavelength region of the observed spectra, 5162–5132 Å, can be obtained for a time interval of around 2×10^3 sec as shown in Fig. 5.17. This time

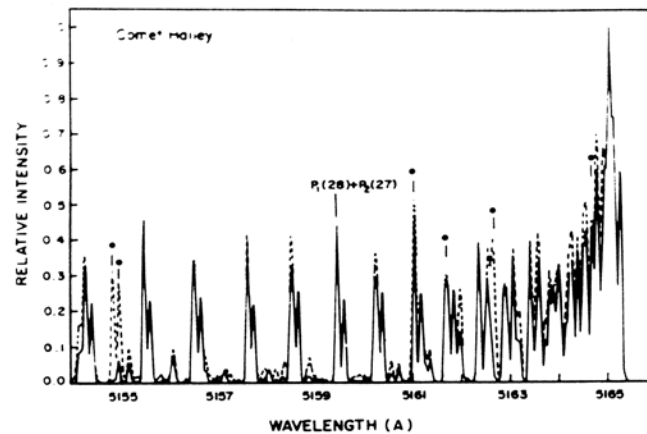


FIG. 2a

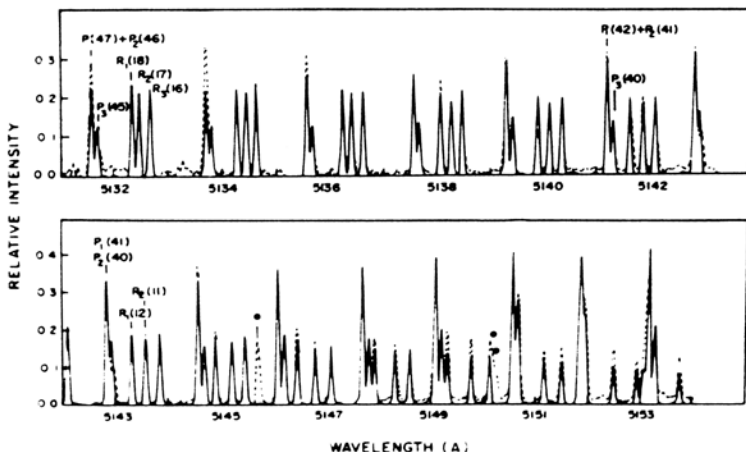


Fig. 5.17 Comparison of the calculated time dependent spectra (Solid line) with the observed spectra (dashed line) for the (0, 0) Swan band in the wavelength region 5166 to 5154 Å of Comet Halley. The calculated curves are for a time interval of 2×10^3 secs and FWHM=0.06 Å. The short line with filled circles show the location of the NH₂ features. Several of the P, Q and R lines are also marked (Krishna Swamy, K.S. 1991. *Ap. J.*, **373**, 266).

scale is consistent with the time $\sim 2.7 \times 10^3$ sec taken by the C₂ molecules with a velocity ~ 1 km/sec, to cross the equivalent radius of the projected area on to the sky. This indicates that the observations have picked up only molecules with the time interval $\sim 2 \times 10^3$ sec from the time of formation indicating that the level populations does not appear to have reached the steady state values.

5.2.2. Vibrational temperature

A mean vibrational excitation temperature may be defined from the Boltzmann law representing the population distribution in various vibrational levels. An expression for vibrational temperature can be written in an analogous manner to that of rotational temperature as

$$N_v = \frac{N}{Q_{\text{vib}}} e^{-G(v)hc/kT} \quad (5.25)$$

where $Q_{\text{vib}} = e^{-G(v)hc/kT}$ is called the vibrational partition function. $G(v)$ represents the energy of the vibrational level v . The emission intensity of a vibrational band can be written as (Chap. 3).

$$I_{\text{em}} = C q_{v'v''} e^{-G(v)hc/kT} \quad (5.26)$$

where $q_{v'v''}$ is the Franck-Condon factor for the band (v', v'') and C is a constant. A plot of $\log (I_{\text{em}}/q_{v'v''})$ versus $G(v)$ gives a straight line from which the vibrational temperature can be determined.

Several attempts have been made to get an estimate of the vibrational temperature of molecules. However, one difficulty with this method is that it is hard to get many bands where the contamination from other bands or from other lines is negligible. So one usually uses the ratio of intensities of two bands or more bands if available. For the case of C₂ molecule, the band sequence flux ratios corresponding to $\Delta v = 0$ and +1 is generally used. The vibrational temperature vibrational temperature obtained for C₂ molecule is around 3000 to 5000°K. This is of the same order as the rotational temperature.

5.3. Abundances of Heavy Elements

The emission lines of heavy elements are seen only for the heliocentric distance $\simeq 0.15$ AU. Comets passing through such small perihelion distances are very rare. One such comet was the Sun grazing Comet Ikeya-Seki in

1965 which had a perihelion distance ~ 0.005 AU. This comet provided the opportunity for observing emission lines of various elements like Na, K, Ca, Ca^+ , Fe, Ni, Mn and so on in the visible region. This made it possible to make an abundance analysis of these elements. These elements are believed to come from the vapourization of the refractory grains.

In a steady state, the relative populations in the upper levels are governed by the Boltzmann's formula reduced by the dilution factor W , which is a measure of the deviation of the energy density of radiation from the equilibrium value i.e. $u_\lambda \propto W \lambda^{-5} 10^{-\theta\chi}$. Therefore the intensity of an emission line is given by

$$I = \left(\frac{8\pi^2 e^2 h}{m} \right) \frac{Ngf}{u\lambda^3} 10^{-\theta\chi} \quad (5.26a)$$

where χ is the excitation potential of the line and $\theta = (5040/T)$. T is the excitation temperature corresponding to the colour temperature of the exciting solar radiation. The term represented by the power of 10 corresponds to the exponential factor in the Boltzmann distribution function. N is the total number of atoms/cm² in the line of sight and u is the partition function of the line. The other quantities have their usual meanings. The above equation can be written as

$$\log \left(\frac{\lambda^3 I}{gf} \right) = -\theta\chi + \text{constant.} \quad (5.27)$$

Therefore, a plot of $\log (\lambda^3 I/gf)$ against the excitation potential χ for all the observed lines will result in a straight line whose slope gives the value of θ . Figure 5.18 shows one such typical plot for FeI lines. The straight line drawn through the points is for $\theta = 1.0$. Knowing the excitation temperature, the total number of atoms can be calculated easily from

$$\begin{aligned} \log N &= \text{constant} + \log(\lambda^3 I) - \log(gf) \\ &\quad + \log u + \theta\chi \end{aligned}$$

The procedure can be repeated for all the observed lines. The value of $\theta = 1.0$ also fitted the other lines. Therefore the number of atoms of various kinds can be determined. The calculated relative abundances of various elements relative to iron is similar to that of the solar value.

The *in situ* measurements of Comet Halley, made with impact ionization mass spectrometer on board the Vega spacecraft, have given the elemental composition of dust. The contribution from the gaseous component has to be added to the dust component, to get an estimate of the total elemental abundances. Using a mean value for the dust to gas ratio of 0.8, the derived

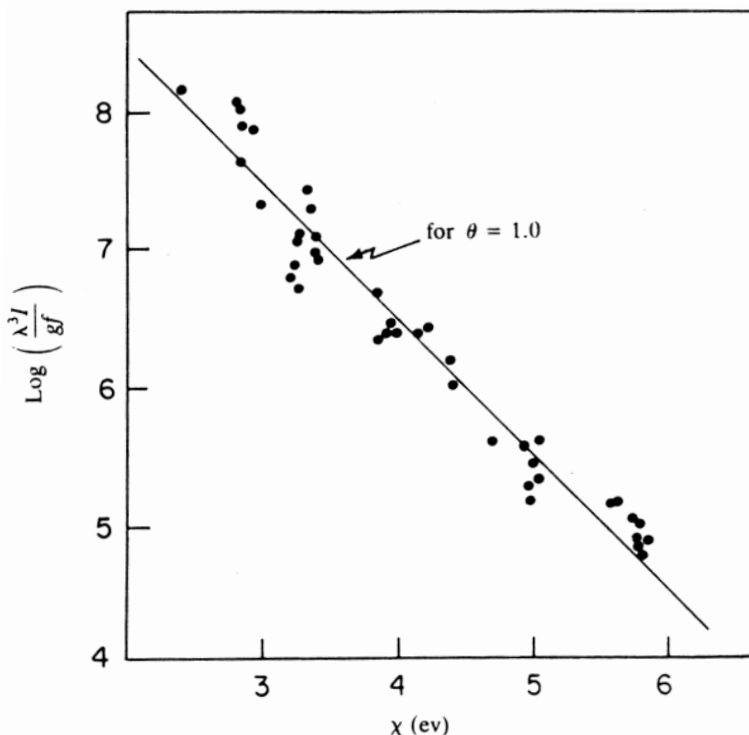


Fig. 5.18 A plot of $\log (\lambda^3 I/gf)$ as a function of the excitation potential of the line. The straight line drawn through the points is for $\theta_{ex} = (5040/T_{ex}) = 1.0$ (Adapted from Arpigny, C. 1977, *Proceedings of the Robert A. Welch Foundation Conferences on Chemical Research XXI*, Cosmochemistry. Houston, p. 9; see also Preston, G.W. 1966. *Ap.J.* **147**, 718).

total abundance of gas and dust for Comet Halley is compared with the Sun in Fig. 5.19. It shows that the elemental abundances in Comet Halley are very similar to the solar values except for hydrogen.

5.4. Isotopic Abundances

The study of the isotopic abundances in comets has attracted considerable attention as it has significant amount of information in it as to the conditions which prevailed at the time of formation of these objects. Fortunately, the most abundant elements, namely, H, C, N and O do have many stable isotopes. Therefore a comparison of the isotopic ratios of

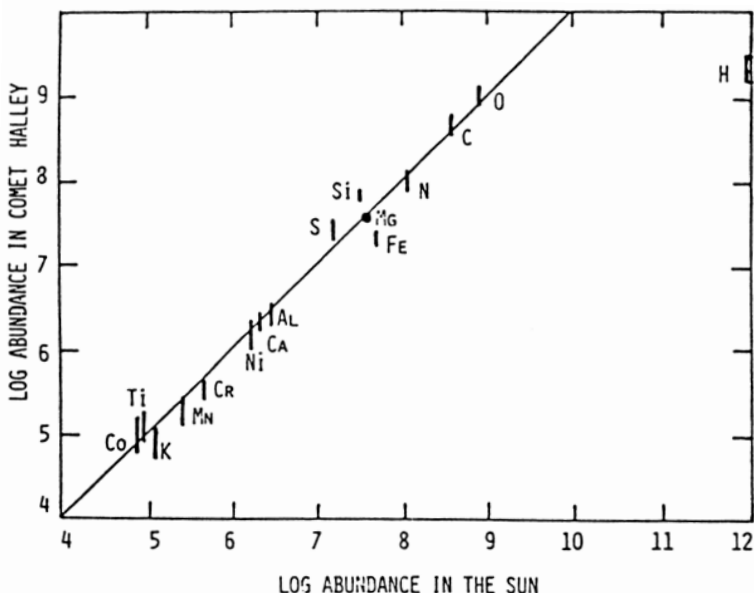


Fig. 5.19 A comparison of the element abundances in Comet Halley and in the Sun showing that they are similar. The abundances refer to $\log N(H) = 12.0$ (Delsemme, A.H. 1991. In *Comets in the Post-Halley Era*, eds. R.L. Newburn, Jr. *et al.*, Kluwer Academic Publishers, p. 377).

these elements in different kinds of objects will reveal the history of the whole evolutionary process. The detection of several complex molecules in comets has given the general feeling that the cometary material and the interstellar material could be very similar in nature. The isotopic ratios could help in clarifying this problem as well.

For a diatomic molecule, the vibrational and rotational isotopic shifts are proportional to $(1 - \sqrt{\frac{\mu}{\mu_i}})$ and $(1 - \frac{\mu}{\mu_i})$ respectively, where μ and μ_i are the reduced masses of the normal and the isotopic molecule. This shows that the expected isotopic shifts from molecules are quite small. Therefore, in order to study the isotopic molecule, it will be a great advantage if the abundance of the isotopic molecule is large, the isotopic line is well separated from the line of the normal isotope and also lie in the less crowded region of the spectrum. This introduces severe constraints on the selection of the molecules. In addition, the spectra should be of higher resolution to separate the isotopic line from the normal line. These restrictions automatically limit the study to bright comets. Due to the difficulties involved

in the spectral and radio astronomical observations the studies have been limited to only a few isotopic species. In principle, the isotopic ratios can be determined better than the absolute abundances as they are not model dependent.

The isotopic ratio $^{12}\text{C}/^{13}\text{C}$ has been determined for several comets based on the analysis of the Swan band intensities of the C_2 molecule. It is well suited for the study as the (1, 0) band of the Swan system which occurs at 4737 \AA is well separated from the $^{12}\text{C}/^{13}\text{C}$ band which occurs around 4745 \AA .

A typical medium resolution scan in the region of interest for the Comet Kohoutek is shown in Fig. 5.20. From a comparison of the observed intensity ratios of these two bands, it is possible to get an estimate for the isotopic ratio of $^{12}\text{C}/^{13}\text{C}$. This method has been applied to many comets. Unfortunately the isotopic line at 4745 \AA is strongly blended with the emission lines of NH_2 molecule. The high resolution scan around 4745 \AA line shows that the blending comes from 4 lines of NH_2 . The blending problem can be taken care with high spectral resolution observations and with better signal-to-noise ratio. To avoid the blending problem, the possibility of using the (0, 0) band of the Swan system has been considered. With a high resolution spectra of Comet West it was possible to resolve completely the rotational structure of the (0, 0) band. However, the isotopic features are rather weak, which makes the derived isotopic ratio uncertain.

The 3883 \AA (0, 0) band of $\text{B}^2\Sigma-\text{X}^2\Sigma$ system of CN has also been used for the determination of carbon isotopic ratio in comets. However, the normal lines of $^{12}\text{C}^{15}\text{N}$, $^{13}\text{C}^{14}\text{N}$, weak lines of (1, 1) band and P-branch lines of the CN system also lie in this wavelength region (Fig. 5.21). All these lines can be resolved in a high resolution spectra. Therefore the isotopic ratio of carbon can be determined. The results of $^{12}\text{C}/^{13}\text{C}$ studies for various comets are summarised in Table 5.4.

The deuterium-to-hydrogen ratio is of great interest as deuterium is most likely to be synthesized in the early universe. The neutral mass spectrometer on board Giotto spacecraft made measurements of the composition of neutral and ion species in Comet Halley with high mass resolution. Therefore it is possible to get the isotopic ratio D/H. The derived ratio from the study of $\text{HDO}/\text{H}_2\text{O}$ is around 3×10^{-4} . Subsequently HDO was detected in Comets Hyakutake and Hale-Bopp from observations of $1_{01}-0_{00}$ rotational line at 464.925 GHz . Following this, HDO was also detected from $2_{11}-2_{12}$ transition at 241.562 GHz and $3_{12}-2_{21}$ at 225.897 GHz in Comet Hale Bopp.

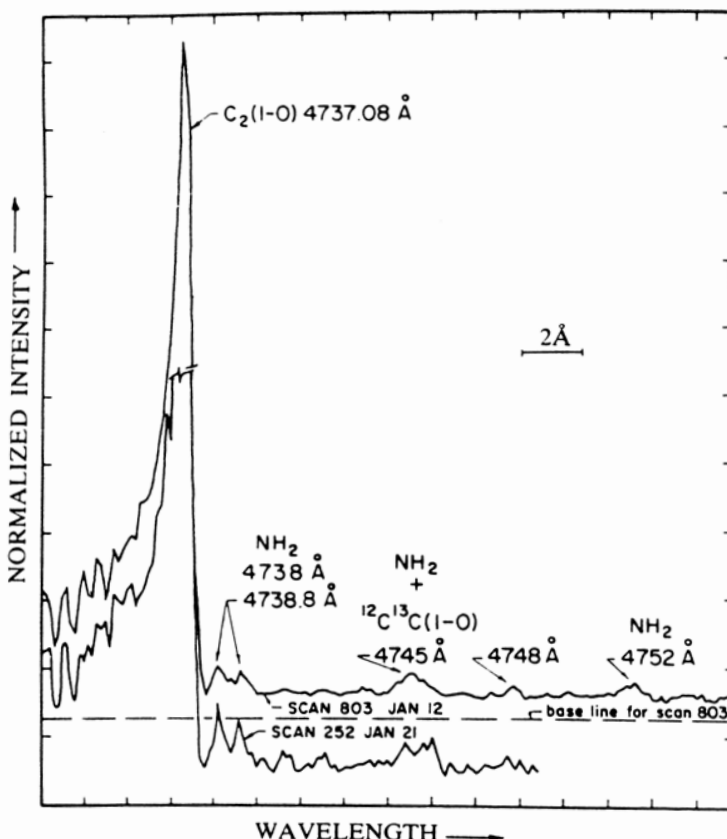


Fig. 5.20 Photoelectric scans of Comet Kohoutek in the region of 4737 Å corresponding to (1, 0) band of the Swan System. Resolution is 0.4 Å. The $^{12}\text{C}/^{13}\text{C}$ feature is around 4745 Å which is blended with NH₂, (Danks, A.C., Lambert, D.L. and Arpigny, C. 1974. *Ap. J.* **194**, 745).

The molecule DCN has been seen through their rotational transition J(5-4) at 362.046 GHz. The derived D/H ratio is 2.3×10^{-3} . The rotational transition of HC¹⁵N, H¹³CN and C ³⁴S has also been detected in Comet Hale-Bopp leading to their isotopic ratios (Table 5.4). The line of J(3-2) of H¹³CN has been detected in Comet Hyakutake.

The fundamental ortho line of H₂¹⁸O at 547.7 GHz has been seen in Comet Ikeya-Zhang. The observed ratio of H₂¹⁸O/H₂¹⁶O is in agreement with the ratio derived from mass spectroscopy from Comet Halley. The results of the measured isotopic ratios are summarized in Table 5.4.

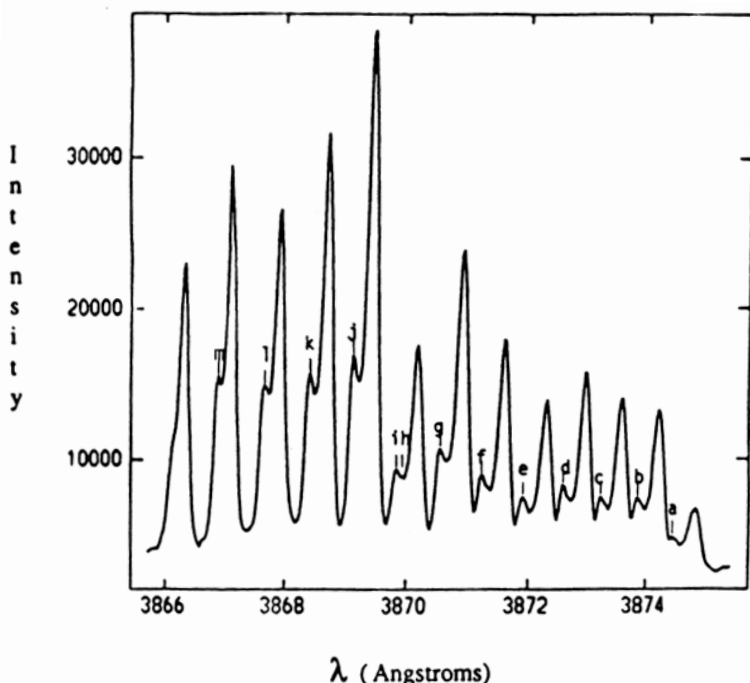


Fig. 5.21 The high resolution spectrum of Comet Halley in the wavelength region from 3866 to 3874 Å. The R-branch lines of ^{12}CN and ^{13}CN overlap in this region. The features marked a to g and i belong to the (0, 0) band of the ^{13}CN molecule while those marked with h and j to m are P-branch lines from the (1, 1) band of the ^{12}CN molecule (Jaworski, W.A. and Tatum, J.B. 1991. *Ap. J.*, **377**, 306).

All the comets indicate D/H ratio in $\text{H}_2\text{O} \sim 3 \times 10^{-4}$. The cometary material is enriched by a factor of around 10 as compared to the D/H ratio in the primordial solar nebula ($\sim 2.5 \times 10^{-5}$) (Fig. 5.22). It is highly likely that this enrichment is due to fractionation effect arising through ion-molecule reactions or grain-surface processes in the solar nebula phase. The lower value of D/H found in planets in comparison to comets appears to be consistent with the idea that the giant planets formed around icy cores with high cometary D/H ratio gathered a large amount of H_2 from the solar nebula with a low protosolar D/H at a later stage.

The other measured isotopic ratios of $^{12}\text{C}/^{13}\text{C}$, $^{16}\text{O}/^{18}\text{O}$ and $^{32}\text{S}/^{34}\text{S}$ are consistent with the solar system value of 89, 500 and 24 respectively.

Table 5.4 Observed isotopic ratios.

Ratio	Molecule	Comet	Value
D/H	H ₂ O	Halley	3.08×10^{-4}
		Hyakutake	2.9×10^{-4}
		Hale-Bopp	3.3×10^{-4}
¹² C/ ¹³ C	HCN	Hale-Bopp	2.3×10^{-3}
		four Comets (a)	93 ± 10
	CN	Halley	95 ± 12
	CN	five Comets (b)	90 ± 10
	CN	Hale-Bopp	165 ± 40
	CN	C/2000 WM ₁	115 ± 20
	HCN	Hale-Bopp	111 ± 12
¹⁴ N/ ¹⁵ N	CN	Hale-Bopp	140 ± 35
		C/2000 WM ₁	140 ± 30
	HCN	Hale-Bopp	323 ± 46
	HCN	Hale-Bopp	330 ± 98
¹⁶ O/ ¹⁸ O	H ₂ O	Halley	470 ± 40
	H ₂ O	153P/2002C1	450 ± 50
³² S/ ³⁴ S	S ⁺	Halley	23 ± 6
	CS	Hale-Bopp	27 ± 3
	H ₂ S	Hale-Bopp	17 ± 4

(a) Ikeya, Tago-Sato-kosaka, Kohoutek, Kobayashi-Bergar-Milon

(b) Halley, Levy, Austin, Okazaki-Levy-Rudenko, Hale-Bopp

Adapted from: Bockelee-Morvan, D. 2005, In *Comets II*, Eds. M.C. Festau, H.U. Keller and H.A. Weaver. Univ. Arizona Press, Tucson, p. 391.

The results for ¹⁴N/¹⁵N is rather puzzling. The high spectral resolution of CN observations for several comets give ¹⁴N/¹⁵N ~ 150 , while radio line observation give ¹⁴N/¹⁵N ~ 300 which is close to the terrestrial value of 270. The lower ratio of 150 observed in Comets Hale-Bopp and WM₁(LINEAR) point to an additional source of CN other than HCN and heavily enriched in ¹⁵N which is still not identified.

The measured isotopic ratios given in Table 5.4 refer to the bulk compositions. However it is possible that departures from the mean value may be present at the microscopic level. Such deviations to the extent of ¹²C/¹³C ratios as high as 5000 has been found in the individual small grains in the coma of Comet Halley. The variations in ¹²C/¹³C of around 2 to 7000 has also been seen in primitive meteorites. The wide ranges in the observed

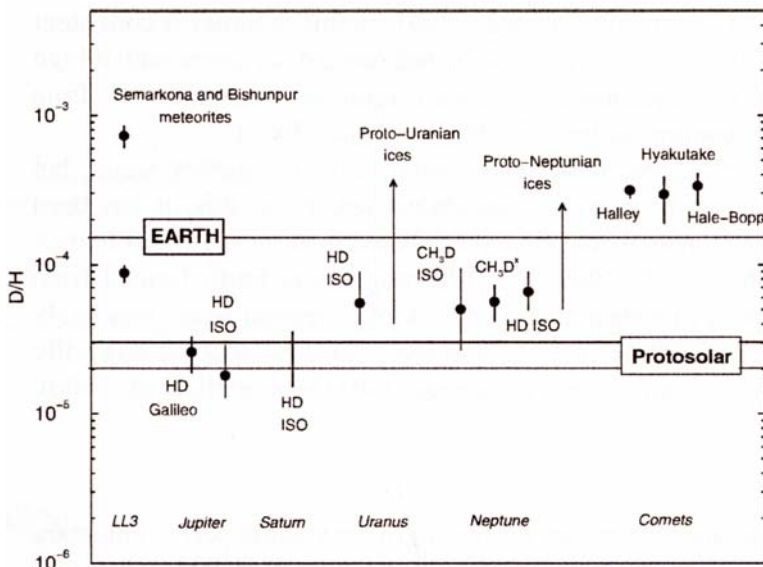


Fig. 5.22 The deuterium to hydrogen ratio in comets is compared with the values observed in planets and solar nebula (photosolar) (Attwedd, K. and Bockelee-Morvan, D. 2003. *Space Sci. Rev.*, **106** 139; Hersant, F., Gautier, D. and Hure, J.M. 2001. *Ap.J.*, **554**, 301).

value of $^{12}\text{C}/^{13}\text{C}$ ratios indicate that these particles are preserved presolar grains that have survived from physical and chemical processes in the interstellar and early solar system environments.

The measured isotopic ratio $^{12}\text{C}/^{13}\text{C}$ from the interstellar medium at the present time seems to vary from 20 to 80. The former and latter values corresponding to the galactic centre region and around solar neighbourhood respectively. This is smaller compared to the cometary value of around 90. The equilibrium value of $^{12}\text{C}/^{13}\text{C}$ based on the hydrogen burning in stars (i.e. CNO cycle) is around 4. The general reduction in the ratio of $^{12}\text{C}/^{13}\text{C}$ in interstellar matter compared to the solar system value is more likely to be produced as a result of the addition of ^{13}C . This could be brought about by the processing of ^{13}C by the CNO cycle in stars. On the basis of the present picture, the processed material of the stars find their way finally into the interstellar medium and thus enrich the medium with ^{13}C isotopes. The observed isotopic ratio of $^{12}\text{C}/^{13}\text{C}$ between the solar system and the interstellar value appears to be consistent to a first approximation with the scenario of chemical evolution which has taken place for the last 4.6 Gyr.

Lastly, mention may be made of the isotopic ratios of light elements like Li, Be, B, etc., as these elements will be destroyed easily in stars even if they were present in the original material. The detection in comets imply that they ought to have been produced more recently by different physical processes. However, the detection of light element isotopes in comets is a difficult problem.

5.5. Summary

The analysis of the spectra shows that the resonance fluorescence process is the excitation mechanism of the observed emission lines in comets. The abundance of various elements obtained from the study of the spectra of Comet Ikeya-Seki as well as *in situ* measurement of Comet Halley show values very similar to those of solar abundances. In addition, the isotopic ratio of $^{12}\text{C}/^{13}\text{C}$ in comets has a value of about 90, which is the same as the solar system value. However $^{12}\text{C}/^{13}\text{C}$ as high as 5000 has been seen in some of the individual dust grains in Comet Halley indicating that they are presolar grains.

Other isotopic ratios such as $^{16}\text{O}/^{18}\text{O}$ and $^{32}\text{S}/^{34}\text{S}$ are found to be similar to the solar values except the D/H ratio. It appears that the abundance of deuterium is enhanced compared to the solar values by a factor of 10 or so. The likely mechanism of such an enhancement could be through the ion-molecular reactions.

Problems

1. Consider the (B–X) transitions of the molecular hydrogen. Write down the equation between the upper and lower populations, $N(v')$ and $N(v'')$, assuming only the absorption and spontaneous emission terms are important. If the population in the lower vibrational levels is determined by the Boltzmann distribution at temperature $T = 2000^\circ\text{K}$, calculate the population in the upper vibrational levels and the resulting emission.
2. Consider the ground electronic state ($X^1\Sigma^+$), the first singlet (A^1II) and the triplet (a^3II) electronic states of the CO molecule. From the statistical equilibrium equations, obtain an expression for the intensity ratio of ($a^3II - X^1\Sigma^+$) to ($A^1II - X^1\Sigma^+$) transitions in terms of the molecular parameters of the molecule and its numerical value. Assume

$\rho B_{21} < A_{21}$ and $\rho B_{31} < A_{31}$. This problem will give an idea of the expected intensities of forbidden transitions compared to those of allowed transitions.

3. Calculate the wavelength of a solar photon of $\lambda = 5000 \text{ \AA}$ at the comet which is at $r = 0.52 \text{ AU}$. The comet is moving in an elliptical orbit with $e = 0.8$ and has a period of 5 years.
4. The relative intensities of the rotational lines of molecular spectra in a comet will vary irregularly with rotational quantum number and the intensity of an individual line will vary irregularly with the distance of the comet from the Sun. Explain why these effects occur and describe how in principle, you could compute the line intensities.
5. In terms of the spectral features observed in the coma of a comet, is it possible to infer the abundances of molecules in the primordial nebula? Explain.

References

The effect of Fraunhofer lines on cometary spectra was first pointed out in
 1. Swings, P. 1941. *Lick Obs. Bull.* **19**, 131.

The application of Resonance Fluorescence Process to molecules can be found in

2. Arpigny, C. 1965. *Mem. Acad. Roy. Belg.* Cl. 8°, **35**, 5.
- For some later work, the following papers may be referred.
3. Krishna Swamy, K.S. 1981. *Astr. Ap.* **97**, 110.
4. Weaver, H.A. and Mumma, M.J. 1984. *Ap.J.* **276**, 782.
5. Kleine, M., Wyckoff, S., Wehinger, P.A. and Peterson, B.A. 1994. *Ap. J.* **436**, 885.
6. Magnani, L. and A'Hearn, M.F. 1986. *Ap.J.* **302**, 477.
7. Schleicher D.G. and A'Hearn, M.F. 1988. *Ap.J.* **331**, 1058.
8. Reyle, C. and Boice, D.C. 2003. *Ap. J.*, **587**, 464.

For the calculation of vibrational transition probabilities, the following book may be referred to:

9. Penner, S.S. 1959. *Molecular Spectroscopy and Gas Emissivities*, Reading: Addison-Wesley Publishing Company.

The early work on C_2 molecule is discussed in

10. Stockhausen, R.E. and Osterbrock, D.E. 1965. *Ap.J.*, **141**, 287.

For later work, the following papers may be referred:

11. Krishna Swamy K.S. and O'Dell, C.R. 1987. *Ap. J.* **317**, 543.

12. O'Dell, C.R., Robinson, R.R., Krishna Swamy, K.S., Spinrad, H. and McCarthy, P.J. 1988. *Ap.J.* **334**, 476.
13. Gredel, R., van Dishoeck, E.F. and Black, J.H. 1989. *Ap. J.* **338**, 1047.
14. Combi, M.R. and Fink, U. 1997. *Ap.J.*, **484**, 879.

Papers pertaining to Prompt Emission lines.

The extensive Laboratory study carried out on H₂O is covered in the following paper

15. Carrington, T. 1964. *J. Chem. Phys.*, **41**, 2012.

The following papers cover the application to Comets.

16. Bertaux, J.L. 1986. *Astron. Astrophys.*, **160**, L7.

17. Budzien, S.A. and Feldman, P.D. 1991. *Icarus*, **90**, 308.

Comet Hyakutake spectral observations is in the following paper:

18. Meier, R. *et al.* 1998. *Icarus*, **136**, 268.

The first detection of Prompt Emission lines in Comet Hyakutake is covered in the paper

19. A'Hearn, M.F., Krishna Swamy, K.S. and Wellnitz, D.D. 2007. *Bull. Am. Astro. Soc.*, **39**, 507.

The following papers deal with polarization of molecular bands.

20. Ohman, Y. 1941. *Stockholm Obs. Ann.* **13**, No. 11, p.1.

21. Le Borgne, J.F. and Crovisier, J. 1987. *Proc. Symp. on Diversity and Similarity of Comets*. Brussels, Belgium.

22. Sen, A.K., Joshi, U.C. and Deshpande, M.R. 1989. *Astr. Ap.* **217**, 307.

The following papers refers to isotopic studies:

23. Altweig, K. and Bockelee-Morvan, D. 2003. *Space Sci. Rev.*, **106**, 139.

24. Bockelee-Morvan, D. 2005. In *Comets II*, Eds. M.C. Festou, H.U., Keller and H.A. Weaver, Univ. Arizona Press, Tucson, P.391.

This page intentionally left blank

CHAPTER 6

Gas Production Rates in Coma

The gaseous molecules vaporized from the nucleus are subjected to a variety of physical processes which could dissociate them step by step. Hence, the species observed in the spectra of comets could comprise contributions arising out of the dissociated products, as well as those released directly by the nucleus or even by dust particles. Therefore, the physical quantity of interest is the production rate of the species and its variation with the heliocentric distance. The production rate of a molecule can be determined either from the observation of the total luminosity or from the surface brightness of a given spectral line, band or a band-sequence.

If the vapourization of H₂O is mainly due to the absorption of the solar energy, then the production rate of H₂O should also have a r^{-2} dependence with the heliocentric distance. Therefore, if the observations show a deviation from the r^{-2} dependence, it is of great significance and has important information with regard to the mechanism of evaporation of the material from the nucleus. It is also of interest to see whether the production rate of the molecules differs from comet to comet and whether it has any correlation with the morphology, dust content, age, etc. of the comet. From these results, one may be able to understand better the evaporation of material from the nucleus as well as the source of the observed radicals and molecules in comets and the structure of the nucleus. Some of these aspects will be the subject of discussion in this chapter.

6.1. Theoretical Models

6.1.1. From the total luminosity

The total production rate of a particular species can be determined from the measurement of the total flux of the radiation from the entire coma of a given line or band. If the mean lifetime of the molecule is τ_i then the coma will contain N_i molecules of this type at any given time so that

$$N_i = Q_i \tau_i, \quad (6.1)$$

where Q_i is the production rate of the species. Since the excitation of the lines is due to the resonance fluorescence process, for an optically thin case, the luminosity of any line or a band is proportional to the total number of the species in the coma and to the fluorescence efficiency factor called the ‘g-factor’. The g-factor actually represents the probability of scattering of a solar photon per unit time per molecule. The luminosity at wavelength λ_i is therefore given by

$$L_i = g_i N_i = g_i Q_i \tau_i. \quad (6.2)$$

Since the observations include the whole extent of the coma, the flux received on the Earth F_i is given by

$$F_i = \frac{L_i}{4\pi\Delta^2}. \quad (6.3)$$

where Δ is the geocentric distance. Therefore, the production rate is given by

$$Q_i = \frac{4\pi\Delta^2 F_i}{g_i \tau_i} \quad (6.4)$$

The production rate can therefore be calculated provided g_i , τ_i and F_i are known. In general, the measurements covering only a given instrumental field of view is available and not over the whole coma. For such cases the total number of species in the field of view, N_i is given by the relation

$$N_i = \frac{4\pi\Delta^2 F_i}{g_i}$$

and hence the column density can be calculated.

The g-factor represents the number of photons per second scattered by a single atom or molecule exposed to the unattenuated sunlight. If the solar photon flux is πF_ν per unit frequency in the neighbourhood of the line, the g-factor for a strict resonance scattering is given by

$$g_\nu = F_\nu \int \alpha_\nu d\nu \quad (6.5)$$

where α_ν is the absorption cross-section. Therefore,

$$g_\nu = \pi F_\nu \left(\frac{\pi e^2}{mc} \right) f \quad (6.6)$$

or

$$g_\lambda = \left(\frac{\pi e^2}{mc^2} \right) \lambda^2 f_\lambda (\pi F_\lambda) \text{ photons/sec/molecule} \quad (6.7)$$

where f_λ is the absorption oscillator strength and πF_λ the solar flux per unit wavelength. For molecules, the relative transition probabilities for downward transitions must be taken into account. Therefore, Eq. (6.7) can be written as

$$g_\lambda = \left(\frac{\pi e^2}{mc^2} \right) \lambda^2 (\pi F_\lambda) f_\lambda \tilde{\omega} \quad (6.8)$$

where

$$\tilde{\omega} = \frac{A_{v'v''}}{\sum_{v''} A_{v'v''}}.$$

Here the A 's are the Einstein coefficients. The g-factor depends upon the oscillator strength and the solar flux. As pointed out in Chap. 3, the solar radiation in the ultraviolet region is dominated by line emissions. Therefore, the Doppler shift due to the comet's heliocentric radial motion can produce large changes in the g-factor as the comet moves in its orbit (see Fig. 5.14). This has to be taken into account in the analysis of the observations. But the average g-factor has been calculated for many molecules and is available in the literature.

The calculation of the *lifetime* of the species involves a knowledge of the photodissociation and photoionization rates, J_d and J_i respectively. These can be calculated from the relation

$$J_{i,d} = \int_{\lambda_c}^0 \sigma(\lambda) \pi F_\odot(\lambda) d\lambda \text{ (sec/molecule)} \quad (6.9)$$

where $\sigma(\lambda)$ is the photodestruction cross-section and $F_\odot(\lambda)$ is the incident solar flux. λ_c represents the threshold for the dissociation or ionization process. For most of the species, the photodissociation lifetime is relevant since the dissociation energies are smaller than those of ionization potentials. However, for the case of the CO molecule, the two are comparable as the dissociation potential ~ 11 eV and the ionization potential ~ 14 eV. The lifetime of the molecules is just the inverse of Eq. (6.9), i.e.,

$$\tau_i = J^{-1} \text{ sec.} \quad (6.10)$$

It should be noted that the dependence of the solar flux with heliocentric distance (Eq. 6.9) also enters in the lifetime of the molecules. Usually, the lifetime is referred to 1 AU. Since both g_i and τ_i depend directly on the solar flux which varies as r^{-2} , the product $g_i\tau_i$ [Eq. (6.4)] becomes independent of r . Because of the presence of large uncertainties in the value of cross-sections as well as the solar fluxes in the extreme ultraviolet region, the calculated J values and in turn the lifetime of the species are also uncertain. For example, the solar flux itself could vary by factors of 2 to 4 during the solar cycle. Therefore, the accurate calculation of the lifetime of a species is one of the main problems at present. The uncertainty in the lifetime of the molecules directly affects the calculated production rates.

6.1.2. From surface brightness distribution

It is possible to get much more information than just the production rates, if the variation of brightness of various emissions with radial distance from the centre of the comet could be observed. It is a common practice nowadays to make such observations using a diaphragm whose field of view is much smaller than the projected size of the coma. A typical observed brightness profile has a flat region near the centre and falls rather steeply in the outer region (Fig. 6.1). If the average brightness of a molecule is denoted as B_i at the projected distance ρ as seen in the sky then

$$B_i(\rho) = \bar{N}_i(\rho)g_i, \quad (6.11)$$

where $\bar{N}_i(\rho)$ is the average column density of the molecule along the line of sight. To get the total number of a species one has to integrate over the model dependent variation of density as a function of the projected distance ρ from the nucleus. This is then to be convolved with the instrumental field of view.

It is generally believed that the observed species are the dissociated or the decayed products of the original complex molecules which were vapourized from the nucleus. Because of the finite lifetimes of these dissociated products, they in turn break up further as they move out in the coma. Therefore, the coma can be divided roughly into three zones: a productive zone, an expansion zone and a destructive zone.

Let us start with the simplest model in which molecules are released by the nucleus with a production rate

$$Q = 4\pi R_0^2 E \quad (6.12)$$

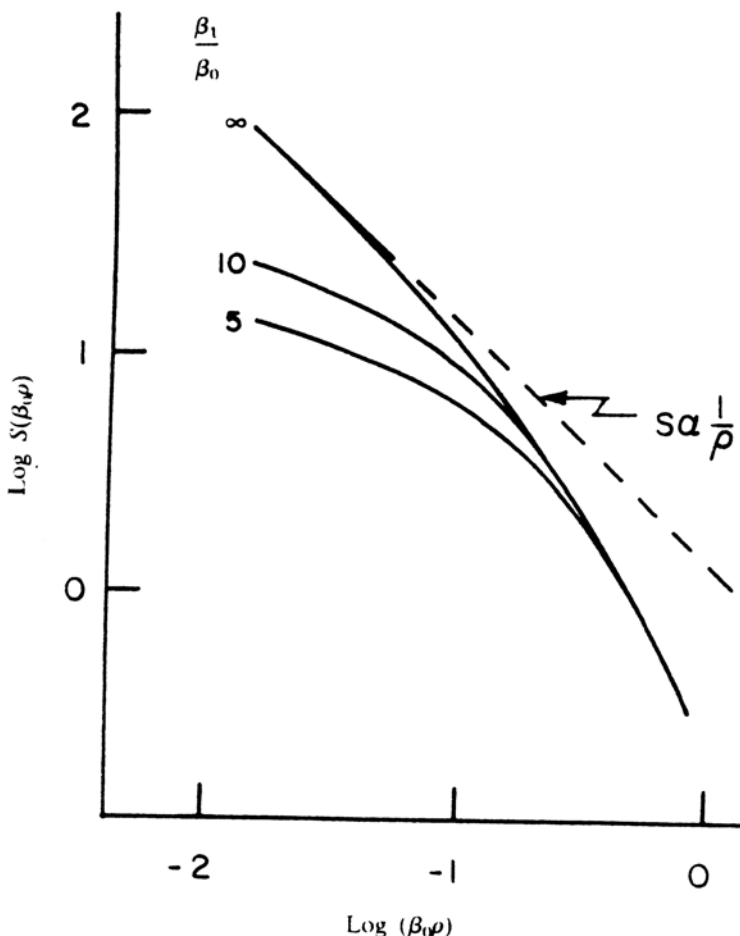


Fig. 6.1 Theoretical surface brightness distributions based on Haser's model for different ratios of the scale lengths of daughter and the parent molecule. (Adapted from D'Dell, C.R. and Osterbrock, D.E. 1962. *Ap. J.*, **136**, 559).

where R_0 is the radius of the nucleus and E is the evaporation rate ($/\text{cm}^2/\text{sec}$). It then expands isotropically with a velocity v . For such a case, the density falls off as R^{-2} where R is the distance from the centre of the coma and it is given by

$$n(R) = \frac{Q}{4\pi v} \frac{1}{R^2}. \quad (6.13)$$

At a projected distance ρ as seen in the sky, the column density is obtained

by integrating along the line of sight and is given by

$$N(\rho) = \frac{Q}{4v} \frac{1}{\rho}. \quad (6.14)$$

The column density, therefore, varies as $(1/\rho)$. The above formalism is very simple and gives only rough estimates.

As the molecules move outwards, they are generally dissociated by the solar radiation. They have a mean lifetime τ . This corresponds to a distance $R_d = v\tau$, where v is the average velocity of the molecule. The density distribution is now given by

$$\begin{aligned} n(R) &= \frac{Q}{4\pi v R^2} e^{-(R/R_d)}, \\ &= \frac{C}{R^2} e^{(-R/R_d)} \end{aligned} \quad (6.15)$$

where

$$C = \frac{Q}{4\pi v}.$$

A slightly more complicated model is based on the parent-daughter hypothesis in which the parent molecules released by the nucleus decay with a mean lifetime τ_1 corresponding to a distance (called *scale length*) of $R_1 = v_1\tau_1$. The daughter products then in turn decay with a lifetime τ_0 corresponding to $R_0 = v_0\tau_0$. For such a two-component model, the number density takes the form

$$n(R) = \frac{C}{R^2} (e^{-\beta_0 R} - e^{-\beta_1 R}). \quad (6.16)$$

Here $\beta_0 (\equiv (\tau_0 v_0)^{-1})$ denotes the reciprocal of the mean distances travelled by or scale lengths of the observed molecules, β_1 denotes the same by the parent molecule before they are dissociated. The Eq. (6.16) can be written as

$$n(R) = \frac{C}{R^2} f(R) \quad (6.17)$$

where $f(R)$ is the function representing the quantity in brackets of Eq. (6.16). If $n(R_1)$ denotes the density at the distance R at which $f(R)$ has its maximum value, then

$$n(R) = n(R_1) \frac{R_1^2}{R^2} \frac{\beta_1}{\beta_1 - \beta_0} \left[e^{-\beta_0(R-R_1)} - \frac{\beta_0}{\beta_1} e^{-\beta_1(R-R_1)} \right]. \quad (6.18)$$

The integration of the above equation along the line of sight at the projected distance ρ from the nucleus gives the column density and hence the surface

brightness at that point for an optically thin case. The resulting expression is of the form

$$N(\rho) = 2n(R_1)R_1^2 \frac{\beta_0\beta_1}{\beta_1 - \beta_0} e^{+\beta_0 R_1} \frac{1}{\beta_0\rho} [B(\beta_0\rho) - B(\beta_1\rho)] \quad (6.19)$$

where

$$B(z) = \frac{\pi}{2} - \int_0^z K_0(y)dy. \quad (6.19a)$$

Here $K_0(y)$ is the modified Bessel function of the second kind of order zero. The Eq. (6.19) can be written as

$$N(\rho) = (\text{constant})s(x) = \frac{(\text{constant})}{x} \left[B(x) - B\left(\frac{\beta_1 x}{\beta_0}\right) \right] \quad (6.20)$$

where $x = \beta_0\rho$. The equation shows that the shape of the surface brightness distribution $s(x)$, depends essentially upon the relative values β_1 and β_0 . The Fig. 6.1 shows a plot of brightness profiles predicted for various values of the ratio β_1/β_0 . The curves become rather flat in the central region for small values of β_1/β_0 , and this means that the two scale lengths do not differ from each other very much. One can also see the deviation from the simple model (constant outflow velocity with no creation or destruction) in which the dependence is given by $1/\rho$.

The total number of molecules $M(\rho)$ within a cylinder of radius ρ centred on the nucleus can be obtained by the integration of Eq. (6.19) over ρ , i.e.,

$$\begin{aligned} M(\rho) &= \int_0^\rho 2\pi\sigma N(\sigma)d\sigma \\ &= 4\pi n(R_1)R_1^2 \frac{\beta_1}{\beta_0(\beta_1 - \beta_0)} e^{\beta_0 R_1} \beta_0\rho [G(\beta_0\rho) - G(\beta_1\rho)] \end{aligned} \quad (6.21)$$

where

$$G(z) = \frac{\pi}{2} - \int_0^z K_0(y)dy + \frac{1}{z} - K_1(z).$$

Here K_0 and K_1 are the modified Bessel functions of the second kind of order 0 and 1 respectively. The above expression can also be expressed more conveniently in terms of the production rate as

$$M(\rho) = \frac{Q\rho}{v} \left[\int_x^{\mu x} K_0(y)dy + \frac{1}{x} \left(1 - \frac{1}{\mu} \right) + K_1(\mu x) - K_1(x) \right] \quad (6.21a)$$

where $x = \beta_0\rho$ and $\mu = \beta_1/\beta_0$. The quantity occurring in bracket depends only on the parameters μ and x which could be tabulated for various values of x and μ .

The above two-stage model usually known as *Haser's model*, can be further extended to three stages in which the daughter products themselves dissociate. Let τ_1, τ_2 and τ_3 denote the lifetime of the parent, daughter and the granddaughter species respectively. If the corresponding velocities are v_1, v_2 and v_3 then $\beta_i = (\tau_i v_i)$ with $i = 1, 2$ and 3 . The densities of the three corresponding species can be expressed conveniently in terms of the production rate Q_1 of the parent molecule as follows.

$$n_1(R) = \frac{Q_1}{4\pi v_1 R^2} \exp(-\beta_1 R) \quad (6.22)$$

$$n_2(R) = \frac{Q_1}{4\pi v_2 R^2} \frac{\beta_1}{(\beta_2 - \beta_1)} [\exp(-\beta_1 R) - \exp(-\beta_2 R)] \quad (6.23)$$

and

$$n_3(R) = \frac{Q_1}{4\pi v_3 R^2} [A \exp(-\beta_1 R) + B \exp(-\beta_3 R) + C \exp(-\beta_2 R)] \quad (6.24)$$

where

$$A = \frac{\beta_1 \beta_2}{(\beta_1 - \beta_2)(\beta_1 - \beta_3)},$$

$$B = \frac{-A(\beta_1 - \beta_3)}{(\beta_2 - \beta_3)}$$

and

$$C = \frac{-B(\beta_1 - \beta_2)}{(\beta_1 - \beta_3)}.$$

The corresponding column density of the species over the field of view of linear radius ρ is given by

$$N_1(\rho) = \frac{Q_1}{4\pi v_1} \frac{2}{\rho} B(\beta_1 \rho), \quad (6.25)$$

$$N_2(\rho) = \frac{Q_1}{4\pi v_2} \frac{2}{\rho} \left(\frac{\beta_1}{\beta_2 - \beta_1} \right) [B(\beta_1 \rho) - B(\beta_2 \rho)] \quad (6.26)$$

and

$$N_3(\rho) = \frac{Q_1}{4\pi v_3} \frac{2}{\rho} [AB(\beta_1 \rho) + BB(\beta_2 \rho) + CB(\beta_3 \rho)] \quad (6.27)$$

where $B(Z)$ is given by Eq. (6.19a). The above procedure can easily be extended to cascade processes involving more than three species.

6.1.3. From number densities

The relation between the emission coefficient j and the number density n of the species for the resonance fluorescence excitation process is given by

$$\frac{j}{h\nu_{\text{em}}} = \frac{\pi e^2 f}{h\nu_{\text{abs}} m} \rho_\nu(r) n P. \quad (6.28)$$

Here ν_{em} and ν_{abs} are the emission and absorption frequencies, $\rho_\nu(r)$ the solar radiation density at the heliocentric distance r and P is the probability that a particular transition takes place in comparison with other decays. All other constants have their usual meanings. The integration of Eq. (6.28) along the line of sight through the comet and up to a projected radius ρ gives the relation

$$\frac{L(\rho)}{h\nu_{\text{em}}} = \frac{\pi e^2 f}{h\nu_{\text{abs}} m} \rho_\nu(r) PM(\rho) \quad (6.29)$$

where $L(\rho)$ is the observed luminosity in the emission line and $M(\rho)$ is the total number of the species in the field of view. The above equation can be written as

$$M(\rho) = \left(\frac{\nu_{\text{abs}}}{\nu_{\text{em}}} \right) \frac{m L(\rho)}{\pi e^2 f \rho_\nu(r) P} \quad (6.30)$$

or

$$\log M(\rho) = \log C + \log L(\rho) + 2 \log r \quad (6.31)$$

where

$$C = \left(\frac{\nu_{\text{abs}}}{\nu_{\text{em}}} \right) \frac{m}{\pi e^2 f \rho_\nu(r) P}.$$

The last term in equation (6.31) arises as solar radiation varies as r^{-2} where r is the heliocentric distance of the comet. The constant C depends upon the transition of interest.

For C_2 molecule, as one generally observes band sequence fluxes with $\Delta V = +1$ or 0, it is necessary to include in the calculation of constant C , the absorptions arising from various vibrational levels from the lower electronic state through the term $(f\rho_\nu(r)/\nu)$. In a similar manner the population of vibrational levels in the upper electronic state enters through the probability P . Therefore, a mean value for the above ratio has to be used, i.e.,

$$\left(\frac{f\rho}{\nu} \right) = \sum_{v''} x_{v''} \sum_{\Delta v} f_{v'', \Delta v} \rho(\nu_{v'', \Delta v}) / \nu_{v'', \Delta v}. \quad (6.32)$$

Here v'' represents the vibrational level in the lower electronic state and Δv the various band sequences being considered. $x_{v''}$ represents the weight factors for the vibrational levels of the lower electronic state. Similarly the transition probability P for the downward transition should also take into account the population distribution in the upper vibrational levels. The Eq. (6.31) gives the abundance of the species of interest within the field of view of the comet as a function of r .

The comparison of the observed surface brightness distribution with the expected distribution of Fig. 6.1, fixes the values of β_0 and β_1 as well as R_1 from its definition. These can then be used to compute $M(\rho)$ from Eq. (6.21) for comparing with the observed distribution [Eq. (6.31)]. This fixes the value of $n(R_1)$ and hence the density distribution in the coma through Eq. (6.18). The observed distribution of $M(\rho)$ can also be used to derive the production rate Q directly from Eq. (6.21a).

The radial outflow decay model has been used extensively in the literature with a high degree of success. Basically from a fit of the expected surface brightness distribution with the observed distribution, it is possible to derive the production rates and the two scale lengths corresponding to the parent and the dissociated product. From a knowledge of the scale lengths, the lifetime of the species can be determined provided the velocity is known. However, it is found that the scale lengths derived from the Haser's model are generally smaller than the values calculated using the estimated outflow speed of the gas and the photodissociation lifetime computed from the solar UV flux and the measured photoabsorption cross-sections. There are some limitations of this model. First of all it is applicable only to photodestruction products. It does not allow for situations where they could be produced through chemical reactions. Other effects like non-radial flow, the effect of solar radiation pressure and the velocity distribution of the species have to be taken into account in a more realistic model. Some attempts have been made in this direction. Mention may be made of the method based on the *vectorial formalism*. In this method, the molecular fragments of a dissociated parent molecule are ejected isotropically in a reference frame attached to the parent molecule. Also, unlike in the case of Haser's model, the effects of velocity and lifetimes are separated which allow the study of velocity dependent phenomena. These are the two main improvements over the Haser's model. Another formalism has been developed based on an average random walk model which is the *Monte Carlo approach*. The calculations are done in 3-dimensions centred on the comet nucleus. The results are then reduced to 2-dimensional maps for compar-

ing with the observation of molecules. It allows the asymmetric ejection of the parent molecules from the molecules such as jets etc. It can also take into account the acceleration due to solar radiation pressure. It includes several dissociation steps for each specie. More physical effects could be incorporated into the model. These two approaches are more complicated than Haser's model. However, these models yield the surface distributions which resemble rather closely with those of Haser's model.

6.1.4. *Semi-empirical photometric theory*

The gas production rate can, in principle, be determined from the knowledge of the observed light curve. The light curve of a comet basically gives the variation of apparent brightness as a function of the heliocentric distance. In general, the observed brightness in the visual region is mainly due to the continuum and the Swan bands of the C₂ molecule. The continuum is made up of scattering by the dust particles in the coma as well as the reflection from the nucleus. Therefore, a simple photometric equation can be written relating the observed light to the light contributed by the dust grains and the nucleus in the same visual band pass. It can be written as

$$A\phi_n(\alpha) + Bf_1(r) + C\phi_d(\alpha)f_2(r) = r^2 10^{0.4[m_\odot - m_1(r) - 5 \log \Delta]}. \quad (6.33)$$

The three terms on the left hand side of the above equation represent the contribution from the nucleus, gas and dust respectively. Here $m_1(r)$ is the apparent visual magnitude of the comet, m_\odot the apparent magnitude of the Sun, $\phi_n(\alpha)$ and $\phi_d(\alpha)$ are the phase functions of the nucleus and the dust, at phase angle α , $f_1(r)$ and $f_2(r)$ are the functional behavior of the gas and dust production with r . The equation (6.33) can be simplified with the assumption that the cometary activity is basically given by the production rate of hydrogen Q_H . This is a reasonable assumption as H₂O is the most abundant molecule in a comet and H is the dissociated product of H₂O. If the gas and dust are well mixed and remain almost the same with several apparitions, then one can write

$$Cf_2(r) \simeq C(r)Q_H(r). \quad (6.34)$$

The observed production rate of C₂ of several comets appears to vary roughly as a quadratic function of Q_H . Therefore, one can write to a first approximation,

$$Bf_1(r) \approx B(r)Q_H^2(r). \quad (6.35)$$

Therefore, Eq. (6.33) can be written in the form

$$P_n R_n^2 \phi_n(\alpha) + B(r) Q_H^2(r) + C(r) Q_H(r) \phi_d(\alpha) = r^2 10^{0.4[m_\odot - m_1(r) - 5 \log \Delta]} \quad (6.36)$$

where R_n and P_n represent the radius of the nucleus and geometric albedo respectively. The Eq. (6.36) can be solved as a quadratic equation in $Q_H(r)$. For further simplification one can write the ratio of the dust scatter to that of the gas in the same band pass as

$$\delta = \frac{C(r) Q_H(r) \phi_d(\alpha)}{B(r) Q_H^2(r)}. \quad (6.37)$$

The term $B(r)$ should be proportional to the local lifetime of the molecule and so it can be written as

$$B(r) = R \tau_{c_2} (r/r_0)^2 \quad (6.38)$$

with the C_2 lifetime referring to $r = r_0 = 1\text{AU}$. Here R refers to the resonance fluorescence efficiency. The Eq. (6.36) can be written as

$$P_n R_n^2 \phi_n(\alpha) + (1 + \delta) R \tau_{c_2} Q_H^2(r) = r^2 10^{0.4[m_\odot - m_1(r) + 5 \log \Delta]}. \quad (6.39)$$

This gives the solution for the hydrogen production rate as

$$Q_H(r) = \left[\frac{r^2 10^{0.4(m_\odot - m_1(r) + 5 \log \Delta)} - P_n R_n^2 \phi_n(\alpha)}{(1 + \delta) R \tau_{c_2}} \right]^{1/2}. \quad (6.40)$$

If the second term involving $P_n R_n^2$ is smaller than the first term, which is the case at shorter distances, it is easier to calculate Q_H from the observed light curve.

6.2. Results

6.2.1. OH and H

Extensive observations of the Lyman α of hydrogen as well as of OH emission at 3090 Å have been carried out for various comets using rockets and satellites. These observations have been used to extract the production rate of OH and H. If OH and H arise from the dissociation of H_2O , the ratio is $Q(\text{H})/Q(\text{OH}) \approx 2$. The analysis of the brightness measurements for the Comet Bennett showed that the dependence of the production rates of H and OH with heliocentric distance had almost the same variation as $r^{-2.3}$ (Fig. 6.2). This implies that both H and OH must have come out of the same parent molecule, which presumably is water. The

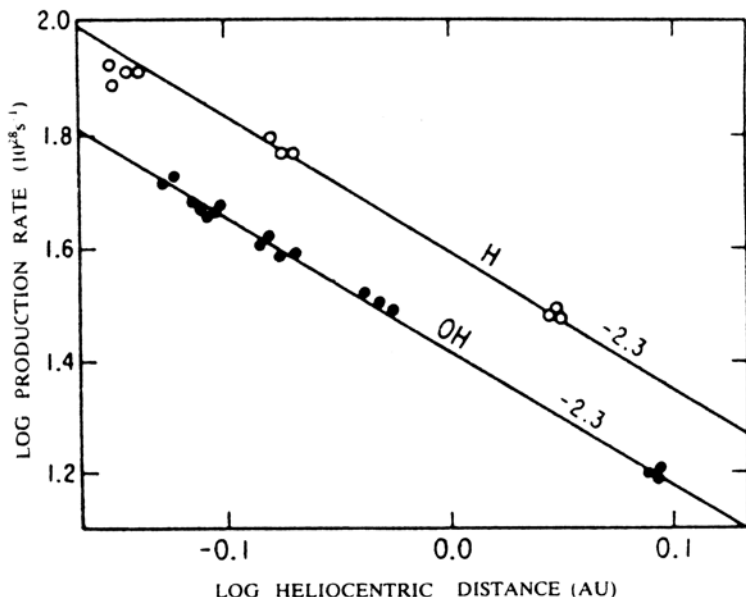


Fig. 6.2 A plot of the production rates of OH and H as a function of heliocentric distance for Comet Bennett (Keller, H.U. and Lillie, C.F. 1974. *Astr. Ap.*, **34**, 187).

derived production rates for OH and H at 1 AU were $(2.0 \pm 0.8) \times 10^{29}$ molecules/sec and $(5.4 \pm 2.7) \times 10^{29}$ atoms/sec respectively. This gives a ratio of $Q(H)/Q(OH) \approx 2.7$. The International Ultraviolet Explorer Satellite (IUE) was well suited for this study as it covers the wavelength region from 1150 to 3400 Å wherein the emissions from H and OH lie (Fig. 4.4). Therefore, it was possible to make simultaneous brightness measurements of these decay products as a function of the radial distance from the nucleus. Such spectra covering a wide range of heliocentric distances give a homogeneous set of observations. From a fit with the expected brightness distribution with those of observations, the production rate of H_2O can be determined for various heliocentric distances. The results for Comet Bradfield indicate the dependence of the production rate with heliocentric distance as $r^{-3.8}$ to $r^{-4.4}$. For Comet Austin (1990 V) the variation is around $r^{-1.8}$ to $r^{-2.8}$. The ranges in the power of r for a given comet come about due to the fact whether the effect of solar activity is included or not in the model calculations. The derived production rates of water in Comet Bradfield can also explain reasonably well the observed brightness distri-

bution of hydrogen and oxygen atoms with two velocity distributions for H atoms of 8 and 20 km/sec (Sec 6.3.1). Therefore, the observed brightness of OH, H and O are consistent with a common source of all the three species, which most probably is H₂O. The heliocentric variation of the production rate of OH for Comet Stephan-Oterma is found to have a dependence, as $r^{-4.8 \pm 0.6}$ for the pre-perihelion distance. The heliocentric variation of OH production rate in Comet Hale-Bopp for pre-perihelion observations is initially steeper ($r^{-3.7}$), then flatter ($r^{-1.8}$) and finally much steeper ($r^{-6.8}$). The typical number densities of H₂O and OH at a distance of 10⁴ km from the nucleus are of the order of $2 \times 10^5/\text{cm}^3$ and $4 \times 10^4/\text{cm}^3$ respectively.

Comet Halley was observed extensively from IUE satellite for Ly α of H emission (1216 Å) and OH emission (3085 Å). The observations of Ly α were analysed based on Monte Carlo models in combination with radiative transfer models. The derived production rate of water from the nucleus centred observations is compared with that derived from OH observations in Table 6.1. The agreement in the production rate of H₂O derived from H and OH observations is good.

Table 6.1 Comparison of H₂O production rates for Comet Halley*.

(r AU)	Log Q(H ₂ O) (from OH, 3085 Å)	Log Q(H ₂ O) (from Ly α , H)
1.45	28.987	28.978
1.13	29.582	29.509
1.02	29.555	29.452
0.84	29.818	29.734
0.98	29.642	29.691
1.32	29.367	29.343
1.85	29.340	29.406
0.84 ^a	29.36	29.45 ^a

*IUE observations.

Adapted from Combi, M.R. and Feldman, P.D. 1993. *Icarus*, **105**, 557.

a. For Comet Hyakutake: Combi, M.R. *et al.* 1998. *AP.J.*, **494**, 816.

The study of the 18 cm line of OH in the radio region should also give information about the production rates and the velocity fields in the coma. This should supplement the information obtained from the study

of the lines in the ultraviolet region. A large amount of work has been carried out on various comets based on the radio frequency lines of the OH radical. Since the radio frequency lines are very narrow and since it is also possible to make high resolution radio observations, it is possible to study the velocity distribution of OH molecule in the coma. In fact, the precision of the velocity field is limited only by the quality of the data. The observed profile is generally asymmetric about the centre. In addition, there is an asymmetry in the spatial brightness distribution in the East-West of the comet's centre. These asymmetries arise due to the fact that the velocities of the OH molecules in the coma are not uniform throughout, i.e., the differential velocity effect is present. The observed asymmetry implies that the OH radicals are not isotropically distributed around the nucleus.

The calculation of the total number of OH molecules from the observed emission is not so simple as the lines arise due to the excitation by ultraviolet radiation where Swings effect is very effective. The expression relating the total flux density emitted by the entire comet to the total number of OH molecules in the ground state is given by

$$F = \frac{A_{ul} ik T_{BG}}{4\pi\Delta^2} \frac{2F_u + 1}{8} N_{OH} \quad (6.41)$$

where T_{BG} is the background emission, F_u is the total angular momentum quantum number of the upper state of the transition, i is the ‘inversion’ of the lambda doublet (Fig. 5.14) and Δ is the geocentric distance of the comet.

The OH production rate can be calculated from the relation $Q_P = N_{OH}/\tau_{OH}$ where τ_{OH} is the lifetime of the OH molecules. In general, for a better estimate it is necessary to take into account the collisional quenching as well as the distribution of molecules and the molecular outflow velocities in the coma in the interpretation of the observed flux in terms of the total number of molecules and hence the production rate. To specify the distribution of OH in the coma requires a model for the production of OH from H_2O and the destruction of OH due to photodissociation and photoionization. The Haser's model is most commonly used for the analysis of OH observations, i.e.,

$$n(OH) = \frac{Q_P}{4\pi r^2 v_{OH}} \frac{l_{OH}}{l_{OH} - l_P} \left(e^{-r/l_{OH}} - e^{-r/l_P} \right) \quad (6.42)$$

where $n(OH)$ is the density of the OH molecule. l_{OH} and l_P are the scale lengths (same as β^{-1} of Sec. 6.1.2) for OH and the parent molecule respectively. v_{OH} is the radial velocity of the OH molecule. Figure 6.3 shows

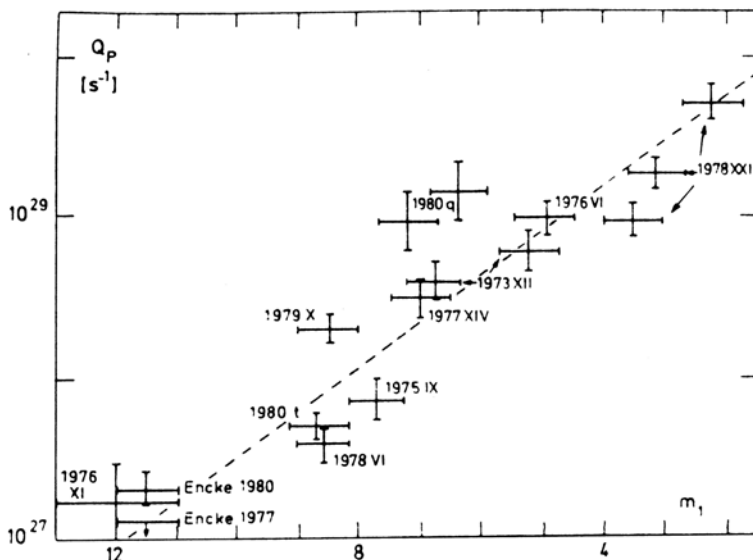


Fig. 6.3 Shows the production of OH as a function of the total visual brightness reduced to $r = \Delta = 1$ AU for various comets. The dashed line drawn is for $\log Q_p = 30.33 - 0.28 m_1$ (Despois, D., Gerard, E., Crovisier, J. and I. Kazes, 1981. *Astr. Ap.*, **99**, 320).

a plot of the OH-parent production rate as a function of the total visual brightness for a number of comets, both referred to $r = \Delta = 1$ AU. The dashed line represents the relation

$$\log Q_P = 30.33 - 0.28m_1. \quad (6.43)$$

It is of interest to compare the production rates of OH obtained from both the radio and the ultraviolet observations for the same comet, to see whether there is any discrepancy between the two determinations. It is found that the ultraviolet production rates are systematically higher compared to those of radio values.

There are several causes for this observed discrepancy. First of all the two measurements are fundamentally different and hence comparison relies on extensive modelling. It requires the knowledge of lifetime of OH and the velocity distribution. The model also depends upon the heliocentric distance, radial velocity, anisotropic out-gassing and the solar cycle. Owing to all these factors, the problem is a complex one. Therefore, the discrepancy appears to be associated with the use of different model parameters which enter in the interpretation of the UV and radio observations. For

example, the lifetime of OH used in the two cases are different. In addition, Λ -doublet OH population is sensitive to collisions in the inner coma and so it has to be taken into account. Therefore, the derived production rate of OH from radio observations depends upon the beam width of the radio telescope and so on. Basically, the physics of the problem is complicated and it involves the specification of too many parameters. So far a comparison of the production rate of OH from UV and radio methods were carried out for different dates of observations, radio telescopes and so on. Therefore, in order to understand better this discrepancy, if it is real, is to use simultaneous UV and radio observations so that the physical characteristics of the coma are roughly the same. Through this procedure it may be possible to put tight constraints on the model parameters. Such an exercise was carried out for Comet Halley observations of 1985-86. The OH observations from IUE satellite and 18 cm radio observations of Comet Halley taken around the same time have been used for the study. The 18 cm data has been analysed with sophisticated models. The derived production rate of OH from OH observations and 18 cm radio observations are given in Table 6.2. The agreement between the radio and UV OH production rates is good.

Table 6.2 OH production rates from UV and radio observations of Comet Halley.

Date (1985)	Method	$Q(OH)$ ($10^{29}/\text{cm}^2$)
2.5 Dec	UV	1.4
3.2 Dec	UV	1.0
15.5 Dec	UV	1.7
5.12 Dec	Radio	1.4
10-12 Dec	Radio	1.2

OH UV (0, 0 band of (A-X)
3085 Å), Radio (18 cm)

Adapted from Gerard, E. 1990. *Astron. Astrophys.*, **230**, 489.

The study of 18 cm line of OH has been carried out routinely on comets. The results for Comet Halley showed a variation of the production rate with the heliocentric distance as r^{-2} for $r < 2$ AU.

The production rate of H₂O can also be determined independently of the study of [OI] 6300 Å and H α (6565 Å) observations of comets. This will provide an independent check on the consistency of O and H arising out of H₂O. Table 6.6 shows the derived values for the production rate of H₂O for Comet Halley, by these two methods based on the observations carried out on the same night and with the same instrument. The agreement between the two is good. Therefore, the production rates of H₂O derived from the H α brightness measurements are consistent with the H₂O production rates derived from the O[¹D] measurements, both of which are based on the coma containing OH, H and O arising out of the dissociation of H₂O. Therefore, at the present time, it is an excellent approximation that H₂O is the source of observed species OH, H and O in comets.

The heliocentric variation of the production rate of H₂O is of particular interest. As already mentioned, if the evaporation of the gases from the nuclei is due to the absorption of the total solar energy, the variation of the production rate of H₂O should also behave as r^{-2} . The results presented earlier showed that for some comets it is in reasonable accord with this dependence. However, for some other comets the variation is vastly different. This is related to the evaporation of the gaseous material from the nucleus which is dependent upon the nature and the composition of the nucleus. Therefore, more complicated models might have to be considered for explaining the observations.

6.2.2. H₂O, H₂

H₂O

2.7 μm band

Before the direct detection of H₂O in Comet Halley, the presence of H₂O in comets was inferred indirectly from observations such as the presence of OH, H, O and H₂O⁺ in comets. The fundamental bands of vibration, especially the ν_3 near 2.7 μm cannot be observed from ground due to strong absorption by the Earth's atmosphere. The first direct detection of ν_3 band at 2.7 μm of H₂O came from the observations carried out with KAO on Comet Halley at $r = 1.13$ AU (Fig. 4.7). It was also detected by VEGA spacecraft. This detection provided direct evidence that H₂O is the dominant volatile component of comets. The total column density of H₂O can be estimated from the measured band brightness and with the use of Haser's

model. It is then possible to calculate the production rate of H_2O . The calculated production rate of $\text{H}_2\text{O} \sim 4 \times 10^{28}/\text{sec}$. The $2.7 \mu\text{m}$ band of H_2O has been observed in other comets like Wilson, Hale-Bopp, Hartley etc.

Radio lines

The pure rotational transitions between low rotational states of water are predicted to be quite strong. These lines lie in the submillimetre wavelength region and can only be observed from space. The line at 557 GHz arising out of $1_{10} - 1_{01}$ transition in H_2O was detected in Comet Lee ($r \sim 1.2 \text{ AU}$) using Submillimetre Wave Astronomy Satellite (SWAS). The estimated production rate of H_2O from the observed intensity and use of Haser's model $\sim 8 \times 10^{28}/\text{sec}$.

Prompt emission lines

The photolysis of water produces OH mostly in the excited states of the ground electronic state $X^2\Pi$ as shown by laboratory studies. The wavelength of vibrational rotational transitions of (1, 0) band arising out of the ground electronic state $X^2\Pi$ lie in the infrared region ($\sim 3 \mu\text{m}$). The transitions from $v'' = 1$ to $v'' = 0$ occurs within $\sim 10\text{ms}$. This type of emission is called *prompt emission* lines which is similar to the ones discussed earlier which lie in the UV region (Sec. 5.1.5).

The prompt emission lines arising from the vibrational rotational transitions of (1, 0) band in the ground electronic state $X^2\Pi$ is shown in Fig. 6.4. The four lines in the region 3042 cm^{-1} to 3048 cm^{-1} are conspicuous.

Many of the nonresonant fluorescent bands of H_2O called *hot bands* which lie in the wavelength region of around $2.9 \mu\text{m}$ can be observed from the ground. Therefore with the same instrument it is possible to make simultaneous measurements of the parent (H_2O , hot bands) and its dissociation product (OH, prompt emission lines) in the infrared region.

If H_2O is the parent molecule of OH prompt emission lines, the spatial distribution of their intensities should be similar, peaking at the centre in contrast to quiescent OH which should exhibit a much flatter distribution. Figure 6.5 shows the observed intensities of H_2O and OH as a function of distance from the nucleus in Comet Lee. They are in good agreement with each other. This type of agreement has been seen from several comets.

The production rate of H_2O can be calculated from the observed inten-

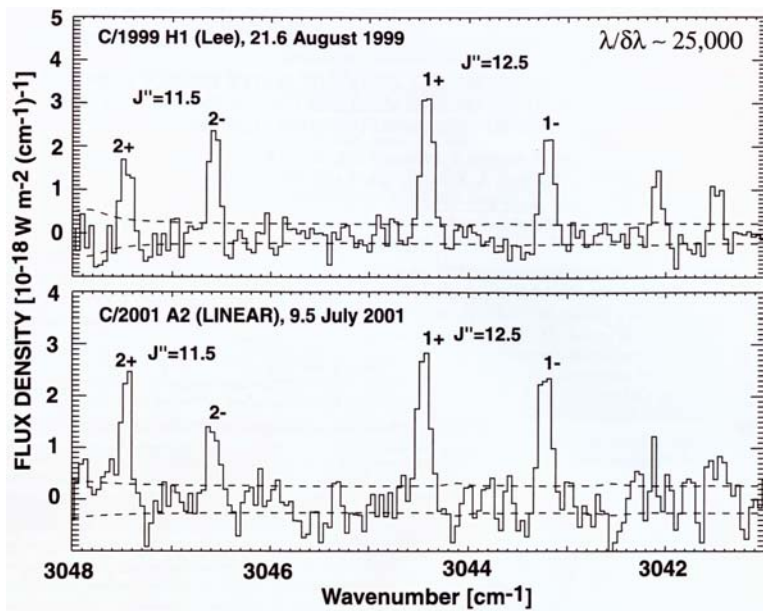


Fig. 6.4 High dispersion spectra of Comets Lee and LINEAR showing quadruplet lines of OH near 3046 cm^{-1} (Bonev, B.P., *et al.* 2004. *Ap.J.*, **615**, 1048, Reproduced by permission of the AAS).

sity of its nonresonant fluorescence lines (hot bands) from the relation

$$Q(\text{H}_2\text{O}) = P \left\langle \frac{F(\text{H}_2\text{O})}{g(hcv)} \right\rangle (\text{GF}) \quad (6.43a)$$

Where $F(\text{H}_2\text{O})$ is the line flux and g is the fluorescene emission factor. P is a parameter which depends upon geocentric distance, the photodissociation lifetime of H_2O and the fraction of H_2O molecules expected in the sample region of the coma. The quantity (GF) represent the growth factor that accounts for the loss of flux near the nucleus.

The equivalent g-factor g_{eq} for OH prompt emission lines which equal the observed production rate of H_2O represented as Q^* can be calculated from an expression similar to equation (6.43a) as

$$Q^* = \frac{F(\text{OH}^*)}{g_{\text{eq}}(hcv)^*} (\text{GF})^*$$

Here all the parameters are similar to those of equation (6.43a), but refer to OH prompt emission lines. These g_{eq} factors can be used to derive the production rate of H_2O in any other comet from the measured fluxes of

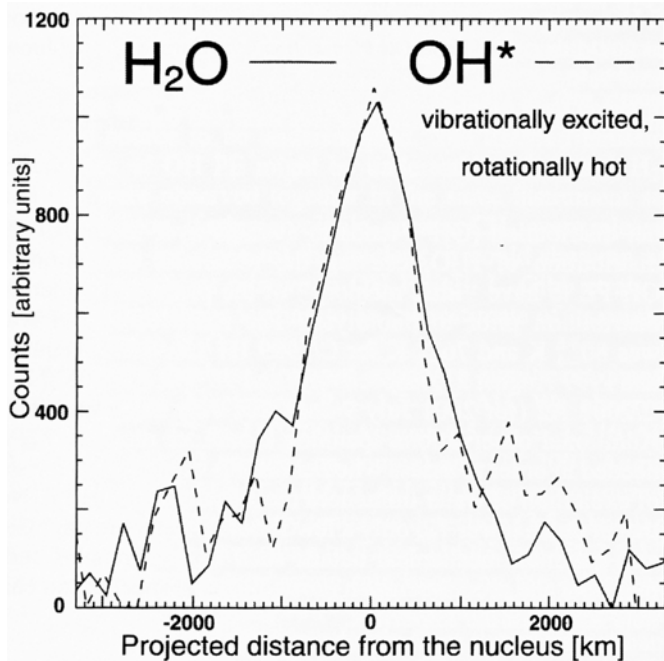


Fig. 6.5 Observed Spatial distribution of H_2O and OH in Comet Lee (Bonev, B.P. *et al.* 2004. *Ap. J.*, **615**, 1048, Reproduced by permission of the AAS).

OH prompt emission lines. This is a simpler way of getting the production rate of H_2O in comets as it is easier to observe OH prompt emission lines from the ground. Therefore OH prompt emission lines provide a proxy for water.

The distribution of OH prompt emission lines seen in $X^2\Pi, v' = 1$ state in comets also refer to the conditions which is vastly different from those carried out under laboratory conditions. Therefore cometary observations of OH prompt emission lines could provide deeper insight into the dissociation dynamics of H_2O .

Total water production

The production rate of H_2O for Comet Halley has been measured by various methods over a wide range of heliocentric distances covering before and after perihelion passage. Integration of the observed production rate of water with time gives an estimate of the total amount of water sublimated from the nucleus during the entire apparition, which comes out to be

1.3×10^{11} kg. For Comet Borrelly, the estimated total amount of water sublimated from the nucleus obtained from integrating the water production rate throughout an apparition is around 1.1×10^{10} kg.

H_2

The strong lines of the hydrogen molecule should appear in the spectral region around 1600 Å. But its identification is not definite. Shorter than around 1170 Å, three H_2 Lyman P1 lines of the (6, v'') bands have been detected in Comet LINEAR with FUSE (Fig. 4.6). These lines are normally not excited but arises due to accidental coincidence of the wavelength of solar Lyman β line with the wavelength P1 line of ($B\ ^1\Sigma_u^+ - X\ ^1\Sigma_g^+$) (6, 0) band. The derived column density of H_2 of $(3.0 \pm 0.6) \times 10^{13}/\text{cm}^2$ is found to be consistent with the H_2O dissociation models. i.e. $H_2O \rightarrow H_2 + O(^1 D)$. It is possible that some of it could be produced directly from the nucleus or by solar wind sputtering of dirty ice grains.

6.2.3. CN , C_2 , C_3 , NH

It is easier to study the spectral lines of the molecules like C_2 , CN , etc in comets using the standard techniques as their lines lie in the visual region. Generally filters are used which can isolate their emission bands. It is also possible to get a homogeneous set of data on many comets covering a large range of heliocentric distances which are of prime importance for investigating the possible physical correlations like the composition variations or the similarities among the comets of various types.

The method based on Eq. (6.31) is particularly suitable for the study of molecules like C_2 , CN , etc., as the total flux of a band or a band sequence in a certain field of view can easily be measured using the standard methods. The total number of the molecules can then be calculated from Eq. (6.31) as the constant can be evaluated using the spectroscopic data for the molecules of interest. The production rate can be calculated from Eq. (6.21a) from molecular column densities knowing the scale length of the two species and for an assumed outflow velocity, $\sim 1 \text{ km/sec}$. The production rates can easily be scaled for any other value of the outflow velocity. The generally used scale lengths for some of the molecules are given in Table 6.3. The results for the heliocentric variation of the production rates of C_2 , CN and C_3 for Comet Bradfield show a dependence as $r^{-3.2}$ compared to $r^{-1.7 \pm 0.3}$ for CN observed for Comet West. For the dusty

Comet Stephán-Oterma, the production rate of CN and C₂ varied approximately as $r^{-4.2 \pm 0.3}$ and $r^{-5.6 \pm 0.4}$ respectively. Therefore the heliocentric variation of the production rate of molecules vary among comets.

Table 6.3 Scale length of molecules at 1 AU.

Molecule	Parent(km)	Daughter(km)	Daughter life time (sec)
OH(0,0)	2.4×10^4	1.6×10^5	1.6×10^5
NH(0,0)	5.0×10^4	1.5×10^5	1.5×10^5
CN($\Delta v = 0$)	1.3×10^4	2.1×10^5	2.1×10^5
C ₃ ($\lambda 4050A$)	2.8×10^3	2.7×10^5	2.7×10^4
C ₂ ($\Delta v = 0$)	2.2×10^4	6.6×10^4	6.6×10^4

Schleicher, D.G. and Farnham, T.L. 2005, In *Comets II*, eds. M.C. Festou, H.U. Keller and H.A. Weaver, Univ. Arizona Press, Tucson, p. 449.

Several studies have been carried out in a systematic manner on a large number of comets by various groups. One such study contains 85 comets. A statistical study of the variation of the production rates of several molecules has been studied.

Comet Halley was observed extensively during its apparition in 1985-86. Therefore extensive good quality data exists on this comet covering a wide range of heliocentric distances, before and after perihelion passage. The results for the heliocentric variation of the production rates of several molecules is shown in Fig. 6.6. The dependence of production rate with heliocentric distance for the molecules C₂, C₃ and CN are quite similar. The slope of NH is also quite similar to those of carbon bearing species. Another feature of Fig. 6.6 is the presence of asymmetry about perihelion in the production rates of these species.

The curve of OH varies gradually with heliocentric distance and also has slight asymmetry about perihelion. The possible difference in the variation in the production rates with heliocentric distance between the minor species and water, the major constituent, has also been seen in several other comets. This appears to indicate decoupling of carbon-bearing species from that of water.

It is of interest to look at the relative abundances of the species among comets. The average relative molecular production rates of several species for Comet Halley is given in Table 6.4. The mean values and the range

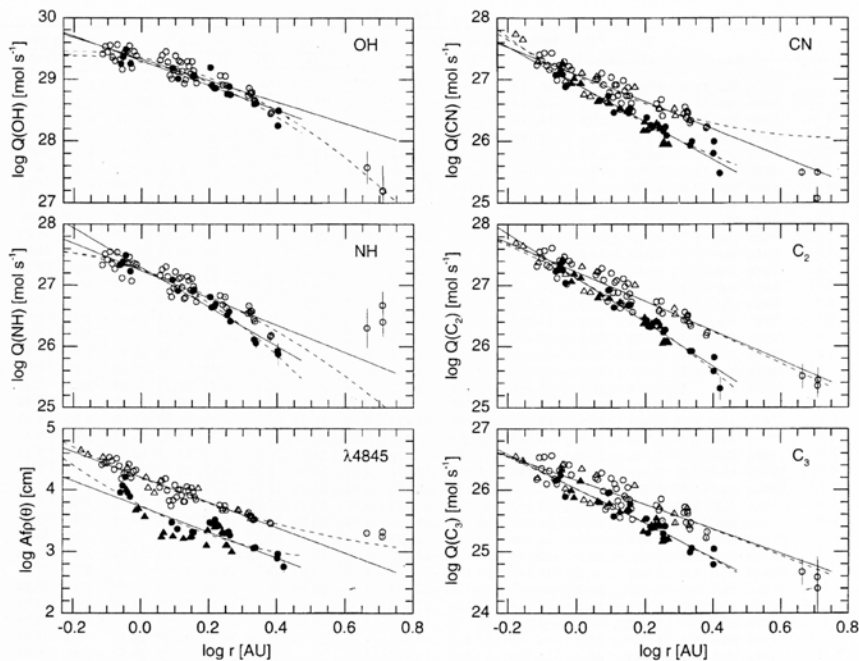


Fig. 6.6 Observed production rates of molecules OH, NH, CN, C₂ and C₃ and A(θ) $f\rho$ plotted as a function of the heliocentric distance for Comet Halley. Filled symbols refer to preperihelion observations while open symbols refer to postperihelion observations. Solid lines and dotted curves are for linear and quadratic fit to the data. (Schleicher, D.G., Millis, R.L. and Birch, P.V. 1998. *Icarus*, **132**, 397).

among all the comets studied in a homogeneous group of 85 comets is also given in Table 6.4. The observed ratios for Comet Halley fall within the typical range of values.

Observations for Comet Borrelly are available over several apparitions. The derived gas production rates of carbon-bearing molecules are larger before perihelion compared to that after perihelion for the same distance. The dependence of production rate with heliocentric distance is similar for CN, C₂ and C₃ (~ -8.1) while OH has a dependence ~ -8.9 . The values are quite similar over different apparitions. The relative abundances of the species for some comets is given in Table 6.4. There are several other comets which have either strong asymmetric or steep heliocentric production rate

Table 6.4 Abundance ratios in comets.

Species	Wild2 ^e	Halley ^b	Borrelly ^d	Wirten ^c	Mean ^a	Range ^a
NH/OH	-2.35 ± .34	-1.86	-2.28±.34	-2.36±.03	-2.37±.23	-2.77 to -1.80
CN/OH	-2.60±.14	-2.32	-2.62±.09	-2.50±.12	-2.50±.18	-2.83 to -2.17
C ₂ /OH	-2.97±.23	-2.21	-2.91±.12	-2.49±.12	-2.44±.20	-2.90 to -2.10
C ₃ /OH	-3.40±.20	-3.20	-3.55±.19	-3.49±.12	-3.59±.27	-4.26 to -3.09
UV Cont.	-25.53±.32		-25.53±.31			
Blue Cont.	-25.40±.13		-25.53±.36			
Green Cont.	-25.28±.24	-25.0	-25.40±.31			
C ₂ /CN		+0.11			+0.06±.0	-0.09 to +.29

Continuum is in $A(\theta)f\rho/Q(OH)$.

- (a) A' Hearn, M.F. *et al.* 1995. *Icarus*, **118**, 223.
- (b) Schleicher, D.G., Millis, R.L. and Birch, P.V. 1998. *Icarus*, **132**, 397.
- (c) Farnam, T.L. and Schleicher, D.G. 1998. *Astron. Astrophys.*, **335**, L50.
- (d) Schleicher, D.G., Woodney, L.M. and Mills, R.L. 2003. *Icarus*, **162**, 415.
- (e) Farnam, J.L. and Schleicher, D.G. 2005. *Icarus*, **173**, 533.

dependence such as, Arend Rigaux, Charyumov - Gerasimenko, Giacobini - Zinner, Kopff and Tempel 2. There are also some comets in which the behaviour of production rates of species remain roughly the same with different apparitions and in other comets it changes from one apparition to another. So there is a wide variation among comets.

On the other hand, Comet Wild 2 shows no asymmetry in their production rates between pre - and post perihelion passages and heliocentric distance. This indicates that C₂/CN production rate remained the same with apparition. So Comet Wild's composition remained constant over time and heliocentric distance.

The different properties seen from comets such as asymmetry in the gas production around perihelion and its variation with heliocentric distance etc. could arise due to seasonal effect of sources from a complex rotating comet nuclei which depends upon pole orientation, its stability, direction of rotation etc.

CN from dust

The detection of CN jets for the first time in Comet Halley indicated the presence of an extended source of CN arising from the grains. This conclusion is based on the fact that the radical CN profiles should be peaked at some distance from the nucleus in contrast to the parent molecule which should be peaked at or near the nucleus. This is similar to the extended source of CO and H₂CO observed from Comet Halley. The statistical study

of 85 comets showed a good correlation between dust to gas ratio with CN to gas ratio in several comets. It also indicated that comets with high dust showed a better correlation supporting the suggestion that dust could be the dominant source of CN in dusty comets. The observed production rate also indicated that this effect is quite weak for C₂ and C₃ and hence their contribution from grains must be small. The variation of dust production rate with CN production rate shows a good correlation between the two indicating that CN originates largely from volatile grains in the coma.

The typical production rates at 1AU for CN, C₂, H, OH and H₂O expressed in the unit of Q(H₂O)=1 are roughly the following:

$$\begin{aligned}Q(\text{H}_2\text{O}) &\approx Q(\text{OH}) \approx 1; \\Q(\text{H}) &\approx 2; \\Q(\text{C}_2), Q(\text{CN}) &\approx 0.01\end{aligned}$$

These values indicate that the production rates of C₂ and CN and other species seen in the visual spectral region are less by a factor of about 100 or so compared to that of H₂O or H. Thus, even though the lines of C₂, CN, etc., dominate the visual spectral region, they are only minor constituents of the cometary material. Therefore, the total amount of gas ejected from the nucleus can be represented to a very good approximation by the production rate of H₂O.

6.2.4. CH, NH₂

The column density of CH for the Comet Kohoutek at $r = 0.5$ AU is about $4 \times 10^{10}/\text{cm}^2$ averaged over 5×10^4 km. Similarly the column density of NH₂ at $r=1$ AU is about $6 \times 10^{10}/\text{cm}^2$ which is the average value over 3×10^4 km. These two molecules have also been observed in the Comet West for the heliocentric distances from 0.60 to 1.58 AU and only the relative values with respect to C₂ are known. The mean relative value of CH and NH₂ with respect to C₂ integrated over the whole coma is determined to be 0.013 ± 0.003 and 0.030 ± 0.013 respectively for distances $r \lesssim 1$ AU. These values show that the abundance of CH is approximately 1 to 2% of C₂ and that of NH₂ about 3% of C₂. The derived production rate of CH and NH₂ for Comet Halley at $r = 0.89$ AU is $(4.1 \pm 1.2) \times 10^{27}/\text{sec}$ and $(1.6 \pm 0.3) \times 10^{27}/\text{sec}$ respectively. This gives a ratio for the production rate of CH and NH₂ with respect to H₂O of about 0.007 and 0.003 respectively.

6.2.5. CO, CO₂

CO

The ultraviolet observations made on the Comet West at the heliocentric distance of 0.385 AU showed the strong bands of (A-X) transitions (near 1500 Å) of the CO molecule. The deduced production rate of CO from this observation based on Eq. (6.4) with $\tau(\text{at 1 AU}) = 1.4 \times 10^6$ sec comes out to be

$$Q(\text{CO}) = 2.6 \times 10^{29} / \text{sec}.$$

Since then the above bands of CO has been seen from all bright comets observed with IUE, HST etc.

The derived production rate of CO relative to H₂O in Comet West was around 0.3 and in Comet Bradfield the ratio was about 0.02. Comet Levy gave a ratio of 0.11 ± 0.02 . Comet Halley gave a ratio of ≈ 0.17 . For several comets belonging to Oort cloud comets, the total abundance of CO varied from 1% to 24% relative to water.

Extended source of CO

The presence of an extended source of CO in Comet Halley came from the *in situ* observations carried out with Neutral Mass Spectrometer (NMS) on board the Giotto spacecraft. This result came from a comparison of the observed distribution of molecules of $m/q = 28(\text{CO})$ with $m/q = 18(\text{H}_2\text{O})$. The observed radial density distribution of H₂O and CO derived from NMS data is shown in Fig. 6.7. The two molecules show entirely different variations. The linear decrease of H₂O is due to the photo-destruction of H₂O. For CO, the initial linear increase is due to the extended source of CO which is likely to arise from CHON dust particles containing H₂CO which photodissociates. The nearly constant variation at large distances is due to the long life of CO against photodestruction.

CO₂

The presence of CO₂⁺ ion in comets implied the presence of CO₂. But CO₂ was observed for the first time in Comet Halley from the infrared spectrometer on board the Vega spacecraft which detected ν_3 fundamental band at $4.26 \mu\text{m}$. Although the band is strong, it cannot be observed from ground due to the absorption of CO₂ in the earth's atmosphere. Subsequently it has been observed in several other comets such as Hale-Bopp, Hartley etc.

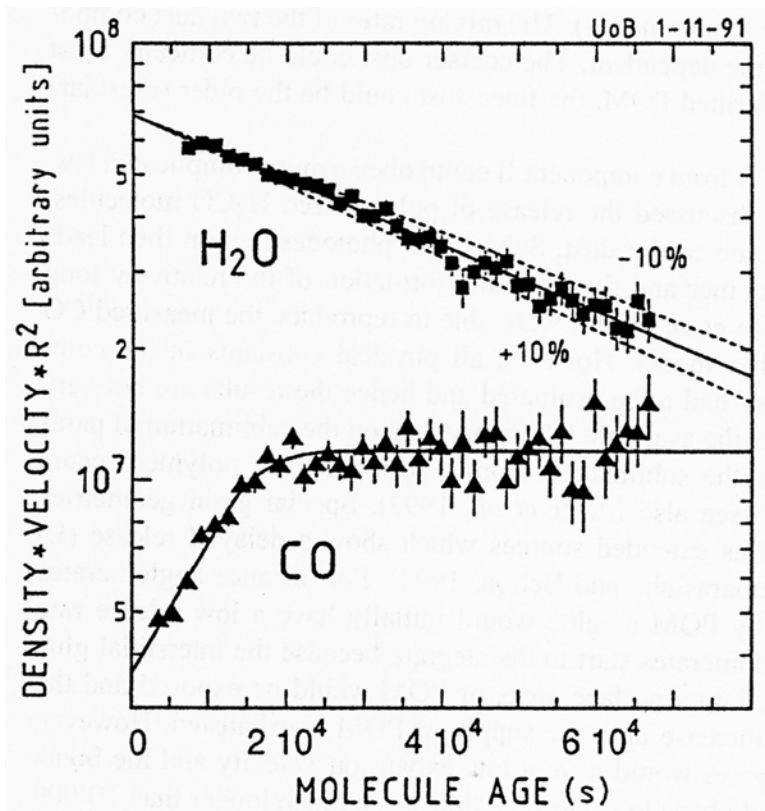


Fig. 6.7 Radical density profiles for H_2O and CO derived from gas mass spectra with NMS on Giotto spacecraft for Comet Halley. The solid line corresponds to a least square fit to the data and corresponds to a photodestruction rate of $k_{\text{H}_2\text{O}} \approx 1.7 \times 10^{-5} \text{s}^{-1}$. The dashed lines refer to photodestruction rate for $\pm 10\%$. (Eberhardt, P. 1999. *Space Sci. Rev.*, **90**, 45).

by ISO. The presence of mass peak at 44 in the Giotto NMS mass spectra also showed the presence of CO_2 in Comet Halley. The derived abundance ratio of $\text{CO}_2/\text{H}_2\text{O}$ is around 3–4% for Comet Halley and 8–10% for Comet Hartley 2. The derived production ratio of CO_2 to water in comets varies around 3–10%. However for Comet Hale-Bopp the estimated production ratio of CO_2 to water at $r > 2.9$ AU was $> 20\%$. Therefore CO_2 is also a trace constituent of the nucleus.

Prompt emission

The Cameron band system of CO seen in comets arises between triplet and singlet electronic states ($a^3\Pi - X^1\Sigma$). These transitions are forbidden dipole ones. Therefore they cannot be excited by resonance fluorescence process. They are most likely to arise from the formation of CO molecules in the $a^3\Pi$ state during the photodissociation of CO_2 . The molecules in the $a^3\Pi$ state then decay to the ground state in a time scale of $\sim 7 \times 10^{-3}$ sec producing prompt emission lines. Therefore the Cameron band emission is directly proportional to the production rate of CO_2 and can be used to trace the abundance of CO_2 .

Two dominant mechanisms for the observed Cameron emission are the photodissociation of CO_2 by solar radiation and the electron impact excitation of CO. The two processes can be distinguished observationally as the rotational temperature of CO molecules produced in the photodissociation of CO_2 is around five times larger than produced by electron impact excitation.

6.2.6. CS, S_2

The other minor species whose production rates are of interest are the sulphur containing molecules, CS and S_2 . The (0, 0) band of CS at 2576 Å has been observed in many comets mainly with the IUE satellite. It has also been observed in the radio wavelength region. If the observed CS comes from CS_2 , then $\text{CS}_2/\text{H}_2\text{O} \approx \text{CS}/\text{H}_2\text{O} \approx 0.4\%$. Therefore, CS_2 is also a trace constituent of the nucleus.

The molecule S_2 was discovered in IRAS-Araki-Alcock from the observations of several bands of (B-X) system near 2900 Å. The molecule S_2 has a short lifetime \sim few hundred seconds at 1 AU. So it is present very close to the nucleus. The derived production rate of S_2 for the Comet IRAS-Araki-Alcock observed at $\Delta = 0.032$ AU is about $2 \times 10^{25}/\text{sec}$. It has also been seen in several other comets. The derived abundance ratio of $S_2/\text{H}_2\text{O} \sim 0.001$.

6.2.7. *Ions*

The plasma tail is dominated by molecular ions of various kinds. The most dominant among them are the ions CO^+ and H_2O^+ whose lines lie in the near blue and in the visible regions respectively. The early estimates for the column densities of CH^+ and CO^+ ions were made based on the

observations of Comets Kohoutek and Bradfield for a projected distance of about 10^4 km from the nucleus and for $r = 0.5$ AU. The deduced column density ($/\text{cm}^2$) of CH^+ , and CO^+ for Comet Kohoutek are of the order of $10^{10.9 \pm 1.1}$ and $10^{12.6 \pm 0.9}$ respectively.

H_2O^+ was first identified in Comet Kohoutek in 1974. An analysis of the surface brightness profiles of H_2O^+ in Comet Bennett and CO^+ in Comet West has been investigated. The calculated production rate of CO^+ for $r = 0.440$ and 0.842 AU is $Q(\text{CO}^+) = 2.4 \times 10^{28}/\text{sec}$ and $0.22 \times 10^{28}/\text{sec}$ respectively with the heliocentric distance variation of $r^{-4.6 \pm 1.0}$. The estimated production rate of H_2O^+ for Comet Bennett is about $Q(\text{H}_2\text{O}^+) = 2 \times 10^{26}/\text{sec}$ at $r = 0.841$ AU. This value may be compared with the early estimates of $Q(\text{H}_2\text{O}^+) = 3.7 \times 10^{24}/\text{sec}$ for Comet Kohoutek at $r = 0.9$ AU and $Q(\text{H}_2\text{O}^+) = 2 \times 10^{23}/\text{sec}$ for Comet Bradfield at $r = 0.6$ AU.

The production rate of H_2O^+ can also be determined from the Doppler shifted emission lines of H_2O^+ 6159 Å and 6147 Å emission doublets in the (0, 8, 0) band based on the Fabry Perot technique. The observed ratio of $Q(\text{H}_2\text{O}^+)/Q(\text{H}_2\text{O})$ for Comet Halley is 1.2×10^{-3} and for Comet Austin is 2.6×10^{-3} . The model based on magnetohydrodynamics and chemistry of cometary coma indicate that for comets, upto 11% of water molecules are finally ionized.



The reported identification of $(\text{B}^2\Sigma_u^+ - \text{X}^2\Sigma_g^+)$ system of N_2^+ ion near 3910 Å has been existing in the literature for the last few decades. The presence of this band in Comet Halley was also reported in 1986. However recent observation based on high spectral resolution and high signal to noise ratio of several comets such as de Vico, Hale-Bopp and Ikeya-Zhang does not seem to show the lines of N_2^+ at 3910 Å. These observations have cast doubt on the earlier detection of N_2^+ in comets, which was mostly based on low-resolution spectra wherein the blending problem is severe arising out of molecules CO^+ , CO_2^+ , CH and CH^+ . The derived upper limit from these observations for $\text{N}_2^+/\text{CO}^+ \lesssim 10^{-5} - 10^{-4}$ which is a very low value. The above study has great implication with regard to the presence of molecule N_2 in comets.

The molecule N_2 is the least reactive among all species containing nitrogen. It is also believed to be the dominant equilibrium species in the early solar nebula. Unfortunately, it is the most difficult molecule to make

any observation. It is difficult to observe from the ground because of the presence of N₂ in the earth's atmosphere. The interpretation of the Giotto Mass Spectral data is also difficult as N₂ and CO have the same mass, 28. Therefore the presence of N₂ in comets is inferred indirectly from the presence of N₂⁺ in comets. The method that is generally used to study N₂ in cometary ices is through the study of its ion (N₂⁺(B - X)(0, 0) band at 3910 Å). Hence N₂⁺ has been used as a proxy for N₂. However, non detection of N₂⁺ in some of the recent comets as discussed earlier and with an upper limit to the abundance ratio of N₂/CO $\lesssim 10^{-5} - 10^{-4}$ has raised several important issues. Some of them are whether comets have varying amount of N₂ or did the depletion took place at a later time or is it related to the place of formation in the solar nebula. May be the general view that neutral N₂ and CO should have been present in the early solar nebula is questionable.

6.2.8. Complex molecules

Expected line intensities

The observations in the radio frequency region referring to source intensity are generally expressed in terms of equivalent brightness temperature, T_B. This is related to the line optical depth τ through the relation, which can be derived from the radiative transfer, as

$$T_B = (1 - e^{-\tau}) \frac{h\nu}{k} \left[\frac{1}{e^{h\nu/kT_{\text{ex}}} - 1} - \frac{1}{e^{h\nu/kT_{\text{bg}}} - 1} \right]. \quad (6.44)$$

Here T_{ex} is the excitation temperature, T_{bg} is the background brightness temperature which can be taken to be 2.7 K and ν is the line frequency. The optical depth at the line centre is given by

$$\tau = \frac{c^2}{8\pi\nu^2} \frac{2J+3}{2J+1} A_{J+1 \rightarrow J} \frac{\langle N_J \rangle}{\Delta\nu} [1 - \exp(-h\nu/kT_{\text{ex}})] \quad (6.45)$$

where $\Delta\nu$ is the line width in frequency units and $\langle N_J \rangle$ is the mean volume density within the observed field in the rotational state J. For most of the molecules, the lines are optically thin and therefore $(1 - e^{-\tau}) \approx \tau$ in Eq. (6.44). The average excitation temperature T_{ex} can be calculated from the

relation

$$\frac{\langle N_{J+1} \rangle}{\langle N_J \rangle} = \frac{2J+3}{2J+1} \exp\left(-\frac{h\nu}{kT_{\text{ex}}}\right). \quad (6.46)$$

In order to proceed ahead, the excitation mechanism of the molecules in a cometary atmosphere is required. To model the radio emission from a molecule, it is necessary to consider the excitation scheme of the molecules by taking into account the rotational, the vibrational and the electronic states of the molecule. However, for most of the molecules in the coma, the main excitation process is the pumping of the fundamental bands of vibration by the solar infrared radiation field and the thermal excitation by collisions in the inner coma. Such species do not have a significant electronic excitation because they are generally predissociative and also they lead to destruction rather than fluorescence. For the case of the stable CO molecule the excitation rate of the ground state $X^1\Sigma^+$ vibrational levels by solar infrared radiation field at 1 AU is about 2.6×10^{-4} / sec for $v'' = 0$ to 1 and 3×10^{-6} / sec for $v'' = 0$ to 2. The rate is $\sim 10^{-6}$ to 10^{-9} / sec for excitation from the ground level to higher electronic states. Hence, the excitation rates are too low to populate electronic states as well as $v'' = 1$ level. Therefore, it is a very good approximation to consider the excitation starting from the $v'' = 0$ ground vibrational state. Rotational excitation by solar radiation is also negligible due to lesser fluxes at the wavelength of rotational transitions.

To a very good approximation, the radiative excitation is dominated by one or two vibrational bands. The balance between the infrared excitation and spontaneous decay completely determines the rotational distribution at fluorescence equilibrium. The fluorescence equilibrium can be evaluated without much difficulty as it depends on the molecular constants and the solar radiation field. However, the collisional excitation due to collisions with H₂O molecules is more complicated. One assumes spherical symmetry and a reasonable value for collision cross-section between the molecule and H₂O and the coma temperature and velocity distribution derived from hydrodynamic models. The molecular mean column densities can then be derived by volume integration within the instrument beam. The excitation temperature, T_{ex} can therefore be estimated from Eq. (6.46). The expected rotational line intensities can be calculated for reasonable values of the relevant parameters in Eq. (6.44).

As an example the relative population distribution of linear molecules CO and HCN is shown in Fig. 6.8. For such molecules, the rotational

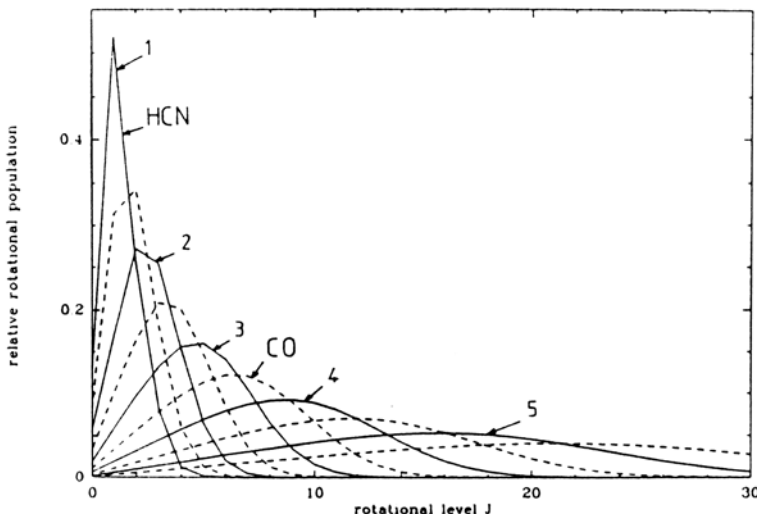


Fig. 6.8 The rotational population distribution under resonance fluorescence equilibrium for CO and HCN is shown as a function of rotational quantum number and for logarithmic ratio of the infrared excitation rate to the rate of rotational de-excitation from the $J = 1$ level (Bockelee-Movany, D. and Crovisier, J. 1985. *Astr. Ap.*, **151**, 90).

population distribution is determined by the ratio of total infrared excitation rate to the spontaneous decay rate of the rotational levels. Therefore, the molecules with large rotational Einstein A coefficients like that of HCN molecule, will have population concentrated mostly in the lowest rotational levels as compared to molecules like CO and HC₃N with small rotational Einstein A values which have populations over a wider range of rotational levels.

Observed molecules

As mentioned earlier, the line intensities in the radio region are generally expressed in terms of equivalent brightness temperature T_B . The brightness temperature is related to the line flux F_{ul} (upper level u, lower level l) through Rayleigh-Jeans relation (i.e. $h\nu \lesssim kT$) of the Planck function. The integrated line area over the velocity is related to the column density through the relation

$$\int T_B dv = \frac{hc^3 A_{ul}}{8\pi k \nu_{ul}^2} \langle N_u \rangle$$

where N_u is the column density in the upper level u and other symbols have their usual meanings. In general, time-dependent excitation models

are required to derive the population distribution in the upper states for calculating the total column density $\langle N \rangle$. Alternately from the observed intensities of several rotational lines, it is possible to estimate the rotational temperature which can then be used for the calculation of population distribution in the upper states. Knowing the total column density of molecules in the coma, the production rate of the molecule can be calculated. This is then used for estimating the relative abundances of molecules in the nucleus.

The number of known molecules in comets before Comet Halley's apparition in 1985-86 were limited in extent. However the concentrated effort made on Comet Halley led to the detection of many new molecules. Subsequently, large number of molecules of various kinds and complexities has been detected in comets. Several lines arising out of isotopes have also been detected. A typical observed spectrum in the radio region is shown in Fig. 4.10. From such observations the production rate of molecules can be derived. A wide variation in the observed abundance of parent species in the coma of comets have been seen. In addition to the detected molecules upper limits have been determined for many other molecules.

Several molecules belonging to CHO group, such as Methanol (CH_3OH), Formaldehyde (H_2CO), Formic acid (HCOOH), Methyl Formate (HCOOCH_3), Acetaldehyde(CH_3CHO) and Ethyl Glycol ($\text{HOCH}_2\text{CH}_2\text{OH}$) have been seen. Surprisingly Ethyl Glycol is the most abundant organic molecule in spite of its complexity and its identification is based on several lines present in the millimetre spectra of Comet Hale-Bopp. The hydrocarbons such as, Methane (CH_4), Acetylene(C_2H_2) and Ethane (C_2H_6) are present. Several sulphur bearing molecules like S_2 , H_2S , OCS , H_2CS etc are present. Some of the complex molecules containing nitrogen are Methyl Cyanide (HC_3N), Isocyanic acid (HNCO) and Formic acid (NH_2CHO).

Comet Tempel 1 showed the presence of PAHs.

The significant result that comes out of abundance studies of molecules is the presence of chemical diversity among comets belonging to Oort cloud and Jupiter-family of comets. For example, the abundance of CO varies by a factor of around 40. The abundance of hydrocarbon CH_4 varies by a factor of about 10, while that of C_2H_6 shows less variation ~ 0.4 to 0.7% . The HCN abundance seems to peak around 0.1% . HNC, the isomeric form of HCN was first detected ($J(4-3)$ line at 363 GHz) in Comet Hyakutake and subsequently in other comets. It is an unstable molecule under laboratory conditions. The ratio of HNC/HCN in Comet Hale-Bopp is found to lie

in the range of 0.03 to 0.15. The abundance of H₂S, H₂CO and CH₃OH show large variations. In general, the abundance of most of the molecules < 10⁻²–10⁻³ relative to water. Also the abundance of the molecules seems to decrease with an increase in their complexity.

The observed diversity in the chemical composition among comets could arise depending upon the local temperature and the nebular composition in the region of their formation. The variation in chemical composition can also arise if there was significant mixing of the nebular material. Therefore it is not surprising that there exists a wide variation in the chemical composition among comets.

The heliocentric variation of the production rate of molecules is of great interest as it is directly related to the cometary ices, sublimation process etc. However, monitoring along the cometary orbit is possible only for bright comets. This was possible in the case of Comets Halley, Hyakutake, Hale–Bopp etc. Since Comet Hale–Bopp was a bright comet and was discovered when it was at 7 AU, it was possible to study the evolution of production rate of a large number of molecules over a wide range of heliocentric distances. In Comet Hale–Bopp, CO was detected in the radio region up to heliocentric distance \sim 14 AU. CO is the main escaping gas at large heliocentric distances as its sublimation temperature is very low \sim 25 K. The results derived from radio observations of molecules on Comet Hale–Bopp, show that the chemical composition of the coma changed with heliocentric distance. In addition, the heliocentric variation of the production rate of molecules is different for different molecules.

Ethylene glycol is a known interstellar molecule and is observed towards Sgr B2. The abundance ratio of ethylene glycol to CH₃OH \sim 0.1 in comets whereas it is \sim 0.001 towards Sgr B2.

Extended source of molecules

As discussed earlier, the results based on measurements carried out with Neutral Mass Spectrometer on Giotto spacecraft of Comet Halley showed different density distributions for the molecules H₂O and CO in the coma. The H₂O distribution showed a R⁻² variation consistent with simple radial expansion from the nucleus, like a parent molecule, while the distribution of CO required an additional extended source. Therefore the basic idea to look for an extended source of any molecule is to examine the observed radial distribution of the molecule in the cometary coma. For parent molecule coming from or near the nucleus the radial distribution of the molecule should fall steeply with radial distance, while for an extended source, the

variation initially is steeper and then flattens out. From the observed radial distribution of molecules in the cometary coma of Comet Hale Bopp, the extended source of H₂CO, OCS and CO has been inferred. In contrast, the observed column density profiles for the molecules H₂O, C₂H₆, CH₄ and HCN were found to be consistent with their release directly from the nucleus.

6.2.9. O, C, N, S

Oxygen

The abundances or the production rates of oxygen atoms can be calculated from the observation of red doublet lines of oxygen atom occurring at 6300 and 6364 Å. Since the line at 6300 Å is quite strong in comets, it has been studied extensively for deriving the production rate of oxygen atoms. Since these lines arise due to photodissociation of H₂O, OH and CO molecules which populate the ¹D state (Fig. 4.11), the column densities of the parent oxygen atoms can be easily obtained. The observed intensity of the line is therefore given by

$$I \propto \frac{\alpha \beta N}{\tau_P} \quad (6.47)$$

where α and β are the yields for the particular state for dissociation and branching ratio respectively. N is the column density of the parents and τ_P is the dissociation lifetime of the parent. The oxygen ¹D production rate of the comet can be calculated using the observed fluxes of the oxygen line that has been corrected for various blending and other effects (F_{corr}). The photon rate is given by

$$P = \frac{F_{\text{corr}} 4\pi \Delta^2}{(h\nu)_{6300}}. \quad (6.48)$$

Here Δ is the comet-earth distance. If the lifetime of the ¹D state is τ sec for the 6300 Å line (~ 100 sec), multiplying P by the lifetime will give the total number of oxygen atoms within a cylindrical column of radius ρ , $M(\rho)$, centred on the nucleus, i.e.,

$$M(\rho) = \frac{F_{\text{corr}} 4\pi \Delta^2 \tau}{(h\nu)_{6300}} \text{ atoms.} \quad (6.49)$$

The production rate is generally calculated using the Haser's model with H₂O as the parent molecule and O as the daughter-product with corresponding scale lengths $l_{\text{H}_2\text{O}}$ and l_0 respectively.

Fabry-Perot observations:

The main difficulty in the measurement of neutral oxygen from 6300 Å emission is the contamination due to NH₂ emission lines. High resolution spectroscopy allows the separation of spectrally NH₂ lines from 6300 Å line thereby providing an uncontaminated 6300 Å line for quantitative studies. High resolution observations also help to avoid the airglow effects. The Fabry-Perot spectrometer can be used for this purpose. An example of the scan of 6300 Å line is shown in Fig. 6.9. For the calculation of the produc-

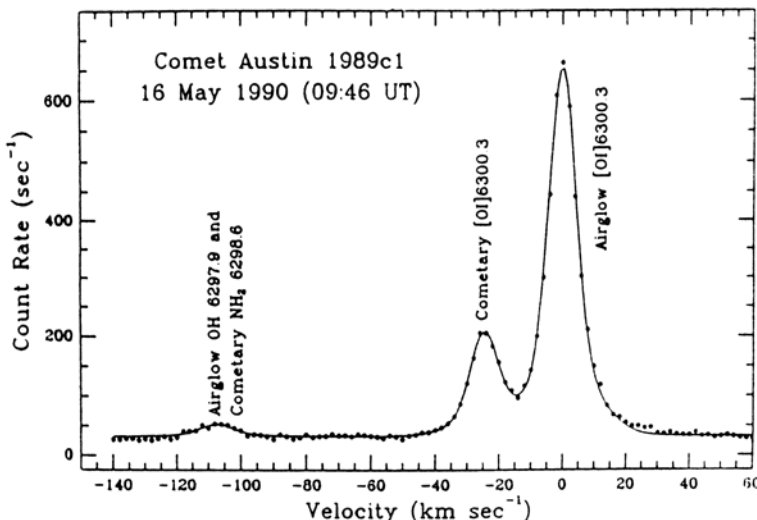
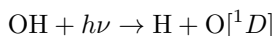
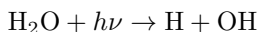
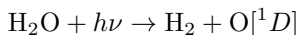
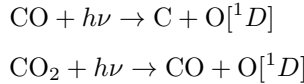


Fig. 6.9 The observation of the cometary [OI] 6300 Å line. The zero point for the velocity scale is set at the position of the terrestrial airglow line. The solid curve represents a Gaussian least square fit to the data (Schultz, D., Li, G.S.H., Scherb, F. and Roesier, F.L. 1992. *Icarus* **96**, 190).

tion rate of O[¹D] atoms, it is necessary to know the photodissociation of molecules responsible for the production of O[¹D] atoms. O[¹D] may be produced by the dissociation of H₂O and OH through the reactions



with respective branching ratios $BR1, BR2$ and $BR3$. $O[{}^1D]$ can also be produced from the reaction



with branching ratios $BR4$ and $BR5$. However, as CO and CO_2 are minor constituents of comets and their photodissociation lifetimes are much larger than those of H_2O and OH, the contribution from these sources to 6300\AA emission is relatively small within the field of view of observations. Therefore, the contribution arising out of CO and CO_2 is generally neglected. The intensity of 6300\AA emission at the projected distance ρ from the nucleus is given by

$$I_{6300}(\rho) = \frac{N_{\text{H}_2\text{O}}(\rho)}{4\pi\tau_1} + \frac{N_{\text{OH}}(\rho)}{4\pi\tau_3}. \quad (6.50)$$

Here τ_1 and τ_3 are the photodissociation lifetime of H_2O and OH leading to $O[{}^1D]$ channels. $N_{\text{H}_2\text{O}}$ and N_{OH} are the column densities of H_2O and OH respectively at ρ . Using azimuthally symmetric parent-daughter Haser model for representing $N_{\text{H}_2\text{O}}$ and N_{OH} , the intensity $I_{6300}(\rho)$ can be written as

$$I_{6300}(\rho) \propto \frac{1}{\rho} \int_0^{\pi/2} \exp\left(\frac{-\rho \sec \theta}{l_1}\right) d\theta$$

$$+ \frac{BR_2 \cdot BR_3}{BR_1 \cdot \rho} \left[\frac{l_1}{l_1 - l_2} \right] \int_0^{\pi/2} \left\{ \exp\left(\frac{-\rho \sec \theta}{l_1}\right) - \exp\left(\frac{\rho \sec \theta}{l_2}\right) \right\} d\theta. \quad (6.51)$$

Here l_1 and l_2 are the Haser parent-daughter photodissociative scale length for the $(\text{H}_2\text{O}, \text{H})$ and (OH, H) respectively. By integrating Eq. (6.51) with respect to ρ , it is possible to calculate the ratio of the total flux in the 6300\AA line to the flux within the field of view of the observation. This ratio is given by

$$AC = \frac{\int_0^\alpha I_{6300}(\rho) \rho d\rho}{\int_0^{\rho_1} I_{6300}(\rho) \rho d\rho} \quad (6.52)$$

where ρ_1 is the projected radius of the field of view of the observation. Hence AC can be calculated, based on the values of the parameters and theoretical branching ratios $BR1, BR2$ and $BR3$. The photodissociation

scale length can be derived from a comparison of Eq. (6.51) with several high spectral resolution images of 6300 Å emission. The production rate $Q(O^1D)$ can be derived from the relation

$$Q(O^1D) = \left(\frac{4}{3}\right)(4\pi\Delta^2\Omega I_{6300})AC. \quad (6.53)$$

Here Ω is the solid angle of the field of view, I_{6300} is the average intensity of the 6300 Å emission within the field of view (in photons /cm² / sec / ster). The factor (4/3) takes into account the fact that 1/4 of the O¹D atoms radiate to the ground state via 6364 Å channel.

To convert $Q(O^1D)$ to $Q(H_2O)$, the ratio of $Q(H_2O)/Q(O^1D)$ has to be known. This ratio can be determined from the photochemical branching ratios. It can also be determined by comparing the production of $Q(^1D)$ with the results of $Q(H_2O)$ derived from other observations. There is a variation in the derived ratios of $Q(^1D)$ to $Q(H_2O)$. The estimated factor for converting O[¹D] production rate to $Q(H_2O)$ from the branching ratios is given in Table 6.5.

Table 6.5 Branching ratios.

Reaction	Theoretical values
$H_2O + h\nu \rightarrow H_2 + O(^1D)$	0.044, 0.054
$H_2O + h\nu \rightarrow H + OH$	0.840, 0.905
$OH + h\nu \rightarrow H + O(^1D)$	0.103

Schultz, D., Li, G.S.H., Scherb, F. and Roesler, F. L. 1993. *Icarus* **101**, 95 and is for solar minimum conditions. The individual references to the above values are given in the paper.

It is around 11.7 for pre-perihelion observations and 13.7 for post-perihelion observations for Comet Halley. The conversion factor for pre-and post-perihelion observations are different as the branching ratio $BR3$ depends upon the heliocentric velocity of OH. The resulting production rate of H₂O is compared with those derived from H α observations in Table 6.6, which shows a general agreement between the two determinations.

The [OI] 6300 Å emission line profile from the coma of Comet Halley was observed with Fabry - Perot during 1986. The observed profile is in good agreement with the calculated profile based on Monte Carlo Particle Trajectory Model. The derived water production rate is $(2.90 \pm 0.13) \times$

10^{30} mol/sec. Fabry - Perot observations of [OI] 6300 Å emission carried out on Comet Hyakutake was also found to be in agreement with model calculated line profile.

Table 6.6 H₂O Production rate for Comet Halley from H α and [OI] 6300 Å observations.

Date of observation	H ₂ O Production rate ($10^{29} s^{-1}$)	
	H α	[OI] 6300 Å
Dec 13, 1985	4.3 ± 0.5	4.42 ± 0.82
— 15, 1985	3.2 ± 0.4	3.71 ± 0.85
— 16, 1985	2.8 ± 0.3	3.22 ± 0.61
Jan 4, 1986	6.3 ± 0.8	7.65 ± 1.5
— 7, 1986	8.3 ± 0.9	9.49 ± 1.8
— 9, 1986	11.6 ± 1.5	12.1 ± 2.3
— 12, 1986	7.8 ± 0.9	11.8 ± 2.3
— 13, 1986	17.5 ± 2.0	18.5 ± 2.6

(Adapted from Smyth, W. H., Marconi, M L, Scherb, F. and Roesler, F. 1993. *Ap. J.* **413**, 756).

Green line of oxygen at 5577.3 Å

The forbidden line of oxygen arising out of the 1S level which lies at 5577.3 Å (1S - 1D) is highly blended with the Swan band sequence of C₂ corresponding to $\Delta v = -1$. The study of this line can also help in clarifying the problem of the parent molecule of oxygen atoms. The H₂O parent molecule model calculations have indicated the intensity of the green line to be weaker by a factor of 10 or so compared to that of the red line. Therefore, if the green line is detected, the intensity ratio of green to red line could help in this regard. One way to extract the 5577.3 Å line of oxygen based on low dispersion spectra is through the comparative spectral synthesis of $\Delta v = -1$ C₂ Swan band sequence. The calculated profile which is a superposition of all the rotational lines arising out of bands (0, 1) to (5, 6) and which has been corrected for the instrumental effect show a slight excess of flux at $\lambda \sim 5577$ Å compared to the expected flux that could be attributed to the contribution of the oxygen line of 5577 Å. These results indicate that the intensity of the oxygen line at 5577.3 Å should be roughly about 3 to 5% of the oxygen line at 6300 Å. A similar ratio was obtained from the measurements on Comet IRAS-Araki-Alcock wherein the line 5577.3 Å could be resolved. The line 5577.3 Å has also been

resolved in Comets Halley, Hyakutake and LINEAR (C/1999S4). Since C₂ is severely depleted in Comet LINEAR, 5577.3 Å line could be seen without any blending with C₂ band. These results are, therefore, consistent with H₂O being the parent molecule for excited oxygen atoms.

The ultraviolet lines occurring at 1304 Å have also been used to derive the production rates of oxygen atoms (Table 6.7). The intercombination doublet at 1356 Å of OI has also been seen in some comets. Since the g factor for this transition is too small, the excitation is likely to arise from electron impact.

Table 6.7 Comparison of column densities of some species in comets.

Comet	Date	$r(au)$	$\Delta(au)$	N(O) ($10^{13}/\text{cm}^2$)	N(C) ($10^{12}/\text{cm}^2$)	N(S) ($10^{12}/\text{cm}^2$)
Bradfield	16 Jan 1980	0.80	0.40	2.5	1.7	1.7
	31 Jan 1980	1.03	0.29	0.8	0.68	1.4
Encke	5 Nov 1980	0.81	0.32	0.40	0.27	0.59
	24 Oct 1980	1.01	0.29	—	—	—
Tuttle	7 Dec 1980	1.02	0.50	1.2	1.0	1.3

(a) Weaver, H.A., Feldman, P.D., Festou, M.C., A'Hearn, M.F. and Keller, H.U. 1981. *Icarus* **47**, 449.

Carbon

The brightness of the carbon line at 1657 Å arising out of the 3P state has been used to derive the column densities of carbon for several comets and are given in Table 6.7. The CI line at 1657 Å was strong in the spectra of Comet West. It could be accounted for from the dissociation of the CO molecule. However in Comet Bradfield carbon emission is quite strong inspite of CO being less abundant. This could indicate the presence of other sources.

The detection of the carbon line at 1931 Å arising from the metastable level 1D state is of particular interest. This is because the parent molecule should be able to explain the presence of carbon both in the 3P (1657 Å line) and 1D states.

There are several molecules which can give rise to carbon atoms such as CO and several other minor species such as CO₂ and so on. The *in*

situ measurements of Comet Halley showed that carbon is contained in CHON grains. Therefore, this is also source of carbon atoms. In fact, the inclusion of this carbon component from the grains to the observed component from the fluorescent lines has removed the problem of carbon deficiency in comets.

Nitrogen, Sulphur

It is not possible to make an estimate directly of the production rate of nitrogen as its resonance spectral line of 1200 Å has not been observed. Therefore, the estimates have to be made indirectly, based on the nitrogen bearing molecules like CN, NH, N₂⁺ etc., and they give a rough value for the ratio (N/O) ≈ 0.1 .

The lines of SI 1812 Å multiplet which was seen first in Comet West has been seen in all the comets. The observed brightness of this multiplet has been used to deduce the column densities for sulphur. The results for some comets are given in Table 6.7.

Table 6.8 gives a rough representation of the elemental abundances of H, C, N, O and S for comets.

Table 6.8 Average abundance ratios.

Ratios	Comets	Sun	CI chondrites
H/O	2.0	1175	0.17
C/O	0.40	0.43	0.10
N/O	0.09	0.13	0.007
S/O	0.03	0.02	0.07

Delsemme, A. H. 1991. In *Comets in the Post-Halley Era* eds. R. L. Newburn, Jr. et al. Kluwer Academic Publishers, Vol. 1, p. 377.

The table shows that the observed ratio of C/O in comets is similar to the solar value. However, the ratio H/O is very much smaller in comets compared to the solar value. This implies that hydrogen is very much depleted in comets. This in turn means that either the hydrogen has escaped from the system or it was not trapped at the time of formation. A plausible physical explanation could be that in the case of the sun it is the gravitational binding while in comets it is the chemical binding which is important. Hence, in the case of the Sun, gravity essentially prevents hy-

hydrogen from escaping, while in the case of comets only a small fraction of hydrogen can be bound in molecules. Therefore, most of the hydrogen as well as H₂ disappear due to their high volatility. On the other hand, the heavy elements like Na, Ca, Fe, Mn, etc are assumed to have sublimated out of the refractory grains and have relative abundances similar to the solar value (Fig. 5.19).

6.3. Analysis of Hydrogen Observations

6.3.1. *Analysis of Lyman α measurements*

The presence of a huge halo of hydrogen gas around comets was predicted by Biermann in 1968 based on the dissociation of the H₂O molecule. In general, the photon energy available for dissociation is much larger than the dissociation energy. Therefore, this excess energy is usually carried away by the dissociated products. For example, in the case of H₂O the excess energy gives a velocity ~ 17.8 km/sec to the hydrogen atom, and this is much larger than the gaseous outflow velocity which is of the order of 0.5 km/sec. Since the lifetime for the ionization of the molecule is $\sim 10^6$ sec, the observed extent of the size of the halo which is given by $v\tau$ is about 10^6 to 10^7 km. Based on this simple physical argument and with a hydrogen gas production rate of 10^{30} to 10^{31} molecule/sec, it was concluded that the comets should be bright in the Lyman α line. The ultraviolet observations made in Lyman α with OAO-2 on Comets Tago-Sato-Kosaka and Bennett confirmed the presence of the hydrogen halo extending up to about 10^6 to 10^7 km around the nucleus. This result was further confirmed through a series of rocket and satellite observations made on various other comets. In recent years, with the availability of better instruments and spatial resolution, it has been possible to get good and high quality isophotes of the Lyman α region. These high quality isophotes and line profile have shown that they extend farther in the direction away from the Sun compared to that in the direction toward the Sun. The isophotes also become more and more elongated in the antisolar direction as the comet goes nearer the Sun. These observations clearly show the effect of intense Lyman α radiation pressure effects. The high quality isophotes also show that the axis of the isophotes is not along the direction of the Sun-Comet line, but is inclined at an angle to this line. The theoretical models have to explain some of these observed effects.

In order to make a comparison with the observed isophotes, the emis-

sion of the hydrogen atoms has to be calculated. The collisions could be important in the inner coma region $< 10^4$ km for the gas production rate of about 10^{30} molecules/sec. However, the dissociation takes place at distances $> 10^5$ km and therefore the collisions are not important. For an optically thin case the emission is given by

$$B = gN \text{ (photons/cm}^2/\text{sec)} \quad (6.54)$$

where g is the emission rate factor and N is the column density of hydrogen atoms. Therefore, the calculation of emission intensities essentially depends upon N , which is model dependent.

To start with, one can assume an isotropic radial outflow without collisions from a point source. The above assumption is reasonable since the observed distribution of molecules is nearly spherically symmetric around the nucleus. This is borne out by the shape of the isophotes in the visible region. Therefore, the assumption of a point source with the radial outflow of material usually termed as the *Fountain model* is reasonable for the interpretation of the hydrogen coma. In this steady state model the hydrogen atoms are released at the rate of Q_H from the nucleus and are pushed away due to solar radiation pressure in the direction away from the Sun with a lifetime t_H .

The lifetime t_H for hydrogen atoms is the sum total of lifetimes due to photoionization (t_{ph}) and to charge exchange with protons (t_{pr}). The calculated photoionization lifetime at 1 AU is $t_{\text{ph}} = 1.4 \times 10^7$ sec. The lifetime for charge exchange with protons of flux $F_w \approx 2 \times 10^8$ proton/cm 2 /sec at 1 AU and for an effective cross-section $\sigma = 2 \times 10^{-15}$ cm 2 is equal to

$$t_{\text{pr}} = \frac{1}{\sigma F_w} = 2.5 \times 10^6 \text{ sec.}$$

Therefore, the total lifetime, t_H is given by

$$t_H = \left[t_{\text{ph}}^{-1} + t_{\text{pr}}^{-1} \right]^{-1} = 2.1 \times 10^6 \text{ sec.} \quad (6.55)$$

The acceleration due to the radiation pressure force is given by

$$b = \frac{h\nu}{m_H c} \left(\frac{\pi e^2}{m_e c} \right) f \frac{F_\odot}{r^2}. \quad (6.56)$$

The velocity distribution of the hydrogen atoms is assumed to be Maxwellian and is given by

$$f(v)dv = \frac{4}{\sqrt{\pi}} \frac{v^2}{v_0^2} e^{-(v/v_0)^2} dv. \quad (6.57)$$

The most probable speed v_0 is related to the mean speed v_H by the relation

$$v_H = \left(\frac{2}{\sqrt{\pi}} \right) v_0. \quad (6.58)$$

The density of hydrogen atoms at a distance r from the nucleus and for a time of travel t is given by

$$n_H = \frac{Q_H}{4\pi v_H r^2} e^{-t/t_H}. \quad (6.59)$$

The distance r has now to be expressed in terms of the orbit of the hydrogen atoms after they are released from the nucleus. The co-ordinate system is chosen such that the nucleus is the origin, the Sun is in the negative z direction and the positive x -axis is in the direction of the Earth. The hydrogen atoms leaving the nucleus follow the parabolic orbits and they can reach any point (x, y, z) with a velocity v through two different trajectories. The total density which is made up of these two components is given by the relation

$$n_H(x, y, z) = \frac{Q_H}{4\pi v} [(a \pm \sqrt{x_0^2 - x^2}) \sqrt{x_0^2 - x^2}]^{-1} \times \exp \left[-\frac{1}{t_H} \left(\frac{2}{b} \right)^{1/2} \sqrt{a \pm (x_0^2 - x^2)^{1/2}} \right]. \quad (6.60)$$

Here $a = z + (v^2/b)$ and $x_0 = \sqrt{x^2 - (z^2 + y^2)}$. The parameter x_0 is a function of y and z and defines a surface of a rotational paraboloid about the z -axis containing all the atoms within the maximum velocity v . The total column density along the line of sight s , including the velocity distribution of atoms, is given by

$$N(s) = \int_0^\alpha \frac{v}{v_H} f(v) 2 \int_0^{x_0} n_H(x, y, z) ds dv. \quad (6.61)$$

The model-based isophotes of Lyman- α can, therefore be calculated for different values of Q_H , t_H and v_H until a fit is obtained. The calculated isophotes for Comet Bennett are shown in Fig. 6.10.

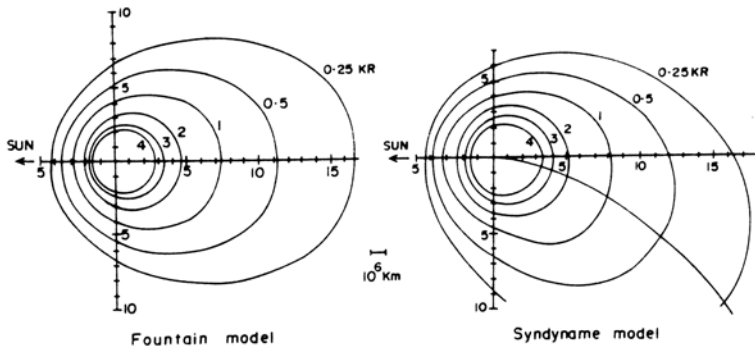


Fig. 6.10 Calculated Lyman α isophotes based on the Fountain and Syndyne models for Comet Bennett for April 1, 1970. The parameters used are: production rate $Q_H = 1.2 \times 10^{30}/\text{sec}$, outflow velocity $v_H = 7.9 \text{ km/sec}$, lifetime $t_H = 2.5 \times 10^6 \text{ sec}$ at 1AU, solar Lyman α flux = $3.2 \times 10^{11} \text{ photons/cm}^2/\text{sec}/\text{\AA}$ (Adapted from Keller, H.U. 1976. *Space Sci. Rev.*, **18**, 641).

The number marked on each isophote gives the intensity expressed in Kilo Rayleighs (KR) where 1 Rayleigh = $10^6 \text{ photons/cm}^2/\text{sec}$. The calculated Lyman- α isophotes based on the above model were in qualitative agreement with the observed isophotes; however in details, there were differences. For example, the calculated isophotes were symmetrical about the sun-comet line while the observed isophotes were inclined at an angle with respect to this line. This reflects the limitations of the model. The main assumption of the model is that the average parameters do not change with time, and this implies a steady state. But this is far from true in a real situation, wherein one has to consider the non-steady situations.

The non-steady state models were then developed and are usually referred to as *Syndyne* models. The formalism is very similar to the case of the formation of the dust tail of comets, wherein one finds dust particles in the tail emitted at different earlier epochs (Chap. 7). The hydrogen atoms coming out of the nuclear region are being acted upon by the forces of radiation pressure and gravitation. The resulting trajectories of the hydrogen atoms in the orbital plane of the comet depend upon the ratio of these two forces generally denoted as $(1 - \mu)$. The particles ejected continuously and having the same value of $(1 - \mu)$, describe a curve called *Syndyne*. The resultant effect of these two forces is to give curvature to the path of the hydrogen atoms. The total column density of the hydrogen atoms is the integral over all these paths corresponding to all the fictitious source points.

At the observation time t_0 , all the points are arranged along the Syndyne and correspond to the same emission time t_e . Let v_P represent some minimum velocity above which the contribution reaches the line-of-sight integral. Then

$$v_P = \frac{s}{(t_0 - t_e)}$$

where s represents the minimum distance from the fictitious source point. The total contribution to the column density at time t is the integral over all the surface densities and is given by

$$N_t(s) = \frac{1}{2\pi} \int_{v_P}^{\alpha} \frac{P_t(v) dv}{v^2 t^2 [1 - (v_P/v)^2]^{1/2}} \quad (6.62)$$

where $P_t(v)dv$ represents the production rate of hydrogen atoms with velocities between v and $v + dv$. Here the subscript t is used to denote the production rate as a function of time, which in turn depends on the heliocentric distance. The total column density arising out of all the fictitious source points on the Syndyne is given by

$$N = \int N_t(s) dt = \frac{1}{2\pi} \int_0^{\infty} dt \int_{v_P}^{\infty} \frac{P_t(v) dv}{v^2 t^2 [1 - (v_P/v)^2]^{1/2}}. \quad (6.63)$$

If the hydrogen atoms decay with a lifetime t_H which may be a function of t , then the exponential factor $\exp[-\int_0^t t_H^{-1}(t') dt']$ has to be included in the expression for $N_t(S)$. Therefore, the expression for the total column density is given by

$$N = \frac{1}{2\pi} \int_0^{\infty} dt \exp \left[- \int_0^t t_H^{-1}(t') dt' \right] \int_{v_P}^{\infty} \frac{P_t(v) dv}{v^2 t^2 [1 - (v_P/v)^2]^{1/2}}. \quad (6.64)$$

The velocity distribution is related to the production rate of hydrogen atoms through the relation

$$P_t(v) dv = \left(\frac{Q_H}{v_H} \right) v f(v) dv. \quad (6.65)$$

Figure 6.10 shows the calculated isophotes for Comet Bennett based on the above model for the same parameters of v_H , t_H , Q_H and F_{\odot} used in the Fountain model. The figure clearly shows that the isophotes are now inclined at a certain angle to the Sun-Comet line and are symmetrical about the Syndyne, and this is consistent with the observations.

The model described above can be improved further by assuming the parent molecules to be released by the nucleus and allowing for the decay of the molecules as they flow outwards. This eliminates the assumption of

the hydrogen atoms being emitted from a point source. In this model the parent molecules are released isotropically from the nucleus. These parent molecules could give rise to two or more decays along their paths with a certain value for the scale length for each decay. This in turn is dependent on the lifetime and the velocity of the molecules. The formalism developed in Sec. 6.1.2 can easily be applied to the present situation.

The models described above has been applied to the Lyman- α observations of many comets with great success. A comparison of the observed and the calculated isophotes allows one to determine quantitatively the production rate, the lifetime and the outflow velocity of hydrogen atoms. The detailed observations of Comet Bennett showed that two Maxwellian velocity distributions in the model calculation corresponding to $v_H = 7$ and 21 km/sec with 50:50 of each are required to fit the observations.

Monte-Carlo approach

In the formulation outlined above many details are still to be understood. This, therefore, led to the consideration of Monte-Carlo approach. The model developed is a three-dimensional time dependent Monte-Carlo particle trajectory model (MCPTM). It takes into account the physical processes which are important in the inner and outer coma of comets. In particular, it includes a physically realistic description of the detailed production mechanism and trajectories of H atoms produced by the photodissociation of H_2O and OH. It takes into account the solar radiation pressure acceleration. The gas dynamic model calculates the velocity and temperature variation in the coma and includes the multiple collisions, photochemical heating, radiative transfer and so on. The model couples the simple gas-dynamic flow of the gas with the MCPTM formalism. Therefore, the gas-dynamic model coupled with MCPTM formalism considers in a consistent way and also in a realistic manner the actual trajectories of as many as $\sim 10^5$ radicals or atoms. The space and column densities and hence the emission rates are then calculated. For comparing with the observation, the calculated results have to be referred to the projection on the sky-plane which in turn depend upon the relative geometry of the Earth, the Sun and the comet at the time of the observations. These are then compared with observations.

The model simulated isophotes based on MCPTM formalism is in agreement with the observed isophotes of Comet Hale-Bopp (Fig. 6.11). Therefore MCPTM formalism which takes into account in detail the important physical processes in the inner and outer extended coma region, is

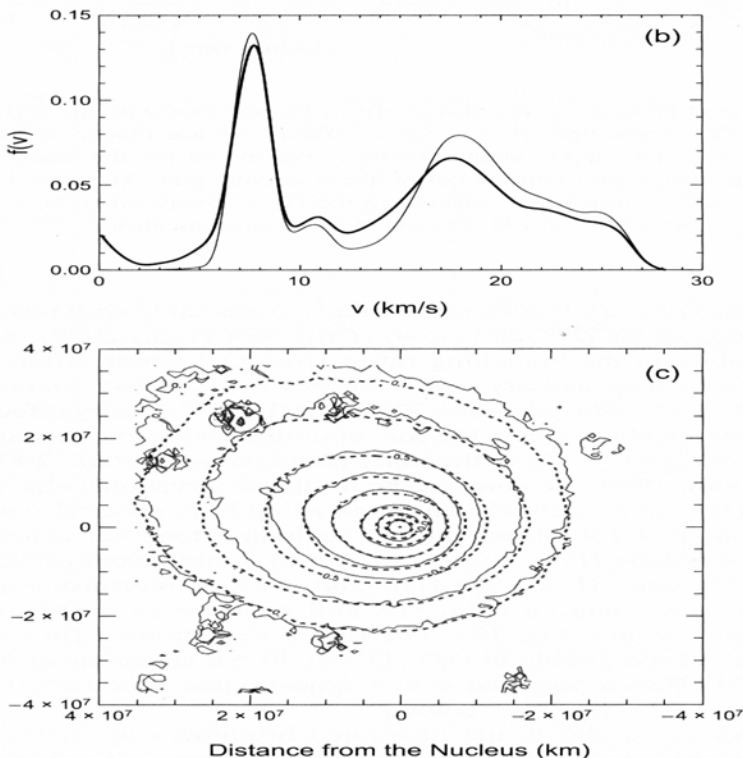


Fig. 6.11 (c) Comparison of the SOHO SWAN observations of Ly α isophote contours (solid lines) of Comet 1995 O1 (Hale-Bopp) at $r = 1.75$ AU with the calculated isophotes based on MCPTM models. (b) Shows the H-atom velocity distribution upon photochemical production (thin line) and after Monte Carlo model calculation (thick line) (Combi, M.R. et al. 2000. *Icarus*, **144**, 191).

a very general method of studying the observations of Lyman α in comets. The additional complications in terms of physics and dynamics can be incorporated as and when the need arises.

6.3.2. Analysis of H α observations

The H α line at 6563 Å can also be used to study the daughter species and could in turn be used to monitor the production rate of H₂O. Unfortunately, this line is usually faint and in addition could be contaminated with geocoronal H α emission, diffuse galactic H α emission particularly when the comet is located near the galactic plane and cometary H₂O⁺ (0, 7, 0) emission at

6562.8 Å. However, the observations carried out with the Fabry-Perot spectrometer, the Doppler shift of the cometary H α may be sufficient to avoid the geocoronal H α emission (Fig. 6.12). The contamination of galactic H α

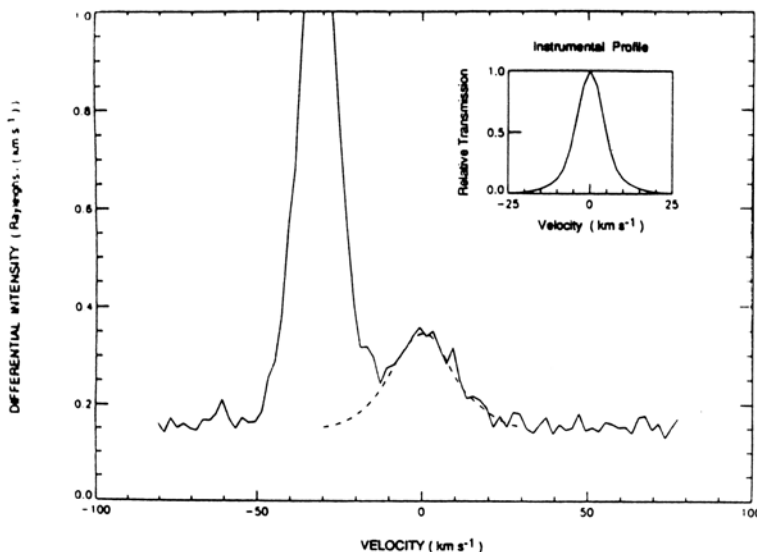


Fig. 6.12 Fabry-Perot observation of H α (6563 Å) line of Comet Halley taken on January 4, 1986. The smaller feature which is centered at zero velocity is the cometary H α emission while the larger feature centered around - 32 km/sec is the geocorona H α emission. The model fit to the observed cometary H α is shown by the dashed line (Smyth, W.H., Marconi, M.L., Seherb, F. and Roesier, F. 1993. *Ap. J.*, **413**, 756).

emission and H₂O⁺ emission can be minimized by taking proper precautions in making the observations. The commonly used Haser's model is not adequate for the analysis of H α emission as the hydrogen atoms have large dispersion in velocities. These had limited the study of H α emission in comets.

As discussed earlier, the Monte-Carlo Particle Trajectory Model (MCPTM) has been successfully applied to Lyman α observations of comets. This formalism can be modified and used for the analysis of observations of H α emission in comets. The main quantity to be determined in the application of MCPTM model is the g-factor for the H α emission. This has to be calculated taking into account the contributions from all the transitions which can give rise to this emission. This involves the knowledge of the transition probabilities of all the relevant transitions which

contribute to this emission and the solar radiation which excites these levels i.e., through excitation and de-excitation. The principal source of H α emission is through the excitation of H atoms by solar Lyman β photons. The actual profile of Lyman β has to be used since H atoms are in motion. For solar minimum conditions the total flux of Lyman β line at 1AU is 3.5×10^9 photons/cm 2 /sec while the corresponding Lyman α flux is 3.1×10^{11} photons/cm 2 /sec. For an accurate calculation of g-facotr for H α emission, in addition to principal contribution from the 3P to 3S transitions, several other secondary contributions have also been considered. The derived g-factor is velocity dependent, as in the case of OH (see Fig. 5.14). The MCPTM can be used to simulate observations of H α emission. The calculated and the observed line profile for Comet Halley is shown in Fig. 6.12. The derived velocities for such a fit require a broad velocity peak from 5 to 9 km/sec representing the bulk of ($\sim 70\%$) of H atoms released and a velocity ~ 8 km/sec due to the dissociation of OH. Additional smaller peaks also appear at around 11 km/sec ($\sim 7\%$) and 22–26 km/sec ($\sim 20\%$) due to the formation of H from OH and at 15 to 19 km/sec due to photodissociation of H₂O. A comparison of the derived production rate of H₂O from H α emission with those derived from 6300 Å emission observations should help in checking the photochemical processes which give rise to atomic oxygen and hydrogen from the parent molecule H₂O. Fortunately such a comparison can be made for Comet Halley, as measurements of H α and 6300 Å emissions were carried out on the same dates, with the same instrument, same calibration procedure and so on. The results derived from such an analysis are shown in Table 6.6. The agreement is reasonable in view of the various uncertainties involved in the calculation of parameters such as, g-factor for H α emission and the branching ratios for the production of O[¹D] atoms from photodissociation of H₂O and OH.

6.4. Related Studies

6.4.1. *Gas-phase chemistry in the coma*

The understanding of the formation of various observed species in the coma has attracted much attention in recent years. They could be produced either through the break-up of complex molecules or by some other physical process, as the gas expands outwards in the coma. Therefore, the distribution of the observed species in the coma does not necessarily reflect the original gaseous material ejected from the nucleus. In addition to the var-

ious physical processes that could modify this gas, the gas-phase chemical reactions among various constituents (neutral and ions) in the inner coma could also alter the original gas. The chemical reactions can take place due to the fact that the timescales involved for many of the reactions are much faster than the solar photodestruction rates at a heliocentric distance of 1 AU. In fact, the early investigations did indicate that ion-molecule could be quite important and various reaction sequences were considered. They did produce substantial amounts of various types of species that have been observed in comets. However, the reaction schemes considered were quite simple so that the calculations could be carried out without much difficulty. But in a real physical situation various networks of chemical reactions have to be considered between neutrals and ions of different atoms and molecules.

The nucleus is assumed to be spherical in shape containing the volatile material in certain proportions. The gases evaporate from the nucleus as a result of the solar heating. The vapourization theory (Chap. 11) could be used to calculate the gas production rate, outstream velocity, temperature, etc., which is consistent with the assumed mixture. The total number density present in the expanding coma gas at a distance r from the nucleus is related to the density at the nucleus surface $n(R_0)$ through the conservation of mass by

$$n(r) = n(R_0) \left(\frac{R_0}{r} \right)^2. \quad (6.66)$$

Here R_0 is the radius of the nucleus. To take into account the various physical processes and the chemical reactions which modify the particular species, it is necessary to have the particle conservation equation. The equation for a general case for a species i can be written in the form

$$\frac{\partial n_i}{\partial t} + \nabla \cdot n_i v_i = \sum_j R_{ji} - n_i \sum_k R_{ik}, \quad (6.67)$$

where n_i and v_i denote the number density and the flow velocity respectively. The first and the second terms on the right-hand side of the equation denote the rate of formation of species i , by processes involving species j and the rate of destruction of species i through processes involving species k . The whole set of equations given by Eq. (6.67) are coupled to each other through sources and sinks which are on the right-hand side of the equation. The assumption of spherical symmetry and a constant outflow velocity for all the species will simplify the equations considerably. Photodissociation and photoionization processes as well as the opacity effects

for the incident solar radiation are taken into account. The various chemical reactions between ions, electrons, neutrals and free radicals have been considered (Table 6.9).

Table 6.9 Gas phase chemical reactions with examples.

Photodissociation	$h\nu + \text{H}_2\text{O} \rightarrow \text{H} + \text{OH}$
Photoionization	$h\nu + \text{CO} \rightarrow \text{CO}^+ + e$
Photodissociative ionization	$h\nu + \text{CO}_2 \rightarrow \text{O} + \text{CO}^+ + e$
Electron impact dissociation	$e + \text{N}_2 \rightarrow \text{N} + \text{N} + e$
Electron impact ionization	$e + \text{CO} \rightarrow \text{CO}^+ + e + e$
Electron impact dissociative ionization	$e + \text{CO}_2 \rightarrow \text{O} + \text{CO}^+ + e + e$
Positive ion-atom interchange	$\text{CO}^+ + \text{H}_2\text{O} \rightarrow \text{HCO}^+ + \text{OH}$
Positive ion charge transfer	$\text{CO}^+ + \text{H}_2\text{O} \rightarrow \text{H}_2\text{O}^+ + \text{CO}$
Electron dissociative recombination	$\text{C}_2\text{H}^+ + e \rightarrow \text{C}_2 + \text{H}$
Three-body positive ion-neutral association	$\text{C}_2\text{H}_2^+ + \text{H}_2 + M \rightarrow \text{C}_2\text{H}_4^+ + M$
Neutral rearrangement	$\text{N} + \text{CH} \rightarrow \text{CN} + \text{H}$
Three-body neutral recombination	$\text{C}_2\text{H}_2 + \text{H} + M \rightarrow \text{C}_2\text{H}_3 + M$
Radiative electronic state deexcitation	$\text{O}^{(1D)} \rightarrow \text{O}^{(3P)} + h\nu$
Radiative recombination	$e + \text{H}^+ \rightarrow \text{H} + h\nu$
Radiation stabilized positive ion-neutral association	$\text{C}^+ + \text{H} \rightarrow \text{CH}^+ + h\nu$
Radiation stabilized neutral recombination	$\text{C} + \text{C} \rightarrow \text{C}_2 + h\nu$
Neutral-neutral associative ionization	$\text{CH} + \text{O} \rightarrow \text{HCO}^+ + e$
Neutral impact electronic state quenching	$\text{O}^{(1D)} + \text{CO}_2 \rightarrow \text{O}^{(3P)} + \text{CO}_2$
Electron impact electronic state excitation	$\text{CO}^{(1\Sigma)} + e \rightarrow \text{CO}^{(1\Pi)} + e$

(Huebner, W.F., Boice, D.C., Schmidt, H.U. and Wegmann, R. 1991. In *Comets in the Post-Halley Era*, eds. R.L. Newburn, Jr. *et al.*, Kluwer Academic Publishers, p. 907).

A step-by-step solution of the coupled Eq. (6.67) gives the number density of the species and its variation with r . Figures 6.13 and 6.14 show the typical results of such calculations for various neutrals and ions. The column densities can be calculated by integrating the number density along the line of sight.

It is interesting to note from the model calculations (Fig. 6.14) that the most abundant ions in the inner coma should be H_3O^+ , NH_4^+ and others. Therefore, in a comet, the most abundant ion in the inner coma should be H_3O^+ . The dominant H_3O^+ in the inner coma arises as a result of the production of H_3O^+ through photoionization of H_2O followed by

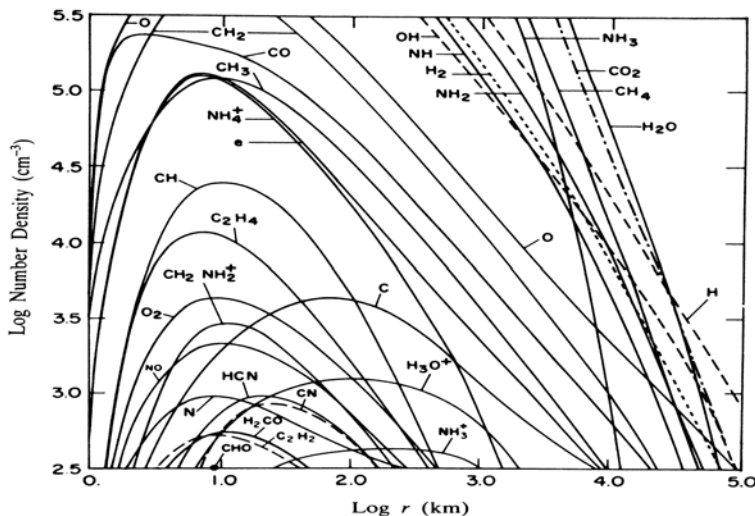
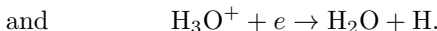
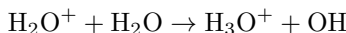
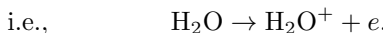


Fig. 6.13 Typical variation of the number density of various species plotted as a function of the distance from the centre of the nucleus. The radius of the nucleus = 1 km and $r = 1$ AU (Huebner, W.F. and Giguere, P.T. 1980. *Ap. J.*, **238**, 753).

ion-neutral reaction and destruction by dissociative recombinations,



Such calculations have been used to identify the species found by Giotto Mass Spectrometer.

6.4.2. *In situ mass spectrometer for ions*

The *in situ* measurements carried out with spacecrafnts on Comet Halley gave confirming evidence for some of the basic ideas of gas-phase chemistry discussed earlier. In fact the gas-phase chemistry has been used extensively in the interpretation of ions observed in the inner coma of Comet Halley to extract the production rates of ions.

The ion mass spectrometer on board the Giotto spacecraft has provided important information about the ions present in the coma of Comet Halley to a distance ~ 1000 km. The mass resolution is excellent. This makes it easier to calculate the ion densities. The instrument measures the distribution of m/q . Therefore, a careful analysis of the data with the

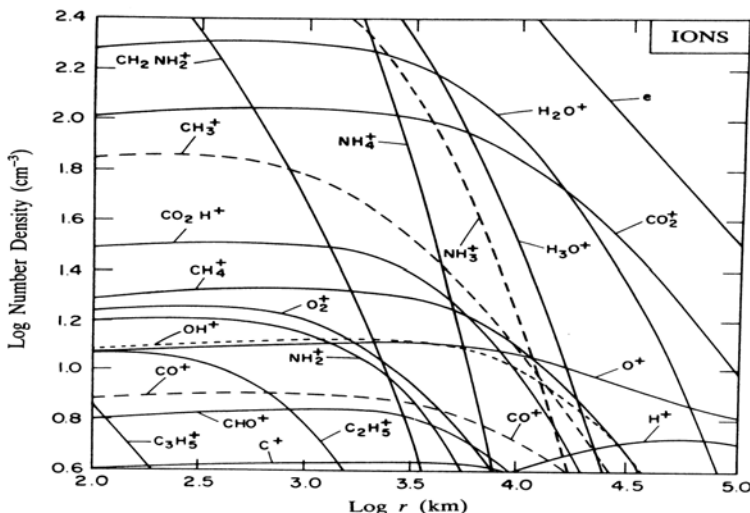


Fig. 6.14 Typical variation of number density of ions plotted as a function of the distance from the centre of the nucleus. (Huebner, W.F. and Giguere, P.T., 1980. *op. cit.*)

theoretical modelling is required before the peaks can be identified with certainty. However, the singly ionized peaks can easily be identified. The peaks at $m/q = 18, 17$ and 16 gave the direct detection of H_2O as these peaks belong to the H_2O group of ions, i.e., H_2O^+ , OH^+ and O^+ . The peak at $m/q = 12$ is certainly C^+ . The peak at $m/q = 19$ is almost certainly H_3O^+ which supported the chemical models. Molecular ions have been detected ranging beyond 100 amu. The major ion species and also some of the secondary ones which can contribute to the observed m/q peaks are shown in Table 6.10.

The important reactions for forming some of these ions are shown in Fig. 6.15. As can be seen from Table 6.10, NH_4^+ can also make contribution to the peak at $q/m = 18$. Similarly, NH_3^+ could contribute to the peak at $q/m = 17$. Several peaks have been seen with the positive ion cluster analyzer on Giotto spacecraft with an alternate mass difference of 14 and 16amu as can be seen from Fig. 6.16. A suggestion has been made that it could arise due to ion fragments CH_2 and O breaking off from the large parent molecule formaldehyde (H_2CO) _{n} , also known as Polyoxymethylene (POM).

Table 6.10 Dominant ion species contributing to mass range detected in the ion mass spectrometer.

M/q	Ion Species		M/q	Ion Species	
12	C ⁺		34	³⁴ S ⁺ , H ₂ S ⁺	
13	CH ⁺ , ¹³ C ⁺		35	H ₃ S ⁺	
14	CH ₂ ⁺ , N ⁺		36	C ₃ ⁺	
15	CH ₃ ⁺ , NH ⁺		37	C ₃ H ⁺ , H ₃ O ⁺ .H ₂ O	
16	O ⁺ , CH ₄ ⁺ , NH ₂ ⁺		38	C ₂ N ⁺ , C ₃ H ₂ ⁺	
17	OH ⁺ , NH ₃ ⁺ , CH ₅ ⁺		39	C ₃ H ₃ ⁺	
18	H ₂ O ⁺ , NH ₄ ⁺		40	C ₃ H ₄ ⁺ , CH ₂ CN ⁺	
19	H ₃ O ⁺		41	C ₃ H ₅ ⁺	
20	H ₂ ¹⁸ O ⁺		42	-	
21	H ₃ ¹⁸ O ⁺		43	CH ₃ CO ⁺	
22	-		44	CO ₂ ⁺ , CS ⁺ , C ₃ H ₈ ⁺	
23	-		45	HCS ⁺ , HCO ₂ ⁺	
24	C ₂ ⁺		46	H ₂ CO ₂ ⁺ , NS ⁺ , H ₂ CS ⁺	
25	C ₂ H ⁺		47	H ₃ CS ⁺ , HNS ⁺	
26	C ₂ H ₂ ⁺ , CN ⁺		48	SO ⁺	
27	C ₂ H ₃ ⁺ , HCN ⁺		49	HSO ⁺	
28	H ₂ CN ⁺ , CO ⁺ , N ₂ ⁺ , C ₂ H ₄ ⁺		50	C ₄ H ₂ ⁺	
29	HCO ⁺ , C ₂ H ₅ ⁺ , N ₂ H ⁺		51	C ₄ H ₃ ⁺	
30	H ₂ CO ⁺ , CH ₄ N ⁺ , NO ⁺ , C ₂ H ₆ ⁺		52	C ₃ H ₂ N ⁺	
31	CH ₂ OH ⁺ , HNO ⁺		53	C ₄ H ₅ ⁺	
32	S ⁺ , O ₂ ⁺		54	-	
33	HS ⁺ , O ₂ H ⁺		55	C ₃ H ₃ O ⁺ , C ₄ H ₇ ⁺	

(Huebner, W.F., Boice, D.C., Schmidt, H.U. and Wegmann, R. 1991. In *Comets in the Post-Halley Era*, eds. R.L. Newburn, Jr. *et al.*, Kluwer Academic Publishers, p. 907).

6.4.3. Temperature and velocity of the coma gas

The knowledge of the temperature and velocity of the coma gas as a function of distance from the nucleus is required for the calculation of the excitation process as well as for the derivation of molecular abundances. This can, in principle, be derived from the model calculations which take into account the thermodynamical and hydrodynamical processes in the coma. For the description of the state of the gas, the equations of mass, momentum and energy have to be considered. The corresponding fluid dynamic equations with velocity u , mass density ρ and pressure P can be written as

$$\frac{\partial \rho}{\partial t} + \nabla \cdot (\rho u) = \dot{\rho}, \quad (6.68)$$

$$\frac{\partial}{\partial t} (\rho u) + (u \cdot \nabla) \rho u + \rho u (\nabla \cdot u) + \nabla P = \dot{q}, \quad (6.69)$$

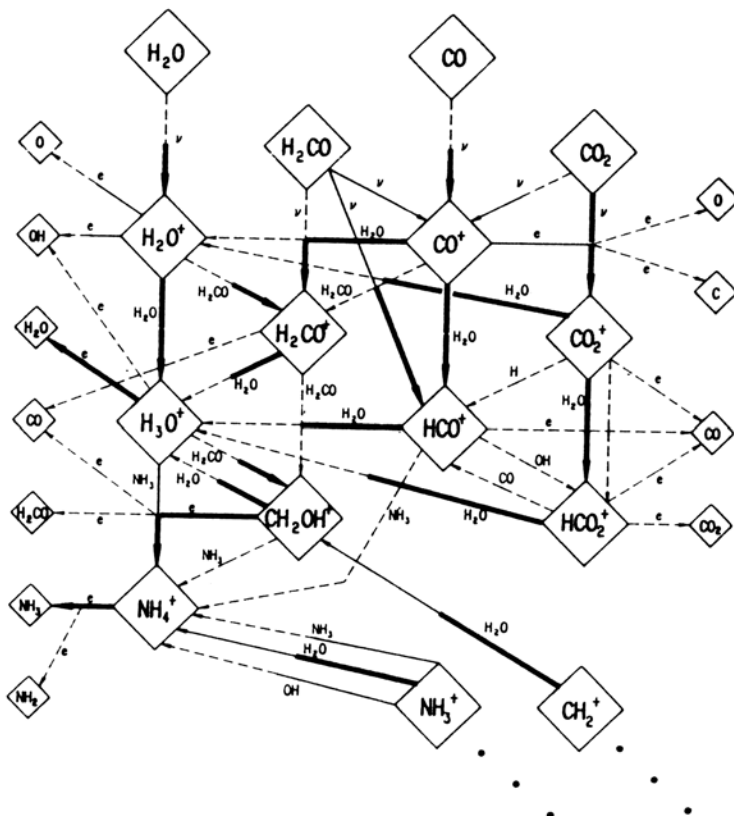


Fig. 6.15 For illustrative purpose, this figure shows the network of major chemical reactions involving the formation and destructive processes that have to be considered in the calculation of abundances of some of the species. The arrow indicates the direction of the reaction ν represents photodissociation or photoionization and e indicates electron dissociative recombination (Huebner, W.F., Boice, D.C., Schmidt, H.U. and Wegmann, R. 1991. In *Comets in the Post-Halley Era*, eds R.L. Newburn, Jr. et al., Kluwer Academic Publishers, p. 907).

$$\frac{\partial}{\partial t} \left(\rho \frac{u^2}{2} + \rho \epsilon \right) + \nabla \cdot \left[\rho u \left(\frac{u^2}{2} + h \right) \right] = \dot{E}. \quad (6.70)$$

Here ϵ and h are the specific internal energy and enthalpy respectively. The quantities on the right hand side represent the sources and sinks for the mass, momentum and energy respectively. These equations have to be solved with the appropriate initial boundary conditions. The equations are generally solved in a one-dimensional form with radial variation. Such

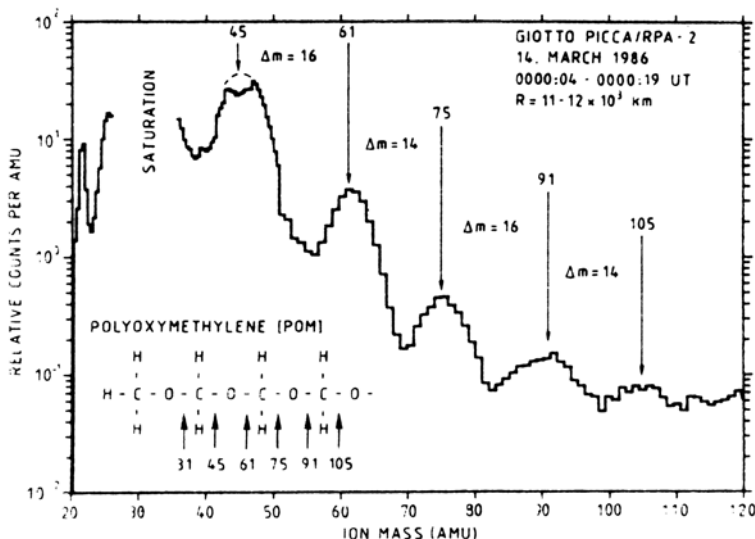


Fig. 6.16 The ion mass spectrum of Comet Halley observed on March 14, 1986 with the Giotto spacecraft at a distance $11\text{--}12 \times 10^3$ km from the nucleus. The peaks at regular intervals with alternate difference in mass number of 14 and 16 have been interpreted as dissociation production of the molecule polyoxymethylene. (Huebner, W.F. *et al.* 1987. *Symposium on the diversity and similarity of comets*, ESA-SP 278, p. 163; see also Vanysek, V and Wickramasinghe, N.C. 1975. *Astrophys. Space Sci.*, **33**, L19).

solutions are sufficient in the inner coma, but in the outer coma where the solar wind interactions occur, the description of the state of the ionic gas may require two or three-dimensional solutions. The corresponding equations for a spherically symmetric coma for the one dimensional case are given by

$$\frac{1}{r^2} \frac{d}{dr} (r^2 u \rho) = \dot{\rho}, \quad (6.71)$$

$$\rho u \frac{du}{dr} + \frac{dP}{dr} = \dot{q} \quad (6.72)$$

and

$$\frac{1}{r^2} \frac{d}{dr} \left[r^2 \rho u \left(h + \frac{u^2}{2} \right) \right] + \left[\frac{\bar{\gamma}}{\bar{\gamma} - 1} \rho u \right] = \dot{Q} - \dot{L}. \quad (6.73)$$

Here $\bar{\gamma}$ is the specific heat ratio for the gas. \dot{Q} and \dot{L} are the energy input and energy loss rates respectively. The above equations can easily be modified to include the dust component. The method is to write the analogous

equations for the interaction of dust and the gas which are therefore treated as separate fluids.

The results of the solution of the equations depend on the various physical processes that have been considered in the terms on the right hand side of the equations. In particular, it depends on the source of energy input, energy loss, chemistry and so on. Therefore, the emphasis on the solution depends upon the problem of interest. For example, several studies have been carried out which mainly emphasize certain aspects like nucleus-coma interface, gas-dust interaction, detailed study of the chemistry or the solar wind interaction and so on. Here again initially simple models were considered.

The inner part of the coma is the collision dominated region (LTE). It decreases in importance moving away from the nucleus. The hydrodynamic flow which is a good approximation in the inner region becomes free molecular flow in the outer region of the coma, with a transition region in between. Therefore, the solutions of the hydrodynamic equations can represent approximately the real solution provided proper quantities are used referring either to LTE or NLTE situations and a suitable form for in-between regions. The photolytic heating is given by the thermalisation of the excess kinetic energy carried off by the photolytic products due to photodissociation or exothermic chemical reactions. The dominant contribution to the heating process comes from the dissociation of H₂O through the channel H₂O+hν → H + OH + Energy. In this process H atoms has an excess of velocity ∼ 17.5 km/sec and OH radical ∼ 1.05 km/sec. This means that collisions have to be important which imply that the time scale for collision must be smaller than the time scale for the expansion of the gas.

The cooling process of the coma gas comes mainly due to H₂O molecules because of its large abundance. The cooling takes place mainly through their strong rotational transitions.

In a real cometary situation, the calculation of photochemical heating is not simple as the coma gas is not in LTE. Also the coma region where the density is high for the local photochemical effect to be highly efficient, depends upon the gas production rate and the expansion velocity in the coma. Since the gas density varies as $1/r^2$, the photochemical heating efficiency decreases slowly and hence it is rather difficult to define a collision zone for heating caused by super-thermal H atoms.

Some of the complications in the calculation of cooling rates have also to be considered. In particular, the water density in the coma is high enough

that some of the lines could be optically thick. The optical depth effect is generally calculated based on escape probability method. The net result being that rotational temperature basically comes out of equilibrium with the gas kinetic temperature. Several of these effects and refinements have been incorporated in the calculation of heating and cooling rates which greatly influence the temperature and velocity of the gas in the coma.

The results of such model calculations provide the velocity and temperature variation in the coma. The resulting temperature distribution is shown in Fig. 6.17. The temperature distribution falls steeply to a minimum temperature ~ 20 K at a distance $\sim 10^2$ km and then increases again. The general shape of the temperature variation is the resultant effect of the relative importance of heating and cooling rates of H_2O and the expansion cooling.

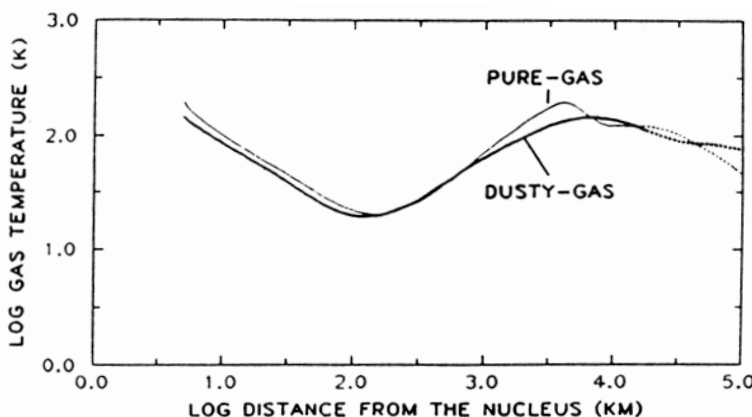


Fig. 6.17 The calculated variation of gas temperature as a function of distance from the nucleus for Comet Halley. (Combi, M.R. 1989. *Icarus*, **81**, 41).

Refined models

All the discussion presented so far pertaining to chemistry, temperature and velocity of the coma gas were based on certain simplifying assumptions in the model calculations. In addition several processes that can occur in the coma were considered individually or in combination with others. But in a real situation, due to the nature of the physical conditions in the coma, various processes operate simultaneously in a complex and intricate manner.

The starting point for all the activities seen in the coma of a comet is due the absorption of solar radiation by various molecules. This leads to photodissociation and ionization of the parent molecules. These in turn fragment giving rise to newer species and the process continues. The energy budget in this process is controlled by the heating and cooling mechanisms which in turn has a great effect on the coma gas. The earlier assumption of considering the gaseous coma as a fluid is reasonable in the inner parts of the coma where the densities are high. But moving outwards from the nucleus to the coma, the density gradually decreases and the flow of the gas becomes more like a free molecular flow. In these regions the description of the gas as a fluid is not applicable. Therefore it is necessary to consider the flow of the gas in the coma in a consistent manner going from a region of higher density to regions of decreasing densities. The presence of dust can also have an effect on the structure of the coma. This comes through the change in the temperature of the dust particles, which in turn can have an effect on the vapourization of volatiles from the CHON dust particles. Therefore the observed structure of the coma gas, is a resultant effect of coma chemistry, physics and dynamics that are intimately connected with each other. Therefore all these effects have to be considered simultaneously in any realistic model.

Several types of such models have been developed. Some of them are, Hydrodynamic model, Monte Carlo Model. Hydrodynamic model has been used extensively for the study of the coma gas. For example, a chemical/dynamical model developed for the study of the coma includes in the chemical reaction scheme involving around 180 species and more than 3500 reactions.

The Monte Carlo approach is the most general and most accurate description of the coma which can take care of all the complexities involved within the coma. One such model is called Direct Simulation Monte Carlo Method (DSMC). This is a time dependent in which the molecular motions of a large number of molecules are followed and simultaneously their response to imposed field. This model has been used widely in the study of the coma gas and has been highly successful. As an example, the observed gas velocity variation in the coma of Comet Halley deduced from Giotto observations is compared with the results based on time dependent DSMC model in Fig. 6.18 for distances between 10^3 and 3×10^4 km. The observed velocities are deduced from the energy shifts of peaks in the neutral mass spectrometer energy spectra and show a variation from a value of about 0.8 to 1.05 km/sec. As can be seen the observed and the model based velocity

distributions are in reasonable agreement.

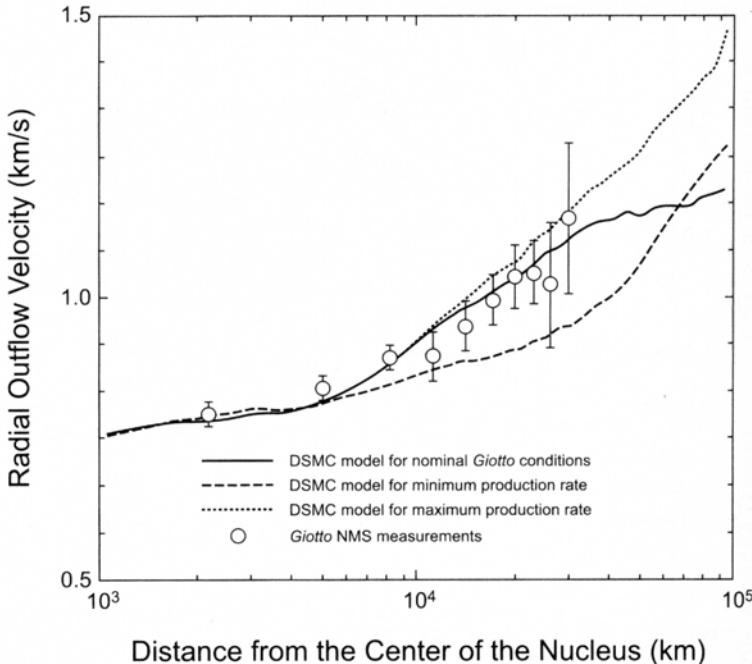


Fig. 6.18 The calculated variation of expansion velocity with distance from the nucleus based on time-dependent DSMC model is compared with the observed variation for Comet Halley deduced from the Giotto measurements (Combi., M.R. 1996. *Icarus*, **123**, 207).

6.5. Parent Molecules

Most of the observed species in comets cannot exist as such in the nucleus. Therefore, it is suggested that they could arise out of the photodissociation process of stable complex molecules. However, it is very difficult to observe these parent molecules directly from the Earth-based observations due to their short lifetime, as they are dissociated in most of the cases very near the nucleus. Hence the information about the possible parent molecule has to come from indirect means and, in particular, mainly from the study of the decay products. However, the spacecrafts which passed by Comets Halley, Tempel 1 and Wild 2 made *in situ* measurements of the inner coma

and have given important and direct information about the possible nature of the parent molecules. In general, there are several ways to approach this problem.

The straightforward approach is to look for the dissociated products of simple parent molecules as in the case of H₂O molecules. There are not many clear-cut cases of this type. The laboratory investigations of the photochemistry of various types of molecules can help a great deal in elucidating the problem of the parent molecules. The laboratory studies have to give information with regard to the products of photodissociation, the energy required to initiate the reaction and also the branching ratios for various paths of the reactions. At present, the data is limited in extent. Also such studies have to be performed for all molecules of astrophysical interest. To start with, the various types of molecules identified in the interstellar space could be used. The calculated photochemical lifetimes of several molecules based on the laboratory data show that for most molecules the lifetime is below 2×10^4 sec at 1 AU. The results based on laboratory photochemical studies should be used only as a guideline when applying the same to a cometary atmosphere. This is due to the fact that the astrophysical situations are vastly different from laboratory conditions.

The surface brightness distribution as a function of the radial distance from the nucleus can give information about the parent molecule (Sec. 6.1.2). The comparison of the observed brightness profiles with those of calculated profiles gives the scale lengths of the species. The lifetime of the species, can therefore, be obtained by dividing the scale length by the expansion velocity. These lifetimes in turn can give information with regard to the possible types of the parent molecule.

Another approach is through the study of gas-phase reactions in the coma. If an agreement can be obtained between the observed and the calculated abundances of various species, one can hopefully trace backwards through the network of reactions and this could help in identifying the plausible parent molecule of various species. However, the procedure may not be very practical in most of the cases.

Another possible method is through the spectral study of the observed lines and particularly from those molecules which give lines arising out of singlet-singlet and triplet-triplet transitions. The idea is to see whether the observed intensities of lines arise preferentially from the singlet-singlet or the triplet-triplet states of the molecule. This could in turn be related to the products arising out of the dissociation of the parent molecule.

The study of forbidden lines can also help in identifying the parent

molecule of the species which gives rise to these lines. By combining different types of studies it is possible to infer the possible nature of the parent molecule of some of the observed species. We may illustrate them with a few examples.

Until the direct detection of H₂O from Comet Halley in 1986, all the earlier observations had built up a strong case for the H₂O as the dominant volatile component of the nuclei of comets. This is basically related to the fact that all the dissociated products of H₂O are seen and they dominate the ultraviolet spectra of comets. But the direct detection of H₂O came from the observation made from the Kuiper Airborne Observatory of the ν_3 band near $\lambda \sim 2.65 \mu\text{m}$ in Comet Halley. The same band was also observed by the infrared spectrometer on the Vega spacecraft. The results based on Neutral Mass Spectrometer (NMS) measurements on the Giotto spacecraft showed that H₂O comprised around 80% of the volatile of Comet Halley.

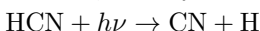
The presence of CO in comets was indicated by the detection of fourth positive bands at $\lambda \sim 1500 \text{ \AA}$. Its abundance relative to water varies from a few percent to around 30%. For Comet Halley, the value derived from various observations is $\sim 17\%$, while NMS data gave a value $\sim 7\%$. The lower value is attributed to CO coming from the nucleus and the rest is believed to arise from an extended source. CO is the second most abundant molecule in comets.

The observation of the ν_3 band of CH₄ around $3.3 \mu\text{m}$ has yielded an estimate for the production rate of CH₄ which is $\sim 1\%$.

Although CO₂ was believed to exist due to the presence of CO₂⁺ ion in comets, it was first detected in Comet Halley from the observation of ν_3 band at $4.3 \mu\text{m}$ from the IKS instrument in the Vega spacecraft and the NMS instrument on Giotto which gave a value $\sim 3\%$ relative to water. The observed distribution of the column density of CO₂ is in good agreement with the ρ^{-1} law. This is consistent with the distribution of R^{-2} expected for parent molecules in the vicinity of the nucleus.

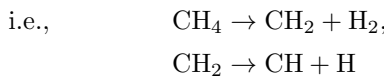
NH₃, NH₂ and NH have been seen in comets. The photodissociation of NH₃ appears to produce mostly NH₂($\sim 95\%$) and very little NH($\sim 5\%$). Therefore the parent of NH₂ is NH₃ and the dominant parent of NH is NH₂.

The photodissociation of HCN, namely



can explain the CN radical both from the point of view of production rates as well as from the kinematic considerations. The molecule C₂N₂ has also been proposed as the parent of CN.

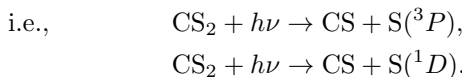
The parent of CH is most like CH₄. Since CH₃ is highly unstable, CH₄ first decays to CH₂ which in turn decays to CH.



The source of S₂ (lifetime ~ 350 sec) has been the subject of considerable debate as the presence of S₂ in the cometary nuclei has great significance for the origin of cometary material. CS₂ hardly photodissociates into S₂. It is highly unlikely that solid S₂ has formed from gas phase condensation, which primarily produces other compounds. So is also with the irradiation of the nucleus by cosmic rays or ultraviolet radiation and so on.

The long-slit spectroscopic observations has been carried out with HST to get the spatial brightness profile of S₂ in Comet Ikeya-Zhang. These observations seems to indicate that most likely S₂ originate from the nucleus. Therefore, S₂ could be a parent molecule.

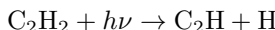
The most plausible parent of CS is the short-lived (life time at 1 AU ~ 500 sec) CS₂ molecule,



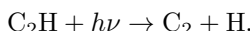
Another possible source of CS is OCS. However the main dissociation process of OCS is CO and S. Hence the contribution of OCS to S is minor.

The S produced from CS₂ and S₂ does not appear to account for the observed amount of sulphur. The molecule H₂S which has been detected in comets may contribute to the observed sulphur.

The analysis of the C₂ brightness profile seems to suggest that it could be formed in a three-step photodissociation process of some parent molecule. The laboratory studies indicate that C₂ can be produced in a two-step process as follows:



followed by



The C₃ molecule is a difficult case for which there are some suggestions. Laboratory studies have shown that C₃ molecule can be formed from C₃H₈. This molecule photodecomposes to give C₃H₃ and C₃H₂ as intermediate products, which can then absorb a photon to give C₃ molecule. C₃H₈ has also been suggested.

Table 6.11 gives a limited list of probable parent molecules of some observed species in comets. Some of the identifications are to be taken with caution as they are still preliminary in nature.

Table 6.11 Possible parent molecules and abundances of some of them.

Observed species	Possible parent molecule
H ₂ O, H ₂ O ⁺ , OH, H, O	H ₂ O
CO ₂ ⁺ , CO ⁺ , CO	CO ₂
CO, CO ⁺ , C	CO
CH	CH ₄
CN	HCN, C ₂ N ₂
HCN	HCN
NH, NH ₂	NH ₃
NH	NH ₂
C ₂	C ₂ H ₂ , C ₃ H ₂ O
C ₃	C ₃ H ₄ , C ₃ H ₈
CS	CS ₂ , OCS
S ₂	S ₂
S	S ₂ , OCS, CS ₂ , H ₂ S, SO ₂

6.6. Chemical Diversity

The surprising result that comes out of the study of the abundances of a large number of molecular species in comets, is the presence of chemical diversity among them. This could help in the understanding of the possible sites of formation of these objects as well as the physical processes that could have taken place leading to such an observed effect.

The other problem of great interest is the bulk composition inside the nucleus of a comet. The only available information for the study is the production rate of volatiles and its variation with heliocentric distance. The natural question that arises is, to what extent the observed ratio of volatiles reflects the bulk chemical composition inside the nucleus. The relation between the two is not simple. It has been realized over the years that the observed ratio of volatiles in the coma which vary with the heliocentric distance and also among comets, may be vastly different from those present in the nucleus even before they were processed by solar radiation. Conclusions on the bulk composition of the nucleus can only be made if the coma composition is integrated over the entire orbit of the comet.

6.7. Summary

We may briefly summarize the results of the discussion presented so far. The study of several comets has shown a wide variation of the production rate of molecules with the heliocentric distance, vastly different from that of r^{-2} dependence. In order to explain such a variation, more complicated models have to be considered. The interesting result is the observed chemical diversity among comets, which has direct bearing on the formation site of comets. Even though the lines of C₂, CN and others dominate the visual spectral region, their production rates are less by a factor of 100 or so compared to that of H₂O or H. These molecules are, therefore, the minor constituents of the cometary material. Most of the elements have abundance ratio very similar to the solar atmospheric value except hydrogen which is very much depleted in comets.

The *in situ* measurements of Comet Halley made by spacecrafts have shown the wide variety of ions present in the coma. The production rates of these species derived for the first time making use of the detailed gasphase chemistry show them to be a minor contributor of the gas. The presence of extended source of molecules give strong evidence to show that grains can also act as suppliers of volatiles in the coma. The expected velocity distribution of the coma gas based on the detailed modelling agrees with the Giotto results. Lastly, the spacecraft observations have detected several possible parent molecules. All the earlier studies indicating H₂O as the parent of OH, H and O have been further reinforced.

Problems

1. Calculate the surface brightenss profiles for a few values of β_1/β_0 as shown in Fig. 6.1.
2. Deduce the values of β_1 and β_0 for the following observed surface brightness distribution: at $\rho = 10^3, 4 \times 10^4$ and 7×10^4 km, the observed values of surface brightness are 350, 35 and 12 kilo Rayleighs respectively. What is the lifetime of the species for an assumed velocity of 1 km/sec?
3. Assume that the diatomic molecule NH is formed due to the collision process of N and H with α as the rate constant for the reaction. What is the resulting concentration of NH for $n_H = 10/\text{cm}^3$, $\alpha = 10^{-10} \text{ cm}^3/\text{sec}$ and for a time scale of 4×10^9 years?

4. Write down the expression for the equilibrium abundances of CH and CH^+ in terms of other abundances for the following reactions: $\text{C} + \text{H} \rightarrow \text{CH} + h\nu$; $\text{C}^+ + \text{H} \rightarrow \text{CH}^+ + h\nu$; $\text{CH} + h\nu \rightarrow \text{CH}^+ + e^-$; $\text{CH} + h\nu \rightarrow \text{C} + \text{H}$; $\text{CH}^+ + h\nu \rightarrow \text{C}^+ + \text{H}$. The rate constants for these reactions are k_1 , k_2 , β_1 , β_2 and β_3 respectively.

References

The calculations of surface brightness distribution for the two component models are discussed in these two papers.

1. Haser, L. 1957. *Bull. Acad. Belg. cl. Sc.*, 5e Ser. **43** 740.
2. O'Dell, C. R. and Osterbrock, D. E. 1962. *Ap. J.* **136** 559.

The values required for the calculation of surface brightness distribution are given in

3. A'Hearn, M. F. and Cowan, J. J. 1975. *Ap. J.*, **80** 852.

The three component model is given in the paper

4. O'Dell, C. R., Robinson, R. R., Krishna Swamy, K. S., Spinrad, H. and McCarthy, P. J. 1988. *Ap. J.*, **334**, 476.

For later work refer to

5. Combi, M.R. and Fink, U. 1997, *Ap. J.*, **484**, 879.
6. Manfroid, J.M., Hutsemékers, D., Jehin, E. et al. 2007, *Icarus*, **187**, 144.

The vectorial formalism model is presented in

7. Festou, M C. 1981. *Astr. Ap.*, **95**, 69.

The Monte Carlo approach and others are discussed in

8. Combi, M. R. and Delsemme, A. H. 1980. *Ap. J.* **237**, 633.
9. Hodges, Jr. R. R. 1990. *Icarus*, **83**, 410.
10. Xie, X. and Mumma, M.J., 1996. *Ap.J.*, **464**, 442.
11. Combi, M.R. 1996, *Icarus*, **123**, 207.
12. Crifo, J.-F., et al. 2005. *Comets II*, eds. M.C. Festou, H.U. Keller and H.A. Weaver, Univ. Arizona Press, Tucson, p. 471.
13. Combi, M.R. et al. 2005. *Comets II*, eds. M.C. Festou, H.U. Keller and H.A. Weaver, Univ. Arizona Press, Tucson, p. 523.
14. Crifo, J.-F. 1990. *Icarus*, **84**, 414.

For some basic parameters, refer to

15. Crovisier, J. 1992. *Infrared Astronomy with ISO*, eds. Th. Encrenaz and M.F. Kessler, Nova Science Publishers, p. 221.
16. Huebner, W.F. et al. 1992. *Astrophys. Space Sci.*, **195**, 1.

The semi-empirical photometry theory is discussed in the following papers.

17. Newburn, R. L. 1981. In *The Comet Halley Dust and Gas Environment*. ESA SP-174, p. 3.
18. Divine, N. *et al.* 1986. *Space Sci. Rev.*, **43**, 1.
- The material for prompt emission lines (See. 6.2.2) is from
19. Mamma, M.J. *et al.* 2001. *Ap.J.*, **546**, 1183.
20. Bonev, B.P., Mumma, M.J., Dello Russo, N., *et al.* 2004. *Ap.J.*, **615**, 1048.
21. Bonev, B.P., Mumma, M.J., Disanti, M.A., *et al.* 2006. *Ap.J.*, **653**, 774.

Papers referring to water production rates

22. Schleicher, D.G., Woodney, L.M. and Mills, R.L. 2003. *Icarus*, **162**, 415.
23. Schleicher, D.K., Mills, R.L. and Birch, P.V. 1998. *Icarus*, **132**, 397.
- Review paper for Sec. 6.2.3.
24. A'Hearn, M.F. *et al.* 1995. *Icarus*, **118**, 223.
- Paper for CN Jet
25. A'Hearn, M.F. *et al.* 1986. *Nature*, **324**, 649.
- Extended source of CO and H₂CO
26. Eberhardt, P., Krankowsky, D., Shulte, W. *et al.* 1987. *Astron. Astrophys.*, **187**, 481.
27. Meier, R. Eberhardt, P., Krankowsky, D. *et al.* 1993. *Astron. Astrophys.*, **277**, 677.
28. DiSanti, M.A., Mumma, M.J., Dello Russo, N. *et al.* 2001. *Icarus*, **153**, 162.
29. Festou, M. 1999. *Space Sci. Rev.*, **90**, 53.

Case of N₂⁺

30. Cochran, A.L. 2002. *Ap. J.*, **576**, L165.
31. Cochran, A.C., Cochran, W.D. and Barker, E.S. 2000. *Icarus*, **146**, 583.

The Discussion about complex molecules is drawn from

32. Bockelée - Morvan, D. *et al.* 2005. *Comets II*, Eds. M.C. Festou, H.U. Keller and W.A. Weaver, Univ. Arizona Press, Tucson, p. 391.
33. Crovisier, J. 1987. *Astr. Ap. Suppl.*, **68**, 223.
34. Crovisier, J. 2005. *Asteroids, Comets and Meteors*, eds. D. Lazzaro, S. Ferraz Mello and J.A. Fernandez, Cambridge University Press, Cambridge, p. 133.
35. Mumma, M.J., Disanti, M.A., Dello Russo, N. *et al.* 2003. *Adv. space Res.*, **31**, 2563.

36. Disanti, M.A., Villanueva, G.L., Bonev, B.P. *et al.* 2007. *Icarus*, **187**, 240.

The following paper pertains to Sec. 6.2.9 of oxygen

37. Schultz, D., Li, G.S.H., Scherb, F. and Roesler, F. L. 1992. *Icarus*, **96**, 190; **101**, 95, 1993.

For later work

38. Smyth, W.H. *et al.* 1995. *Ap. J.*, **440**, 349.

39. Morgenthaler, J.P. *et al.* 2001. *Ap. J.*, **563**, 451.

40. Oliverson, R.J. *et al.* 2002. *Ap.J.*, **581**, 770.

The following paper refers to discussion of Ly α observations.

41. Keller, H.U. 1976. *Space Sci. Rev.*, **18** 641.

Monte-Carlo approach is presented in

42. Combi, M. R. and Smyth, W. H. 1988. *Ap. J.*, **327**, 1044.

43. Combi, M. R., Bos, B. J. and Smyth, W. H. 1993. *Ap. J.*, **404**, 668.

Some papers pertaining to H α observations.

44. Smyth, W.H., Marconi, M.L., Scherb, F. and Roesler, F. 1993. *Ap. J.*, **413**, 756.

45. Morgenthaler, J.P. *et al.* 2002. *Earth Moon and Planets*, **(90)**, 77.

The basic formulation of gas phase chemistry in the coma can be found in

46. Huebner, W. F. and Giguere, P. T. 1980. *Ap. J.*, **238** 753.

For later work

47. Rodgers, S.D. and Charnley, S.B. 2002. *MNRAS*, **330**, 660.

48. Rodgers, S.D. *et al.* 2005. *Comets II*, eds. M.C. Festou, H.U. Keller and W.A. Weaver, Univ. Arizona, Tucson, p. 505.

The following papers give some results based on in situ measurements.

49. Balsiger, H. *et al.* 1986. *Nature*, **321**, 330.

50. Eberhardt, P. Meier, R., Krankowsky, D. and Hodges, R. 1994. *Astr. Ap.*, **288**, 315.

51. Meier, R., Eberhardt, P., Krankowsky, D. and Hodges, A.R. 1994. *Astr. Ap.*, **287**, 268.

52. Krankowsky, D. 1991. In *Comets in the Post-Halley Era*, eds. R. L. Newburn, Jr., *et al.* Kluwer Academic Publishers p. 855.

53. Keller, H.U. *et al.* 2005. *Comets II*, eds. M.C. Festou, H.U. Keller and W.A. Weaver, University Arizona, Tucson, p. 211.

54. Kissel, J., Krueger, F.R., Silen, J. *et al.* 2004. *Science*, **304**, 1774.

55. Tuzzolino, A.J., Economou, J.E., Clark, B.C. *et al.* 2004. *Science*, **304**, 1776.

The following papers may be referred for parent molecules.

56. Krasnopoesky, V. A. 1991. *Astr. Ap.*, **245**, 310.

57. Feldman, P.D., Cochran, A. and Combi, M.R., 2005. In *Comets II*, eds. M.C. Festou, H.U. Keller and H.A. Weaver, Univ. Arizona Press, Tucson, p. 433.

This page intentionally left blank

CHAPTER 7

Dust Tails

The gaseous material released by the nucleus was studied in the previous chapter. This material also carries with it a large amount of dust. The idea that the dust particles are dragged into the tail by the effect of radiation pressure was first suggested by Bessel in the 1830's. This concept was refined by Bredichin around 1900. These ideas were put on a firm basis by Finson and Probstein in the 1950's. These authors have worked out in great detail the dynamics of grains based on fluid and kinetic concepts and the resulting intensity distributions. Some of these aspects will be considered in this chapter.

7.1. Dynamics

Consider the case of only pure dust tails. The dust emitted by the nucleus is subjected to two opposite forces. The solar radiation pressure acting on the dust particles tries to push it away from the Sun while the force of solar gravity tries to pull it towards the Sun. Since the two forces vary as $(1/r^2)$, one usually defines an effective gravity, essentially given by the difference of the two forces. The Keplerian orbit mechanics is then used for the study of the dynamics of the dust particles. The ratio of radiation pressure to gravitational force is denoted by $(1 - \mu)$ where

$$(1 - \mu) = \frac{F_{\text{rad}}}{F_{\text{grav}}} \quad (7.1)$$

The expressions for F_{rad} and F_{grav} for a spherical particle can be written as

$$F_{\text{rad}} = \frac{\pi d^2}{4} \frac{Q_{\text{pr}}}{c} \left(\frac{F_{\odot}}{4\pi r^2} \right) \quad (7.2)$$

and

$$F_{\text{grav}} = \frac{GM_{\odot}}{r^2} \left(\frac{\rho_d \pi d^3}{6} \right). \quad (7.3)$$

Here F_{\odot} is the mean solar radiation field impinging on the grain of diameter d and density ρ_d . Q_{pr} is the efficiency factor for radiation pressure (Chap. 8). Therefore Eq. (7.1) becomes

$$(1 - \mu) = C(\rho_d d)^{-1} \quad (7.4)$$

$$\text{where } C = \frac{3Q_{\text{pr}} F_{\odot}}{8\pi c GM_{\odot}} = 1.2 \times 10^{-4} Q_{\text{pr}}.$$

The nature of the orbit of the particle is decided by the value of $(1 - \mu)$. There are two cases of interest that have to be considered. Firstly, particles are ejected continuously as a function of time by the nucleus. The locus of the particles which have the same value of $(1 - \mu)$ is called the *Syndynome* or *Syndyne* curve (Chap. 6). Physically this means that particles of the same size are emitted by the nucleus. The other case involves the distribution of particles emitted at any one particular time, as in the case of an outburst. These particles will have varying $(1 - \mu)$ values and the locus of the curve which describes this situation is called *Synchrone*.

The cometocentric coordinate system used to describe a comet tail is shown in Fig. 7.1. Here ξ and η represent the coordinates in the orbit plane of the comet. The third coordinate ζ is in the direction perpendicular to the plane of the orbit. Let the position of the comet be at A corresponding to the time of observation t . Consider the position of the comet corresponding to earlier times say t_1, t_2, t_3 and t_4 along its orbit. For simplicity assume the particles to be emitted from the nucleus with zero relative velocity and also of the same size. This implies that they have the same value of $(1 - \mu)$. The orbit of the particles can be worked out and the position on these trajectories for the time of observation t can be calculated. The final positions are also marked as t_1, t_2, t_3 and t_4 in the tail. Therefore the observed tail is just the locus of the dust particles in the (ξ, η) plane, that were emitted at different earlier times. This represents the Syndynome or Syndyne curve. The farther one goes along the tail, the earlier the time at which the particles were emitted. However, in a real situation, the particles are emitted with a certain velocity spread, which gives rise to the observed spread in the tail. The assumption that the particles have the same size is not very realistic as generally particles of various sizes are emitted at any instant of time. The actual trajectories of the particles are sensitive to

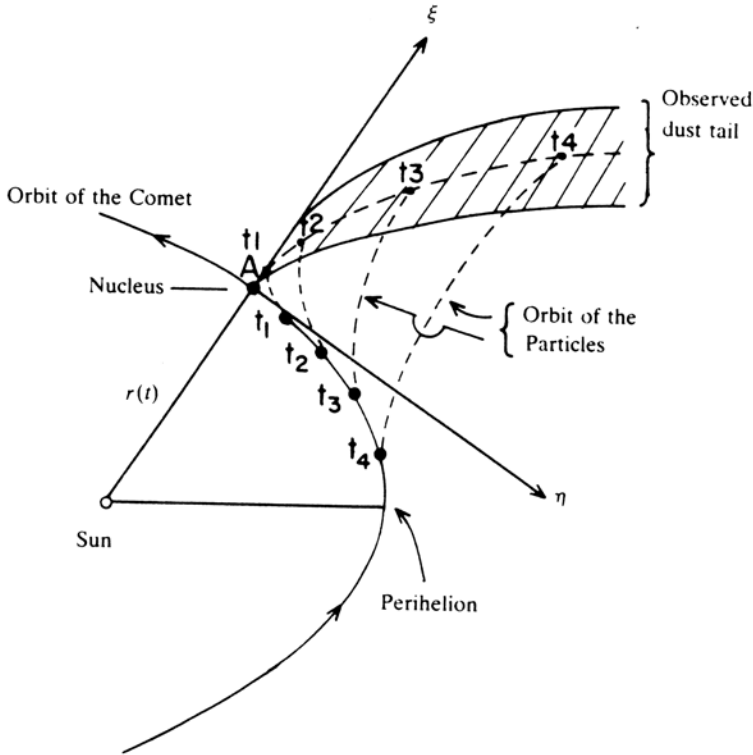


Fig. 7.1 Trajectories of the particles and the formation of the dust tail.

the particle size as can be seen from Eq. (7.4). The smaller size particles would have moved farther compared to those of larger size particles. All these effects have been incorporated in the dynamic model. Some of the calculated Syndynes and Syncranoes are shown in Fig. 7.2.

As mentioned already, in a real situation the dust particles are emitted continuously as well as with varying sizes from the nucleus for which

$$(1 - \mu) \propto (\rho_d d)^{-1}. \quad (7.5)$$

Let $\dot{N}_d(t)$ represent the dust production rate of all sizes in particles per second. For simplicity it is assumed that the distribution of particle sizes remains constant along the orbit of the comet. The particle distribution function g is given by

$$g(\rho_d d)d(\rho_d d) \text{ such that } \int_0^\infty g(\rho_d d)d(\rho_d d) = 1. \quad (7.6)$$

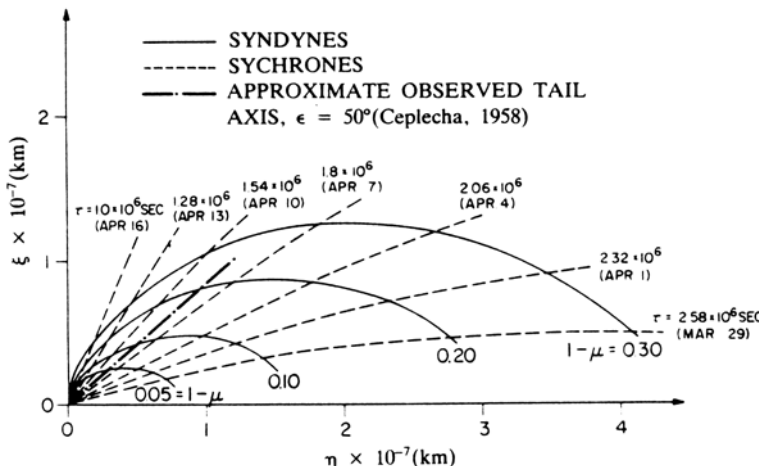


Fig. 7.2 Syndynes and Sychrones for Comet Arend-Roland on April 27, 1957. Time $\tau = 1.71 \times 10^6$ sec at perihelion on April 8. The position of the observed tail of the comet is also shown. (This figure as well as the other figures of this chapter are taken from Finsen, M.L. and Probstein, R.F. 1968. *Ap. J.* **154**, 327 and 353).

The quantities $\dot{N}_d(t)$ and $g(\rho_d d)$ are usually obtained from the fitting of the model with the observations.

For the calculation of the orbit of the particle, it is necessary to know the initial velocities of the dust particles coming out of the nucleus. The model for the calculation of the velocity of the dust particles is based on the steady state fluid approach. The flow is assumed to be spherically symmetric with the same temperature for the gas and dust at the nucleus and dust particles having a uniform size. The gas and the dust coming out of the nucleus are coupled through drag forces, computation of which is based on molecular drag coefficient. With no relative velocity to start with, the particles are accelerated outwards. The solution of the conservation equations gives the velocity of the dust particles. These calculations which are quite involved show that the dust particles reach their terminal speed within about 20 radii of the nucleus. This is indeed a very short distance and hence one generally uses terminal speed for the dust particles in the tail calculations. The terminal speed denoted as v_i can be expressed in the functional form as

$$\frac{v_i}{(C_p T)^{1/2}} = g(\mathcal{M}, \beta) \quad (7.7)$$

$$\mathcal{M} = \frac{\dot{m}_d}{\dot{m}_g} \text{ and } \beta = \frac{16}{3} \pi \rho_d d R_0 (C_p T)^{1/2} / \dot{m}_g$$

where \dot{m}_d is the mass flow rate for the dust and \dot{m}_g that of the gas. Therefore \mathcal{M} represents the dust-to-gas mass ratio. Here R_0 is the radius of the nucleus of the comet, T is the initial temperature of the gas and C_p the specific heat at constant pressure. Figure 7.3 shows a plot of the velocity of the dust particles as a function of β . Therefore the velocity can be written

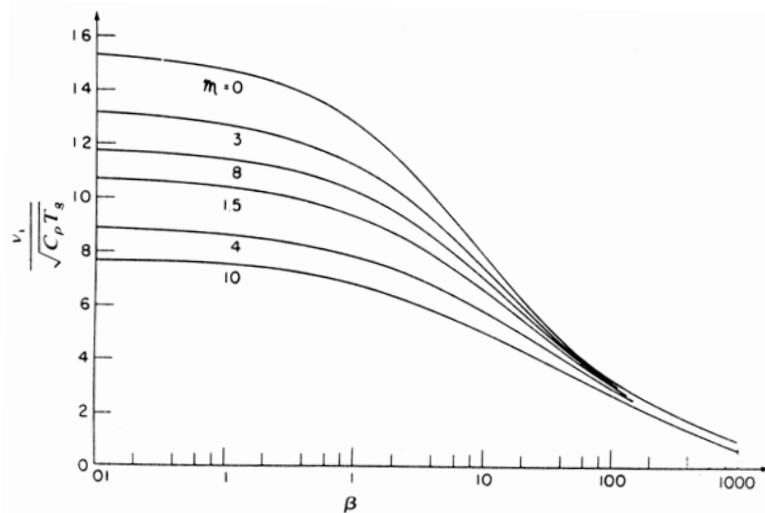


Fig. 7.3 Speed of the dust particles emitted from the inner head region (see text).

in the form

$$v_i = v_i(\rho_d d, \dot{N}_d, \dot{m}_g) \quad (7.8)$$

where T and R_0 are known. Based on these results, it is generally assumed that the dust comes out of the nucleus in a spherically symmetric manner whose speeds are given by the results shown in Fig. 7.3. The results of more detailed and realistic dust particle size distribution calculations show that the derived velocities are similar to those in Fig. 7.3, except that the terminal dust velocity is smaller by about 20% with respect to the single size dust particles. One can also keep \dot{m}_g , the gas mass flow rate, as a variable. This value can be obtained by comparing the theoretical calculations with the observations.

In order to compare with the observed isophotes, the total emission from the comet along the line of sight has to be calculated. It is necessary to calculate the integral of the number density along the line of sight, which is termed as surface density. Since the optical thickness in the dust tail

is small, the surface density is directly proportional to the light intensity. There are two approaches for calculating the surface density distribution in the tail. One procedure is to use the particles of various sizes emitted and then integrate over all the times (Synchrone approach). The other method is to consider one particle size and then integrate over all the sizes of the particles (Syndyne approach). The two approaches give the same result as they involve double integral involving $(1 - \mu)$ and time in both the cases. Only the order of integration in these two cases is reversed. For illustrative purposes, a brief discussion of the Syndyne approach will be presented.

Consider the position of the comet observed at a particular time t_c measured from the time of perihelion passage which is taken to be zero. For a given value of $(1 - \mu)$, the particles lying on a Syndyne curve would have been emitted at time

$$t = t_c - \tau \quad (7.9)$$

where τ increases along the Syndyne curve with zero value at the Syndyne origin. The number of particles emitted in the time τ and $\tau + d\tau$ and in the size range (ρ_{dd}) and $(\rho_{dd}) + d(\rho_{dd})$ is given by

$$\dot{N}_d(t)d\tau g(\rho_{dd})d(\rho_{dd}). \quad (7.10)$$

This has to be multiplied by the light scattering function to get the total scattered intensity. The scattered intensity is proportional to the cross-sectional area of the particle and hence varies as $(\rho_{dd})^2$. Working in terms of $(1 - \mu)$ rather than (ρ_{dd}) , the new weighted distribution function can be written as

$$f(1 - \mu)d(1 - \mu) \propto g(\rho_{dd})(\rho_{dd})^2d(\rho_{dd}) \quad (7.11)$$

such that $\int_0^\infty f(1 - \mu)d(1 - \mu) = 1$. Therefore the Eq. (7.10) can also be expressed as

$$\dot{N}_d d\tau f(1 - \mu)d(1 - \mu). \quad (7.12)$$

These particles then follow well-defined orbits in the plane of the orbit of the comet. However what is actually seen is the projection of these orbits in the plane of the sky. Therefore, the expected intensities in the plane of the sky has to be calculated. The total modified surface density is obtained by integrating over various Syndyne tails for all values of $(1 - \mu)$. The final expression is of the form

$$D = \int_{(1-\mu)_a}^{(1-\mu)_b} \dot{N}_d f(1 - \mu) \left[2v_i \tau \frac{dx}{d\tau}(\tau; 1 - \mu; t_c) \right]^{-1} d(1 - \mu) \quad (7.13)$$

Here $dx/d\tau$ represents the rate of change of length along the given Syndyne axis with respect to τ . Physically it represents the effect on the surface density due to dispersion in the longitudinal direction with respect to the tail axis. On the other hand the other term $v_i\tau$ arises due to the dispersion in the lateral direction. The Eq. (7.13) involves the functional parameters $\dot{N}_d(t)$, $f(1 - \mu)$ and $v_i(\tau; 1 - \mu; t_c)$. These can be determined from a comparison of the expected and the observed intensity distributions. From a knowledge of these three parameters, all other quantities of interest can then be determined.

The above formalism has been applied very successfully to Comet Arend-Roland as can be seen from Fig. 7.4. Near perihelion, the gas and

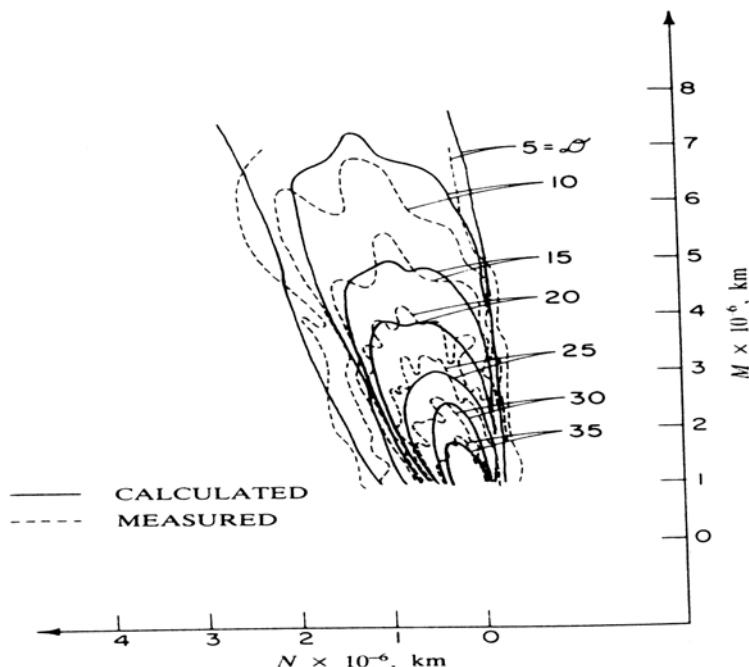


Fig. 7.4 Measured and calculated isophotes for Comet Arend-Roland for May 1, 1957. D is the density level.

the dust emission rates are about 7.5×10^7 gm/sec and 6×10^7 gm/sec. This gas emission rate corresponds to a value of about 1.5×10^{30} molecule/sec. The dust to gas ratio for Comet Arend-Roland is about 0.8 and the average size of the particles in the tail is $\sim 1 \mu\text{m}$. The particles in the observed dust

tail of Comet Arend-Roland correspond to those which have been emitted about 10 to 15 days on either side of the perihelion passage. The method has also been applied successfully to several other comets.

Although Finson and Probstein formalism has been very successful in the studies of tail morphology, it has several limitations. All the grains are assumed to be of the same kind and it is difficult to distinguish between different kinds of grains. The observation of comets has clearly shown a wide variation in the chemical and physical nature of grains. The value of Q_{pr} is also not constant but is dependent upon the sizes of the particles. If the grains of various sizes are emitted continuously, it is difficult to separate the effects depending on the time of ejection from those due to the size and properties of the grains. Therefore several studies have been carried out to take care of some of the above limitations. However, these studies with complicated numerical integration techniques, loose the great advantage of the simplicity of the Finson and Probstein approach. But they are highly successful.

One of these is the Inverse Monte Carlo dust tail model. In this model, the orbit of sample dust particles are calculated which takes into account the anisotropy in dust ejection, dust ejection velocity for each dust particle etc. for modelling the cometary dust tails. The model has been applied to large number of observed cometary dust tails with good agreement. The model also calculates the dust mass rate and the time dependent size distribution function. The time average of size distribution function gives a value of $\alpha = -3.5$ for the power law index. The resulting dust size range between 1 μm and about 1 cm.

7.2. Anti-tail

Many comets generally show a short tail in the solar direction which is called the *anti-tail* (see Fig. 1.15). The anti-tail really do not point towards the sun. It is related to the geometry of the system. The theory developed for the dynamics of the grains of dust tails can also explain the presence of anti-tail in comets. The calculated Synchrones and Syndynes for Comet Arend-Roland are shown in Fig. 7.5 which shows the presence of Synchrones in the direction of the Sun. The size of the particles giving rise to these synchrons is $\gtrsim 10 \mu\text{m}$, which is much larger than those present in the dust tails which is $\lesssim 1 \mu\text{m}$. The appearance of the anti-tail of Comet Arend-Roland changed with time within an interval of a few days. This

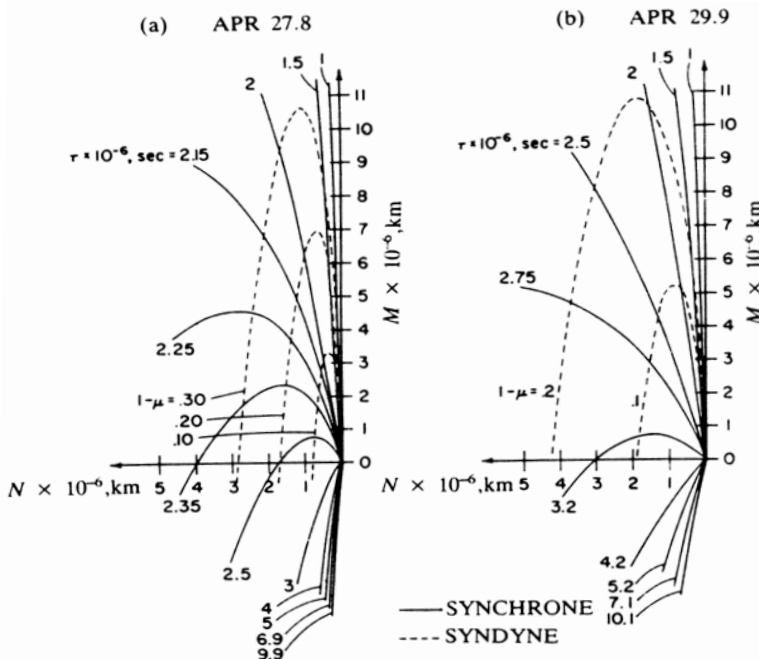


Fig. 7.5 Calculated Syndynes and Synchrones for tail and anti-tail for Comet Arend-Roland.

arises due to the changing pattern of the positions of the synchrones. If the synchrones are crowded together, then the anti-tail will be seen as a narrow tail, while if the synchrones are spread out, the anti-tail will be a broad one. The visibility of an anti-tail depends mainly on the sun-comet-earth geometry. It can be seen clearly only when the orbit of the comet cuts the orbital plane of the Earth.

The anti-tail of Comet Kohoutek could be seen shortly after perihelion. Comet Halley also displayed anti-tail after its perihelion passage. In general, the anti-tail is more favourable for observation after perihelion.

The dynamical theory of grains has been applied very successfully to the observed anti-tail of many comets. In fact, the predictions of the anti-tail based on the theory have later been confirmed through observations. The large size grains present in the anti-tail is also consistent with the estimated size of the particles based on the absence of $10 \mu\text{m}$ emission feature in the anti-tail of Comet Kohoutek (Chap. 9). The presence of anti-tail of comets is therefore generally explained as due to the effect of large size particles.

It is evident from the dynamical theory of grains that the size of the particles along the tail should vary and it depends upon the nature of Synchrone and Syndyne curves. Since the polarization measurements are sensitive to particle sizes, they could effectively be used for determining the sizes of the particles. The polarization measurements on comets do seem to indicate the variation of the particle size along the tail of the comet.

7.3. Dust Trails

Dust trails were first seen on Comet Tempel 2 from the observations carried out with the Infrared Astronomical Satellite. They are very narrow with length to width ratio of around 200 to 1. Many of the trails are found to coincide with the orbit of comets. Dynamical calculations show that the observed dust trails are coincident with large size particle trajectories indicating the presence of particles in the size range of about millimetre to centimetre. These particles are ejected out at low velocities \sim a few m/s from the nucleus. The narrowness of the trail indicate that the velocity dispersion is quite low and are therefore stable against perturbing forces over periods of atleast a few orbital revolutions. Therefore the observed dust trails is the resultant effect of the build up of large particle emissions over several orbits. The observations carried out with ISO could spatially resolve the dust trail in Comet Encke. Because of very large particles present in dust trails, it may be too faint to be seen in the visible region. However it has been detected along the orbit of Comet Kopff in the visible region when the comet was at $r = 3.01$ AU. Therefore study of dust trails in comets in the visible region should help in a better understanding of the nature of very large size particles.

7.4. Sodium Gas Tails

A narrow, straight and long tail along with a diffuse tail superposed over the dust tail composed of sodium atoms has been seen in the bright Comets Hale-Bopp and Hyakutake. These were seen in the images taken with filters centred on the sodium D lines at 5890 Å. These are similar to plasma tail and dust tail that are generally seen in comets. The straight sodium tail extending upto $\sim 10^7$ km is located between the ion tail and the prolonged radius vector. The straight tail could arise from the dissociation of some molecule containing sodium which is then dragged out due to radiation

pressure. The diffuse sodium tail could arise by the release of sodium from dust grains due to some physical processes, such as evaporation and sputtering. It is possible that sodium tails could be a common feature of comets.

7.5. Dust features

The high quality photographs near the nuclear region show highly complicated structure of various kinds as can be seen from Fig. 7.6. This arises

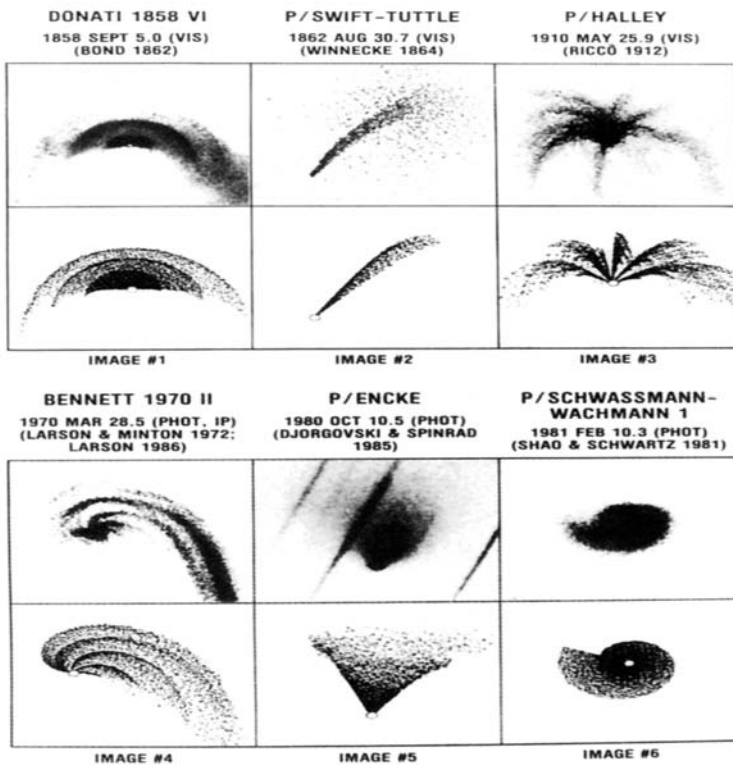


Fig. 7.6 The top rows show the various types of features observed in six comets in the vicinity of the nucleus. The bottom rows show the computer simulated images. There is a good similarity between the two. The Sun is at the top. (Sekanina, Z. 1991. In *Comets in the Post-Halley Era*, eds. R.L. Newburn, Jr., et al. Kluwer Academic Publishers, p. 769).

due to the complicated flow pattern of the grains after they are released from the nucleus. To a first approximation it can be described in terms of the resulting force between the gravitational, F_{grav} and radiation F_{rad} , forces acting on the grains (Sec. 7.1). The trajectories of the grains under such a force in a cometocentric system are approximately parabolic in nature. Different patterns could be produced depending on the parameters of the grains like radius, density and the material property (Fig. 7.7). In a

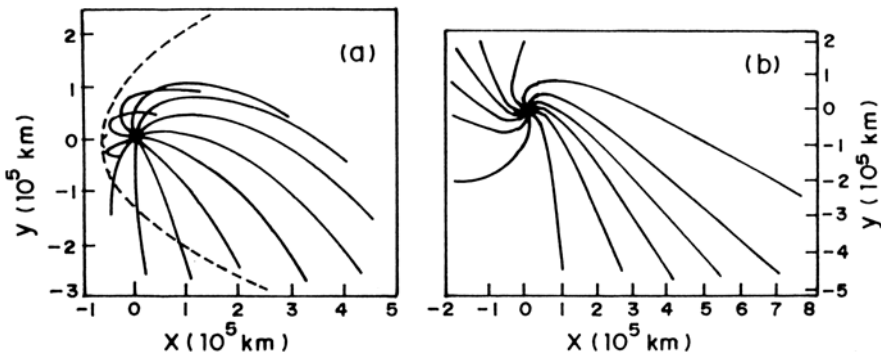


Fig. 7.7 Dust particle trajectories for Comet Halley released from the nucleus at the time of perihelion passage. (a) and (b) correspond to particle sizes of $10\mu\text{m}$ and 0.8 mm respectively. The dotted curve shows the resulting envelope (Fertig, J. and Schwehm, G. 1984. *Adv. Space Res.* **4**, 213).

real situation the spin of the nucleus, its associated precession and nutation and the cometary activity has to be considered. These will give rise to complex behaviour of the flow patterns of the dust particles in the near nucleus region. For example, arising from a single active area on the nucleus, the spiral jets unwind and develop into expanding parabolic envelopes and so on. It is rather difficult to take into account all these effects in the model calculations. Therefore several attempts have been made to understand the observed features in terms of simple hydrodynamic models. Another approach that has been attempted is to understand the flow patterns through computer generated synthetic images by varying the parameters. As can be seen from Fig. 7.6, the computer simulation technique can in principle reproduce the diverse patterns of the observed dust structures of comets. However the disadvantage of this method is that there are many parameters involved which have to be adjusted by trial and error method to match the observations, such as the angles associated with spin axis positions and its relation to Earth and Sun, rotation period, position of active regions, dust

properties and so on. Therefore it is possible to have multiple solutions in this approach. To limit the number of solutions, it is preferable to fix some of the parameters based on some other observations.

Several other fine features have also been seen in comets. The streamers seen are straight and curved structures which converge towards the nucleus. They are generally associated with synchrones. For example the streamers seen in Comet West (1976 VI) have been attributed to particles of different sizes expelled simultaneously from the nucleus in the form of an outburst. Therefore long streamers are indicative of large dispersion of particle sizes, whereas a narrow width reflects a short duration outburst. Several well separated dust streamers have been seen in the images of Comet Halley. The analysis of these streamers is consistent with the interpretation that they represent diffuse synchrones of dust particles. The time interval between these streamers is found to be around 2.2 days which corresponds to the rotational period of the nucleus.

Another kind of feature, called *striae* has been seen in several comets. These are characterized by a series of parallel narrow bands at large distances from the nucleus. They do not start from the nucleus. The mechanism of formation of striae is not clear at the present time.

The dynamical theory developed to explain the shape of the dust tail of comets has been very successful in explaining the observations. In particular it can explain quantitatively the observed isophotes of dust tails of comets. It has also been possible to get production rates of the gas and dust and therefore the dust to gas ratio. The theory is also very successful in explaining the presence of anti-tail in comets. Several sophisticated models have been carried out over the simple dynamical theory, which can explain in detail the observed dust tail of comets.

Problems

1. A grain of size a and density ρ is moving in a medium of hydrogen density N_H due to the effect of radiation pressure of a star of temperature T and radius R . The grain is being slowed down by the drag force due to the hitting of the grain and sticking to it. Show that the terminal speed of the grain is given by

$$v_t = \left(\frac{R^2 \sigma T^4}{m_H c} \right)^{1/2} \frac{1}{N_H^{1/2} r}.$$

- Hint: Use the conservation of momentum of the particle for calculating the drag force.
2. Why does the length of the dust tail change with heliocentric distance?
At what distance from the Sun will the tail have the maximum extent.
 3. How does the tail of a comet look, when it passes by Jupiter at a close distance?

References

The theory of dynamics of dust tails is worked out in detail in these papers

1. Finson, M.L. and Probstein, R.F. 1968. *Ap. J.* **154**, p. 327. (Paper I), p. 353 (Paper II).

Other relevant papers are the following

2. Crifo, J.F. 1991. *In Comets in Post-Halley Era*, eds. R.L. Newburn, Jr. *et al.*, Kluwer Academic Publishers, Vol. **2**, p. 937.
3. Fulle, M. 1989. *Astr. Ap.* **217**, 283.
4. Fulle, M. 2005. In *Comets II*, eds. M.C. Festou, H.U. Keller and W.A. Weaver, Univ. Arizona Press, Tucson, p. 565.
5. Grün, E. and Jessberger, E.K. 1990. *In physics and chemistry of comets*. ed. W.F. Huebner. Springer-Verlag. p. 113.
6. Richer, K. and Keller, H.U. 1987. *Astr. Ap.* **171**, 317.
7. Sekanina, Z. and Farrell, J.A. 1978. *A.J.* **87**, 1836.

Dust Trail

8. Eaton, N., Davis, J.K. and Green, S.F. 1984. *MNRAS*, **211**, 15.
9. Sykes, M.V., Lebofsky, L.A., Hunten, D.M. *et al.* *Science*, 1986. **232**, 1115.

Detection in the visible for the first time

10. Ishiguro, M., Watanabe, J., Usui, F. *et al.* 2002. *Ap. J.*, **572**, L117.

Cometary dust features can be seen in

11. Rahe, J., Donn, B. and Wurm, K. 1969. *Atlas of Cometary Forms*, NASA SP-198 U.S. Govt. Printing Office, Washington D.C.

The following papers discuss model calculation of features

12. Vasundhara, R., Chakraborty, P., Muneer, S. *et al.* 2007. *A.J.*, **133**, 612.
13. Sekanina, Z., Brownlee, D.E., Economou, T.E. *et al.* 2004. *Science*, **304**, 1769.

CHAPTER 8

Light Scattering Theory

The dust particles present in comets scatter and absorb the incident solar radiation. In fact, it is the scattered solar radiation which makes the dust tail of comets visible. The infrared radiation that has been seen from comets is also directly related to the amount of incident radiation absorbed by the dust particles. Therefore the theory of scattering of light by small particles is basic to the study of cometary grains. The aim is to determine, from theory, the distribution of intensity of the scattered radiation and the polarization as a function of the scattering angle. It is also of interest to know the cross sections for the absorption and scattering processes, which determine the albedo of the particles. The efficiency factor for the radiation pressure is also of interest, as was discussed in the last chapter. All these quantities depend upon the shape, structure and composition of the grain. The theories of scattering have been developed for well-defined particle shapes like spheres, concentric spheres, cylinders, spheroids and so on. However, grains in general are likely to be irregular in shape, inhomogeneous and fluffy in nature. The theory of scattering from such grains is highly complex. Hence, at the present time attempts are being made to study the scattering from such grains from the theoretical points of view with certain approximations. The study is also being pursued through experimental means. We will briefly discuss some of these aspects in this chapter.

8.1. Mie Scattering Theory

8.1.1. Efficiency factors

The theory of scattering by spherical particles of homogeneous composition involves the solution of Maxwell's equations with appropriate boundary conditions on the sphere. This was worked out by Mie in 1908 and independently by Debye in 1909. Since an excellent account of the solution of this scattering problem, generally known as Mie Theory, is discussed in many books, we will summarize here only the results with particular reference to the case of cometary dust.

The scattering properties of a particle depend upon the following quantities: (1) the property of the medium, usually specified by the complex refractive index, $m = n - ik$, where n and k are the refractive and absorptive indices respectively. (2) the wavelength of the incident radiation (λ) and (3) the size of the particle (a). As a result of radiation interacting with the particle, part of the radiation is absorbed and part of it is scattered. Therefore, the total amount of radiation lost from the incident beam (extinction) is the sum total of the absorbed and the scattered components. These are generally expressed in terms of the dimensionless efficiency factors, Q_{sca} and Q_{abs} for the scattering and absorption components. The efficiency factor for the total extinction is given by

$$Q_{\text{ext}} = Q_{\text{sca}} + Q_{\text{abs}}. \quad (8.1)$$

If C_{sca} , C_{abs} and C_{ext} denote the corresponding cross sections, then

$$C_{\text{sca}} = \pi a^2 Q_{\text{sca}} \quad (8.2)$$

$$C_{\text{abs}} = \pi a^2 Q_{\text{abs}} \quad (8.3)$$

and

$$C_{\text{ext}} = \pi a^2 Q_{\text{ext}}. \quad (8.4)$$

The main aim is to determine the efficiency factors Q_{sca} and Q_{abs} from the scattering theory. They are given by

$$Q_{\text{sca}} = \frac{2}{x^2} \sum_{n=1}^{\infty} (2n+1) \{ |a_n|^2 + |b_n|^2 \} \quad (8.5)$$

$$Q_{\text{ext}} = \frac{2}{x^2} \sum_{n=1}^{\infty} (2n+1) \{ \text{Re}(a_n + b_n) \} \quad (8.6)$$

where the dimensionless parameter $x = (2\pi a/\lambda)$ and Re represents the real part. The scattering coefficients a_n and b_n are given by

$$a_n = \frac{\psi'_n(mx)\psi_n(x) - m\psi_n(mx)\psi'_n(x)}{\psi'_n(mx)\zeta_n(x) - m\psi_n(mx)\zeta'_n(x)} \quad (8.7)$$

$$b_n = \frac{m\psi'_n(mx)\psi_n(x) - \psi_n(mx)\psi'_n(x)}{m\psi'_n(mx)\zeta_n(x) - \psi_n(mx)\zeta'_n(x)}. \quad (8.8)$$

ψ_n and ζ_n are the modified Bessel functions known as the Riccati-Bessel functions. The addition of a prime to the Riccati-Bessel functions denotes the differentiation with respect to their arguments. Riccati-Bessel functions can be expressed in terms of Bessel functions, J , as follows

$$\psi_n(y) = \left(\frac{\pi y}{2}\right)^{1/2} J_{n+1/2}(y) \quad (8.9)$$

and

$$\zeta_n(y) = \left(\frac{\pi y}{2}\right)^{1/2} [J_{n+1/2}(y) + i(-1)^n J_{-n-1/2}(y)] \quad (8.10)$$

where y represents either mx or x . The third Riccati-Bessel function can be defined as

$$\chi_n(y) = (-1)^n \left(\frac{\pi y}{2}\right)^{1/2} J_{-n-1/2}(y) \quad (8.11)$$

The functions $\psi_n(y)$ and $\chi_n(y)$ are connected through the identity

$$\zeta_n(y) = \psi_n(y) + i\chi_n(y). \quad (8.12)$$

In addition to energy, light carries momentum. Therefore a beam that interacts with the particle will exert a force on the particle called radiation pressure. With the assumption that all the photons absorbed by the particle transfer all their momentum and hence exert a force in the direction of propagation, the efficiency for radiation pressure is given by the difference between the total extinction and the amount of scattered light.

$$\text{i.e. } Q_{\text{pr}} = Q_{\text{ext}} - \overline{\cos \theta} Q_{\text{sca}} \quad (8.13)$$

where

$$\begin{aligned} \overline{\cos \theta} Q_{\text{sca}} &= \frac{4}{x^2} \sum_{n=1}^x \left\{ \frac{n(n+2)}{n+1} [\text{Re}(a_n)\text{Re}(a_{n+1}) \right. \\ &\quad + \text{Im}(a_n)\text{Im}(a_{n+1}) + \text{Re}(b_n)\text{Re}(b_{n+1}) \\ &\quad \left. + \text{Im}(b_n)\text{Im}(b_{n+1})] + \frac{2n+1}{n(n+1)} [\text{Re}(a_n)\text{Re}(b_n) + \text{Im}(a_n)\text{Im}(b_n)] \right\} \end{aligned} \quad (8.14)$$

where Re and Im represent the real and imaginary quantities. The efficiency for radiation pressure is of interest in the study of dynamics of grains. The value of $\overline{\cos\theta}$ is also sometimes known as the asymmetry factor.

$$\text{i.e. } g = \overline{\cos\theta}. \quad (8.14a)$$

The value of $g = 0$ for a particle that scatters isotropically and $g > 0$ for preferentially scattering in the forward direction. For complete forward scattering $g = 1$. For $g < 0$ the scattered radiation is in the backward direction. The cross sections given by Eqs. (8.5) and (8.6) refer to a particle of a given size. However, in general, a medium will consist of particles of various sizes. If $n(a)$ represents the number of particles per unit volume in the size range a and $a + da$ then the total extinction is given by the expression

$$Q_{\text{total}}(\lambda) = \int \pi a^2 Q_{\text{ext}}(a, \lambda) n(a) da. \quad (8.15)$$

8.1.2. Albedo

Another quantity of interest is the amount of energy scattered from the incident beam, called the *albedo* of the particle. In the general case, when the scattered contributions from diffracted, refracted and reflected components are taken into account, the albedo of the particle is defined as

$$\gamma = \frac{Q_{\text{sca}}}{Q_{\text{ext}}}. \quad (8.16)$$

If the diffraction component is not taken into account, it is called the bond albedo. Therefore the bond albedo is defined as the ratio of the energy refracted and reflected by the particle in all directions to the energy incident on the geometric cross section.

$$\text{i.e. } A_B = \frac{1}{G} \int \sigma_r(\theta, \phi) d\omega \quad (8.16a)$$

Here $\sigma_r(\theta, \phi)$ is the differential scattering cross-section. For the case when there is symmetry with respect to the direction of incident radiation, then

$$\sigma_r(\theta, \phi) = \sigma_r(\theta).$$

The geometric albedo A_p is defined as the energy scattered by the particle at $\theta = 180^\circ$ (backward scattering) to that scattered by a white disk

of the same geometric cross section, scattering according to Lambert's Law ($\sigma_r(180^\circ) = G/\pi$).

$$\text{i.e. } A_p = \frac{\pi}{G} \sigma_r(180^\circ). \quad (8.16b)$$

The bond albedo A_B is related to the geometrical albedo A_p by the relation

$$A_B = A_p \cdot q \quad (8.16c)$$

where

$$q = 2 \int_0^\pi j(\theta) \sin \theta d\theta.$$

Here $j(\theta) = \sigma_r(\theta)/\sigma_r(180^\circ) \equiv F(\theta)/F(180^\circ)$, the ratio of the phase functions and q is known as the phase integral. For isotropic scattering, $A_B = 1$ and $A_p = 0.25$ and therefore $q = 4$.

8.1.3. Scattered intensity

The major physical quantity of interest is the intensity of the scattered radiation as a function of the scattering angle. If I_0 is the original intensity impinging on the grain, the intensity of the light scattered into unit solid angle for the scattering angle θ defined with respect to the incident beam (Fig. 8.1) is given by $F(\theta)I_o$, where $F(\theta)$ denotes the phase function. Therefore a plot of $F(\theta)$ versus θ gives the angular distribution of the

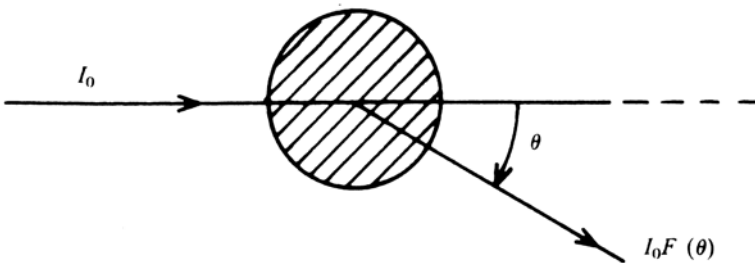


Fig. 8.1 Schematic diagram of a scattering process. θ is the scattering angle and $I_o(\theta)F(\theta)$ is the intensity of the scattered radiation from the original incident radiation of I_o .

scattered radiation and is known as scattering diagram. The scattering phase function is related to the complex scattering amplitudes $s_1(\theta)$ and $s_2(\theta)$ as

$$\begin{aligned} F(\theta) &= \frac{1}{2k^2} [|s_1(\theta)|^2 + |s_2(\theta)|^2] \\ &= i_1 + i_2 \end{aligned} \quad (8.17)$$

where $k = (2\pi/\lambda)$. The quantity i_1 and i_2 are essentially the components of intensity in the direction perpendicular and parallel to the scattering plane. The scattering plane contains the incident radiation and the direction of the scattered wave. The expressions for $s_1(\theta)$ and $s_2(\theta)$ are given in terms of the scattering coefficients a_n and b_n as

$$s_1(\theta) = \sum_{n=1}^{\infty} \frac{2n+1}{n(n+1)} \{a_n \pi_n(\cos \theta) + b_n \tau_n(\cos \theta)\} \quad (8.18)$$

$$s_2(\theta) = \sum_{n=1}^{\infty} \frac{2n+1}{n(n+1)} \{b_n \pi_n(\cos \theta) + a_n \tau_n(\cos \theta)\} \quad (8.19)$$

where

$$\pi_n(\cos \theta) = \frac{1}{\sin \theta} P_n^1(\cos \theta) \quad (8.20)$$

and

$$\tau_n(\cos \theta) = \frac{d}{d\theta} P_n^1(\cos \theta). \quad (8.21)$$

Here P_n 's are the Legendre polynomials.

8.1.4. *Polarization*

The scattered intensities i_1 and i_2 in the two directions are a function of the scattering angle. Therefore the polarization of the resulting radiation is defined as

$$P = \frac{i_1 - i_2}{i_1 + i_2}. \quad (8.22)$$

The value of $|P|$ varies from 0 to 1. The sign of P could be positive or negative. Positive and negative signs imply that the scattered light is polarized perpendicular or parallel to the scattering plane respectively. The value of P for the scattering angles, $\theta = 0^\circ$ and 180° , is equal to zero as $i_1 = i_2$. In addition to linear polarization, circular polarization also may be seen in certain favourable cases. The circular polarization arises if the refractive indices are different for the two states of polarization. In general, the circular polarization is one or two orders of magnitude smaller than that of linear polarization.

8.2. Approximate Expressions

So far we have been considering the exact expressions for the efficiency factors for the scattering and the extinction by the spherical particles. In many practical situations, like in the infrared and far infrared regions, where the condition that the size of the particle is very much less than the wavelength of the radiation, i.e., $x \lesssim 1$ is satisfied, the approximate analytical expressions of Eqs. (8.5) and (8.6) may be used. Under the above condition, the Eqs. (8.5) and (8.6) reduce to

$$Q_{\text{sca}} = \frac{8}{3}x^4 \operatorname{Re} \left\{ \frac{m^2 - 1}{m^2 + 2} \right\}^2 \quad (8.23)$$

and

$$Q_{\text{abs}} = -4x \operatorname{Im} \left\{ \frac{m^2 - 1}{m^2 + 2} \right\}. \quad (8.24)$$

If further m is real, i.e. no absorption, then

$$Q_{\text{sca}} = Q_{\text{ext}} \approx \frac{8}{3}x^4 \left| \frac{m^2 - 1}{m^2 + 2} \right|^2 \quad (8.25)$$

and $Q_{\text{abs}} = 0$.

8.3. Computation of Cross Sections

The actual evaluation of the efficiency factors has been considered in detail by various investigators. Various methods have been proposed for the calculation of efficiency factors starting from the simple expansion techniques. The main problem is to calculate the coefficients a_n and b_n and this is quite tedious. The calculation of a_n and b_n involves a knowledge of the quantities ψ_n , ψ'_n and others which in turn depend upon the Bessel functions with complex arguments. The computation of these quantities becomes complicated when the refractive index is complex. However they can be calculated easily using recurrence relations with the help of a computer. The following recurrence relations can be used to derive the Riccati-Bessel functions.

$$\psi_n(y) = \frac{2n - 1}{y} \quad \psi_{n-1}(y) - \psi_{n-2}(y) \quad (8.26)$$

$$\psi'_n(y) = -\frac{n}{y} \quad \psi_n(y) + \psi_{n-1}(y) \quad (8.27)$$

$$\chi_n(y) = \frac{2n-1}{y} \quad \chi_{n-1}(y) - \chi_{n-2}(y) \quad (8.28)$$

and

$$\chi'_n(y) = \frac{n+1}{y} \quad \chi_n(y) - \chi_{n+1}(y) \quad (8.29)$$

with

$$\psi_0(y) = \sin y \quad (8.30)$$

$$\psi_1(y) = \frac{\sin y}{y} - \cos y \quad (8.31)$$

$$\chi_0(y) = \cos y \quad (8.32)$$

and

$$\chi_1(y) = \frac{\cos y}{y} + \sin y. \quad (8.33)$$

Therefore all the functions that enter in a_n and b_n can be generated. Hence the efficiency factors can be computed for any given value of m and x . The number of terms to be included in Eqs. (8.5) and (8.6) depend upon the parameters x and m . If x is large, more terms have to be included in the calculation of a_n and b_n . However with the availability of computers it is easy to sum over all the terms till the required accuracy is achieved in the calculated efficiency factors. Many investigators have developed efficient computer programs for the calculation of these quantities which are readily available in the literature.

8.4. Results

For astrophysical situations, one seems to deal with the real part of the refractive index of the particles, which is of the order of 1.3 to 1.6 (Chap. 9). Therefore, for illustrative purposes, the extinction cross-section is plotted as a function of x for constant indices of refraction of 1.3 and 1.6 in Fig. 8.2. Since the indices of refraction are assumed to be constant, the nature of the curves remains the same when the size or wavelength is changed. But in a real situation, the refractive index of the material is a function of the wavelength which has to be incorporated. The results of such calculations give a better physical picture and show more structures in the curves arising due to the material property. The curves in Fig. 8.2 display several interesting features. A series of broad maxima and minima can be

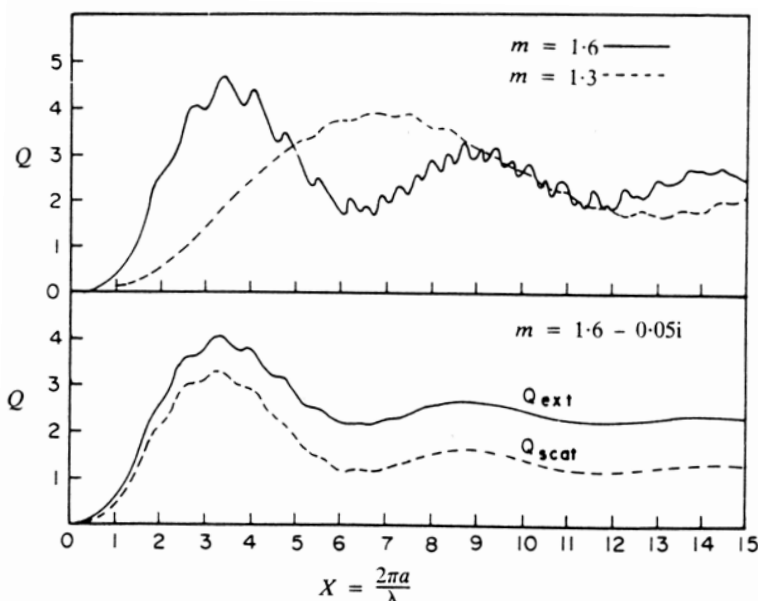


Fig. 8.2 The efficiency factors for extinction and scattering for spheres calculated from the Mie Theory are plotted as a function of the dimensionless parameter X . The results are shown for three sample cases. (Adapted from Wickramasinghe, N.C. 1973. *Light scattering functions for small particles*. London: Adam Hilger).

seen easily. Superposed on these band features are the small irregular fine structures generally called the ripple structure. The curve for small values of x refers to Rayleigh scattering region, where it varies as $(1/\lambda^4)$. For intermediate values of x , the variation is given by $(1/\lambda)$. For large values of x , the value of Q_{ext} approaches a value of 2. It is interesting to note that the limiting value 2 is twice as large as the cross section given by the geometrical optics. This is essentially related to the fact that the geometrical optics is strictly not valid in the neighbourhood of the edges of the object. So one has to use the diffraction theory. The additional factor of πa^2 comes due to this reason. The effect of absorption in the Q_{ext} is to reduce the strength of the resonances and the curve becomes smooth (Fig. 8.2). For very large values of x , the absorption and scattering contribute almost equally while for small values of x , the total extinction is mainly contributed by the absorption process. The effect of increase in the absorption coefficient is to reduce the albedo of the particle.

The scattering intensity for various angles is shown in Fig. 8.3. The

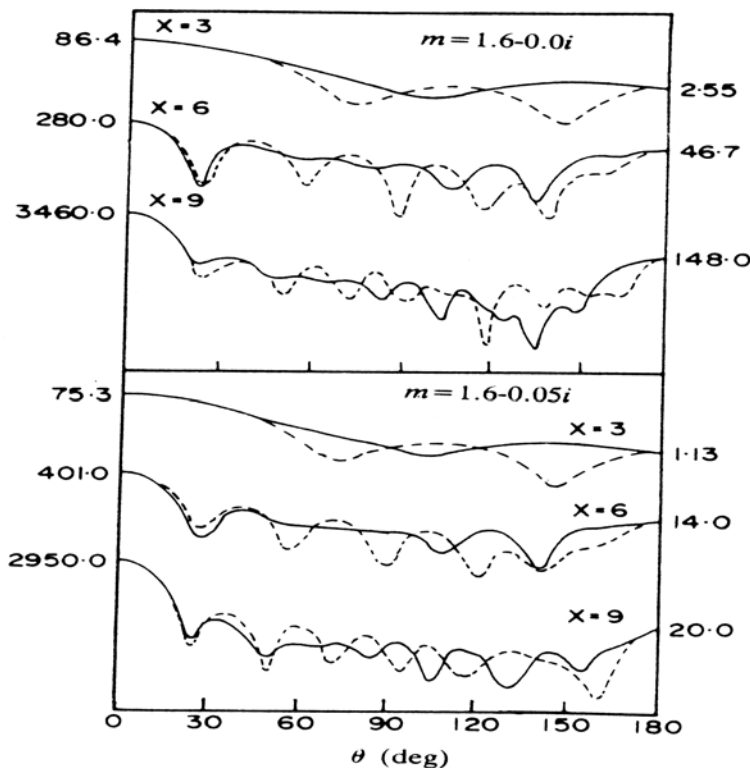


Fig. 8.3 The intensities I_1 (dashed curve) and I_2 (solid curve) are plotted as a function of the scattering angle for two representative values of the refractive index. Each curve is labeled by the parameter X . (Adapted from Wickramasinghe. N.C. 1973. *op. cit.*).

values of the intensity at 0° and 180° are marked in the margin of the curve. The most important point to note from the curve is that the scattering is mostly in the forward direction ($\theta = 0^\circ$) and it oscillates with the scattering angle. The scattering diagrams for a few cases are shown schematically in Fig. 8.4. For isotropic scattering the intensity is the same in all directions. For Rayleigh scattering i.e., particle size \lesssim wavelength of the incident radiation, the phase function $\propto (1 + \cos^2 \theta)$ where θ is the scattering angle. This dependence shows that the resultant diagram shown by the solid line is a superposition of two different components. One component which is isotropic, is shown by dashed lines and the second component is shown by two lobes. The Mie scattering diagram for $m = 1.3$, $x \approx 1$ and $x > 1$ is also shown in Fig. 8.4. Here as x increases, the scattering becomes more

and more forward peaked.

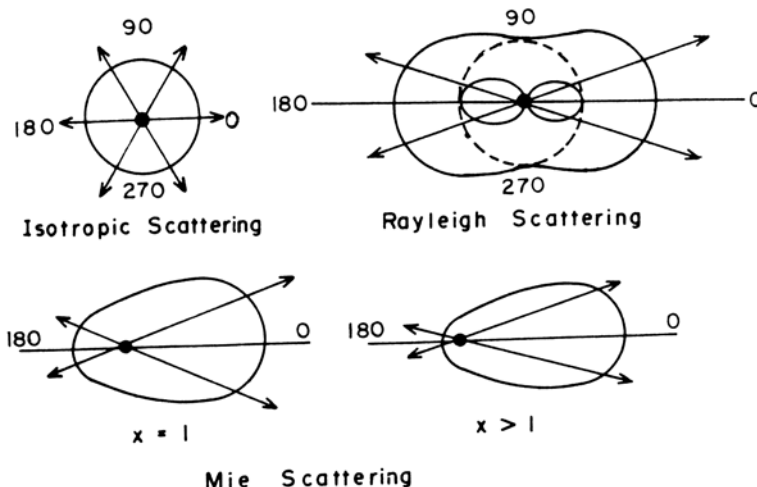


Fig. 8.4 Schematic scattering diagrams for various cases.

However, in any real situation, there will be a distribution of particle sizes. Therefore the cross-sections have to be averaged over the size distribution function. Several analytical expressions have been used for averaging the cross-sections. For the purpose of illustration Fig. 8.5 shows the results for the size distribution of the form

$$n(r) = \text{constant } r^{(1-3b)/b} e^{-r/ab} \quad (8.34)$$

where $a = r_{\text{eff}}$ and $b = v_{\text{eff}}$. Here r_{eff} and v_{eff} represent a mean radius for scattering and a measure of the width of the size distribution function respectively, $b = 0$ refers to the case of single particles. The effect of the size distribution function is to average out the ripple structure which smoothens it out. It also dampens the resonance effects. Therefore the curve becomes smooth. The results for phase function and linear polarization are shown in Fig. 8.6. Although the results refer to a particular size distribution function, the general trend and nature of the results are similar for any other size distribution function.

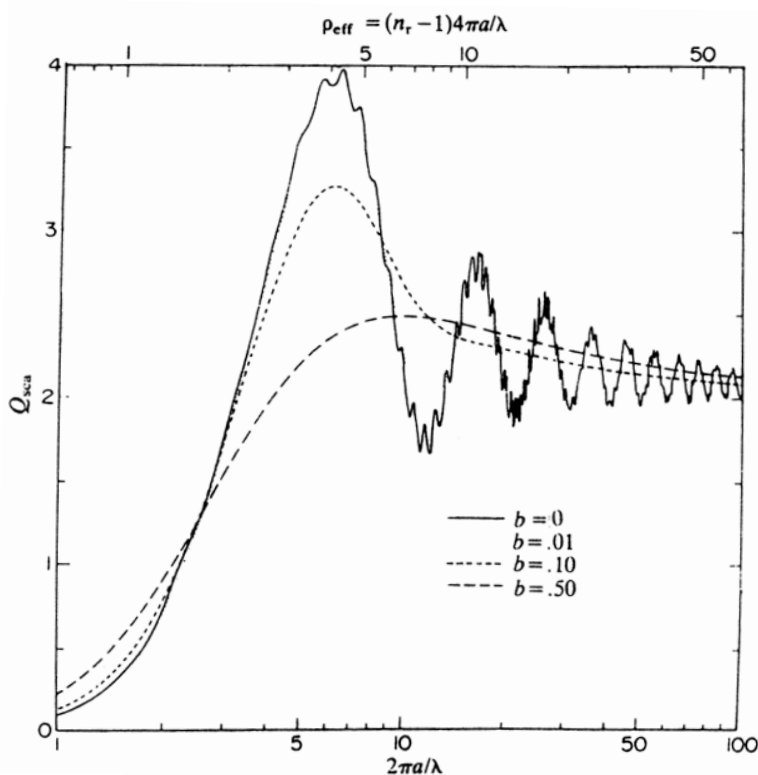


Fig. 8.5 A plot of the efficiency factor for scattering as a function of the dimensionless parameter $X = (2\pi a/\lambda)$. The curves represent the averaged value summed over the size distribution of the form $n(r) = \text{const. } r^{(1-3b)/b} e^{-r/ab}$. The refractive index is $n = 1.33$, $k \equiv n_i = 0$. (Hansen, J. E. and Travis, L.D. 1974. *Space Sci. Rev.* **16** 527).

8.5. Particles of Other Types

So far, the discussion has been limited to the case of spherical particles with homogeneous and isotropic internal structure. Even in this case the mathematical solution is highly complex in nature. However in a real situation, the particles are far from being spherical in shape. Therefore considerable effort has been spent in the study of particles of other shapes through theoretical and numerical means. Several classical methods of solving scattering problems have been used. To name a few, separation of variables, perturbation methods, fields expanded in vector spherical harmonics among others have been used. The exact solutions for scattering from spheroids,

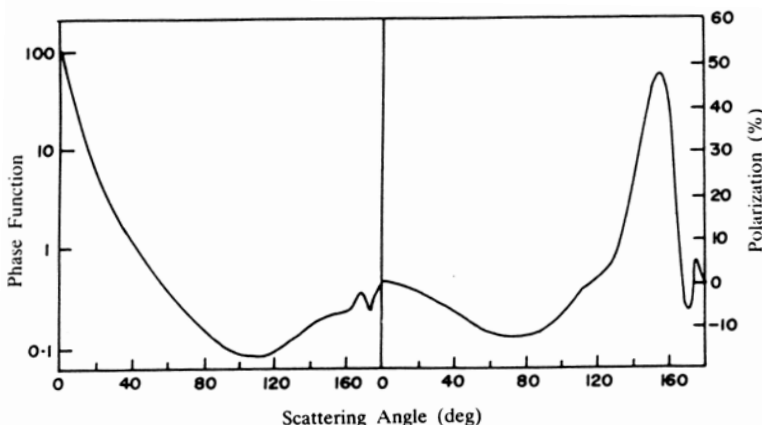


Fig. 8.6 Phase function and polarization for single scattering are plotted as a function of the scattering angle for wavelength of 5500 Å and $n = 1.33$, $k \equiv n_i = 0$ (Adapted from Hansen, J. E. and Travis, L. D. 1974. *op. cit.*).

infinite cylinders, concentric spheres have been worked out and are available in many books. The cases of cylinders with oblique incident, as well as concentric cylinders have also been investigated mathematically. The approximate formulae for the limiting cases are also available for concentric spheres, cylinders etc. However, even the well defined shape for the particles introduces many more additional parameters due to their shape, orientation etc. compared to that of spheres.

Two possibilities exist for the case of spheroids. They could be prolate or oblate. For infinite cylinders, the exact solution has been derived for the case when the particle diameter is much smaller than its length. In the case of concentric spheres there are various possibilities depending on the inner and outer radii and their relative refractive indices. Even from such well-defined shape of particles the computation of cross sections is quite complicated and lengthy. In addition, the computation time could be quite large and particularly so for larger size particles. Therefore efforts are being made to develop efficient methods for the calculation of cross sections from such well-defined particles.

The general results for nonspherical cases are qualitatively very similar to those for spheres, with a Rayleigh like increase, broad scale interference structure with finer ripples superposed over it. As a typical case, the results for the extinction efficiencies in the case of infinite cylinders for $n = 1.33$ and $m = 1.33 - 0.05i$ are shown in Fig. 8.7. Here Q_E and Q_H denote

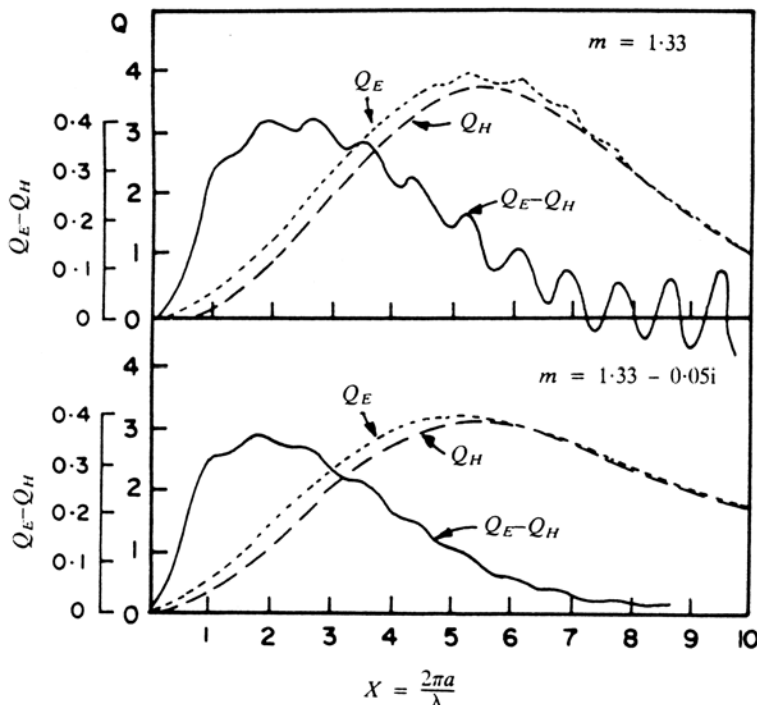


Fig. 8.7 A plot of the efficiency factors for extinction of cylinders oriented normal to the incident radiation for two values of refractive index. Q_E is for the electric vector E of the incident radiation parallel to the axis and Q_H is for the magnetic vector H of the incident radiation parallel to the axis. The polarization is also shown as $Q_E - Q_H$. (Adapted from Greenberg, J. M. 1978. In *Cosmic Dust*. ed. McDonnel, J. A. M. New York: John Wiley and Sons, p. 187).

the value of Q for the case of electric vector and the magnetic vector of the incident radiation parallel to the axis of the cylinder. The radius of the cylinder is ' a '. The polarization ($Q_E - Q_H$) is also shown in the same figure. The effect of absorption as pointed out before, is to dampen the polarization oscillations.

The discussion so far was limited to the ideal situations wherein the particles are assumed to have definite and regular shapes. However, in general, the dust particles in a real case are far from the above situations. It is more likely that they will be irregular in shape. They could also be fluffy, porous and could have surface roughness. Therefore several attempts have been made to consider the general case of scattering by an arbitrary parti-

cle. The general solutions involve the calculation of the effect on individual atoms by the incident field and also the combined fields of all other atoms. As the general case is almost impossible to solve, it necessarily involves making certain approximations and finally the cross sections have to be derived from numerical methods. Several studies have been carried out based on perturbation approach, T-matrix method also known as the extended boundary condition method, study of statistical description of roughness in the frame work of the potential theory and so on.

However a method which has been successfully used is to subdivide the particle into several smaller identical elements, which itself is a collection of large number of atoms, and can be represented as a dipole oscillator. The average field due to the combined effect of all these individual oscillations is then calculated. This is the well known *Discrete Dipole Approximation* (DDA) method. Another approach that has been investigated is to make use of the integral representation of the macroscopic Maxwell's equations. In this method, the particles are assumed to be an aggregate of small cubic volumes at the lattice site of which are located sub volumes, of identical and homogeneous character. This is mathematically equivalent to that of DDA except that the computation is based on the calculation of volume element polarizations. The advantage of DDA method is that it can be applied to particles of arbitrary shape, structure and composition. A sample representation of a fluffy particle in terms of subparticles which is considered in the computation of cross sections is shown in Fig. 8.8. The nature of fluffiness i.e. creating porosity in the grain, depends upon the number of dipoles, their sizes and the separation between them. The number of dipoles used in the calculation could be as large as 10^5 . Each of the dipoles in the grain could be small enough to be thought of as Rayleigh-limit inclusions. Extensive calculations have been carried out for the study of scattering properties of such a grain under the DDA formalism for examining the effects of porosity, size of the dipoles, topology of the grain and so on, on the derived results. A sample result for the extinction from a prolate spheroid is shown in Fig. 8.9. The validity of DDA results has to be tested by comparing the results with those derived from well-defined shapes.

In the past, the scattering from regular particles like spheres, spheroids etc., but with inhomogeneous composition, has been studied by replacing the inhomogeneous grain with a homogeneous grain by using an effective dielectric constant. The idea being that the effective dielectric constant of the material provides the correct light scattering characteristics of the heterogeneous medium. It can be calculated either from the Maxwell-Garnett

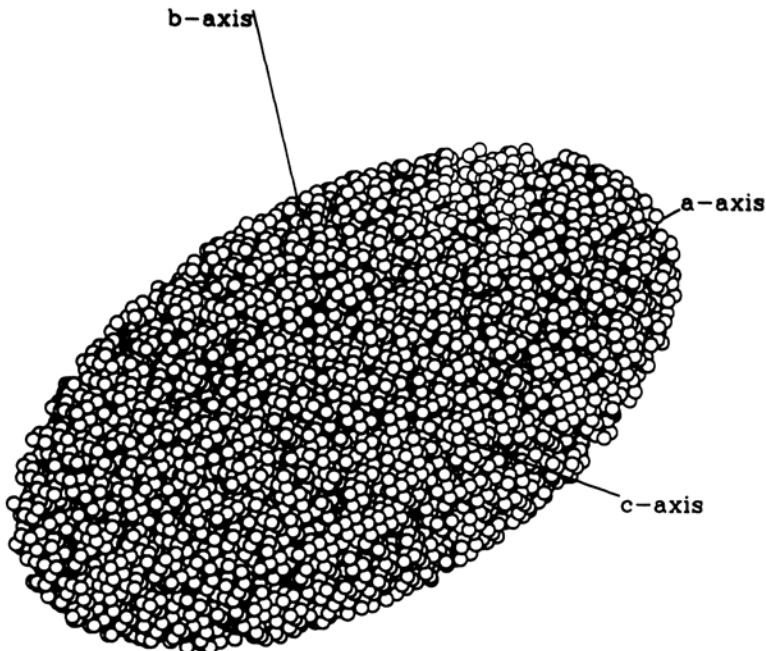


Fig. 8.8 The model of the dust particle (a prolate pseudospheroid with $2a = 60$, $2b = 2c = 30$ in units of the lattice spacing d) used in the calculation of cross-section under Discrete-Dipole approximation. In this grain model 60% of the original 28256 dipoles have been removed (Wolff, M. J., Clayton, G. C., Martin, A. G. and Schulte-Ladbeck, R. E. 1994. *Ap. J. Letters*, **423**, 51).

theory or the Bruggeman theory (Sec. 8.6). It is therefore of interest to compare the results obtained from such calculations with those derived from DDA formalism, for the same grain parameters. Figure 8.9 shows such a comparison. The agreement in general is found to be better, as the number of dipoles in the DDA formalism is increased. Ultimately, how good are the calculations has to be tested by comparing with the observations. In general, the results based on these theories seem to represent astronomical observations better compared to the case of spherical particles. However the results based on spherical dust particles can be used to limit the range of cometary grain parameters.

It is easier to carry out laboratory measurements on larger size particles rather than on micron size particles. Therefore several studies have been carried out using the microwave techniques. If the optical constants of the material in the microwave and optical wavelength regions are the same, then

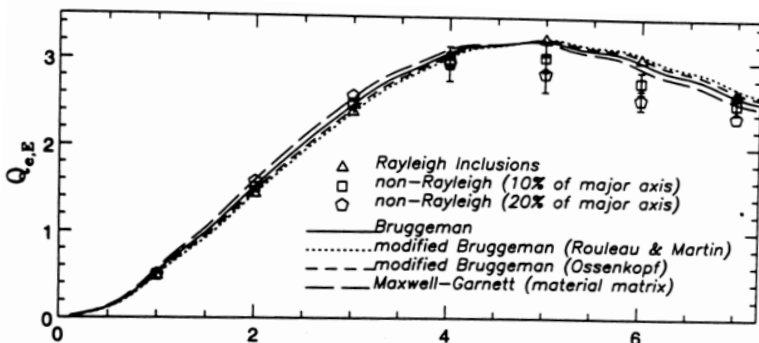


Fig. 8.9 The calculated efficiency factors for extinction with 40% porosity. The results are for two orientations of the incident electric vector E and H which are parallel and perpendicular to the major axis of a 2:1 prolate spheroid. The DDA results for both Rayleigh and non-Rayleigh vacuum inclusions are compared to the various mixing rules (continuous curves). The base grains have 3558, 8320 and 14440 dipoles for the ranges $x \leq 2$, $3 \leq x \leq 4$ and $x \leq 5$ respectively (Wolff, M. J. et al. 1994. *loc. cit.*).

the results based on the microwave studies carried on larger size particles are also valid for smaller size particles in the visible wavelength region, as the characteristic parameter x is the same. Therefore, various kinds of measurements like extinction, angular scattering and so on have been carried out in the microwave region on particles of various shapes such as cylinders, spheroids, spheres and irregular particles. The results of such studies agree reasonably well with those of calculated values, thus giving some credibility for the theories.

8.6. Optical Constants

The calculation of cross sections requires the knowledge of the gross material property of the grain. This is generally represented by the refractive index, $m = n + ik$, or the dielectric constant $\epsilon = \epsilon' + i\epsilon''$, of the medium. The optical constants represent a measure of the capacity of electrons in the material to oscillate for the incident radiation. m and ϵ are generally complex quantities. These two quantities are not independent of each other. Knowing one set of quantities, the other set can be calculated. The relations for ϵ' and ϵ'' are given by

$$\epsilon' = n^2 - k^2 \quad \text{and} \quad \epsilon'' = 2nk. \quad (8.35)$$

similarly the relations for n and k are given by

$$n = \left[\frac{(\epsilon'^2 + \epsilon''^2)^{1/2} + \epsilon'}{2} \right]^{1/2} \quad (8.36)$$

and

$$k = \left[\frac{(\epsilon'^2 + \epsilon''^2)^{1/2} - \epsilon'}{2} \right]^{1/2}. \quad (8.37)$$

The determination or the use of either refractive index or the dielectric constant depends upon the physical situation being considered.

The optical constants of materials are not directly measurable quantities. But they have to be determined from laboratory measurements of some property of light in combination with the suitable theory. Various types of measurements can be made for the determination of the optical constants of the material. They could be the measurement of the extinction coefficient from a set of thin slabs, transmittance and reflected light at near normal incidence or for various incidence angles, measurement of the phase shift of the reflected light and so on. The theoretical formulation for the interpretation of the above types of measurements are available. The choice of the method depends upon the material to be measured, experimental techniques available and so on. Various methods have been used to derive the optical constants of several types of material. However the most commonly used and probably the best method for the determination of optical constants is the use of dispersion relations, generally known as the Kramers-Kroning relations in combination with the reflectance measurements. Basically, the dispersion relation is an integral over the whole range of photon energies, which relate the dielectric function to the measured quantity like the extinction coefficients or the reflectance measurements. The real and imaginary parts of m or ϵ are not independent of each other but are interrelated through these dispersion relations.

The determination of optical constants of materials from the laboratory measurements are quite difficult and cumbersome. The sample has to be perfectly smooth to avoid scattering effects, it should be homogeneous and thin slab and so on. Most of the optical constants derived from laboratory measurements are of that of pure substances. In addition the wavelength coverage may not be extensive. Therefore one might have to make use of the derived optical constants over the limited wavelength regions available, to cover the wavelength region from ultraviolet to far infrared. The optical constants for several material like graphite, carbon, amorphous carbon, silicates and so on which are of interest for cometary studies are available.

The optical constants for several terrestrial rock samples and moon samples have also been measured. The measured refractive indices of silicates for different Mg/Fe ratio show wide variation. This will have great effect on grain temperature and hence on the infrared emission from such grains. Since these materials are not strictly homogeneous, the measurements in principle, should provide some sort of average dielectric constants of these materials. The cometary grains are inhomogeneous in character. Therefore the best way to get the refractive index of the material of interest is through laboratory studies. Since it is almost impossible to study all the cases of interest in the laboratory, a theoretical treatment of the problem becomes a necessity.

The dust grains present in the astrophysical environments are highly inhomogeneous in character. In general, it is not easy to calculate the average optical properties of inhomogeneous medium even if the property of the individual constituents are known. So one has to use various approximations. This has given rise to the concept of an effective dielectric constant for the material. This has given rise to several theories. The two theories that are most commonly used are the Maxwell-Garnett theory dating back to 1904 and the Bruggeman theory proposed in 1935. In the Maxwell-Garnett theory, the composite grain consists of matrix material in which small spherical inclusions are embedded having dielectric constants ϵ_m and ϵ_i respectively with f as the volume fraction of inclusions. The inclusions are assumed to be spherical in shape with sizes smaller than or nearly equal to the wavelength under consideration. The problem is to calculate the average electric field of the medium from the knowledge of the individual electric fields E_i and E_m of the two components arising out of the interactions, which are by themselves averages over a smaller volume. With the assumption that the relations for the electric fields, polarization vector and the relations between E_i and E_m as well as between ϵ_i and ϵ_m also hold for the average fields, the following relation for the average dielectric constant is derived.

$$\epsilon_{av} = \epsilon_m [(2\epsilon_m + \epsilon_i - 2f(\epsilon_m - \epsilon_i))/(2\epsilon_m + \epsilon_i + f(\epsilon_m - \epsilon_i))]. \quad (8.38)$$

Here the average dielectric constant is independent of the position in the composite medium. This is generally known as the Maxwell-Garnett rule or simply as the M-G rule.

In the Bruggeman theory, there is no distinction between the matrix and the inclusions as in the case of Maxwell-Garnett theory. Here the grains are aggregate of small particles with their own dielectric constant (ϵ_i) and

volume fraction (f_i). The effective dielectric constant for such a case is given by the expression

$$\sum_i \frac{f_i(\epsilon_i - \epsilon_{\text{eff}})}{(\epsilon_i + 2\epsilon_{\text{eff}})} = 0. \quad (8.39)$$

The value of ϵ_{eff} is derived from the solution of the above equations. However there may be some convergence problem if there is a wide variation in optical constants. Maxwell-Garnett theory is more popular and is generally being used. The applicability and accuracy of the above relations has to be tested based on the comparison between the computed values and those of laboratory measurements of two component mixtures. The laboratory measured dielectric constants of several two component mixtures are in agreement with the effective dielectric constant values derived from Eq. (8.38). Therefore the M-G rule can be used to derive the average optical constants of a two component medium. It is possible to extend the method for a multicomponent mixture as well as for the shape distribution for the inclusions, which of course introduces several additional parameters.

The dust in comets are more complicated than the simple models considered in the theoretical treatments as summarized so far. For a real situation it is necessary to specify several parameters for the aggregate like the size, shape and the refractive index of the material and for the inclusions, the degree of porosity, size, shape, location and their orientation. To consider so many parameters in the actual calculation of cross-section becomes difficult from the practical point of view as well as computing time required. In spite of this, in recent times DDA and other methods have been used extensively in cometary studies. The codes for some of these methods are available.

Problems

1. Show that for the condition $(2\pi a/\lambda) \lesssim 1$ and with refractive index $m = n - ik$, Q_{abs} is given by

$$Q_{abs} = \frac{a}{\lambda} \frac{48\pi nk}{(n^2 - k^2 + 2) + 4n^2k^2}.$$

2. Express the above relation for Q_{abs} in terms of the dielectric function ϵ_1 and ϵ_2 .
3. Calculate Q_{sca} and Q_{abs} for ice particles of $m = 1.3 - 0.05i$, $a = 2 \times 10^{-5}$ cm and $\lambda = 5 \mu\text{m}$.

4. For a particle size distribution of the form $n(a)\alpha a^{-3}$ for $a_1 < a < a_2$, calculate the constant of proportionality such that the total number is unity.
5. Assuming $m=1$, $a \ll \lambda$ and the size distribution of Problem 3, get an expression for the total Q_{abs} .
6. Discuss the physical reason for the occurrence of Kinks in the extinction curve. Why does it smooth out when integrated over the size distribution function?

References

The theory of scattering from spheres can be found in these classic works:

1. Debye, P. 1909. *Ann. Physik*, **30**, 59.
2. Hulst, Van de 1957. *Light Scattering by Small Particles*. New York: John Wiley and Sons.
3. Mie, G. 1908. *Ann. Physik*, **25**, 377.

A discussion of albedos can be found in

4. Hanner, M.S., Giese, R.H., Weiss, K. and Zerull, R. 1981. *Astr. Ap.*, **104**, 42.

The theory of core-mantle particles is worked out in

5. Guttler, A. 1952. *Ann. Phys.*, Lpz. 6 Folge, Bd. 11,5.

The case of core-mantle and cylindrical particles is included in

6. Wickramasinghe, N.C. 1973. *Light Scattering Functions for Small particles*, London: Adam Hilger Limited.

A good account is also given in the book

7. Bohren, C.F. and Huffman, D.R. 1983. *Absorption and Scattering of Light by Small particles*. John Wiley, New York.

The idea of Discrete-Dipole approximation was proposed in the following paper.

8. Purcell, E.M. and Pennypacker, C.R. 1973. *Ap. J.* **186**, 705.

More recent work can be found in the following papers.

9. Draine, B.T. and Goodman, J.J. 1993. *Ap. J.* **405**, 685.
10. Hage, J.I. and Greenberg, J.M. 1990. *Ap. J.* **361**, 251.
11. Wolff, M.J., Clayton, G.C., Martin, P.G. and Schulte-Ladbeck, R.E. 1994. *Ap. J. (Letters)*, **423**, 51.
12. Wolff, M.J., Clayton, G.C. and Gibson, S.J. 1998. *Ap.J.*, **503**, 815.
13. Kimura, H. Kolokolova, L. and Mann, I. 2006. *Astron. Astrophys.*, **449**, 1243.

14. Kolokolova, L., Hanner, M.S. and Levasseur - Regourd, A. -Ch. 2005. *Comets II*, eds. M.C. Festou, H.U. Keller and M.A. Weaver, Univ. Arizona Press, Tucson, p. 577.

Maxwell-Garnett and Bruggeman rules are discussed in

15. Bohren and Huffman 1983. *Absorption and Scattering of Light by Small particles*, John Wiley, New York.

CHAPTER 9

The Nature of Dust Particles

As was pointed out in the previous chapter, when radiation is incident on a dust particle (also called the grain), it can scatter as well as polarize it. The absorbed energy by the dust particles can also be radiated in the infrared region and this has been seen in comets. There may be also spectral features in the infrared region depending on the composition of the dust particle. The radiation pressure acting on the particle can give rise to dynamical effects as discussed in Chap. 7. Each of these physical effects could be used to infer the nature and the composition of the cometary grains. The *in situ measurements* of Comets Halley, Wild 2 and Tempel 1 performed by the instruments on board the spacecrafts have given valuable information about the nature and the composition of dust particles. The laboratory studies of dust samples collected from Comet Wild 2 has revealed for the first time the true nature of the cometary dust particles. While it is known that comets do exhibit a great deal of variability, there still exists a general overall pattern of behaviour in their observed properties. The emphasis here is on this general pattern of the observed properties of comets. Here we would like to consider some of these effects.

9.1. Visible Continuum

Comets in general posses a continuum in the visible region of the spectrum. The strength of the continuum varies from comet to comet and with the heliocentric distance. The observed continuum is attributed to the scattering of the solar radiation by the dust particles. Therefore, the dusty comets should have a strong continuum. What is of interest, of course, is the dependence of the continuum as a function of the wavelength. The usual method adopted for getting the variation of continuum with wave-

length is to compare the observed energy distribution of a comet with the energy distribution of the Sun or a similar star. But the cometary spectrum in the visible region is dominated by the emission features from the molecules. Therefore, the continuum has to be corrected for these emission features or a spectral region has to be selected where the emission features are absent or minimal. From these observations, it is possible to determine the relative continuum intensities of comet with respect to the Sun or a star similar to the Sun. This yields the wavelength dependence of the observed continuum of the comet. Since the dependence arises due to the scattering of the dust particles in the comet, the interpretation of these observations should give information about the nature of the particles.

Let I_0 be the intensity of the incident solar radiation and r , Δ represent the sun-comet and the comet-earth distances respectively. The intensity of the scattered radiation at the Earth at an angle θ is given by (Chap. 8).

$$I_{\text{scat}}(r, \Delta, \theta, \lambda) = \frac{I_0(\lambda)}{2k^2 r^2 \Delta^2} [i_1(\lambda, \theta) + i_2(\lambda, \theta)] \quad (9.1)$$

where $k = 2\pi/\lambda$. This has to be integrated in general with a size distribution function. Therefore, the problem reduces to the calculation of $I_{\text{scat}}(r, \Delta, \theta, \lambda)$ for a given size distribution function and for the assumed grain properties represented by the refractive index of the material, $m = n - ik$. The mean scattering intensities can be calculated from the Mie Theory as discussed in the previous chapter. Therefore, the expected intensity distributions can be calculated for various input parameters which could then be compared with the observations.

There exists a large number of broad band observations of comets in the wavelength region from 0.5 to 20 μm . To have an idea of the expected results from the scattering component of the cometary grains, some of the comets around a few heliocentric distance values and covering various scattering angles can be grouped together. Since the main interest is in the general shape of the wavelength dependence of the observed fluxes and not in the absolute amount, the shape of the curves could be shifted to obtain a mean dependence of the observed fluxes. This procedure enables one to extend the wavelength range of the scattered radiation for comets up to $\lambda \approx 4 \mu\text{m}$ as can be seen from Fig. 9.1. There exists a close relation in the various observations. The shape of the observed solar flux variation with the wavelength is nearly the same as that of the observed shape. This shows that it is rather difficult to extract the properties of dust particles in comets from the study of broad band-pass observations. This is borne out

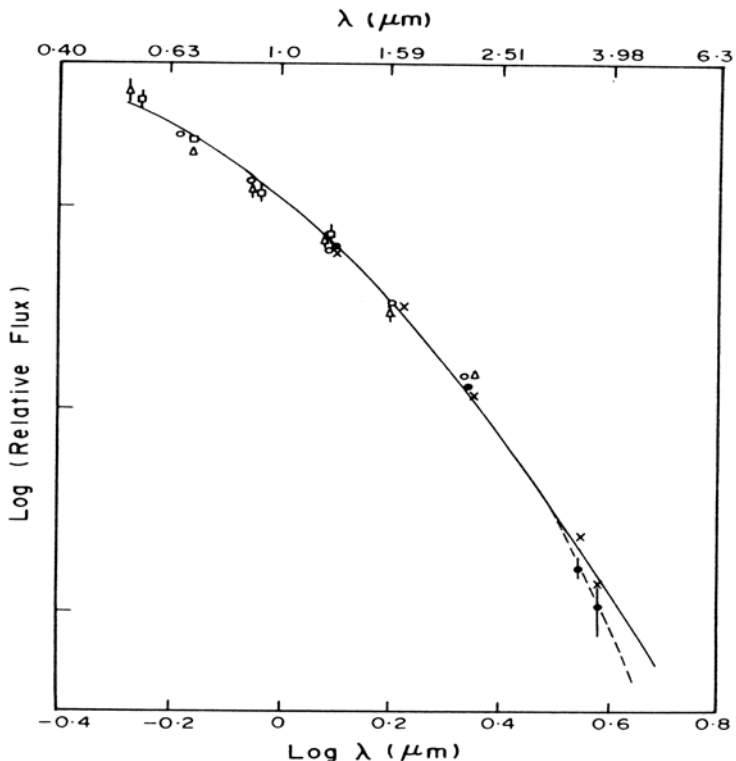


Fig. 9.1 Superposed plot of relative observed fluxes of eight comets as a function of wavelength for heliocentric distances r grouped around 0.3 AU(\square), 0.7 AU(\triangle), 1.0 AU(\circ), 2.5 AU(X) and 3.75 AU(\bullet). They cover the scattering angles from around 30 to 177°. The continuous curve shows the shape of the observed solar flux and the dashed curve is for Mie calculations with $m = 1.38 - 0.039i$ and $N(a) \propto a^{-3.5}$. Observational data: Bradfield (1974 III) and Kohoutek (1973 XII) (Ney E.P. 1974 *Icarus* **23**, 551); Bradfield (1980 XV) (Ney, E.P. 1982. In *Comets*, ed. L.L. Wilkening, Univ. Arizona Press, Tucson, p 323); P/Crommelin (1984 IV) (Hanner, et al. 1985. *Astr Ap* **152**, 177); P/Giacobini-Zinner (1985 XIII) (Hanner, M.S. et al. 1992. *AJ*, **104**, 386); Halley (1986 III) (Bouchet, P. et al. 1987. *Astr. Ap.* **174**, 288; Tokunaga et al. 1988, *AJ*, **96**, 1971); West (1976 VI) (Ney, E.P. and Merrill, K.M. 1976. *Science* **194**, 1051); Wilson (1987 VII) (Hanner, M.S. and Newburn, R.L. 1989. *AJ*, **97**, 254).

from the extensive studies of near infrared colour like J-H and H-K, which show that they cannot be used as a distinguishing feature for the study of the properties of cometary grains. It also indicates that in general, the results expected from the scattering effects of grains are not drastic.

There have been several refined studies of the continuum measurements

of comets in the visible region. However, the results are somewhat confusing. In some comets, the observed wavelength distribution of the scattered radiation has almost the same dependence as that of the solar radiation, while for others, it produces a large reddening. This arises due to several factors. As mentioned earlier, the wavelength dependence of the scattered radiation is derived from observations by comparing the observed continuum with the energy distribution of the Sun. In this procedure, it is very essential to take into account properly the contribution of the molecular emissions, before the dust scattered component can be extracted. This is a difficult and a major problem in scattering studies, as the molecular bands are quite strong and dominate in the visual spectral region. This leaves very few clear windows or spectral regions where the observations could be carried out. However, the situation improves moving towards the red region. It may also be noted that the continuum becomes stronger as the dust to gas ratio increases and the emission bands become weaker as the heliocentric distance of the comet increases. The other difficulty associated with the early observations is connected with poor spectral resolution. A combination of these difficulties and the poor response of the detectors could have been responsible for the differing results of earlier studies. In recent years it has been possible to overcome some of these difficulties and it is now possible to get somewhat reliable and consistent results.

From the observational point of view, it is convenient to describe the scattered radiation or colour from the observed spectra in terms of a quantity called ‘reflectivity’, which is merely the ratio of the flux $F(\lambda)$ to the solar flux $F_{\odot}(\lambda)$ at the same wavelength, i.e.,

$$S(\lambda) = \frac{F(\lambda)}{F_{\odot}(\lambda)}. \quad (9.2)$$

To be consistent with the cometary spectra, the solar spectrum has to be made smooth to the instrumental resolution of the cometary spectra before the ratio is determined. The normalized reflectivity gradient is defined as

$$S'(\lambda_1, \lambda_2) = \left(\frac{ds}{d\lambda} \right) / \bar{S}. \quad (9.3)$$

Here $(ds/d\lambda)$ represents the reflectivity gradient in the wavelength interval between λ_1 and λ_2 , and \bar{S} is the mean reflectivity in the same wavelength region defined as

$$\bar{S} = N^{-1} \sum S_i(\lambda). \quad (9.4)$$

The reflectivity gradient $S'(\lambda_1, \lambda_2)$ gives a measure of the colour. If $S'(\lambda_1, \lambda_2) > 0$, it indicates grain reddening.

The reddening curve, in principle, can be extended to the ultraviolet and infrared wavelength regions by combining various observations. However, the main difficulty is that since the observations are performed with different instruments, different wavelength regions etc., it is hard to connect them with one another. An attempt to combine the data obtained from the IUE and ground-based observations, along with infrared observations of Comets Bowell, Stephen-Oterma and Cernis, has succeeded in getting the reddening curve for the coma in the wavelength region $\lambda = 0.26$ to $2.5\mu\text{m}$. This showed a gradual reddening with an increase in wavelength. In more recent times, the reflectivity and the reflectivity gradient have been determined in a systematic manner from the study of several comets in the spectral region from 0.5 to around $3\mu\text{m}$. This broad coverage in wavelength came about as a result of the combination of the scanner observations in the wavelength region of 0.35 to $0.7\mu\text{m}$ and the near infrared observations. In these studies, several wavelength regions in the cometary spectra, as far as possible, free of molecular emissions, were selected. This criterion is particularly difficult in the continuum measurements in the ultraviolet region, where they are susceptible to emission lines in the spectral region. The derived average behaviour of S' based on a large number of comets is shown in Fig. 9.2. The results for Comet Halley also show a similar behaviour of the reflectivity gradient with wavelength. These results clearly show that the average S' decreases systematically from ultraviolet into the near infrared wavelength region. In particular, it shows a strong reddening in the ultraviolet region which decreases slowly with an increase in wavelength. The neutral point being around $\lambda \sim 2\mu\text{m}$ and the blue beyond $\lambda \sim 3\mu\text{m}$. Therefore, comets in general, appear to show an average behaviour for the reddening as shown in Fig. 9.2, although there are some exceptions. In addition, there could be spatial as well as temporal variation in colour in the coma.

Colours of dust grains can also be determined from the difference in the values of $A(\theta)f\rho$ (Sec. 9.1.4) between the two continuum filters used in photometric measurements. Observations of several comets indicate the presence of reddening.

It is also possible to determine the distribution of surface brightness of the continuum radiation. The results based on several comets show that the brightness varies with the nucleocentric distance up to about 10^5 km or so, with an average power index of around -1 . The particles generated near the nucleus, as they expand outwards with a constant velocity, will give rise to a surface brightness variation with an index of -1 . The close

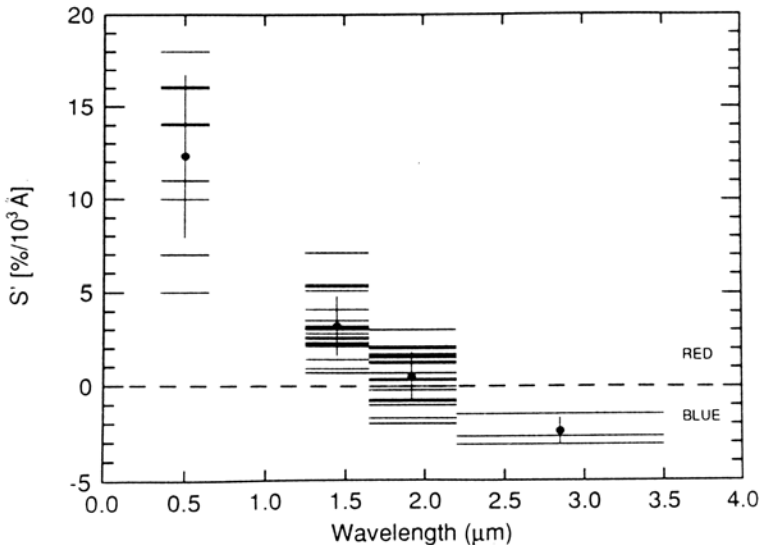


Fig. 9.2 The observed normalized reflectivity gradient $S'(\lambda_1, \lambda_2)$ between wavelengths λ_1 and λ_2 expressed in percent per $10^3 A$ is shown as a function of the wavelength for more than a dozen comets. The horizontal line represents the observational value for each comet over the interval between λ_1 and λ_2 . The filled circle represents the mean value of S' with each measured wavelength interval. The dashed line is for neutral scattering with $S'(\lambda_1, \lambda_2) = 0$. Continuum colours due to scattering changes from red ($S' > 0$) to blue ($S' < 0$) as the wavelength changes from optical to near-infrared regions (Jewitt, D.C. and Meech, K.J. 1986. *Ap J* **310**, 937).

agreement between the observed and the expected variation shows that the fountain model is reasonable. However, with an increase in distance from the nucleus, the effect of radiation pressure on the grains will start becoming important causing distortion in the observed surface brightness curve. This is evident from the observed isophotes of comets which show spherical symmetry close to the nucleus, but distorted at larger distances. Also, the asymmetry in the coma due to sunward ejection of the dust particles becomes prominent. In these situations, the surface brightness in the coma is also a function of the phase angle. Therefore, the surface brightness profile of comets can be described reasonably well with the geometrical dilution of the expanding gas for distances not too far from the nucleus. But, with the increase in distance, the radiation pressure effect becomes important and it dominates at large distances causing deviations from the -1 index law.

The interpretation of reddening results in terms of the physical characteristics of the dust grains is complicated, as it involves several parameters,

including the variation in scattering angle, and is also generally based on the Mie theory of scattering for spheres. Also, in general, it is rather difficult to entangle the influence of size and the composition of the dust grains.

The early reddening observations of the tails of Comets Arend-Roland and Mrkos were found to give a fit with model grains with the refractive index of iron and sizes $\sim 0.3\mu$. The scattered radiation from the head regions of Comets Arend-Roland and Mrkos could also be fitted with particles with the refractive indices between 1.25 and 1.50 (dielectric) and the size distribution proportional to a^{-4} for the sizes of the particles. The interpretation of later observations of Comets Kohoutek, Bradfield, West and others seems to indicate the particle sizes to be submicron or micron and slightly absorbing. The expected intensity distributions have been carried out for various types of silicate materials as well as for various values for the constant refractive index (n) with a small absorption part (k). These comparisons indicate that $n \approx 1.5$ to 1.6 , $k \leq 0.05$ and the particle size $\sim 0.2\mu$. The observed colour trend of Fig. 9.2 is consistent with dust grain sizes, $a \geq 1 \mu\text{m}$ and slightly absorbing.

9.1.1. Albedo

The average value for the albedo of cometary particles can be obtained from a combination of very simple physical arguments and observations. The observation required for such a study is the scattered radiation at the visible wavelength and the total integrated infrared flux from a comet. These are readily available for many comets. The basic physical idea behind such a simple method is that the continuum in the visual region arises due to the scattering process which depends on the scattering efficiency of the grain. On the other hand the observed infrared radiation is dependent on the amount of impinging energy absorbed by the grain, which depends on the absorption efficiency of the grain. For small optical depths and also neglecting phase dependence effects, the optical surface brightness can be written as

$$S_{\text{opt}}(\lambda) = \frac{F_{\odot}(\lambda)\tau}{4\pi} = \frac{F_{\odot}(\lambda)N_d l \pi a^2 Q_{\text{sca}}(a, \lambda)}{4\pi}. \quad (9.5)$$

Here N_d is the column density of the dust particles and l is the representative path length. The infrared surface brightness can be approximated as

$$S_{\text{ir}} = \frac{\langle Q_{\text{abs}} \rangle \pi a^2 F_{\odot} N_d l}{4\pi}. \quad (9.6)$$

Here $\langle Q_{\text{abs}} \rangle$ represents a mean absorption efficiency for the grain and $F_{\odot} = \int F_{\odot}(\lambda) d\lambda$, the integrated solar radiation. It is possible to derive an expression for the average albedo γ of the particles from the above equations. This is given by

$$\frac{\gamma}{1 - \gamma} = \frac{F_{\odot} S_{\text{opt}}(\lambda)}{S_{\text{ir}} F_{\odot}(\lambda)}. \quad (9.7)$$

The estimated values of albedo for several comets is ~ 0.1 . In the above method, the phase dependent scattering is neglected. The derived albedo for Comet Giacobini-Zinner to around 0.07 to 0.15.

9.1.2. Phase function

The average scattering function or phase function, i.e., the scattered intensity as a function of the scattering angle, is another important parameter in defining the nature of the particle responsible for it. The average scattering function can be obtained by observing the coma of the comet as a function of the heliocentric distance or by scanning along the outward direction of the tail. In such observations the quantity that is changing is basically the scattering angle.

It is considerably difficult to derive the phase function, since the physical conditions within the coma change with the scattering angle. The approximate phase function has been derived from the ratio of the visual flux, which represents the scattered radiation, to the infrared brightness that represents the absorbed energy, for the scattering angles between 30° and 150° . Since they both come from the same volume of dust, the ratio is simply proportional to the scattering function of the grains. The derived phase function for several comets is shown in Fig. 9.3. The phase function shows a forward scattering lobe for scattering angle $\leq 40^{\circ}$ with almost a flat shape for an angle between 60° and 150° . The observation of Comet Halley carried out upto a scattering angle of 178.63° does not indicate a strong backscattering peak. The results for Comets Ashbrook-Jackson, Bowell and Stephen-Oterma also show a similar behaviour of Comet Halley. Therefore, there appears to be no evidence for the presence of backscattering peak. The results for Comet Machholz follow the general trend of the continuum curve for scattering angles less than about 50° . The values for Comet Hale-Bopp is about 50% higher compared to that of Comet Halley for scattering angles around 140° . The nature of the observations is more in conformity with the expected results from non-spherical particles (Fig. 9.3(b)).

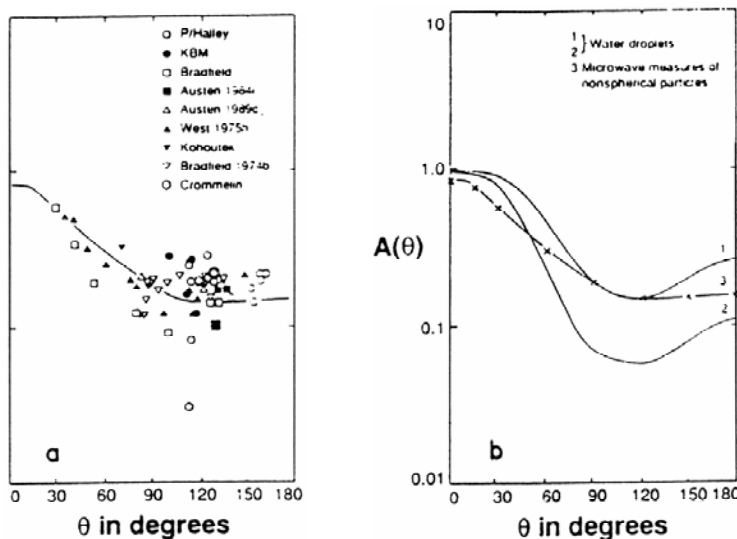


Fig. 9.3 (a) A composite phase diagram of the observed ratio of the reflected to the infrared flux as a function of the scattering angle derived for several comets. For comparison with the data, the curve 3 from (b) is also shown. (b) shows the laboratory data from spherical (curves 1 and 2) and nonspherical particles (curve 3) (Gehrz, R. D. and Ney, E. P. 1992. *Icarus*, **100**, 162).

The phase function for Comet Halley has been determined for phase angles between 1.5° and 66° . This in combination with other results should give the phase curve over the entire range of phase angles.

The observed phase function is consistent with the expected distribution of micron size particles with an index of refraction in the ranges $1.3 \leq n \leq 2.0$ and $k \geq 0.05$.

With regard to albedo, the estimated albedos for different comets have to be compared at the same scattering angle. The geometric albedo A_p at $\lambda \sim 1.2 \mu\text{m}$ is roughly around 0.025 for scattering angles in the region of around 150° .

9.1.3. Dust production rate from continuum

The production rate of grains can be calculated from a knowledge of the total number of dust particles in the field of view required to explain the observed scattered flux at the earth, F_{earth} . It is given in gm/sec by the

expression

$$Q_D^{\text{opt}}(r) = \frac{4\pi\Delta^2 F_{\text{earth}}}{\delta} \left[\frac{\bar{M}}{\bar{E}_\lambda} \right] \bar{V} \quad (9.8)$$

where

$$\bar{E} = \int_{a_{\min}}^{a_{\max}} \frac{I_0(\lambda)}{2k^2} \frac{R_\odot^2}{r^2} [i_1(\lambda, \theta) + i_2(\lambda, \theta)] n(a) da \quad (9.9)$$

and

$$\bar{M} = \frac{\int_{a_{\min}}^{a_{\max}} \frac{4\pi}{3} a^3 \rho n(a) da}{\int_{a_{\min}}^{a_{\max}} n(a) da}. \quad (9.10)$$

Here δ is the linear radius of the projected field of view, ρ is the density of the grain material and Δ is the geocentric distance. The mean velocity of grains is defined by

$$\bar{V} = \frac{\int_{a_{\min}}^{a_{\max}} a^3 V(a) n(a) da}{\int_{a_{\min}}^{a_{\max}} a^3 n(a) da}. \quad (9.11)$$

In the above expression, $n(a)da$ represents the number of grains of size a in the size range between a and $a+da$ and $V(a)$ is the velocity of grains of size a . The summation has to be carried over minimum, a_{\min} and maximum, a_{\max} size ranges of the size distribution function. The other symbols have their usual meanings.

The calculation of dust production rate from the nucleus requires the knowledge of the density of the grains, the dust particle velocities and the size distribution of grains. However the density of grains in comets is quite uncertain. Although the instruments on board the spacecrafcts to Comet Halley were not designed or calibrated to measure the density accurately, some estimates have been made which are around 0.3 to 1.0 gm/cm³. The compositional measurements from Giotto and Vega spacecrafcts indicate an average value of ~ 1 gm/cm³ for the carbon type of particles and a value ~ 2.5 gm/cm³ for the silicate type particles. The density measurements of the actual interplanetary dust particles indicate a value ~ 1 gm/cm³. In view of the uncertainties, a canonical value of 1 gm/cm³ is generally used as the production rate roughly scales with the density.

The velocity of the grains has to be obtained from the study of the dust-gas dynamics in the coma. Either the dust velocities calculated based on a simplified expression for the dust or by the results based on detailed dust-gas dynamics may be used.

The size distribution function for cometary dust is generally taken as

$$n(a)da \propto a^\alpha da \quad (9.12)$$

where α is a constant. The value of α is generally ~ -3.5 (Sec. 9.3). Some variation in the above type of function has also been used.

The production of dust can be calculated from Eq. (9.8), provided the scattered continuum is known. As discussed earlier, it is rather difficult to get accurately this quantity due to the presence of strong emission bands in the visual spectral region. This will also introduce uncertainty in the derived production rate of grains. However, the difficulty associated with band emissions improves in the red wavelength region. In addition, the observed fluxes in the near infrared region of comets essentially refer to the scattered radiation by the dust particles. Therefore, it may be advantageous to use the observed fluxes in this spectral region for the calculation of production rate. Some sample calculated results are given in Table 9.1. It is interesting to note that the derived production rate of grains from the observed scattered fluxes and infrared fluxes agree reasonably well.

Table 9.1 Production rate of grains (Kg/s).

Comet	Date	r(au)	Δ (AU)	From IR emission*	From scattered radiation
Halley	25 Aug 85 (Pre)	2.81	3.16	2.4(4)	3.4(4)
	26 Sept 85 (Pre)	2.40	2.18	5.8(4)	5.0(4)
	8 Jan 86 (Pre)	0.90	1.29	2.9(6)	2.2(6)
	2 May 86 (Post)	1.65	0.85	5.3(5)	3.8(5)
	30 May 86 (Post)	2.05	1.75	2.5(5)	2.4(5)
Kohoutek	10 Dec 73 (Pre)	0.65	1.2	2.0(6)	2.5(6)
	16 Dec 73 (Pre)	0.48	1.1	2.0(6)	3.4(6)
	1 Jan 74 (Post)	0.23	1.0	5.0(6)	8.0(6)
	4 Jan 74 (Post)	0.33	0.9	3.3(6)	3.8(6)

* Krishna Swamy, K.S. 1991. *Astr. Ap.* **241**, 260.

Pre: Pre-perihelion observation.

Post: Post-perihelion observation.

9.1.4. *Dust production from $A(\theta)f\rho$*

In view of the difficulties associated with deriving accurate scattered radiation of dust from continuum observations as well as its interpretation, sometimes it may be sufficient to use a quantity which represents the average property of the grain. This will be particularly useful in the inter-

comparison of observations of various comets. Therefore, a quantity $A(\theta)f\rho$ has been used extensively as a proxy dust production in comets and it is given by

$$A(\theta)f\rho = \left[\frac{2\Delta r}{\rho} \right]^2 \left(\frac{F_{\text{com}}}{F_{\odot}} \right) \rho. \quad (9.13)$$

Here $A(\theta)$, f and ρ represent the average grain albedo for the phase angle of observation θ , filling factor of the grains in the field of view and the linear radius of aperture projected on the comet respectively. F_{com} is the observed cometary flux. The filling factor f is given by

$$f = \frac{N(\rho)\sigma}{\pi\rho^2} \quad (9.14)$$

where $N(\rho)$ is the number of grains in the field of view and σ is the average grain cross-section. If the column density $N(\rho) \propto \rho^{-1}$, as in the case of the radial outflow model, the quantity $A(\theta)f\rho$ becomes independent of the field of view or the geocentric distance. The advantage of the quantity $A(\theta)f\rho$ is that it can be directly determined from the measurable quantities. Since $A(\theta)f\rho$ depend upon the phase angle, some correction may be needed on the measurements. The resulting values of $A(\theta)f\rho$ which has been corrected to zero phase angle represents the intrinsic production of dust of the comet. In addition there could be some deviation in the projected density from ρ^{-1} variation, which could have some effect on the measurements made with different aperatures. The quantity $Af\rho$ allows comparison of dust production rates of comets.

The calculated dust production rate $A(\theta)f\rho$ from observations for Comet Halley is shown in Fig. 6.6. The resulting variation of $Af\rho$ corrected to zero phase angle is quite similar to Fig. 6.6. The power law constant which are for the pre- and post-perihelion observations give values of -2.96 and -2.25 respectively. The interesting feature is the pre- and post perihelion data do not converge near perihelion in contrast to those of other gas species.

In contrast of Comet Halley, Comet Borrelly has heliocentric distance dependence for OH of -8.9 which is very steep. Other observed molecules have also similar steep slopes. These variations are vastly different from that of $A(\theta)f\rho$ which has a power law slope of around -3 . In addition it does not show any asymmetry about perihelion.

The dust-to-gas ratio is just the ratio $A(\theta)f\rho/Q(\text{OH})$. Since the heliocentric variation of gas and dust is vastly different in Comet Borrelly, the derived gas-to-dust ratio varies during each apparition. There is a strong

asymmetry for the dust between pre- and post-perihelion data in the case of Comet Wild 2. The dust-to-gas ratio was found to have a variation of two orders of magnitude between different comets in the study of a sample of 85 comets. The variation that have been seen among different apparitions in the same comet could be due to evolutionary effect.

As can be seen from the above discussion, there appears to be a wide variation in the dust-to-gas ratio in comets and its variation with heliocentric distance. These could be the consequence of strong seasonal effect which is also present in the gas species as pointed out earlier.

9.2. Polarization

9.2.1. Linear polarization

The scattered light from cometary dust is usually linearly polarized, which implies that the electromagnetic wave has preferential plane of oscillation. For randomly oriented particles the electromagnetic wave oscillates either perpendicular (called positive polarization) or parallel (called negative polarization) to the scattering plane.

The polarization of the scattered radiation is another important observation which can give information as to the nature and size of the particle. In fact, it is found that the polarization is quite sensitive to the shape, structure and sizes of the dust particles.

The appearance of bright Comets Arend-Roland and Mrkos gave a good opportunity for making the first good polarization measurements. The measured polarization at $\lambda \sim 5000 \text{ \AA}$ and for the phase angle of $\sim 100^\circ$ for both the comets is about 20%. Until the recent measurements on Comet Halley, there were not many systematic continuum polarization measurements on a single comet over an extended range of heliocentric distances and/or for scattering angles from 0 to 180° . The available observations were referred either to the fixed scattering angles or to fixed heliocentric distances. The observations were also referred to mostly in the visual spectral region based on the use of broad-band passes. Therefore, as in the case of continuum measurements, the possible contribution of the molecular emission features has to be taken into account. The observed variations of the polarization with scattering angle for several comets are shown in Fig. 9.4. They show a well defined mean polarization curve as a function of the scattering angle. The polarization shows negative values for scattering angles $\geq 160^\circ$, a gradual increase with a decrease in scattering angle reaching maximum

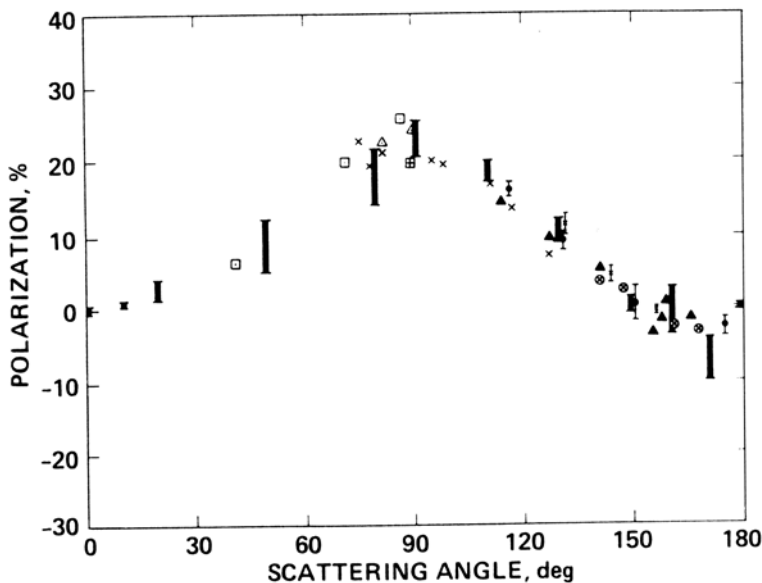


Fig. 9.4 The observed dust polarization in several comets denoted by various symbols is plotted as a function of the scattering angle. The existence of negative polarization for scattering angles around 170° can be seen. The observations clearly delineate a well defined polarization curve as a function of the scattering angles. The dark vertical bars are the calculated values (Krishna Swamy, K. S. and Shah, G. A. 1988. *Monthly Notices*, **233**, 573).

polarization value ~ 20 to 30% around $\theta \sim 90^\circ$ and then decrease for θ 's $< 90^\circ$. The observed negative polarization is typically around -2% and is parallel to the scattering plane. The neutral point is around the scattering angle of $\sim 160^\circ$. The polarization becomes perpendicular to the scattering plane for scattering angle less than 160° . The extensive polarization measurements carried out in Comet Halley from the visible to the near-infrared wavelength region show a very similar behaviour as shown in Fig 9.4. This general behaviour could be taken as a representative of quite conditions of the coma. There could be a variation of polarization with the level of activity of the nucleus, such as the presence of jets, bursts or in active comets.

For interpreting polarization observations, Mie theory has been used extensively. From a comparison of the observed polarization with those of calculations, it is possible to restrict the ranges in the input parameters for the dust particles. In general, the smaller size particles have a

complicated polarization behaviour with respect to the wavelength and the scattering angles. In order to reproduce the observed value of polarization, one requires the complex part of the refractive index to be small. This is also consistent with the result that a high value of the complex part cannot produce negative polarization for large scattering angles. Therefore, roughly one can put a range for the parameters n and k of $1.3 < n < 2.0$ and $0.01 < k < 0.1$ and particle size $\geq 1\mu$.

The usual procedure adopted is to calculate the polarization as a function of the scattering angle for a grid of real and imaginary part of the refractive index, particle size distribution and then to try to get the best fit to the observations. Such an analysis was carried out for Comet Halley based on the size distribution of grains derived from Vega measurements. This leads to an average refractive index of the grain for the visible region, $n = 1.39 \pm 0.01$ and $k = 0.035 \pm 0.004$. The observed linear polarization with the scattering angle for several comets is also consistent with such a refractive index (Fig. 9.4). The calculations for rough particles, including both silicate and graphite grains, also give a good fit to the Comet Halley polarization measurements.

So far the discussion pertained to the average behaviour of the observed polarization in various comets. However the polarization data seems to indicate a wider dispersion in polarization values for scattering angle less than 150° . It seems to fall into two distinct classes corresponding to the maximum polarization. This is shown in Fig. 9.5. One group such as Comets West, Halley, Levy 1990XX etc. corresponds to comets with high polarization of around 25–30%. The other group of comets such as Kobayashi-Berger-Milon, Austin etc. appears to belong to low polarization values around 10–15%. The polarization observations of the bright Comet Hale-Bopp limited to scattering angles $> 132^\circ$ show distinctly higher values than the above two groups. Efforts are being made to understand the real nature of these two apparently two classes of comets.

The polarization also shows wavelength dependence. The wavelength dependence of polarization has been carried out on several comets. The characteristic feature is that the polarization increases with increase in wavelength from the visible region. It also depends upon the scattering angle. This was noticed in Comet Halley and later confirmed based on other comets. However few comets have shown that the degree of polarization decreases with increase in wavelength as was observed in Comet Giacobini-Zinner. The polarization changed from 8% at 4430 Å to 5% at 6420Å observed at phase angle 44° . This type of behaviour was also seen

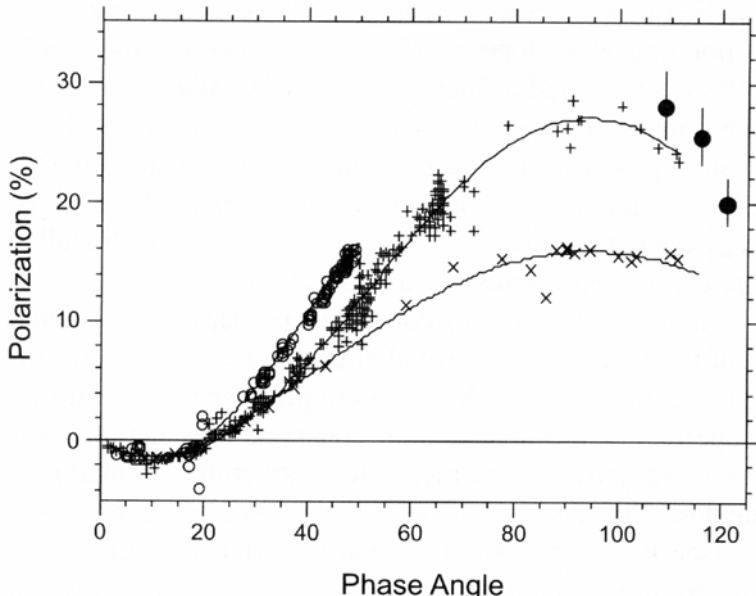


Fig. 9.5 The observed polarization of comets for phase angles 0.3 to 120°. They seem to divide comets into classes depending on the maximum polarization (Levasseur-Regourd, A.-Ch, Hadamcik, E. and Renard, J.B. 1996. *Astron. Astrophys.*, **313**, 327).

in Comet Halley based on Giotto measurements. This has also been seen in Comet Tempel 1. The reason for the increase or decrease in polarization with wavelength is basically related to the sizes of the dust particles in relation to the wavelength of the observation. This is due to the fact that the dust particles are efficient scatters when the size of the dust particles is of the order of wavelength of the incident radiation. Therefore the polarization dependence depend upon the size of the dust particles at a given wavelength.

An extensive polarimetric measurements of the tail of Comet Ikeya-Seki carried out in 1965 when the comet was at $r \approx 0.3$ AU showed the surprising result that the polarization value changed from +0.20 to -0.42% with scattering angles from 116 to 136° respectively, for $\lambda = 0.53 \mu\text{m}$. The neutral point (zero polarization) was found to be around a scattering angle of 125°. The linear polarization measurements carried out along the tail of Comet Halley in April 1986, at $r = 1.3$ AU showed that they are very similar at 1000 km, 3000 km from the nucleus and for the envelope around the nucleus, for the scattering angles between 125 to 160°. These

observations showed that there was no change in the crossover angle of linear polarization and there was also no drastic modification of the grains as they were transported from the nucleus out to distances of around 1.6×10^6 km.

The expected polarization calculated as a function of the particle size shows that it is possible to produce positive and negative polarizations for grain composition of silicate type and not for that of dirty ice (ice with a small complex part), graphite or iron. Figure 9.6 shows the typical result obtained for grain composition of olivine. As the polarization is very

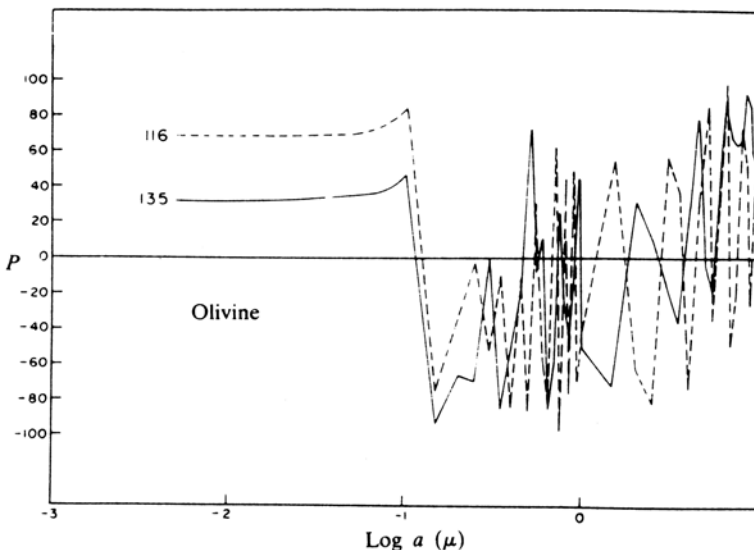


Fig. 9.6 Expected polarization versus particle sizes for $\lambda = 5300 \text{ \AA}$ and for two scattering angles of 116° and 135° . The oscillations will smoothen out with the use of a size distribution function (Krishna Swamy, K. S. 1978. *Astrophys Space Sci.* **57**, 491).

sensitive to particle sizes, it is possible to get reversal in polarization, if there is a variation of particle size along the tail of the comet.

At the present time, there exist several kinds of observations pertaining to scattering and polarization properties of cometary dust. Any proposed cometary dust model should be able to explain simultaneously all these observations. Attempts are being made to develop such a model. One such model proposed to explain all the observed characteristics in the visual spectral region uses aggregates of 10 to 1000 monomers with sizes $\sim 0.1 \mu\text{m}$ composed of silicate, carbonaceous material and iron-bearing sulphides with volume fraction of one-third silicates, two-thirds carbona-

ceous material and a small amount of iron-bearing sulphides. The resulting mean refractive index derived for this mixture based on Maxwell-Garnet mixing rule and consistent with the Comet Halley's *in situ* abundances is $m_{av} = 1.88 + 0.47i$ for $\lambda = 4500 \text{ \AA}$ and $m_{av} = 1.98 + 0.48i$ at $\lambda = 6000 \text{ \AA}$. The result based on this model can reproduce the correct behaviour of the observed characteristics of comets such as, the observed shape of angular dependence of scattering intensities and polarization. The model can account for all the observed trends and also the mineral composition of cometary dust is consistent with the elemental abundances derived from other considerations. This has led to consideration of more realistic model which can explain the observations in a quantitative manner.

9.2.2. Circular polarization

So far, the discussion pertained to linear polarization. It is also of interest to see whether circular polarization can be detected in comets as it can give additional information about the grains. The expected circular polarization is of the order of 0.5% for certain values of scattering angles which is quite small compared to the linear polarization. Circular polarization was first detected in Comet Halley with an average value of around 1.7×10^{-3} . This was followed by Comet Hale-Bopp which had a circular polarization of -0.26% in 1997. Since then circular polarization has been measured in Comets D/1999 S4(LINEAR), C/2001 Q4(NEAT) etc. The circular polarization seen from comets show left circularly polarized light. This can be seen from Fig. 9.7 where the phase dependence of circular polarization is shown for several comets. The figure also show the increase in circular polarization (absolute value) with phase angle.

The circular polarization is produced only in the case when an incident unpolarized light after scattering by an ensemble of particles violating mirror symmetry. This can arise due to the intrinsic property of the particles itself or it could be due to an external cause. The external processes could due to multiple scattering in an anisotropic medium or scattering by aligned non-spherical particles. Scattering by optically active (Chiral) particles belongs to the other class where the property is intrinsic to the particle.

For multiple scattering to be the cause of the observed circular polarization, the optical depth must be appreciable. The estimated optical depth in a cometary atmosphere appears to be reasonable and therefore in principle this mechanism can account for the observed circular polarization.

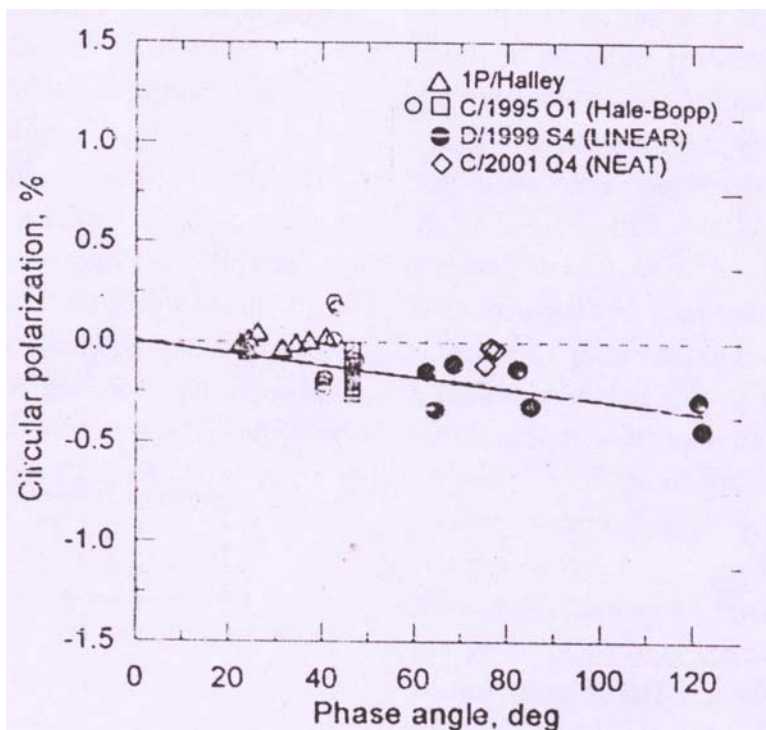


Fig. 9.7 The variation of circular polarization with phase angle for Comets Halley, Hale-Bopp, LINEAR and NEAT (Rosenbush, V., Kiselev, N. and Kolokolova, L. 2008. *Organic Matter in Space*, eds, Kwok S. and Sandford S., Cambridge Univ. Press, Cambridge, p. 311).

In the case of scattering by aligned non-spherical particles, the main problem is associated with the mechanism of alignment of the particles.

The other class of particles is where the circular polarization arises from scattering of light by dust particles composed of optically active material (Chiral). The property of such a material is that they have different refractive indices for left and right circularly polarized light which automatically separate the two polarizations.

It is interesting to note that the above effect is quite strong in complex organic molecules. This is due to the fact that they exist in two forms called Left-handed(L) and Right-handed(D). They arise mainly because the organic molecules are optically active as well as possess circular dichroism. The biomolecules on the earth are only L-amino acids and D(sugar). This is also found to be case in the case of Murchison meteorite (an extrater-

restrial source). Therefore the dust particles present in comets must be Chiral organic in character. This is consistent with the left-handed circular polarization seen from comets. The model based results are in reasonable agreement with the observations.

These studies are highly relevant, as comets are believed to have transported organic molecules on to the earth by cometary impacts (Sec. 13.6). It is intriguing that the biomolecules present on the earth, L-amino acids, could actually be the ones that were transported from comets during earlier times.

9.3. Grain Sizes

Dust particle detectors were used on Giotto and Vega missions to Comet Halley to record dust impact rate and thus to measure the mass distribution of particles. The instrument from both the missions covered together the mass range of around 10^{-6} to 10^{-16} gm. The size distribution of particles can therefore be inferred from these mass measurements. The cumulative mass distribution function for the observed data is consistent with $\alpha = -3.7$ ($n(a) \propto a^\alpha$). The measured mass distribution of dust particles for particles masses $> 10^{-6}$ gm is found to be much flatter compared to smaller masses. This indicated that the total mass is mostly contributed by large size particles. The *in situ* mass distribution of dust particles in the coma of Comet Wild 2 was also carried out by the stardust misssion. The results of these measurements was found to be similar to that of Comet Halley. The *in situ* measurements also showed the dominance of small size particles, $a \leq 0.1 \mu\text{m}$, which cannot generally be detected through observations made in the visible region.

It is possible to deduce the size distribution function of the dust particles from the model fitting to the observed dust tail of comets. These studies indicate the size distribution function is characterized by the power law index of -3.5 . The analysis of the nucleus of Comet Tempel 1 acquired with camera aboard Rosetta spacecraft in the orange filter 6450 Å with the Monte Carlo approach gave an index of -3.0 for the power law size distribution function.

Large size particles are also present in comets. This comes from several observations. The absence of $10\mu\text{m}$ silicate emission feature in the anti-tail of Comet Kohoutek puts a lower limit to the particle size, $a \geq 5 \mu\text{m}$ (Sec. 9.4.2). This conclusion is also consistent with the results based on

dynamical considerations of the anti-tail which gives for the particle sizes, $a \geq 15 \mu\text{m}$. Supportive evidence for the presence of large size dust particles comes from the study of meteor showers which are associated with comets. In addition dust trails seen in comets require millimetre to centimetre size dust particles.

The dust particles emitted from comets span a wide range in sizes, from submillimetre to millimetre to centimetre. The derived size distribution of dust particles based on various studies is a representative value for all comets, but it could vary from comet to comet and can also vary within the coma. The variation in the size distribution of dust particles with distance in the coma can arise as a resultant effect of sorting of particles due to radiation pressure effect and sublimation of volatiles. The power law index, $\alpha \approx -3.5$ of the size distribution function, is also characteristic of interstellar grains and is typical of collisionally evolved bodies.

9.4. Infrared Measurements

There are very few windows in the infrared region that are available for ground based observations, as most of the infrared radiation is absorbed by the Earth's atmosphere (Fig. 9.8). Therefore, most of the observations are carried out with broad band passes. Several such systems exist which have been used by different observers with slight variations in their mean wavelengths and band widths. (Table 9.2).

Table 9.2 Infrared band passes and their wavelengths.

Band pass	Arizona System		IRTF System	
	Wavelength (μm)	$\Delta\lambda$ (μm)	Wavelength (μm)	$\Delta\lambda$ (μm)
J	1.26	0.20	1.20	0.3
H	1.60	0.36	1.60	0.3
K	2.22	0.52	2.2	0.4
L	3.54	0.97	3.55	1.05
L'	-	-	3.78	0.57
M	4.80	0.60	4.7	0.57
N	10.6	5.0	10.50	5.0
Q	21.0	11.0	20.6	9.0

Adapted from Hanner, M.S. and Tokunaga, A.T., 1991. In *Comets in the Post-Halley Era*, eds. R.L. Newburn, Jr *et al.* Kluwer Academic Publishers, p. 70.

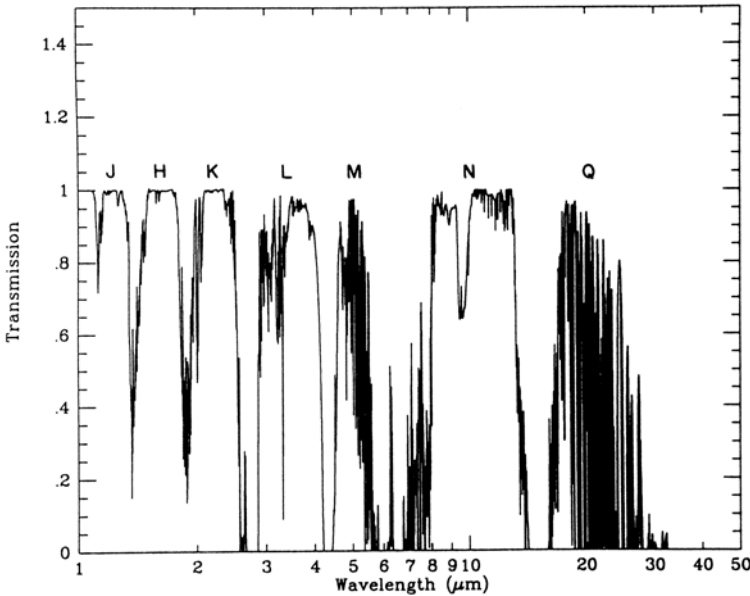


Fig. 9.8 The atmospheric transmission is plotted as a function of wavelength for the region of 1 to 20 μm . The spectral band passes corresponding to *J* to *Q* are also shown (Courtesy Charlie Lindsey).

The first infrared observations made on Comet Ikeya-Seki in 1965 in the wavelength region of 1 to 10 μm showed clearly that the comet was very bright in the infrared wavelength region and its colour temperature was higher than that of a black body at the same heliocentric distance. These results have been confirmed based on the infrared observations of many more comets. Most of the observations on comets before Comet Halley were limited to broad band infrared observations in the spectral region around 2 to 20 μm . However, for Comet Halley it has been possible to get very good broad band and spectroscopic data in the middle infrared and far-infrared wavelength regions based on ground based, airborne and spaceborne instrumentation.

The infrared observations of comets can provide another independent method for extracting significant information on the physical nature of the cometary grains. This is due to the fact that the observed infrared radiation arises from the re-radiation of the absorbed energy by the dust particles

which in turn depends on the nature and composition of the dust. From a detailed comparison of the cometary infrared radiation with the expected infrared fluxes based on grain models, it is possible to infer the physical and the chemical nature of cometary grains. The grains are considered to be in radiative equilibrium with the incident solar energy. The equilibrium temperature of the grain is, therefore, determined by a balance between the absorbed radiation which is mostly in the ultraviolet and visible regions and the emitted radiation which is in the far infrared region. This can be expressed by the condition

$$F_{\text{abs}}(a) = F_{\text{em}}(a, T_g) \quad (9.15)$$

where

$$F_{\text{abs}}(a) = \left(\frac{R_\odot}{r}\right)^2 \int F_\odot(\lambda) Q_{\text{abs}}(a, \lambda) \pi a^2 d\lambda \quad (9.16)$$

and

$$F_{\text{em}}(a, T_g) = \int \pi B(\lambda, T_g) Q_{\text{abs}}(a, \lambda) 4\pi a^2 d\lambda \quad (9.17)$$

where $F_\odot(\lambda)$ representing the incident solar radiation field at wavelength λ , $Q_{\text{abs}}(a, \lambda)$ is the absorption efficiency and $B(\lambda, T_g)$ is the Planck function corresponding to the grain temperature T_g . The difference in the geometrical areas between the two sides arises as the grains absorb in one direction and emit in all the directions. The calculation of the grain temperature involves a knowledge of the size and composition of the grains. Knowing the grain temperature, it is possible to calculate the infrared emission from Eq. (9.17).

In general, the emission has to be integrated over the size distribution function to get the total infrared emission from the grains. Therefore, the total infrared emission at the Earth is given by

$$F_{\text{em}}(\lambda, r) = \frac{1}{\Delta^2} \int_0^\alpha n(a) \pi a^2 Q_{\text{abs}}(a, \lambda) B(\lambda, T_g) da \quad (9.18)$$

where $n(a)da$ represents the relative number of grains in the size interval between a and $a + da$ and Δ is the geocentric distance of the comet. If there are grains of various types present at the same time, then the total observed infrared radiation is the sum total over all the grain types, j , i.e.,

$$F_{\text{total}}(\lambda, r) = \sum_{i=1}^j F_{\text{em}}(\lambda, r)_i x_i \quad (9.19)$$

where x_i is the fraction of the grain population of type i . The corresponding mass of grains of type i is given by

$$M_i = \int_o^{\alpha} \frac{4\pi}{3} a^3 \rho_i n(a) da \quad (9.20)$$

where ρ_i is the density of the i^{th} type of the material.

The important observation which gave some clue to the possible nature of the grain was the detection of a broad $10 \mu\text{m}$ emission feature in Comet Bennett (C/1969 Y1). Another feature at $20 \mu\text{m}$ also appears to be present in many comets (see Fig. 9.9). However, the whole profile does not show up in these broad band observations as the last band pass is at around $20 \mu\text{m}$. The observed features at 10 and $20 \mu\text{m}$ are widely believed to be due to a silicate type of material (Sec. 9.5). The moderate resolution observations of Comet Halley made in the $10 \mu\text{m}$ region with Kuiper Airborne Observatory has given important information about the nature of the silicate material in showing that it is in crystalline in nature.

Observations of the $10 \mu\text{m}$ feature in the spectra of comets show that the apparent strength of this feature varies from comet to comet and also with the heliocentric distance for the same comet. The strength of the 10 and $20 \mu\text{m}$ features is a function of the particle size. It becomes weaker with an increase in size of the particles (Sec. 9.4.2). Therefore, silicates can still be the dominant component of the grain even if no $10 \mu\text{m}$ feature is evident in the spectra. Another new emission feature near $3.4 \mu\text{m}$ was detected in the spectra of Comet Halley. This also appears to be a common feature of most of the observed comets. The $3.4 \mu\text{m}$ feature is a characteristic of the C-H stretching vibrations and indicates the presence of some form of hydrocarbons. Taken together, the infrared spectra of comets suggest, there are two components to the grains – silicates and some form of carbon.

Several attempts have been made to reproduce the observed infrared radiation from comets using models based on assumed optical properties for the cometary dust particles. They include models such as, assuming constant refractive index for the material or its variation with wavelength or a mixture of materials such as silicate and some form of carbon with some size distribution function etc. (See Sec. 9.5.2).

9.4.1. *Dust production from infrared observations*

The production of dust can also be determined from the observed infrared radiation of comets. The observed infrared radiation at the Earth,

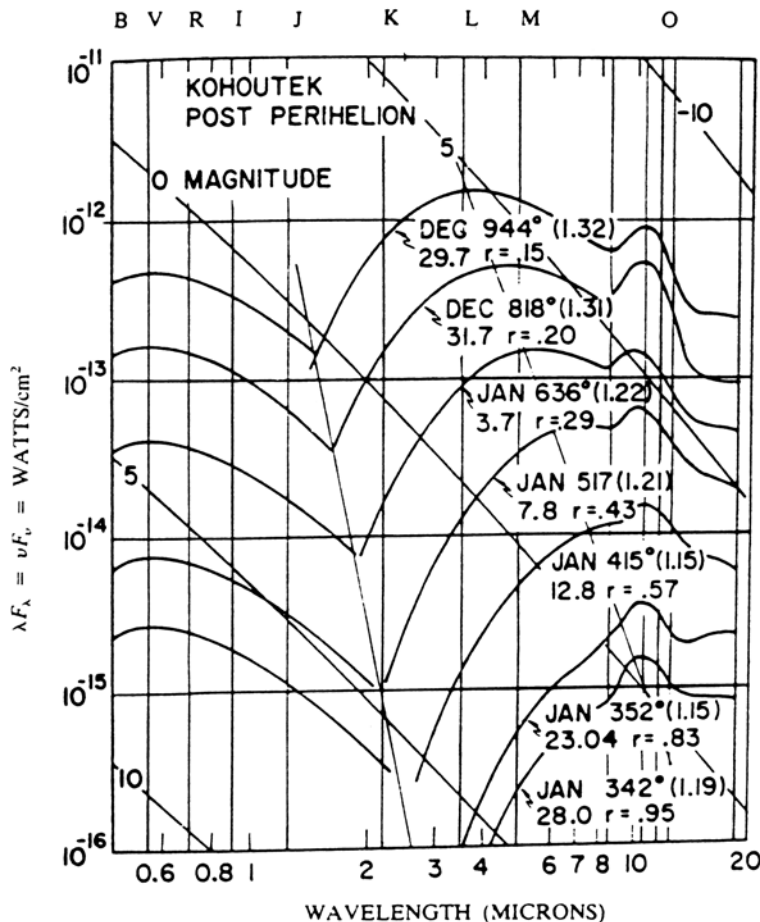


Fig. 9.9 Observed infrared fluxes plotted as a function of wavelength for Comet Kohoutek. The fitted black body temperature for each of the curves along with the factor by which the temperature exceeds the black body temperature is also shown. (Ney, E. P. 1974. *Icarus*, **23** 551).

F_{earth} is related to the total number of grains in the coma, $N(r)$ through the relation

$$F_{\text{earth}} = \frac{E_\lambda}{4\pi\Delta^2} \quad (9.21)$$

where E_λ represents the infrared radiation of the comet given by

$$E_\lambda = B(\lambda, T_g)Q_{\text{abs}}(a, \lambda)4\pi a^2 N(r). \quad (9.22)$$

Here Δ is the geocentric distance. A rough estimate for the production rate can be obtained from the relation

$$Q_D(r) \simeq \frac{N(r)}{\tau} \quad (9.23)$$

where τ is the lifetime of the grain. This gives an average dust mass rate of about 4×10^6 gm/sec for the assumed lifetime of the grain $\tau \simeq 4 \times 10^4$ sec. However, in general, it is necessary to take into account the effect of the size distribution of grains. Therefore, the production rate of grains in gm/sec, as in the case of continuum can be calculated from the relation

$$Q_D^{iR}(r) = \frac{4\pi\Delta^2 F_{\text{earth}}}{\delta} \left[\frac{\bar{M}}{\bar{E}_\lambda} \right] \bar{V} \quad (9.24)$$

where

$$\bar{E}_\lambda = \int_{a_{\min}}^{a_{\max}} B(\lambda, T_g) 4\pi a^2 Q_{\text{abs}}(a, \lambda) n(a) da. \quad (9.25)$$

The expressions for \bar{M} and \bar{V} are given by Eqs. (9.10) and (9.11). All the symbols which occur in these equations are described in Sec. 9.1.3 or have their usual meanings. The calculation of the production rate of grains from Eq. (9.24) involves the knowledge of density, velocity and size distribution function for the grains. A discussion regarding these quantities is also outlined in Sec. 9.1.3. The production rate of grains has been calculated for various comets. The results for Comet Halley for heliocentric distances between 2.8 and 0.6 AU show a close relation with an r^{-4} dependence, while the results for Comet Kohoutek show a close relation for heliocentric distances between 0.15 and 1.5 AU with an r^{-2} dependence. It is interesting to see whether there exists a general behaviour of the production rate of dust with the heliocentric distance in comets. This could be carried out by the superposition of the shape of the derived dust production rate with the heliocentric distance of various comets and the results are shown in Fig. 9.10.

The gas (composed of H_2O) and the dust coming out of the nucleus of a comet flow outwards in such a way that the gas carries the dust with it. Therefore, to a first approximation, the heliocentric variation of the dust production rate and the water production rate should be very similar as can be seen from Fig. 9.10. The dependence of r^{-2} for $r \leq 1$ AU arises due to the solar flux falling off as r^{-2} and it then deviates from this dependence due to the effect of temperature dependence of the vapour pressure. The ratio of gas to dust for a representative sample of comets is given in Table 9.3.

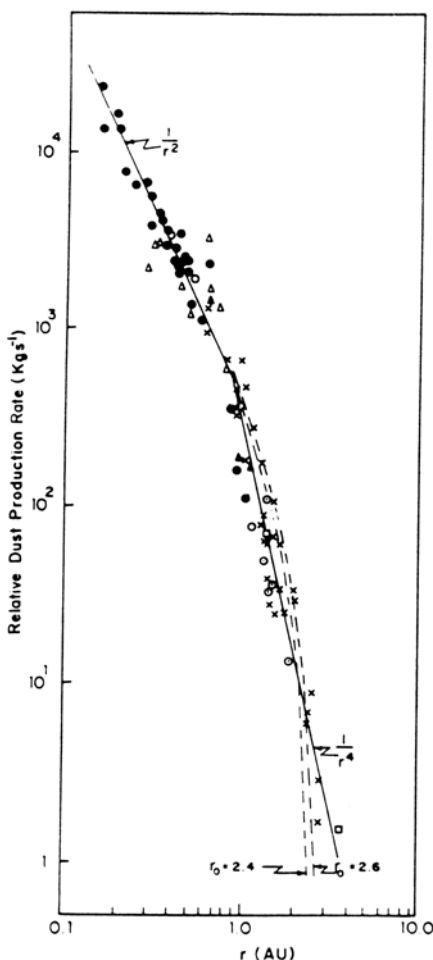


Fig. 9.10 A composite diagram showing the general shape of the variation of the dust production rate with heliocentric distance is derived from several comets, denoted by various symbols. There is a tight relation with heliocentric distance r showing r^{-2} variation up to $r \leq 1$ AU and r^{-4} for $r \geq 1$ AU. The dashed curve shows the shape of the derived water production for $r_0 = 2.4$ and 2.6 respectively (Krishna Swamy, K. S. 1991. *Astron. Astrophys.*, **241**, 260).

Table 9.3 Gas to dust ratio in comets ($r = 1$ AU).

Comets	$Q(H_2 O)$ (Kg/sec)	$Q(\text{dust})$ (Kg/sec)	$H_2 O/\text{dust}$
Bennett (1970 II)	1.5(4)	1.5(3)	10
Churyumov-Gerasimenko (1982 VIII)	1.1(2)	5.4(1)	2
P/Crommelin (1984 IV)	1.8(2)	1.2(3)	0.1
P/Encke	2.1(2)	2.8(1)	7
P/Giacobini-Zinner (1985 XIII)	1.2(3)	3.8(2)	3
P/Grigg-Skjellerup (1982 IV)	9.0(1)	2.0(1)	5
P/Halley (1986 III)	1.5(4)	5.4(3)	3
IRAS-Araki-Alcock (1983 VII)	2.2(2)	2.0(2) ^a	$\lesssim 11.1$
Kobayashi-Berger-Milon (1975 IX)	6.0(2)	1.0(2)	6
Kohoutek (1973 XII)	9.2(3)	4.6(2)	20
Sugano-Saigusa-Fujikawa (1983 V)	8.1(1)	2.0	40
West (1976 VI)	1.5(4)	3.5(3)	4
Wilson (1987 VII)	1.1(4)	1.8(3)	6

(Krishna Swamy, K.S. 1991. *Astron. Astrophys.*, **241**, 260).

9.4.2. Anti-tail

The characteristic feature of Comet Kohoutek was the presence of the anti-tail seen shortly after the perihelion passage. The infrared measurements of this comet made on the same day showed the presence of $10 \mu\text{m}$ emission in the coma and in the tail, but not in the anti-tail (Fig. 9.11). The absence of $10 \mu\text{m}$ feature in the anti-tail immediately puts a lower limit to the particle size, as can be seen from Fig. 9.12. The figure shows the shape of the emission curves for grains of silicate type for different sizes and for grain temperatures of interest. It shows that the strength of the $10 \mu\text{m}$ feature is a function of the particle size and for $a \geq 5 \mu\text{m}$, the feature actually disappears. The 10 and $20 \mu\text{m}$ features in small size grains show up as they are optically thin. As the size of the particle gets larger and larger, the material becomes optically thick and the feature gets washed out. Therefore, the particles present in the anti-tail appear to be of a much larger size compared to those present in the coma or in the tail region. This conclusion is also consistent with the results based on dynamical considerations of the anti-tail which gives for the particle sizes, $a \geq 15 \mu\text{m}$. The strength of the silicate feature can change from comet to comet. It can also change with time for the same comet as was the case for Comet Bradfield. This comet had the silicate signature in the observations of March

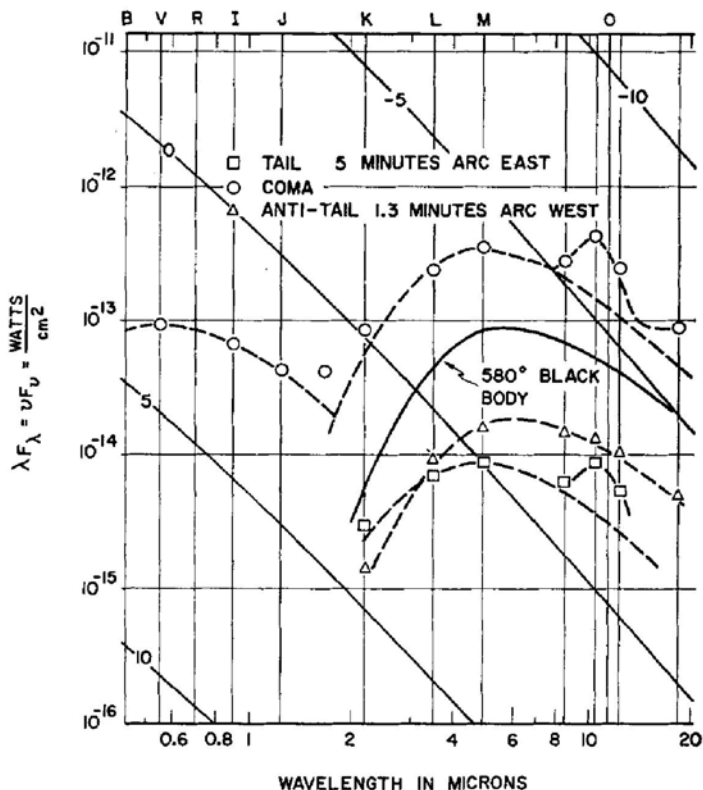


Fig. 9.11 Measured energy distributions in the coma, tail and anti-tail of Comet Kohoutek are plotted as a function of wavelength. Observations refer to January 1.7, 1974. The absence of 10 micron feature in the anti-tail observations can be seen. (Ney, E. P. 1974. *op. cit.*).

21.9, 1974 ($r = 0.51$ AU and $\Delta = 0.73$ AU), but was clearly absent in the observations of April 5.8, 1974 ($r = 0.67$ AU and $\Delta = 0.69$ AU). These observations show that the sizes of the emitted grains (Fig. 9.12) could vary from comet to comet, as well as with the heliocentric distance for the same comet. The supporting evidence for the large size particles in the anti-tail also comes from the colour temperature measurements of Comet Kohoutek. It showed that the colour temperature for the anti-tail was much cooler and therefore closer to the black body temperature than that of the coma and the tail temperature.

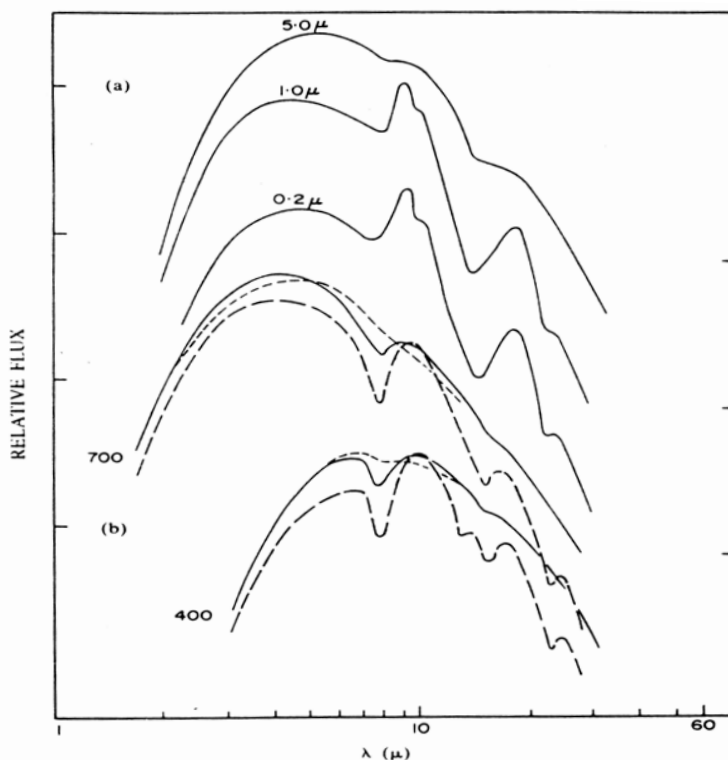


Fig. 9.12 Shape of emission curves for different sizes, grain temperatures and for material of moon samples are shown. (a) For moon sample 12009, $T_g = 550^{\circ}\text{K}$ and sizes of 0.2, 1.0 and 5.0 microns. (b) For moon sample 14321, $T_g = 400$ and 700 K. Long-dashed, continuous and dashed curves refer to particle sizes of 2, 5 and 10 microns respectively. (Krishna Swamy, K. S. and Donn, B. 1979. *A.J.*, **84**, 692).

9.5. Spectral Feature

The most direct way of getting information about the composition of the grain is through the detection and identification of characteristic spectral features such as the vibration-rotation bands of molecules. It is important to note that such bands retain their identity even when the molecules are in the solid state.

9.5.1. Silicate signature

As already remarked, the clue to the possible chemical composition of the cometary grain came from the infrared measurements themselves, with the first detection of a broad emission feature at $10\mu\text{m}$ in Comet Bennett. This was confirmed by the observation of many other comets, although the strength may vary from comet to comet with heliocentric distance.

The next logical step is to try to identify the nature of the material responsible for giving rise to this feature. Laboratory measurements of the absorption spectra of various types of rocks and minerals carried out at room temperature or at liquid nitrogen temperature (89°K) have a common property in showing strong and broad absorption feature around $10\mu\text{m}$ (Fig. 9.13). This is attributed to Si-O stretching vibrations. From the similarity between the laboratory spectra and the cometary spectra, it is suggested that the $10\mu\text{m}$ feature observed in cometary spectra is due to some type of silicate material. There is the other broad feature present in the laboratory spectra around 20 micron arising out of Si-O-Si bending vibrations. This feature has also been seen in cometary spectra confirming the silicate nature of dust. The laboratory spectra in addition to showing the main features at 10 and $20\mu\text{m}$, also show a few other secondary features which are the characteristics of the particular types of silicate material. If these features show up, then it could be used as a diagnostic of the dust composition. The silicate material also shows another feature around 30 to $33\mu\text{m}$ as was observed in the laboratory absorption spectra of $\gamma-\text{Ca}_2\text{SiO}_4$, Olivine (Mg_2SiO_4) or other silicates. Unlike the 10 and $20\mu\text{m}$ features, the feature around $30\mu\text{m}$ seems to depend more on the chemical composition of the material.

The observed shape of the $10\mu\text{m}$ feature in comets should be able to provide information about the composition of the grains, since different silicate materials have different band profiles depending upon Si-O stretching frequencies. The observations carried out on Comet Halley with the Kuiper Airborne Observatory and ground-based telescopes clearly showed a well defined spectral feature at $11.2\mu\text{m}$ located inside the broad $10\mu\text{m}$ emission feature (See Fig. 9.14). This feature is attributed to crystalline olivine [$(\text{Mg}, \text{Fe})_2\text{SiO}_4$] based on good spectral match with the observed spectral emissivity of Mg-rich olivine. The strong $10\mu\text{m}$ emission feature has been seen from a number of comets. Comet Hale-Bopp had the strongest silicate emission among all the observed comets. It was also unusual in showing a strong silicate feature even at 4.6 AU pre-perihelion. A typical $10\mu\text{m}$

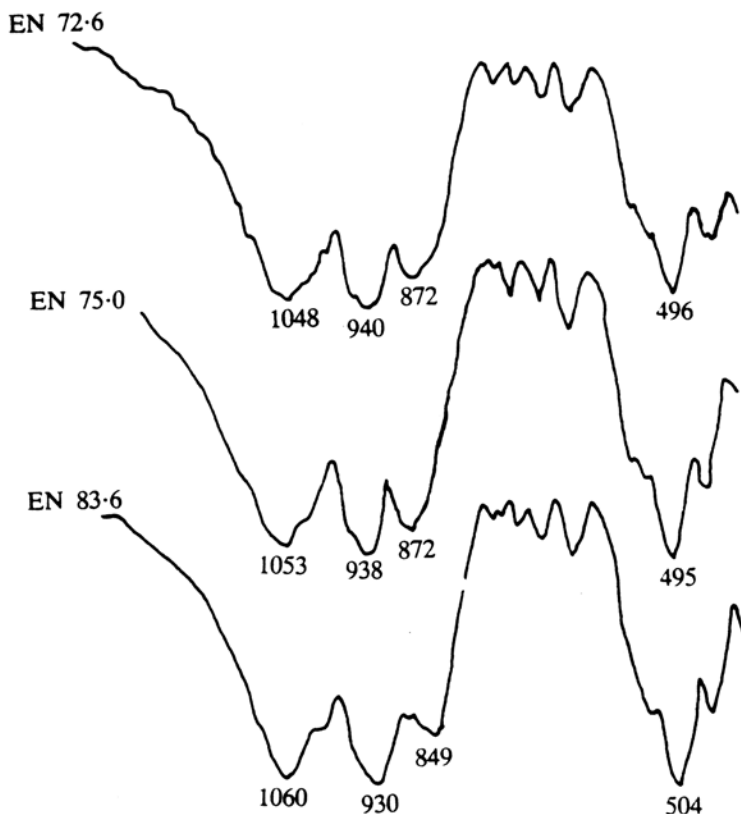


Fig. 9.13 Absorption spectra of Orthopyroxene ionosilicates. Sample curves shown (in cm^{-1}) are for the enstatite-hypersthene series of En_{62} , En_{75} and En_{84} . (Adapted from Lyon, R. J. P. 1963. NASA Technical Note, NASA TN D-1871).

spectral feature observed in a comet is shown in Fig. 9.14.

There are three strong feature at 9.2, 10.0 and 11.2 μm . The other features which are minor in nature is at 10.5 and 11.9 μm . The 11.2 μm feature is due to crystalline olivine, as was seen earlier, in the Kuiper Airborne Observations on Comet Halley. Crystalline olivine has also a secondary peak at 10 μm and a weak feature at 11.9 μm . The broader 10 μm maximum in the cometary spectra is characteristic of amorphous olivine. The characteristic signature of pyroxene [$(\text{Mg},\text{Fe})\text{SiO}_3$] is the presence of a feature at 9.2 μm . Therefore the cometary 9.2 μm feature corresponds to amorphous Mg-rich pyroxene. Crystalline pyroxene has also a feature near 9.3 μm .

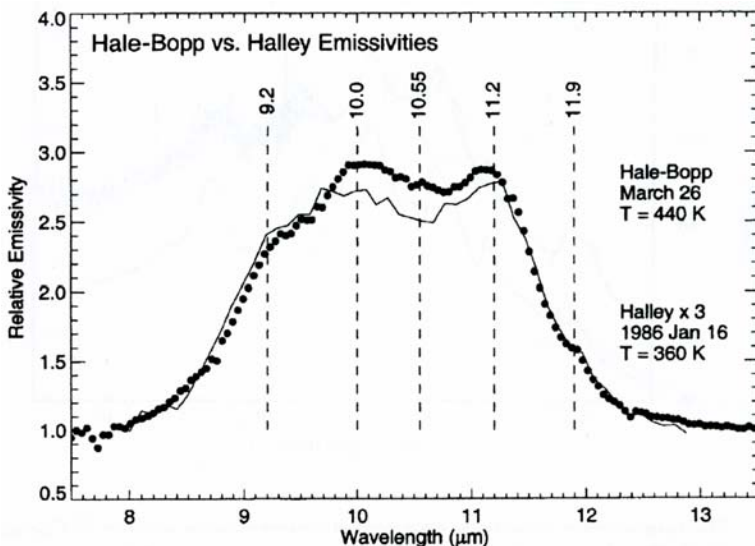


Fig. 9.14 Shows the shape of the emission feature around $10 \mu\text{m}$ in Comets Halley ($r = 0.79 \text{ AU}$, line) and Hale-Bopp ($r = 0.92 \text{ AU}$, dots) with various spectral signatures. (Hanner, M.S. et. al. 1999. *Earth, Moon and Planets*, **79**, 247).

Crystalline pyroxene in general have a wide range of spectral features. The peak at $10\text{--}11 \mu\text{m}$ contribute to the width of total feature and the structure near $10.5 \mu\text{m}$.

9.5.2. Mineralogy of dust particles

Comet Halley

The mineralogical composition of dust particles was first obtained for Comet Halley based on *in situ* measurements. This came from the studies of mass spectra of around 5000 particles made with instrument on board Giotto and Vega Spacecrafts. The mass spectra basically provide the elemental composition of the dust particles. The mass spectra clearly indicated the presence of dust particles with rock-forming elements Mg, Si, Ca, and Fe. It also showed the presence of dust particles containing both rock and CHON elements (Sec. 9.6).

The next step is to get some information on the mineralogical composition of the dust particles. From a knowledge of the abundances of various elements, it is possible to make a systematic analysis of the variation among

the observed grains and make some broad classification of its composition. For this purpose the cluster analysis method can be used. Cluster analysis is a statistical method of grouping a set of data points to look for correlations among them. This method has been applied to classify Comet Halley's dust particles. In this study, the abundant inorganic elements Na, Mg, Al, Si, S, Ca and Fe have been considered. The result of these studies and with the observed distribution of Fe/(Fe+Mg), Mg-Fe-Si, Mg-Fe-O and Mg-Fe-S, it has been possible to characterise the particles into a few major mineral groups. The resulting major mineralogical composition of dust particles in Comet Halley is given in Table 9.4. As can be seen from the table, the dominant component is the Mg-Si-O rich particles (olivine, pyroxene etc.). The other group comprising around 10% are the particles of Fe, Ni and sulphides. These particles could consist of Pyrrhotite ($Fe_{1-x}S$) and Pentlandite($Fe Ni_9 S_8$). All these results indicate that the cometary dust is an unequilibrated heterogeneous mixture of minerals containing both high and low temperature condensates.

Table 9.4 Estimated mineralogical composition of Comet Halley Dust.

Mineral group	Estimated proportion	Mineral chemistry	possible minerals
Mg silicates	> 20%	Fe-poor, Ca-poor	Mg-rich pyroxene and/or olivine
Fe sulfides ~ 10%	some Ni-rich	pyrrhotite, pentlandite	
Fe metal	1-2%	Ni-poor	kamacite
Fe oxide < 1%		magnetite	

Schulze, H., Kissel, J. and Jessberger, E.K. 1997, From *Star Dust to Planetesimals*, ASP Conference Series, Vol. **122**, p. 397, eds. Y. Pendleton and A.G.G.M. Tielens, By the kind permission of the Astronomical Society of the Pacific Conference Series.

Comet Hale-Bopp

The remarkable spectra taken with Infrared Space Observatory in the wavelength region 5 to 45 μm on Comet Hale-Bopp at heliocentric distance, $r = 2.9$ AU showed the true nature of the grain material. The spectra show clearly five strongest emission features at 10, 19.5, 23.5, 27.5 and 33.5 μm (Fig. 9.15). The wavelength of all peaks correspond to Mg-rich crystalline olivine (forsterite, Mg_2SiO_4) when compared with the laboratory spectra. Minor features present in the spectra are attributed to crystalline pyroxene

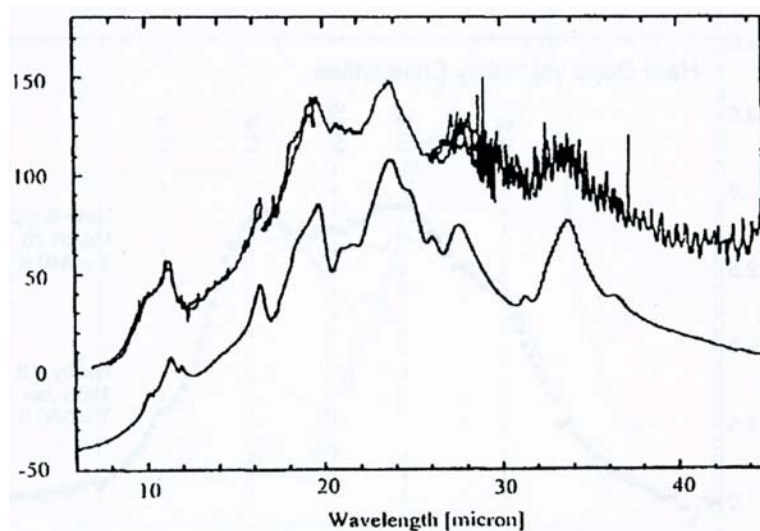


Fig. 9.15 The upper curve shows the silicate emission features in Comet Hale-Bopp observed with ISO, in the wavelength region 5 to 45 μm . The lower curve shows the modeled spectrum of forsterite from the laboratory data (Crovisier, J. et al. 1997. *Science*, **275**, 1904).

$[(\text{Mg},\text{Fe})\text{SiO}_3]$. The agreement between the two is excellent. The infrared observations of comets have clearly shown that silicate grains in comets are Mg-rich. Models have been proposed to match the observed infrared spectra of Comet Hale-Bopp based on a mixture of silicate minerals. A good fit could be obtained with the following five emission components: black body 1($T = 280$ K), black body 2($T = 165$ K), Mg-rich olivine (forsterite, cry O1), Ortho pyroxene (cry O-pyr) and amorphous (Am Pyr) silicates. The relative abundances of silicates are Cry O1:Cry O-pyr: Am pyr = 0.22:0.08:0.70. The temperature of silicate grains used in the model is 210 K. Therefore the spectral structure indicate complex mineralogy for cometary silicates containing both crystalline grains of olivine and pyroxene as well as amorphous silicates. The observed mineralogy in Comet Hale-Bopp is similar to pyroxene-rich and olivine-rich chondritic aggregate IDPs thought to originate from comets. The grains in Comet Hale-Bopp is also Mg-rich which is also in agreement with the chemical composition in the coma of Comet Halley.

The ISO spectra of young stars with a dust disk such as Herbig's Ae/Be star HD 100546 is strikingly similar to that of Comet Hale-Bopp as can be

seen from Fig. 9.16. This shows the similarity in the mineralogy of the grain material.

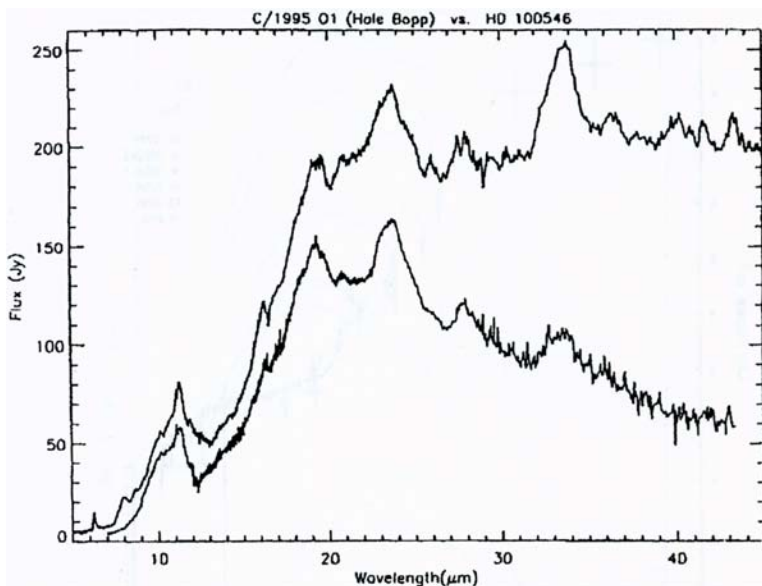


Fig. 9.16 Comparison between the ISO-SWS spectrum of Ae/Be star. HD 100546 (top curve) with the corresponding spectrum from Comet Hale-Bopp (bottom curve). The striking resemblance between the two curves can clearly be seen (Malfait, K., Waelkens, C., Waters, L.B.F.M. *et al.* 1998. *Astron. Astrophys.*, **332**, L25).

Comet Tempel 1

Deep Impact mission gave the first opportunity to look at the deeper layer material ejected from Comet Tempel 1. The spectral characteristics of this material was observed by the Spitzer Space Telescope in the spectral region from 5–35 μm . The emission from the normal coma and the nucleus, which is representative of the pre-impact spectrum was subtracted out from the observed spectrum. The resulting emission spectrum represent basically the emission from the ejected material. This is shown in the Fig. 9.17. The conspicuous features in the spectrum are carbonates in the region 6.5 to 7.2 μm , pyroxenes in the region 8 to 10 μm , olivines at 11 μm and sulphides in the region 27 to 29 μm . The calculated spectral emission model is based on measured thermal emission spectra of micrometer size

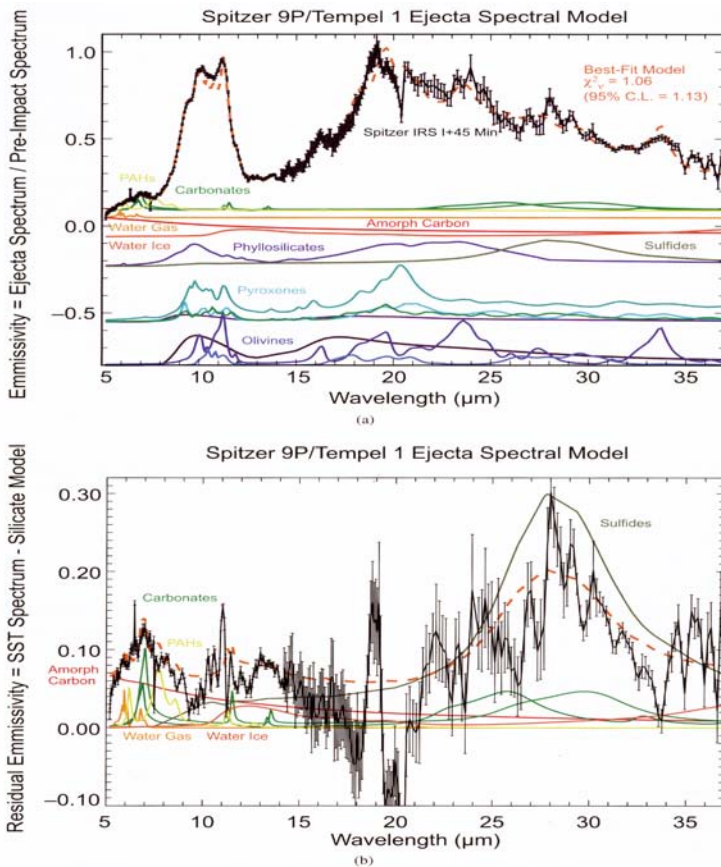


Fig. 9.17 (a) Comparison of the observed spectrum of Comet Tempel 1 ejecta obtained from Spitzer's Space Telescope at $r = 1.51$ AU with the best fit model using various kinds of materials for the dust particles. (b) The residual spectrum after subtracting the best fit model (a). The best fit with non-silicate species are overlaid in the figure (Lisse, C.M. et al. 2007. *Icarus*, **187**, 69).

particles of over 80 mineral species. The particle composition, size distribution and temperatures were determined through search in phase space. Several checks were applied for the correctness of the model such as, minerals detected are the major species seen IDPs, the derived abundances are consistent with solar system abundances as well as the deduced particle distribution and temperature agrees with the findings of instruments on Deep Impact etc. The phase space search eliminated large number of mineral species from the Comet Tempel 1 ejecta. The best model fit to the

observed spectrum is shown in Fig. 9.17(a). It clearly shows the presence of compositional signaturers due to rich silicates and phyllosilicates, carbonates, water-ice, amorphous carbon, sulphides and polycyclic aromatic hydrocarbons(PAHs). Figure 9.17b show the residual emission features after subtracting the best-fit model curve to the observed curve (Fig. 9.17(a)). The non-silicate species which give a fit to the residual emission spectra is also shown in Fig. 9.17(b). The list of all the identified features in the emission spectra of Comet Tempel 1 is given in Table 9.5. The derived relative atomic abundances of Si, Mg, Fe, Ca and Al in the ejecta dust of Comet Tempel 1 are similar to the relative abundances in the solar system and C1 chondrites. The emission spectra of Comet Tempel 1 ejecta clearly show the presence of PAH from the detection of features at 5.2, 5.8, 6.2, 7.7 and 8.2 μm . Therefore the spectral structure present in the infrared spectra of Comet Tempel 1 has shown the complex mineralogy of these dust particles.

Table 9.5 Dust composition of Comet Tempel 1 ejecta from model fitting.

Species	Molecular Weight	N_{moles} (rel.)
Olivines		
Amorph olivine(MgFeSiO_4)	172	0.35
Forsterite(Mg_2SiO_4)	140	0.70
Fayalite(Fe_2SiO_4)	204	0.18
Pyroxenes		
Amorph pyroxene($\text{MgFeSi}_2\text{O}_6$)	232	0.06
Ferrosilite($\text{Fe}_2\text{Si}_2\text{O}_6$)	264	0.50
Diopside($\text{CaMgSi}_2\text{O}_6$)	216	0.18
Orthoenstatite($\text{Mg}_2\text{Si}_2\text{O}_6$)	200	0.16
Phyllosilicates		
Smectite nontronite	496	0.07
$\text{Na}_{0.33}\text{Fe}_2(\text{Si},\text{Al})_4\text{O}_{10}(\text{OH})_2 \cdot 3\text{H}_2\text{O}$		
Carbonates		
Magnesite(MgCO_3)	84	0.11
Siderite(FeCO_3)	116	0.17
Metal sulphides		
Niningerite($\text{Mg}_{10}\text{Fe}_{90}\text{S}$)	84	0.92
Water		
Water ice(H_2O)	18	0.27
Water gas(H_2O)	18	23.7
'Organics'		
Amorph carbon(C)	12	1.45
PAH($\text{C}_{10}\text{H}_{14}$)	(178)	0.022

Adapted from Lisse, C.M. *et al.* 2007. *Icarus*, **187**, 69.

The results of Comet Tempel 1 are consistent with the Comet Halley flyby results which showed the presence of silicates, water, sulphides and carbonates.

The same model has been used for the re-analysis of ISO Spectrum in the region 2.4 to 4.5 μm of Comet Hale-Bopp ($r = 2.8$ AU) and the young stellar object HD 100546. The results are qualitatively similar in showing emission signatures due to silicates, carbonates, Phyllosilicates, water ice, amorphous carbon and sulphides. But there are some differences as well.

Comet Wild 2

The Stardust mission which collected samples of dust particles from Comet Wild 2 has given interesting results with regard to their mineralogy. It showed the importance of sulphur and nitrogen chemistry in the dust particles. It is likely that sulphur atom which is generally associated with mineral phase result have came from mineral such as troilite.

Infrared studies of these particles has shown the presence of amorphous silicate. Among crystalline silicates, forsterite, enstatite, olivine and diopside with pyroxene has been seen. FeNi metal grains and FeNi sulphides have been seen. The range of Fe/Mg ratios seen in the particles indicate that Comet Wild 2 is unequilibrated. The presence of particles with nitrogen-rich chemistry and lower abundance of O implies that nitriles or polycyanides may have been present. The interesting finding is that dust particles which are mineralogically similar to meteoritic Calcium-Aluminium-rich inclusions have been found. Ca-Al-rich dust particles are the oldest samples in the solar system and contain minerals in abundance.

Deep Impact mission of Comet Tempel 1 provided detailed mineralogical composition of this comet. Among the various minerals, only forsterite was seen in both the Comets Tempel 1 and Wild 2. Iron sulphide has been seen in Comet Wild 2, but not FeMg sulphides. The major difference between the two comets is the presence of carbonates and hydrated silicates in Comet Tempel 1 but not in Wild 2 samples. These species have been seen from meteorites. Its formation is generally believed to arise from hydrothermal alteration inside a wet parent body.

The vast difference in the observed mineralogy between the two Jupiter family of Comets Tempel 1 and Wild 2 could be due to several reasons. It is possible that the two comets themselves are different or it could have been formed in different regions. In addition the synthesis of observed infrared

spectra of Comet Tempel 1 was carried out with laboratory minerals which may be different from those present in comets that have gone through various processes. Since comets were formed from aggregates of materials, it is quite possible that some comets possess hydrated silicates due to melting of ice. Lastly Comet Tempel 1 site of impact appeared to show the presence of impact craters. Therefore it is possible that the hydrated silicates could have been formed inside Comet Tempel 1 due to the impact. However this appears not the case for Comet Wild 2.

9.5.3. *The C-H stretch feature*

A new emission feature near $3.4 \mu\text{m}$ was first detected by Vega 1 spacecraft in the spectra of Comet Halley. This was confirmed by several ground-based observations. The laboratory absorption spectra of organic materials both in gaseous and solid phase generally show a strong feature around $3.4 \mu\text{m}$. Most of the C-H stretching vibrations fall in the wavelength regions around 3.1 to $3.7 \mu\text{m}$ (see Fig. 3.4). Therefore, the observed feature in Comet Halley is attributed to C-H stretching of some organic material. The $3.4 \mu\text{m}$ feature has subsequently been seen from several other comets indicating the common nature of cometary organics. This feature is also seen from some IDPs collected in the stratosphere. The intensity of the $3.4 \mu\text{m}$ feature as observed by Vega spacecraft seemed to vary inversely with the projected distance from the nucleus in a manner similar to the parent molecule indicating the possible detection of a new parent molecule.

The apparent profile of $3.4 \mu\text{m}$ feature in several comets is around $3.36 \mu\text{m}$ (Fig. 9.18). In addition, there is evidence for the presence of two weaker features at 3.28 and $3.52 \mu\text{m}$. The vibrational frequencies of CH_3 group occur at $3.37 \mu\text{m}$ and $3.48 \mu\text{m}$ and that of CH_2 group at $3.42 \mu\text{m}$ and $3.50 \mu\text{m}$. Therefore, the observed features in comets appear to indicate the presence of spectral signatures of $-\text{CH}_3$ and $-\text{CH}_2$ functional groups. The structure, width and the intensity of the observed $3.4 \mu\text{m}$ emission feature suggest that several of these species may be present.

The feature at $3.52 \mu\text{m}$ is attributed to ν_3 band of Methanol (CH_3OH). Other rotational-vibrational lines of methanol occurring at $3.33 \mu\text{m}(\nu_2)$ and $3.37 \mu\text{m}(\nu_9)$ contribute to the broad $3.36 \mu\text{m}$ emission. Detailed modelling with methanol indicate a residual feature. This could come either from other weaker lines of methanol, for which the required data is not available or it could come from some other species.

The other feature present at $3.28 \mu\text{m}$ is characteristic of aromatic com-

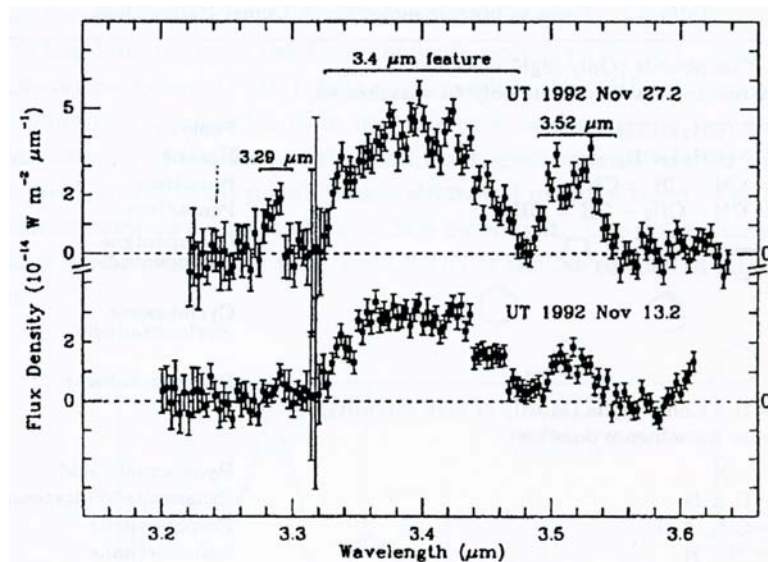


Fig. 9.18 The spectral feature around $3.4 \mu\text{m}$ region observed from Comet 109P/Swift-Tuttle at $r = 1.0$ AU (Disanti, M.A. et al. 1995. *Icarus*, **116**, 1).

pounds(PAHs). The feature seen at $3.29 \mu\text{m}$ from interstellar matter is generally associated with other features occurring at $6.2, 7.7, 8.6$ and $11.3 \mu\text{m}$. Some of these features have also been seen in the infrared observations of Comet Tempel 1.

The spectra of the Comet Tempel 1 showed an increase in the ratio of organics to water after the impact. The organic feature was also found to be broader and contained more structures after the impact. This indicates the presence of many new species that were below the detectable limit prior to the impact.

The $3.4 \mu\text{m}$ cometary feature has also been seen from interstellar clouds, molecular clouds, HII regions and so on. But the characteristic feature is different indicating the variation of carbonaceous material present in different environments.

9.5.4. Ice signature

All the available evidence indicates that H_2O is the major component of the nucleus of a comet. Therefore, it is interesting to look for ice grains in the cometary comae.

Large size particles of ice grains could be stable against sublimation around 1 AU. However, even with a small amount of absorbing material present, the high temperature attained by the grain can entirely sublimate the icy grain. Therefore it should be looked for in comets at large heliocentric distances where the temperature of the grain is low enough that the icy grains are present. The strong OH production seen in Comet Bowell at $r > 4$ AU has been attributed to icy grains.

A more direct method of detecting the presence of icy grains in comets is to look for the absorption bands of ice in the infrared region. Laboratory investigations have shown that ice band has features near 1.5, 2.2 and 3.1 μm . Among these, 3.1 μm feature is the strongest. These bands have been looked for in several comets. The observations on Comets Bowell and Cernis at $r \sim 4$ AU gave an indication of the presence of 3.1 μm absorption feature. A broad and shallow absorption feature appears to have been detected in Comet Hale-Bopp when the comet was at 7 AU.

The strong water-ice band at 3.1 μm has been definitely detected for the first time from Comet Tempel 1 from the infrared observations of the ejecta from the Deep Impact experiment. This is shown in Fig. 9.19. This indicate that large amount of icy grains from the nucleus of Comet Tempel 1 was lifted gradually after impact without being evaporated. This shows that the excavated pristine material from a depth of 10 to 20 meters consist of water-ice particles of sizes $\sim 1 \mu\text{m}$.

9.6. Properties Derived from Direct Measurements

Comet Halley

The important information about the chemical composition of dust particles in Comet Halley has been obtained from the dust impact mass analyzer PUMA 1 and 2 on Vega and PIA on Giotto spacecrafts. Dust particles striking a silver target placed in front of the mass spectrometer generate a cloud of ions and the positive charge are mass analyzed, which indicates its chemical composition. Several thousand mass spectra of dust particles were recorded by the instruments. These studies indicated broadly three classes of particles (Fig. 9.20): (1) mostly made up of light elements such as H, C, N and O indicative of organic composition of grain called 'CHON' particles (2) similar to CI Chondrites but enriched in carbon and (3) primarily O, Mg, Si and Fe suggestive of silicate grains. Therefore, the Comet Halley

grains were found to be essentially composed of two end member particle types - a silicate and a refractory organic material (CHON) in accordance with the infrared observations.

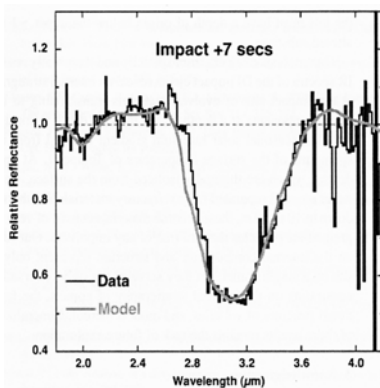


Fig. 9.19 Comparison of the observed broad feature in the region of $3 \mu\text{m}$ from the ejecta of Comet Tempel 1 with the model spectra of $0.5 \mu\text{m}$ diameter water ice particles. There is a good fit (Sunshine, J.M. et al. 2007. *Icarus*, **190**, 284).

The possibility of the presence of core-mantle structure of dust particles comes from the fact that on the average CHON ions appear to have a higher initial energy than the silicate ions. The observed ion abundances have been transformed to atoms based on laboratory calibration from the knowledge of the ion yields with different projectiles. The resulting composition of Comet Halley's dust indicate that the abundances of rock forming elements in Halley's dust are within a factor of two relative to the solar system abundances. The abundances of H, C and O are more than that of CI-chondrite believed to be the unaltered meteorites from the early solar system. This can be interpreted to mean that the Halley dust is more primitive than CI-chondrites. The puzzle of carbon depletion in comets also seems to have been resolved as they are tied up in the refractory organics. Due to uncertainties in converting the ion intensities to atomic abundances, there could be a factor of two uncertainties in the final derived abundances. The derived gas to dust ratio is ~ 1.1 to 1.7 . The estimated density of silicate dominated grain indicates a value $\sim 2.5 \text{ gm/cm}^3$, while CHON dominated grain indicates a value $\sim 1 \text{ gm/cm}^3$. Several refractory grains show $^{12}\text{C}/^{13}\text{C} \approx 5000$ which is drastically different from the normal value ~ 89 . This indicate that the carbon coming out of different nucleosynthesis sites has been incorporated in the Comet Halley dust particles.

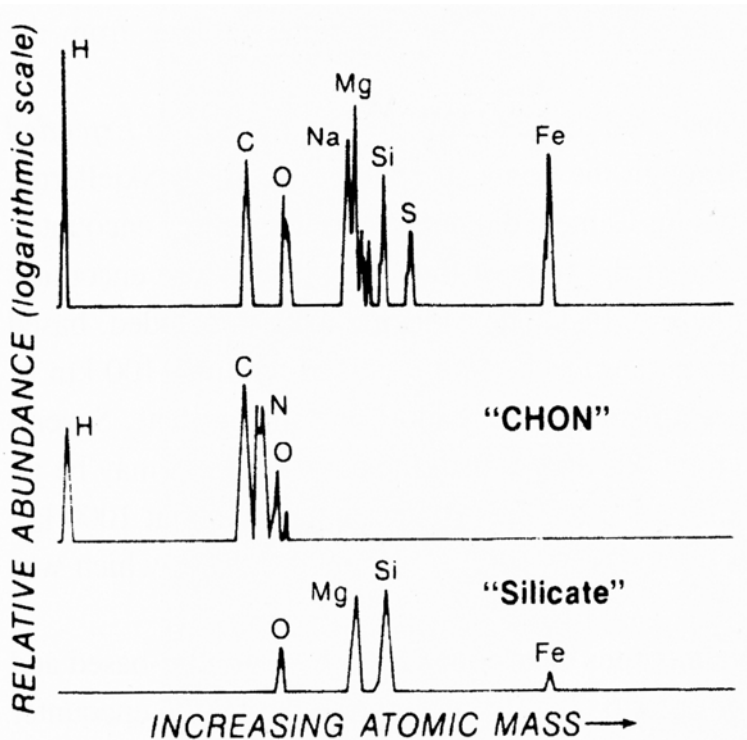


Fig. 9.20 Composition of dust particles seen by dust impact mass analyzer by Vega spacecraft from Comet Halley (Kissel, J. et al. 1986. *Nature*, **321**, 336).

The possible presence of polymerized formaldehyde (H_2CO_n) (also called polyoxymethylene, POM) in the dust grains of Comet Halley has been proposed based on the results of the positive ion cluster analyzer (PICCA) experiment conducted aboard the Giotto spacecraft (Fig. 6.16). The dust grains contain a large number of organic compounds (Table 13.8), e.g., unsaturated hydrocarbons like pentyne, hexyne, etc; Nitrogen derivatives like hydrocyanic acid etc; Aldehydes and acids like formaldehyde, formic and acetic acid etc. Many more molecules are expected to be present in the dust. It is quite possible that a large number of molecules might have also been destroyed due to the high velocity of impact $\sim 78 \text{ km/sec}$.

Comet Wild 2

The stardust spacecraft flew past the nucleus of Comet Wild 2 within

a distance of 234 km on 2 Jan 2004. The particles ejected from the nucleus of Comet Wild 2 were collected when they hit silica aerogel with a speed of 6.12 km/sec. Stardust collected more than 1000 dust particles of sizes in the range of about 5–300 μm . Stardust mission was meant for collecting dust samples from Comet Wild 2 and bring back to earth for laboratory investigation. The stardust spacecraft also contained a time-of-flight spectrometer called CIDA (cometary and interstellar dust analysis) which was used for the study of the composition of dust particles in the coma. These two studies have given detailed information about the composition of dust particles of Comet Wild 2.

The CIDA instrument was similar to that in PUMA 1 and 2 on the Vega spacecraft and PIA instrument on Giotto of Comet Halley. The CIDA instrument is a time-of-flight mass spectrometer and is based on the fact that the dust particles with enough velocity striking a silver target produce either positive ions or negative ions depending on the voltage applied. The flight time of these ions from the time of impact to the time of detection give a direct measure of the mass of these ions.

The dominant ion detected from CIDA instrument was CN^- . This indicates the dominance of nitrogen-rich chemistry. It was found that O^- and OH^- ions were minor in abundance which show that oxygen chemistry play a minor role in these dust particles. Hence water-ice cannot be a major constituent of these dust particles.

The importance of sulphur chemistry in the dust particles came out of the detection of the two isotopic lines of SH^- (mass-to-charge ratio $m/z = 33$ and 35). it is possible that sulphur atom which is generally attributed to mineral phases of cometary dust could have come out of minerals such as troilite to organic phase by some radiative process during the time (several billion years) the dust particles spent in interstellar space and later in the nuclei of comets.

In the positive ion mass spectra, three types of species have been detected. They are CH^+ ion($m/z = 13^+$), traces of N^+ , NH^+ , O^+ , OH^+ and unsaturated organic species containing some nitrogen.

Therefore studies based on CIDA instrument of Comet Wild 2 indicate that H_2O and CO were absent in the dust particles, nitrogen chemistry appears to be dominant and sulphur must have come out of mineral phase of the cometary dust.

The stardust samples collected from Comet Wild 2 have been subjected to multiple experimental techniques. They show the presence of organic aromatic matter(PAHs). As shown in Fig. 9.21 it contains benzene(78 amu,

C_6H_6), phenol(94 amu, C_6H_5OH), naphthalene(128 amu, $C_{10}H_8$) and their alkylated derivatives, acenaphthylene(152 amu, $C_{12}H_8$), phenanthrene(178 amu, $C_{14}H_{10}$), pyrene(202 amu, $C_{16}H_{10}$), perylene(252 amu, $C_{20}H_{12}$) etc. The features present at 101, 112, 155 and 167 amu could arise from O and N substituted aromatic species. The higher mass spectra extending to about 800 amu could be attributed to polymerization of smaller aromatics as a result of chemical processing due to radiation processes, such as cosmic rays, solar heating etc.

Glycine which is an amino acid and is an important constituent of living systems has been detected for the first time in the dust particles of Comet Wild 2.

Infrared spectra of dust particles show the presence of non-aromatic functional groups as can be seen from the absorption features present at 3322 cm^{-1} (-OH), 3065 cm^{-1} (aromatic CH), 2968 cm^{-1} (-CH₃), 2923 cm^{-1} (-CH₂-), 2855 cm^{-1} (-CH₃ and -CH₂-) and 1706 cm^{-1} (C=O).

The observed spectra indicate the presence of aromatic, aliphatic, carboxylic and N-containing functional groups. The organics in Comet Wild 2 is found to be considerably richer in O and N relative to both meteorite organic matter and the average composition of Comet Halley.

Isotopic measurements have given some interesting results. D/H ratio in some of the dust particles was found to be about three times larger than the terrestrial value. D and H were heterogeneously distributed within the samples and is associated with C. This indicates that it is organic in character. The enrichment of ^{15}N was also seen in some dust particles. The higher value of D and ^{15}N suggest that cometary material contain materials from those of interstellar and/or protostellar environments.

All the studies carried out on dust particles from Comet Wild 2 has shown the rich diversity of organic materials. They show a wide variety of forms in molecular structure and molecular complexity. The distribution of organics is heterogeneous inside as well as between the dust particles indicating that they are unequilibrated material that experienced very little processing after incorporating into dust particles. The enrichments in D and ^{15}N in the dust particles indicate the presence of presolar material.

9.7. Radiation Pressure Effects

The dust particles released from the nucleus are subjected to radiation pressure forces which push them to different distances from the nucleus and

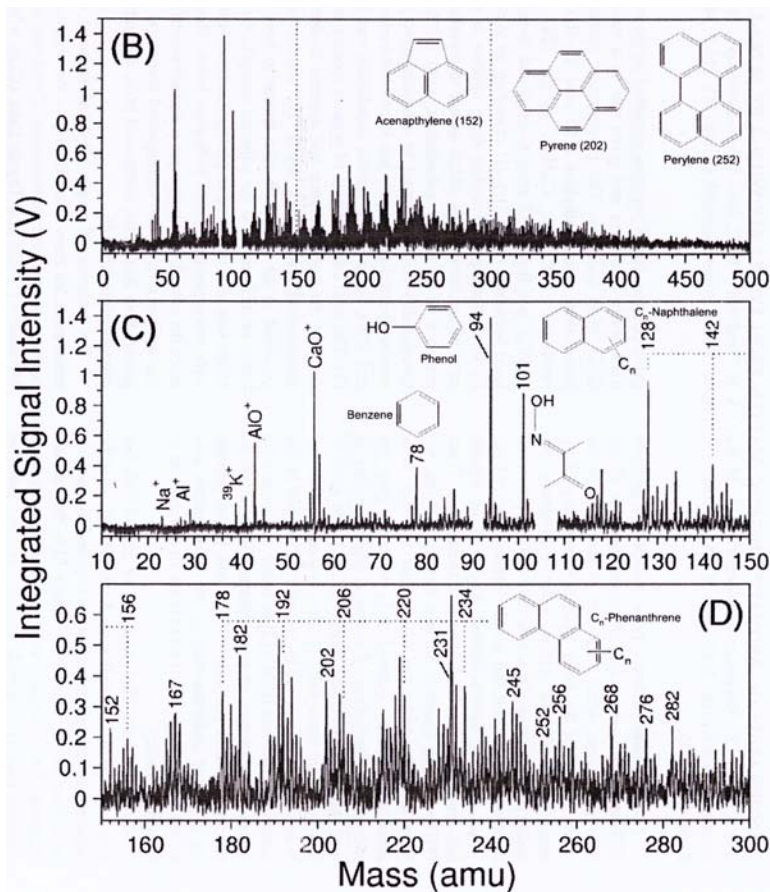


Fig. 9.21 Mass spectra of stardust sample C2115, Track 22 of Comet Wild 2. The complex distribution of aromatic species covering molecular weights upto 500 can be seen in (B). The expanded portion of mass range is shown in (C) and (D). The complex nature of organics present can be seen (Clemett, S.J. et al. 2007. *Lunar and Planetary Science*, **38**, 2091.

this ultimately gives rise to the observed dust tail as discussed in Chap. 7. The dust tail is composed of various Syndynes and each curve is defined in terms of a parameter $\beta \equiv (1 - \mu)$, which is the ratio of solar radiation pressure to gravity. These Syndynes when projected on to the photographs of the tail give a range of β values which encompass the observed tail. The maximum value of β fixes the minimum size of the particles that can exist in the tail. Others will essentially be pushed away from the system. From such

comparisons, it is possible to get the maximum value of β denoted as β_{\max} for various cometary tails. Table 9.6 gives a list of β_{\max} values obtained for various comets. They show that there are no particles in the tail which

Table 9.6 Values of β_{\max} obtained for various comets* ($r = 1$ AU).

Comet	β_{\max}	Comet	β_{\max}
1957 III	0.55	1970 II	1.9
1957 V	2	1970 II	3.8 ^a
1962 III	2.5	1973 XII	0.8 ^b
1965 VIII	1.1-1.4	1976 VI	2
1965 VIII	0.8 (farthest part)	1976 VI	2.5
1965 VIII	2.5 (near the head)	Several Comets	2.5

a. from IR photometry; b. from Colorimetry(*Saito, K., Isobe, S., Nishioka, K. and Ishii, T. 1981. *Icarus* **47**, 351.)

are subjected to radiation pressure forces beyond about $\beta_{\max} \simeq 2.5$. This apparent cut-off in the value of β can be used to infer the properties of the dust particles. However, the interpretation is not straightforward as it involves various parameters of the grains, which means one has to invoke various grain models. As an example, Fig. 9.22 shows a plot of the variation of β as a function of the radius of the particle for different types of particles. It can be seen that for small size particles most of the curves are flat except for the silicate type (Basalt) of materials. The observed maximum value of $\beta_{\max} \simeq 2.5$ seems to lie in between these two general shapes of the curves.

9.8. Summary

We may now briefly summarize the main characteristic properties of cometary grains based on the discussion presented so far. In order to reduce the ambiguity, it is important as well as necessary to consider various types of observations which have to be satisfied simultaneously by any grain model. However, it may not be practicable in all the cases. In the absence of such detailed studies, it is even worthwhile to restrict the parameters

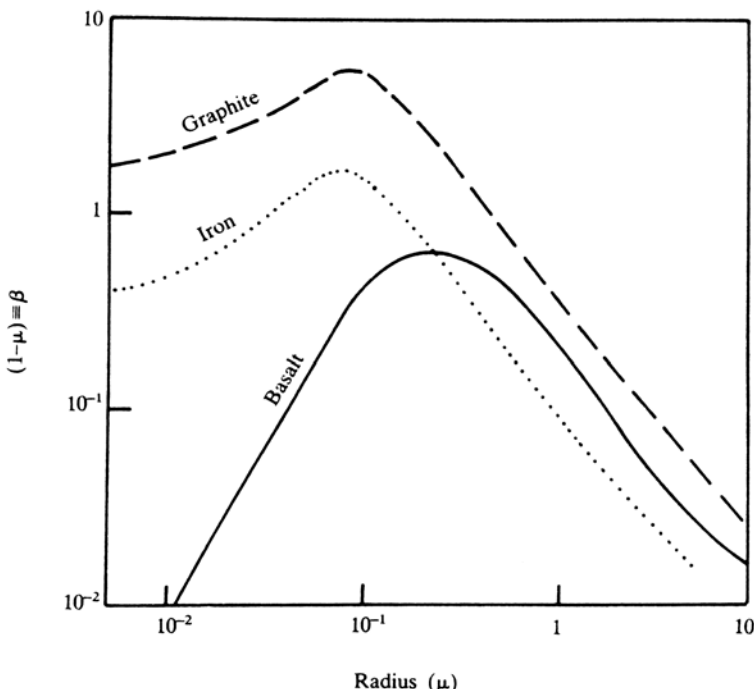


Fig. 9.22 The variation of radiation pressure force $(1 - \mu) \equiv \beta$ with the radius of the particle for three types of material is shown. (Adapted from Saito, K., Isobe, S., Nishioka, K. and Ishii, T. 1981. *Icarus*, **47**, 351.)

which define the grain characteristics within certain possible ranges.

The optical continuum measurements, the polarization measurements as well as scattering phase function in the visual region give a limit for the refractive index as $1.3 < n < 2.0$ and $k \leq 0.1$.

These are based on single particle models or multi-component models based on different compositions and size distribution functions. Models based on aggregates of large number of monomers with sizes of $\sim 0.1 \mu\text{m}$ composed of several compositions have also been considered. Any realistic model has to explain all the observations pertaining to cometary dust. Attempts are made to develop such a model.

The silicate nature of grain came from the detection of 10 and $20 \mu\text{m}$ features from comets. The evidence for the second component to the cometary grain namely organics, came from the discovery of CHON particles in Comet Halley as well as the detection of $3.4 \mu\text{m}$ feature in the infrared

observation. Therefore, the two major components of the cometary dust are silicates and some form of carbon.

The true mineralogical composition of cometary dust particles came from the mid and far-infrared observations of Comets Halley, Hale-Bopp, Tempel 1 and Wild 2 and the laboratory studies of cometary dust of Comet Wild 2. They showed the presence of silicates of various kinds including crystalline type, carbonates, water ice, amorphous carbon, sulphides, PAHs etc. Calcium-Aluminium-rich inclusions, the oldest samples in the solar system containing minerals in abundance, which condensed around 1400 K was seen. The dust particles also show rich diversity of organics. The detection of Glycine in cometary dust indicate the presence of ingredient for the formation of living systems. There is enrichment of ^{15}N and D in the dust particles indicating the presence of presolar grains. Therefore cometary dust is an unequilibrated heterogeneous mixture of materials containing both high and low temperature condensates and also contains presolar grains. This also indicated for the first time, that large scale mixing must have taken place in the solar nebula.

Problems

1. Derive an expression for the variation of the temperature of a black body as a function of distance from the Sun. Assume that the energy distribution of the Sun can be represented by a black body of temperature 6000°K. What will happen if the body is a planet with no atmosphere or if there is an atmosphere?
2. Calculate the grain temperature for graphite grains of $a = 0.2 \mu\text{m}$ at 1 AU from the Sun. How much does this value differ from that of black body temperature at the same distance?
3. Suppose in the above problem, the grain has some impurity which gives $Q_{abs} = 1$ at 1 mm. What will happen to the temperature of the grain?
4. Calculate the number of electrons and atoms or molecules required to explain the observed scattered radiation in comets at $r = 1 \text{ AU}$ and for $\lambda = 5000 \text{ \AA}$. Take the value of the scattered intensity to be 50% of the solar intensity at that wavelength. What is the expected wavelength dependence of these?
5. Suppose the heavy elements like O, C, N hit the grain and stick to it with a probability α . If the temperature of the gas is T and assuming the mean velocity to be given by the Maxwellian distribution, deduce

the expression for the rate of growth of the grain. What is the time required for an ice grain of initial radius of $0.01 \mu\text{m}$ to grow to $1 \mu\text{m}$, if $\alpha = 1$, $T = 100^\circ\text{K}$ and $n_H = 10/\text{cm}^3$

6. A grain releases a molecule and reduces in size due to protons hitting the surface of the grain. Deduce an expression for the rate of decrease of grain size with time, if β is the probability for the release of a lattice molecule when the proton hits the surface. What is the time required to destroy completely an ice grain of size $1 \mu\text{m}$ with $N_H = n_e = 10/\text{cm}^3$, $T = 10^4 \text{ K}$ and $\beta = 0.1$?
7. Assuming solar constant of $1.4 \times 10^6 \text{ ergs/cm}^2 \text{ sec}$ and spherical completely absorbing particles of density 3.0, calculate the limiting radii of particles to be retained in the solar system released from Comet Encke at aphelion distance of 4.10 AU and perihelion distance of 0.34 AU.
8. Compare the importance of radiation pressure on the motion of the dust compared with the force of gravity at the orbit of Venus. Calculate the time required for the dust to be driven out to the distance of the Earth by radiation pressure alone.

References

The following paper gives a good account on dust

1. Kolokolova, L, Hanner, M.S., Levasseur-Regourd, A.-Ch *et al.* 2005. In *Comets II*, eds., M.S. Festou, H.U. Keller and H.A. Weaver, Univ. Arizona Press, Tucson, P.577.

The early work on continuum studies can be found in these two references:

2. Liller, W. 1960. *Ap. J.* **132** 867.
3. Remy-Battiau, L. 1964. *Acad. r. Belg. Bull. el. Sci. 5eme Ser.* **50** 74.

The following papers may be referred for later work:

4. Jewitt, D. C. and Meech, K. J. 1986. *Ap. J.* **310**, 937
5. Hanner, M.S. 2003. *JQSRT*, **79-80**, 695.
6. Wolf, M.J., Clayton, G.C. and Gibson, S.J. 1998. *Ap.J.*, **503**, 815.
7. Mann, I., Kimura, H. and Kolokolova, L. 2004. *JQSRT*, **89**, 291.
8. Mason, C.G., Gehrz, R.D., Jones, T.J. *et al.* 2001. *Ap.J.*, **549**, 635.

The determination of grain albedo can be found in the following papers

9. O'Dell, C.R. 1971. *Ap. J.*, **166**, 675.
 10. Hanner, M.S. and Newburn, R.L. 1989. *Astron. J.*, **97**, 254.
- $A(\theta)f\rho$ was introduced in the following paper

11. A'Hearn, M.F., Schleicher, D.G., Feldman, P.D., *et al.* 1984. *Ap.J.*, **89**, 579.

The early measurement of polarization was done by

12. Bappu, M.K.V. and Sinvhal, S.D. 1960. *M N* **120** 152.

The existence of negative polarization in comets was shown in the following two papers:

13. Kiselev, N.N. and Chernova, G.P. 1978. *Soviet Astron.* **22** 607.
14. Weinberg, J.L. and Beeson. D.E. 1976. *Astron. Astrophys.* **48** 151.

For later work the following may be consulted

15. Dollfus, A. 1989. *Astr. Ap.* **213**, 469.
16. Mukai, T., Mukai, S. and Kikuchi, S. 1987. *Astr. Ap.* **187**, 650.
17. Harrington, D.M., Meech, K. Kolokolova, L., *et al.* 2007. *Icarus*, **187**, 177.

The possible division of comets based on observed linear polarization is in the following papers

18. Levasseur-Regourd, A. -Ch., Hadanicik E. and Rehard, J.B. 1996. *Astron. Astrophys.*, **313**, 327.
19. Levasseur-Regourd, A. -Ch., Zolensky, M. and Lasue, J. 2008. *Planetary and Space Science*, **56**, 1719.
20. Jockers, K., Kiselev, N., Bonev, T. *et al.* 2005. *Astron. Astrophys.*, **441**, 773.

Circular polarization could be due to organics is discussed in the following paper

21. Rosenbush, V. Kolokolova, A., Lozarian, A. *et al.* 2007. *Icarus*, **186**, 317.

In situ studies are discussed in the following papers

22. Mazets, E.P., Aptekar R.L., Golenetskii, S.V. *et al.* 1986. *Nature*, **321**, 276.
23. McDonnell, J.A.M., Lamy, P.L. and Pankiewicz, G.S. 1991. In *Comets in the Post-Halley Era*, eds. R.L. Newburn, M. Neugebauer and J. Rahe, Kluwer Academic Publishers, P. 1043.
24. Nordholt, J.E., Reisenfeld, D.B., Wiens, R.C. *et al.* 2003. *Geophys. Res. Lett.*, **30**, 18.
25. Tuzzolino, A.J., Economou, T.E., Clark, B.C. *et al.* 2004. *Science*, **304**, 1776.

The first infrared measurements made on Comet Ikeya-Seki is reported by

26. Becklin, E E and Westphal, J A. 1966. *Ap. J.*, **145** 445.

The following paper reports the first detection of 10 μm emission feature in Comet Bennett.

27. Maas, R., Ney, E.P. and Woolf, N.J. 1970. *Ap. J.*,**160**, L101.
Interpretation of infrared observations and mineralogy of grains can be found in the following papers
28. Krishna Swamy, K.S. and Donn, B 1968. *Ap J* **153**, 291.
29. Krishna Swamy, K.S., Sandford, S., Allamandola, L.J. *et al.* 1988. *Icarus*, **75**, 351.
30. Oishi, M., Okuda, H. and Wickramasinghe, N C 1978. *Publ. Astro. Soc. Japan*, **30**, 161.
31. Crovisier, J., Brooke, T.Y., Leech, K. *et al.* 2000. *Thermal Emission Spectroscopy and Analysis of Dust Disks and Regoliths*, eds. M.L. Sitko, A.L. sprague and D.K. Lynch, ASP Conference Ser. Vol. 196, P.109.
32. Wooden, D.H., Harker, D.C., Woodward, C.E., *et al.* 1999. *Ap.J.*, **517**, 1034.

Study of complex mineralogy of dust is in the following papers

33. Crovisier, J., Leech, K., Bockelee-Morvan, D. *et al.* 1997. *Science*, **275**, 1904.
34. Lisse, C.M., Kraemer, K.E., Nuth III, J.A. *et al.* 2007. *Icarus*, **187**, 69.
35. Hanner, M.S. and Bradley, J.P. 2005. In *Comets II*, eds. M.C. Festou, H.U. Keller and H.A. Weaver, Univ. Arizona Press, Tucson, p. 555.

The following papers discusses the complex nature of organics

36. Sandford, S.A. 2008. In *Organic Matter in Space*, Eds. S. Kwok and S.A. Sandford, Cambridge University Press, Cambridge, P.299.
37. Brownlee, D., Tsou, P., Aleon, J. *et al.* 2006. *Science*, **314**, 1711.
38. Kissel, J. Krueger, F.R., Silen, J. *et al.* 2004. *Science*, **304**, 1774.
39. Kissel, J. and Krueger, F.R. 1987. *Nature*, **326**, No. 6115, 755.
40. Disanti, M.A., Villanueva, G.L., Bonev, B.P. *et al.* 2007. *Icarus*, **187**, 240.
41. Biver, N., Bockelee-Morvan, D., Boissier, J., *et al.* 2007. *Icarus*, **187**, 253.
42. Clemett, S.J., Nakamura-Messenger, K., McKay, D.S. *et al.* 2007. *Lunar and Planetary Science*, **38**, 2091.

The first detection of Glycine in Comet Wild 2 is reported in the following paper

43. Elsila, J.E., Glavin, D.P. and Dworkin, J.P. 2009. *Meteorites and Planetary Science*, **44**, 1323.

The observed C-H(3.4 μm) feature in Comet Tempel 1

44. A'Hearn, M.F. 2005. In *Asteroids, Comets and Meteors*, eds. D.Lazzaro, S. Ferraz-Mello and J.A. Fernandez, Cambridge Univ.

Press, p. 33.

The first definite detection of strong $3.1 \mu\text{m}$ ice dust feature in Comet Tempel 1 is reported in the following paper

45. Sunshine, J.M., Groussin, O., Schultz, P.H. *et al.* 2007. *Icarus*, **190**, 284.

CHAPTER 10

Ion Tails

The ion tails of comets provide a unique and natural place for the study of various plasma processes. Many of the features seen in the ion tails of comets change on a short-time scale as well as on a long-time scale. The formation of ion tails is basically due to the interaction of the solar wind plasma with the cometary plasma. The detailed dynamical model calculations for such an interaction process had indicated the presence of Large Scale Structures like bow shock, ionosphere and so on. The *in situ measurements* of Comets Giacobini-Zinner, Halley Borrelly, etc. showed not only the presence of these features but also indicated the plasma to be highly complex, containing instabilities, waves, turbulence and so on. Some of these aspects will be discussed here. In addition, some of the large scale features that have been seen in the ion tail of comets will also be discussed.

10.1. Evidence for the Solar Wind

The existence of the solar wind was first postulated based on the study of the ion tail of comets. The model was put on a firm footing with the work of Parker based on the hydrodynamic expansion model of the solar corona. The model predicted in detail the expected nature of the solar wind as well as the resulting shape of the interplanetary magnetic field. These were confirmed later on with observations made through satellites.

The idea of the solar wind came from the photographic observations of comets which showed that certain features like knots in the ion tails were moving away along the tail. The velocity and the acceleration of the features obtained from successive photographs showed clearly that these features were moving in the anti-solar direction with high velocities. The typical velocity is about 100 km/sec. A measure of the deceleration is generally

expressed in terms of the effective gravity parameter $(1 - \mu)$ as defined in Chap. 7. The typical values of $(1 - \mu) \approx 10^2$ were quite commonly observed in the ion tails of many comets. This indicates an outward force which is 10^2 times larger than the solar gravity. One force which could operate and give rise to this motion on an atom or a molecule is the radiation pressure. The expression for the radiation pressure is given by

$$F_{\text{rad}} = \left(\frac{F_{\odot}}{c} \right) \left(\frac{\pi e^2}{mc} f \right) \quad (10.1)$$

where F_{\odot} is the solar flux at the comet and all other quantities have their usual meanings. It was found that the Eq. (10.1) fails to explain the observed accelerations of features in the ion tail by several orders of magnitude. This led Biermann to hypothesize the existence of the solar wind, i.e., the high velocity corpuscular radiation coming from the Sun, which accelerates the ions in the tail through the momentum transfer. In fact he developed a very simple expression for this interaction and obtained the equation

$$\frac{dv_i}{dt} \approx \frac{e^2 N_e v_e m_e}{\sigma m_i}. \quad (10.2)$$

Here the quantities with the subscript e refer to electrons and i to ions, N_e is the electron density and v_e is the velocity of electrons, σ is the electrical conductivity. In order to explain the observed accelerations, the above equation requires the solar wind velocity to be of the order of a few hundred kilometers per second and the density of about 600 electrons/cm³. These values may be compared with the present day velocity of about 400 to 500 km/sec and the density of about 5/cm³.

10.2. Dynamical Aberration

More support for the solar wind hypothesis came from the study of the orientation of ion tails of comets. The tail axes of ion tails are found to lag behind by a few degrees with respect to the radius vector. The lag arises due to the resultant effect of the solar wind velocity and the velocity of the comet. This is known as the dynamical aberration. Figure 10.1 shows the geometry of the comet tail on the plane of the sky. Here r , t and $-v$ denote the radius vector, the tail vector and the negative velocity vector of the comet. For the interpretation of ion tail orientation, it is convenient to use the plane of the comet's orbit as the reference frame. The observational

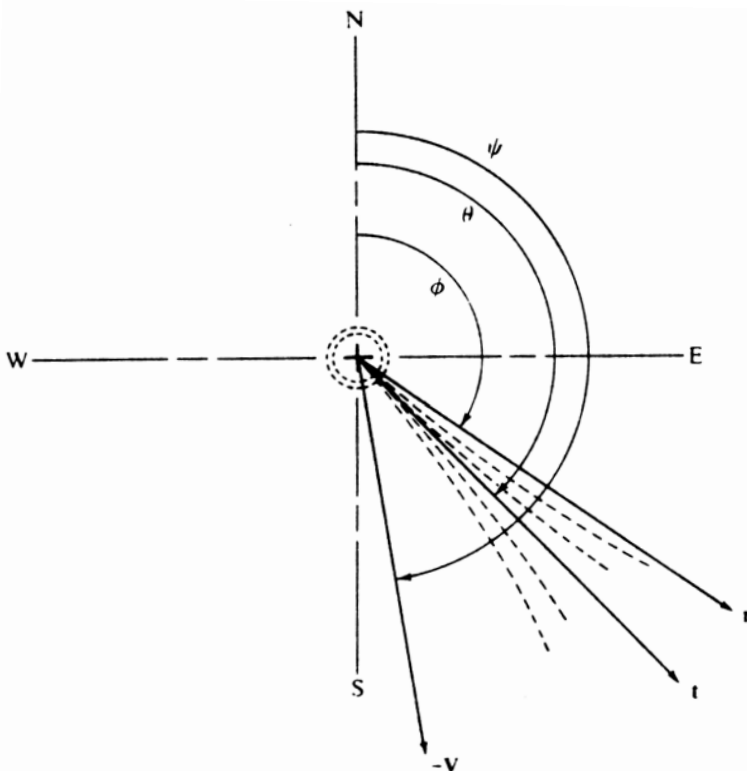


Fig. 10.1 The geometry of the comet tail (dashed lines) projected on to the plane of the sky. The position angles ϕ , θ and ψ denote the prolonged radius vector, the comet tail and the direction of comet's velocity back along the orbit respectively. (Belton, M.J.S. and Brandt, J.C. 1966. *Ap. J. Suppl.* **13**, 125).

data is the position angle θ of the tail axis on the plane of the sky. From a knowledge of the various quantities as shown in Fig. 10.1, the orientation of the tail in the comet's orbital plane can be calculated (Fig. 10.2) with the assumption that it also lies in the same plane. The aberration angle ϵ is then the angle of the tail with respect to the radius vector. The basic equation used for the interpretation of dynamical aberration observation is given by

$$\mathbf{t} = \mathbf{w} - \mathbf{v} \quad (10.3)$$

where \mathbf{t} is the tail vector which lies in the orbital plane of the comet, \mathbf{w} is the solar wind velocity and \mathbf{v} is the comet's orbital velocity. Physically the above equation means that the direction of the tail is the direction of the

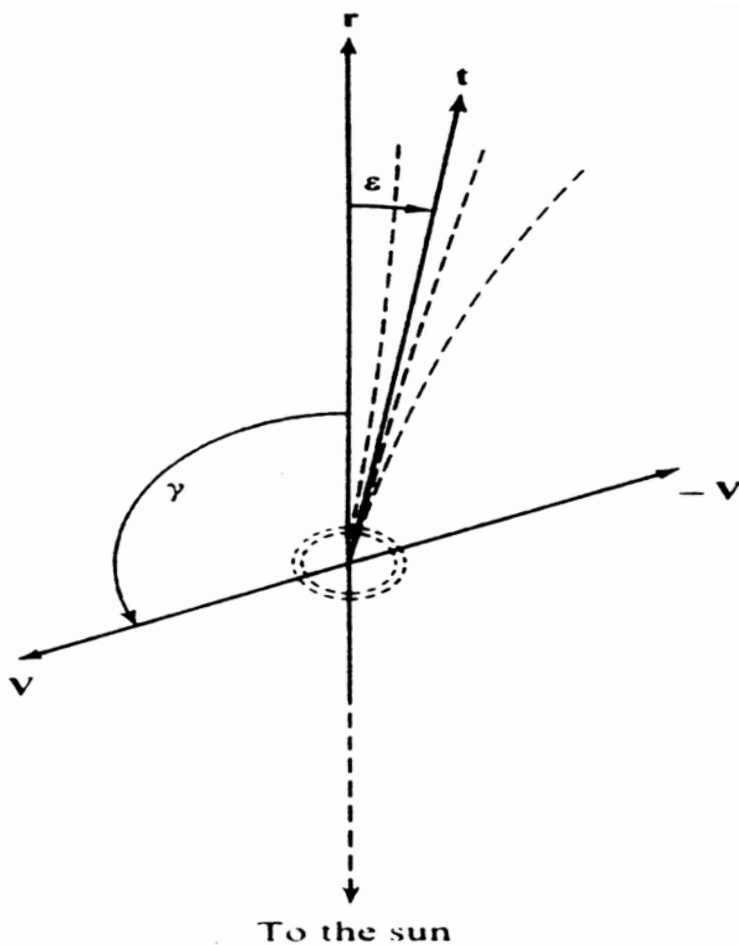


Fig. 10.2 The geometry of the comet tail projected on to the plane of the comet's orbit. The aberration angle ϵ and the angle γ are shown. (Belton, M.J.S. and Brandt, J.C. 1966. *op. cit.*).

solar wind as seen by an observer riding on the comet. If the solar wind velocity is resolved into radial (w_r) and azimuthal (w_ϕ) components, the aberration angle for a comet near the solar equator is given by

$$\tan \epsilon = \frac{v \sin \gamma - w_\phi \cos i}{w_r - v \cos \gamma} \quad (10.4)$$

where i is the inclination of the comet's orbit to the plane of the solar equator and γ is the angle between the radius vector and the direction of

v. All the quantities in the above equation are known except for w_r and w_ϕ . Since the value of w_ϕ is small, the value of w_r can easily be calculated from Eq. (10.4). Since the observations on comets cover a wide variety of situations, it is possible in principle to get not only w_r and w_ϕ but also their variations. If w_ϕ has an appreciable value, it should show up in the aberration angle between the direct (D) and retrograde (R) comets. The above method has been applied to about 60 comets covering approximately 1600 observations. The resulting averages for the aberration angles for direct and retrograde comets are

$$\langle \epsilon \rangle_D = 3.7^\circ$$

and

$$\langle \epsilon \rangle_R = 5.5^\circ.$$

Assuming w_r and w_ϕ are the same for the two cases and using the average values for other parameters, the resulting mean values for w_r and w_ϕ are

$$\langle w_r \rangle = 450 \pm 11 \text{ km/sec}$$

and

$$\langle w_\phi \rangle = 8.4 \pm 1.3 \text{ km/sec.}$$

In the above discussion, it was assumed that the tail of the comet lies in the orbital plane of the comet. This assumption can be relaxed and the velocity field of the solar wind can also be taken into account. The following variations for w_ϕ and w_θ which are found to be consistent with the observational and theoretical evidences have been used in the comet tail orientation problem

$$w_r = \text{constant}, w_\phi = w_{\phi,o} \frac{(\cos b)^{2.315}}{r} \quad (10.5)$$

and

$$W_\theta = w_m \sin 2b \quad (10.6)$$

where b is the solar latitude, $w_{\phi,o}$ and w_m denote the azimuthal speed in the plane of the solar equator at 1AU and the maximum value of w_θ . The results of analysis are given in Table 10.1. It is also possible to get the minimum solar wind speed which actually refers to the larger values of ϵ . The minimum value obtained for the solar wind speed is around 225 ± 50 km/sec. All these results are in good agreement with the direct space probe measurements. The presence of the azimuthal component of the

Table 10.1 Parameters of solar wind derived from ion tails.

Parameter	Published sample	Total sample (includes unpublished data)
ω_r (km/sec)	402 ± 12	400 ± 11
$\omega_{\phi,o}$ (km/sec)	7.0 ± 1.8	6.7 ± 1.7
ω_m (km/sec)	2.6 ± 1.2	2.3 ± 1.1
Number of observations	678	809

(Brandt, J.C. and Mendis, D.A. 1979. In *Solar System Plasma Physics*, Vol. II, eds. C.F. Kennel, L.J. Lanzerotti and E.N. Parker. Amsterdam: North Holland Publishing Company.)

solar wind was also first deduced based on the study of ion tails which was later confirmed through the direct space probe measurements, vindicating the simple aberration picture of the ion tails of comets. It is also remarkable that it can give so much of information without a detailed knowledge of the interaction between the solar wind and the tail plasma.

From the above discussion, it is apparent that the derived results based on the use of Eq. (10.3) are in good agreement with the gross observed properties of plasma tail of comets. Having established the validity of Eq. (10.3), it is now possible to reverse the problem and calculate approximately the expected general shape of the plasma tail from the same equation. This formalism is known as the *Wind Sock Theory*. Therefore the existence of solar wind was well established from the cometary studies before its detection by spacecraft at a much later time. The above studies indicate the importance of knowing the nature, structure and composition of solar wind for a full understanding of the comet and solar wind interaction.

10.3. Theoretical Considerations

The comet acts as an obstacle to the free flow of the solar wind. Therefore one can approach the problem of the interaction of the solar wind with the cometary atmosphere purely from the theoretical considerations. The presence of fine structures in the plasma tail of comets indicates the existence of magnetic field in comets for its confinement. Otherwise the fine structure will be washed out due to thermal motions.

Therefore the theoretical study of the interaction between the solar wind and cometary ions is a complicated problem as the interaction is coupled

through the interplanetary magnetic fields. The basic idea of the comet-solar wind interaction was provided by Alfven in 1957 and is shown in Fig. 10.3. When the solar wind with its frozen-in-magnetic field encounters

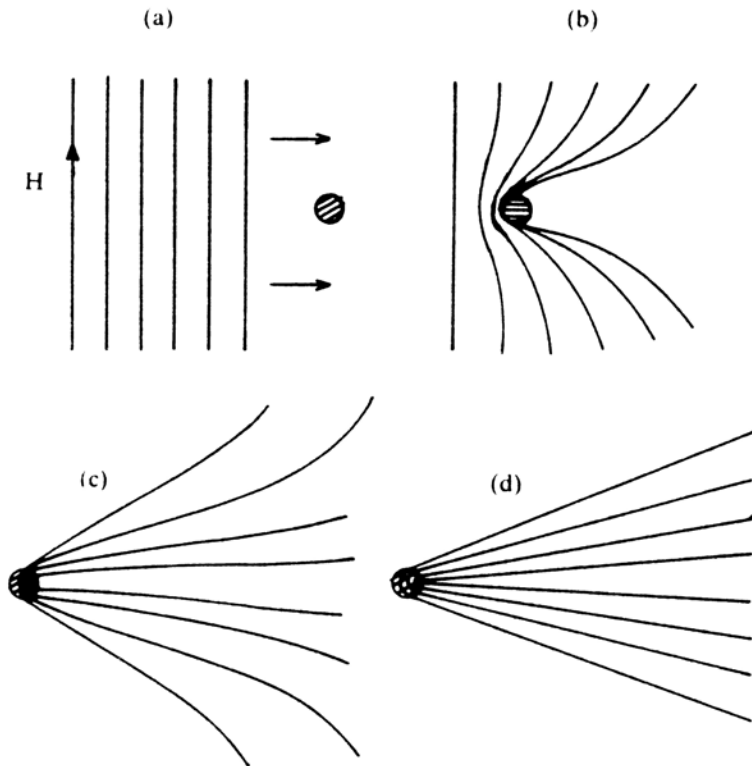


Fig. 10.3 A schematic representation of the “piling up” and “curling up” of interplanetary magnetic field by the coma of the comet. The gradual formation of the ion tail is shown in (a), (b), (c) and (d). (Adapted from Alfven, H. 1957. *Tellus* **9**, 92).

a comet containing ionized molecules, these molecules cannot cross the field lines. Instead they spiral around the magnetic lines and hence they are attached to the field lines. The cometary ions trapped in the field line is called ‘mass loading’. Since the cometary ions have low velocities, they are essentially at rest with respect to the solar wind speed of ~ 450 km/s. This reduces the flow speed. This effect is stronger near the nucleus than well away from the comet. These field lines wrap around the comet’s ionosphere and it is finally dragged into the tail as shown in Fig. 10.3. It also helps

in transfer of momentum between solar wind plasma and the cometary ions and this formalism can explain in a natural way the presence of narrow and straight streamers in the ion tail of comets. This is the basis of all the plasma models.

In a simple model, the plasma can be assumed to act as a fluid in the sense of fluid dynamics, allowing the use of simple hydrodynamic methods to predict the flow pattern of the plasma. Even without detailed modelling, it was suggested around 1964 that the expansion of the ionized coma gas should act as an obstacle to the supersonic solar wind flow which should result in a bow shock at a distance of around 10^4 to 10^5 km from the nucleus. The particle distribution functions can usually be determined from the conservation laws, namely, continuity, momentum and energy equations including the effect of electric and magnetic fields. These are to be supplemented with the equations for the magnetic field and the electric field. These equations constitute the magnetohydrodynamic equations (MHD) for the plasma and provide a good description of most of the plasma processes in the coma. The results of accurate one-and-two-dimensional models with spherical gas flow showed that a weak bow shock is expected with a Mach number 2. In recent years, more realistic and sophisticated models have been constructed, which takes into account various physical processes including chemistry in the neutral and ionized coma and its interaction with the solar wind. The interaction of the ionized coma with the solar wind lead to deviations from spherical symmetry. The assumption of axial symmetry is also destroyed due to the embedded magnetic field. Therefore a detailed description of the region would require a 3-dimensional magnetohydrodynamic model. These MHD models describe the macroscopic flow patterns and the characteristic boundaries expected from such interactions. The result of one such detailed 3-dimensional MHD calculation is shown in Fig. 10.4. The model takes into account momentum exchange from ion-neutral collisions, photoionization, mass-loading through ion pick up and the Lorentz forces of the transverse magnetic field. The simulation also takes into account the detailed physics and chemistry of the coma together, as they are intimately connected.

The results show that a bow shock occurs around 5×10^5 km from the nucleus for Comet Halley parameters. The ions are heated by the shock to around 2.2×10^6 K. However they cool down very fast due to collisions and charge exchange. The temperature of electrons is not affected by the shock and they lose their energy due to electron impact reaction. A sharp boundary exists at a distance of around 4800 km where the flow velocity

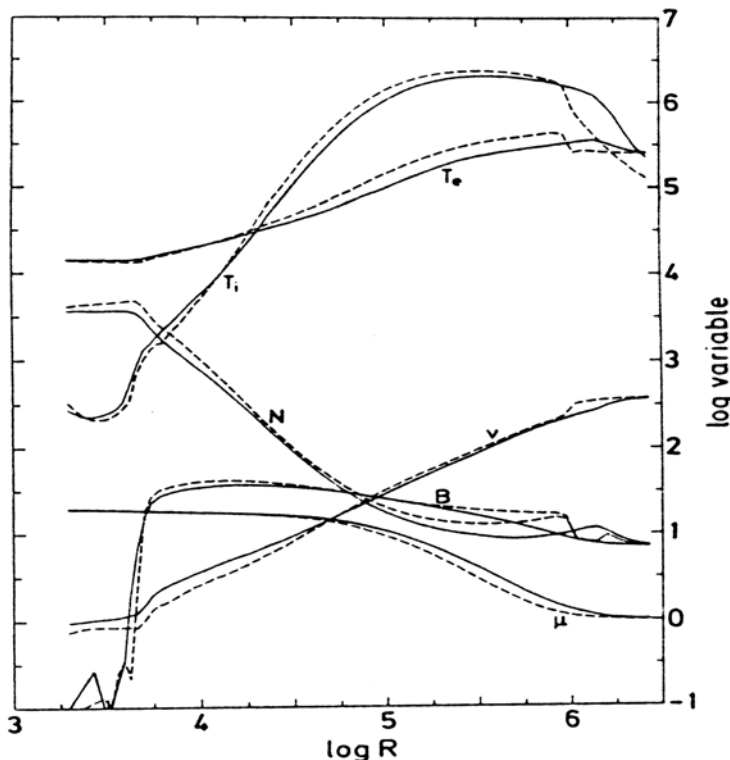


Fig. 10.4 Variation of physical quantities as a function of distance from the nucleus (R in km) for axisymmetric model (dashed lines) and the three dimensional model (solid lines). T_i =ion temperature (K), T_e =electron temperature (K), v =velocity (km/sec), N =Number density (/cm 3), B =magnetic field strength (nT) and μ =mean molecular weight (Wegmann, R., Schmidt, H.U., Huebner, W.F. and Boice, D.C. 1987. *Astr. Ap.* **187**, 339).

falls steeply. This is the contact surface which separates the contaminated solar wind from the pure cometary plasma inside. Therefore at this surface two plasmas of different origin converge. The magnetic field is compressed by the shock and it reaches a value of about 53 nT in the stagnation zone. The value drops suddenly at the contact surface. The variation of physical parameters as shown in Fig. 10.4 arise as a result of balance of different effects.

The overall morphology of the flow of plasma near a comet is schematically shown in Fig. 10.5. They can be understood as follows. At large distances from the comet the interaction of the solar wind is collisionless

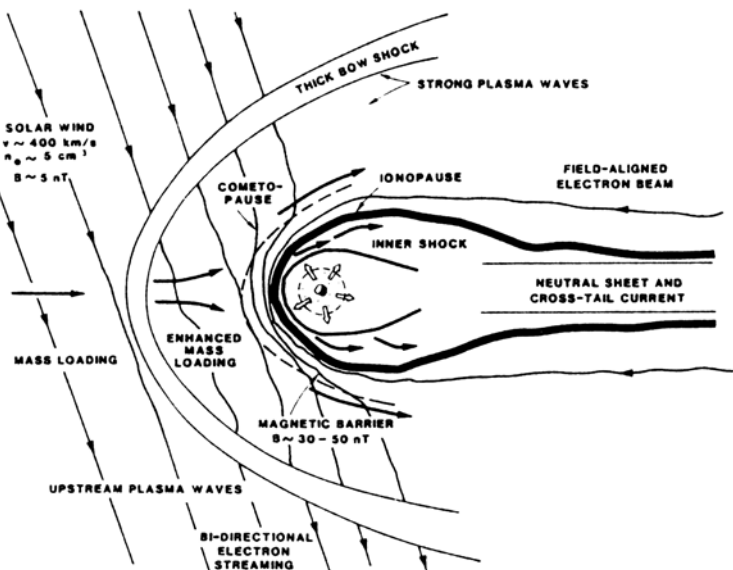


Fig. 10.5 Schematic representation of the global morphology produced by the interaction of the solar wind with the cometary atmosphere shows the flow pattern and the presence of various discontinuities arising from such an interaction (Mendis, D.A. 1988. *Ann. Rev. Astr. Ap.* **26**, 11).

as the cometary material is neutral. Once the ions are created, they are accelerated due to the interplanetary magnetic field (B) and the motional electric field of the solar wind, $E = V_{sw} \times B$ where V_{sw} is the solar wind velocity. The most important source of ionization of the gas is the photoionization by the extreme ultraviolet radiation. The charge exchange transfer of solar wind protons with cometary neutral also contribute to the ionization process. The ions formed move with a typical speed of around 1 km/sec in the cometary frame of reference, while the solar wind velocity is 400 km/sec. The newly formed ions which are initially at rest are accelerated by the motional electric field of the solar wind leading to a cycloidal motion with both gyration and $E \times B$ drift motion. The gyration speed depends upon the angle between the solar wind velocity and the magnetic field. This assimilation of the cometary ions into the magnetized solar wind is called 'mass loading' of the inflowing solar wind. The dynamics of the solar wind containing cometary ions depend upon the overall pressure and density associated with these ions. The thermal speed of ions, picked up by the solar wind, is of the order of solar wind speed. The picked up energy of

the ions in the upstream in the solar wind reference frame is typically about 10–20 keV for O^+ , whereas the solar wind protons have thermal energies ~ 10 eV. Therefore the picked up ions are quite hot and the pressure due to these ions dominate the total pressure even at large cometocentric distances. With the decrease in cometocentric distance, more and more ions are added to the solar wind and hence the total pressure increases. As solar wind progressively gets ‘mass loaded’, due to momentum conservation, the solar wind slows down. As the solution of the fluid equation cannot go continuously from supersonic to subsonic state, this results in a weak bow shock at a critical level of mass-loading. This depends crucially on the mean molecular weight. Therefore the cometary bow shock arises purely as a result of mass-loading process and is unique among the solar system objects. Many of the energetic ions like O^+ , C^+ and H^+ are generated upstream of the comet. Moving inwards from the shock, the solar wind continues to interact with the cometary material of increasing neutral density. These outflowing neutrals play an important role in slowing down the incoming solar wind through collisions. Therefore cometary ions which are produced down-stream of the shock are less energetic ($E \sim 1$ keV) compared to those produced upstream of the shock. In a real situation there is a slow gradation in the energy of the picked up ions and hence in the solar wind reference frame, energy of the pick-up ions decreases with decreasing cometocentric distance. Therefore the plasma found in the inner regions of coma contains ions of different populations made up of energetic ions picked up far upstream, and relatively cold ions picked up locally. Finally, the velocity decreases rapidly, giving rise to a sharp boundary called ‘cometopause’. In this transition region, collisions dominate. Near ‘cometopause’, the hot and warm cometary ions disappear from the plasma through charge exchange collisions with the neutrals. Inside the ‘cometopause’, the speed is very low, the ions are abundant and are modified by collisions and chemistry. This also leads to compression of the magnetic field giving rise to the magnetic barrier. The boundary of the field free cavity is called ‘diamagnetic cavity boundary surface’. It is also called contact surface, the ionopause or the tangential discontinuity. This boundary separates the purely cometary plasma and the mass-loaded solar wind plasma. The basic physical mechanism of its formation is due to the balance between the outward ion-neutral frictional force (due to the flow of neutrals past stagnated ions) and an inward directed electromagnetic ($J \times B$) force. Here the mass loading term is less important. The presence of another shock inside the cometary ionopause has been suggested in order to decelerate the supersonic outward flowing

cometary ions and divert them into the tail.

10.3.1. Comparison with observations

The *in situ* measurements of Comets Giacobini-Zinner, Halley and Borrelly which provided detailed data, confirmed the large scale picture of the solar wind interaction with comets at close heliocentric distances. Out of the three comets, extensive and detailed *in situ* data exists for Comet Halley due to six spacecrafts passing close to the nucleus of this comet.

The ICE spacecraft passed by Comet Giacobini-Zinner on Sept.11, 1985. The observations indicated the presence of a bow shock around 130,000 km from the nucleus. The detection of the high energy particles and plasma waves was an important result that came out of these studies. These high energy ions are basically the ions that were picked up by the solar wind magnetic field and accelerated as they are dragged by the solar wind. This process generates plasma waves. The curling of the magnetic field was also seen in the observations. The reversal of the magnetic polarity was also seen from spacecraft measurements. Far from the nucleus, plasma had typical solar wind speed of about 500 km/s. The density was around 5 ions/cm³ and an electron temperature of around 250,000 K. Around the closest distance of the spacecraft to the nucleus of 7800 km, the flow speed was about 30 km/sec, electron density of 600/cm³ and electron temperature of 15000 K. The measured ions were mostly water-group ions, such as H₂O⁺ and H₃O⁺.

While the bow shock of Comet Giacobini-Zinner was not well defined, the presence of a bow shock at a distance $\sim 1 \times 10^6$ km from the nucleus in Comet Halley was clearly identified by instruments aboard spacecrafsts, measuring plasma, magnetic field and plasma wave. The detection of bow shock in Comet Halley has resolved the controversy about its existence. The spacecraft measurements, has also given detailed information on the structure of the bow-shock. For example, the water group ions O⁺, OH⁺, H₂O⁺ and H₃O⁺ showed a sudden enhancement following the bow shock. Inside the bow-shock, in the cometo-sheath region the flow speed was found to decrease continuously due to ion pick up and the plasma becomes more dominated by cometary ions. The phase space density distribution of cometary H⁺ ions showed a shell-like structure at a distance of around 8×10^6 km upstream of the bow-shock in Comet Halley. This pattern arises due to the fact that the velocity distribution of pick up ions which should be in the form of a ring with velocity component $v_{\perp} = V_{sw} \sin \alpha$ perpendicular to

the interplanetary magnetic field and a drift velocity $v_{11} = V_{sw} \cos \alpha$ along B and relative to the solar wind is unstable and leads to various plasma instabilities. As a result of wave-particle scattering, the H^+ ions diffuse along the sphere transforming the ring-like structure to shell-like structure.

Many of these features have also been seen from Comet Borrelly from measurements carried out with Deep Space 1.

The existence of cometopause at a distance of around 10^5 km came from the observation that the density of the solar wind protons was found to decrease rapidly approaching this distance, while the comet ion density increased rapidly with $1/R^2$ radial dependence for $R < 10^5$ km (Fig. 10.6). At a cometodistance $\sim 1.4 \times 10^5$ km there was also a sudden decrease of

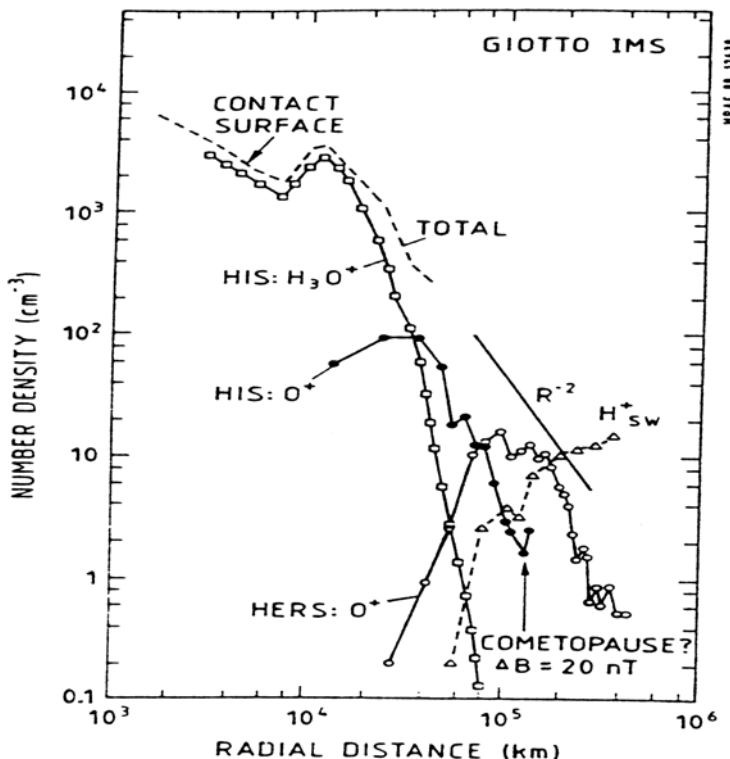


Fig. 10.6 Number density profiles of water group ions and solar wind protons as measured by Giotto ion mass spectrometer (see Ip, W.-H. 1989. *Ap. J.* **343**, 946).

electrons with energies ≥ 10 eV while the magnetic field strength increases

from 6 nT to 26 nT. For radial distances $< 2 \times 10^5$ km the dominant ions change progressively from O^+ , OH^+ and H_2O^+ to H_3O^+ (Fig. 10.7). The dominant ions inside 10^4 km are H_2O^+ and H_3O^+ which continuously increase towards the nucleus as indicated by the models. The ions C^+ and S^+ were also found to be very abundant.

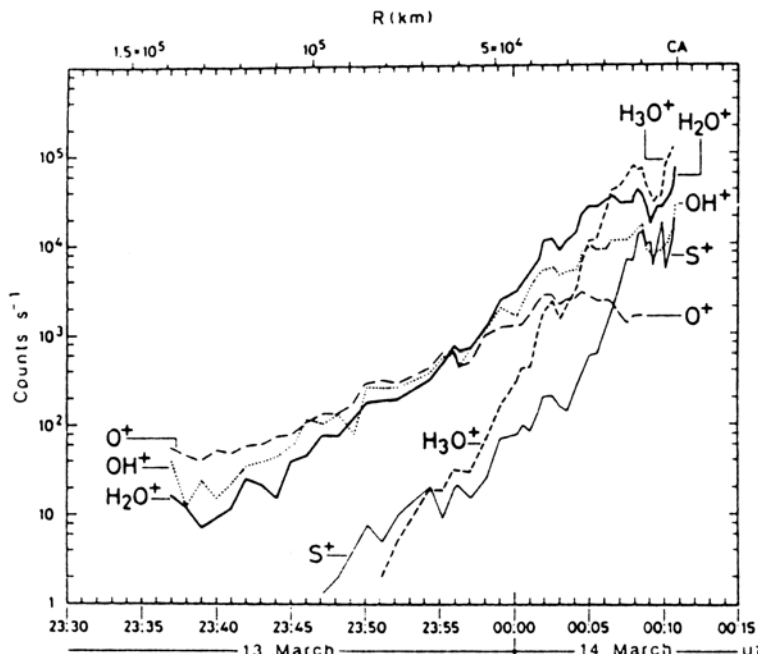


Fig. 10.7 The variation of abundances of several species as measured by ion mass spectrometer on Giotto from Comet Halley. R is the distance of Giotto from the nucleus and the time refers to UT at the ground station (Balsiger, H. et al. 1986. *Nature* **321**, 330).

The Giotto measurements of magnetic field, plasma temperature and plasma speed is compared with that of model calculations in Fig. 10.8 and Fig. 10.9. There is overall agreement between the models and observations. The ion temperature dropped from 2600 K to 450 K at a distance of around 4700 km. These results confirmed the presence of tangential discontinuity. The interesting result that Giotto magnetometer measurements showed is that there was a dramatic drop in the magnetic field ~ 50 nT to zero at cometocentric distance ~ 4600 km from the nucleus inbound. In the outbound the magnetic field of zero rose to about 65 nT at distance of about

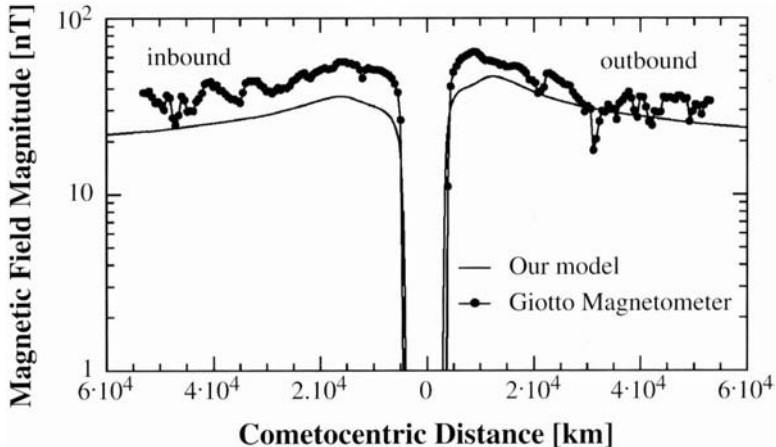


Fig. 10.8 The Giotto measurements of variation of magnetic field is compared with modeled results (Gombosi, J.I., De Zeeuw, D.L. and Haberte, R.M. 1996. *J. Geophys. Res.*, **101**: 15, 233).

3800 km. The region bound by these two distances is devoid of magnetic field. The upper limit for the magnetic field strength in the stagnant plasma region can be estimated from balance between the magnetic pressure and the solar wind ram pressure

$$\text{i.e., } \frac{B_s^2}{2\mu_0} = n_{\text{sw}} m_{\text{sw}} V_{\text{sw}}^2 \quad (10.7)$$

Using for solar wind number density $n_{\text{sw}} \sim 5/\text{cm}^3$ and $V_{\text{sw}} \sim 400 \text{ km/sec}$, the calculated value of $B_{\text{max}} \sim 60 \text{ nT}$. This is what is observed.

The width of the field-free cavity is about 8500 km. The boundary of the cavity separate the two regions of the plasma wherein the inner side containing mainly pure cometary plasma while the outer region containing a mixture of cometary plasma and solar wind plasma. In essence the outflowing cometary plasma hinders the flow of solar wind with its magnetic field inside this surface. The location at which the inner edge of the ionopause occurs can also be estimated from the balance between the magnetic force and the ion-neutral drag force. This gives a distance $\sim 4335 \text{ km}$ for inbound and $\sim 3470 \text{ km}$ for the outbound for the Giotto encounter. These are in reasonable accord with the observed values mentioned above.

The general results of plasma measurements carried out in Comet Borrelly are quite similar to those of Comet Halley. The approximate composition as determined from the closest approach data is as follows: 63% OH⁺,

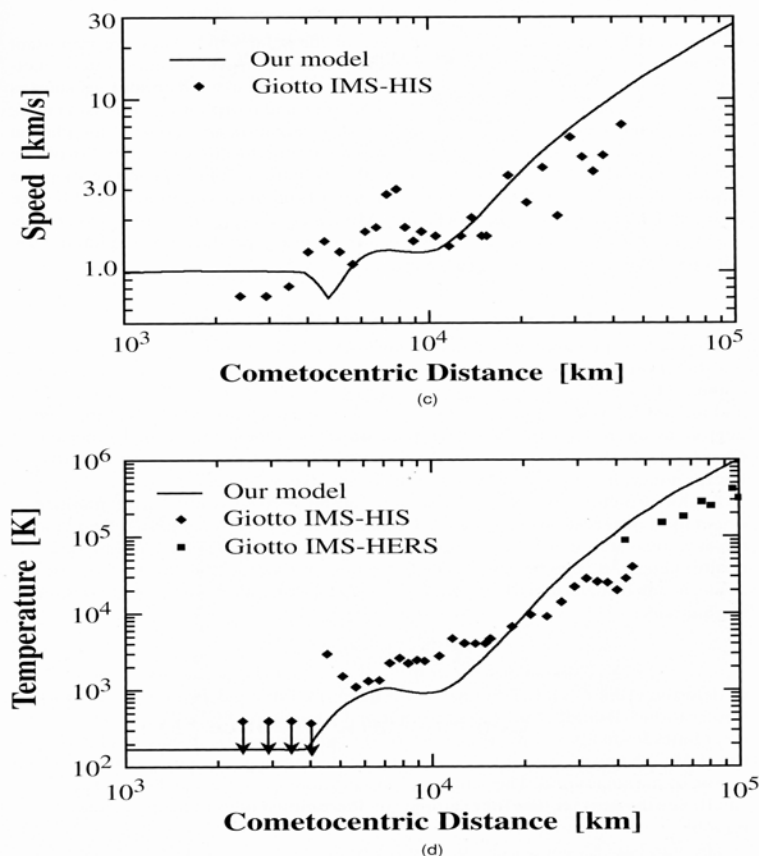


Fig. 10.9 The Giotto measurements of variation of speed and temperature of ions are compared with modeled results (Gombosi, J.I., De Zeeuw, D.L. and Haberte R.M. 1996. *J. Geophys. Res.*, **101**:15, 233).

25% H_2O^+ , 2.5% C^+ , 2% N^+ and 8% CH_3^+ .

10.4. Instabilities and Waves

It was suggested that there could be some instabilities present in the plasma due to the mass-loading of the solar wind by the newly created ions. The nature of the pick up cometary ions by the solar wind depend upon the orientation of the solar wind flow to the interplanetary magnetic field (IMF) \mathbf{B} . When the IMF is orthogonal to the solar wind V_{sw} , i.e. $\mathbf{B} \perp V_{\text{sw}}$ the

$V_{sw} \times B$ motional electric field makes the newly created ions gyrate around the magnetic field. In this case the anisotropy in their gyro velocities (as they can have both the zero velocity and twice the solar wind velocity), can give rise to three types of low frequency instabilities, namely the ion-cyclotron instability, a parallel propagating nonoscillatory mode and a fluid mirror instability. In the other extreme case, when the IMF is parallel to the solar wind velocity vector i.e. $B \parallel V_{sw}$, there is no $V_{sw} \times B$ solar wind force acting on the cometary ions. For such a situation the ions form a beam in the solar wind plasma frame moving at a velocity $-\bar{V}_{sw}$ relative to the ambient plasma. This can lead to two types of instabilities, a right handed resonant helical beam instability and a nonresonant instability. However the coupling between the solar wind and the cometary ions becomes complicated if the solar wind flows obliquely to the magnetic field at an angle θ . Therefore, in principle, various kinds of plasma instabilities and waves could be generated due to the ion pick up by the solar wind, depending upon the complex local conditions of the plasma. The *in situ* plasma and magnetic field measurements of Comets Giacobini-Zinner and Halley by the spacecrafts have shown the presence of a large number of waves of various kinds. They are highly complex and difficult to interpret. Only a few of these results will be mentioned here.

One of the main results that came out of the study of the Comet Giacobini-Zinner by the ICE spacecraft is the detection of the water group (16 to 19 amu) ion cyclotron frequency from spectral power analysis. This has also been detected in Comet Halley observations. Several peaks with cyclotron fundamental at 7 mHz and its harmonics at 14, 21, 29 and 39 mHz has been seen in the cross-spectral densities of the solar wind proton velocity and magnetic field. The fundamental mode at 7 mHz is linearly polarized and the higher harmonics are either linearly or highly elliptically polarized. The cometary influence extends to a distance of around 2×10^6 km.

Waves have been detected upstream of the bow shock for Comets Giacobini-Zinner and Halley. A variety of polarizations have been detected from circularly polarized waves propagating at large angles relating to the ambient field to highly elliptical polarized waves. The detection of short duration magnetic pulses during $\theta = 90^\circ$ intervals was rather an unexpected result. The field variations have a duration of around 6 to 7 sec and is comparable to the proton cyclotron frequency in the spacecraft frame. These pulses are mostly transverse oscillations.

At distances $\sim 3 \times 10^4$ to 18×10^4 km from the comet the magnetic field experiment detected mirror mode waves which are characterized by

irregular dips in the magnetic field. Similar structures have been seen from Giotto Spacecraft in Comet Halley and ICE on Comet Giacobini-Zinner. Higher frequency whistlers have been seen near the bow shock of Comet Giacobini-Zinner and it is an integral part of the magnetosonic wave. Several mechanisms for the formation of whistlers have been proposed such as through generation of dispersive whistlers derived from hybrid simulation results, generation of pick up of heavy ions and protons at the distorted steepened fronts of the magnetosonic waves and so on.

The waves of extremely low frequency (ELF) in the region 10 to 1500 Hz and of very low frequency (VLF) in the region 10^3 to 10^6 Hz generated by cometary pick up ions and photoelectrons are present in Comets Giacobini-Zinner and Halley upto distances of about 2×10^6 km from the nucleus. The Comet Halley emission was about an order of magnitude more intense than as seen from Comet Giacobini-Zinner. Some of the wave modes that has been seen in comets are shown in Fig. 10.10. They show the electron plasma oscillations (EPO), the ion acoustic waves, electromagnetic whistlers and lower hybrid resonance (LHR) waves.

An indication of the presence of strong turbulence even upto distances $\sim 2 \times 10^6$ km from the nucleus came from the detection of strong wave activity. In addition to high level plasma activity, large-amplitude magnetic field variation were observed. The turbulence measured by Vega and Giotto Spacecrafts of Comet Halley showed that the magnetic field fluctuations were smaller compared to that observed in Comet Giacobini-Zinner. There is a clear correlation between the magnetic field variations and solar wind plasma measurements which suggest the waves are fast-mode magnetosonic waves. The observed magnetic field turbulence spectrum follows a power law spectrum with an index of about 2, which is sufficiently different from the fully developed Kolmogorov spectrum with a spectral index of 5/3. This indicates that the cascade has not progressed far enough.

The detection of strong turbulence has led to several theoretical investigations. Both analytical treatments and numerical simulations have been applied to interpret these results. They could arise due to the presence of cyclotron harmonic emission, which would add power at the higher frequencies; or if ions have a finite temperature, it will shift the wave frequencies to higher values or due to non-linear effect of the waves and so on. It is quite possible that several processes could lead to a smooth power law spectrum. It is found that resonant wave-particle interactions and ion-shell formation can lead to a wave power law spectrum with an index of around 2.0.

Though a large number of substructures have been identified in the *in*

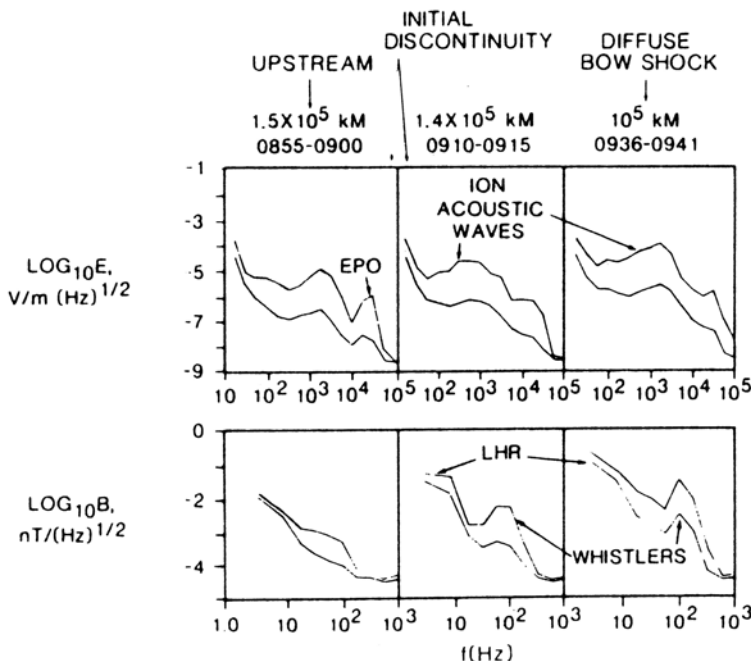


Fig. 10.10 Several wave modes seen in Comet Giacobini-Zinner in the upstream and downstream are shown. This includes electron plasma oscillations (EPO), ion acoustic waves, electromagnetic whistler modes and lower hybrid resonance (LHR) waves (Scarf F.L. et al. 1987. *Astr. Ap.* **187**, 109).

situ measurements, the mechanism of formation of such structures is not clear.

10.5. Acceleration of Cometary Ions

The possibility that cometary ions could be accelerated to high energies in the coma due to the turbulent plasma environment came from the analogy with the diffuse shock acceleration at the Earth's bow shock. The existence of such accelerated ions in Comet Giacobini-Zinner came from the observations carried out with the ICE spacecraft. The measurement showed large flux of cometary ions of about 100 keV even upto distances $\sim 10^6$ km from the nucleus. Large anisotropy in their distribution was also detected. The *in situ* measurements of Comet Halley confirmed the presence of appreciable fluxes of energetic cometary ions in the coma, but

it extended even beyond 100 keV and upto about 0.5 MeV.

The maximum energy that a newly formed ion can have in the rest frame of the spacecraft is given by

$$E_{\max} = \frac{1}{2} m_i (2V_{\perp})^2 = 2m_i V_{sw}^2 \sin^2 \alpha \quad (10.8)$$

where $2V_{\perp}$ is the total velocity comprising of the drift speed V_{\perp} and roughly an equal amount of gyration speed. V_{sw} is the solar wind speed and α is the angle between the solar wind velocity and the interplanetary magnetic field. For $V_{sw} \simeq 400$ km/sec, the maximum energy E_{\max} that water ions can have ~ 60 keV corresponding to $\alpha = 90^\circ$. There should be a sharp cut off in the energy distribution beyond this value. However the observations indicating that the energy spectra extended upto ~ 0.5 MeV clearly showed that significant ion acceleration must have occurred. The value of $\alpha = 90^\circ$ or 0° correspond to the extreme cases of velocity vector of the ions in the direction of the solar wind (E_{\max}) or in the opposite direction (E_{\min}) and should therefore lead to anisotropies in the energy distribution.

The possible mechanisms for the acceleration of ions has led to several studies of wave-particle interactions. The cometary ions could be accelerated through diffuse shock acceleration process near the bow shock. This process is basically related to random multiple scattering of charged particles across the shock front, separating the supersonic and subsonic sides, a form of first order Fermi acceleration. Another mechanism is the stochastic acceleration process, a form of second order Fermi acceleration process. Here the mechanism is the scattering of the particles by the waves in the turbulent cometary plasma. In the diffuse acceleration process, the accelerated ion population builds up ahead of the bow shock with a characteristic length scale given by K/V_{sw} where K is the diffusion coefficient of the medium normal to the shock. For the case of ion acceleration at the bow shock of Comet Halley, the estimated distance is $\sim 10^6$ km. The diffuse shock acceleration process is more important in this region and for energies ≤ 100 keV. For energies > 100 keV and for distance $> 5 \times 10^6$ km far from the bow shock, the acceleration through stochastic process or the second-order Fermi acceleration process is of major importance. Support for the stochastic acceleration process also seems to come from the observations that can be fitted well with an exponential velocity distribution of cometary ions. Other mechanisms that have been considered for ion acceleration process include the lower hybrid turbulence that could be generated by the comet ion pick up process as well as by the bow shock formation and ion cyclotron wave absorption.

The presence of intense electron plasma oscillations and ion-acoustic waves in the Comets Giacobini-Zinner and Halley indicate that electron heating and acceleration should take place. Some of the processes considered for electron heating are ion acoustic wave instability, cross-field streaming instabilities, lower hybrid wave acceleration and so on.

10.6. Large Scale Structures

Different kinds of plasma processes must be taking place in the ion tail of comets. This is evident from the photographs of bright comets which show a wide variety of unusual large scale dynamical phenomena. A wide variety of plasma tails can be seen from the Atlas of Cometary Forms. Many of these interesting phenomena appear to be controlled to a large extent by the microscopic plasma physical processes arising out of the comet-solar wind interactions. There are many other features which arise due to the dominance of the solar wind. Therefore any change in the solar wind property in a small or on a large scale is reflected directly in the behaviour of the cometary plasma. Some of the characteristic features arising out of these processes are given in Table 10.2. It should be noted that most of the observed features are transient in nature. Since the ion tail is basically a plasma column of large extent and is also bright, it gives a splendid opportunity for the study of spatial and temporal variations. It can also help in distinguishing the phenomena connected with the processes taking place inside the tail like instabilities etc. from those introduced by the fluctuations in the solar wind.

Table 10.2 Plasma process and the possible associated events.

Physical process	Lead to observed features
Change in the solar wind conditions	Changes the orientation of the ion tail, bends the tail
Development of instabilities	Enhancement of ionization, flares, condensations, filaments, rays, helices, waves, etc.
Magnetic field lines disconnected	Disconnected tails

10.6.1. Tail rays or streamers

The filamentary structure in the ion tails of comets is quite common and is also very conspicuous (Fig. 1.18). The shape of these streamers appears to show the importance of magnetic fields. Since the CO⁺ ions present in the ion tail follow the direction of the magnetic field, the streamers are made visible through CO⁺ emission. These rays going in the anti-solar direction grow with time and can extend from smaller lengths of about 10³ km to longer lengths of about 10⁶ km. The rays are distributed almost symmetrically around the comet tail axis. They also seem to turn towards the main tail axis. The time scale for coalescing process is around 10 to 15 hours. Since the time of formation of a new streamer is about one hour, usually streamers as many as 20 to 25 can be seen at any given time. These streamers do not interact with each other. They appear to originate from a small volume very close to the nucleus, at a distance of the order of 10³ km from the nucleus. In addition to seeing the streamers originating from the coma, streamers starting from the tail have also been noticed. Since these rays do not originate from the ionized region, the mechanism of formation of these rays has to be different. Two possibilities have been suggested either they are produced by nonlinear compressional waves or the cometary ions trace the magnetic field lines. Observations appear to show the first explanation to be unlikely although there are problems with the second explanation. The ion stream could also arise due to the effect of magnetic sector boundaries in the IMF (Sec. 10.6.6) The IMF following the sector boundary reconnects at the front side of the ionosphere. This can lead to ion streamers. In the coma, in addition to magnetic lines of force, neutral sheets or surfaces also curl around and their behaviour will be similar to the observed reversal of directions in the interplanetary medium. It has been suggested that the streamers represent the enhanced plasma which is confined to these neutral tubes or surfaces. These ions are concentrated in the neutral zones as a result of the field gradients on either side of the neutral regions. Also these neutral regions prevent the field lines of opposite polarity merging with each other leading to annihilation. These neutral tubes are nearly cylindrical, centred on the tail axis and when seen edge-on, they appear as rays. They appear symmetrical about the tail axis and this is consistent with the observations. It is quite possible that strong shock waves in the sunward direction can generate keV electrons and energetic protons. These high energy electrons streaming along the magnetic field lines can result in high ionization in a short time scale which

can give rise to streamers.

10.6.2. Knots or condensations

The plasma tails are filled with structures such as bright knots or condensations which are basically ion concentrations. With the use of time sequence photographs, it is possible to follow these knots as a function of time for a period of a few hours to a day. From such measurements, the velocity and acceleration can be determined. Their velocities lie in the region of around 20 km/sec near the head to around 250 km/sec at distances far from the head. This corresponds to a value of $(1 - \mu)$ of around 100 with wide variation. Several attempts have been carried out for an understanding of these results. In particular whether the observed motions are the mass motions or some form of disturbance traveling down the tail. Even though the collision mean free path for the particles is large, it is still a reasonable approximation to treat the interaction between the solar wind and the cometary plasma as a fluid-like interaction. Based on such a hypothesis, several other mechanisms for the observed acceleration have been suggested. One suggested process is that the acceleration will result when the plasma is squeezed out of the flux tubes by the magnetic pressure gradients. Another point of view is that the enhancement of the momentum transfer takes place due to some form of instability setting in the plasma. It is not clear at the present time whether the observed motions are the mass motions or some form of disturbance propagating down the tail. Doppler measurements carried out in the near-nucleus region of plasma tail indicate speeds of around 30 km/sec and extend to distances of around 3×10^5 km. The derived acceleration is found to increase with distance. Therefore it is likely both mass motion and waves are present in the plasma tail of comets.

10.6.3. Oscillatory structure

The photograph of Comet Kohoutek taken on 13 January 1974 when it was at $r = 0.58$ AU and $\Delta = 0.81$ AU, clearly showed the presence of a wavy structure in the ion tail, moving approximately at a speed of about 235 km/sec. (Fig. 1.16). The feature appeared to be a helical structure. The radius and the wavelength of the structures are about 2.3×10^5 km and 1.4×10^6 km respectively. The wavy structure had an extension of about 3.6×10^6 km and was about 1.6×10^7 km away from the nucleus. These oscillations have been interpreted in terms of "kink instability" based on

the studies of the Earth's geomagnetic tail. The theoretical work developed for the Earth's geomagnetic tail has been successfully applied to the comet tails. In brief, an azimuthal component of the magnetic field is produced, in a cylinder of plasma when a current flows through the longitudinal magnetic field. This finally gives rise to a helical field. The phase speed of the helical kink turns out to be simply the Alfvén speed of the tail plasma, which is given by

$$C \approx \frac{B}{(4\pi\rho)^{1/2}} \quad (10.9)$$

where B is the magnetic field and ρ is the mass density. For a number density of CO^+ ions of 10 to $10^3/\text{cm}^3$, the magnetic field lies in the range of

$$100\gamma \leq B \leq 1000\gamma.$$

10.6.4. “Swan-like” feature

Another large scale dynamical structure in the tail of Comet Kohoutek can be seen in the photograph of 11 January, 1974 (Fig. 1.17). This is generally termed as “Swan-like” feature because of its appearance. The size of the feature is estimated to be about 5×10^6 km and is situated at a distance of about 15×10^6 km from the nucleus. The feature was found to move away from the nucleus with an apparent speed of about 250 km/sec. The Swan feature is not a mass flow but rather a propagating hydromagnetic wave phenomenon. In fact it could be the kink instability in an advanced stage of growth.

10.6.5. Bend in the tail

The changes in the solar wind conditions can reflect directly in the observations of ion tails. This was established for the first time, based on the photographic observations of Comet Bennett. It was shown that the kinks observed in the tail of this comet were correlated with the solar wind events as observed from the satellite measurements.

A striking example of this type can be seen from the photograph of Comet Kohoutek taken on 20 January 1974, where a large bend can be seen. This is shown in Fig. 10.11. It is interesting to investigate whether this bend is correlated with the solar wind properties for that date. The properties of the solar wind are obtained by the observations made by

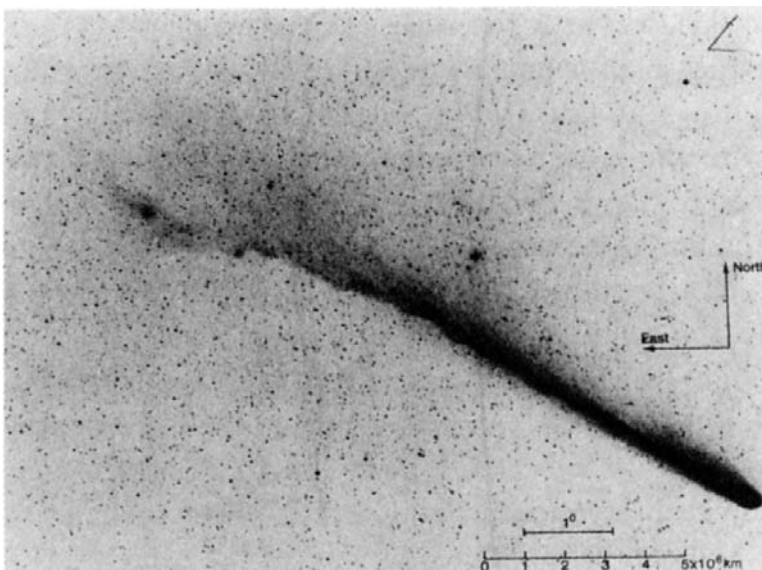


Fig. 10.11 Photograph of Comet Kohoutek taken on January 20, 1974 which shows the large scale bending of the tail. (Brandt, J.C. and Chapman, R.C. 1981. *Introduction to Comets*. Cambridge: Cambridge Univ. Press). Illustration credited to Joint Observatory of Cometary Research, NSA.

the Earth orbiting Satellite IMP-8. These observations have been used in conjunction with the theory to predict the nature and structure of the ion tail projected on to the sky for the day of the observation. There was a good agreement between the expected and the observed comet tail configurations. These results clearly showed that the observed large-scale tail curvature coincided with the compression region of a high speed solar wind stream. Generally a high speed solar wind stream causes enhanced geomagnetic activity which usually shows up in the geomagnetic records. A geomagnetic storm was actually detected on January 24 to 27, corresponding to the Comet Kohoutek observations. Figure 10.12 shows schematically the tail configuration and the bend. The direction of the solar wind is shown by the arrows. It can be seen that in region A, the tail has the same direction as the direction of the solar wind. This means that the tail has taken the equilibrium position. In region B, the flow of the solar wind is across the tail and has not yet adjusted to the direction of the solar wind. On the other hand the segment C is well aligned with the head of the comet, as the tail has not yet been affected by the solar wind. This is a striking example



Fig. 10.12 Schematic representation of Fig. 10.11. The left portion shows overall kink and the right portion shows some details. The inferred solar wind direction is shown by arrows. (Adapted from Jockers, K. 1981. *Icarus*, **47**, 397).

which clearly shows that the comet tails are very effective for monitoring the changing conditions of the interplanetary plasma.

10.6.6. Disconnection events

Another interesting and characteristic feature quite often seen in the plasma tail of comets is the disconnection events which have been noted since early times. The photograph of Comet Morehouse shows the abrupt disconnection of the tail as shown in Fig. 10.13. This is a common property of all comets. The disconnection events appear to be cyclic in the sense that after a tail gets disconnected a new tail appears to form and this process seems to repeat itself. A possible mechanism for such phenomena

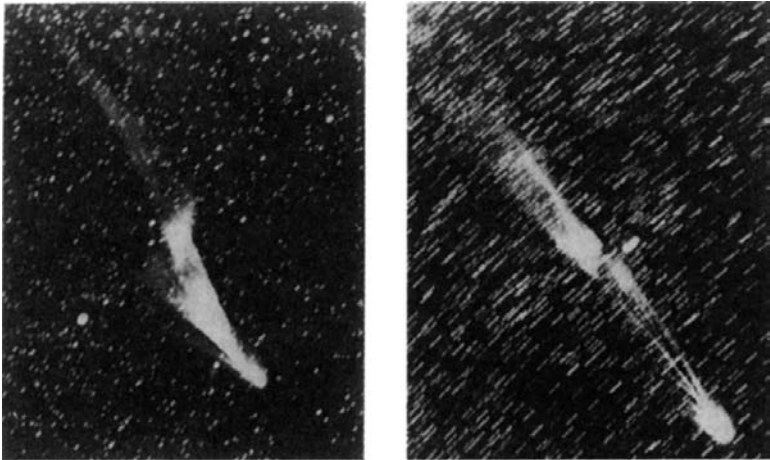


Fig. 10.13 Photograph of Comet Morehouse showing a tail disconnection event. Left and right photographs refer to September 30, 1908 and October 1, 1908 respectively. (Niedner, M.B. and Brandt, J.C. 1979. *Ap. J.* **223**, 671).

can be understood from Fig. 10.14. The explanation is essentially related to the presence of magnetic sector boundaries in the interplanetary magnetic field (IMF). A sector boundary is defined as the boundary between a region in which the field lines are directed primarily towards the Sun (in the ecliptic plane) and a region in which the field lines are directed primarily away from the Sun (in the ecliptic plane). The two regions with opposite magnetic field polarity are separated by a thin layer of the heliospheric current sheet (HCS). When the comet ionosphere crosses the magnetic sector boundary of the IMF at which the magnetic field direction reverse by 180° i.e. HCS, it disconnects the existing tail and it will move in the anti-solar direction. A new tail will then form with the reconnection of the field lines with the opposite field orientation until a new magnetic sector comes along. The process is repeated. Therefore if a bright comet is observed for a long time, it is possible to observe many events as described above. In the reconnection phase, the magnetic energy may be dissipated in the form of an increase in brightness or ionization or flares etc., and it may show up in the observations. There is some observational evidence to suggest that these things do happen. Comet Halley showed a disconnection event on March 8.4, 1986. The presence of magnetic sector boundary at this time was verified from observations of Vega 1 and Vega 2 spacecrafcts. Comet Hyakutake also showed a spectacular disconnection event on March 24.6,

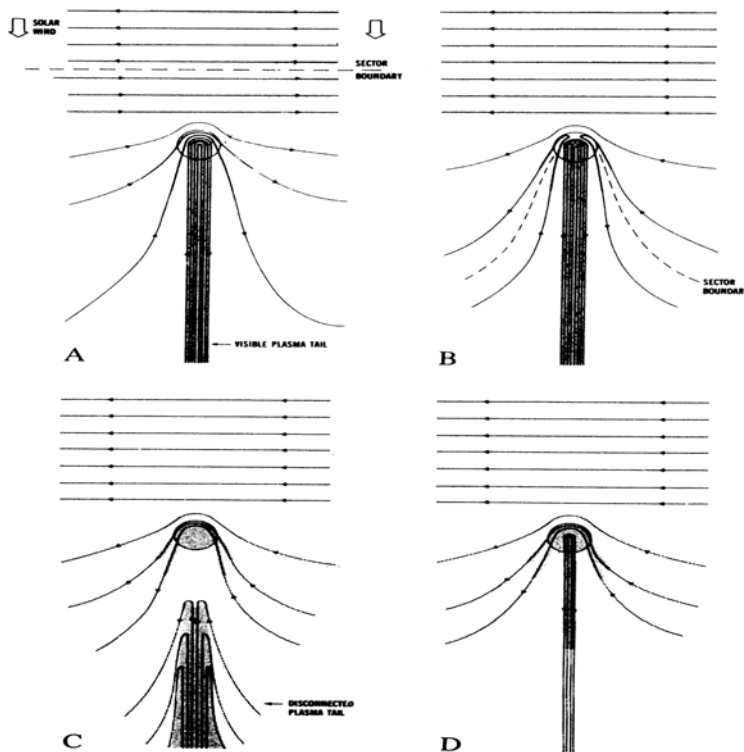


Fig. 10.14 Process of formation of disconnected plasma tail of a comet due to the passage of an interplanetary sector boundary. Tail ways are shown by the shaded portions. (Niedner, M.B. and Brandt, J.C. 1979. *op. cit.*).

1996. This was also in agreement with the calculated position of the magnetic sector boundary. Therefore all the observations are in agreement with the magnetic sector boundary reconnection model.

10.7. X-rays

X-ray emission is generally associated with a high temperature plasma of about 10^6 K or so. Therefore the detection of X-rays from Comet Hyakutake with ROSAT satellite in 1996 was a great surprise. The motivation to look for X-rays in Comet Hyakutake appear to have come from a study of the possible production of X-rays as a result of high speed collision between interplanetary dust particles and the dust particles in the comet.

Comet Hyakutake was considered to be a favourable comet for the possible detection of X-rays as the comet was very bright and came very close to the earth. Strong X-ray emission was indeed detected for the first time from this comet. Following the detection of X-ray from Comet Hyakutake, ROSAT archival data base was searched for the possible presence of other comets with X-ray emission and several comets were found. In recent times, many more comets have been detected in the X-ray region from X-ray satellites. Therefore X-ray emission can be considered to be a common feature of all comets.

Several characteristic features associated with X-ray emission from comets have been seen. X-ray images appears to show similar spatial morphologies, which is crescent shaped extending upto about 10^5 km with the brighter peak displaced toward the Sun (Fig. 10.15). The X-ray emission

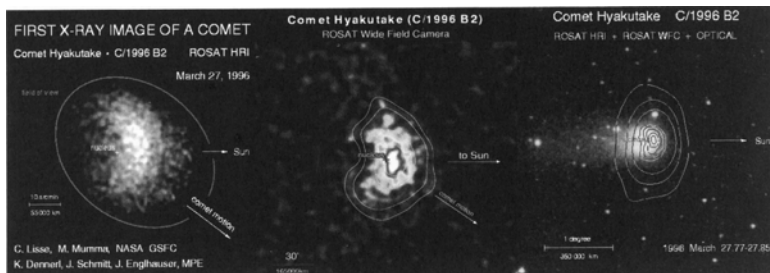


Fig. 10.15 Shows the images of Comet Hyakutake taken on 26–28 March 1996. The first two are the X-ray images taken with ROSAT. The third image is in the visible light with X-ray emission contours superimposed. The mark “+” denotes the location of the nucleus and the direction of the Sun is towards the right (Lisse, C.M. *et al.* 1996. *Science*, **274**, 205).

is confined to the cometary coma. In the case of Comet Hyakutake the location of the emission peak from the nucleus was about 2×10^4 km. These give an indication of the possible encounter of solar wind with the extended cometary atmosphere. The X-ray emission was not associated with extended dust or plasma tails. The X-ray emission was also found to be variable. The observed total luminosity of Comet Hyakutake was about 4×10^{15} ergs/sec for an aperture radius at the comet of 1.2×10^5 km. In the case of Comet Levy the observed soft X-ray luminosity in the energy range 0.2 to 0.5 keV was about 2×10^{16} ergs/sec. Observations of several comets have shown that total X-ray luminosity correlates with the gas production rate. The time variation of X-ray emission show a correlation

with solar wind proton flux and oxygen ion flux, but no correlation with solar X-ray flux. Longtime monitoring of rapid changes in gas production and the observed X-ray flux in comets (such as an outburst) has shown a direct link between the two. Earlier X-ray observations carried out at low energy resolution could not resolve the possible presence of emission lines. However with the availability of higher resolution instruments, the spectrum was found to be dominated by emission lines from highly charged C, N and O and not by continuum (Fig. 10.16).

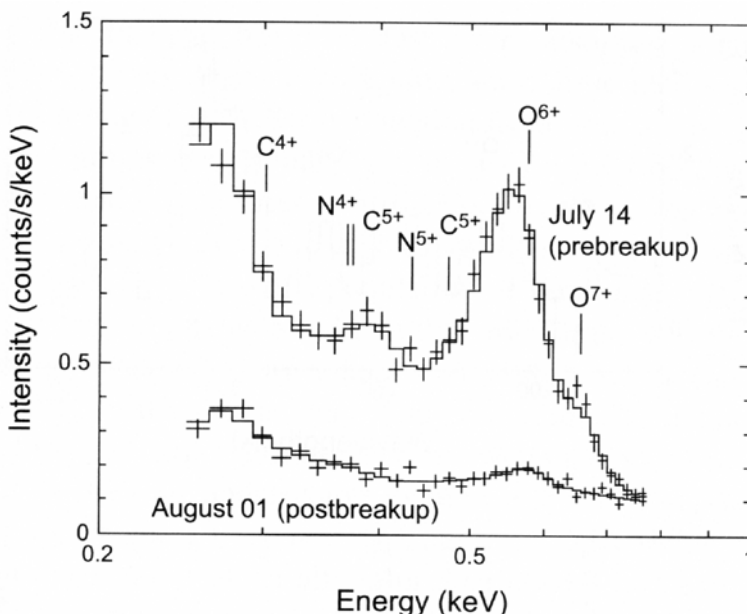


Fig. 10.16 X-ray spectrum of Comet C/1999S4 (LINEAR) observed with Chandra X-ray Observatory (crosses). The six-line best-fit model spectrum is shown as solid line (Lisse, C.M. et al. 2001. *Science* **292**, 1343).

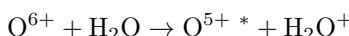
Any physical mechanism proposed to explain the observed X-ray emission in comets has to be consistent with all the observed characteristics of this emission. These include thermal bremsstrahlung associated with collision of solar wind electrons with neutral gas or dust, scattering of solar X-rays by cometary small dust particles, charge exchange of solar wind heavy ions with cometary neutrals, K-shell ionization of cometary neutrals by electron collision etc.

In the Thermal bremsstrahlung mechanism, the electrons of solar wind

are deflected from the nuclei of atoms on collision and give rise to continuum radiation. For such a process the electron energies have to be larger than 100 eV (i.e. $T > 10^6$ K). In the K-shell mechanism the collision between a fast solar wind electron and an atom can remove the orbital electron from the inner shell of the atom. However in these mechanisms the expected luminosity are smaller by a factor of around 100 to 1000 compared to observations. This is due to the fact that flux of high-energy solar wind electrons near comets are not enough. Also X-ray emission has been observed upto larger distance from the nucleus ($\sim 10^5$ to 10^6 km) beyond the bow shock and the energies of solar wind electrons at these distances is only around 10 eV. In addition the presence of multiple emission lines indicate non-viability of continuum or K-shell line models.

There are also difficulties associated with mechanisms involving dust models. The scattering of solar X-ray radiation by cometary dust particles of sizes $\sim 1 \mu\text{m}$ in size cannot produce the observed X-ray luminosities. This problem can be overcome by involving the presence of small dust particles of size of the order of the wavelength of observed X-ray emission, $\sim 10\text{--}100 \text{\AA}$, which can scatter the solar X-ray radiation efficiently. The abundance of such dust particles in comets is not known. However there was some indication of the presence of such dust particles in Comet Halley from Vega flyby spacecraft. Other problems associated with dust particles are X-ray emission correlates with gas production rate, time variation of X-ray emission correlate with solar wind ion flux etc. In view of these considerations the charge exchange collisions of highly charged solar wind ions with cometary neutral species and the collision of high energy solar wind electrons with cometary neutrals are plausible processes. Charge exchange mechanism produce lines while electron neutral collision produce a continuum. In both of these mechanisms, neutral species in the cometary coma is the target.

The heavier minor species in the solar wind exist in highly charged states such as O^{7+} , O^{6+} , N^{6+} , C^{5+} , Ne^{8+} , Si^{9+} etc. In the charge exchange mechanism, these highly charged ions charge exchange with cometary neutral species and produce ions in an highly excited state. A typical example of such a process is,



Here O^{6+} ion in collision with an abundant neutral molecule such as H_2O produce O^{5+*} in an excited state denoted as $*$ and H_2O^+ ion. Other abundant neutral molecules can be OH , CO etc. The excited state of the

ion O⁵⁺* decay spontaneously giving rise to photons in the X-ray region. It is possible to make an estimate of the X-ray power density for the case of a single collision with the solar wind ion in the coma from a simple expression,

$$P_x = \alpha n_{sw} u_{sw} n_n. \quad (10.10)$$

where n_{sw} , u_{sw} and n_n represent solar wind proton density, solar wind speed and density of the neutral species respectively. The parameter α includes all other quantities pertaining to solar wind, atomic and molecular details. The variation of neutral density of the species with r in the coma for a spherical symmetric case is given by $n_n = Q/(4\pi r^2 u_n)$ where Q is the production rate of the specie. Integration of equation (10.10) over the observed volume of the neutral species result in the X-ray luminosity which is roughly within a factor of 2 to 3 of the observed X-ray luminosity. The X-ray luminosity is also proportional to the gas production rate which is in agreement with the observations.

The cometary gas density is high close to the nucleus and hence collisions are frequent. This results in solar wind ions being converted to a low charged state ion and therefore X-rays cannot be excited. This could explain the observed crescent - shaped X-ray emission. The model spectra based on charge exchange mechanism were in good agreement with the low resolution cometary X-ray emission.

For a better understanding of the X-ray emission including the observed X-ray line emissions, it is necessary to invoke detailed Magneto Hydrodynamic models (MHD) for the interaction of the solar wind with the cometary gas which allows variation in plasma density, temperature, velocity etc. The variation in the neutral density of species such as H₂O, CO₂, CO, OH etc. can be included through Haser's model. The details of the charge-exchange mechanism such as, the abundance of various ions and its variation and the cascading process leading finally to X-ray emission should be an integral part of this study. Such sophisticated models have been carried out to calculate the expected X-ray emision around a comet. The simulated X-ray emission are found to be in good agreement with the observed images (i.e. isophotes). The X-ray line emission spectra can also be calculated. These are in good agreement with the observed spectra (Fig. 10.16). Therefore the observed characteristics of X-ray emission from various comets can be explained based on charge-exchange model.

10.8. Summary

The existence of solar wind came from the studies of the orientation of ion tail of comets, long before its detection by spacecrafts. The whole problem of comet-solar wind interaction is a highly complex one. The exact nature and the location of the different discontinuities depend upon the various physical processes that can take place during the interaction. What happens in a particular situation depends upon the complex interaction of the plasma, turbulence, solar activity and so on. However the large scale structure as predicted by the MHD calculations like bow shock, ionopause, magnetic cavity and so on have been confirmed from the *in situ* measurements of Comets Giacobini-Zinner, Halley and Borrelly. This shows that the mechanism of interaction between the solar wind and cometary plasma giving rise to various structures is fairly understood at the present time. The measurements also showed the plasma to be highly complex in showing the presence of strong turbulence, various instabilities, waves, high energy particles and so on. Various mechanisms have been proposed to explain the origin of these observed features. Strong X-ray emission is a common feature of all comets.

All the properties of the ion tail that have been discussed so far can be classified as belonging to the “typical” comets. In these comets the ion-tails are more or less similar and behave in a certain manner except for the presence of certain characteristic features in the tail in some cases. The major aim has been to understand the gross behaviour of such “typical” comets.

Problems

1. Take for the velocity of the solar wind $v = 450 \text{ km/sec}$ and the proton density $n = 5/\text{cm}^3$. Calculate the magnetic field required to counteract the solar wind pressure.
2. Does the magnetic field exist in comets? Can you suggest some method to probe the magnetic field associated with a comet?
3. Calculate the Alfvén speed in the tail of comets.
4. Discuss the relative importance between cometary plasma and laboratory plasma

References

The evidence for the existence of solar wind is discussed in this paper

1. Biermann, L. 1951. *Zs. f. Astrophysik* **29**, 274.

For a complete theoretical discussion of the solar wind, refer to

2. Parker, E.N. 1963. *Interplanetary Dynamical Processes*. New York: Interscience Publishers.

The phenomena of dynamical aberration is discussed in the following papers.

3. Belton, M.J.S. and Brandt, J.C. 1966. *Ap. J. Suppl.* **13**, 125.
4. Brandt, J.C. and Mendis, D.A. 1979. In *Solar System Plasma Physics*, Vol. II, eds. C. F. Kennel, L.J. Lanzerotti and E.N. Parker. Amsterdam: North-Holland Publishing Company p. 253.
5. Hoffmeister, C. 1943. *Zs. f. Astrophysik* **23**, 265.

The Wind-Sock theory for the ion tail is discussed here.

6. Brandt, J.C. and Rothe, E.D. 1976. In *The Study of Comets*, eds. B. Donn. M. Mumma, W. Jackson, M.F. A'Hearn and R. Harrington, NASA SP 393, Washington D.C. p. 878.

The basic idea of the solar wind interaction is given in this paper.

7. Alfven, H. 1957. *Tellus* **9**, 92.

The theoretical model of the Comet-Solar Wind interaction is from

8. Wegmann, R. *et al.* 1987. *Astr. Ap.*, **187**, 339.

Later work

9. Gombosi, T.I., De Zeeuw, D.L. and Häberli, A.M. 1996. *J. Geophys. Res.*, **101**, 15, 233.
10. Ip, W. -H. 2005. In *Comets II*, eds. M.C. Festou, H.U. Keller and H.A. Weaver, Univ. Arizona Press, Tucson, p. 605.

The confinement of ions very close to the nucleus was discussed by

11. Wurm, K. 1963. In *The Moon, Meteorites and Comets*, eds. B.M. Middlehurst and G.P. Kuiper, Chicago: The University of Chicago Press p. 575.

The following atlas gives cometary plasma tails of various forms.

12. Rahe, J. Donn, B and Wurm, K. 1969. *Atlas of Cometary Forms*, NASA SP-198, Washington D.C. GPO.

A good discussion of the *in situ* plasma measurements can be found in the following papers:

13. Flammer, K.R. 1991. *In Comets in the Post-Halley Era*. eds. R.L. Newburn, Jr. *et al.* Kluwer Academic Publishers. p. 1125.

14. Tsurutani, B.T. 1991. In *Comets in the Post-Halley Era*. eds. R.L. Newburn, Jr. *et al.* Kluwer Academic Publishers. p. 1171.
15. Ip,-W.H. and Axford, W.I. 1990. In *Physics and Chemistry of Comets*, Springer Verlag, p. 172.

The electron temperature is discussed in the paper

16. Eberhardt, P. and Krankowsky, D. 1995. *Astron. Astrophys.*, **295**, 795.

Model for Disconnection event was proposed in the following paper

17. Niedner, M.A. and Brandt, J.C. 1978. *Ap. J.*, **123**, 655.

18. Brandt, J.C., Caputo, F.M., Hoeksema, J.J. *et al.* 1999. *Icarus*, **137**, 69.

Possibility of detection of X-ray from comets is discussed in the paper

19. Ibadov, S. 1996. *Adv. Space Res.*, **17**:(12), 93.

Discovery of X-rays from Comet Hyakutake is in the following paper

20. Lisse, C.M. *et al.* 1996. *Science*, **274**, 205.

For later work, refer to the following papers

21. Cravens, J.E. 2002. *Science*, **296**, 1042.

22. Lisse, C.M., Cravens, T.E. and Dennerl, K. 2005. In *Comets*, eds. M.C. Festou, H.U. Keller and H.A. Weaver, Univ. Arizona Press, Tucson, p. 631.

23. Wickramsinghe, N.C. and Hoyle, F. 1996. *Astrophys. Space Sci.*, **239**, 121.

This page intentionally left blank

CHAPTER 11

Nucleus

Though the nucleus is responsible for most of the observed phenomena, its nature is the least understood. As the nucleus cannot be observed directly from the Earth because of its small size, the information with regard to their possible nature, structure and composition has to come from indirect means. The flybys to Comets Halley, Tempel 1, Wild 2 and Borrelly have given new insights into this area.

11.1. Morphology

Several surprising results came out on the surface characteristics of the nuclei of comets from spacecraft flybys. The spacecrafsts Giotto, Vega 1 and Vega 2 were the first to take the images of the nucleus of the Comet Halley. Based on different aspects seen by the three spacecrafsts, the actual three dimensional shape of the nucleus was constructed. It clearly showed the nucleus is not spherical in shape, but highly irregular. It resembles more like a ‘peanut’ or a ‘potato’. The surface has many features such as valleys, hills and craters. The nucleus was also found to be large as well as quite dark in nature. The salient feature was that the gas emission was not uniform over the entire surface of the nucleus but comes out as discrete jets. Due to rotation of the nucleus the jets will become active only when they are exposed to the solar radiation. The jets cover around 10% of the surface of the nucleus.

The close-by images of Comet Borrelly by Deep Space 1 mission showed the nucleus to be shaped like a ‘foot print’ (Fig. 11.1). The images also showed jets as was seen in Comet Halley. The terrain appeared to be highly complex with some craters. They also show bumps, troughs and other features. The nucleus of Comet Wild 2 observed in stardust mission

was found to be oblate. It contains depressions ranging in size up to about 2 km across. Some of the depressions are not circular and have complex structures. They could have been formed by impact, sublimation, ablation or a combination of all of these processes.

The images of Comet Tempel 1 taken by Deep Impact showed the presence of circular depressions and terrains. One dramatic feature seen was the presence of layers over the entire surface of the nucleus of the comet (see Fig. 11.8). Such layers are also found in Comets Borrelly and Wild 2 based on the images taken by the earlier spacecrafts.

The Comets Borrelly, Wild 2 and Tempel 1 belong to the same group of Comets, namely Jupiter family, but their appearances are vastly different, as can be seen from Fig. 11.1. This could either be connected with the processes that could have taken place on the surface itself or could possibly be due to different internal histories.

11.2. Theory of Vapourization

When the solar radiation impinges on the surface of the nucleus, part of the energy is absorbed and part of it is reflected. The reflected part depends upon the albedo of the nucleus. The absorbed energy gives rise to the surface temperature which sublimates the material and also gives rise to the thermal emission. The absorbed energy also depends upon the angle between the incident radiation and the normal to the surface.

The amount of energy radiated from the surface is dependent upon the temperature, which in turn is related to the chemical composition and the structural properties of the nucleus. The sublimation of the gases depends upon the latent heat and its variation with temperature. The penetration of the heat flow inside the nucleus also depends upon the conducting properties of the material. The presence of dust in the coma can also have an effect on the vapourization of the volatile components. Therefore the amount of volatile constituents that come out of the surface of the nucleus is a very complicated function involving many unknown factors. Hence, until we have better ideas with regard to the above processes, one has to resort to simplifying assumptions in writing down the equation for the energy flow.

The temperature of the nucleus is determined by the balance between the amount of absorbed and the emitted energy. The energy balance equation for the simple model of a spherical nucleus which takes into account the thermal re-radiation and the heat used to transform the vapourizing



Fig. 11.1 Comparison of the images of nucleus of Comets Tempel 1 (upper right), Wild 2 (upper left) and Borrelly (bottom) taken from space crafts. The morphological structure of each of these comets is entirely different (Thomas, P.C. et al. 2007. *Icarus*, **187**, 4).

ice into gas for the steady state condition can therefore be written as

$$\frac{F_{\odot}(1 - A_v)}{r^2} \cos z = (1 - A_{IR})\sigma T^4 + Z(T)L(T). \quad (11.1)$$

Here F_{\odot} is the solar radiation at 1AU. A_v and A_{IR} are the bond albedo of the nucleus in the visible and infrared region and r is the heliocentric distance. $Z(T)$ and $L(T)$ represent the vapourization rate of the gas in molecule/cm²/sec and the latent heat for sublimation in ergs/molecule. T

is the surface temperature and z is the solar zenith distance. The vapourization rate $Z(T)$ can be deduced by relating it to the equilibrium vapour pressure of ice. Under the equilibrium conditions the number of molecules coming out of the nuclear surface will be balanced by the number hitting the surface. The number of molecules hitting the surface for such a situation is equal to $\frac{1}{4}N\bar{v}$. Therefore

$$Z(T) = \frac{1}{4}N\bar{v} \quad (11.2)$$

where N is the gas density and \bar{v} is the mean speed for the Maxwellian distribution of velocities which is given by

$$\bar{v} = \left(\frac{8kT}{\pi m} \right)^{1/2} \quad (11.3)$$

Here m is the average molecular weight of the gas. Using the above relation for \bar{v} and with the use of the relation $P = NkT$, $Z(T)$ can be written as

$$Z(T \text{ or } r) = \frac{P}{(2\pi mkT)^{1/2}}. \quad (11.4)$$

The total production rate of the molecule is given by

$$Q(r) = S < Z(r) >$$

where $< Z(r) >$ represents the production rate averaged over the solar zenith distance z and S is the surface area of emission. The integration over z can be avoided under some simplifying assumption. For a non-rotating nucleus of radius r_n , the cross section for the absorption of solar energy is πr_n^2 , while for a fast rotating nucleus the incident energy is uniformly distributed over the entire surface $4\pi r_n^2$. The corresponding value of $< \cos z >$ is 1 and $1/4$ for the slow rotator and fast rotator models respectively. The equations show that even the very simple energy balance equation requires the specification of the six parameters, namely A_v , A_{IR} , L , P , η and S . Here η represents the geometrical factor related to $\cos z$. Since it is a multivariable problem, it is necessary to make some assumptions to limit the number of free parameters. This depends upon the problem under investigation. It then fixes certain parameters and others are derived from comparing with observations. This procedure is just a method of simplifying the problem and therefore the results have to be weighted in terms of the assumptions made in the problem.

Since H_2O is the dominant component of the nucleus of a comet, the values for L and P corresponding to H_2O are generally used. The vapour

pressure can also be calculated from Clasius-Clapeyron equation

$$P = P_r \exp \left[\frac{L(T)}{RT} \left(\frac{1}{T_r} - \frac{1}{T} \right) \right]$$

where T_r and P_r are the reference point. The vapour pressure in general is very sensitive to temperature. Therefore, the general variation of the production rate of H_2O and OH as a function of the heliocentric distance should reveal something about the vapourization of ice from the nucleus of a comet and should in turn give information about the overall nature of the nucleus of a comet. A simultaneous solution of Eqs. (11.1) and (11.4) iteratively will give the unknown $Z(T)$ and T , for assumed values of the parameters that enter in the above two equations. The results for the variation of Z as a function of the heliocentric distance for different cases are shown in Fig. 11.2. The curves depend upon the values of A_v and A_{IR} . The

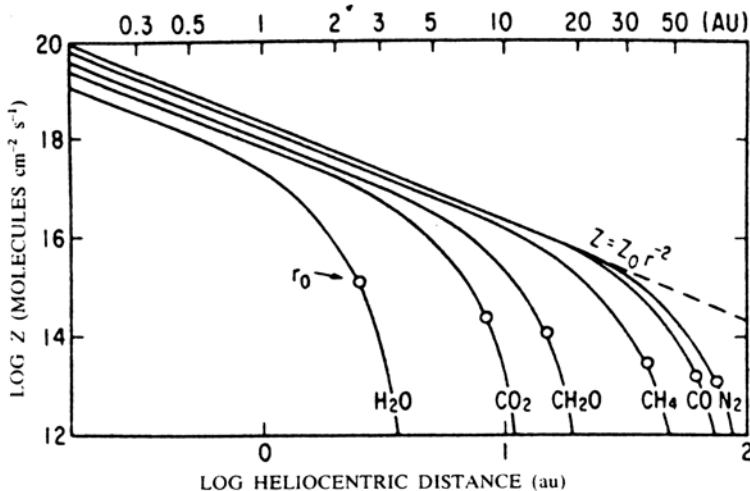


Fig. 11.2 The vapourization rate Z , for various snows as a function of the heliocentric distance. The distance after which the vapourization becomes negligible is denoted as r_0 . (Delsemme, A.H. 1982. In *Comets*, ed. Wilkening, L.L. Tucson: Univ. Arizona Press, p. 85).

curves are almost the same if $A_v = A_{IR}$. For unequal values of A_v and A_{IR} the maximum difference in the results arises in the shift of the curves in $\log r$ by about ± 0.2 . Figure 11.2 shows r^{-2} dependence in the beginning and then shows a rapid fall in the sublimation rate of water for distances between

2 and 3 AU. The calculated behaviour of the curve is basically related to the steep dependence of vapour pressure on temperature. The sublimation rate is nearly proportional to the impinging energy if the temperature is greater than a certain critical value. This is the case for small values of r and hence Z varies as r^{-2} . For distances greater than a certain value, the sublimation rate falls down steeply with temperature and this gives rise to the observed effects. The cometary observations also show a similar cut-off around these distances, after which they are not generally seen. This effect is particularly so in the case of short period comets where the cut-off is around $r \sim 3$ AU. These observations are in striking agreement with the expected curve for the sublimation of H₂O. Therefore the observations by itself seem to indicate that H₂O may be the dominant constituent of the nucleus. In addition, the vapourization theory gives the total production rate of rough order with the observed rates of several comets where the water controls the sublimation process.

Based on the above model, it is rather difficult to explain high volatiles that has been seen in some comets at large heliocentric distances of around 3 AU, where it is unlikely that water will evaporate. This led to the suggestion of Clathrate Hydrate model. The clathrates are basically loose crystal lattices of H₂O in which molecules like CH₄, CO₂, etc are loosely packed. These molecules are not chemically bound but they are bound by weak Van der Waals forces. The cut-off distances for such types of clathrates lie in the range of about 5 AU or so. Therefore the comets which have been observed beyond $r \gtrsim 3$ AU are likely to arise out of this structured ice material. This was a significant step in the understanding of the cometary nuclei. In this connection it is interesting to note that OH has been detected in Comet Halley at $r = 4.9$ AU with $\log Q(\text{OH}) \sim 29$ and in Comet Hale-Bopp at $r = 5.13$ AU with $\log Q(\text{OH}) \sim 27.19$.

In the derived production rate of various volatiles shown in Fig. 11.2 the value for the albedo for the nucleus of $p_v \sim 0.7$ was used. However extensive observations carried out on Comet Halley followed by other comets indicated that the albedo of the nucleus is quite low and is around 0.04. The effect of this low albedo for the nucleus on the production rate of H₂O show a change in slope in the region of around $r = 4$ to 6 AU for H₂O production. Beyond this distance, production rate of H₂O decreases but is still not negligible. Therefore there is still some water coming out of the nucleus at large distances.

Although clathrate hydrate model was in conformity with earlier cometary observations, later laboratory studies indicated a major difficulty

in their formation. These experimental studies showed that clathrate hydrates is produced under high pressure conditions and hence not applicable to comets, which are produced at low pressure and temperature. Besides, the abundances of the observed species are quite high and is not possible to trap so much in the clathrate hydrate icy matrix. This has led to a new model where water-ice is most likely to be present in amorphous form. Amorphous ice exists at lower temperatures of around 77 K or less. The study of solar nebular models have shown that these conditions exist at distances > 7 AU. Hence interior of comets is most likely to have amorphous ice, as comets were formed under low temperature and low pressure conditions.

Amorphous H₂O - ice can trap large amount of volatiles and when heated, their trapped volatiles are released. For temperature starting around 90 K, amorphous form of ice changes over to crystalline form with the release of energy. This corresponds to distances of around 8 to 20 AU where large amount of traped gases may be released. In this connection it is intereresting to note that volatile species of various kinds were seen in abundance from Comet Hale-Bopp beginning at distances of around 7 AU. These are most likely to be produced by amorphous to crystalline H₂O - ice phase transitions rather than produced by sublimation due to solar heating.

The early results of the vapourization of H₂O from the nucleus had met with reasonable success in explaining the gross observed nature of the light curves of various comets. However observations have shown that the light curve for pre-and post-perihelion passages are not symmetrical in shape and gas comes out in jet form at some discrete active regions on the nucleus. The active areas are hardly a few percent of the surface area of the comets. The use of constant values of A_v, A_{IR}, L and P in modelling means that the material property of the nucleus is the same for all comets. Several attempts have been made to refine the models that take into account factors like, thermal properties of the surface layers, rotation period of nucleus, the effect of diurnal heating and cooling individually or in combination. Though these studies have met with partial success, these simple models have been quite useful for an understanding of the general trend as well as qualitative study of Comets.

Refined Models

The striking feature of a comet is their varied features along the orbit of a comet. Hence complicated models have to be considered which take into account several processes simultaneously. Some of the processes con-

sidered are, diurnal temperature variation over the surface of the nucleus, heat conduction to the interior through the entire nucleus, possibility of the outer dust mantle enveloping the icy nucleus, cometary ice being in amorphous state which can lead to crystallization, porosity, radioactive heating from the short lived isotope ^{26}Al . Since half life of ^{26}Al is less than about 0.7 million years, it would have decayed during the early stages of the solar system, within few million years and thus providing a heat source. The initial mass fraction of ^{26}Al in the solar nebula $\approx 7 \times 10^{-7}$. In comets it could be smaller on the average by an order of magnitude, as the time of cometary formation did not exceed a few million years. The change over from amorphous to crystalline state could provide additional source of energy. Therefore there are three sources of energy available to comets; namely solar radiation, radioactivity and process of crystallization. When the comets are near the sun, solar radiation dominates the other two sources. On the other hand, the energy source through radioactive decay is important that are far from the sun. However crystallization from amorphous ice can occur at any stage in the cometary evolution once the threshold temperature is reached.

Heat could flow inwards or outwards from any region of the nucleus. The effect of heat and gas diffusion in the nucleus results in chemically differentiated layers. In particular the top layers of the nucleus should contain mostly least volatile material followed by layers of water ice and dust and the deeper layers should contain dust, ices and most volatiles such as CO and CH_4 .

The built up pressure from the gases released from the interior of the icy nucleus, forces the gas to flow towards the surface. The flow of the gas drags the dust particles from the icy solid matrix. It is possible that the built in pressure could be high enough to make cracks in the porous matrix leading to out-gassing. Large size particles reaching near the surface may lead to formation of a dust mantle resulting in diminishing cometary activity. Therefore the observed activity of a comet is a resultant effect of several physical processes involving the structure of the nucleus, heat conduction and energy sources. Several attempts have been made to study the nuclei of comets taking into account all these details. The model considered is a porous agglomerates made up of amorphous ice, dust and volatiles such as CO, CO_2 , HCN, N_2 etc. Such a model results in explaining the overall observed activities of comets. The thermal evolution and the resulting pattern in the activities from the nucleus of a fragile and porous comet leads to the structured nature of the nucleus of comet as shown in Fig. 11.3.

This is quite different from that of a solid body of a nucleus made up of ice sublimating from the surface due to solar heating as in the earlier models.

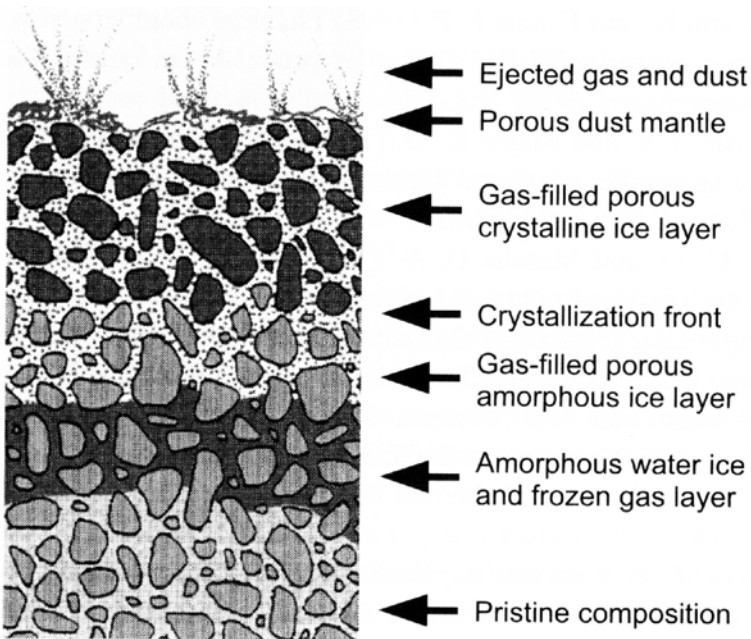


Fig. 11.3 Schematic representation of the layered structure of a cometary nucleus with pristine composition deep inside and the modified layers arising as a result of various physical processes taking place (Prialnik, D. 1999. *Earth, Moon and Planets*, **77**, 223).

The analytical expression for the vapourization of water from an icy nucleus can be written as

$$\begin{aligned} Z &= Z_o \alpha \left(\frac{r}{r_o} \right)^{-m} \left[1 + \left(\frac{r}{r_o} \right)^n \right]^{-k} \\ &= 7Z_o g(r) \quad g(r) = \alpha \left(\frac{r}{r_o} \right)^{-m} \left[1 + \left(\frac{r}{r_o} \right)^n \right]^{-k} \end{aligned} \quad (11.5)$$

where $r_o = 2.808$ au, $m = 2.15$, $n = 5.093$ and $k = 4.6142$. The value of α is chosen such that $z = z_o$ for $r = 1$ AU, which gives $\alpha = 0.111262$. As will be discussed later, the vapourization from an icy type of nucleus can explain in principle the observed nongravitational forces in comets (Sec. 11.10).

11.3. Outbursts

Outbursts have been seen quite frequently in comets. It is basically related to a sudden increase in the production of volatiles from the nucleus. Comet Schwassmann-Wachmann is well known for its large outbursts and flares up frequently. These outbursts can brighten the comet by a factor of 100 or more compared to the quiescent brightness. Initially, the comet looks star-like in appearance. After the outbursts, a halo forms and eventually it fades away leaving behind the original nucleus. The whole process might take around 3 to 4 weeks. The outbursts from Comet Schwassmann-Wachmann have been seen regularly from heliocentric distances of around 5 to 7 AU. Comet Halley showed an outburst when it was at $r = 14$ AU. It is rather difficult to understand such a phenomena based on the sublimation of H_2O from the nucleus, as the production rate of H_2O falls down steeply for $r \gtrsim 3$ AU. A number of suggestions and ideas have been proposed to explain the origin of these outbursts. It has been suggested that exothermic chemical reactions involving free radicals or pockets of volatile gas stored beneath the surface takes place until the pressure would build up which leads finally to explosions. The phase change from amorphous to crystalline ice at temperatures above 140 K is an exothermic process giving about 24 cal/gm, which is a substantial amount of energy and could trigger the outbursts. Since the phase change is critically dependent upon the temperature, the outburst should depend on the heliocentric distance.

Therefore crystallization of amorphous ice appears to be the best mechanism for explaining the appearance of outbursts in comets. The three physical processes of interest are crystallization, conduction and sublimation and their relative time scales. For understanding the resultant effect of these processes inside a porous nucleus, which are complicated in nature, it becomes necessary to resort to numerical methods.

When the surface of the nucleus is heated due to solar heating, the heat wave moves inwards. This results in amorphous ice to crystallize liberating trapped gases. Part of the released gas move inwards into the colder regions and eventually condense at different location inside the nucleus depending upon the temperature in that region. The recondensation process results in the release of heat which in turn affects the chemical composition of its surroundings. During the next perihelion passage the heat wave generated reaches these regions and is used to sublimate condensed gases rather than the crystallization of amorphous ice. This is the process by which alternative layers of crystallization and amorphous ice are created. Such layers

extend from about 10 metres to about a few hundred metres below the surface of the nucleus. When the heat wave from the surface reaches to some of these layers the trapped volatile species are suddenly released leading to pressure build-up. These gases move to the surface through pores, cracks etc. This gives rise to an outburst. The resulting production rate of different volatiles could be vastly different. This could explain the observed activities in comets (Fig. 11.4).

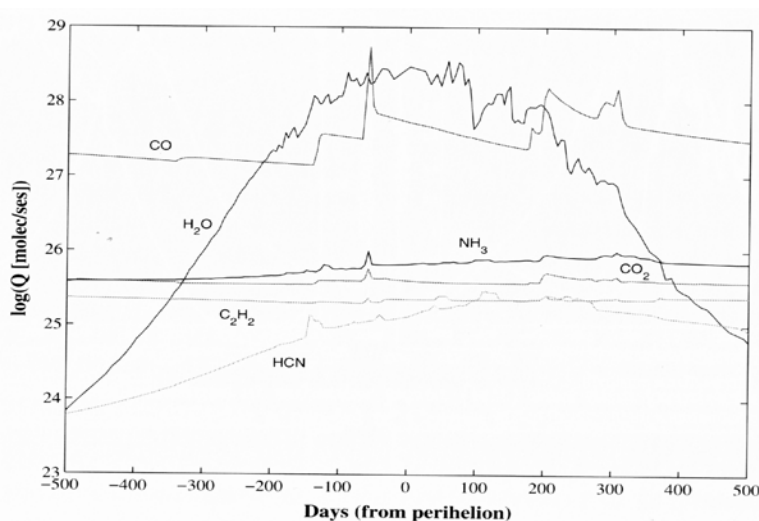


Fig. 11.4 The production rate of volatiles based on model calculations for Comet 9P/Tempel 1 is plotted as a function of time measured from the perihelion point (Prialnik, D. 2005. In *Asteroids, Comets and Meteors*, IAU Symposium No. 229, eds, Lazzaro, D.Ferraz-Mello, S. and Fernandez, J.A., Univ. of Cambridge Press, Cambridge, p. 153).

Model calculations have also been carried out to long time scales to understand the outburst seen in comets at large heliocentric distances. These results indicate that such bursts are related to fine-tuning of time scales of re-condensation of volatiles and crystallization of amorphous ice. It is possible to attain a temperature ~ 200 K in a narrow region and for a brief period of time which can lead to sudden release of trapped gases which is seen as an outburst. It is also possible to get repetitive outbursts if phase transition time scale is comparable to diffusion time scale of moderately volatile gases.

11.4. Albedo and Radius

The dimension of the nucleus of a comet cannot be obtained directly as it cannot be resolved. The general method which is commonly used is from the photometry of the comet at far off distances from the Sun. At these distances the comet is more or less stellar in appearance. This comes about due to the fact that at these distances, the temperature of the nucleus will be so low that the sublimation of the gases from the nucleus cannot take place. Therefore one is essentially seeing the nucleus of the comet. Hence the observed radiation at these distances essentially comes from the reflection of the incident solar radiation by the nucleus of comet. From such photometric observations, the radius of the nucleus R can be obtained from the relation

$$R^2 = r^2 A^{-1} \phi(\alpha)^{-1} 10^{0.4[V_\odot - (V_c - 5 \log \Delta)]} \quad (11.6)$$

where $\phi(\alpha)$ is the phase function according to Lambert's Law, A is the albedo for the nucleus, V_\odot and V_c are the absolute magnitudes of the Sun and the comet respectively. Equation (11.6) has been applied to several comets using photometric magnitudes and a reasonable range of values for the albedo of the nucleus. However, it is possible to get simultaneously the values of radius and the albedo of the nucleus from the following simple physical considerations.

The photometric observations of comets made at great distances from the Sun give only the total brightness which is AS where S is the effective cross section of the nucleus for the reflection of the solar radiation. It can be estimated from the observed magnitudes. It is also possible to get the value of the quantity $(1 - A)S$ from the theory of vapourization of ice-water from the nucleus when the comet is near the Sun wherein the vapourization is maximum. The integration of Eq. (11.1) over the nucleus gives the relation

$$\frac{F_\odot(1 - A_v)S}{r^2} = 4\sigma(1 - A_{IR})ST^4 + 4SZL. \quad (11.7)$$

For reasonable values of the albedo A_v and for the heliocentric distance less than about 0.8 AU, the radiative contribution term in the above equation can be neglected. Therefore Eq. (11.7) reduces to

$$(1 - A_v)S = \frac{4SZLr^2}{F_\odot} = \frac{QLr^2}{F_\odot} \quad (11.8)$$

where $Q = 4SZ$ represents the production rate of water which can be obtained from the observed production rates of OH or H in comets (Chap. 6).

The value of L , the latent heat for vapourization of water is 11500 calorie/molecule for $T = 200^{\circ}\text{K}$. From a knowledge of AS and $(1 - A_v)S$ it is then possible to get the albedo and radius from the following equations:

$$S = (1 - A_v)S + AS \quad (11.9)$$

and

$$A_v = \frac{A_v S}{A_v S + (1 - A_v)S}.$$

The method is valid if the effective area is roughly the same for the reflected light and for the vapourization equilibrium. However, there could be a difference in the areas in a real situation. In addition, there is some difficulty in separating the contributions to brightness from the nucleus and coma. The quantity $(1-A)S$ can also in principle be determined from the infrared observations of the nuclei of comets. To a first approximation, $(1-A)S$ is directly proportional to the thermal emission in the $10\text{--}20 \mu\text{m}$ region provided the vapourization process from the nucleus does not take a significant fraction of the absorbed energy.

Even at large heliocentric distances a faint coma is still present. Therefore direct photometric observations have the problem of separating the light from the nucleus from the surrounding coma radiation. The coma contribution can be minimized with the use of high spatial resolution observations of the nuclei of comets. In this approach the brightness of the nucleus is observed as a delta function over a slowly varying coma contribution. Therefore the brightness distribution of a comet can be represented as

$$B(\rho) = a[1/\rho + b\delta(\rho)] \quad (11.10)$$

Where ρ is the projected distance from the nucleus. The first term in equation (11.10) represents the variation of the coma brightness for a constant source with inverse square dependence of space density. The delta function $\delta(\rho)$ represent the contribution arising from the nucleus, while a and b are constants. A fit to the observed brightness variation will give the contribution from the nucleus which can be used to get the radius of the comet for an assumed value for the albedo. If the rotational light curve is available it is possible to get the semi axes for the nucleus.

The direct determination of the size of the nucleus of a comet was made possible by the study of Comet Halley. The images taken by the spacecrafts

directly give the projected dimension. Based on different aspects seen by the three spacecrafts, Vega 1, 2 and Giotto, it is then possible to reconstruct the actual three dimensional shape of the nucleus. Figure 11.5 shows one best image obtained from Giotto. It clearly shows the irregular shape of the nucleus. Other comets which have been studied with spacecraft are Borrelly, Wild 2 and Tempel 1 etc. The albedo can be estimated from a knowledge of the area of the nucleus and the observed photometric magnitudes (equation 11.9).

The radius and albedo of cometary nuclei for comets are given in Tables 11.1 and 11.2. There is some variation in the observed radius, while albedos have low values. Low value of albedo indicate that the cometary nuclei are very dark.

Table 11.1 Sizes of cometary nuclei.

Comet	$a \times b \times c$ (km \times km \times km)
Halley	$7.65 \times 3.61 \times 3.61$
Tempel 2	$8.2 \times 4.9 \times 3.5$
Borrelly	$4.0 \times 1.6 \times 1.6$
Tempel 1	$14.4 \times 4.4 \times 4.4$
Wild 2	$1.65 \times 2 \times 2.75$

Table 11.2 Albedo and radius of cometary nuclei.

Comet	Geometric albedo	Radius(km)
Eucke	0.046	2.3
Tempel 1	0.05	3.1
Borrelly	0.03	-
Neujmin 1	0.03	10.6
Halley	0.04	-
Hale-Bopp	0.04	30
Swift Tuttle	0.02	11.8
IRAS-Araki-Alcock	0.03	3.5
Arend-Rigaux	0.04	4.6

Lamy, P.L., Toth,I., Fernández, Y.R. and Weaver, H.A., 2004, In *Comets II*, eds. M.C. Festou, H.U. Keller and H.A. Weaver, Univ. of Arizona Press, Tucson p. 223.

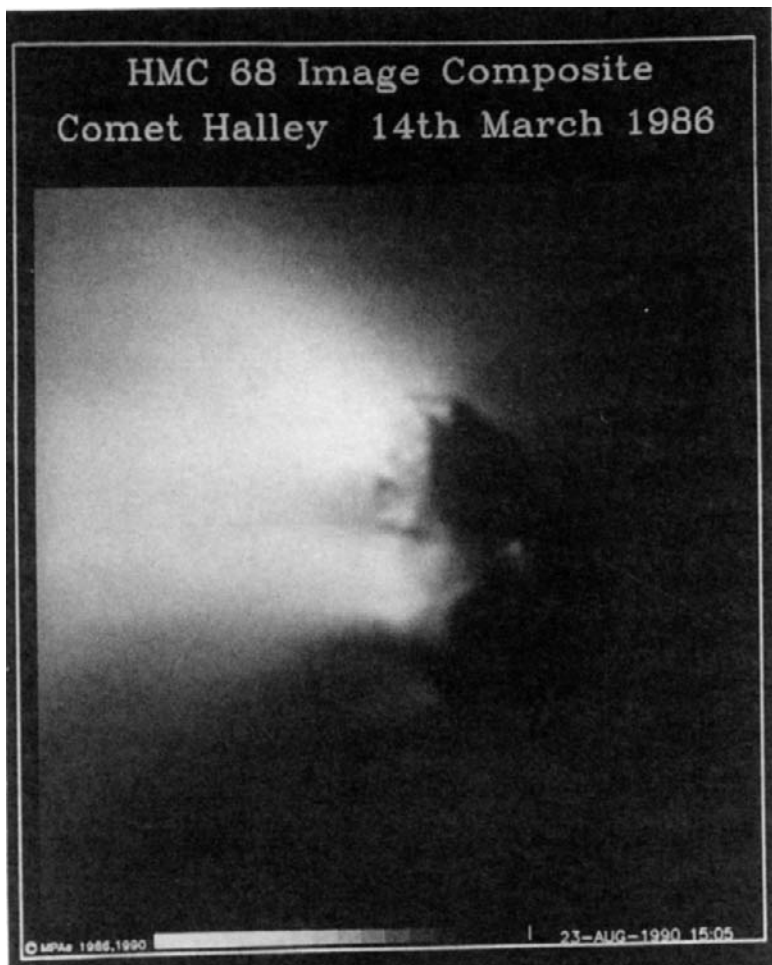


Fig. 11.5 Composite image of the nucleus of Comet Halley made from several images obtained from Halley Multicolour Camera on board Giotto Spacecraft (Courtesy Keller, H.U., Copyright Max-Planck - Institut für Aeronomie, Lindau, Germany).

11.5. Mass, Density and Surface Gravity

Mass

It is rather difficult to make an estimate of the mass of the nuclei of

comets. A rough estimate can be made from a knowledge of their sizes and densities.

Another method that has been generally used for getting the mass of the nucleus is through change in the orbital period caused by non-gravitational force arising from the sublimation of water ice from a rotating nucleus. This force arising from the outflow of the material is related to the mass of the nucleus of the comet through Newton's second law of motion, $F=ma$. This method has been applied to several comets. The derived masses lie in the range of around 1 to 5×10^{13} kg. The derived mass for Comet Tempel 1 from the same method is $(5.8 \pm 3.0) \times 10^{13}$ kg.

The study of the ejecta plume created by the impactor in Comet Tempel 1 by the Deep Impact mission has been used to make an estimate of the local gravity at the impact site. This is used for making an estimate of the bulk density for an assumed shape and a uniform mass distribution inside the nucleus. The derived mass is 4.5×10^{13} kg. This value based on direct observations is consistent with the mass derived above from non-gravitational force modelling. This therefore gives credibility to the indirect method of estimating the mass of the nucleus of comets through non-gravitational force modelling technique.

The perturbation produced by a close encounter of flyby spacecraft with a comet could in principle be used to extract the nuclear mass. However the expected perturbation is below the detectable limit of the present day instruments.

The discovery of satellites around asteroids has raised the prospect of the likely presence of satellites around cometary nuclei. The main advantage of a binary system is that it is possible to derive the mass of the system using Kepler's laws from the observed orbits. However the detection of a satellite companion to cometary nucleus is difficult because of its small size and also due to the presence of coma even at large heliocentric distances. If and when cometary binaries are detected, it will give a direct method of estimating the mass of the nuclei of comets.

Density

The determination of bulk density of the nucleus of a comet is important as it can give information about the structure of the nucleus. It can be estimated provided the mass and the total volume (including voids and pore spaces) of the nucleus are known.

Volume can be estimated from direct spacecraft imaging or from telescopic observations that can yield the appropriate radius and axial ratios

of individual nuclei. Spacecraft imaging has been carried out for several comets such as Halley, Tempel 1, Wild 2, Borrelly etc.

The charge-coupled device (CCD) photometry of nuclei when they are far from the sun (and presumably inactive) provide an estimate of their brightness. It is possible to make an estimate of the radius of the nucleus and hence volume for a typical cometary albedo of 0.03 - 0.04.

The estimated bulk density lies in the region of around 0.2-0.8 gm/cm³. The density of the fully compacted comet material consisting water-ice, organics and dust is expected to be in the range $1.2 < \rho_{\text{compact}} < 1.65$ gm/cm³. Therefore the results appear to indicate a somewhat lower value for the bulk density of the nucleus of comets. This indicates that the nucleus could be fluffy. The estimated bulk porosity of the nucleus is about 0.3 to 0.6.

Surface Gravity

The impactor from the Deep Impact spacecraft that collided with Comet Tempel 1 made a crater and ejected the material giving rise to an ejecta plume. The ejecta plume was imaged continuously from the flyby spacecraft at a distance of around 700 km. These images show clearly that the ejecta cone remained attached to the surface throughout the encounter. This interesting observation indicates that the formation of the crater was controlled by gravity.

The images of the ejecta plume taken by the spacecraft showed the expansion of the base of the conical solid ejecta with time. The particles forming the solid ejecta follow paths in the gravitational field of Comet Tempel 1 at any given time. Making few assumptions such as, the cone is nearly axially symmetric, scaling relations derived from laboratory studies for gravity dominating cratering is valid and the properties of ejecta flow could be extrapolated to this observed impact, it was possible to make an estimate of the strength of gravity from the observed expansion of the base of the conical ejecta. The estimated local gravity at the impact site of Comet Tempel 1 is about $g_{\text{nuc}} = 3.4 \times 10^{-4}$ m/sec².

11.6. Rotation

The rotational state of the nucleus of a comet is important for an understanding of the physical properties of the nucleus of a comet and its surface. The evolution of the spin state and the nucleus gives information

about the changing pattern of the observed activities of a comet. It also plays a key role in a better understanding of the activity of the nucleus of a comet resulting due to gas evaporation from the nucleus, generally called ‘non-gravitational force’. These studies are being carried out observationally to deduce the rotation period of the nucleus and the orientation of the spin axis of comets and its interpretation in terms of physical and dynamical models.

The time period of nuclear rotation can be estimated from some time-dependent property associated with the comet. It could be the observation of a certain repetitive feature, sequence of images of the nucleus, from an analysis of modelling of light curves or the non-gravitational force and so on.

The successive expanding halos with velocities of about 0.5 km/sec seen in the photographic observations of several comets have been interpreted on the basis of the rotation model for the nucleus. Parabolic envelopes have also been seen in the coma of comets. With the assumption that these arise out of the repetitive ejection of material from a single active area, it is possible to make an estimate for the rotation period of the nucleus. The procedure is to get the time at which the material was ejected, called the zero time. If the zero time can be found from concentric halos, then the time interval between the two zero times gives the rotation period. From the measured diameters of the halos or from the latus recta of the parabolic envelopes, the rotational velocities of a large number of comets have been determined. This method is generally known as ‘zero age’ method. The basic assumption involved in the halo method is that the halo structure arises mainly due to the rotation of the nucleus.

Many comets seem to show broad, fan-shaped coma coming out of the central condensation and in the general direction of the Sun. The width appears to change from comet to comet and with time. These have been interpreted in terms of anisotropy in the out-gassing. This can clearly be seen from the densitometer tracings of the inner part of the Comet Pons-Winnecke which are shown in Fig. 11.6. These have been interpreted in terms of the orientation of the spin axis of the nucleus.

The continuous monitoring of continuum or molecular emission lines over an extended period of time can give information about the periodicities connected with the rotation of the nucleus. The rotational light curves derived from photometric observations when the comet is far off from the sun can be used to extract the shape and the rotational period of the nuclei of comets. The idea being that the periodic temporal variation of the

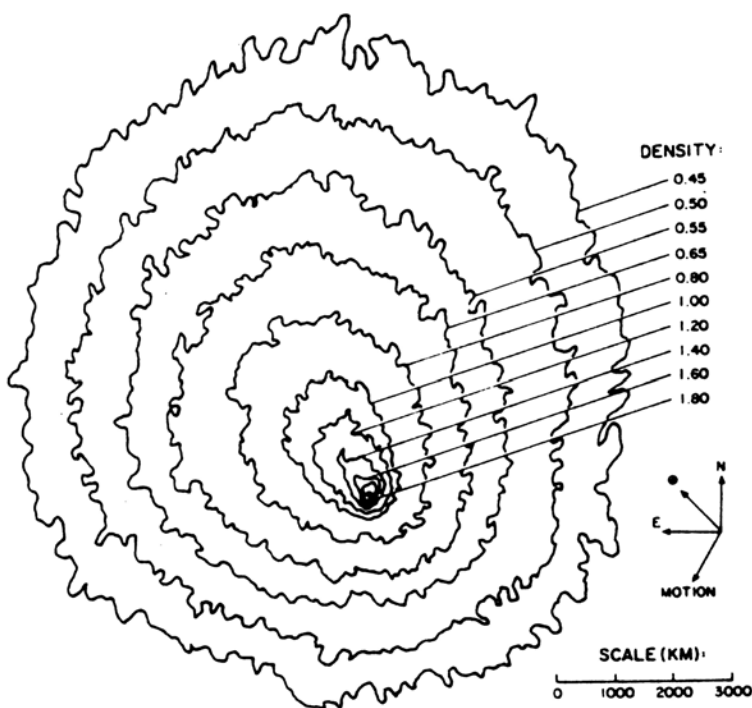


Fig. 11.6 The densitometer tracings of the photograph of June 25, 1927 in the inner part of the fan of Comet Pons-Winnecke are shown here. The jet near the nucleus in the sunward direction and the curvature effect as one goes outwards can be seen. The circled dot denotes the direction of the Sun. (Sekanina, Z. 1981. *Ann. Rev. Earth Planet Sci.*, 9, 113). Reproduced with permission from Annual Reviews Inc.

brightness is interpreted in terms of the rotation of an elongated body. At present observations are carried out at visible and infrared wavelength regions for producing light curves. High spatial resolution observations carried out with HST at various times can be used to derive the flux contribution from the nucleus and hence the rotational light curve. The time period can be extracted from the light curve through various methods such as Autocorrelation analysis, period dispersion minimization method etc. The derived rotational time period for Comet Tempel 1 is 41.27 h. Based on various methods, the time periods of rotation of many comets have been determined. Unfortunately there is lot of variation in the derived periods for the same comet. The diversity in the derived values are illustrated with two examples.

For Comet Encke, the zero age method gave a value of 6.5 hrs. The periodic variation in the photometric magnitude gave a value of 22.4 hrs. The photometric data obtained near aphelion could be satisfied with periods of 22.6 hrs, 15.1 hrs, 11.1 hrs or 7.5 hrs. Later studies have put some doubt on 15.1 hrs period. It is possible that the observed periods may represent harmonically related periods. If this is the case, then the observed periodicities could relate to the basic period of 7.4 h. However it is not clear whether this is the case.

For Comet Halley several values have been derived. The ‘zero age’ method gave a period of about 10 hrs. The most direct evidence came from the morphology of sun ward jets. A rotational period of around 52 hours was estimated from the processing of spiral jets seen in the photographs taken during the 1910 apparition. The comparison of Vega 1 and Vega 2 camera observations gave a rotational period of 52–54 hours. However the images of features like jets near-nucleus show a period \approx 2.2 days. A time period of about 7.4 days was obtained from the time series studies of the narrow-band photometric observations of the coma. The same time period was also indicated by the morphology of jets of free radicals, Lyman α emission and the 18 cm OH line, but nothing around a period of 2.2 days. Therefore there is conflicting results derived from various methods. Images taken from Vega 1, Vega 2 and Giotto spacecrafts could refer to different viewing geometries and timings of the nucleus of Comet Halley that might complicate the interpretation of the observed images. But on the whole there appears to be two rotational periods corresponding to 2.2 and 7.4 days.

For a non-spherical nucleus there could be several possible rotation states. It can rotate around the long or short axis. It can also have nutation motion. The rotation could be in its lowest rotational state energy or in an excited state. Depending on the state of the nucleus, it can have one or two time periods and their harmonics. Several attempts have been made to understand the observed periodicities of Comet Halley in terms of rotational, precessional or nutational motion of the nucleus. From a detailed model study of the nucleus of Comet Halley, it has been possible to understand the observed time periods. In this model the nucleus is considered to be a prolate spheroid with dimensions of $17 \times 8.5 \times 8.5$ km. It takes into account five active areas on the surface of the nucleus that are active only when they are exposed to the sun and provide torques to the nucleus. The model can explain reasonably well the ground based data as well as the interpretation of visible data from spacecraft. The resulting

model indicate that long axis of the nucleus precess around the rotational angular momentum vector in 3.69d at an angle of 66° . In addition the long axis rotates around its own axis with a period of 7.1d.

A rotation period of 26 h has been deduced for Comet Borrelly based on ground based and HST observations. A linear jet emanating from the nucleus was seen from the Deep Space 1. Several observations about this feature indicate that the jet is along the rotation axis of the nucleus and also spinning close to its lowest energy spin state.

Based on the above brief discussion, it is evident that the periodicities depend upon the state of the nuclei. In particular, on the shape, activity and their location, jets, how the gas comes out and so on. This leads to the complex nature of the periodicities in the observed spectra than indicated by the assumed simple models. Hence the interpretation of the observed periodicities is a difficult matter and is comet dependent.

11.7. Nucleus Composition

The major goal of cometary studies is to determine the chemical composition of the nuclei of comets. Therefore the evolution of the activity of a comet along its orbit is important for an understanding of the chemical nature of the nucleus. In view of this, extensive studies have been carried out with regard to the variation of gas production ratio of species as a function of the heliocentric distance for various comets. The observed production rates of various species are found to vary with heliocentric distance and from comet to comet. Therefore the coma abundances of species cannot directly reflect the composition of the nucleus of a comet. This problem has been investigated based on the model for the nucleus.

As discussed earlier the structure of the nucleus of a comet is a complicated function of various physical processes that could take place inside the rotating porous nucleus containing amorphous ice and volatiles. These result in structured layers with different composition. The top layers containing the least volatile material and the deepest layers containing the most volatile species. This structured layer nucleus can be used to calculate the production rate of the species and the integration over the entire orbit will give the total amount of material ejected during one orbit of the comet. The deduced abundance ratios for each specie can then be compared with the abundance ratios for the same specie in the nucleus. The results of such studies have shown that the abundance ratios of the ob-

served species in the coma integrated over the entire orbit of the comet is a better representation of the composition of the nucleus of a comet. This implies that one has to take into account the change in coma composition with heliocentric distance.

Comet Hale-Bopp was a bright and active comet which made it possible to study this problem in greater detail. The comet was observed over a large range of heliocentric distances of 1 to 7 AU. The expected abundances in the coma from the structured layer chemical model that takes into account the gases arising from, the surface of the nucleus (sublimation), the interior of the porous nuclei and the distributed source, can be calculated. These results can be compared with the observed ratios to deduce the composition of the nucleus. A mixture composed of 35% amorphous H₂O, 7%CO₂, 13%CO (50% trapped in the amorphous ice) and 45% dust give a good fit to the observed data as can be seen from Fig. 11.7. The fit to the observed data will be much better if the distributed source of CO were subtracted. The deduced abundance ratio for the nucleus is similar to the expected abundance ratios from a condensable component of molecules at a lower temperature from a mixture of solar abundance elements.

11.8. Mass Loss

The volatiles sublimating from the nucleus of a comet, eventually leave the system. Therefore the mass loss of volatiles in comets can be used to make an estimate of the lifetime of a comet. For this purpose, the observed mass loss rate of water from the nucleus of a comet per revolution may be used. For Comet Borrelly, the total amount of water sublimated from the nucleus during an apparition is around 1.1×10^{10} kg and the estimated mass of the nucleus from non-gravitational force modelling is around 1 to 5×10^{13} kg. Therefore the comet can last for about 1000 to 5000 passes. Taking a typical value of 5 yrs for the time period for short period comets, the observed mass loss rates indicate that the lifetime of a short period comet is limited to about 5×10^3 to 3×10^4 yrs.

When most of the volatiles are lost from the nucleus, it might go into an extinct state. It is possible that some of them may be in the asteroidal belt. As more and more volatiles sublime, the very low tensile strength material of the nucleus may become more fragile leading to disintegration of the nucleus into large number of pieces, which then takes on their own path.

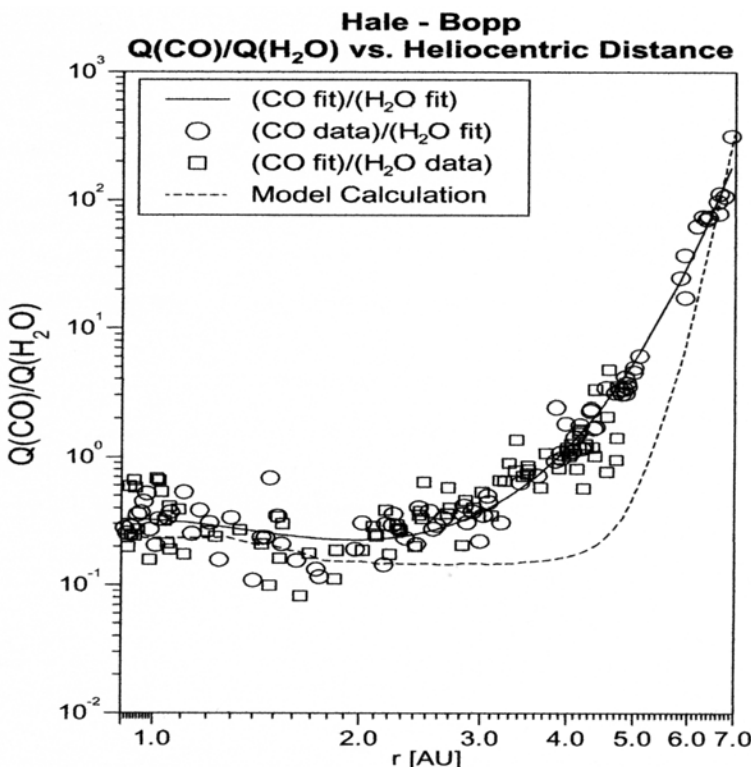


Fig. 11.7 Mixing ratio $Q(\text{CO})/Q(\text{H}_2\text{O})$ is plotted as a function of the heliocentric distance for Comet Hale-Bopp. The dashed line is the model fit. The model fit will be much better if the distributed source is subtracted from the observations (Huebner, W.F. and Benkhoff, J. 1999. *Space Sci. Rev.*, **90**, 117).

11.9. Structure

There is no direct method of knowing the internal structure of the nucleus. Therefore one has to infer the possible nature of the structure of the nucleus from the observed characteristics of comets. The observational fact that the splitting of the nuclei is quite commonly seen in comets implies that the nuclei should be quite brittle. Otherwise it will not break that easily. The important point is that the splitting process does not totally destroy the nucleus. Comets split into several components when it passes within the Roche limit of the planet. The Roche limit is defined as the distance from the planet at which a smaller body like a comet which is porous

and with weak tensile strength will be torn apart due to tidal forces. The classic example is the Comet Shoemaker-Levy 9 which came with in 0.001 AU of Jupiter in 1992 and disintegrated into 21 pieces due to tidal forces (Figs. 1.8, 1.9). The splitting phenomenon also gives a chance to compare the different split components with the original nucleus and through this one may be able to get some information about the changes with depth. The splitting of Comet West into four components (Fig. 1.7) has been analyzed in some detail. The components are observed to separate out with extremely small velocities of the order of one meter per second. After their initial velocity they are all subjected to non-gravitational separation forces produced as a result of the jet action resulting out of vapourization of ice (Sec. 11.10). The observations can be fitted very well with such a physical model. Comet LINEAR (1999S4) split up into several pieces during its passage around the sun in 2000. The observations of several other split comets, which have different time-period can also be explained in a similar manner. These results show that the different pieces coming out of comets of extreme ages show the same behaviour with regard to the vapourization process. The splitting of the nuclei of comets appear not to depend upon whether the comet is of short period or long period or on their orbits or happens before or after perihelion etc. The splitting of comets also appears to be more or less random in character. The outburst seen in many comets indicate the nucleus could be fragile as well as porous. In general the new comets appear to exhibit more activity than short-period comets at large heliocentric distances. This may indicate that the outer layers of new comets may be extremely loose with more volatile material contained in it or there could be a halo of volatile material around the nucleus.

The erosion of the nuclear surface can take place during its long exposure at far off distances from the Sun due to the bombardment of cosmic rays, the solar wind etc.

The gross material strength of comets can be obtained from the estimates of the tidal forces acting on the Sun grazing comets, split comets and from other considerations. The gravitational compression force ($\lesssim 10^5$ dynes/cm²) is quite small and cannot compress the icy material of the nucleus. The tensile strength against the tidal disruption of Sun grazing comets indicates a value in the range of 10^3 to 10^5 dynes/cm². Similar order of strength of the material in the nucleus is estimated from the period of rotation of the nucleus. These values are small and they indicate the material to be weak. The strength of the material can also be estimated based on the study of meteor trajectories as they plunge into the Earth's

atmosphere since they are believed to be cometary debris (Chap. 13). They also give value of about 10^3 to 10^5 dynes/cm 2 . The estimated values for the tensile strength for cometary material in the nucleus may be compared with the values for solid water-ice and rocky material which is $\approx 4 \times 10^6$ dynes/cm 2 . It shows the cometary material to be of low material strength. In addition to this, the particles collected at high altitudes appear to be fluffy. The estimated low bulk density for the nuclei of comets indicate the material to be fulffy and loosely packed in the nucleus.

There are also other types of observations which can give some clue to the structure of the nucleus. It is well known that comets go around in their orbits many times. These observations show that only a thin layer of the material comes out of the nucleus keeping the core of the nucleus intact. More support for this comes from the Sun grazing comets which survive even after such an encounter. Also the jet force arising out of the vapourization of the gases modifies only the trajectory of the comet and it does not destroy the nucleus as a whole.

All these observations appear to show that the nucleus cannot be composed of a cluster of small particles termed as the sand-bank model. In the sand-bank model the particles are independent of each other but they follow similar orbits around the Sun. In this case there is no real body at the centre although there is a high concentration of particles at the centre. The images of the nucleus of Comet Halley, Tempel 1, Wild 2 and Borrelly taken from spacecraffts have clearly shown the nucleus to be a one solid chunk. The images have also given enormous information about the surface morphology and topology of the nucleus of comets.

Modelling cometary nuclei which can reproduce the observed characteristic behaviour of comets can also provide internal properties of a comet. The earlier model based on the assumption that the solar radiation is the only source of energy responsible for the observed cometary behaviour has been superseded by more sophisticated models. This is due to the fact that the cometary nucleus likely to contain amorphous ice and its subsequent crystallization could provide an additional source of energy. In addition, there could be another source of energy arising from short-lived radionuclide ^{26}Al . Models which take into account these three sources of energy, namely solar radiation, through crystallization process and radioactive decay and the high porosity of the nucleus have been considered. These studies indicate the stratified structure of the nucleus (Fig. 11.3).

Comets are formed as a natural product in a contracting solar nebula. The resulting nuclear structure could be aggregates of smaller icy planetes-

imals. This concept has led to models such as fluffy aggregate, primordial rubble pile and icy-glue. The collisional evolution appears to have played a role as well for the cometary nuclei. Infact all the evidences seems to indicate that the structure of nuclei of comets is processed rubble pile of smaller ice planetesimals of previous generation. Therefore the general feeling at the present is that the processed models such as fluffy aggregates or the collisionally evolved rubble pile models are the best representation of the interior structure of a cometary nucleus.

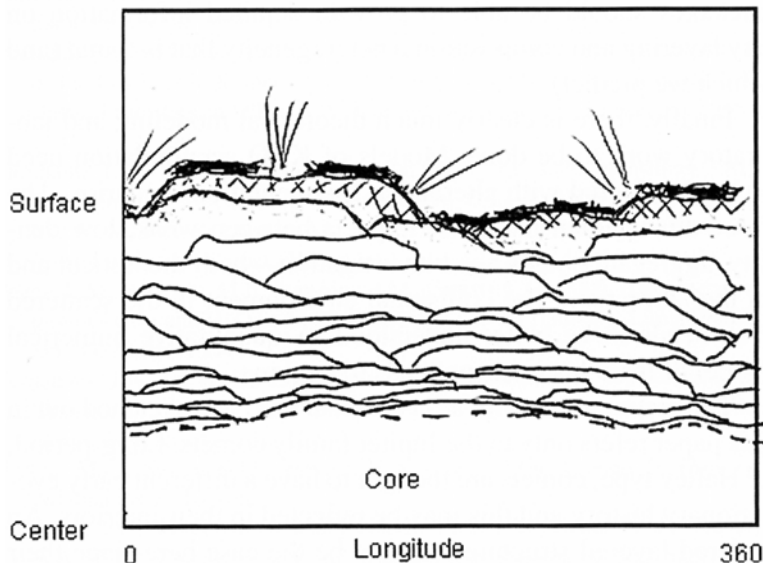


Fig. 11.8 Schematic diagram showing the persisting layers that have been seen on the surface and deeper layers of Comet Tempel 1 based on the images taken by Deep Impact spacecraft. Such features has also been seen in Comets Wild 2 and Borrelly (Belton, M.J.S. *et al.* 2007. *Icarus*, **187**, 332).

The highest spatial resolution images of Comet Tempel 1 obtained from Deep Impact showed clear evidence for the presence of layering over the surface of the comet (Fig. 11.8). Such layering structures are also present in the earlier images of Comet Borrelly and Wild 2. However the layering present in Comet Tempel 1 is very conspicuous. The appearance of such a feature on a large scale in three comets belonging to Jupiter family of comets has led to the suggestion that layering could be a common feature in the internal structure of these comets. These observations have been

interpreted in terms of a new proposed model called ‘talps’ or ‘layered pile’ model. In this model the interior of a cometary nuclei consists of a core, overwhich a randomly staked layers are piled up (Fig. 11.8). This model can explain several observed characteristics of comets. The consequence of such a model is that the nuclei of Jupiter family of comets are primordial in nature and the structure of the nucleus has not changed much from the time of their formation.

11.10. Non-gravitational Forces

The orbit of a comet can be computed by well-known methods based on Newton’s law of gravitation. The accuracy of the determined orbit depends upon the number of observations available for the comet. The orbit of short-period comets can be determined accurately as they can be observed many more times than that of long-period comets. The orbit of a comet is generally perturbed strongly by the planets as they enter the inner part of the solar system. The perturbation induced due to such an encounter can be incorporated in the orbit calculation and these complications have become easier to handle with the availability of high speed computers. However in spite of such accurate orbit calculations, it has been noticed that they seem to differ from the observed position of comets at each revolution. The well-known comet for which this is striking is the Comet Encke, discovered in 1786 and having a period of 3.3. years. It persists in returning at each revolution about $2\frac{1}{2}$ hours too soon. This was noticed by Encke himself as far back as 1820. The deviations from the observed position of comets are typically a fraction of a day and is more in some comets. Observationally it is found that out of several comets studied some came earlier than the predicted time and others later than the predicted time. This means that some are accelerated and the others decelerated, which demonstrated conclusively that there was an additional nongravitational force acting on the comet which was not included in the orbit calculations. It was noticed from observations that this nongravitational force decreased substantially with an increase in the distance between the comet and the Sun. Enckes first suggestion that the observed deviation could arise from a resisting medium was not in conformity with the observations. However the basic model based on the sublimation of gases from the icy conglomerate nucleus has been able to explain the observations reasonably well. Refinements have been considered to this model due to the presence of complex features on

the surface of the nuclei of comets.

The equation of motion of a comet in the rectangular coordinate system used in the orbit calculation procedure can be written as

$$\frac{d^2\mathbf{r}}{dt^2} = -\mu \frac{\mathbf{r}}{r^3} + \frac{\partial R}{\partial \mathbf{r}} \quad (11.11)$$

Here μ is the product of the gravitational constant and the mass of the Sun. The term on the right-hand side of Eq. (11.11) takes care of the planetary perturbations i.e., R is a planetary disturbing function. The above equation was generalized to include nongravitational forces as

$$\frac{d^2\mathbf{r}}{dt^2} = -\mu \frac{\mathbf{r}}{r^3} + \frac{\partial R}{\partial \mathbf{r}} + F_1 \mathbf{r} + F_2 \mathbf{T} + F_3 \mathbf{N}. \quad (11.12)$$

Here F_1 , F_2 and F_3 represent the additional acceleration components, F_1 is along the radius vector defined outward along the Sun-Comet-line, F_2 is perpendicular to r in the orbit plane and towards the comet's direction of motion and F_3 normal to the orbit plane. r , T and N are the three unit vectors along the three direction of forces. Since the nature of F_1 , F_2 and F_3 was not known, one can write

$$F_i = A_i f(r) \quad (11.13)$$

and to see what form of $f(r)$ can remove the observed discrepancy. The component of the force F_3 is generally present for active comets, but it is difficult to determine a meaningful solution due to its periodic nature and also the average non-gravitational acceleration is determined from the solution over three or more apparitions. Therefore for most of the comets the value of A_3 is put equal to zero. The change in the semi major axis introduced due to the radial and transverse perturbing acceleration (R_P , T_P) is given by the equation

$$\frac{da}{dt} = \frac{2}{n(1-e^2)^{1/2}} \left[(e \sin \nu) R_P + \frac{P}{r} T_P \right]$$

where n , e , ν and r represent the orbital mean motion, eccentricity, true anomaly and the heliocentric distance respectively. P presents the orbital semi-latus rectum, $a(1-e^2)$. The derived empirical function $f(r)$ was found to agree well with the form $g(r)$ given by the Eq. (11.5). Knowing the function $f(r)$, the constants A_i can be calculated. These nongravitational parameters are actually obtained from the least square fit to the definitive orbit of the comet. Therefore the empirical work on the nongravitational force has been put on a firm basis based on a physical model. In recent years the expression (11.5) has been used in all the orbit calculations.

These ideas fit in well with the matter ejected from a rotating icy model of the nucleus which can be understood from Fig. 11.9. When the solar radiation impinges on the nucleus, the material evaporates from the surface and moves out in the direction of the incident radiation. This results in a jet action, a force pushing the comet away from the Sun. If the nucleus is rotating then there will be a time delay between the heating and the ejection of the gas from any point on the surface. If the rotation is in the same direction as its motion around the Sun, the delayed jet action will have a forward component which will increase the orbital period of the comet (Fig. 11.9(b)). As a result it will go into a higher orbit and so it will show up later than the predicted time. On the other hand, if the nucleus rotates in the opposite direction to the motion around the Sun (Fig. 11.9(c)) the jet action will have a backward component. This will reduce the period of the comet and hence it will show up earlier than the predicted time. Therefore, depending on the direction of rotation of the nucleus, some of them will be accelerated and some will be retarded, which is consistent with the observation.

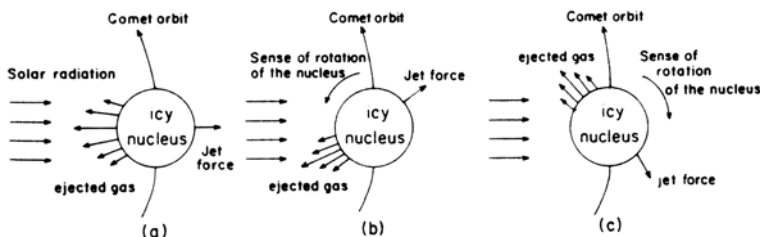


Fig. 11.9 The result of outgassing on the cometary nucleus: (a) the nucleus does not rotate; (b) the nucleus rotates along the direction of motion around the Sun. The jet force is also along the direction of motion increasing thereby the period of the comet; (c) the nucleus rotates in the opposite direction to the direction of motion around the Sun. The jet force is now in the opposite direction to its motion resulting in a decrease in the period of the comet.

It is now possible to make a meaningful comparison of the nongravitational parameters A_1 and A_2 for different comets as they represent the relative mass loss rates. However, there was still a major problem requiring the outgassing to be much higher than what was known at that time based on the line emission of C_2 and CN in the visual region of the spectrum (Chap. 6). Otherwise the jet force was not enough to exert an adequate force on the comet. This problem was resolved with the discovery of the

presence of a huge halo of hydrogen gas around Comet Bennett in the 1970's through the detection of the Lyman α line radiation (Chap. 6). The observed decrease of nongravitational effect with an increasing distance from the Sun can also be explained based on the vapourization model. The nongravitational parameter indicates that about 1% of the material is lost from each comet in one revolution which is consistent with other estimates (Sec. 11.8). To take care of the active emission areas from the surface of the nucleus, an effective sublimation rate $Z(z, r)$ (molecules/cm²/s) at a heliocentric distance r and the Sun's local zenith angle z is defined as

$$Z(z, r) = Z_0(r)\mathcal{G}(z, r)$$

where Z_0 is the sublimation rate at the subsolar point and $\mathcal{G}(z, r)$ (≤ 1) is the relative sublimation rate at the Sun's Zenith angle z . If there are several sources then it has to be averaged to get the rotation-averaged acceleration.

The transverse component given by the parameter A_2 is quite sensitive to the effects of episodical events in the orbital motions of comets. The determination of non-gravitational parameters require at least three consecutive apparition and in addition at least three independent values of the parameters A_2 is required for the study of temporal variations. This limits the study to short period comets for which astrometric observations have been made for 5 or more apparitions. Such observations have been used to determine the values of A_1 and A_2 for a large number of comets. These have been used to understand the diurnal effects and seasonal effects in comets. Diurnal effect refers to the short term variations arising due to outgassing from uneven exposure of individual sources to sunlight caused by the rotation of the nuclei. Seasonal effects are the long term variations associated with producing the asymmetric curve in the production rate with respect to perihelion.

The non-gravitational parameter for the Comet Kopff which was positive before 1930 changed over to negative value around 1940. On the other hand for Comet Halley the value of A_2 has not changed over a long time period. This indicate that Comet Halley has been out-gassing at almost the same rate over this long period of time.

In the discussion so far, it has been generally assumed that the parameter representing the component of the force normal to the orbital plane, A_3 is equal to zero. This is due to fact that the introduction of the parameter A_3 did not seem to improve the orbital solutions implying that it is hard to extract the value of A_3 i.e. essentially indeterminate. Therefore A_3 is the least understood parameter and it requires further study. With this

in view, several attempts have been carried out, in recent years, to detect the contribution from the normal component of the transferred momentum. Using various mathematical techniques, the three non-gravitational parameters A_1 , A_2 and A_3 have been derived for a number of comets. The results are rather consistent in showing that the value of A_3 is not large. Therefore with the availability of accurate values for the parameters A_1 , A_2 and A_3 representing the component of non gravitational perturbation in the radial, transverse and normal directions it may be possible to study the time evolution of the orbits, precession of the spin axis, wobbling and so on.

All the studies carried out so far for the last two decades or so, were based on the symmetric models for the non-gravitational effects in the equation of cometary motion. The implicit assumption in the symmetric model is that the non-gravitational effects are the same on either side of the perihelion position. However, in a real situation the non-gravitational effects are more of perihelion asymmetrical in nature. The evidence for such an effect comes from the non-random distribution of the active regions on the surface of the nucleus and the observed asymmetrical nature of the light curve of comets, which basically reflect their out gassing histories. Therefore the results based on symmetrical non-gravitational acceleration model is being questioned. However, it should be noted that the symmetric models have been very successful in providing accurate ephemerides but the derived physical properties of comets should be taken with caution. Therefore attempts are being made to take into account the asymmetrical nature of the non-gravitational force in comets by considering the out gassing as accurately as possible.

An approach that has been attempted is a slight modification of the symmetrical non-gravitational acceleration model. In this procedure the possible asymmetry in the out-gassing is taken into account by shifting the time (DT) for a few days before or after perihelion passage so that it coincides with the maximum value of the water vapourization curve. DT=0 corresponds to the symmetric case. Therefore the expression for the asymmetric non-gravitational acceleration model at any time t is given by $g(r')$, where $r' = r(t') = r(t - DT)$. The new calculations are similar to the symmetric model case except that the function $g(r')$ is evaluated for the heliocentric distance corresponding to the time $t - DT$, rather than for t itself. The time shift DT is varied till a best fit to the anisotropic observations is found and this in general agrees with the shift seen in the maximum of the light curve from the perihelion. It is found that the asymmetric

model appears to provide better orbital solution compared to symmetric models. The new approach is being applied to the study of several comets. The results based on a few comets have shown that the radial and transverse non-gravitational parameters derived from non-symmetric models are different from symmetric models and hence in their inferred physical properties. Over long periods of time the value of DT may change its value and sign. The value of DT is about 40d for Comet d'Arrest and is also stable over many observed apparitions of the comet. On the other hand for Comet Giacobini-Zinner DT = + 14 days during 1959–1973 and - 13 days during 1972–1987. For comet Halley DT = + 20 days and this is consistent with the post-perihelion peak observed in the light curve. There are some comets which show long term non-gravitational effect to be irregular as well as the value change rapidly. These could be understood in terms of forced precession model of a rotating non-spherical cometary nucleus.

Since the non-gravitational force is the resultant effect of the redistribution of the momentum that is transferred to the nucleus by the sublimating gas, it is a complicated function of several factors like shape, structure, nature and areas of active regions, jets, direction of the ejection of gas and so on of the nucleus. The resultant effect is to complicate the rotational as well as the orbital motion of the nucleus of a comet, which shows up as peculiarities in the observations (Fig. 11.10). It also depends upon sudden activation or deactivation of discrete emission centres in the nuclear surface.

All these complicated effects which varies from comet to comet and affect the non-gravitational perturbations have to be considered for getting accurate orbit of comets.

11.11. Ortho to Para Ratio of Molecules

The nuclear spin of two similar atoms in a molecule such as H₂, give rise to segregation of rotational levels of the molecule depending upon the total nuclear spin angular momentum (I). Therefore it was postulated based on Quantum Theory the existence of two forms of molecular hydrogen called Ortho - H₂ and Para -H₂ and got experimental confirmation of this prediction, a great success story. Later work found that in ortho - H₂, the two hydrogen atoms spin in the same direction (I=1,↑↑) and have rotational levels with odd J values. In para - H₂, the nuclei of two hydrogen atoms spin in the opposite direction (I=0,↑↓) and have rotational levels with even

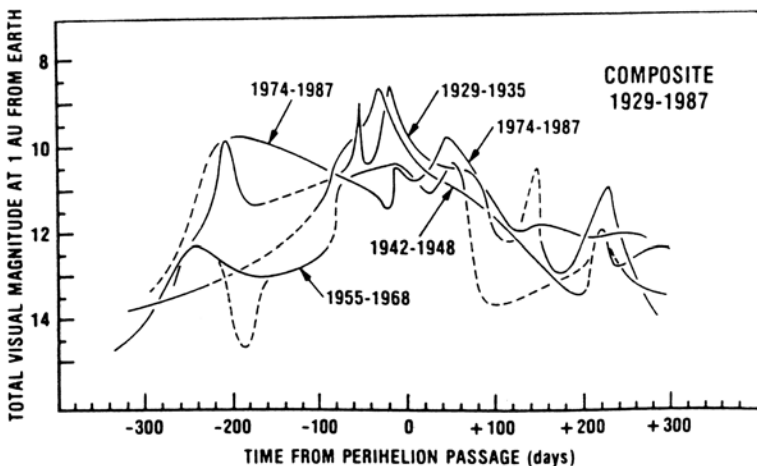


Fig. 11.10 A composite figure showing the light curves of Comet Schwassmann-Wachmann 2 for the period from 1929–1987. The negative times correspond to the inbound orbit and positive times to outgoing orbit. The long-term variations as well as erratic behaviour can be seen (Sekanina, Z. 1993. *Astron. Astrophys.* **271**, 630).

J values. Radiative and collision transition between the rotational states of ortho and para molecules are strongly forbidden.

The H_2O molecule also exists as ortho - $\text{H}_2\text{O}(I=1)$ and para - $\text{H}_2\text{O}(I=0)$ depending upon whether hydrogen nuclear spins are in parallel or in anti-parallel state with statistical weight of $(2I+1)$. The lowest rotational level of ortho - H_2O is higher than the lowest level of para - H_2O by 24 cm^{-1} . Therefore the ratio between the total populations of ortho - H_2O and para - H_2O states depend upon the temperature called the *Spin temperature*. This temperature refers to the temperature for a given ortho to para ratio under local thermodynamic equilibrium.

In thermal equilibrium the ortho-to-para ratio (OPR) can be determined from the rotational distribution of the molecules

$$\text{i.e., } OPR = \frac{(2I_o + 1) \sum(2J + 1) \exp\left[\frac{-E_o}{kT}\right]}{(2I_p + 1) \sum(2J + 1) \exp\left[\frac{-E_p}{kT}\right]}.$$

Here o and p refer to ortho and para rotational levels. J and E refer to rotational quantum number and energy of the levels respectively. The above equation can be evaluated as a function of temperature using energy

level diagram of H_2O molecule. The results are shown in Fig. 11.11. For high temperatures the population ratio of ortho-to para H_2O approach the statistical weight $2I+1$ which is 3 for H_2O . As can be seen from the figure, the statistical equilibrium value of OPR=3.0 is achieved for temperatures greater than around 60K. For lower temperatures the OPR is less than the statistical equilibrium value.

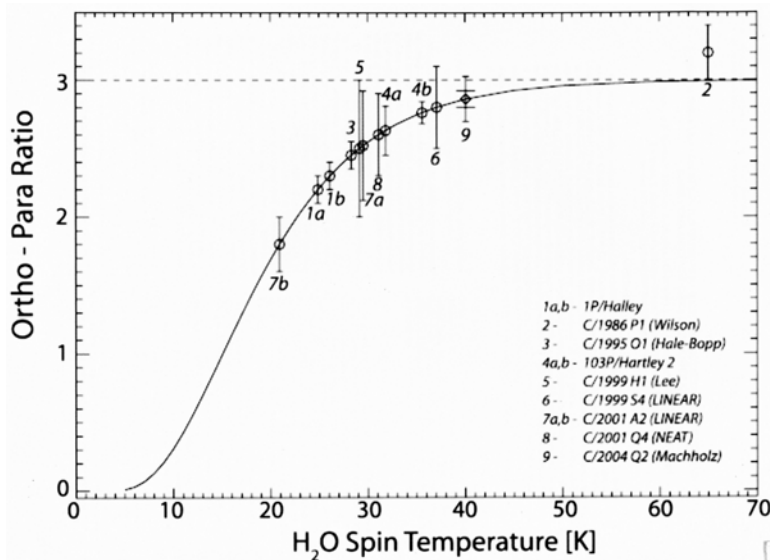


Fig. 11.11 The time dependent Ortho to Para ratio is shown by the solid curve. The observed ratio for H_2O in various comets is also shown (Bonev, B.P. et al. 2007. *Ap. J.*, **661**, L97).

Since the nuclear spin conversion in H_2O is forbidden during radiative transitions or non-destructive collisions, the OPR formed at a particular temperature is essentially frozen-in and OPR is believed to remain the same throughout the coma. Therefore the observed OPR should give an indication of the spin temperature that existed when water molecule was formed and hence the location in the solar system where comets were formed. Therefore ortho-to-para abundance ratio of cometary H_2O could give information about the region of formation of comets in the solar system about 4.6 Gyr ago. In view of this, the determination of ortho-to-para ratio of H_2O in comets is of particular interest.

The first determination of ortho-to-para ratio of H_2O was for Comet

Halley in 1985-86 based on the observed lines of ortho and para in the $2.9\text{ }\mu\text{m}$ spectral region. Since then OPR ratio of water has been determined for a large number of comets. This is determined from a comparison of the observed spectra with the synthetic spectra based on fluorescence model.

The molecules NH_3 and CH_4 which exhibit ortho and para states and whose lines lie in the radio and infrared spectral regions have also been used to determine the OPR in comets. Although OPR ratio of NH_3 can be determined directly from their observed spectral lines, it is more advantageous to get this ratio from the study of NH_2 molecule whose lines are quite strong and lie in the visible spectral region. As a typical case, a comparison between the observed spectra and the best fit synthetic spectra for NH_2 is shown in Fig. 11.12 for Comet Ikeya-Zhang.

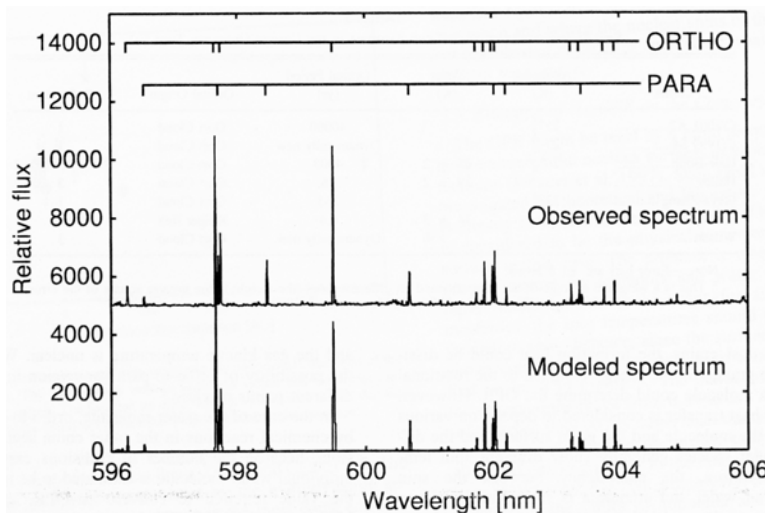


Fig. 11.12 Comparison between the observed and modeled spectra of NH_2 A (0, 9, 0) - X (0, 0, 0) band in Comet Ikeya-Zhang for April 19, 2002. The best fit for OPR of NH_2 is 3.22 for the model spectrum indicating spin temperature of 32 K for NH_3 (Kawakita, H. et al. 2004. *Ap.J.*, **601**, 1152, Reproduced by permission of the AAS).

The observed OPR of NH_2 is used to get the OPR of NH_3 with the assumption that NH_2 is the major photodissociation product of NH_3 and the application of nuclear spin selection rule to photodissociation reaction of NH_3 into NH_2 and H is valid. The spin temperature determined from the study of H_2O , NH_3 and CH_4 for several comets are given in Table 11.3 and shown in Fig. 11.11 for H_2O . The striking feature of Table 11.3 is the

grouping of the observed spin temperature of H₂O, NH₃ and CH₄ around 30 K with some scatter, even though the observations refer to different heliocentric distances, gas production rates or the orbital period of comets. This indicate that the spin temperature appears to reflect the temperature of the region of formation of these molecules and hence of comets. If the spin temperature reflect the place of formation of comets in the solar nebula, then one expects spin temperature of Jupiter family of short period comets (originally in the Kuiper Belt region which is farther than 30 AU in the solar nebula) must be smaller than Oort cloud comets (originally in the region of giant planet region of 5–30 AU from the sun). However the spin temperature of these two types of comets indicate that both Oort cloud comets and Jupiter family comets were formed under similar conditions in the solar nebula and hence have a common origin. This is possible if the cometary material had originated from a presolar molecular cloud at 30 K. Even though the observed spin temperature of H₂O, NH₃ and CH₄ of comets cluster around 30 K, there are deviations as well. Of particular interest is Comet Wilson and other comets whose OPR of H₂O is close to the statistical equilibrium value of 3 (spin temperature is \gtrsim 50 K). These have raised the question of the real meaning of the observed OPR of molecules in comets and the corresponding spin temperature.

Although the nuclear spin conversion is forbidden, the constancy of nuclear spin temperature over large time scales is not clear at the present time. Some laboratory studies have indicated that the radiative nuclear conversion time for H₂O is much larger compared to that of CH₄. Also if equilibrium took place within the coma, the spin temperature should vary with heliocentric distance of the comet. On the other hand if equilibrium took place inside the nucleus, the nuclear spin temperature should vary with the orbit of the comet. i.e. the spin temperature should differ between short period and long period comets. Therefore laboratory study of cometary analogs can help in a better understanding of the conditions under which nuclear conversion can take place. This in turn can help in clarifying to what extent the observed spin temperature represents the formation history of comets.

Table 11.3 Nuclear spin temperature in comets.

Comet	H ₂ O	NH ₃	CH ₄	Orbit
Halley	29±2			OC
Wilson	> 50			OC
Hale-Bopp	28±2	26 ⁺¹⁰ ₋₄		OC
Hartley 2	36±3			JF
Lee	30 ⁺¹⁵ ₋₆			OC
S4 LINEAR	≥30	27 ⁺³ ₋₂		OC
A2 LINEAR	23 ⁺⁴ ₋₃	25 ⁺¹ ₋₂		OC
WM1 LINEAR		30 ⁺⁵ ₋₃		OC
Ikeya-Zhang		32 ⁺⁵ ₋₄		OC
NEAT	31 ⁺¹¹ ₋₅	31 ⁺⁴ ₋₂	33 ⁺² ₋₁	OC
MACHHOLZ	>34			OC
Tempel 1		24± 2		JF
Enake	≥33			JF

Kawakita, H. *et al.* 2006, *Ap.J.*, **643**, 1337. Bonev, B.P., Mumma, M.J., Villanueva, L. *et al.* 2007, *Ap.J.*, **661**, L97. Kawakita, H. *et al.* *Icarus* 2007, **127**, 272. OC (Oort cloud); JF (Jupiter family)

11.12. Binary Systems

The discovery of binaries among Asteroids, Near Earth Asteroids, Transneptunian objects and Trojan Asteroids have raised high prospects of finding satellite around cometary nuclei. The detection of a satellite around the cometary nucleus will be of great significance as it will provide a direct method of getting the mass of the cometary nucleus. If the mass is known and size can be determined by an independent method, the density of the material can be determined. This will give an insight for an understanding of the properties of the nucleus such as, porosity, structure of the nucleus etc. However in a real situation, detection of a binary is a difficult task as the nucleus itself is small and in addition coma is present even at large distances. Hence, so far there is no definite observational evidence for the existence of satellites around cometary nuclei.

There are several possible scenarios for the formation of a satellite around a cometary nuclei. Capture of an external object is highly unlikely process. The nucleus can fragment and the pieces can assemble to reform into a satellite. It could also bi-furcate into two co-orbiting bodies.

The splitting of cometary nuclei is a common phenomena. So the fragments can be produced. However due to non-gravitational force, the fragments may drift apart quite fast and not allowing for the formation of a

stable binary configuration. Even if a satellite can form, its motion around a non-spherical rotating and an active cometary nucleus could be highly complex. Therefore the detection of a satellite around a cometary nuclei is a real challenge from the observational point of view.

11.13. Summary

The vapourization theory of water from the nucleus could explain reasonably well the visibility of comets at around the heliocentric distances of 3 AU. However, it had difficulty in explaining comets seen at distances much beyond 3 AU. This led to clathrate model. Such a configuration is not practicable as it can be produced only at high pressure conditions, which is not the case in the case of comets. The working model at the present time is that the nucleus contains amorphous ice, and release energy when it crystallizes. Consequently, the repetition of heating and cooling processes inside the nucleus creates a layered structure with different compositions. The most volatiles lie in the near central regions and less volatiles near the surface layers of the nucleus. This model can reasonably explain all the observed activities of a comet such as bursts, random or repetitive, outbursts at large heliocentric distances etc. The flybys to several comets have given surprising results with regard to the morphological structure of the nucleus. The tensile strength of the nucleus is quite low and hence it is fragile. Therefore the nucleus can break up easily, which has been seen in several comets. The ortho-to-para ratio of several molecules indicate a formation temperature ~ 30 K which implies that comets are formed in the low temperature region of the solar nebula. The surface gravity of Comet Tempel 1 has been determined for the first time from the observation of ejecta plume. The non-gravitational force which arise due to the net transfer of momentum to the nucleus, is a complicated function which depends upon the shape, active areas and their location, rotation, jets, outbursts etc. of the nucleus. Similarly all these effects has influence on the nuclear rotation giving rise to one or several time periods for the rotation of the nucleus of a comet.

Problems

1. Do you expect the vapourization rate of gases from the nucleus to be constant at every revolution around the Sun?
2. Consider a nucleus made up of ice 1 km in radius, with mass loss rate of 10^8 gm/sec and a period of 5 years. If the comet is assumed to be active for about a year at every revolution, how much does the nucleus shrink per revolution? What is the lifetime of the nucleus?
3. A comet of radius 1 km is moving with an orbital velocity of 60 km/sec at 1 AU. Calculate the amount of out-gassing required if the gas comes out at 1 km/sec from the sun-lit hemisphere of icy nucleus so that the non-gravitational force is about 1% of the orbital force.
4. How do you reconcile the fact that the nucleus contain mostly water but the observed geometrical albedo for Comet Halley is 0.04.
5. If the nucleus of a comet was made up of 80% CO₂ and rest is made up of other molecules like H₂O, CO and others, what will be the scenario of such a comet?
6. What are the consequence if the nucleus is a hard solid body instead of fragile and fluffy in nature?

References

The following papers cover morphology of comets

1. Brownlee, D.E. *et al.* 2004. *Science*, **304**, 1764.
2. Britt, D.T., Boice, D.C., Buratti, B.J. *et al.* 2004. *Icarus*, **167**, 45.
3. Thomas, P.C., Viverka, J., Belton, M.J.S. *et al.* 2007. *Icarus*, **187**, 4).

The following paper gives a good account of the vapourization theory

4. Delsemme, A.H. 1982. In *Comets* ed. Wilkening, L.L. Univ. Arizona Press, Tucson, p. 85.

A good account for later work is given in the following papers:

5. Meech, K.J. and Svoren, J. 2005. In *Comets*, Eds. M.C. Festou, H.U. Keller and W.A. Weaver, Univ. Arizona Press, Tucson, p. 317.
6. Prialnik, D., Benkhoff, J. and Podolak, M. 2005. In *Comets*, Eds, M.C. Festou, H.U. Keller and W.A. Weaver, Univ. Arizona Press, Tucson, p. 359.

A good summary of albedo and radius of comets is given in the following paper:

7. Lamy, P.L., Toth, I., Fernandez, Y.R. *et al.* 2005. In *Comets*, eds. M.C. Festou, H.U. Keller and W.A. Weaver, Univ. Arizona Press, Tucson, p. 223.

The mass and density is covered in the following papers.

8. Davidson, B.J.R. and Gutierrez, P.J. 2006. *Icarus*, **180**, 224.
9. Richardson, J.E., Melosh, H.J., Lisse, C.M. *et al.* 2007. *Icarus*, **190**, 357.
10. Weissman, P.R., Asphaug, E. and Lowry, S.C. 2005. In *Comets II*, eds. F.C. Festou, H.U. Keller and W.A. Weaver, Univ. Arizona Press, Tucson, p. 337.

First direct determination of the surface gravity of Comet Tempel 1, is in the following paper.

11. A'Hearn, M.F., Belton, M.J.S., Delamere, W.A., *et al.* 2005. *Science*, **310**, 258.

The rotation of the nuclei of comets is covered in the following paper

12. Samarasinha, N.H., Mueller, B.E.A., Belton, M.J.S. *et al.* 2005. In *Comets*, eds. M.C. Festou, H.U. Keller and W.A. Weaver, Univ. Arizona Press, Tucson, p. 281.

The following papers refer to nucleus composition

13. Huebner, W.F. and Benkhoff, J. 1999. *Space Sci. Rev.*, **90**, 117.
14. Huebner, W.F. and Benkhoff, J. 1999. *Earth, Moon and Planets*, **77**, 217.

For structure, outburst etc. of cometary nuclei, see papers

15. Belton, M.J.S., Thomas, P, Veverka, J., *et al.* 2007. *Icarus*, **187**, 332.
16. Prialnik, D., Benkhoff, J. and Podolak, M. 2005. In *Comets*, eds. M.C. Festou, H.U. Keller and W.A. Weaver, Univ. Arizona Press, Tucson, p. 359.

The existence of non-gravitational force in comets was proposed for the first time in a classic paper by

17. Whipple, F.L. 1950. *Ap.J.* **111**, 375.

For a good summary of non-gravitational forces in Comets, refer to:

18. Yeomans, D.K., Chodas, P.W., Sitarski, G. *et al.* 2005. In *Comets*, eds. M.C. Festou, H.U. Keller and W.A. Weaver, Univ. Arizona Press, Tucson, p. 137.

The first determination of Ortho-to-Para ratio is in the following papers:

19. Mumma, M.J., Weaver, H.A. Larson, H.P. 1986. *Science*, **232**, 1523; *Astron. Astrophys.*, **187**, 419.

For later work, refer to the following papers:

20. Bonev, B.P., Mumma, M.J., Villanueva, L. *et al.* 2007. *Ap.J.*, **661**, L97.
21. Kawakita, H., Russo, N.D., Furusho, R. *et al.* 2006. *Ap.J.*, **643**, 1337.
22. Kawakita, H., Jehin, E., Manfroid, J. *et al.* 2007. *Icarus*, **187**, 272.
A good account of binary systems is in the following paper
23. Noll, K.S. 2006. In *Asteroids, Comets and Meteors*, eds. D. Lazzaro, S. Ferraz-Mello and J.A. Fernandez, Cambridge University Press, Cambridge, p. 301.

This page intentionally left blank

CHAPTER 12

Origin

There are many ideas and hypothesis with regard to the origin of comets. Some of these date back to Laplace and Lagrange. Dynamical simulations in conjunction with available observations, although scarce, have given new insights into this area of study. Some of these aspects will briefly be discussed in this chapter.

12.1. Evidence for the Oort Cloud

During early times, the emphasis in the study of comets was mainly on the determination of their orbits. This resulted in the accumulation of a lot of data with regard to the orbital characteristics of comets, which gave an insight into some of the physical problems. One such fundamental aspect, which came out of these studies - namely, nongravitational force has already been discussed in the previous chapter. Another significant result refers to the problem of the origin of comets themselves. Several general characteristic properties can be noted just from the stability of comets. The long-period comets, mostly in parabolic orbits, appear to come from all directions in the sky. The short period comets, have low inclination to the ecliptic plane and have a strong association with the planetary system. Any reasonable theory of the origin of comets has to explain these features. Various concepts, ideas, hypothesis and theories, have been put forward over the years discussing the merits and demerits of interstellar vs solar system origin of comets. Therefore the whole subject was in a confused state. In a classic paper, Oort in 1950 proposed the unification of the origin of comets within a reasonable and consistent framework. This has given rise to a rapid development of the subject and a better understanding of the whole phenomena.

Table 12.1 Distribution of original values of semimajor axes, a (AU).

	$1/a$		Number of comets
	\leq	0.00005	10
0.00005	-	0.00010	4
0.00015	-	0.00015	1
0.00020	-	0.00020	1
0.00025	-	0.00050	1
0.00050	-	0.00075	1
	>	0.00075	0

Oort, J. 1950, *Bull. Astr. Inst. Netherlands* **11**, 91.

Even with limited observational material available on about 19 long-period comets at that time, Oort showed that a simple plot of the number of comets versus the inverse of semi major axis, $1/a$ (equivalent to orbital energies) of the original orbit gave a conspicuous peak near value zero (i.e. nearly parabolic orbits) (Table 12.1). The original orbit refers to the orbit of the comet before it enters the planetary system.

The peak observed in the $1/a$ distribution cannot be due to chance but represents the real characteristic property. This is based on the fact that the observed dispersion in $1/a$ is much smaller than it would have been if it had passed through perihelion passage once. Even one passage can bring in a dispersion in $1/a$ which is much larger than the observed values. Therefore most of the comets must have come into the solar system for the first time, generally called ‘new’ comets. Most of these comets appear to come from the region of say 30,000 to 50,000 AU. This led Oort to recognize the existence of a spherical cloud of comets around the Sun at this distance but still gravitationally bound to it. This is generally called the “Oort cloud”. It should be pointed out that as far back as 1932, Opik had suggested the possibility of the presence of such a cloud surrounding the solar system. With more accurate and high precision data available in recent years on a large number of comets the idea proposed by Oort has been confirmed and all the results deduced earlier based on the limited data remain more or less the same. It is remarkable that such an important work came out, based just on 19 cometary orbits. Figure 12.1 shows the histogram of the number of comets versus the original $1/a$ values based on comets with well-determined orbits. The observed distribution has a sharp

peak of comets at near zero. The figure also shows a continuous distribution of tightly bound orbits. Most new comets have aphelion distance of around 50,000 to 100,000 AU. The corresponding major axis is around 25,000 to 75,000 AU. More recent determination give a value for the semi major axis of about 36,000 AU. These distances are almost comparable to the distances of nearby stars. Oort recognized the fact that the peak in Fig. 12.1 should be the source of long period comets, a gravitationally bound spherical cloud of comets at distances greater than 10^4 AU from the sun. Recent simulation studies have shown that the inner part of the Oort cloud at distances of around 3000–10,000 AU may also be the source of long period comets.

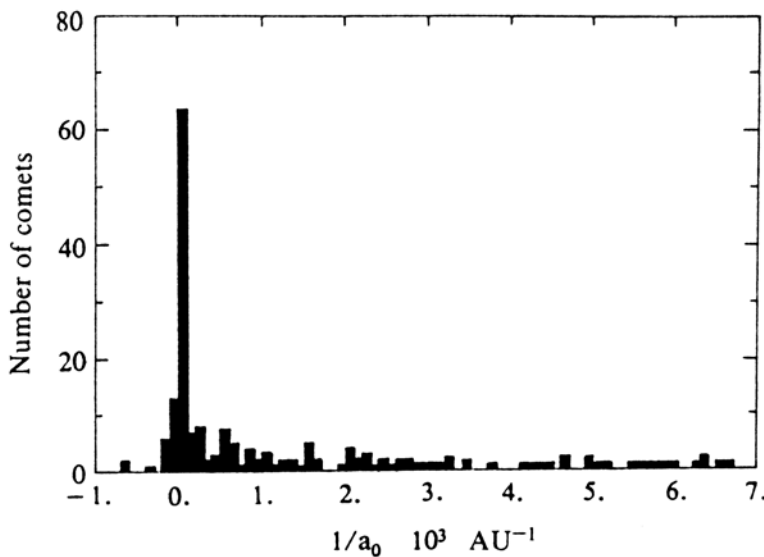


Fig. 12.1 A histogram of the number of comets plotted as a function of the original inverse semi major axes for the observed long-period comets. The sharp peak of comets near zero value of original $1/a$ represent the new comets from the Oort cloud. (Marsden, B.G., Sekanina, Z. and Everhart, E. 1978. *A.J.*, **83**, 64).

Oort made an estimate of the total number of comets in the Oort cloud to be about 1.9×10^{11} based on the observed flux of dynamically new comets for an influx rate of about 1 comet per year within 1.5 AU from the sun. More recent dynamical models gave a value for the number of comets in the Oort cloud to be in the range of $(0.4 \text{ to } 1.3) \times 10^{12}$. The present day mass for comets with $a > 20,000$ AU and H (absolute magnitude) < 11 is around $7M_{\oplus}$ and the total present day mass of the Oort cloud is estimated

to be around $38M_{\oplus}$.

Cometary fading

It is observed that the number of returning comets after the Oort cloud spike decreases more steeply compared to the expected rate based on models which takes into account planetary and stellar perturbations. This is generally known as ‘Cometary Fading’. Dynamical model calculations have shown that this effect cannot be attributed to modelling effect, but must be due to the intrinsic property of the comet. Three possibilities have been suggested. They are ‘disruption or splitting’ process due to low tensile strength of the nucleus, loss of volatiles called ‘Extinct State’ or formation of non-volatile mantle on the surface of the nucleus called ‘Dormant State’ of the comet. Dynamical calculations once again seems to rule out the extinct and dormant state of the comet for the observed cometary fading. Therefore more likely that the catastrophic splitting of comets is the dominant physical loss process for the observed cometary fading. Therefore comets after few passes through the solar system are split up into a large number of smaller bodies which then move independent of each other. Such a process might have resulted in well known Kreutz group of comets containing more than few hundred comets.

12.2. Evolution and Properties of Oort Cloud

The transformation of comets from the Oort cloud to the observable comets can be understood in a quantitative fashion in the following manner. Due to stars perturbation, many comets leave the cloud for ever and some others enter the planetary system. Among these some may happen to come close and are observable as “new” comets. When a fraction of these comets encounter the planets, particularly Jupiter, they are perturbed and leave the system altogether after their first encounter. Some of these get caught in the solar system, and are seen as long-period comets. By repeated encounters with the giant planets, enough of them are progressively transferred from long-period orbits to intermediate-period orbits and finally into short-period orbits. A large number of investigations have been carried out for an understanding of some of these problems through analytic, semi-analytic and numerical calculations. With the availability of high speed computers, the Monte Carlo approach has been used to simulate the dynamical evolution of comets in the Oort cloud, wherein it is possible to

investigate the effect of varying initial conditions. The idea is to consider a large number of comets in the Oort cloud and study their time evolution by taking into account the perturbations due to various sources. The orbits of comets could be followed until they escape from the system in a hyperbolic orbit. It is the cumulative effect of the changes in the comets orbital energy during each passage through the planetary system which is important in deciding the fate of the final orbit of the comet. Due to large computer time involved, some approximations have to be made to obtain results within a reasonable length of time.

The results of Monte Carlo simulation for 10^5 hypothetical comets gives a good match to the observed distribution in $1/a$. (Fig. 12.1). On the average a long-period comet with perihelion distance < 4 AU makes around five passages through the planetary region before taking on some final state with a mean life time of about 6×10^5 years. In addition to the perturbing forces normally considered, arising due to planetary encounters and passing stars that continually change the orbital elements of comets, other type of perturbing forces have been shown to be important. One is due to the existence of Giant molecular clouds with a typical mass $\sim 3 \times 10^5 M_\odot$ and radius $\sim 20pc$ respectively. The Giant Molecular Cloud encounters are rare with the mean interval of about 3 to 4×10^8 yr. This has been shown to be a major perturber of the orbits of comets in the Oort cloud. Just as stars passing the Oort cloud perturb the orbit of comets, in a similar way the distribution of stars in the Galaxy can also have a major perturbing effect on the orbits arising due to ‘tidal’ distortions. This arises due to the gradient of the gravitational force in the solar neighbourhood which is slightly different at the position of the Sun and the comet. As a result the galactic acceleration is different at the two locations which leads to a net tidal force acting on the comet with respect to that of the Sun. This effect has been taken into account in a more realistic manner in recent dynamical calculations. The relative importance of various perturbers for the net influx of comets can be seen from Table 12.2. The results are for a radial distribution of comets in the Oort cloud of the form $n(r) \propto r^{-3}$ and normalized to unity for the influx rate caused by random passing stars. For ranges around $7 \times 10^3 \leq a_{\text{original}} \leq 4 \times 10^4$ AU of the Oort cloud the effects of forces other than planetary perturbations are important.

The structure and stability of the Oort cloud has also been studied based on the N-body simulation with the inclusion of various perturbations.

Table 12.2 Influx rate of comets from the Oort clouds.

Perturber	Relative number
Random stars	1.0
Intermediate size molecular cloud	124
Vertical galactic tidal force	1.72
Close stellar passage ($D_{\odot} = 10^4$ AU)	62.1

Adapted from Fernandez, J.A. and IP.W.-H. 1991. In *Comets in the Post Halley Era*. eds. C.L. Newburn *et al.* Kluwer Academic Publishers. p. 487.

This approach tries to simulate the actual physical system, wherein the interaction of all the bodies is taken into account. It is possible to study physical processes through this approach, such as the exchange of energy and angular momentum between the cloud and the stars and so on. A comparison of the mean square velocity of the cloud with the escape velocity at any particular layer would show whether it can escape from the system. The results show that the inner regions are stable, while the outer layers can escape from the system.

The dynamical half-life of comets in the Oort cloud due to the effect of passing star is estimated to be about 3 Gyr at 25,000 AU. It is around 1 Gyr at 50,000 AU. The effect of Giant molecular cloud on the Oort cloud is comparable that of passing star. The resultant effect of stellar perturbation is that, around 5% of comets should survive at 50,000 AU for 4.5 Gyr. Similar is the case at 30,000 AU. This indicates that the comets in the outer region of the Oort cloud decrease with time. One way to replenish is by capture of comets from interstellar space. This is a highly unlikely process as it involves a three body gravitational interaction for dissipating the excess hyperbolic energy. The other possibility being that the supply of comets is provided by the inner regions of the Oort cloud. However it is not at all clear at the present time whether the comets are depleted at such a rate from the outer regions of the Oort cloud that it requires to be replenished in view of several simplifying assumptions made in the model calculations.

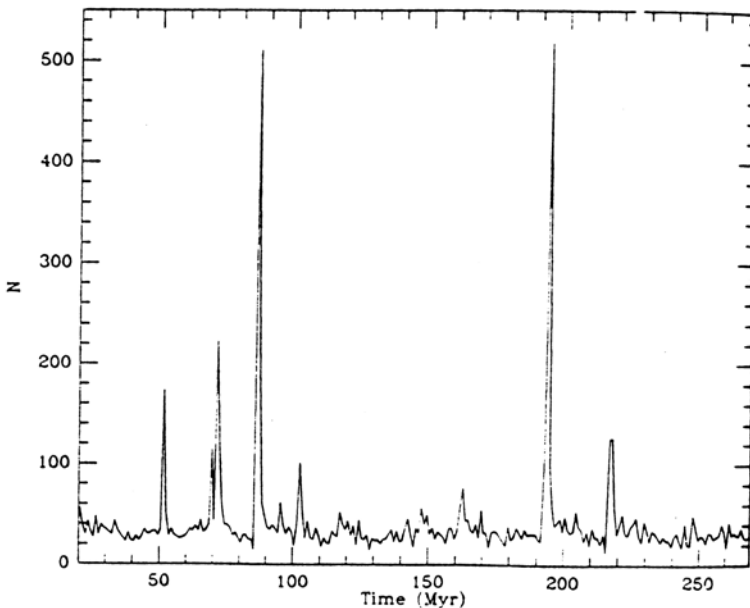


Fig. 12.2 The results of Monte Carlo simulation showing the number of new long-period comets entering the terrestrial planets region $q < 2$ AU from the Oort cloud. The spikes represent the comet showers arising due to random stars penetrating the Oort cloud (Courtesy Heisler, J.).

Cometary Showers

The studies based on Monte Carlo calculations have indicated that influx of cometary flux from the outer regions of the Oort cloud could vary roughly by a factor of 2 to 3. These are a sort of common phenomena. Sometimes it is possible that the passing stars happen to penetrate the Oort cloud, or the stars could be of relatively high mass, or pass the cloud with small impact parameter. In these situations the orbit of comets could be changed by a larger amount. The net effect will be to scatter more long-period comets into the solar system, which will increase drastically the observable comets giving rise to cometary shower (Fig. 12.2). Monte Carlo simulations have been carried out for such situations to get an idea of the expected results. The impact rate increases by a factor of around 300 for the case of star passing at a distance of \sim to 3×10^4 AU from the Sun and seems to last for around 2 to 3×10^6 years. The increase in flux rate arises due to the fact that comets coming from the inner part of the Oort

cloud have relatively shorter time periods compared to those coming from outer regions and hence perturbed more due to planetary perturbations and in turn make more revolutions. However such close stellar encounters are quite rare and the frequency of occurrence could be perhaps once in 3 to 5×10^8 years or so. In a similar way, a sudden increase in the influx of comets from the Oort cloud can increase by a factor as high as 10^3 for a close encounter with a Giant molecular cloud ($M \sim 5 \times 10^5 M_\odot$) or even higher rate of influx for the penetrating Giant molecular cloud. But such occurrences may occur at intervals of several times 10^7 years.

The distribution of comets is a complicated function of the various physical mechanisms which could operate on the Oort cloud. Therefore the enhancement of ejection of comets could vary in a periodic fashion, random or in some complicated way, depending on the manner in which the disturbances act on the Oort cloud. This could have catastrophic or moderate effects on the geophysical, biological or climatic changes on the earth. They could possibly appear in terrestrial records. In view of these considerations, it has been suggested that the random cometary showers could contribute substantially for the formation of craters on planets and the Moon and also the biological extinction events on the Earth. Also the statistical study of the fossil records has been interpreted in terms of biological extinction events that may be taking place with a time scale of approximately 26×10^6 years (Fig. 12.3). An interesting measurement was carried out at the sea floor looking for iridium concentration for the period from 33 to 67 Myr ago. The results showed an increase by a factor of around 13 near the Cretaceous-Tertiary boundary (referring to 66 Myr). This can be explained in terms of a strong comet shower which enhanced the iridium concentration. The expected value from such a process agrees within a factor of two of the observed value seen at the Cretaceous-Tertiary boundary. At present these may be considered as possibilities rather than evidence in support of them, as more work needs to be done from both observational and dynamical points of view.

The Oort cloud has been considered to be a cold storage place for long-period comets without much happening until it is perturbed by a perturbing force. In recent years, it has been suggested that during the life time of the Oort cloud the outer layers of the cometary nuclei could be modified due to various physical processes such as, bombardment by galactic cosmic rays, solar wind, heating due to nearby supernova explosions, luminous stars passing by, impact due to various debris and so on.

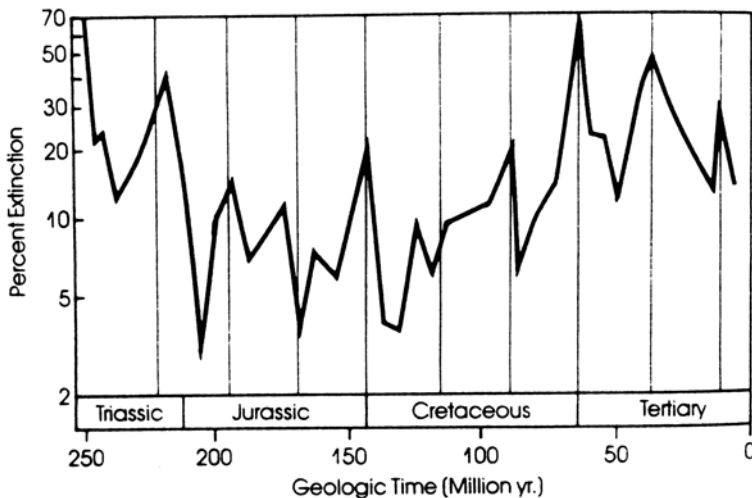


Fig. 12.3 A statistically significant mean periodicity of about 26 million years is indicated by the extinction records for the past 250 million years. (Raup, D.M. and Sepkoski, J.J. 1984. *Proc. Nat. Acad. Sci.* **81**, 801).

12.2.1. Short period comets

The long-period comets, after random-walk through the planetary system, which reduces the semi-major axis of the orbit, could finally give rise to short period comets. The important work of Everhart in 1972 showed clearly that such a dynamical mechanism can be an efficient process. The question to ask is whether such a mechanism can produce the number of observed short-period comets.

Estimates of the expected number of short period comets from long period comets by diffusion process has been made and it varies considerably. The dynamical calculations have shown that the ratio of the initial population of near parabolic orbits to the number of long period comets gravitationally bound to the system after N perihelion passages varies as $N^{1/2}$. The ratio of the observed long period comets to short period comets is ~ 5 and hence $N \sim 25$. This indicates that after around 25 passages or so, around 90% of the original comets are lost from the system. It is quite possible that some of the long period comets can be transformed into short period comets after an unusually long number of revolutions. It is estimated that around 2×10^3 revolutions are required for transforming a long period comet to short period comet with $P < 20$ years. The transformation can

also take place only over a restricted region, $4 < q < 6$ AU and $0 < i < 9^\circ$, with an efficiency factor of one captured comet for about 10^2 long period comets. In addition, other physical processes such as sublimation, breaking of the nucleus and so on could also prevent the long-period comet turning into a short-period one. Therefore the existing dynamical calculations show that roughly one comet out of a total of 10^3 comets can end up as a short-period comet. Hence the major difficulty in the process of producing long-period comets to short-period comets through diffusion process in the solar system is that the resulting number of short-period comets are too small compared to the observed number. Also the long-period comets tend to preserve their inclination as they evolve into short-period comets, in contrast to those of observed short-period comets, whose orbits are confined to inclinations $\lesssim 30^\circ$ or so. In addition, the original population of long period comets with random inclinations would lead to a certain fraction of short period comets with retrograde orbits, which is not seen. These are some of the major difficulties and therefore it is necessary to consider other mechanisms for the production of short period comets.

In order to produce low inclination, short period comets, the source has also to be confined to a flattened disk of comets. This has led to the hypothesis that the Trans-Neptunian population of comets could be the source of short period comets. The possibility of the existence of such a source of comets had been suggested by Kuiper in 1951. He postulated a remnant of the accretion disk of planetesimals in the solar nebula, which never managed to accrete into planets. This is now termed as ‘Kuiper Belt’. The Kuiper Belt is also called ‘Edgeworth-Kuiper Belt’ as Edgeworth had shown the possible presence of comets beyond pluto in 1949. This idea has been elaborated later on by several investigators and showed that such a residual population of planetesimals could have remained bound to the solar system. The short period comets produced from such a comet belt are far more efficient than produced through long period comets from the Oort cloud.

Detailed simulation studies have shown that Oort cloud is composed of two parts, namely the spherical outer cloud and the inner cloud which is flattened. The boundary between the two regions is around 20,000 AU. Long period comets come from the the spherical distribution of the Oort cloud, Halley type comets come from the inner flattened disk of the Oort cloud and Jupiter family of comets come from the Kuiper belt. It now appears likely that most Jupiter family comets arise from the related structure called the scattered disk.

Extensive dynamical evolution studies over forward and backward in time spanning up to 10^7 yr has been carried out. The comet was followed until it became either an unbound system from the sun or a sun-grazer. These studies show that around 92% of comets were ejected from the solar system and around 6% of comets were destroyed by becoming sun-grazers. It also showed that around half of the comets of sun-grazing type were of Halley type of comets. The median life time of short period comets $\sim 4.5 \times 10^5$ yr and that of JFCs $\sim 3.2 \times 10^5$ yr. The distribution of comets based on simulation studies is in agreement with the observed distribution of Jupiter family of comets. These studies are consistent with the earlier work in showing that Kuiper belt is the source of JFCs. Simulations also indicate that JFCs and HTCs switch between them in about a dozen times in a time scale of 4.5×10^5 yr.

Since the Kuiper Belt is believed to be the source of short period comets (i.e. Kuiper Belt objects, KBOs) considerable effort went into looking for KBOs and the first such object was discovered in 1992. Since then, large number of transneptunian objects (KBOs) have been detected. The estimated number of KBOs of sizes ~ 100 km with $30 < a < 50$ AU is about 10^5 . Simulation studies for the dynamics of KBOs show that the orbital characteristics of the scattered KBOs that enter into the solar system are quite similar to those of Jupiter family comets.

12.3. Origin of the Oort Cloud

The reservoir of comets generally called the Oort cloud is quite well established. The observable long-period comets can be understood reasonably well, based on the time evolution of new comets coming out of the Oort cloud. Therefore the origin of long-period comets essentially reduces to the problem of the origin of the Oort cloud. Various hypothesis have been proposed to explain the origin of the Oort cloud. They can all be divided roughly into two groups, interstellar and the solar system. The other possibility of comets forming at the present location of the Oort cloud itself is not feasible due to the extremely low densities, which make it difficult for the growth of the particles.

If interstellar comets do exist and enter the solar system at times then they should be seen with hyperbolic orbits. However, no such comet has been observed for the last 200 years or so. This observation can be used to put a limit on the number of interstellar comets in the solar neighborhood

to be $\leq 10^{-4}$ AU $^{-3}$. This shows that the number of interstellar comets entering the solar system at the present time is not large. In addition, capturing hyperbolic comets from interstellar medium is a highly unlikely process as a third body is required to dissipate the excess kinetic energy involved. It is quite possible that passage of the solar system through a Giant molecular cloud or dense region might result in the capture of comets leading to bound orbits around the Sun. One can also think of other scenarios which could have given rise to the Oort cloud. Although these are possible in principle, however there appears to be no concrete viable models based on such mechanisms.

The other possibility that comets is of solar system in origin implying that they were formed at the same time and as a part of the formation of Sun and planets has received considerable interest and attention. On this hypothesis, cometary material should be similar to that of the solar system material. This is borne out by the measurement of the isotopic ratio of $^{12}\text{C}/^{13}\text{C}$ in comets ~ 100 , comparable to the terrestrial value of 89.

However, the formation of comets in the inner solar system is highly unlikely due to the fact that the presently known chemical composition of comets requires a temperature at the time of formation to be quite low $\lesssim 100$ K to keep the volatiles like H₂O, CO₂, CO, NH₃ and CH₄ from evaporating. This led to the other possibility that the comets were formed in the outer parts of the nebula that formed the planets. The chemical composition of the solar system bodies can roughly be divided into three classes depending upon the characteristics of the elements present in them. For example, gases such as hydrogen, helium and noble gases stay as gas even at low temperatures, ice melts at moderate temperature and lastly the terrestrial materials like silicon, magnesium, and iron melt at higher temperatures. Table 12.3 shows the relative abundances of various elements in the solar system bodies. It is clear that Jupiter and Saturn were formed mostly of the original solar material like the Sun, while Uranus, Neptune and Comets were formed in the colder regions which account for the icy material. Therefore, probably comets were formed beyond Saturn.

Additional evidence for the low formation temperature of $T \leq 35$ K, comes from the observation of S₂ in comets. Additional support comes from the study of ortho and para ratio of H₂O, NH₃ and CH₄ in comets which indicate the temperature of formation of ice ~ 35 K. Thus there are several observational results which seem to show that comets are formed

Table 12.3 Relative abundances of atoms by mass in the solar system.

Elements		Sun	Terrestrial planets and meteorites	Jupiter	Saturn	Uranus, Neptune and comets
Gaseous	H	1.0	Trace	0.9	0.7	Trace
	He					
Icy	C					
	N	0.015	Trace	0.1	0.3	0.85
	O					
Earthy	Mg					
	Si	0.0025	1.0	Trace	Trace	0.15
	Fe					
	etc.					

Whipple, F.L. 1972. In *Motion, Evolution of Orbits and Origin of Comets* eds. Chebotarev, G.A. Kazimirchaka-Polonskaya, E.I. and Marsden, B.G. Dordrecht: D. Reidel Publishing Company, p. 401.

far from the Sun and in the cooler regions of the solar nebula, placing them beyond Uranus-Neptune zone, possibly the Kuiper belt.

In this connection it is interesting to note that Oort had proposed early on that asteroid belt could be the source region for the long-period comets. It was Kuiper who was the first to propose that due to the icy nature of the comet, they are more likely to be formed in the region of orbits of giant planets, a concept that has withstood over time.

The ejection of minor bodies appears to be a natural consequence of the accumulation process of giant planets. Due to gravitational perturbations of various planets, the orbit of some of these bodies can detach themselves from the bound system. Monte Carlo simulations have demonstrated clearly that such mechanisms can be present in the system. The results of such calculations have shown that the planets tend to eject icy planetesimals from their present zones to eccentric long period orbits with semi-major axis $\leq 10^3$ AU. At these distances the perturbations due to stellar and galactic sources tend to be important to push the orbits further into the region of the Oort cloud and thus detaching them away from the zone of influence of planetary perturbations. This can finally lead to a cloud with more comets at its centre compared to its outer region, similar to the Oort cloud. A typical result of the Monte Carlo calculations for the assumed initial hypothetical comet distribution confined to the ecliptic plane is shown in Fig. 12.4. They show the expected distribution in the plane perpendicular to the plane of the Galaxy for different times. The comets are more or less

randomized both in eccentricity and inclination in a time period of around 4.5×10^9 years and for distances beyond around 10^4 AU. It is also found that relatively more icy planetesimals are ejected out of Uranus-Neptune region compared to Jupiter-Saturn region. The dynamical calculations, thus indicate that the Oort cloud can be produced as a natural by-product of the various processes that could take place in the solar system during its lifetime.

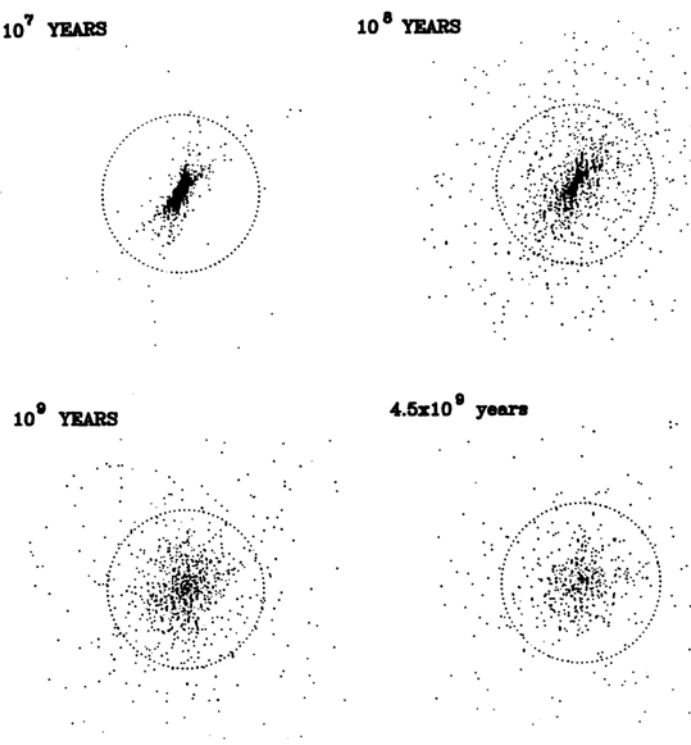


Fig. 12.4 The results of dynamical evolution of a cloud of comets ejected from Uranus-Neptune zone are shown projected onto a plane perpendicular to the galactic plane for several time intervals. The dotted circle with a radius of 2×10^4 AU separates the inner and outer Oort clouds (Duncan, M., Quinn, T. and Tremaine, S. 1987. *AJ*, **94**, 1330).

The best way to study the structure of the Oort cloud is to directly image the comets and make a statistical analysis. This is still a long dream as the object would have a magnitude ~ 42 in the inner region ~ 3000 AU and ~ 60 magnitudes at around 20,000 AU in the Oort cloud that it will not

be possible to detect them in the foreseeable future. It is possible in principle to detect objects in the inner regions of the Oort cloud through occultation of stars. This is again a long term goal. Therefore the only method that is available at the present time is to study the orbital distribution of known comets for inferring the structure of the Oort cloud. This is again a difficult proposition as many new comets may not come within 10 AU of the sun due to Jupiter, which can deflect many of them.

Until a few years ago the detection of objects in the Kuiper belt (\sim 40 AU) was a distant dream. But not any more as several hundred objects known as Kuiper belt objects have been detected. In the same spirit the objects will be looked for in the inner region of the Oort cloud with the hope of finding some in the not too distant future.

Although the presence of the Oort cloud is well-founded, questions pertaining to its origin, physics, dynamics, structure and stability are still uncertain. One method to get some idea of the age of the cloud is through the study of the isotopic ratios of elements. The $^{12}\text{C}/^{13}\text{C}$ ratio available for comets indicates a ratio of about 100. This ratio is more like the solar system value (89) rather than the average value of about 40 to 80 of the interstellar material (Chap. 5). This seems to show that comets were formed out of the solar nebula material about 5 billion years ago.

Dynamical studies which take into account the various perturbations indicate that the Oort cloud can account for the observed long period comets. The perturbation of the Oort cloud due to the encounter with Giant molecular cloud and galactic tidal force is found to be important, in addition to planetary encounters and passing stars. The passage of a perturber close to the Oort cloud can give rise to shower of comets. It can have severe effect on the Earth's environment, as revealed by the interpretation of geo-physical, biological and terrestrial records. The formation of short period comets from long period comets through diffusion process in the solar system has some difficulties, including accounting for the observed number of short period comets. This has led to the hypothesis that the source of short period comets may lie beyond the orbit of Neptune between 30 and 50 AU, probably the remnant of the non-accumulated material. This region is generally known as Kuiper belt. As ejection of minor bodies appears to be a natural consequence of the accumulation process of Giant planets, this process could have been responsible for accumulation of comets during the lifetime of solar system in the region of space, where one now finds the Oort cloud.

12.4. Taxonomy

The general scenario that emerges from the study of origin of comets is that, icy planetesimals (comet nuclei) reside mostly in the two regions of the solar system, namely Kuiper - Edgeworth Belt and Oort cloud(OC). The OC comets are the ones ejected from the giant - planet region of the solar nebula ($\sim 5\text{--}30$ AU). OC comets include long period comets and dynamically new comets. The Jupiter-family of comets (short period and Halley-type, JFCs) originate from Kuiper-Edgeworth Belt (>30 AU). Dynamical studies indicate that comets present in the Oort cloud originated roughly in equal proportion from each giant planet and the Kuiper belt. These studies have also shown the possibility of radial transport of material inward and outward of giant - planet region during the formation period of comets. During this time the nebular temperature was around 200 K near Jupiter (~ 5 AU) and around 30 K near Neptune (~ 30 AU). These studies indicate that JFCs should have been formed at lower temperature environment compared to those of long period comets. Therefore there would be variation in chemical composition among these classes of comets as well as differences in the same group. Therefore the study of the chemical composition of comets should give information on the proto-solar nebula chemistry and in turn on the processes that could have taken place in the early solar nebula.

The study of the molecular composition of volatiles in comets has helped a great deal in this regard. The molecular composition of a large number of comets derived from observations in the radio region has clearly shown a wide variation in the observed chemical composition among comets. Table 12.4 give the average volatile composition of five OC comets which differ substantially from that of OC Comet 1999S4(LINEAR). The Comet C/1999S4(LINEAR) is really an unusual comet. It is possible that the five comets which have similar composition, except CO and CH₄, were formed in the low temperature region, probably formed beyond 30AU from the sun, while Comet S4(LINEAR) could have formed around 5–10 AU.

Extensive compositional surveys have been carried out on a large number of comets. One such survey relates to the study of the production rates of C₂, C₃, OH, NH and CN in a homogeneous data set of 85 comets. It contained 39 Jupiter-family comets 8 Halley-type comets 8 dynamically new comets and 27 long-period comets. Although the overall chemical com-

Table 12.4 Composition of Oort cloud comets.

Comets	CO	CH ₄	C ₂ H ₂	C ₂ H ₆	HCN	CH ₃ OH
Average of 5 comets ^a	1.8-17	0.5-1.5	0.2-0.3	0.6	0.2-0.3	2
LINEAR	0.9 ±0.3	0.18 ±0.06	<0.12	0.11±0.02	0.10±0.03	<0.15

a: Comets Lee, Hale-Bopp, Hyakutake, Ikeya-Zhang, McNaught-Hartley

Adapted from Mumma, M.J. *et al.* 2003, Adv. Space Res., **31**, 2563.

position was similar in these comets, there was significant compositional grouping of comets likely to be related to their place of formation. In particular, there was a depletion of production rate ratio of C₂/CN (carbon-chain molecules) in a large number of short period comets belonging to Jupiter-family. This led to the classification of comets into two groups called, comets with typical mean values of C₂/CN ratio (0.06 ± 0.10) and comets with depleted abundance ratio of C₂/CN (-0.61 ± 0.35). The results of these studies also indicated that approximately one-half of Jupiter-family of comets belongs to a typical class, while the rest of the comets belong to the depleted class with varying degree of C₂/CN ratio. This has given rise to a new terminology ‘Comet Taxonomy’ in which comets are distinguished based on their carbon-chain production ratio, C₂/CN, as typical or depleted. Most likely the depleted comets originate in the Kuiper belt. This has direct relevance to the long standing question whether all or part of Jupiter-family of comets come from the Kuiper belt. The depletion of C₂/CN in some comets is attributed to primordial rather than due to evolutionary effect as no correlation with dynamical age was seen.

There are other types of observations which have direct bearing on the primordial chemical composition of the solar nebula and in turn on the formation sites of comets.

Deep Impact studies of Comet Tempel 1 and the studies of Stardust samples of Comet Wild 2 have provided detailed mineralogical content of dust particles in these comets. The presence of crystalline silicate and calcium - and aluminium - rich inclusions (CAIs) in the dust particles indicate that they must have been formed at higher temperatures ~ 1400 K or so. Therefore these dust particles are believed to have been formed in the hotter and hence in the inner regions of the solar nebula. Since these dust particles came from the icy comet that was formed in the Kuiper belt (outskirts of the solar system), this require mixing of material from the inner regions of the solar system with that of Kuiper belt region.

The enhancement of D, $^{12}\text{C}^{13}\text{C}$ and $^{15}\text{N}^{13}\text{C}$ seen in the dust particles from comets indicate that cometary material contain presolar material. Therefore there is also mix of solar system material with that of interstellar and proto-stellar material. All these studies could provide clues to the place of origin of comets in the solar system. They could also help in the understanding of the physical processes that led to larger scale mixing in the solar nebula. These studies could in turn provide important information with regard to the origin and evolution of the solar system.

12.5. Summary

Oort showed from the study of 19 comets, the existence of gravitationally bound spherical cloud of comets at distances larger than 10^4 AU, called the Oort cloud. The comets in the Oort cloud are perturbed by various forces which make them leave the system. Some of them are captured by the solar system and it can account for the observed long period comets. The formation of Oort cloud is by the accumulation of icy planetesimals ejected from the giant-planet region ($\sim 5\text{--}30$ AU). This is a natural outcome of the various processes that could have taken place in the solar system during its life time.

The diffusion process of long period comets in the solar system cannot explain the observed number of short period comets. Therefore short period comets is believed to come from a different source (>30 AU) called Kuiper Belt. Large number of objects in this region, called Kuiper Belt objects (KBOs) have been seen whose characteristics are similar to those of Jupiter family of comets. Therefore the general picture at the present time is that, long period comets comes from the spherical distribution of the Oort cloud, Halley type comets comes from the inner flattened region of the Oort cloud and Jupiter family of comets comes from the Kuiper Belt. Therefore comets are formed in the colder regions of the solar system which account for the icy material. There is also evidence for the large scale mixing of the material between inner and outer regions of the solar nebula.

Problems

1. How can one say from the appearance of a comet in the sky whether it is a new comet coming from the first time or whether it is one which has already been seen?

2. What is Jupiter's family of comets? What is the most probable origin of these comets?
3. Is there any evidence that the Oort cloud was formed about 5×10^9 years ago? Can you think of some other process by which the Oort cloud be of more recent origin, formed some 10^6 to 10^7 years ago?
4. Is there any way to test observationally the existence of the Oort cloud?

References

The basic idea of the cloud of comets is from the classic paper

1. Oort, J. 1950. *Bull. Astr. Inst. Netherlands* **11**, 91.

Other relevant paper

2. Kaib, N.A. and Quinn, T. 2009. *Science*, **325**, 1234.

Earlier references to the cometary clouds can be found in

3. Opik, E. 1932. *Proc. Am. Acad. Arts and Sciences*, **67**, 169.

The best book on the origin of Comets is the following:

4. Bailey, M.E., Clube, S.V.M. and Napier, W.M. 1990. *The origin of Comets*. Pergaman Press.

A good account of several aspects are given in the following papers:

5. Dones, L., Weissman, P.R., Levison, H.F. *et al.* 2005. In *Comets*, Eds. M.C. Festou, H.U. Keller and H.A. Weaver, Univ. Arizona Press, Tucson, p. 153.

6. Morbidelli, A. and Brown, M.E. 2005. In *Comets*, eds. M.C. Festou, H.U. Keller and H.A. Weaver, Univ. Arizona Press, Tucson, p. 175.

Papers pertaining to KBOs: First Detection

7. Jewitt and Luu, J. 1993. *Nature*, **362**, 730.

The following paper may be referred for a good summary

8. Barucci, M.A., Doressoundiram and Cruikshank, D.P. 2005. In *Comets*, Eds. M.C. Festou, H.U. Keller and H.A. Weaver, Univ. Arizona Press, Tucson, p. 647.

For a discussion pertaining to Taxonomy see also Section 6.6

This page intentionally left blank

CHAPTER 13

Relation to Other Solar System Studies

Comets appear to have a close relationship with other objects of the solar system like asteroids and meteorites. The meteor streams which often appear in the sky are also believed to come out of the cometary material. The study of the nature and composition of dust particles collected at high altitudes through rockets and satellites indicates that they could be of extraterrestrial origin and are generally associated with comets. In recent years comets have also attracted great attention in view of their possible impact on the life of our planet. This has come about basically from the observation that the complex molecules of various kinds appear to be present in the nuclei of comets. This in turn is related to the chemical composition of the primordial material of the solar system. We would like to elucidate some of these aspects here.

13.1. Asteroids

The minor planets of the solar system were classified as objects having dimensions less than Pluto. The Ceres which was discovered in 1801 was classified as a minor planet. This was followed by the discoveries of other minor planets called Pallas in 1802, Juno in 1804 and Vesta in 1807 and so on. However, these objects turned out to be far fainter than expected as their orbits are closer than Jupiter's distance. It was realized that these are of different kind of objects. Hence, minor planets are also called asteroids. The largest concentration of asteroids is in the range of 2 to 3.5 AU, placing them between the orbits of Mars and Jupiter. This is generally called the *asteroid belt*. There are two other minor concentrations of asteroids known as Hildas and Trojans which are located at distances of around 4 and 5 AU respectively. It is estimated that more than around 100,000 asteroids have

been seen at least once. The computed orbits are accurately known for a large number of asteroids. The period for most of the asteroids is in the range of around 3 to 6 years. They revolve round the Sun in the same direction as the principal planets. Most of them have orbits which lie nearly in the plane of the Earth's orbit and the average inclination is about 10° . The average eccentricity of the orbits is around 0.15 with sharp cut offs on either side.

Observing the light curve, it is possible to determine the rotation period and shape of asteroids. The rotation period of most of the asteroids is of the order of a few hours. For example the rotation period of Eros $\sim 5^h 17^m$ and that of Juno $\sim 7^h 13^m$. The deduced mean geometrical albedo of asteroids is rather low, ~ 0.05 which implies that they are extremely dark objects. The diameter of asteroids can vary from the lower set limit of about 100 meters to about 1000 km as seen in the case of Ceres. Most of the asteroids are found to be extremely irregular in shape. This indicates that they were most probably produced out of the break up of some parent body. In addition, the collisions of asteroids within the belt is quite frequent and this leads to erosion and fragmentation.

Since 1965, space missions such as, the Mariner Series, the Vikings and the Hubble space telescope have been used for the study of asteroids. The two Martian satellites, Phobos and Deimos, two likely captured asteroids have been studied in great detail. They are found to be approximately elliptical in shape with radii of $13.5 \times 10.8 \times 9.4$ km and $7.5 \times 6.2 \times 5.4$ km respectively. The mass of Phobos derived from the perturbations of the spacecraft is around 1.3×10^{19} gm. The estimated average density of Phobos and Deimos is around 2.0 gm/cm³ and the geometric albedo ~ 0.06 . High resolution observations have shown many surface features, including large craters. More recent spacecraft missions which passed by closer to asteroids have given detailed information about their shapes, sizes and surface features. Table 13.1 gives a list of some of the spacecraft missions to asteroids. The NEAR-shoemaker spacecraft after circling the asteroid 433 Eros for a year landed finally on this asteroid. The ultraviolet observations carried out with satellites on a large number of asteroids show that the geometrical albedo decreases towards shorter wavelengths. For example, the geometric albedo for Ceres at wavelengths 4300 and 2600 Å is about 0.031 and 0.023 respectively. It is seen that the albedo of asteroids seem to be almost in the same range as that of cometary nuclei.

Table 13.1 Spacecraft to asteroids.

Spacecraft	Name of the asteroid	Diamension of the asteroids (diameter, km)	Remarks
Galileo	Gaspara	19 × 12 × 11	Craters present, S-type
	243 Ida Dactyl	56 × 24 × 21	Craters present, S-type
NEAR-Shoemaker	253 Mathilda	52	Large craters present, density ~1.3g/cm ³ C-type
	433 Eros (NEA asteroid)	34 × 13 × 13	Craters present density ~2.7g/cm ³ S-type, landed on Feb. 12, 2001
Deep space 1	9969 Braille	2.1 × 1 × 1	Detected magnetic field
Stardust	5535 Annefrank	6.6 × 5.0 × 3.4	Appear angular, flat surfaces
Hayabusha	NEA 25143	0.5	Exhibit rocks and boulders, smooth areas, no impact craters
	Itokawa		

Infrared observations have given information about the surface composition of asteroids through the detection of characteristic bands of minerals. The relative abundances of silicates like olivine, pyroxene, feldspar and so on has been determined. Most of them fall broadly into two types with respect to their chemical composition: the C type, the darkest asteroids due to the presence of carbonaceous material and the S type which has silicates like olivine and pyroxene. The C type asteroids are more numerous comprising around 60% of the observed asteroids.

The emission spectra of Trojan asteroid (624) Hektor is compared with the spectra of cometary dust in Fig. 13.1. This emission spectra is similar to the spectra of Comets Hale-Bopp and Schwassmann-Wachmann.

The origin of asteroids is still not known but they could be of cometary origin. The short-period comets after many revolutions could become inactive as most of the volatiles would have vapourized. Depending on the presence or absence of volatiles, comets are called ‘Dormant’ (the volatiles are not coming out due to mantle formation) or ‘Extinct’ (when volatiles

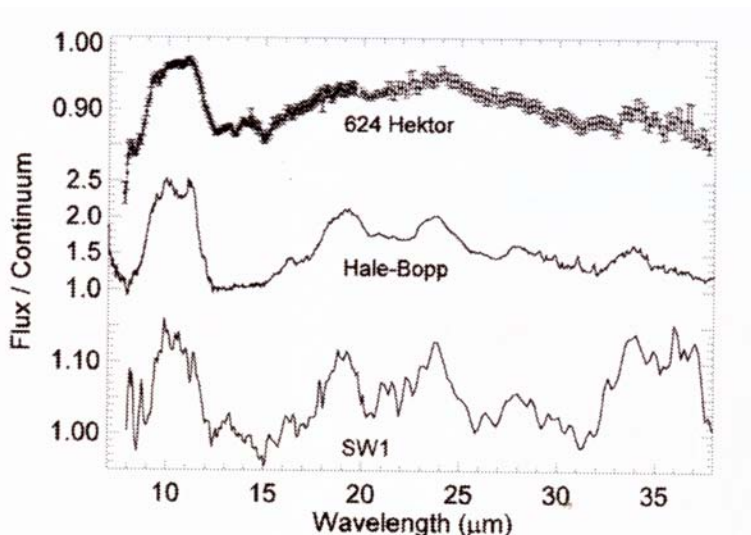


Fig. 13.1 Comparison of the emission spectrum in the wavelength range of 5 to 40 μm of Comets Hale-Bopp and Schwassmann-Wachmann 1 with a Trojan asteroid Hektor. There is similarity between them (Fernandez, Y.R. *et al.* 2007. In *Asteroids, Comets and Meteors*, IAU Symposium 229, Cambridge University Press, Cambridge, p. 121).

have evaporated). Such residual nuclei of comets are *indistinguishable* from those of asteroids. There are two other suggestions with regard to the origin of asteroids and are found in the belt itself. The irregular shape of the asteroids indicates that they were produced due to the break up of some parent body at its present location. There is the other possibility that the material that exists in the present location, is the material that could not have accreted into a planet due to some reason.

There are a number of asteroids with large orbital eccentricities and they are found to come regularly to the Earth. Their perihelion lies interior to Earth's aphelion and are called 'Apollo objects', named after the first object of this kind to be discovered. There is another class of asteroids which includes those which have somewhat larger orbits with perihelion of around 1.02 to 1.3 AU and are called 'Amor objects'. In general these two populations are not fundamentally different from each other and are often called with a single population as Earth-approaching Apollo-Amor objects. The mean dynamical life time of Earth-crossing objects is $\sim 10^7$ to 10^8 yrs, which is short compared to the age of the solar system. Therefore there should be a constant source of these objects. Dynamical simulations have

shown that the orbit of comets can evolve into asteroid orbits. Therefore some of the asteroids can be extinct or dormant comets. It is likely that the Earth-crossing asteroids are old and non-active comets. In fact, the traditional distinction between asteroids and comets is becoming nebulous at the present time, as some of the asteroids with comet like orbits could be dormant comets. There are some asteroids which appear to be parent objects to some meteor streams, for example the orbit of (3200) Phaeton coincides with that of the Geminid Stream.

There could be comets which orbit in the main asteroid belt. An interesting example of this type is the Shoemaker-Levy 9 prior to its capture by Jupiter. Before it was captured by Jupiter, it was located in the Hilda asteroid zone. There could be other comets, in the Hilda group of asteroids.

The object 2060 Chiron discovered in 1977 was classified as an asteroid. It has an orbital period of 51 years and eccentricity of 0.38. It has a semi-major axis of 13.7 AU which lies in between Saturn and Neptune. Suddenly in 1988, brightness variations were seen and coma was formed and it was detected. The emission bands of CN were also detected in 1990. Extensive observations of this object indicated that Chiron is a comet. Calculations based on the cometary nucleus model as discussed earlier (see Sec. 11.2) can explain the observed out-gassing and indicated that it will last for a long period of time.

The asteroid 4015 is an interesting object in which a comet nucleus has become an asteroidal object. This object was discovered in 1979 and was classified as an asteroid. When the accurate orbit of this object became available, it was possible to identify an object during its earlier time in its orbit. The object which had the same orbit as that of asteroid 4015 and was identified in the Palomer sky survey images taken in 1949 was actually a comet and called Wilson-Harrington. It had plasma tail at that time. This is an example of a comet turning into an asteroid. This is now called 4015 Wilson-Harrington.

The other example is the object 7968 Elst-Pizarro (133/E-P) which resides in the main asteroid belt but show recurrent comet-like activity, such as showing temporary dust tail etc. The cause of such activity could be that volatile regions may be located near one of the rotational poles of the nucleus. When this region tilts towards sun, it is exposed to solar radiation. This sublimes volatiles leading to comet-like activities. The cases of such unusual behaviour could arise from population of asteroid-comet transition objects. Therefore there may be large number of comets posing as asteroids in the asteroidal belt. They could be there in dormant or extinct state. It

is difficult to identify these objects. Even though cometary nuclei contain much more ice than asteroids, it is likely that evolved comets may have many characteristics similar to asteroids.

These studies seem to indicate that whether the volatiles are present or not depend upon the dynamical life time, life time for the volatile component to disappear and on the processes that could have taken place inside the nucleus. Hence, depending upon these factors it is possible to have different situations.

Binaries

The search for satellites of asteroids (if any) dates back to 1801 and it had been an unsuccessful one. The serendipitous discovery of a satellite around the asteroid 243 Ida came from the images taken by the Galileo spacecraft when the spacecraft visited 243 Ida in 1993. The satellite called Dactyl is about 1.5 km across and orbits Ida at a distance of approximately 85 km with a period of 1.5 days. Both Ida and Dactyl are S - type asteroids. This led to the detection of satellites around a large number of asteroids. The advantage of a binary system is that it is possible to derive the system mass from the observation of their orbits. But in practice it is rather difficult to calculate the orbits because the data is limited. Hence the orbits and the masses have been determined for a small number of binary asteroids. For example, the estimated mass of (87) Sylvia, the main belt asteroid, is around 14.78×10^9 kg and that of 243 Ida is around 0.042×10^9 kg. In the main belt the dominant process for the formation of binaries is through collisions. Numerical simulations have shown that after collision the fragment may be captured or the fragment may be re-accreted around the remnant primary. The asteroid Sylvia has been found to be a triplet system. Numerical simulations have shown that collisions can produce triplets as well as binaries.

13.2. Meteorites

The meteorites are extra-terrestrial bodies which survive the passage through Earth's atmosphere and fall to the ground. This is generally accompanied by a flash of light in the Earth's atmosphere like that of a meteor. Only the largest objects of some several tens of meters in diameter create large impact craters when they hit the ground. Large number of meteorites are known at the present time. Relatively more meteorites are found in

Antartica as they are preserved over long periods of time. It is possible that due to the fragmentation of the body as it passes through the Earth's atmosphere, it may be scattered over hundreds of kilometers on the Earth.

Since early times, meteorites have been studied extensively as they were shown to be extra-terrestrial in origin. Also, these are only extra-terrestrial objects that were available for laboratory investigation for a long time. Large number of meteorites have been studied over the years with regards to their structure, morphology, chemical composition, origin etc. The two meteorites of particular interest are the Murchison and Allende meteorites. Murchison meteorite fell near Murchison in Australia in September 1969. Allende meteorite fell near Pueblito de Allende in Maxico in February 1969. Since Murchison and Allende meteorites were very large in , large amount of material were available for laboratory investigation. Hence extensive investigations of various kinds were carried out in the laboratory on these two meteorites. The great advantage being the material from these meteorites were picked up soon after their fall and hence the contamination is minimal.

A detailed analysis of the chemical and mineralogical composition of several meteorites indicate that they can broadly be classified into three groups. They are iron, stony-iron and stony meteorites (Table 13.2). The iron meteorites are essentially pieces of metal containing Fe-Ni alloy. The Stony-iron contains mixture of stony material and metallic iron. The stony meteorite consists of mostly silicate type of material (They are generally mistaken for terrestrial rocks). Stony meteorites are further classified into two types, chondrites and achondrites. The most common form of stony meteorite is the ordinary chondrite in which mm size spheroidal globules called chondrules are present. Chondrules are essentially silicate mineral assemblages which had an independent existence prior to the formation of the meteorite. The sub-group in chondrites is called carbonaceous chondrites which are darker stones containing relatively high carbon content. They are also well known for having mm sized refractory inclusions (Ca-Al-rich inclusions). The mineralogy in dominated by oxides and silicates. The stony meteorite without chondrites are called achondrites and are relatively rare. The chondrites have a composition which is similar to that of the photosphere of the sun, for all but the most volatile elements. This suggest that chondrites are the materials that formed at the same time as the sun from the solar nebula and since then, they have undergone very minimal chemical modification. The idea of primitive character of chondritic meteorites is also strengthened by their radiometric age, which is roughly the age of the solar system. On the other hand, achondrites differ in com-

position considerably from that of the sun. The percentage fall of these types of meteorites are around 94% stony (chondrites, 86%; achondrites, 8%), 5% iron and 1% stony-iron.

Table 13.2 Main meteoritic groups.

Group	Main Characterization	Main Components
Iron meteorites	More than 90% metal	Nickel-Iron
Stony meteorites:	More than 75% stony material	
(i) chondrites	chondrules	Silicates, solar in composition except volatile elements
(ii) Achondrites	No chondrules	Silicates, differ from solar composition
Stony-Iron meteorites:		
(i) Pallasites	Olivine in Fe-Ni alloy network	Olivine, metal
(ii) Mesosiderites	silicate and metal grown together	silicate, metal

Meteorites are classified into two groups depending on their presumed origin. They are called as Primitive meteorites and Differentiated meteorites. The primitive meteorites are not subjected to high temperature and high pressure environment. Therefore the material remain the same from the time of formation. However differentiated meteorites contain highly processed material as a result of internal heating. They could also be the fragments of differentiated parent bodies. Most of the stony meteorites are primitive. Iron and stony-iron are differentiated meteorites. Most likely, the iron must have originated from the metallic core of the parent body and stony-iron must have come from the layers between the core and the mantle composed of silicate materials. This is possible if the bodies in the asteroid belt could differentiate and due to collisions many of them could be fragmented.

Large number of minerals of various types has been identified in meteorites. The important minerals are olivine and pyroxene. The sulphide in chondrites is almost always FeS(troilite). In addition a variety of organics

have been identified in Murchison meteorite. Several of these are common with biological systems

Presolar Grains

Interesting results came out of the study of anomalous isotopic composition of several elements in meteorites. These anomalies have been seen mostly in inclusions. Here the isotopic anomalies refer to values in comparison to that of average solar system isotopic composition for a given element. In particular, the noble gases are so rare, any deviation from the average value can be quite significant.

It is hard to explain these observed isotopic anomalies in terms of the local production mechanisms such as irradiation, mass fractionation process or known radioactive decay. Hence, these anomalies represent materials (grains) injected into the solar system from nucleosynthetic sites. These are generally called as *presolar grains*.

Presolar grains detected in meteorites are mostly carbon bearing, namely diamond, graphite and silicon carbide (Table 13.3). Diamond particles are more abundant than those of presolar graphite and SiC particles. The isotopic ratio of $^{12}\text{C}/^{13}\text{C}$ determined from single SiC grains has values around 40 to 70 (Fig. 13.2). Spherical graphite grains show variation in $^{12}\text{C}/^{13}\text{C}$ ratio of around 2 to 6000 as compared to the solar value of 89 (Fig. 13.2).

The source of some of the presolar diamond particles could be supernovae (Table 13.3). This comes from the fact that Xe isotopes ^{134}Xe , ^{136}Xe and ^{124}Xe , ^{126}Xe present in diamonds is produced by the r - and p - processes respectively. The presence of isotopic signature of s - process elements in SiC grains suggest that around 99% could arise from AGB stars. The rest of 1% SiC grains called X - grains appear to have come from supernova ejecta. Isotopic abundances of carbon in presolar spherical graphite particles has indicated the complexity of the grain in showing that contributions can come from various stellar sources such as Wolf-Rayet stars, supernova, AGB (Asymptotic Giant Branch) atmospheres etc. This can be seen from the distribution in $^{12}\text{C}/^{13}\text{C}$ ratio as shown in Fig. 13.2.

Figure 13.3 shows a section of a spherical grain from the Murchison meteorite. It shows clearly the presence of a TiC at its centre. It is clear that TiC must have acted as a nucleus for the graphite to condense. The spherical graphite grain with TiC at its centre clearly indicates that it

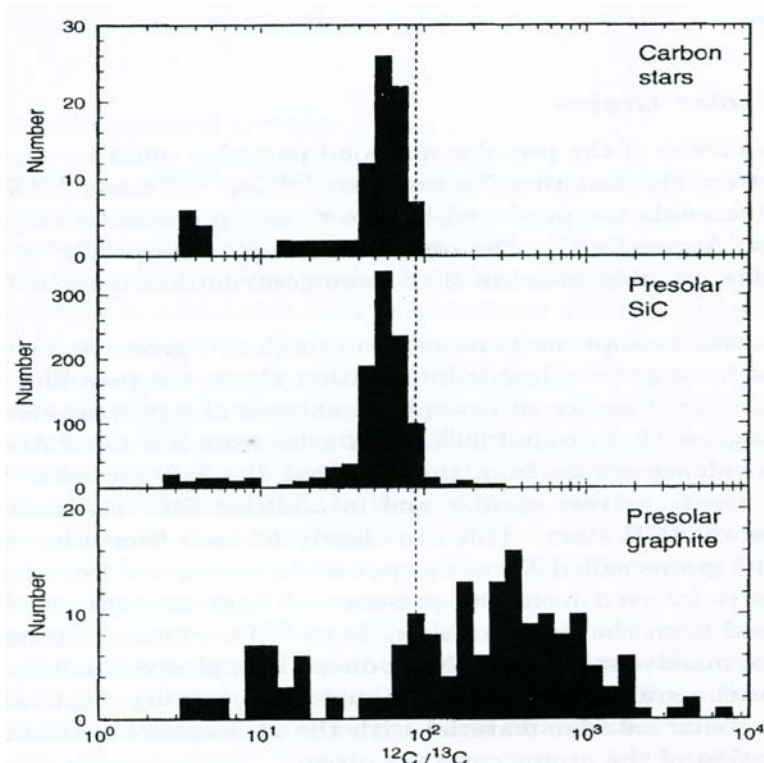


Fig. 13.2 Shows the distribution of the isotopic ratio $^{12}\text{C}/^{13}\text{C}$ in the atmosphere of Carbon Stars and presolar SiC and graphite grains seen in meteorites. The dashed line refers to the solar system value of 89. The source of presolar SiC grains is consistent with that of carbon stars. The presolar graphite grains appear to come from various sources (Whittet, D.C.B. 2003. *Dust in the Galactic Environment*, Institute of Physics Publishing, Bristol).

is presolar graphite grain. It must have originated from a carbon star. Presolar oxide grains have also been identified in meteorites. PAHs have been detected in samples of Allende and Murchison meteorites. Many of the meteorites show enhanced D/H and $^{15}\text{N}/^{14}\text{N}$ ratios in bulk samples. The primary carrier of these anomalous ratios are the organic compounds.

FeS grains in meteorites are also presolar in origin. Oxide grains are likely to have been produced in oxygen-rich environment. Hence, pre-solar grains formed in a distant environment could have been incorporated into the solar nebular material with normal isotopic composition, out of which

Table 13.3 Presolar grains detected in meteorites.

Composition	Diameter (μm)	Origin
C(diamond)	0.002	SN
SiC	0.3 - 20	AGB, Nova
C(graphite)	1 - 20	AGB, SNII, Nova
SiC (type X)	1 - 5	SN
Al_2O_3 (corundum)	0.5 - 3	RG,AGB
Si_3N_4	~ 1	SN II

Hoppe, P.M. and Zinner, E. 2000. *J. Geophys. Res.*, **105**, 10371: Reproduced by permission of American Geophysical Union.

the planetary bodies of the solar system were formed. The volatiles of the pre-solar inclusions could have been lost during the process of accretion into the bodies.

Comets can in principle, explain the origin of primitive meteorites, but not the processed mateorites which have gone through thermal evolution. Hence fragement of asteroids may be a better source of observed meteorites.

The similarity between the meteorites and asteriods comes primarily from their composition, which is reflected in their emission spectrum of these objects. Figure 13.4 shows the emission spectrum of Trojan asteroid Hektor and two meteorites ALH 77003 and Tagish Lake. There is a great similarity between Hektor and Comets Hale-Bopp and Schwassmann-Wachmann 1. These studies indicate that C type asteroids could possibly be the source of carbonaceous chondrites while S type asteroids may be the source of some stony meteorites.

13.3. Meteor Streams

Another interesting aspect, presumably associated with the cometary dust particles, is the meteor showers seen in the sky. The small particles comprising the meteor streams revolve round the Sun, producing meteor showers whenever their orbit crosses the Earth orbit. They are actually made visible as they burn away in the Earth's atmosphere. Many of the meteor showers are seen regularly at specific times of the year (Fig. 13.5). The most spectacular display in the sky ever recorded is that of the Leonid meteors which were seen in the month of November of 1833. In a span of a few hours, roughly about 20,000 meteors appear to have been seen. At

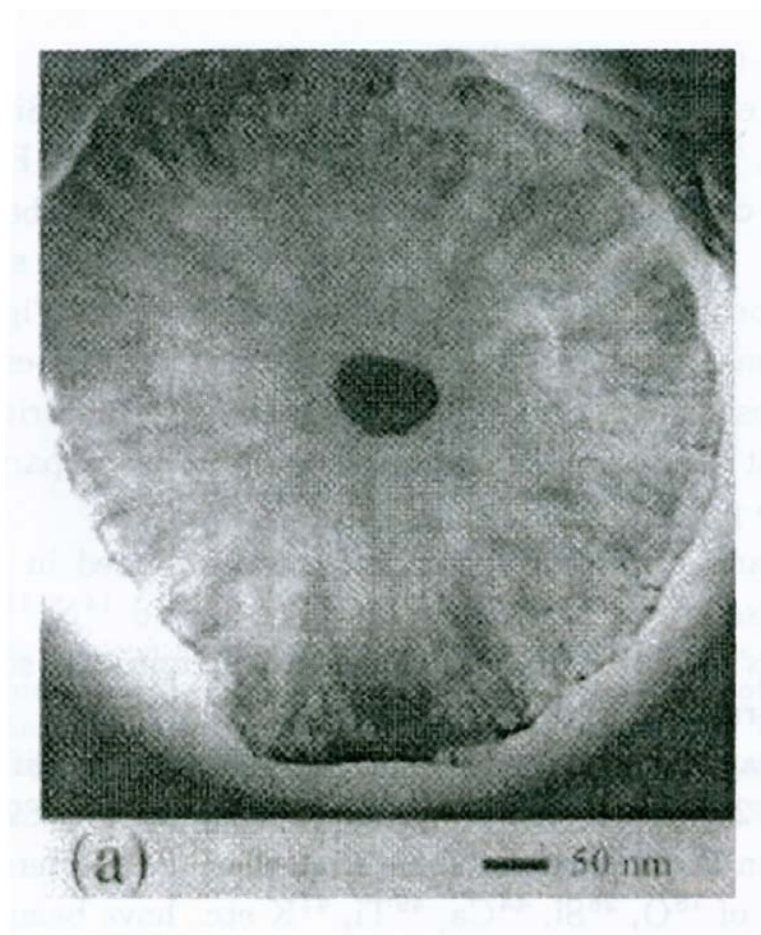


Fig. 13.3 A transmission electron micrograph of a thin section of presolar graphite grain from Murchison meteorite. The long nucleus at its centre is in TiC crystal of $0.07\ \mu\text{m}$ in size. This must have acted as a nucleation centre for graphite to condense (Bernatowicz, T.J. 1997, In *From Stardust to planetesimals*, eds. Pendleton Y.J. and Tielens A.G.G.M., *ASP Conf. Ser.*, **122**, p. 227: By kind permission of the Astronomical society of the Pacific Conference services).

the present time several hundred meteor streams exist in the solar system. What is of interest of course is the orbital characteristics of these meteors. From the observed direction and velocity, it is possible to get the orbit of the individual meteors in the Swarm.

It has been found that the elements of orbits of many of the meteor

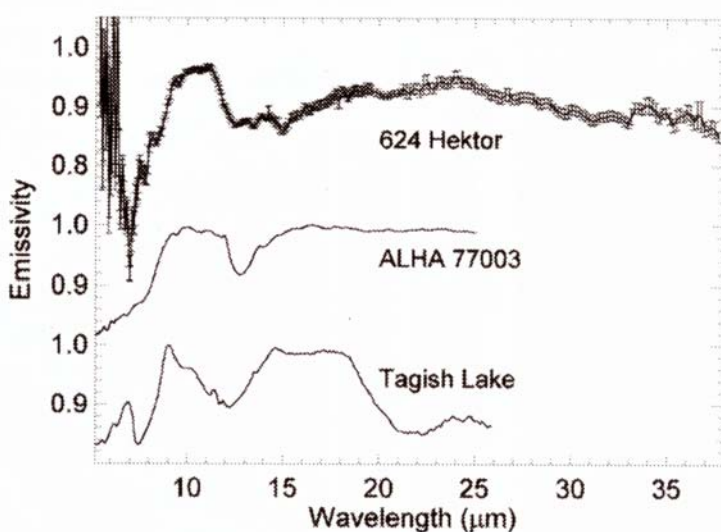


Fig. 13.4 Comparison of the emissivity in the wavelength range 5 to 40 μm of two meteorites ALH 77003 and Tagish Lake with the Trojan asteroid Hektor. There is similarity in the curves (Emery, J.P., Cruikshank, D.P. and van Cleve, J. 2006. *Icarus*, **182**, 496).

showers are very similar to those of the orbits of the known comets. In 1866, Schiaparelli showed that the Perseids shower had the same orbit as the Comet Swift-Tuttle. The showers Eta Aquarids and Orionids have the same orbit as Comet Halley and can be seen during the months of May and October. Of course, not all the meteor showers have been identified with the individual comets. Conversely, not all the known comets are associated with the corresponding meteor streams. Since the association between the two is well established only for a few cases out of a large number of known comets (Table 13.4) and meteor streams, at first sight these results might cast some doubt on the real association between the two. This could arise partly due to inaccuracies in the measured parameters of the orbit of the meteor stream. A more important reason could be that the dynamical evolution of the meteor stream could have modified the orbit such that it is different from that of the parent comet. Therefore a simple comparison of the two orbits may not be appropriate. On the other hand, the position of the perihelion of the comet and the meteor shower is a better indication of the real association as has been shown to be true for a large number of cases. Therefore, on a closer examination, the association between the comets and

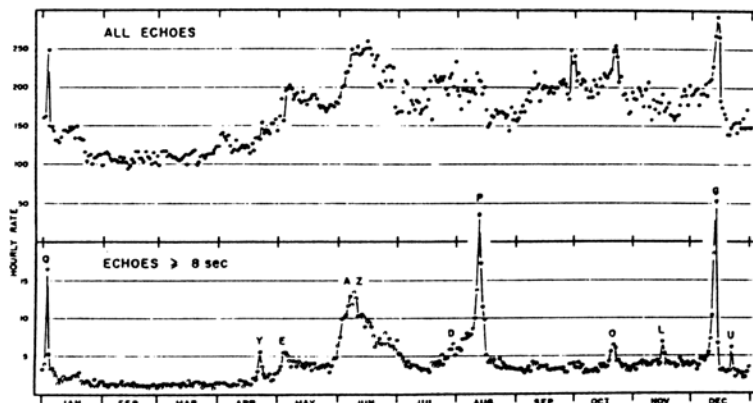


Fig. 13.5 A typical hourly rate of meteors seen throughout the year as observed by the Ottawa Meteor radar. The top figure represents total echo count and the bottom curve is for echos having duration ≥ 8 secs. The peaks represent showers corresponding to Q (Quadrantid), Y(Lyrid), E(η Aquarid), AZ (Arietid-Zeta-Perseid Complex), D(δ Aquarid), P (Perseid), O (Orionid), L(Leonid), G(Geminid) and U(Ursid) (McIntosh, B.A. 1991. *Comets in post-Halley Eta*, eds. R.L. Newburn, Jr., Kluwer Academic Publishers, p 557).

the meteor showers seems to be real. Let us first examine the formation of a Swarm of particles from a comet in a qualitative manner. The dust particles coming out of the nucleus are carried away by the gas. Since the flow of the dust from the nucleus is maximum near about the time of perihelion passage, it is also the place where most of the dust is introduced into the meteor stream. Each of these dust particles becomes independent and the orbit of these particles differs from that of a comet. The orbit of the dust particles depends upon its velocity and the effect of radiation pressure. This varies with the size of the particles and their physical properties. Very small size particles are blown out of the system. The particles both lead and lag behind the comet and eventually lead to a continuous belt within a few revolutions of the period of the comet. The various particles in the meteor stream are subjected to various dispersive and degenerative effects, like gravitational perturbation by the planets, collisions and radiation pressure and so on. Therefore the orbit of these particles evolves into orbits which are difficult to predict. This may result in the orbit of particles in the meteor stream quite different from that of the orbit of the parent body. In fact the perturbations could disrupt the orbits of the particles such that it may make them sway away for crossing the Earth's orbit. This can possibly

explain rather poor association between the comets and the meteor showers. But from the good correlation between the perihelion, it can be inferred that the meteor streams are of cometary origin.

Table 13.4 Comets and their associated showers.

Comet	Associated shower	period of visibility
1P/Halley	η Aquarids Orionids	April 19 - May 28 Oct.2- Nov.7
109P/Swift-Tuttle	Perseids	July 17 - Aug.24
21P/Giacobini-Zinner	Draconids	Oct 6 - 10
55P/Tempel-Tuttle	Leonids	Nov 14 - 21
8P/Tuttle	Ursids	Dec 17 - 26
1861 G1	Lyrids	April 16 - 25

It is interesting to see from Fig. 13.5 that some profiles have two maxima and others have one. This could be related to the fact that the orbital parameters of the particles released from the comet before and after perihelion passage could differ slightly, which is a function of the mass and ejection velocity of the particles. This difference increases with time possibly leading to two streams close to each other.

A very interesting study pertains to Comet Tempel-Tuttle and its associated Leonid meteor streams covering the meteor data over the period 902 to 1969. The comet and the meteor showers have roughly the same period of about 33 years. The comet itself does not appear to have been observed prior to 1366, although the Leonid meteors have been recorded even upto the year 902 A.D. From the presently known orbit of the Comet Tempel-Tuttle, the orbit could be extrapolated backwards in time and the dates around which the meteor showers must have taken place can be calculated. A comparison of the calculated and the observed dates for the period between 902 to 1997 is shown in Table 13.5. The agreement between the two suggests that most of the particles of Leonid showers are from the Comet Tempel-Tuttle.

Table 13.5 Computed and observed dates of Leonid Meteor Showers.

Computed (Based on Tempel-Tuttle orbit)	Shower maximum time (observed)
902 Oct 12.7	Oct 13
1035 Oct 13.2	Oct 14
1202 Oct 18.7	Oct 18
1366 Oct 22.4	Oct 21,22,23
1538 Oct 25.0	Oct 26
1625 Nov 7.5	Nov 4,5,6
1799 Nov 12.5	Nov 11,12
1866 Nov 13.7	Nov 14.1
1900 Nov 15.7	Nov 15-16
1932 Nov 16.5	Nov 16-17
1969 Nov 17.0	Nov 17.4
1997 Nov 17.4	

Yeomans, D.K. 1981. *Icarus* **47**, 492.

13.4. Particles Collected at High Altitudes

Particle collection at high altitudes of the Earth's atmosphere is another way of studying extraterrestrial dust particles and their possible origin. Various methods have been used for the collection of particles based on recoverable rockets, balloons and aircraft. These particles are generally called Interplanetary dust particles (IDPs). The extensive collection of IDPs from the rarefied air in the stratosphere is carried out with NASA U2 aircraft, which flies at a height of about 20 km. The particles collected from these flights are subjected to a thorough laboratory investigation, not only to isolate the terrestrial contamination but also to study the morphological, structural and chemical properties of individual IDPs, in spite of their small size. Large number of the particles can be attributed either to rocket exhaust or to other known particle types. Many other particles cannot be explained as contamination from known causes and they could be extraterrestrial in origin. Roughly all these particles can be classified into three categories; 60% as chondritic, 30% as iron-sulfur-nickel and 10% as mafic silicate types. The chondritic particles are aggregates of small size grains of about 1000 Å. The size of the particles varies from 4 to 25μ . The grains are highly porous as well as compact. The elemental abundances of Fe, Mg, Si, C, S, Ca, Ni, Al, Cr, Mn and Ti in the first category of particles are in close agreement with the bulk compositions of chondritic meteorites. The abundances of C, S, Na and Mn indicate that the particles

are volatile rich in composition and also have a black appearance because of the high content of carbon. The composition of iron-sulphur-nickel type of particles is similar to that of meteoritic troilite. The silicates are olivines and pyroxene. Evidence for the extraterrestrial origin of these dust particles comes from several sources. The direct proof for the extraterrestrial nature comes from the observations of the presence of solar noble gases, the deuterium enrichment (i.e. large D/H ratio) and the presence of solar flare tracks in mineral grains within the particles. Their extraterrestrial nature is also indicated by the presence of ^{10}Be , which is produced by cosmic ray bombardment.

The infrared transmission spectra between 2.5 and 25 μm of a large number of chondrites type of IDPs shows the presence of a strong 10 μm silicate absorption feature and possibly the 3.4 μm feature. They can be classified into three groups as olivines, pyroxene and layer-lattice silicates. Particles in the olivine and pyroxene group are mostly crystalline in nature rather than amorphous. The carbonaceous material typically present is around 2–8% of the particle by mass. Carbonates are the important secondary material in layer-lattice-silicate IDPs, due to the presence of their characteristic feature at 6.8 μm . The Raman spectra of several IDPs show double peaks at $\sim 1360 \text{ cm}^{-1}$ and 1600 cm^{-1} , (7.38 and 6.25 μm). These are due to C - C vibrations of carbon. They are characteristic of aromatic molecular units smaller than 25A. This indicates the presence of PAHs of some kind.

The infrared spectra of two Pyrrhotite - rich grains from IDPs are shown in Fig. 13.6. They show a strong and broad feature around 23.5 μm which is identified with FeS stretch feature (troilite). This is similar to circumstellar feature. Iron sulphide was also identified in the dust component of Comet Halley during the spacecraft encounters.

The major form of non-crystalline silicate in IDPs are the GEMS (Glass with Embedded Metal and Sulphides). The sizes of GEMS is around 0.1 to 0.5 μm in diameter. It contains nanometer sized FeNi metal and Fe - rich sulphide grain embedded in silicate grains. The bulk composition of GEMS are approximately chondritic for the major rock forming elements.

The chemical and mineralogical information indicate that pyroxene-rich IDPs and olivine IDPs are from comets (Fig. 13.7). The overall properties pertaining to the physical and chemical nature of these particles strongly suggest that many of them are of cometary origin containing possibly some component of presolar origin. Supporting evidence comes from the presence of meteor showers as well as the factual information that the vapourized

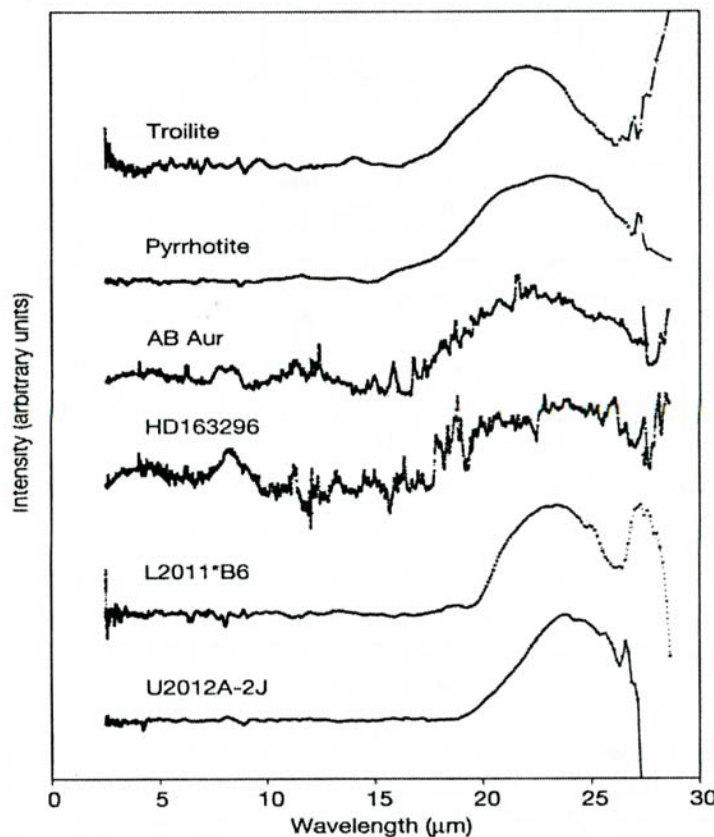


Fig. 13.6 Infrared Spectra of IDPs (U2012A-2J and L 2011*B6), Herbig Ae/Be stars (AB Aur and HD 163296) and FeS (troilite). The residual spectra for AB Aur and HD 163296 is shown after subtracting the best model fit from the observed spectra. The dust components used in the model are, glassy silicate, forsterite, carbonaceous material, metallic iron and water ice. The mineral of U2012A-2J is dominated by pyrrhotite and that of L2011*B6 by low-NiFi-Sulphides (Keller, L.P., Hony, S., Bradley, J.P. *et al.* 2002. *Nature*, **417**, 148).

material of the comet at each apparition is dispersed into the interplanetary medium, some of which may find its way on to the Earth.

FeS grains seen in IDPs, meteorites, comets, young and old stars indicate the similarity among them.

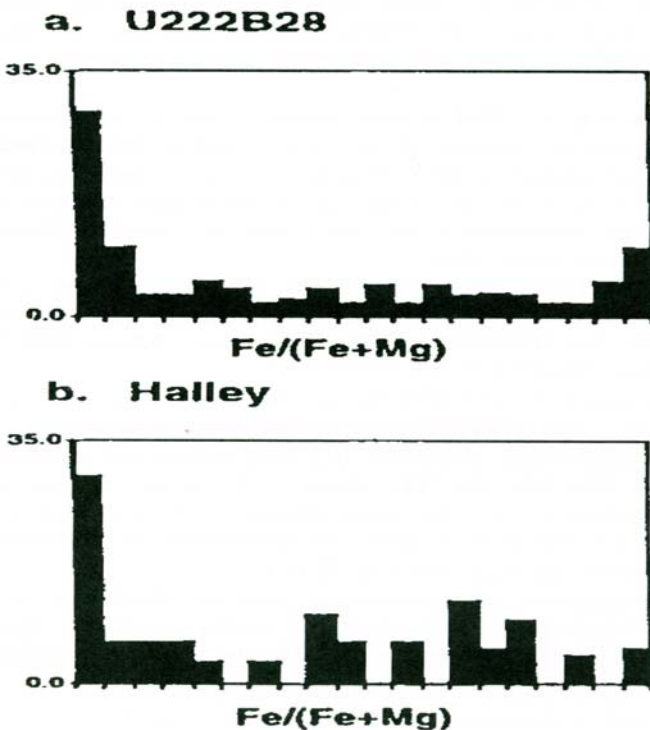


Fig. 13.7 Histograms comparing the submicrometre-scale distribution of $\text{Fe}/(\text{Fe} + \text{Mg})$ in IDPs with Comet Halley dust. The horizontal scale range from 0 to 1. (a) Chondritic porous pyroxene IDP U222B28 which contains abundant Mg-rich silicates, mostly enstatite (Mg SiO_3) and some forsterite (Mg SiO_4) result in large $\text{Fe}/(\text{Fe} + \text{Mg})$ data points near zero. (b) Halley(PUMA) mass spectrometry data (Bradley, J.P., Snow, T.P., Brownlee, D.E. and Hanner, M.S. 1999. In *Solid Interstellar Matter: The ISO Revolution*, eds. L. d'Hendecourt, C. Joblin and A. Jones, Springer-Verlag, p. 297: with kind permission of Springer Science and Business Media).

13.5. Primordial Material

The material out of which the Sun and the planets were formed does not refer to the original material present at the time of formation of the universe about 13×10^9 years ago, but rather to the modified material which existed around 4.5×10^9 years ago. During all these times, the interstellar material was being constantly enriched with heavier elements through the element building in stars followed by ejection of this material into the interstellar

medium. The same process has been happening since the formation of the solar system to the present time. It is not clear at present at what time in the history of the universe the Oort cloud was formed and hence its chemical composition is also not known. This will in turn be reflected on the original chemical composition of comets. For example, if the comets were formed along with other solar system bodies about 4.5×10^9 years ago, they would have the same composition as that of the solar system material. But on the other hand, if they were formed more recently they would have a different composition reflecting the contemporary interstellar abundances. One method to get information about the possible nature of the primordial cometary material and hence the time scale or the age is through the study of the isotopic ratios of various elements. As is well known, the relative abundances of various isotopes preserve the life history of the formation process and hence help in understanding the nature of the original material. The isotopic ratio of several elements has been determined for comets (Table 5.4). The measured isotopic ratios are $^{12}\text{C}/^{13}\text{C} \sim 90$, $^{14}\text{N}/^{15}\text{N} \sim 300$, $^{32}\text{S}/^{34}\text{S} \sim 22$ and $^{16}\text{O}/^{18}\text{O} \sim 450$ and is similar to terrestrial values of 89, 270, 24 and 500 respectively. Therefore the nature of the material at the time of formation of the Oort cloud is similar to that of the primordial cometary material.

13.6. Chemical Evolution

The origin of life on Earth has intrigued mankind since early times. In the standard scenario, the production of organics is the starting point of the whole complex process, as all life on Earth is composed of organic material. It is remarkable that relatively only a smaller number of organics appears to have been used in forming life system among a variety of organics that is possible. The compounds of major interest are those normally associated with water and organic chemistry in which carbon is bonded to itself and to other biogenic elements. The biogenic elements, H, C, N, O, S and P, are generally believed to be essential for all living systems. In 1953, Miller showed that when gaseous mixture of NH_3 , CH_4 and H_2O is subjected to an electrical discharge, it produced various kinds of organic molecules including amino acids. This remarkable experiment showed for the first time the possibility of synthesis of organic molecules from a mixture of simple gases in the presence of an energy source. This led to the suggestion that a similar type of process could have taken place in the early stages of

the earth leading to organics, the basic ingredient for the formation of life. However, studies have indicated that these simple molecules are unlikely to be present as major constituents in the early atmosphere as they are most probably photolyzed in a time scale of year or so. In addition, other studies indicate that the early Earth's atmosphere contained mostly CO₂, H₂O and N₂, which makes it difficult for the formation of organics. The existing observations show that the amount of organics in the solar system objects seems to increase with distance from the Sun. Therefore, it is intriguing that the organics necessary for chemical evolution is found in the outer solar system, whereas water, an essential ingredient for the life formation, is found in the inner solar system. This led to the suggestion that the organics might have been transferred from outer to inner regions of the solar system by some means, possibly through comets. Therefore the general conclusion is that it is highly unlikely that the biogenic could have formed on the Earth itself and therefore it had to be transported to the Earth through some means. The early chemical evolution was then believed to be followed by biological evolution, finally leading to life on the Earth. Even though this scenario is being taken as a working model, it is not at all known at the present time, how the whole process can take place in such a manner.

In recent years, the possible role of comets during the early chemical evolution on the Earth has been put forward. This is basically related to the fact that molecules of various complexities have been seen in comets. In particular, observations of Comet Halley showed for the first time the presence of organics in comets through the detection of CHON particles. The composition of these grains showed that they are made up of highly complex organic molecules of various kinds. Comet Halley observations indicated the possible presence of Phosphorus in the mineral core of the particles. Therefore, all the biogenic elements (H, C, N, O, P and S), essential for living system, have been detected in comets. The direct evidence for the existence of building blocks of life in comets came from the detection of Glycine (an amino acid) for the first time in Comet Wild 2. There are several ways in which the organic material could have been incorporated into comets. It could have been incorporated directly at the time of formation from the material in the solar nebula which is a typical interstellar cloud. More than 150 molecules have been detected in interstellar clouds, most of which are organic in character. Therefore, organics in comets could be interstellar in origin.

There are several observations to show that the earth does seem to

receive cometary material, such as meteor showers, dust particles collected at high altitudes, sedimentation at deep sea, cratering rates and so on. Geological evidences also indicate that comet collision with earth must have been high during earlier times. Therefore, the influx of cometary material could have injected large amounts of simple and complex organic molecules on the Earth. Particularly, the molecules accreted during the early times of planet formation when the comet collision was high could have triggered the chemical evolution cycle on the Earth. However, it is not clear whether these complex molecules could survive during the time of impact. This depends to some extent on the dynamics of the process.

At the present time there is evidence for the presence of some form of life on the Earth on or about 3.5×10^9 yrs ago. For times earlier than this, it is anyone's guess. Is it then possible that the organic molecules pouring from comets on to the Earth, particularly during the early times, might have started the whole cycle of chemical evolution, finally leading to the origin of life on the earth?

It is interesting to note that the presence of Glycine in comets and its delivery to objects indicate that the building block of life is pervasive in the universe which support the hypothesis that life is a cosmic phenomena.

In fact earth is most likely place as it had liquid water, proper oxidation - reduction ratio and right chemistry to get the whole process started. This suggestion has been further extended to the possibility that some sort of basic primitive cells themselves could have come from the cometary material on to the Earth. It is interesting to see the similarity of the relative abundances in comets and in living organisms as shown in Table 13.6. In this connection it is also interesting to see the extreme conditions under which microorganisms can exist. It is indeed remarkable that many microorganisms have been found to be able to survive under extreme environmental conditions, such as boiling water, freezing water, irradiation etc. They seem to adapt themselves to these environments and they are able to survive and grow. But one basic limitation is that they require liquid water. It has been suggested that ^{26}Al present in the early stages of solar system, which has a half life less than 0.7 million years, would have decayed within a few million years of formation of the solar system giving heat that could have melted the cometary material. Therefore it appears that comets *could have* played an important role in the process of chemical evolution, which finally led to life on Earth. However, many of the evidences brought forth to arrive at this conclusion have not yet been firmly established.

Table 13.6 Relative abundances in life and in comets^a.

Element	Bacteria	Mammals	Comets
Hydrogen	63.1	61.0	56
Oxygen	29.0	26.0	31
Carbon	6.4	10.5	10
Nitrogen	1.4	2.4	2.7
Sulphur	0.06	0.13	0.3
Phosphorous	0.12	0.13	0.08 ^b
Calcium	-	0.23	-

a. In %

b. (0.08) is the cosmic abundance.

Delsemme, A.H. 2000. *Icarus*, **146**, 313.

13.7. Terrestrial Water

It is interesting that around 70% of the Earth's surface is covered with water (sea water, oceans). The origin of this terrestrial water has been the subject of investigation for a long time. There is no general agreement on this issue at the present time. It might have come from the earth itself or it could have come from an external source such as comets.

As mentioned earlier, water could have been released by the earth itself. This refers to the accumulation of primordial water from the solar nebula adsorbed on to the grains when it was formed from the accreting disk. The amount of water accreted by the earth may be around 1–3 earth oceans of water. However the accretion process leading to the formation of the earth passed through several violent events, during which it could have also been melted in the final stages. It is not clear as to what fraction of the accumulated water was retained by the earth during the accretion process.

The other suggestion is that the ocean water on the earth could have come from the accumulation of the material from comets when the impact rate was much significant in the past during the formative stages of the earth. The D/H ratio of Jupiter and Saturn most probably representing the material referring to solar nebula gas has a value 2.1×10^{-5} . This is consistent with D/H ratio derived from the solar wind implanted into lunar soil. The D/H ratio derived from three Comets Halley (3.2×10^{-4}), Hale-Bopp (3.3×10^{-4} and Hyakutake (2.9×10^{-4}) $\sim 3 \times 10^{-4}$). Therefore the D/H ratio of these comets is about two times that of terrestrial water D/H

ratio (1.5×10^{-4}). Several laboratory studies have shown that D/H ratio in sublimating ice can increase or decrease with time depending upon the fractionation process (such as ion-molecule reaction etc) and on the nature of the material. It is possible that comets which contributed water to earth may be different from the comets for which D/H ratio has been measured.

13.8. Impact of Outside Bodies

The impact of outside bodies in the solar system is a natural phenomena. This becomes obvious from the craters seen on the surface of planets and their satellites, including the earth. The minor bodies which impinge on the objects in the solar system are the comets and asteroids. But in recent years the distinction between comets and asteroids is becoming nebulous as many asteroids are extinct comets or dormant comets. There is also a group of short period comets which come close to the earth. The impacting body possess tremendous amount of energy and can cause devastating effect on the object being collided. In this connection it is interesting to know whether there is any evidence for such a process to have taken place on the earth's surface. The impact could have moderate or catastrophic effects on the geophysical, biological or climatic changes on the earth. They could possibly appear in terrestrial records.

There are several craters present on the earth's surface like, crater in Arizona, U.S.A. which is approximately 1.2 km in diameter and 100 meter deep. This crater is believed to be due to the impact of a iron meteoroid of size 30 metres moving with a speed of about 20 km/sec about 50,000 years ago.

The Tunguska event of 30 June 1908 in Central Siberia in which all the forest trees near Tunguska river were flattened upto about 30 to 40 km was by a shock wave. This shock wave was created by the incoming object which did not survive to hit the ground but exploded at an altitude of about 8 km. For many years, the cause of this event was considered to be a comet. However it is likely that stony-iron meteorite must have been responsible for this event as minute fragments of iron -nickel were found in the areas. The diameter of this stony-iron material could be around 60 meters.

Many meteorites survive through the earth's atmosphere and fall on the earth's surface. They are generally identified due to their characteristic appearance. There are some meteorites which are destroyed before they reach

the earth's surface. Two well known meteorites of this type are the Murchison and Allende meteorites. Before they could reach the earth's surface, they exploded and shattered into pieces whose remnants were recovered. Both the meteorites are carbonaceous chondrites.

As mentioned already, fossil records suggest the presence of biological extinction event repeating on the earth with a period of around 26 my. It is suggested that cometary showers impinging on the earth could have caused such phenomena.

The credibility for the hypothesis that outside bodies impinge on the earth came when 20 pieces of Comet Shoemaker-Levy 9 pierced through Jupiter's atmosphere during the period from July 17 to 22, 1994. This is indeed an historical event that was witnessed from earth. Therefore it is possible that such an event can happen on the earth in the future and hence poses danger to earth. Therefore efforts are made to see how to prevent such an event taking place on the earth. For this purpose the sky is being monitored continuously to look for objects which might come close to the earth, catalogue them and keep track of these objects. Some of them are Near-Earth Object Survey, the Near-Earth Asteroid Tracking. The Near-Earth objects (NEOs) are defined as asteroids and comets which have perihelion distances of 1.3 AU or less. The total number of NEOs/NEAs is estimated to be around 700–1300.

The only way to avoid the collision is to destroy the object or change its track. Several suggestions have been put forward which can achieve these objectives. One suggestion is to explode the object. But one problem with this approach is that it would shatter the body into pieces, some of which might still head towards the earth. This is blast-and-hope strategy i.e. nothing comes towards the earth. Another way is to land a spacecraft on the surface of the object in order to gently push it off the course. This involves a rather complicated maneuvering. Another suggestion is to push a heavy object near the incoming object for long enough time that it could produce sufficient gravitational tug to change its orbit. Similarly, solar radiation pressure beaming on the object may be used to alter the orbit of the incoming object.

All these suggestions require a spacecraft to be put out there at the right time, but it requires lot of advance planning. Hopefully with man's ingenuity backed by sophisticated technology, it is possible to come out with a simpler way of tackling this problem.

13.9. Overview

The nature of the original material of the solar nebula (a typical interstellar cloud) and its relation to comets and other objects in the solar system and their inter-relationship is of great interest. This is shown schematically in Fig. 13.8.

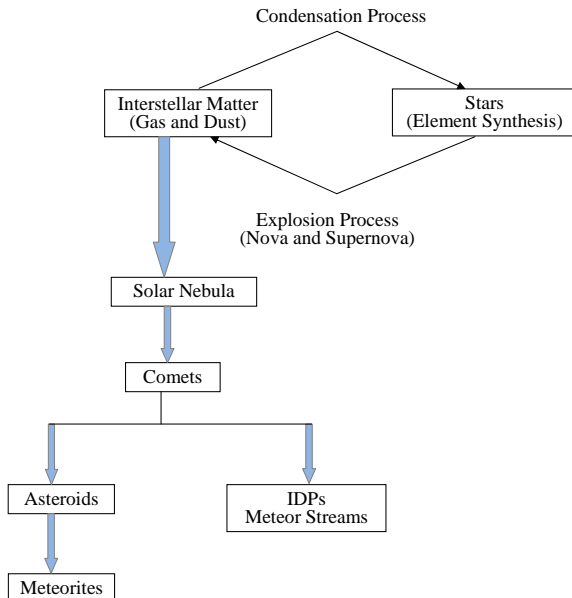


Fig. 13.8 A Schematic representation showing the comets formed out of a typical interstellar cloud (solar nebula) containing presolar grains emitted from stars, novae and supernovae and its relation to other objects in the solar system.

The observed silicate dust mineralogy is quite similar among IDPs, meteorites, asteroids, comets and in circumstellar shell of stars. The high value of the isotopic ratio of several elements observed in some of these objects as compared to solar system value indicate the presence of presolar grains. In particular, the presolar grains with high value of $^{12}\text{C}/^{13}\text{C}$ ratio, contribution must have came from various stellar sources such as Wolf-Rayet stars, novae, supernovae, AGB atmospheres etc. The source of IDPs rich in deuterium is attributed to molecular clouds. Similarly FeS grains have been seen in IDPs, meteorites, comets and from young and old stars. The presence of FeS grains in all these kinds of objects give a direct link between

the solar system material (comets) to the presolar material. Therefore it is likely that sulphur is tied up in grains as FeS. Hence it is likely, that the solar system bodies formed out of the solar nebular material had already crystalline FeS grains.

Carbon chemistry or organics may be used as a probe for a qualitative discussion of this cosmic connection. Before coming to a discussion of this aspect, it may be worthwhile recapitulating some of the points regarding organics seen in various objects in the solar system and in interstellar space.

Evidences for the presence of organic molecules in interstellar clouds came from the observations made in the radio frequency region. A compilation of some of these molecules is given in Table 13.7. A close look at the table reinforces the belief of the presence of numerous different organic compounds in interstellar clouds. The exact nature of the organic component of the dust is also not known. But it could be Polycyclic Aromatic Hydrocarbon (PAHs).

The characteristic feature of the solar system is that the rocky planets (Mercury to Mars) form the inner region and icy planets form the outer regions (Jupiter to Neptune) and are separated by asteroids. The reducing atmosphere of the outer planets consisting of H, He, CH₄ and NH₃ is conducive to the formation of organic molecules. In fact several carbon compounds have been detected on Jupiter. Complex organic chemistry is operating on Titan, the Satellite of Saturn. The Earth has also organic material as the life on Earth goes back to about 3.5×10^9 years.

The new class of grains present in comets, called CHON particles, established that a large fraction of the comet is made up of very complex organics. They are shown in Table 13.8. They provide evidence for the existence of many classes of cyclic and acyclic organic compounds. They include unsaturated hydrocarbons such as Pentyne, hexyne etc, nitrogen derivatives such as hydrogenic acid, aminoethylene etc., Heterocyclics with nitrogen such as purine and pyridine etc. HCN and H₂CO volatiles, allemine and pyrimidines and their derivatives which are biologically more significant has been seen in comets. The possible presence of Formaldehyde Polymers (H₂CO)_n has also been suggested. It is quite possible that CHON particles contain many more molecules than identified so far due to the fact that the impact velocity of the dust at the dust mass spectrometer was very high (~ 70 km/sec), which could possibly have destroyed many of them. The carbon content in cometary dust is close to 25% by weight. The organics present in the dust particles of Comets Wild 2 and Tempel 1 have been studied extensively. The collected samples from Wild 2 has been put

Table 13.7 Some of the observed interstellar molecules.

(a) Inorganic species (stable)					
Diatomeric	Tri-atomic	4-atom	5-atom		
H ₂ ^a HCl ?	H ₂ O ^a	NH ₃ ^a		SiH ₄ ^b	
CO ^a PN	H ₂ S ^a				
CS ^a NaCl ^b	SO ₂ ^a				
NO AlCl ^b	OCS				
NS KCl ^b					
SiO ^a AlF ^b					
SiS ^a					
(b) Organic molecules (stable)					
Alcohols	Aldehydes and ketones	Acids	Hydrocarbons		
CH ₃ OH methanol	H ₂ CO	formaldehyde	HCN ^a	C ₂ H ₂ ^b acetylene	
EtOH ethanol	CH ₃ CHO	acetaldehyde	HCOOH	C ₂ H ₄ ^b ethylene	
	H ₂ CCO	ketene	HNCO	CH ₄ methane	
	(CH ₃) ₂ CO?	acetone			
Amides	Esters and ethers		Organic-sulfur		
NH ₂ CHO	formamide	CH ₃ OCHO	methyl formate	H ₂ CS	thioformaldehyde
NH ₂ CN	cyanamide	(CH ₃) ₂ O	dimethyl ether	HNCS	isothiocyanic acid
NH ₂ CH ₃	methyldamine			CH ₃ SH	methyl mercaptan
Parafin derivatives	Acetylene derivatives		Other		
CH ₃ CN ^c	methyl cyanide	HC ₃ N _a	cyanoacetylene	CH ₂ NH	methyleneimine
EtCN	ethyl cyanide	CH ₃ C ₂ H	methylacetylene	CH ₂ CHCN _a	vinyl cyanide
(c) Unstable molecules					
Radicals	Ions	Rings	Carbon chains	Isomers	
CH C ₃ H ^{a,c}	CH ⁺	SiC ₂ ^b	C ₃ S ^a	HNC ^a	
CN ^a C ₃ N ^a	HCO ⁺	C ₃ H ₂ ^a	HC ₅ N ^a	CH ₃ NC	
OH ^a C ₃ N ^a	N ₂ H ⁺	C ₃ ^a	HC ₇ N ^a		
SO ^a C ₄ H ^a	HOCO ⁺		HC ₉ N ^a		
HCO C ₅ H	HCS ⁺		HC ₁₁ N ^a		
C ₂ ^b C ₆ H	H ₃ O ⁺ ?		CH ₃ C ₃ N		
C ₂ H ^a C ₂ S ^a	HCNH ⁺		CH ₃ C ₄ H		
C ₂ ^b CH ₂ CN	H ₂ D ⁺ ?		CH ₃ C ₅ N [?]		

(Turner, B.E. 1989, Space Sci. Rev., **51**, 235).

a Seen in CSE as well as ISM sources.

b Seen only in CSEs.

c Both linear and cyclic forms.

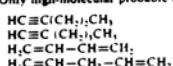
to intensive laboratory investigations. The results of these investigations corroborate Comet Halley results. All these studies have given startling results in showing the presence of wide range of organics of various types, the existence of which was hard to imagine. The overall character of the dust in comets i.e. silicate and carbon, is similar to that of interstellar grains.

The mineralogical composition of meteorites reflect differing degrees of thermal evolution indicated by Stony-iron and iron meteorites. Carbona-

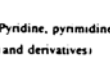
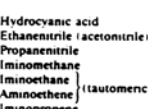
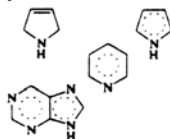
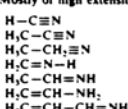
Table 13.8 Types of organic molecules in Comet Halley dust.

C—H— Compounds

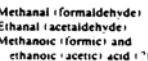
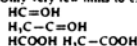
(Only high-molecular probable due to volatility; hints only to unsaturated)

**C—N—H— Compounds**

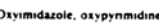
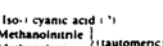
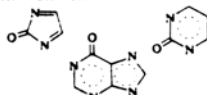
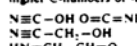
(Mostly of high extensity; also higher homologues possible)

**C—O—H— Compounds**

(Only very few hints to existence)

**C—N—O—H— Compounds**

(Amino-, Imino-, Nitrie of -ole, -alc, -ene, -keto- only probable with higher C-numbers; no cyclic aromatics)



Structure isomers are additionally possible. Several types may form tautomers, mesomers and conformational isomers. Thus the molecules given here serve only as examples of the class of substances possibly present in the organic component of the dust. We are not sure yet if oxygen-containing species are present.

(Kissel, J. and Krueger, F. R. 1987. *Nature*, **326**, No. 6115, 755).

ceous chondrites seems to be primitive in the sense that they have not altered much their state from the time of formation. The organic material found in carbonaceous chondrites is highly complex. In Murchison meteorite, different amino acids have been identified. Many of them occur on earth biologically. A few of the different compounds seen are the following: Carboxylic acids, aliphatic and aromatic hydrocarbons, amines and amides, alcohols, ketones, purines, pyrimidine etc. The organic matter found in meteorites probably existed in the solar system a billion years before the appearance of life on the Earth. There are many similarities between the organic compounds in dust in comets and chondrites. The carbon content in carbonaceous chondrites is ~ 3 to 5%, which is low by almost an order of magnitude compared to cometary dust. There is also an indication that they must have passed through a high temperature phase as well (~ 400 K) in order to explain some of the compounds present in them. Therefore it is unlikely that comets are the source of meteorites as they remained at low temperature. Hence asteroids is most likely the source of meteorites. Observations show similarities between asteroids and meteorites. The isotopic anomaly seen in chondrules in meteorites is attributed to outside material survived and accreted and are therefore pre-solar grains.

Many of the IDPs which are thought to be of cometary origin is carbonaceous in character.

The various objects in the solar system are generally believed to have been formed as a by product of the formation of the Sun. The Sun was formed out of a typical interstellar cloud referred to as the primitive solar nebula. Model studies have shown that when contraction of the cloud takes place, the material will form a disk around a central core due to conservation of angular momentum. This material composed of gas and dust will accumulate in increasing numbers and form a thin disk of particles. This will then become unstable against gravitational forces and separate out from the system. These rings then clump together and form planetesimals and move in circular orbits around the centre of the nebula. These planetesimals act as nuclei for the formation of planets. This is also responsible for the nearly coplanar arrangement of planets and for a common direction of revolution of the planets around the Sun.

Condensation model calculations have shown that different types of material condense out of different temperature and densities, which imply different distances from the Sun. So there could be materials of high temperature phase, low temperature phase as well as a mixture of the two in the solar system objects. Carbon compounds can be vapourized upto around 2

to 3 AU and water upto around 5 AU. Therefore terrestrial planet zones will be rocky and the outer planet zones will be made up of water, methane, ammonia and CO₂-ice. This is in rough accordance with the gross properties of objects seen in the solar system. However, the detailed understanding of the whole problem is far from clear. The exact nature of compound produced depend upon various factors such as temperature, density, chemical composition of the constituents and various physical processes such as heating, cooling, annealing, selective evaporation, fractionation and so on. It is found from laboratory experiments that all the compounds seen in carbonaceous chondrites can be produced from CO, H₂ and NH₃ on a Fe₂O₃ or clay catalyst at a temperature of around 400 to 430 K. Hence it is not surprising that there is a systematic change in composition going outwards from the Sun. Comets are produced in a cold temperature phase in the outskirt of the Solar System and so it has kept most of the molecules it had from the original material.

During the time interval of the formation of the Solar System, materials could have been injected into the solar system from outside (like from a supernova explosion). Some of this material may be preserved in the solar system objects as inclusions etc. In addition, comets colliding with Earth during the early stages of the formation could have deposited organic material, which might have started the chemical evolution on the Earth. Comets could also account for the biosphere on the Earth.

Therefore the organic material present in interstellar clouds and in solar system objects are the same material to start with but may look different in some of the solar system objects at the present time due to variable thermal evolution in these objects depending on their radial distance from the Sun (Cosmic Evolution).

So far we have been discussing the possible interrelationship between various solar system objects and comets. In certain cases the relationship to comets is more direct than in others. This is partly due to lack of good data as well as to the inadequacy in our present understanding of the nature of these objects. With further studies, it is hoped to understand the origin of the solar system itself and possibly even the origin of life on the Earth.

Problems

1. In the study of the origin of life, one deals mainly with the elements H, C, N and O. Explain.
2. Is there evidence of life beyond the Earth? If the answer is negative,

discuss why?

3. Explain how the number of planetary systems in the Galaxy, with life, like on the Earth can be estimated
4. The meteor streams seen in the sky appear to diverge from a point in the sky. Explain.
5. What is the range of velocities at which meteors encounter the Earth? What is the explanation for the limiting values?
6. What has Titus-Bodes law to do with the question of asteroid belt?
7. Meteorites are said to act as beacons to the past. Explain.

References

The following reference gives a good account of asteroids

1. Bottke, W.F.Jr., Cellino A., Paolicchi, P. and Binel, R.P. (eds). 2003. *Asteroids III*, Univ. Arizona Press, Tucson.

The following reference gives a good description of meteorites

2. Lauretta, D.S. and McSween, H.Y. Jr. (eds.) 2006. *Meteorites and the Early Solar System II*, Univ. Arizona Press, Tucson.

For Presolar grains reference may be made to

3. Lugardo, M. 1995. *Stardust from Meteorites*, World Scientific, Singapore.

The technique of particle collection at high altitudes and the results of such studies are given in the following review articles.

4. Brownlee, D.E. 1978. In *Cosmic Dust*. ed. McDonnell, J.A.M. New York: John Wiley and Sons. p. 295.
5. Sandford. S.A. 1987. *Fund. Cosmic Phys.* **12**, 1.

The early work on the various processes leading to element building in stars is discussed in the classic paper:

6. Burbidge, E.M., Burbidge, G.R., Fowler, W.A. and Hoyle, F. 1957. *Rev. Mod. Phys.* **29**, 547.

For more discussion reference may be made to

7. Prantzos, N., Vangioni-Flam, E. and Casse, M. (eds.) 1993. *Origin and Evolution of the Elements*, Cambridge: Cambridge University Press.

The Oparin-Haldane hypothesis of the Origin of Life can be found in

8. Ponnamperuma, C. 1982. *Extraterrestrials: Where are they?* eds. Hart. M.H. and Zuckerman, B. New York: Pergamon Press, p. 87.

The other view point of cometary origin can be found in the following references.

9. Hoyle, F. and Wickramasinghe, N.C. 1981. *Comets and the Origin of Life* ed. Ponnampерuma, C. Dordrecht: D. Reidel Publishing Company, p. 227.
10. Wickramasinghe, N.C. 2009. *Astrobiology*, World Scientific Publishers, Singapore.

The following book may be referred for solar system studies.

11. Lewis, J.S. 1995. Physics and Chemistry of the Solar System, Academic Press.

The following papers pertains to Terrestrial water, Impact of outside bodies, asteroid-comet connection and binaries.

12. Drake, M.J. and Campins, H. 2006. In *Asteroids, Comets and Meteors*, eds., D. Lazzaro, S. Ferraz-Mello and J.A. Fernandez, Cambridge Univ. Press, Cambridge, P.381.
13. Morrison, D. et al. 2003. In *Asteroids III*, eds. W. Bottke, A. Cellino, P. Paolicchi and R. Binzel, Univ. Arizona Press, Tucson.
14. Toth, I, 2006. In *Asteroids, Comets and Meteors*, eds. D. Lazzaro, S. Ferraz-Mello and J.A. Fernandez, Cambridge Univ. Press, Cambridge, p. 67.
15. Noll, K.S. 2006. In *Asteroids, Comets and Meteors*, eds. D. Lazzaro, S. Ferraz-Mello and J.A. Fernandez, Cambridge Univ. Press, Cambridge, p. 301.

This page intentionally left blank

CHAPTER 14

Problems and Prospects

14.1. Epilogue

So far we have discussed in some detail our present understanding with regard to various cometary phenomena which is summarized in Fig. 14.1. We have a reasonable knowledge of the origin, nature and composition of comets. Though much progress has been achieved in the last ten years since the publication of the second edition, many of the aspects are still not well understood.

Over the years, our knowledge with regard to comets has improved enormously from the studies based on several bright Comets like Ikeya-Seki, Kohoutek, West, Bradfield, Hale-Bopp, Hyakutake and others. The Comet IRAS-Araki-Alcock, which came to within about 4–7 million kilometers from the Earth in May 1983, gave the opportunity to observe a comet at such a close approach. Comet Kohoutek gave a big boost to cometary science in 1974 through a concentrated and co-operative effort made by the scientists working in various fields. This venture actually created an interest among the physicists, chemists and biologists as well, in problems connected with cometary science. It also created an increased interest among the astronomers who normally work in other fields. At present we have beautiful techniques for both the ground based and space observations in different spectral regions, remarkable new instrumentation, (ground based equipment and computers), which are much better than what was available about 30 to 40 years ago. With these advances, phenomenal progress in the understanding of comets has been achieved.

However, there are still questions which cannot be answered, either from ground based or satellite observations. The only way to understand these problems is through probes or missions to comets which can pass

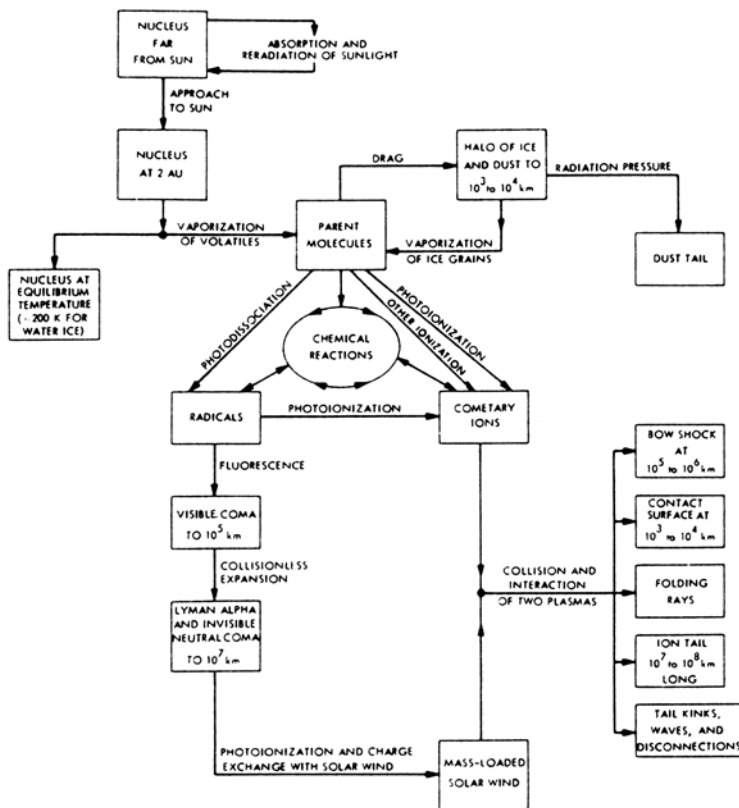


Fig. 14.1 The various processes arising out of the interaction of solar radiation and solar wind with a comet, which result in the observed features in a comet are shown in a block diagram (Report of the Science Working Group, The International Halley Watch, July 1980).

close to the nucleus. This was achieved with remarkable success for the first time during the apparition of Comet Halley in 1986. A target for space missions has to satisfy several requirements. First, the comet's orbit should be predicted accurately. This means that the arrival time of the comet can be predicted well in advance. This is very essential because of large time periods that are involved for developing experimental packages and the necessary preparations for making space flights. The comet should be bright, as well as exhibit as far as possible all the observed phenomena for the maximum scientific return. The condition that the orbit should be well known mean that the comet should have returned at least a few times

and this eliminates new comets. It leaves only the short-period and the intermediate-period comets as potential candidates. Comet Halley satisfied all the requirements for a space mission and is also the most famous of the known comets, which has been observed for the last 2000 years (Table 14.1).

Table 14.1 Perihelion passages of Comet Halley.

240 B.C.	May 25 (probably observed)	912	Jul 19
164	Oct 13 (not observed)	989	Sep 6
87	Aug 6	1066	Mar 21
12	Oct 11	1145	Apr 19
66 A.D.	Jan 26	1222	Sep 29
141	Mar 22	1301	Oct 26
218	May 18	1378	Nov 11
295	Apr 20	1456	Jun 10
374	Feb 16	1531	Aug 26
451	Jun 28	1607	Oct 27
530	Sep 27	1682	Sep 15
607	Mar 15	1759	Mar 13
684	Oct 3	1835	Nov 16
760	May 21	1910	Apr 20
837	Feb 28	1986	Feb 10

ESA Giotto mission pamphlet, 1981 (upto 1910)

The *in situ* studies of Comet Halley have been followed by Comets Giacobini-Zinner, Grigg-Skjellerup, Borrelly, Tempel 1 and Wild 2 (Table 1.3). In addition, the cometary material brought back to earth from Comet Wild 2 gave the first opportunity to study the true nature of the cometary material. All these studies gave a large number of unexpected results as well as showed the complexity of the physical processes occurring in the coma. These observations, combined with ground based and satellite observations, covering the entire range of the electromagnetic spectrum from X-rays to radio wavelengths provided the complete set of data on several comets. These results have increased our knowledge about cometary science in a dramatic way.

14.2. Future studies

Although space missions to comets provided a remarkable insight into our understanding of the cometary phenomena, still there are several fun-

damental questions, which remain to be answered with regard to the origin and evolution of comets, structure and composition of the nucleus, parent molecules, the interaction of solar wind with cometary plasma, relation to chemical and biological evolution and so on. In addition, the space missions to comets provided only snap shots of the physical and chemical conditions in these comets, as the observations could be carried out only for a very limited time period of a few hundred to a few thousand seconds or so. Hence one should have a cautious approach in extending these data to other comets and in deriving general conclusions. Much more data on other comets, similar to that achieved for several comets, is needed before arriving at general conclusions regarding the similarities and differences among comets of different types. It will also be of interest to probe the nucleus of a long period comet, coming directly from the Oort cloud, in order to examine the possible presence of the aging effect among comets.

The next logical step would be to achieve long duration close encounter of a short period comet to study the time evolution of the development of the coma as a function of the heliocentric distance. This can provide information about the nucleus, the elemental and molecular composition of the gas and the dust, solar wind interaction and so on. These studies will go a long way in comparison to those of flybys. This can be achieved by putting a satellite with instruments around a comet and tracking it as it moves with the comet. It should also probe the nucleus with a penetrator for physical and chemical studies. This is the objective of Rosetta mission which will rendezvous with Comet 67P/Churyumov-Gerasimenko around 2014. It will also have a Lander for making on-spot studies. The Rosetta mission with planned capabilities is an ambitious program.

A new generation of powerful ground based optical/IR/Radio telescopes of large collecting area will be available in the near future. Combining this feature with advanced instrumentation and state of the art in optical and IR detectors will provide excellent opportunities for making very high resolution imaging, spectroscopy, polarimetry and so on. The extraordinary sensitivity combined with high spatial resolution should give exciting results. It will also be possible to extend the observations to faint objects. These will be supplemented with high quality observations carried out with satellites in the UV and X-ray regions. With these instruments, it should be possible to extend the observations to faint objects and also look for comet-like objects in the Oort cloud. There is, thus, a bright future for cometary observations, with both the ground based and above the atmosphere instruments.

The laboratory simulation studies of the processes that could occur in a cometary environment is another important input necessary for an understanding the behaviour of comets. Of course, it is very difficult to create the actual cometary environment in the laboratory. In addition, it is very difficult to simulate a cometary target as we do not know the exact compositions and the physical state of a comet. However, studies carried out on approximating the conditions of real comets will help for the development of more realistic comet models.

Future studies, based on combined effort of space missions, ground based and above the atmosphere observations, laboratory investigations and theoretical studies should give new insights into the structure, evolution and origin of comets. Hopefully, through a series of such studies, it will be possible to resolve many of the basic and fundamental problems which have no answers at the present time. These studies should also give enormous information with regard to the early history of the solar system; physico-chemical, dynamical and thermodynamic conditions existing at that time; the information and relation to other solar system objects; the relation to interstellar molecules, chemical evolution, the origin of life and Exobiology, space plasma physics and so on. Therefore cometary science is an exciting area of study for years to come.

This page intentionally left blank

Index

- aberration angle, 305–307
absorption, 227, 228, 233, 235, 240
abundances, 95, 129, 131, 132, 137, 138, 176, 196, 197, 203, 206, 208, 345, 359, 360, 392, 393
abundances of Heavy Elements, 128
acceleration, 303, 321–323, 325
age, 356, 358
albedo, 227, 230, 231, 235, 255–257, 260, 299, 340, 341, 344, 350–352, 355, 377
annealing, 68, 69
anti-tail, 18, 23, 220, 221, 225, 268, 269, 276, 277
appearance, 1–3
asteroids, 401, 402
Atlas of Cometary Forms, 323, 336
Atlas of Representative Cometary Spectra, 93
atomic spectroscopy, 51

band polarization, 123
band sequence, 55, 57
Bayeux tapestry, 2
bend in the tail, 326
binary systems, 379
biological extinction, 388
black body of temperature, 70
black body radiation, 49
blocking coefficients, 99
Boltzmann Distribution, 64
Borrelly, 22, 25, 29, 303, 355

bow shock, 310, 313, 314, 319, 320, 322
brightness, 10, 12–15, 30
brightness profile, 144, 205, 254
Bruggeman rules, 248

 C_2 molecule, 113
C-H stretch, 85, 288
chemical composition, 279, 283, 290
chemical diversity, 206
chemical evolution, 421, 422, 431
chemical subgroups, 57
CHON particles, 28, 90, 167, 201, 290
circular polarization, 232, 266
clathrate hydrates, 344
collisional excitation, 106, 107, 122, 172
column densities, 162, 169, 172, 176, 178, 181, 182, 188, 193
coma, 88–90, 92, 105, 107, 115, 118, 120, 135, 138
cometary fading, 384
cometary showers, 387
complex molecules, 86, 90, 144, 174, 191, 202, 209
composition, 129, 132, 162, 165, 175, 206, 339, 340, 347, 348, 359, 360, 392, 396, 397, 401, 403, 407–411
Condon parabola, 60
continuum, 249–253, 255, 256, 259, 261, 274, 297, 299
Cretaceous-Tertiary boundary, 388

- Deep Impact, 22, 31, 284, 290
 density of grains, 258
 diatomic molecules, 58
 dielectric constant, 241, 243–246
 disconnection events, 328
 discovery, 1, 4, 6, 16, 28
 Discrete-Dipole approximation, 242, 247
 Dissociative Equilibrium, 49
 Doppler shift, 50
 dust features, 223
 dust particles, 249, 250, 254, 255, 257, 259, 261, 264, 267–270, 281, 282, 285, 287, 290, 292–294, 296, 298
 dust production, 151, 259, 260, 272
 dust tail, 17, 18, 22, 27, 217, 220, 222, 225, 226
 dust trails, 222
 dust-to-gas ratio, 260
 dynamical aberration, 305, 336
 dynamics, 213, 220, 226
 efficiency factors for scattering, 233
 electronic transition moment, 62, 63, 104, 112
 electronic transitions, 54, 56, 59, 61, 74
 elemental abundances, 129, 130, 182
 emission lines, 57, 60, 66, 70–72, 74
 energy density, 48, 49
 energy level diagram, 96, 98, 109, 121
 equation of state, 49
 equilibrium constant, 50
 evolution of orbits, 393
 excitation temperature, 110, 125, 128, 129
 expanding halos, 356
 extended source, 167
 extended source of molecules, 175
 extraterrestrial dust particles, 416
 Fabry-Perot, 91, 94, 177, 190
 filamentary structure, 324
 flares, 15, 16, 348
 fluorescence efficiency factor, 123, 142
 fluorescence process, 95, 102, 105, 118, 121, 122
 flyby missions, 27
 forbidden lines, 90, 92, 93
 Forbidden Transitions, 90, 121
 Fountain model, 184, 187, 254
 Franck-Condon factors, 60, 62, 63
 Fraunhofer lines, 96, 98, 99, 102, 103, 138
 Future studies, 437, 439
 g-factor, 142, 143, 160, 190, 191
 gas to dust ratio, 94
 gas-phase chemistry, 194
 grain Sizes, 268
 grain temperature, 271
 Greenstein effect, 105
 Hölñ-London factors, 62, 63
 Hale-Bopp, 435
 Halley, 1, 2, 5–7, 16, 20–22, 24–29, 76, 77, 83, 85, 87, 88, 154, 157, 158, 161, 163–168, 170, 174, 175, 179–182, 191, 194, 198, 200–202, 204, 207, 209
 halos, 16, 20
 Haser's model, 145, 148, 150, 151, 155, 159, 176, 190
 heating efficiency, 199
 heavy elements, 128, 183
 heliocentric variation, 154, 158, 162, 163, 175
 heteronuclear molecule, 56
 homonuclear molecule, 56
 hot band, 83, 159
 Hyakutake, 82, 85, 88, 115, 116, 329, 435
 hydrodynamic flow, 199
 hydrogen lines, 13, 16, 21
 ice band, 290
 icy-conglomerate model, 24
 Impact of outside bodies, 424, 433
 in situ measurements, 23, 194, 281
 Infrared band passes, 269
 infrared lines, 85

- infrared observations, 253, 270, 272, 283, 289–291, 298, 301
interplanetary dust particles, 258, 416
interplanetary magnetic fields, 309
Interstellar molecules, 428
ion tail, 18, 22, 29, 303, 304, 309, 310, 323–325, 327, 335, 336
ion-molecule reactions, 192
isotopic abundances, 130
isotopic shift, 58
- Kramers-Kroning relation, 244
Kuiper belt, 30, 390, 391, 393, 395–397
- Lambda doubling, 64
lifetime of the molecule, 142, 152
linear polarization, 232, 237, 261, 264–266, 300
long period comets, 7, 29, 383, 389, 390, 396, 398
Lyman α isophotes, 186, 189
Lyman α line of hydrogen, 16, 152
- magnetic sector boundaries, 73, 324
mass loss, 82, 360, 367, 377
mass of grains, 272
mass spectrometer, 88, 194, 196, 201
material strength, 362, 363
Maxwell-Garnett rule, 245
meteor showers, 411, 413–415, 417, 422
meteorites, 401, 406–411, 413, 416, 418, 424, 425
Mie Theory, 228, 235
mineralogy of dust, 28, 281
minor constituents, 166, 178, 207
missions, 22
molecular bands, 77
Molecular spectroscopy, 54
molecules, 141–144, 146, 147, 151, 153, 155, 160, 162–164, 166, 167, 169–177, 181–184, 187, 188, 192, 199, 201, 203
Monte Carlo Model, 189, 201
Monte-Carlo approach, 188, 210
- Morphology, 339
Morse potential, 63
multi-component models, 297
- new comets, 9, 395, 396
non-gravitational force, 354, 356, 360, 369, 370, 375–378
nucleus, 77, 82, 87, 90, 105, 107, 108, 115, 118, 339–346
nucleus composition, 359
- observed species, 27, 89
Oort cloud, 9, 29, 30, 383–388, 390, 391
- optical constants, 242–246
orbital elements, 41, 43
origin, 4, 8, 10, 29, 30, 311, 335, 381, 391, 392, 395, 435, 438, 439
- ortho-to-para ratio, 371, 372, 376
- oscillations, 19, 24, 265, 319–321, 323, 325
- outbursts, 16, 348
- oxygen line, 121, 122, 180
- parent molecules, 27, 146, 187, 188, 202–204, 206, 207, 210
- parent-daughter hypothesis, 146
- particle collection, 416, 432
- phase function, 231, 236, 237, 256, 257, 297
- photochemistry, 203
- photochemistry of water, 65
- photodissociation, 143
- photoionization rates, 143
- photometric theory, 151
- Planck's law, 47
- plasma tail, 18–20, 308, 325, 328, 330
- polarization, 227, 232, 239, 240, 245, 261–268, 297, 300
- Polycyclic Aromatic Hydrocarbons, 69, 85, 286
- polyoxymethylene, 198
- presolar grains, 9, 409
- primordial material, 401, 419
- production rate, 141, 142, 144, 147, 148, 150–167, 169, 170, 174–177,

- 179, 182–184, 186–189, 191, 192, 199, 204, 206, 207
- Prompt emission, 79, 114, 159
- radial velocity, 37, 45, 50
- radiation pressure, 214, 225, 227, 229, 230, 254, 269, 294–297, 299
- radicals, 87, 88, 90
- radio lines, 65, 118
- Rayleigh, 186
- reddening, 252–255
- relative abundances, 163, 164, 174, 183
- RKR potential, 63
- rotation, 339, 345, 356–358
- rotation of the nucleus, 25
- rotational structure, 98, 114, 132
- rotational temperature, 126, 128
- rotational transitions, 86
- sand bank model, 363
- scale length, 146, 162, 178, 179, 188, 203
- Scattered intensity, 231
- Scattering functions, 247
- scattering theory, 228
- sector boundary, 324, 329, 330
- Shoemaker-Levy 9, 2, 14, 16, 17
- short period comets, 381, 389–391, 395, 398
- silicate feature, 276, 279
- silicate structure, 67
- size, 339, 340, 346, 351, 354, 375, 407, 412, 414, 416, 424
- Sodium Gas Tails, 222
- solar constant, 70
- solar radiation, 9, 70, 95, 96, 99–103, 105, 114, 129
- solar wind, 72–74, 303–315, 317–320, 322, 323, 325–328, 331–333
- solar wind interaction, 308, 309, 314
- space mission, 19
- spacecrafts to comets, 25
- spectra, 75–79, 81–83, 85–88, 90–93
- spectral features, 249, 278, 281
- spectroscopy, 47
- splitting, 14, 15
- stardust, 22, 31, 287
- statistical equilibrium, 98, 101, 103, 105, 111, 114, 137
- streamers, 310, 324, 325
- structure, 24, 29, 56, 57, 63, 67, 68, 72, 73, 96, 97, 110, 113
- sun-grazing comets, 7, 8, 27, 77, 89
- surface brightness, 144, 145, 147, 150, 170, 203, 207, 208, 253–255
- surface gravity, 353
- Swan band sequence, 180
- Swings effect, 96, 119, 121, 155
- Syndynname, 186, 187, 214
- Syndyne, 214, 218, 222
- synthetic profile, 102, 108, 114
- tails, 9, 10, 17, 18, 22, 323–326, 328, 331, 336
- Taxonomy, 396
- Tempel 1, 22, 25, 28, 29, 85, 174, 284, 289, 290, 355, 375
- temperature, 270, 271, 273, 274, 277, 279, 282, 283, 285, 290, 298, 392, 396
- terminal speed, 216, 225
- terrestrial water, 423
- theory of vapourization, 340
- tidal force, 17
- time evolution, 108
- Tunguska event, 2, 424
- turbulence, 303, 320, 322, 335
- ultraviolet, 21, 22, 79, 81, 143, 144, 155, 156, 167, 181, 183, 204, 205
- ultraviolet coma, 26
- vapourization theory, 344
- velocities in the coma, 155
- vibrational structure, 101
- vibrational temperature, 109, 111, 128
- vibrational transitions, 61
- visible coma, 82
- waves, 303, 314, 319–325, 335

- Wild 2, 22, 25, 28, 29, 31, 87, 287,
292, 355 X-rays, 330, 437